

AD-A119 663

PALISADES INST FOR RESEARCH SERVICES INC NEW YORK

F/6 9/5

IEEE CONFERENCE RECORD OF 1980 FOURTEENTH PULSE POWER MODULATOR--ETC(U)
1980

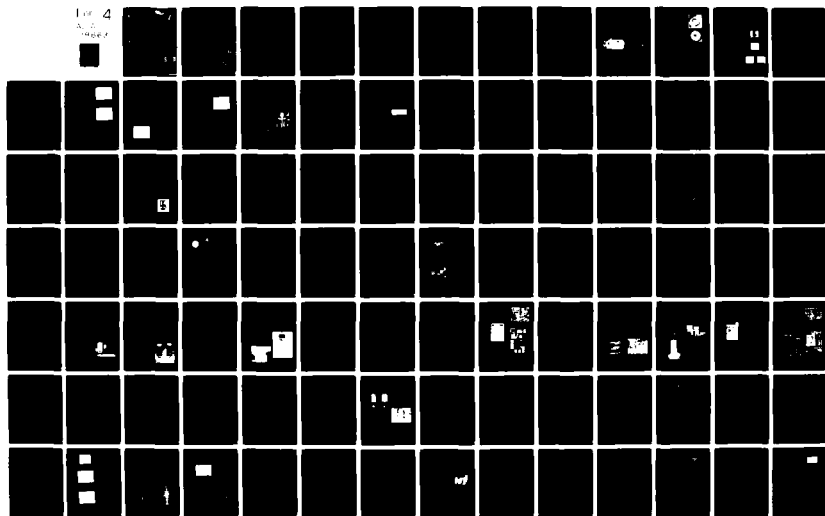
UNCLASSIFIED 80-CH-1573-5-ED

NL

Fig. 4

A. 2

WAVEFORM



AD A119663

80 CH 1573-6 ED



IEEE

CONFERENCE RECORD OF

1980 FOURTEENTH PULSE POWER
MODULATOR SYMPOSIUM

June 3-5, 1980

DTIC FILE COPY

Sponsored by the
IEEE Electron Devices Society
In cooperation with the
Advisory Group on Electron Devices
and under the management of
Palisades Institute for Research Services, Inc.

DTIC
ELECTE
SEP 28 1982

S D
D

DISTRIBUTION STATEMENT A

Approved for public release;
Distribution Unlimited

82 09 27 070



IEEE

CONFERENCE RECORD OF

1980 FOURTEENTH PULSE POWER
MODULATOR SYMPOSIUM

Sponsored by the
IEEE Electron Devices Society
In cooperation with the
Advisory Group on Electron Devices
and under the management of
Palisades Institute for Research Services, Inc.



Accession For	
NTIS GRA&I	<input checked="" type="checkbox"/>
DTIC TAB	<input type="checkbox"/>
Unannounced	<input type="checkbox"/>
Justification	
By <i>Per Ltr. (Acc. # E2-1667)</i>	
Distribution <i>10 (4 Aug 80)</i>	
Availability Codes	
Dist	Avail and/or Special
<i>A</i>	

Library of Congress Catalog Card No.: 80-8193

Printed in USA

Copyright © 1980 by The Institute of Electrical and Electronics Engineers, Inc.
345 East 47th Street, New York, N. Y. 10017

Available from
IEEE Single Copy Sales
145 Hoes Lane
 Piscataway, N. J. 08854

FOREWORD

High-energy pulser development since WW-II has evolved into two separate technologies. The first technology is concerned with *repetition-rate pulse modulators* for radars, air traffic management, lasers, linear accelerators, countermeasures, and industrial control. The second technology is presently concerned with *high-energy pulsed power* single-shot machines for nuclear effects simulation and for particle acceleration and fusion power generation experiments.

The Pulse Power Modulator Symposium has been previously concerned with the technology of repetition-rated pulse modulators, including power conditioning, switching and auxiliary devices, subsystem design, novel techniques, and systems applications. At this past Symposium papers from both technologies were presented. The sessions were well attended by representatives of both communities. Each community had the opportunity to learn from each others experience. However, since the Symposium is conducted with single sessions the time for presentation and discussion of each paper is limited. This eliminates in-depth discussion and postpones the providing of this information until the Proceedings are issued. Fortunately, Palisades Institute issues the Proceedings on a timely basis to the participants and thereby lessens the problem.

The International Pulsed Power Conference will be held in 1981 and the Fifteenth Pulse Power Modulator Symposium will be held in 1982. This ensures a good coverage of both technologies.

The theme of the Fifteenth Pulse Power Modulator Symposium will be limited to the basic technology of repetition-rated systems. The program will provide more time for presentation and discussion: The program committee will, therefore, have to be more discerning in their selection of papers. The criteria will require extended abstracts (500 words) to judge the quality, timeliness, and significance of the research and development work. The committee will encourage more application papers on the latest technological needs, such as nanosecond pulsers for millimeter-wave systems. If appropriate, they will arrange poster sessions.

We wish to express our appreciation to:

Matt Kuhn, president, IEEE Electron Devices Society, for his welcoming remarks and the continuing support of the society;

Ben Leon, vice-president, IEEE, for being guest speaker at the banquet;

The Advisory Group on Electron Devices and Palisades Institute personnel—Leonard Klein, Hildegard Hammond, Joan Gorman, and Jay Morreale for their logistic support;

and the committee members, session chairmen, authors, and attendees for contributing to a successful symposium.

The officers of the Fifteenth Pulse Power Modulator Symposium Executive Committee will be:

Chairman: Ken Baile, Naval Surface Weapons Center
Honorary Chairman: Sol Schneider, Consultant
Program Co-Chairmen: John L. Carter, U.S. Army Electronics & Technology Lab
Ron Pollard, Naval Surface Weapons Center
Sol Schneider,
Symposium Chairman
John E. Creedon
Program Chairman

1980 PROGRAM COMMITTEE

S. Schneider; Symposium Chairman

J. E. Creedon; Program Chairman
Electronics Technology and Devices Laboratory (ERADCOM)

L. H. Klein; Secretary and Treasurer
Palisades Institute for Research Services, Inc.

H. Menown; Overseas Representative
English Electric Valve Company, U.K.

N. S. Nicholls; Overseas Representative
Royal Signals & Radar Establishment, U.K.

R. Fitch
Maxwell Laboratories

R. A. Gardenghi
Westinghouse Electric Corporation

A. S. Gilmour, Jr.
State University of New York at Buffalo

B. R. Gray
Air Force Rome Air Development Center

A. H. Guenther
Air Force Weapons Laboratory

M. Kristiansen
***Texas Tech University**

P. N. Mace
Los Alamos Scientific Laboratory

T. H. Martin
Sandia National Laboratories

J. O'Loughlin
Air Force Weapons Laboratory

L. Reginato
Lawrence Livermore Laboratory

M. F. Rose
Naval Surface Weapons Center

J. Stover
Hughes Aircraft Company

D. Turnquist
EG&G, Inc.

R. A. Verga
Air Force Aero-Propulsion Laboratory

Symposia included papers on:

TABLE OF CONTENTS

PAGE

SESSION I: SPARK GAPS

A Low-Jitter Spark Gap for Repetitively Pulsed Parallel Capacitor Banks <i>G. J. Rohwein, Sandia National Laboratories</i>	1
Subnanosecond Trigger System for ETA <i>E. G. Cook, E. J. Lauer, L. L. Reginato, D. Rogers, and J. A. Schmidt, Lawrence Livermore National Laboratory</i>	5
The FXR One-Nanosecond-Jitter Switch <i>H. B. McFarlane and R. Kihara, Lawrence Livermore National Laboratory</i>	9
Switching System for the FXR Accelerator <i>R. D. Scarpetti and C. D. Parkison, Lawrence Livermore National Laboratory</i>	12
Statistical and Formative Times in Small Gas Spark Gaps <i>D. D. Lindberg, R. J. Gripshover, and J. W. Rice, Naval Surface Weapons Center</i>	17
Design and Performance of a High Repetition Rate Spark Gap Switch at 50-kW Power Levels <i>J. T. Naff, R. J. Sojka, and E. P. Zeehandelaar, Physics International</i>	21
Spark Gap Electrode Erosion Data <i>D. M. Barrett, R. A. Peir, and T. R. Burkes, Texas Tech University</i>	25
Laser-Triggered Switch Modification to VEBA <i>J. R. Bettis, J. K. Burton, R. K. Parker, M. Herndon, and A. K. Kinkead, Naval Research Laboratory</i> <i>A. H. Guenther and E. J. Kobiela, Air Force Weapons Laboratory</i>	28
Laser-Triggered Rail Gaps <i>R. S. Taylor, A. J. Alcock, and K. E. Leopold, National Research Council of Canada</i>	32
UV Preilluminated Gas Switches <i>L. P. Bradley, E. L. Orham, I. F. Stowers, and J. R. Braucht, Lawrence Livermore National Laboratory</i>	38
X-Ray Triggered Switching in SF ₆ Insulated Spark Gaps <i>E. L. Neau, Sandia National Laboratories</i>	42

SESSION II: THYRATRONS

Development of Instant-Start Thyratrons <i>D. Turnquist, T. Lynch, and S. S. Merz, EG&G, Inc.</i> <i>N. Reinhardt, Consultant</i>	46
An Economical High Current Fast Recovery Thyatron System <i>T. P. Donaldson, L. J. Kettle, H. Menown, C. V. Neale, B. P. Newton, and R. Sheldrake, English Electric Valve Co., Ltd.</i>	54
High-Power Tetrodes with Pyrolytic Graphite Grids in Switch Tube Service <i>B. R. Gray, Rome Air Development Center</i> <i>S. G. McNees, Eimac Division of Varian</i>	56
Application and Circuit Considerations of the X2062J and K Switch Tubes <i>S. G. McNees, Eimac Division of Varian</i>	65

SESSION III: GENERAL SWITCHING

Design of Large Area E-Beam Controlled Switch <i>L. A. Miles and E. E. Nolting, Naval Surface Weapons Center</i> <i>I. M. Vitkovitsky and D. Conte, Naval Research Laboratory</i>	68
Influence of the Density of the Surrounding Medium on the Electrical Behavior of Exploding Foils <i>T. L. Berger, Naval Surface Weapons Center</i>	73
The Crossatron Switch—A Cold Cathode Discharge Device with Grid Control <i>R. J. Harvey, Hughes Research Laboratory</i>	77
10-kHz Vacuum Arc Switch Ignition <i>A. S. Gilmour, Jr. and R. F. Hope III, State University of New York at Buffalo</i> <i>R. N. Miller, University of Central Florida</i>	80
Design of a Triggered Vacuum Gap for Crowbar Operation <i>J. E. Thompson, R. G. Fellers, T. S. Sudarshan, and F. T. Warren, Jr., University of South Carolina</i>	85

TABLE OF CONTENTS

	PAGE
SESSION IV: SYSTEMS	
Phase Stability Improvement Techniques for Transmitters with Line-Type Modulators <i>E. M. Piechowiak, Westinghouse Electric Corporation</i>	92
Magnetron/Modulator Interface Design Considerations <i>N. S. Nicholls, Royal Signals & Radar Establishment</i>	97
An All-Solid-State Inverter Charged Modulator with Precision Pulse-to-Pulse Regulation <i>E. H. Hooper, Westinghouse Electric Corporation</i>	98
High Efficiency Pulse Power Supply for a Semiconductor Laser Illuminator <i>R. R. Shurtz, B. H. Ahn, C. W. Trussell, J. E. Miller, and D. J. Horowitz, Night Vision and Electro-Optics Laboratory</i>	104
Multiple Output Modulator for Microwave Diode Pulse Power Generators <i>S. Levinson, Norden Systems, Inc.</i>	110
A Switching-Class ELF Power Amplifier <i>B. Kruger, NAVELEX</i> <i>J. Rodgers and G. Hanna, Continental Electronics Manufacturing Co.</i> <i>W. North, GTE Products, Inc.</i>	115
SESSION V: COMPONENTS	
Development of High-Reliability Multikilohertz Repetition-Rate Fast-Discharge Components <i>G. McDuff, K. Rust, W. J. Sarjeant, and P. N. Mace, Los Alamos Scientific Laboratory</i>	122
Electromechanical Shock in Pulse Power Components <i>T. R. Burkes, Texas Tech University</i> <i>W. J. Sarjeant, Los Alamos Scientific Laboratory</i>	125
Hydrostatic Pressurization of Oil-Impregnated Capacitors to Achieve Extended AC Lifetimes <i>W. A. Fitzsimmons and M. Kang, National Research Group, Inc.</i>	130
Development of Solid Dielectric Energy Storage Lines <i>R. G. Little and W. Halverson, Spire Corporation</i>	134
High Power Capacitor Technology <i>R. D. Parker, Hughes Aircraft Company</i>	137
Low Inductance Impedance Transforming Techniques for Injection Laser Arrays <i>B. H. Ahn, R. R. Shurtz, C. W. Trussell, and J. E. Miller, Night Vision and Electro-Optics Laboratory</i>	144
The Electrical Performance of Water Under Long Duration Stress <i>D. B. Fenneman and R. J. Gripshover, Naval Surface Weapons Center</i>	150
Experiments on Wafer Capacitor Electrode Conditioning by Ion Bombardment <i>V. H. Gorman and D. B. Fenneman, Naval Surface Weapons Center</i>	154
SESSION VI: MODULATORS	
Repetitive Megamp per Microsecond di/dt Pulsers for Driving Sub-Ohm Transmission Line Neutrino Particle Detectors <i>G. J. Krausse, C. G. Dalton, and W. J. Sarjeant, Los Alamos Scientific Laboratory</i>	161
A Modulator for Cathode-Pulsed Millimeter Wave Extended Interaction Oscillators with Fine Control of Pulse Shape <i>D. S. Ladd, G. W. Ewell, and J. C. Butterworth, Georgia Institute of Technology</i>	164
Three Pulse Width Solid State Magnetic Switching Modulator for the AN/SPS-67 Radar <i>S. T. Adams and R. Mgrdechian, Norden Systems, Inc.</i>	169
Generation of Nanosecond Pulses with a Thyatron Switch <i>M. Wziner and W. Beattie, U.S. Army ET&D Lab (ERADCOM)</i>	179
Design Issues and Engineering Techniques for Repetitively Pulsed Systems <i>J. J. Moriarty and G. K. Simcox, Raytheon Company</i>	183
Design of a 250-kW 1-kHz Laser Pulsar System <i>D. B. Cummings and B. Yen, Physics International</i>	187
SESSION VII: MARX GENERATORS	
High Repetition Rate Thyatron Marx Bank <i>T. F. Ewamzky, U.S. Army ET&D Laboratory (ERADCOM)</i>	191

TABLE OF CONTENTS

	PAGE
Development of a 50-Hz 250-kV 500-ns 500-kW Average Power Pulse <i>M. T. Buttram, Sandia National Laboratories</i>	195
Strip-Line Multichannel-Surface Spark-Gap-Type Marx Generator for Fast-Discharge Lasers <i>M. Obara, S. Suzuki, Y. Ishibashi, and T. Fujioka, Keio University</i>	201
A Low-Inductance 300-kJ 1.2-MV Marx Generator for the LASL-Antares Laser Facility <i>J. Harrison, H. Kent, T. Olson, G. Santamaria, and R. White, Maxwell Laboratories</i>	209
SESSION VIII: MAGNETIC INSULATION	
Implications of Electron Trajectories for Design of Magnetically Insulated Diodes <i>J. P. Shannon and F. S. Felber, Maxwell Laboratories</i>	214
Terawatt Power Division and Combination Using Self-Magnetically Insulated Transmission Lines <i>J. T. Crow and G. D. Peterson, Sandia National Laboratories</i>	219
Simulation of Power Flow in Magnetically Insulated Convolutes for Pulsed Modular Accelerators <i>D. B. Seidel, B. C. Goplen, and J. P. VanDevender, Sandia National Laboratories</i>	222
Measurement of Fast-Risetime Megampere Currents by Quartz Gauge <i>R. R. Williams, D. H. McDaniel, and R. W. Stinnett, Sandia National Laboratories</i>	227
SESSION IX: POWER CONDITIONING / REGULATION	
A High-Precision Pulse-Forming Network (PFN) Voltage Regulator <i>R. Sunderland, Marconi Radar Systems, Ltd. N. S. Nicholls, Royal Signals & Radar Establishment</i>	230
An 8-MVA Modulator/Regulator for Neutral Beams <i>D. B. Remsen, Jr. and T. H. Overett, General Atomic Company</i>	237
An 80-kV 100-A Modulator/Regulator Controls <i>H. Aslin and R. Hartline, Systems, Science, and Software</i>	241
A Thyatron Inverter Circuit to Drive a Capacitive Load for the Production of Ozone <i>H. Menown, B. P. Newton, R. Sheldrake, and R. L. Snelling, English Electric Valve Co.</i>	245
Vacuum Arc Switched Inverter Operation at 10 kHz <i>A. S. Gilmour, Jr. and R. F. Hope III, SUNYAB R. N. Miller, Consultant</i>	247
Commutation Switch Voltage Limiting by Current Waveform Control <i>A. S. Gilmour, Jr., SUNYAB</i>	255
Driving Parallel Flashlamps with a Compensated Pulsed Alternator <i>B. M. Garder, B. T. Merritt, and W. L. Gagnon, Lawrence Livermore Laboratory W. L. Bird, W. F. Weldon, and R. C. Zowarka, University of Texas</i>	259
SESSION X: KICKERS	
High Power Pulse Generators for Fast Pulsed Magnets Developments and Operation Experience <i>H. Kuhn and G. H. Schröder, CERN</i>	264
Generation of Current Pulses of Quasi Triangular Shape with Fast Power Thyristors <i>V. Rödel, G. H. Schröder, and E. B. Vossenberg, CERN</i>	272
A Two-Step High-Voltage Pulse Generator <i>D. C. Flander, D. Grier, K. D. Metzmacher, and P. Pearce, CERN</i>	280
Rapid-Cycling Synchrotron (RCS) Single-Stage Kicker Magnet <i>D. E. Suddern and G. J. Volk, Argonne National Laboratory</i>	289
Fast-Extraction Modulators for Los Alamos Scientific Laboratory Proton Storage Rings <i>W. C. Nunnally, D. W. Hudgings, and W. J. Sarjeant, Los Alamos Scientific Laboratory</i>	292
SESSION XI: ACCELERATORS	
Overview of the ETA/ATA Pulse Power <i>L. L. Reginato and R. E. Hester, Lawrence Livermore Laboratory</i>	297
Pulsed Power Accelerators for Particle Beam Fusion <i>T. H. Martin, G. W. Barr, J. B. VanDevender, R. A. White, and D. L. Johnson, Sandia National Laboratories</i>	300

TABLE OF CONTENTS

	PAGE
Preliminary PBFA-II Design <i>D. L. Johnson, J. P. VanDevender, and T. H. Martin, Sandia National Laboratories</i>	305
Computer Models in the Design of FXR <i>G. E. Vogtlin and R. W. Kuenning, Lawrence Livermore Laboratory</i>	310
A Versatile 0.5-TW Electron Beam Facility for Power Conditioning Studies of Large Rare-Gas/Halide Lasers <i>J. J. Ramirez, Sandia National Laboratories</i>	314
Analysis of Performance of Rail Gun Accelerators Powered by Distributed Energy Stores <i>R. A. Marshall and W. F. Weidon, University of Texas at Austin</i>	318
List of Attendees	323
Author Index	331

A LOW JITTER SPARK GAP SWITCH FOR REPETITIVELY PULSED PARALLEL CAPACITOR BANKS*

G. J. Rohwein

Sandia National Laboratories, Albuquerque, New Mexico 87185

Abstract

A two-section air insulated spark gap has been developed for switching multi-kilojoule plus-minus charged parallel capacitor banks which operate continuously at pulse rates up to 20 pps.

The switch operates with less than 2 ns jitter, recovers its dielectric strength within 2 to 5 ns and has not shown degraded performance in sequential test runs totaling over a million shots. Its estimated life with copper electrodes is $> 10^7$ shots. All preliminary tests indicate that the switch is suitable for continuous running multi-kilojoule systems operating to at least 20 pps.

Introduction

Repetitively pulsed particle accelerators are being developed at Sandia National Laboratories for a variety of fusion research applications. One type of accelerator incorporates a low voltage parallel capacitor bank and a voltage step up pulse transformer instead of a Marx generator to charge the high voltage pulse forming line of the accelerator. Figure 1 is a photograph of an experimental transformer charging system which develops 1.5 MV from a ± 25 kV primary capacitor bank and operates at a pulse rate up to 20 pps.

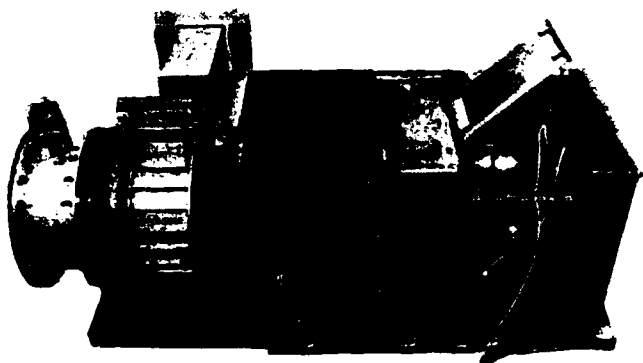


Fig. 1. 1.5 MV repetitive pulse transformer charging system.

One of the components in the transformer charging systems that has required a significant amount of development effort is the primary capacitor bank switch which in tens-of-kilojoule systems must carry current amplitudes of hundreds of kiloamps and withstand both current and voltage reversals. The only type of switch presently available which can meet this service requirement on a repetitive basis is a gas insulated spark gap. However, when the total current exceeds 60 to 80 kA the switch current must be divided into a number of channels to avoid excessive electrode erosion. This may be accomplished with a single switch if repeatable multi-channel operation can be assured. The other and more practical option is to use parallel single-channel switches simultaneously triggered. The

*This work was supported by the U.S. Dept. of Energy, under Contract DE-AC04-76-DP00789.

latter approach was taken in developing the two-section spark gap described in this report.

The switch shown in Fig. 2 has two identical two-electrode sections with one section attached directly to the high voltage terminal of each capacitor. The output electrodes of the two sections are connected with a copper strip to complete the circuit between the capacitors. A capacitor pair with individual switches thus forms a single module of a capacitor bank, Fig. 3. The switches are triggered by applying a high voltage pulse to the electrically common output electrodes through the spark plugs in the housing.

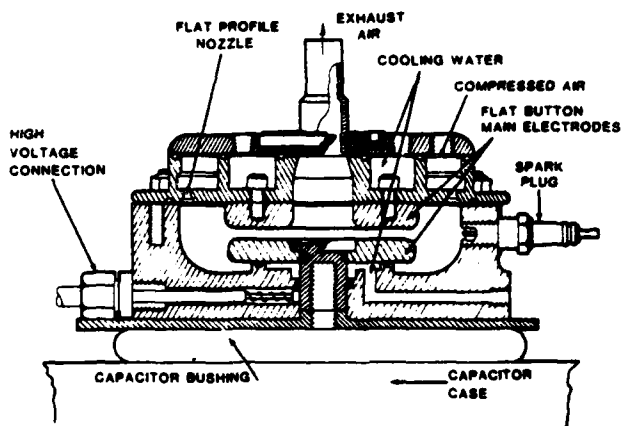


Fig. 2. One switch section.

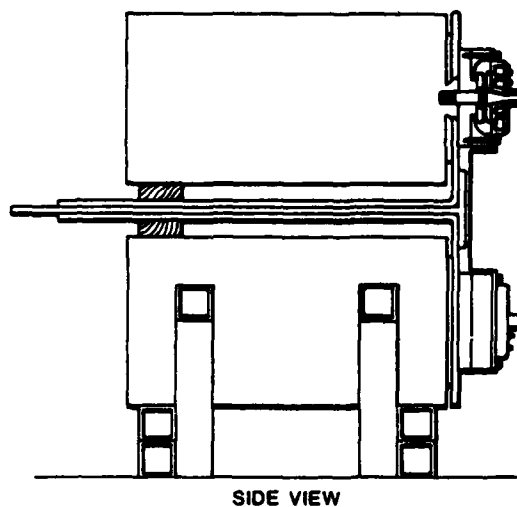


Fig. 3. Capacitor pair with switch attached.

Both switch sections are cooled by a combination of air and water. Compressed air is injected tangentially at supersonic velocity into the switch volume through flat profile nozzles in the cover plate to produce a high speed vortex flow pattern in the plane of the flat electrodes. The injected air provides rapid mixing and cooling of plasma debris which is

One of the primary motivations in developing the two-section switch instead of a more conventional three-electrode switch was that the switch sections provide DC voltage isolation for the high voltage capacitor terminals. No exposed high voltage collector plates or mounting hardware is required which could lead to insulation flashover during the DC charge periods. This arrangement permits a simplified insulation lay-up around the capacitors and output transmission plates. A second advantage of the two-section switch is ease of maintenance. A switch section may be opened, removed, or replaced in a matter of minutes. No special tools or gaging procedures are required to assemble or service the switch.

Initial development was carried out with one switch pair on a 1.2 kJ, ± 25 kV system. This machine was recently expanded to a 5 kJ, ± 30 kV system with three parallel switches and is in the initial stages of testing. It is shown schematically in Fig. 4. Following these tests a 50 kJ, ± 50 kV capacitor bank with 26 parallel switches will be constructed.

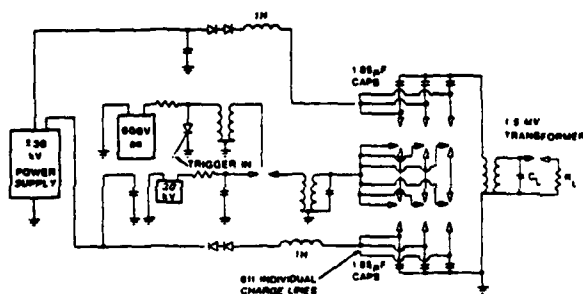


Fig. 4. Schematic of 5 kJ system.

Discussion

Each section of the switch has two 10 cm diameter flat button electrodes which have an effective switching area of approximately 70 cm². When triggered with a voltage pulse rising at 4 kV/ns or faster, shot to shot breakdowns occur more or less randomly over the electrode surfaces which distributes the wear evenly. Figure 5 is a photograph of the breakdown distribution over the electrode surfaces. Although the flat electrodes require a higher trigger voltage than spherical or cylindrical contours, they provide longer shot life and less change in triggering characteristics over the life of the switch. The rapid turbulent mixing associated with the high speed rotational air flow also contributes to the random breakdown distribution by maintaining a constant air quality between the electrodes.

To produce the supersonic vortex in the switch volume it is necessary to supply compressed air to the channel in the switch cover at over twice the static operating pressure in the switch volume. Air expanding through the nozzles will reach sonic velocity in the nozzle throats and supersonic velocities in the final expansion stage. Typically, primary air is supplied at between 100 and 150 psig for switch operating pressures between 20 and 45 psig. It should be noted that for a given supply pressure (P_s) the nozzles maintain



Fig. 5. Switch electrodes showing breakdown distribution.

a constant mass rate of flow through the switch until the absolute pressure in the switch exceeds 0.53 P absolute. The internal switch pressure must therefore be controlled by varying the back pressure in the exhaust line which in this case is accomplished with a throttling valve.

When operated in the 1.2 kJ system with + 25 kV charge on the capacitor bank, the peak current through the switches is 62 kA and the total charge transfer per shot is 0.062 coulomb which includes a single 30 percent current reversal in the discharge cycle. Based upon an erosion rate for copper of 57×10^{-6} g/C measured in a different switch operating with a similar waveform,² the estimated life of the two-section switch for 1 mm erosion will be approximately 1.2×10^7 shots using copper electrodes. When the switches are converted to tungsten alloy electrodes, the life will probably increase.

The triggering range of the switch for various conditions is shown in Fig. 6. Note that the dynamic self-break (prefire) curves for two air flow rates lie close to the static self break line at low charge voltages but diverge gradually as the voltage increases. The points plotted represent one or more prefires per hundred shots. This characteristic illustrates the dependence on effective gas scavenging in preventing prefires. The wedge shaped curves in the lower right part of the graph are triggering threshold lines for three trigger voltages. The regions to the right and left of the wedge tips represent a transition in triggering mode. Everywhere to the left

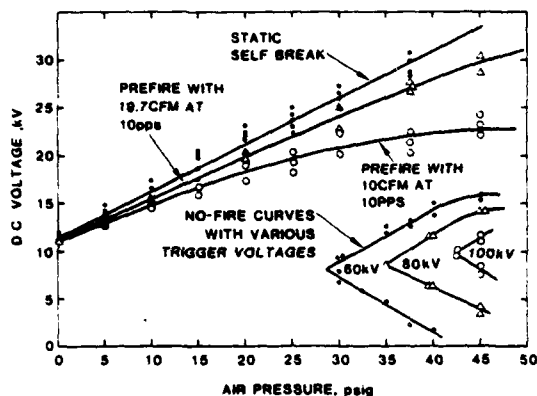


Fig. 6. Triggering range.

of a tip and below the self-break curve both halves of the switch breakdown simultaneously from the trigger pulse. To the right and above the wedges, the switch breaks down in a cascade mode where one section breaks from the trigger pulse and the other breaks subsequently from the total charge voltage appearing across the second gap. The regions enclosed by the wedge curves are no-fire zones where only one gap fires from the trigger pulse but the other does not breakdown from the total charge voltage. As the trigger voltage is raised or lowered, the no-fire zone correspondingly moves to the right and left.

Triggering

With the flat symmetrical electrodes, there is very little electric field enhancement to assist the trigger pulse in breaking down the gaps. Consequently, the gaps must be highly over voltaged to obtain reliable triggering and low jitter. The problem of fast triggering is complicated by the relatively high capacitance inherent in the large-area electrodes which is approximately 50 pF for two switch sections. It was necessary, therefore, to develop a special trigger generator for the switches.

The generator shown in Fig. 7 is small oil-mylar insulated spiral strip transformer with a gain of slightly over 10. It is equipped with an 8 nF primary capacitor and a spark gap switch which can be operated between 5 and 30 kV. The trigger generator therefore develops voltages up to 300 kV across the secondary winding which was designed with a shunt capacitance of approximately 60 pF. Figure 8 is a record of the unloaded pulse transformer output. The transformer output voltage is initially held off by a pressurized peaking gap. Near maximum voltage the gap self fires and delivers a trigger pulse to the main gaps through matched length trigger leads. The trigger leads connect to the main gaps through surface discharge spark plugs inserted through the side of the housing. With the base of the spark plug connected to the output electrode of the main gap, the plug is forced to breakdown before the voltage rises on the main gap. The main gaps thereby receive U.V. illumination simultaneous with the application of the trigger pulse. A comparison of Figs. 9 and 10 shows the contribution of preionization to switch triggering. Without the plugs the trigger voltage rises approximately 20 kV higher before switch breakdown occurs.

Since the charged capacitance of the secondary winding of the trigger transformer discharges into the

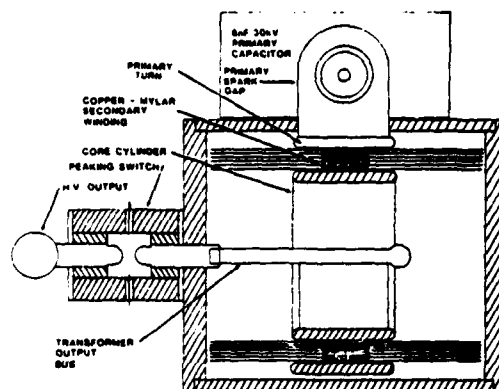


Fig. 7. Trigger generator.



Fig. 8. Trigger generator output, unloaded.
V = 25 kV/div
T = 10 ns/div
Primary voltage 15 kV



Fig. 9. Trigger pulse with no spark preionization in main gaps.
V = 20 kV/div
T = 10 ns/div
Bank charge voltage, ± 15 kV

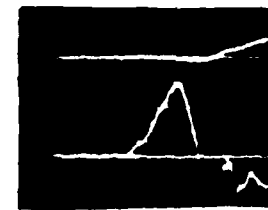
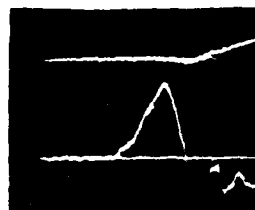


Fig. 10. Ten overlaid trigger pulses with spark preionization in main gaps.
V = 20 kV/div
T = 10 ns/div
Bank charge voltage, ± 15 kV

switch capacitance, the trigger pulse has the characteristic shape of one capacitor charging another through a series inductance which is given by the familiar equation:

$$V_{sw}(t) = \frac{V_{tg} C_{tg}}{C_{tg} + C_{sw}} (1 - \cos \omega t)$$

where

V_{sw} is the main switch trigger voltage
 V_{tg} is the voltage of the secondary capacitance of the trigger generator
 C_{tg} and C_{sw} are the trigger generator and switch capacitances, respectively
 ω is the radian frequency.

The main switches breakdown during the rise of the trigger pulse, typically within 20 ns. The principal criteria, however, is that the rate of rise be 4 kV/ns or faster. Figure 10 is a record of the trigger voltage with 10 overlaid traces. The top trace is the initial rise of current in the capacitor bank. A series of multiple trace measurements taken over a voltage range of + 5 to 25 kV show a consistent time to breakdown of 18 to 20 ns. The time jitter at each voltage step was less than the trace resolution of approximately 2 ns.

Dielectric Recovery and Switch Prefire

The repetitive pulser system in which the switches were tested had no interstage switches between the modulator section and the capacitor bank. Consequently, there was no zero-voltage or grace period between shots to allow the switches to recover their dielectric strength. To avoid prefires, therefore, the dielectric recovery rate had to exceed the recharge rate on the bank capacitors. The approximate recovery characteristics of the switch were determined by varying the primary charging capacitors and inductors to control the recharge rate and the air flow in the switch to control the recovery rate.

The switches recovered reliably to + 25 kV with a recharge period of 2.1 ms when the total air flow through the switches exceeded 36 scfm. With recharge periods of 3 ms and 4 ms, 28 scfm and 20 scfm were required, respectively, for reliable switch recovery. For most routine testing, the 4 ms charge period was used. Although these tests indicate that the compressed air demand could be reduced substantially below 20 scfm with a 50 to 100 ms recharge period, additional charging inductors will be required to verify this assumption.

Conclusions

The two-section spark gap has demonstrated low jitter, fast dielectric recovery and sufficient endurance to be of interest for large repetitively pulsed capacitor banks. Application to a 50 kJ system is planned. Although designed for 10 to 20 pps service, it could be adapted with minor modifications to systems operating up to at least 100 pps.

References

1. G. J. Rohwein, A Repetitive Pulse 1.5 MV Resonant Transformer, CLEOS/ICF Meeting, San Diego, CA, Feb. 26-28, 1980.
2. M. T. Buttram and G. J. Rohwein, Operation of a 300 kV, 100 Hz, 30 KW Average Power Pulse, Proc. of 13th Pulse Power Modulator Symposium, Buffalo, NY, June 20-22, 1978.

SUBNANOSECOND TRIGGER SYSTEM FOR ETA*

E. G. Cook, E. J. Lauer, L. L. Reginato
D. Rogers & J. A. Schmidt

University of California
Lawrence Livermore National Laboratory
Livermore, California

Summary

A high-voltage trigger system capable of triggering 30, 250 kV spark gaps; each with less than ± 1 ns jitter has been constructed. In addition to low jitter rates, the trigger system must be capable of delivering the high voltage pulses to the spark gaps either simultaneously or sequentially as determined by other system requirements. The trigger system consists of several stages of pulse amplification culminating in 160 kV pulses having 30 ns risetimes. The trigger system is described and test data provided.

Introduction

The Experimental Test Accelerator (ETA) is a 5 MeV, 10 kA linear induction accelerator. The accelerator has a five pulse burst at 1 kHz capability and a maximum average repetition rate of 5 pps. The ETA can be divided into two subsections; the injector and the accelerator. The injector is the source of the 40 ns electron beam and provides the first 2.5 MeV of accelerating potential. The accelerator consists of ten induction accelerating cells spaced along the beamline, each of which increases the beam energy by an additional 250 kV.

The source of the accelerating voltage is a water filled 10.5 Ω Blumlein charged to 250 kV. The energy stored in each Blumlein is delivered to the induction cells by triggering the Blumlein spark gap.

Each of the ten induction units (250 kV each) within the injector, is driven by two Blumleins. All the injector spark gaps must be triggered simultaneously with a jitter of less than ± 1 ns in order to generate the proper accelerating waveforms and potential.

The accelerating voltage must be present across the accelerator induction units when the electron beam propagates down the beam tube so the ten accelerator spark gaps are triggered sequentially. The jitter requirement for the accelerator spark gaps are the same as the injector's.

Trigger Requirements

Before a trigger system can be developed, the characteristics of the spark gap and its associated coupling and bias circuits must be understood. As seen in Figure 1, the ETA spark gap is a coaxial switch having three concentric tantalum electrodes which are the anode, trigger, and cathode.¹ The

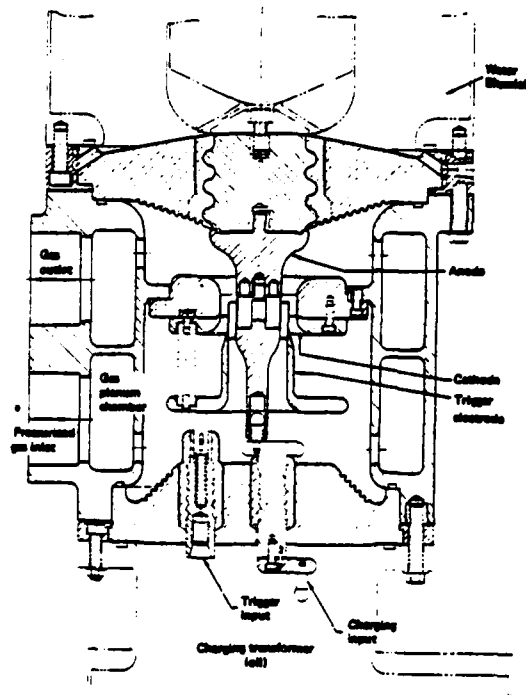


FIGURE 1. CROSS SECTION OF ETA SPARK GAP

trigger electrode is positioned at the electric field mid-potential and in addition is biased to the Blumlein half voltage point by a resistive divider.

In the spark gap trigger circuit schematic shown in Figure 2, the negative trigger pulse is capacitively coupled to the trigger electrode. The coupling capacitor (~ 100 pF) and the stray capacitance (~ 30 pF) of the trigger electrode to the anode and cathode (ground) form a voltage divider which couples approximately 75% of the trigger pulse to the trigger electrode.

Testing of the prototype ETA spark gap established a set of trigger parameters which provided satisfactory triggering. The testing indicated a minimum trigger pulse of 160 kV (at the

*Lawrence Livermore National Laboratory is operated by the University of California for the Department of Energy under Contract No. W-7405-Eng-48.

*This work is performed by LLNL for the Department of Defense under DARPA (DOD) ARPA Order 3718, Amendment #12, monitored by NSMC under Contract No. N60921-80-WR-M0188

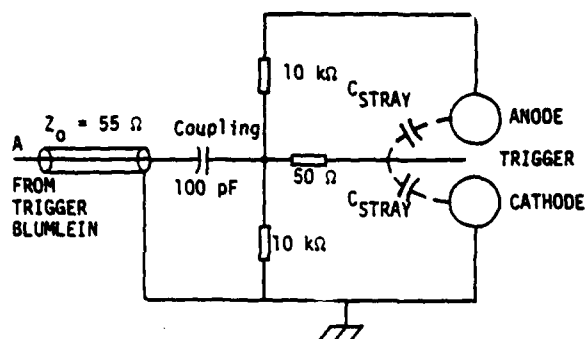


FIGURE 2. TRIGGER CIRCUIT FOR ETA SPARK GAP

drive side of the coupling capacitor) with a 10-90% risetime not to exceed 30 ns is required. These trigger levels are for a Blumlein charge voltage of 250 kV; less trigger voltage is needed at smaller charge levels. A gas mixture of nitrogen and 6-8% SF₆ is used in all spark gap jitter measurements. The maximum operating gas pressure is 120 psi and the gas flow rate thru the spark gap is approximately 5 cm/ms.

Trigger System

Trigger Blumlein

The number of triggers needed led to the concept of using standard ETA water Blumleins as trigger sources. The risetime of the Blumlein output pulse at < 20 ns 10-90% is adequate. In addition, the low source impedance (10.5Ω) enables a single Blumlein to drive several 55Ω (nominal impedance) cables simultaneously. The limitation to the number of cables that may be driven by a single Blumlein is a function of the impressed cable drive voltage. Since the Blumlein output risetime is less than the required cable's electrical length, voltage doubling occurs at the spark gap end of the cable and the drive voltage need be only about 80 kV. This requires an attenuator between the Blumlein and trigger cables but this allows the number of trigger cables to increase since the overall parallel cable impedance can be less than 10Ω. For convenience and versatility, each trigger Blumlein drives ten trigger cables. This arrangement requires two trigger Blumleins for the injector and one for the accelerator, but provides the flexibility of independent control. The output of a trigger Blumlein and the corresponding trigger voltage on the spark gap side of the coupling capacitor are shown in Figures 3a and 3b respectively. The 10-90% risetime of both signals is < 20 ns.

Of course, the trigger Blumleins also require fast low-jitter triggers. These triggers are best provided by another Blumlein. This Blumlein, the master trigger, must have its output attenuated to match into the trigger cables. Jitter in the master trigger Blumlein is not as critical since all machine timing sequences are initiated by its output pulse, however, other physics constraints necessitate a consistent master trigger pulse.

Spark Gap Trigger Transformer

The master trigger spark gap requires a trigger pulse which satisfies the trigger parameters. This trigger pulse is supplied by a special transformer. The transformer used is built on the same principles as the induction accelerator cells. This is an application of magnetic induction (Faraday's Law).

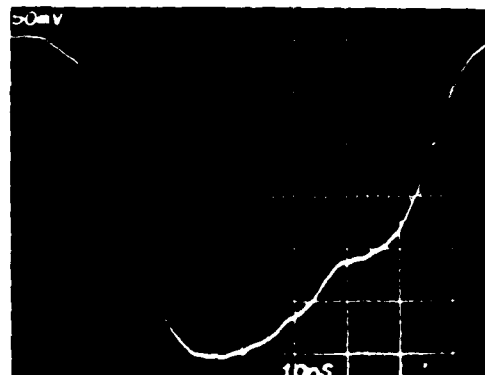


FIGURE 3A. TRIGGER BLUMLEIN OUTPUT

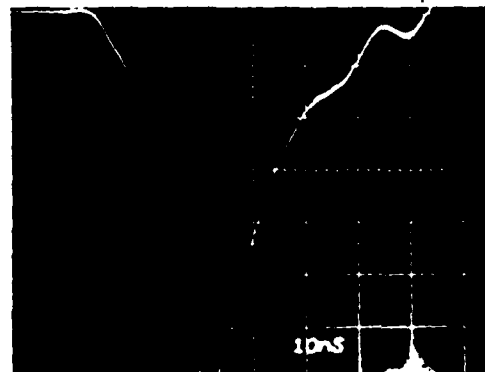


FIGURE 3B. TRIGGER VOLTAGE ON SPARK GAP SIDE OF COUPLING CAPACITOR

In the cross-section of the transformer as seen in Figure 4, each of the nine ferrite toroids is supported in a metal can which forms a single turn around the ferrite. When driven by a voltage pulse the resulting flux swing in the ferrite induces a voltage into the metal rod in the center of the transformer. In this manner each of the ferrite toroids represents a 1:1 transformer and the output of the transformer is simply the sum of the voltages across the individual 1:1 transformers. The result is a 9:1 step-up transformer having a risetime approximately equal to the risetime of the individual voltage drives to the transformer inputs.

When filled with transformer oil the internal dimensions of this transformer approximately a 50Ω impedance to match into the drive cable and minimize reflections. The drive impedance to each of the nine sections of the transformer is 5.0Ω (~50 Ω/9). The drive for each section is a .02 μF capacitor switched into the drive cables with a thyatron. Both the capacitor and thyatron are built into a low inductance housing to minimize

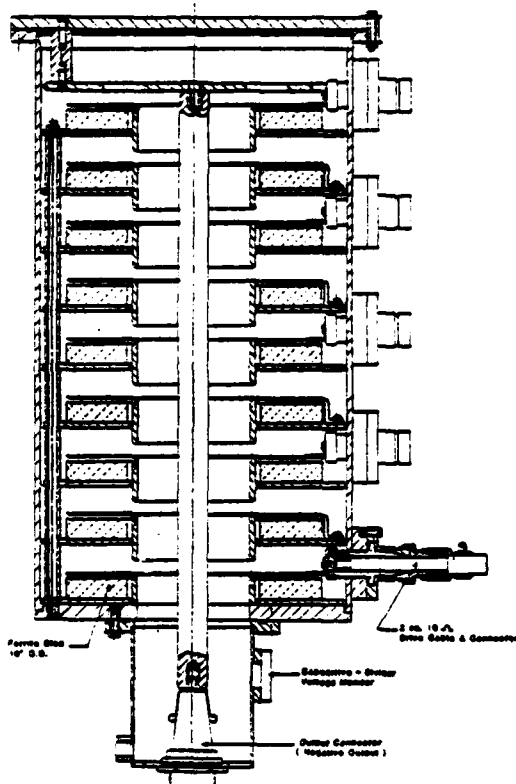


FIGURE 4. CROSS SECTION OF SPARK GAP TRIGGER TRANSFORMER

risetime. The capacitor is resonantly charged. The transformer's output pulse width is primarily dependent upon the available volt-seconds of the ferrite. The ferrite (Stackpole 7D-B) is chosen to have sufficient cross-sectional area such that a DC or pulsed reset is not required to ensure the required output pulse width. Since the transformer drives an open circuit (spark gap coupling capacitor), the output pulse oscillates and thereby keeps the ferrite from remaining in saturation. The transformer output pulse into the spark gap is shown in the oscillogram in Figure 5.

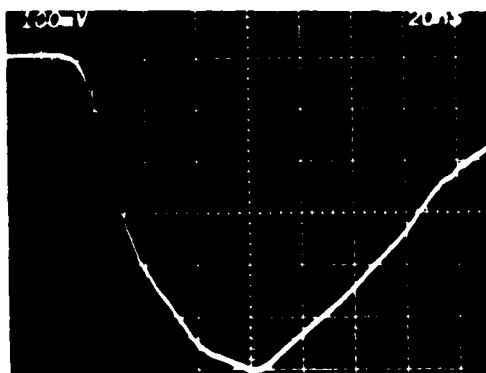


FIGURE 5. SPARK GAP TRIGGER TRANSFORMER OUTPUT (8 PULSES)

A simplified schematic of the overall trigger system is shown in Figure 6. The trigger sequence is started just prior to the Blumleins being fully charged. A low level trigger signal passes through an amplifier which in turn triggers the nine thyratrons to the trigger transformer. The trigger transformer triggers the master trigger Blumlein spark gap. At this time all timing control is lost; all further spark gap trigger pulses are automatic. The cable lengths between the master trigger, the two injector trigger Blumleins and the accelerator trigger Blumleins determine the respective timing between injector and accelerator. Since propagation delays through the Blumleins and spark gaps are constant, cable lengths from the trigger Blumlein are varied to delay trigger pulse arrival times between spark gaps on the accelerator for sequential triggering. All trigger cables from injector trigger Blumleins to injector spark gaps are the same length.

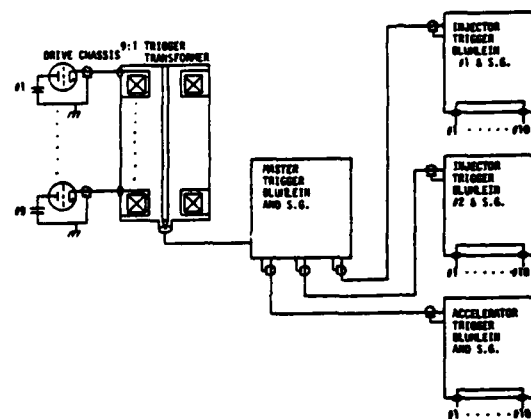


FIGURE 6. SIMPLIFIED BLOCK DIAGRAM - ETA SPARK GAP TRIGGER SYSTEM

Measurements and Results

Measurements of spark gap jitter are made on two different systems. Initial measurements were taken on the test spark which is triggered by a trigger transformer having a risetime of only 100 ns. Later measurements are recorded from the trigger, injector, and accelerator spark gaps which are triggered by the faster risetime Blumlein source. In both cases, a digital time interval counter having a time resolution of 0.1 ns is used. The time interval counter measurements are initiated by a signal taken from the spark gap trigger pulse and terminated by the attenuated Blumlein output pulse. Propagation delays through the Blumlein and cables are constant so the jitter is the difference between measurements. For large numbers of measurements, the jitter is simply the deviation around the mean.

The measurements on the test spark gap were extensive. The parameters varied included spark gap voltage, trigger pulse amplitude, gas pressure and gas mixture. Jitter distributions based on approximately one hundred measurements were tabulated and plotted for each operating point. While the trigger pulse was not optimum, these measurements established the operating conditions and limits of the spark gap, the gas system, and the trigger system.

Jitter data for the trigger, injector, and accelerator spark gaps is generated while the ETA machine is being pulsed. Jitter measurements

recorded for the trigger Blumleins, injector and accelerator spark gaps are relative to the master trigger. A minimum of one hundred data points are recorded for a given operating condition. The jitter information is presented in two formats - an actual plotting of the jitter distribution about a normalized mean and in terms of the standard deviation around the mean.

The jitter data for one of the injector trigger Blumleins is shown in Figure 7. This spark gap operating at near optimum conditions exhibited a σ_{ITB} of 0.85 ns (one standard deviation). The output of the trigger Blumlein triggers the spark gap having the jitter distribution shown in Figure 8. The total deviation with respect to the master

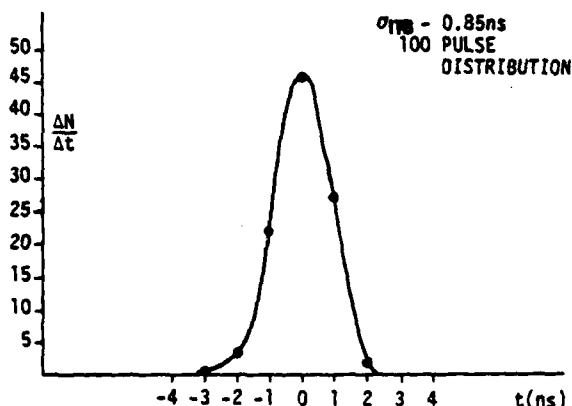


FIGURE 7. JITTER DATA DISTRIBUTION FOR INJECTOR TRIGGER BLUMLEIN S.G.

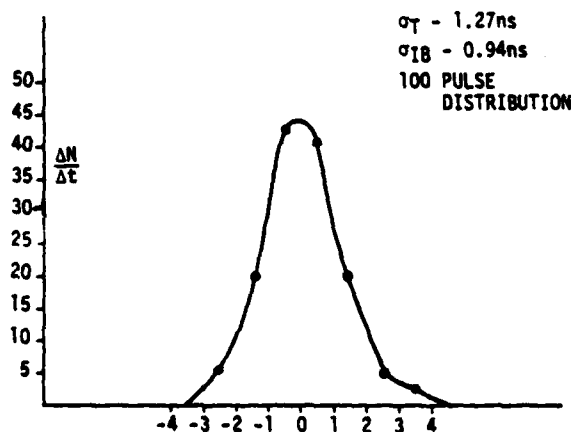


FIGURE 8. JITTER DATA DISTRIBUTION FOR INJECTOR BLUMLEIN S.G.

trigger and including the jitter of the injector trigger Blumlein is 1.27 ns. Using the relationship $\sigma^2_{\text{Total}} = \sigma^2_{ITB} + \sigma^2_{IB}$, one standard deviation for the injector spark gap is 0.94 ns. These distributions are representative of all injector and accelerator spark gaps operating under the same conditions.

In the burst mode of operation jitter data is more difficult to obtain. A relative measure of overall system jitter is made by examining an overlay of the burst pulses. Figure 9 is a 5 pulse overlay of the sum of the injector accelerating voltages.

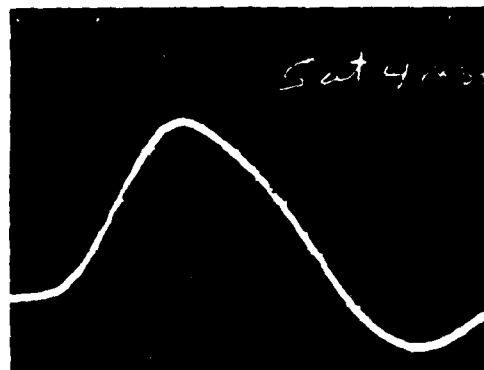


FIGURE 9. FIVE PULSE BURST OF SUMMED INJECTOR VOLTAGE

Conclusion

We have built a trigger which satisfies the spark gap jitter requirements for ETA. The primary limitation of the trigger system is the rather narrow window of operating parameters which yield low-jitter. The limiting factor is the trigger amplitude which must be less than 160 kV to protect the trigger cable and connectors. Modifications to extend the operating range by using cables and connectors capable of operating at higher trigger levels are in progress.

1A. Faltens, L. Reginato, R. Hester, A. Chesterman, E. Cook, T. Yokota and M. Dexter, High Repetition Rate Burst-Mode Spark Gap, UCRL #80934, June 15, 1978.

2E. Lauer, Measurements of Distributions in Firing Time Delay of the ETA Test Spark Gap Switch, ATA Note #64, March 21, 1979.

NOTICE

This report was prepared by the UCRL as an account of work sponsored jointly by the U.S. Department of Energy and the Defense Advanced Research Projects Agency. Neither the U.S. Government, nor any of its employees, nor any of its contractors, subcontractors, or their employees, makes any warranty, express or implied, or assumes any legal liability or responsibility for the accuracy, completeness or usefulness of any information, apparatus, product or process disclosed, or represents that its use would not infringe previously owned rights.

NOTICE

Reference to a company or product name does not imply approval or recommendation of the product by the University of California, the U.S. Department of Energy, or the Defense Advanced Research Projects Agency.

THE FXR ONE-NANOSECOND-JITTER SWITCH*

H. Bruce McFarlane and Ronald Kihara
Lawrence Livermore National Laboratory

Summary

A switching system using low-jitter spark gaps has been designed for a 20 MeV Flash X-Ray (FXR) linear induction accelerator that is being built at the Lawrence Livermore National Laboratory. The accelerator, which is now under construction, will consist of 54 modules connected in tandem. Each module will contribute up to 400 keV of energy to the electron beam traversing it.

The experimental work included a test of one accelerator module designed to produce 400 keV. Of particular concern was the thorough characterization of the Blumlein switch in terms of lifetime, voltage hold off and operating pressure range to produce minimal jitter and an acceptably low prefire rate.

We recorded the data by means of a computer-based data-acquisition system which was set up for later, automatic data reduction and display of the results. Optimization of the spark gap operating parameters resulted in a firing jitter of less than one nanosecond rms.

Introduction

Prototype tests of the FXR 20 MeV linear induction accelerator included a test of one accelerator module. The objectives of this test were to subject all the elements of the typical single accelerator module to numerous discharge cycles. We have recently completed 20,000 discharges using a coaxial midplane spark gap as the Blumlein switch. It is the purpose of this paper to report the results of these tests.

Experimental Setup

The one-module test stand is shown schematically in Figure 1.

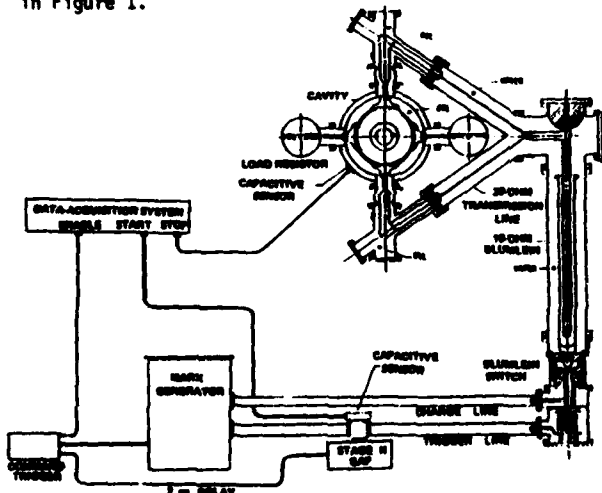


Fig. 1 - Block diagram of one-module test.

*Work performed under the auspices of the U. S. Department of Energy under Contract No. W-7405-Eng. 48.

The Blumlein is charged by a 4-stage Marx generator. Each stage consists of an 80 nF capacitor. The four-stage, 20 nF Marx charges the 10-ohm, water-dielectric Blumlein through an inductor in about 2 microseconds. The Blumlein switch short circuits one end of the Blumlein near the peak of its charge. The trigger line is charged to the proper midplane voltage through a tap on the Marx generator.

The command trigger is split to send an ENABLE pulse to the data acquisition system (DAS), trigger the Marx generator, and also pass through a cable time delay to trigger the stage II gap near the peak of the Blumlein charge cycle.

The output from the stage II gap supplies the trigger to the main Blumlein switch and also sends a START pulse to the DAS. The Blumlein pulse energizes the accelerating cavity. At the cavity a capacitive voltage divider senses the signal and sends it as the STOP pulse to the DAS. The time between the STOP and START pulses is counted as the relative switching delay in the Blumlein switch. By analyzing a number of pulses, a measure of the time-jitter in the Blumlein switch is obtained.

The coaxial midplane spark gap switch is depicted in cross section in Figure 2. The coaxial geometry provides low inductance and hence a short pulse rise time. The midplane trigger electrode provides a large unbalance in electrode voltage and hence a short arc-formation time.

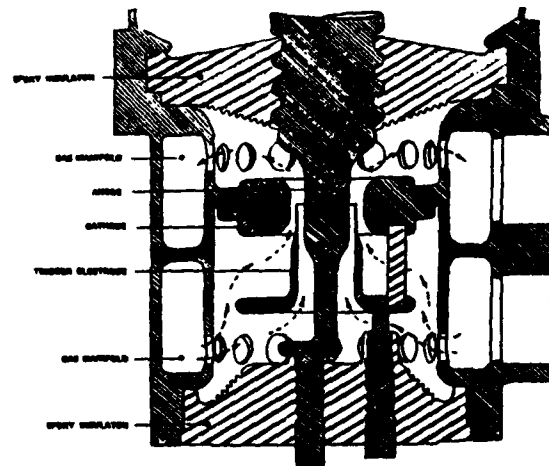


Fig. 2 - Cross section view of coaxial midplane spark-gap switch. The dashed line shows pattern of gas flow used to cool gap.

Jitter and Prefire Measurements

We constructed curves of the number of no-fires, prefires, and acceptable shots for selected values of voltage at different operating pressures. In both these tests and the jitter tests of the Blumlein switch, we charged the Blumlein to 290 kV by charging the Marx generator to 80 kV.

At this voltage we ran several runs of 50 events each at pressures ranging from 320 kPa to 730 kPa absolute. No no-fires were recorded even at the highest pressures. As the pressure was lowered we experienced some prefires. Figure 3 is a graph of the pressure vs. number of prefires at 290 kV on the gap.

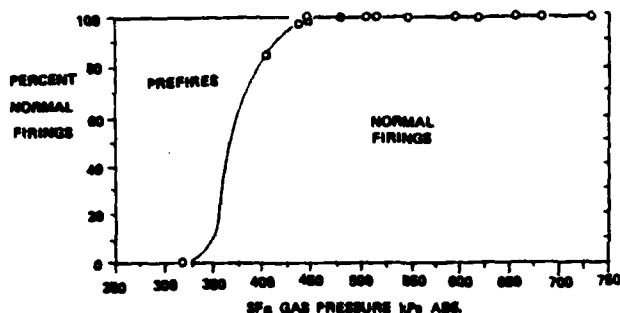


Fig. 3 - Percentage of normal firings of main Blumlein gap vs. gas pressure. Each point resulted from 50 firings at that pressure. No no-fires were detected, even at highest operating pressure.

The procedure we used was to set the desired pressure on various spark gaps (Marx, Stage II, Blumlein), then charge and discharge the system at intervals of 3 seconds. Suitable gas flows were maintained through the discharge devices to sweep out ionization products. In the case of the Blumlein switch a flow of 0.5 litres/second of SF₆ gas was used to cool the electrodes. Three signals are presented to the data acquisition system (Figure 4).

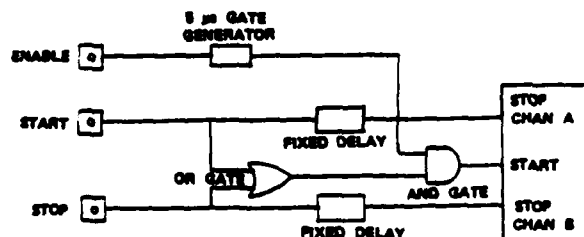


Fig. 4 - The data-acquisition system (DAS). By subtracting the count of channel A from that of channel B, we obtained the relative firing delay of the main Blumlein gap.

The first is an ENABLE signal without which no further data will be recorded. This signal comes from our command trigger. The reason for setting up the recording system this way is to preclude any data from Marx generator prefires. Occasionally the Marx prefired, and we felt that the data was then unreliable since the Stage II gap had not been triggered properly. The ENABLE signal starts a 5μs gate generator that drives one-input of a two-input AND gate.

The Stage II gap triggers the Blumlein gap. Part of this signal is also sent to the DAS as the START input. The STOP signal is derived from the cavity. As noted earlier, the time between START and STOP signals is a measure of the time the main Blumlein gap takes to fire. The clocks on the DAS are started by the START or STOP signals, whichever arrives at an OR gate first. The clock on channel A is stopped by a delayed START signal while channel B is stopped by the STOP signal, also delayed.

The information from each clock is recorded in a disc file with an event number. A series of events are recorded into the file with a unique name for later correlation with experimental conditions noted in the log. The DATE, TIME, DEVICE UNDER TEST, PRESSURE, and VOLTAGE are recorded in the file.

Later the recorded information is processed to produce a printed record showing each event and the delay time. If channel A shows a large number (overflow) and channel B is small, a prefire is presumed. If channel B registers an overflow it is indicative of a no-fire. The printout shows the maximum and minimum delay times recorded, and values for the MEAN and RMS DEVIATION (σ) are printed. This latter term is defined as follows:

$$\sigma = \sqrt{\frac{\sum (X - \bar{X})^2}{n}}$$

where σ is the rms deviation
 \bar{X} is the sample mean
 X_i is the sample value
 n is the number of samples

Data from the disc files is analyzed. The difference between the maximum and minimum delay times is divided into time slots of equal length. The number of events having delay times in each slot are counted. The results are then plotted on a bar graph such as Figure 5. The bar graph is an easy way to see if there are any gross statistical aberrations in the data.

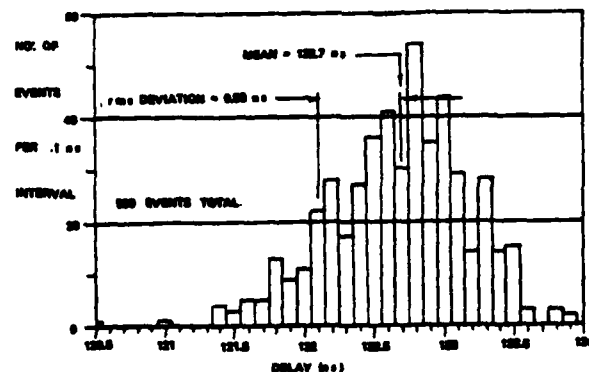


Fig. 5 Delay histogram of typical one-module test run of 500 events. Main-Blumlein-gap pressure (SF₆): 755 kPa abs., gap voltage: 290 kV.

We ran more than 20,000 discharges to life test the Blumlein switch. Each group of 500 or 1000 discharges was analyzed to see if any of the gap statistics were changing. We made a plot of each

We also used a more reliable and faster-rising trigger pulse from our Stage II gap on the four-module test than we used on the one-module test. It may be for this reason that the delay statistics recorded from the first of the four-modules show a jitter of even less than for the one-module test. In the example of Figure 6 the jitter is only 0.35 ns.

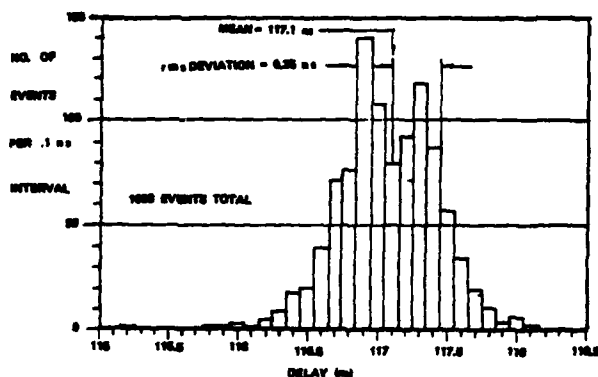


Fig. 6 - Delay histogram of typical four-module test run of 1000 events. Gap voltage: 300 kV, gap pressure: 445 kPa abs.

Another change made prior to the four-module tests was the reorientation of the cavity to a symmetrical lateral feed rather than from the top and bottom. This change eliminated the right-angle bend and also shortened the water transmission line. The new configuration is shown in Figure 7.

NOTICE

This report was prepared as an account of work sponsored by the United States Government. Neither the United States nor the United States Department of Energy, nor any of their employees, nor any of their contractors, subcontractors, or their employees, makes any warranty, express or implied, or assumes any legal liability or responsibility for the accuracy, completeness or usefulness of any information, apparatus, product or process disclosed, or represents that its use would not infringe privately-owned rights.

Reference to a company or product name does not imply approval or recommendation of the product by the University of California or the U.S. Department of Energy to the exclusion of others that may be suitable.

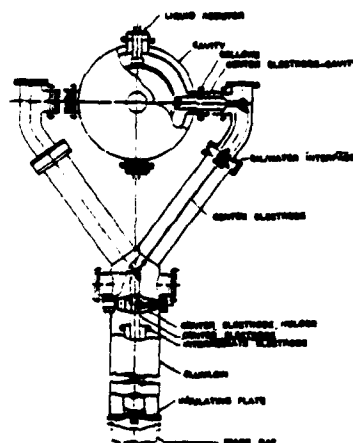


Fig. 7 Schematic drawing of Blumlein and cavity used on four-module test stand.

The shape of the output pulse obtained from the four-module test (Figure 8) is better than the pulse from the single-module test. The top of the pulse is relatively flat, the rise time is about 30 ns (10% - 90%) and the width about 80 ns (FWHM).



Fig. 8 Cavity voltage on four-module test.
Horizontal: 50 ns/div., vertical: 250 kV/div.

Conclusion

The electron beam of the FXR linear induction accelerator travels at near-relativistic velocity through a series of 54-pulse modules. Each pulse must coincide with the arrival time of the beam. This requires timing accuracy of 1 nanosecond or less. We have tested a coaxial midplane spark gap switch and have shown it to have a statistical time jitter over a large number of pulses of 0.35 ns rms. The use of an automatic data recording and reduction system allowed us to measure each pulse that was fired and to reduce the data to statistical bar graphs.

SWITCHING SYSTEM FOR THE FXR ACCELERATOR*

R. D. Scarpetti & C. D. Parkison
Lawrence Livermore Laboratory
P.O. Box 808, L-153
Livermore, California 94550
(415) 422-8502

Summary

A switching system has been designed for a 20 MeV flash x-ray linear induction accelerator which is being built at Lawrence Livermore Laboratory. The switching system fans out a single command pulse and amplifies it to obtain the voltage necessary for reliable, low-jitter triggering of the accelerator components. This system consists of two major subsystems: (1) the Blumlein Charging Subsystem which first triggers thirteen Marx generators, and then charges 54 water-filled Blumleins, and (2) the Blumlein Triggering Subsystem which triggers the already-charged Blumleins to produce a 90 nanosecond, 400 kV pulse in each of 54 ferrite-loaded accelerator modules. The first subsystem consists of charged high voltage cabling with two parallel switch gaps either of which will trigger the Marx generators. The major components of the second subsystem are three stages of switch gaps along with the necessary high voltage cabling. Two parallel first stage switch gaps trigger thirteen second stage gaps, which in turn trigger 54 third stage Blumlein switch gaps synchronous with the passage of the electron beam pulse. These spark gaps are operated at a voltage of 150 to 350 kV with a 1/3 hertz repetition rate. Varying the cable lengths creates the actual delay times in the triggering of each component. Redundancy is built into the system to insure the high reliability which is essential for the flash radiography application.

Introduction

Flash X-Ray (FXR) is a 20 MeV, 2 KA linear induction accelerator composed of 54 accelerating cavities. Six of these cavities make up a 1.5 MeV electron injector and the remaining 48 cavities, arranged in four module sections, each accelerate the electron beam 380 kV. The accelerator has an overall length of 39 meters. FXR uses thirteen Marx generators for energy storage and 54 water-filled Blumleins as pulse-forming networks to supply a 90 ns, 380 kV pulse to each of the 54 ferrite loaded accelerating cavities. The operating sequence is as follows. Each of the Marx generators charges up 4 cavity Blumleins. When the Blumleins are at peak charge they are triggered and send a 90 ns 300 kV pulse to the accelerating cavities. A mismatch between the Blumlein and cavity results in a 90 ns 380 kV pulse across each of the cavity gaps resulting in an overall beam energy of 20 MeV.

An overview of the FXR accelerator is given by B. Kulke¹ and specifics are given by G. E. Vogtlin and R. W. Kuenning² and H. B. MacFarlane and R. Kihara³ at this conference. This paper will deal with the means by which each of the accelerator components are triggered.

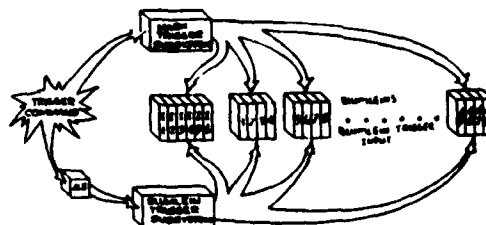
The purpose of the Switching System is to first charge and then trigger each accelerator Blumlein to

produce the accelerating voltage across each accelerator module gap coincident with the passing of the electron beam. Since this machine will be used for radiography shots, which are expensive one-time shots, it is essential that the accelerator be very reliable. Therefore the Switching System itself must have a high reliability.

The predicted lifetime of this accelerator is about twenty years. Over this time the accelerator will have fired several million shots. (Most of these shots will be for machine tuning and hardware checking, and a small percentage will actually be radiography shots). Therefore it is necessary for the Switching System to have a long lifetime (approximately millions of shots) with very little down-time for periodic maintenance and repairs. Another requirement is that the system readily accept machine upgrades, since at present machine upgrades are expected which would increase the beam energy from 20 MeV to as much as 50 MeV.

The Switching System is composed of two major subsystems, the Blumlein Charging and the Blumlein Triggering Subsystems. The first triggers the Marx generators which in turn charge the accelerator Blumleins, and the second triggers these already charged Blumleins (Fig. 1).

THE MARX TRIGGER SUBSYSTEM CAUSES THE ACCELERATOR BLUMLEINS TO CHARGE, WHILE



THE BLUMLEIN TRIGGER SUBSYSTEM TRIGGERS THE ALREADY CHARGED ACCELERATOR BLUMLEINS

FIGURE 1

The Blumlein Trigger Subsystem

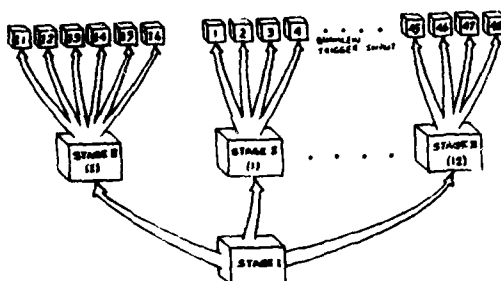
As stated earlier, the purpose of this subsystem is to trigger each of the accelerator Blumleins at the proper time to obtain optimum acceleration of the electron beam. Optimum

*Work performed under the auspices of the U.S. Department of Energy by the Lawrence Livermore National Laboratory under contract No. W-7405-Eng-48.

acceleration creates a beam of maximum energy with minimum energy spread.

The Trigger Subsystem can be broken down into three levels or stages. The purpose of each stage is to amplify the trigger signal of the previous stage. Initially a single one kilovolt trigger signal is fed into the first stage. This stage amplifies the signal into thirteen 125 kV trigger pulses. These thirteen trigger pulses enter the second stage and are further amplified to fifty-four 150 kV trigger pulses. The signals then go on to trigger each of the fifty-four Blumleins (Fig. 2).

THE BLUMLEIN TRIGGER SUBSYSTEM CAN BE BROKEN UP INTO THREE LEVELS OR STAGES.



EACH STAGE OF THE BLUMLEIN TRIGGER SUBSYSTEM FEEDS OUT TO THE NEXT STAGE

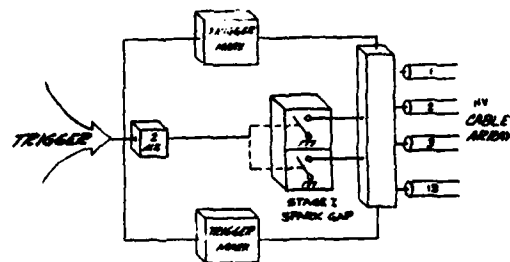
FIGURE 2

a. Stage 1

The block diagram of the first stage of the Trigger Subsystem is shown in Fig. 3. The first stage consists of an array of 13 High Voltage Cables, two spark gaps, and the output from two Marx generators, all connected at a common point. These two Marx generators, or trigger Marxes, are two-stage, 250 nF devices. They are modified versions of the thirteen Marx generators which charge the accelerator Blumleins. Each of these thirteen Marxes is a five stage, 75 kV per stage, 100 nF Marx generator. The trigger Marx is a single five stage Marx split into two two-stage trigger Marxes, (one complete stage is dropped), each having its own charging and triggering circuit. The capacitors, spark gaps, and remaining circuit elements of the trigger Marxes are identical to those of the five stage Marxes, minimizing the number of on-hand spare parts needed. The trigger Marx charging supply is also identical to the charging supplies of the accelerator Marxes.

The spark gaps for this first stage are identical to the spark gaps that will be used to trigger the accelerator Blumleins. The spark gap electrodes are coaxial with the trigger electrode located midway between and concentric with the two main electrodes. Past testing has shown that this type of gap has an inductance of about 60 nanohenrys. H. B. McFarlane³ has completed a set of experiments in the gap which show it has low no-fire, pre-fire characteristics and has an RMS jitter of less than 1 ns when operated with SF₆ at voltages of 325 kV. Since the spark gaps on the switching system will

THE TRIGGER MARXES ARE ERRECTED AND CHARGE THE THIRTEEN TRIGGER CABLES



REDUNDANT MARXES BETTER INSURE THAT THE CABLE ARRAY IS CHARGED

FIGURE 3

be operated at 125 kV, further testing at this lower voltage is necessary.

A -120 kV pulse with a 10-90% rise time of 10 ns or less will trigger these spark gaps. This pulse will be generated by a four stage 4.2 nF Marx. A three-stage version of this Marx has had extensive use at the Lawrence Berkeley Laboratory Electron Ring Accelerator⁴. There it has proven itself to be highly reliable with a tested lifetime of over 10 million shots. The only design change we will make will be adding another stage, making it a four stage -30 kV/stage unit.

The cable array will be high voltage cable rated at 350 kV dc. This cable has a characteristic impedance of 67.6Ω, a capacitance of 23 pF/ft and a phase velocity of .63 times the speed of light in vacuum.

The cable array consists of thirteen cables varying in length from 30.2 to 48.2 meters. The difference in length between each of the thirteen cables corresponds to the electron transit time between the adjacent four cavity sections (Fig. 4).

THE TIME IT TAKES FOR THE TRIGGER PULSE TO REACH EACH STAGE II GAP IS DEPENDENT UPON THE LENGTH OF EACH TRIGGER CABLE. THE DIFFERENCE IN LENGTH BETWEEN EACH CABLE CORRESPONDS TO THE ELECTRON TRANSIT TIME BETWEEN EACH SECTION.

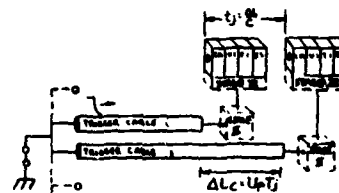


FIGURE 4

The junction where the trigger cables, trigger Marxes and Stage 1 gaps come together is called the fanout assembly. The trigger cables plug into ceramic damping resistors which are attached to the center conductor of the fanout assembly. The fanout assembly is shown in Fig. 5 and is 71 cm. long by 19 cm wide by 20 cm deep. The cables are arranged in two rows of eight. (The three extra connectors are for minor upgrades to the accelerator.) The two coaxial spark gaps are arranged on either side of the fanout housing while the output from the trigger Marxes enter from the bottom. This entire assembly is mounted on top of an oil filled tank containing the trigger Marxes, charging inductor along with the rest of the Stage 1 hardware.

STAGE 1 FANOUT ASSEMBLY

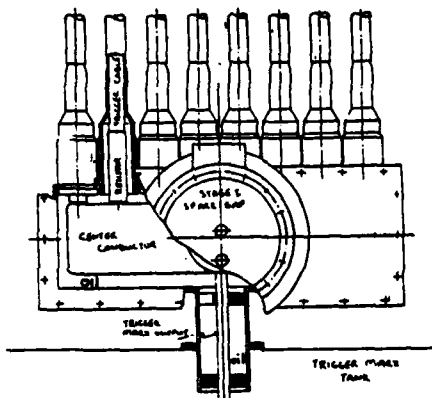


FIGURE 5

When the Marx generators are triggered, they resonant-charge the cable array to 125 kV in 2 microseconds. At peak charge, the two spark gaps are triggered, shorting the cable array to ground, and setting up a -125 kV traveling wave in each of the 13 cables. Each of these cables is terminated in a 100 pf isolation capacitor. Since these capacitors are much smaller than the cable capacitance, the -125 kV trigger pulse effectively sees an open circuit and is almost entirely reflected. The forward traveling wave combined with the reflected wave results in a >125 kV pulse which is used in the second stage of the Trigger Subsystem. In order to minimize the ringing in the cable array, 15 ohm resistors will be placed in series with each of the cables. This design was modeled by computer simulation and the resulting waveform is shown in Fig. 6. Notice that there is an acceptable voltage reversal on the cable. It is believed that this will result in an increase in the average cable's lifetime. The unwanted effect of this series resistor is that it drops the amplitude of the trigger pulse by $Z_0/(Z_0 + r)$, where r is the resistor and Z_0 is the line impedance. For the present case the trigger pulse is dropped to 0.82 of its initial amplitude. These inline resistors will be ceramic, 6 inches long and 1 inch in diameter.

In order to resonant charge the cable array in 2 microseconds, a 15 microhenry inductor will be placed in series with the Marx and cable array. The Marx itself has an inductance of about 2μh. The cable array contains 1683 feet of cable at 22.8

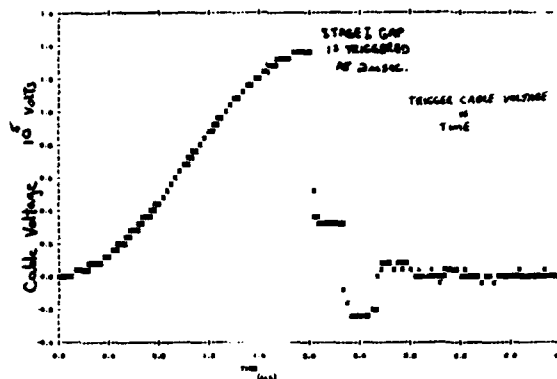


FIGURE 6

pf/ft corresponding to a total capacitance of 38.4 nf. Since the electron transit time in the largest cable (48.2 m) is much shorter than the 2μs charging time, the cable array can be treated as a single capacitor of 38.4 nf. Therefore the cable charging circuit can be represented simply by a Marx capacitance, a charging inductor, and a lumped cable capacitance as shown in Fig. 7. This figure represents the two possible conditions: first, if only a single Marx erected and second, if both Marxes erected. The voltage gain on the trigger cable is given by:

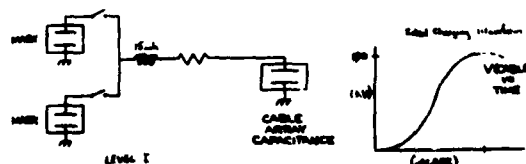
$$\frac{2C_m}{C_m + C_c} \quad (1)$$

where C_m is the Marx capacitance and C_c is the cable capacitance. The charging time, t_c , of the cable is given by

$$t_c = \pi\sqrt{LC} \quad (2)$$

where L is the equivalent charging inductance and C is the equivalent circuit capacitance. The actual voltage gain and cable charging time will depend on whether one or both of the Marx generators erected.

THE THIRTEEN TRIGGER CABLES ARE RESONANT CHARGED TO 150 KV IN ~2 μs.



(SINCE THE CAPACITANCE THAT IS LOADED, THE TRIGGERING CABLES CHARGE AS CAPACITORS.)

FIGURE 7

The reason for redundant trigger Marxes is to ensure that the cable array will be charged. If the cable array is not charged then the entire accelerator will not function leading to a failure of the radiography shot.

It can be shown that both the charging times and voltage gains are relatively insensitive to having one or both Marxes erect. (The voltage gain in the cable array varies by 6% dependent on whether one or both Marxes erect, while the charging time varies by less than 1%.)

Since the cable array is not a single capacitor, but is, instead, a set of thirteen transmission lines having round trip transit times of 320 ns to 510 ns. As a result the voltage waveform will be distorted from the ideal $(1 - \cos \omega t)$ waveform characteristic of a resonant-charge because of voltage reflections at the cable ends. In order to study this distortion, a computer code was used to model the real situation. A plot of the charging waveforms at the common end is shown in Fig. 8. From the plot you can see that there are only minor distortions. When the cable array is at its peak charge, the two coaxial stage I spark gaps are triggered, setting up a traveling wave through the cable array. A 16 ohm resistor is put in series with the trigger Marxes in order to critically damp the oscillations set up as a result of the stage I gaps firing. Two gaps are used in parallel operation in order to increase system reliability.

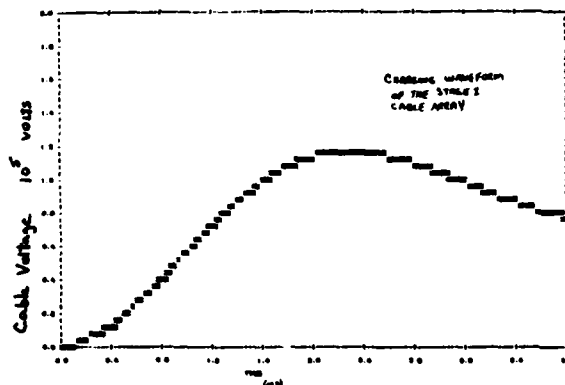


FIGURE 8

The switching system is designed to function properly if either of these gaps trigger.

b. Stage II

The diagram for the second stage of the Trigger Subsystem is shown in Fig. 9. This stage consists of thirteen spark gaps. A set of four trigger cables are attached to each of 12 of the stage II gaps. Each of these cables is terminated in the trigger circuit of the Blumlein stage III spark gaps. A set of six trigger cables is attached to the thirteenth spark gap and is used to trigger the Blumlein spark gaps on the six injector Blumleins. The stage II gaps and the associated trigger cabling will be charged from a tap-off from the accelerator Marxes which charge the Blumleins. Therefore, the trigger cables leading to the stage III gaps are

charged to 150 kV as the Blumleins themselves are being charged to 300 kV. The trigger electrodes of the stage II gaps are located at the midplane and will be charged to 75 kV. A capacitor is needed in the trigger circuit to isolate the trigger electrode at 75 kV from the stage I trigger cable at 125 kV. This capacitor will be 100 pf or roughly 10 times the capacitance of the trigger electrode and either main electrode of the stage II gaps. A trigger pulse from the stage I cable triggers the stage II gap, shorting the stage II cables to ground and setting up a -150 kV traveling wave in the cable. The wave will then trigger the stage III gap and fire the Blumleins.

EACH TRIGGER CABLE IS TERMINATED IN A STAGE II SPARK GAP TRIGGER CIRCUIT.

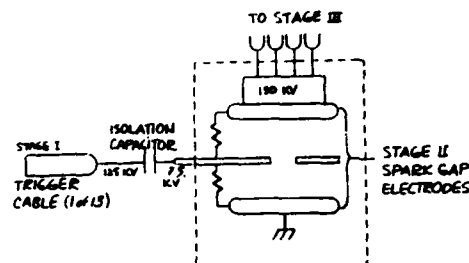


FIGURE 9

c. Stage III

This stage is made up of the 54 Blumlein spark gaps. The Stage II trigger cables are connected to the trigger electrodes of the gaps through a resistor. The purpose of this resistor is to minimize cable ringing in the Stage III triggering cable.

Order of Firing

Varying the cable lengths to each gap determines the timing of the triggering of each Blumlein spark gap. After the stage I gap is fired, the trigger pulse reaches each of the stage II gaps at the appropriate time dependent upon the cable length and sends negative trigger pulse to each of the 54 Blumlein stage III gaps. These trigger pulses reach each stage III gaps at different times again dependent on the length of each of the stage III trigger cables.

The Blumlein Charging Subsystem

The purpose of the Blumlein Charging Subsystem is to trigger the thirteen accelerator Marxes so that each accelerator Blumlein is at its peak charge coincident with the time that the stage III gap is triggered. The charging subsystem is identical to the first stage of the Blumlein Trigger Subsystem. Each of the thirteen trigger cables is terminated in the trigger circuit of each of the Marx generators. Since the Marx trigger electrodes are maintained at ground potential, a 100 pf isolation capacitor is placed at the trigger cable termination.

10. The overall Switching System is shown in Fig.

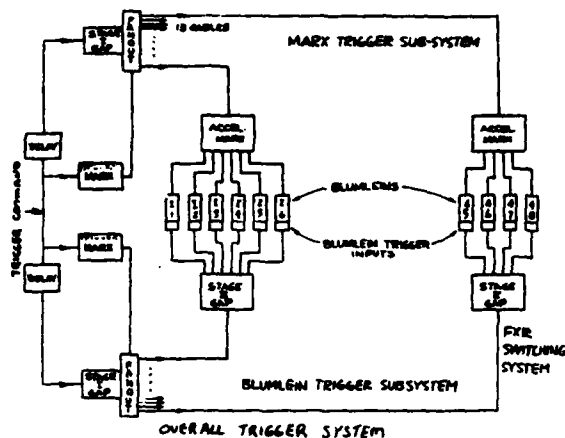


FIGURE 10

Conclusion

The FXR accelerator must be highly reliable if it is to be a successful radiography machine. The Switching System, with its redundant systems, should

prove to be very reliable. The system is easily modified for accelerator upgrades by adding similar subsystems in parallel with the existing systems.

FXR is scheduled for completion late in 1981. The building and testing of the Switching System will begin in the next few months.

Acknowledgements

The authors wish to acknowledge D. A. Barrett for his work on the initial design of the Switching System and the entire FXR staff for its helpful input.

References

1. B. Kulke et al., "Design of a 20 MeV, 4 KA Linear Induction Accelerator," 1980, IEEE International Conference on Plasma Science (May 1980).
2. G. E. Vogtlin and R. W. Kuenning, "Computer Models in the Design of FXR," Fourteenth Pulse Power Modulator Symposium, (June 1980).
3. H. B. McFarlane and K. Kihara, "The FXR One Nanosecond Jitter Switch," Fourteenth Pulse Power Modulator Symposium, (June 1980).
4. Glen R. Lamberton et al., Experiments on Electron Rings at Berkeley, Particle Accel., 5 pp. 113-120, (1973).

STATISTICAL AND FORMATIVE TIMES IN SMALL GAS SPARK GAPS*

D. D. Lindberg
R. J. Gripshover
J. W. Rice

Naval Surface Weapons Center
Dahlgren, Virginia 22448

Summary

The study of electrical breakdown in small, flowing gas spark gaps can provide data on the time to breakdown, and the temporal dependence of the current, resistance, power dissipation and energy loss during the first few nanoseconds of the breakdown. A transmission line terminated in a spark gap has been used in these studies. The finite rise time of the voltage charging the transmission line prior to breakdown of the spark gap creates problems that limit the range of spark gap parameters (especially overvoltage) for which valid data can be obtained. Two methods of easing these limitations have been developed. One is a modification of the experimental apparatus to obtain faster rise times; the other a data processing technique. Together they permit the experiment to cover a broader range of parameters where statistical times of the spark gap are as short as 10ns.

Introduction

Measuring the time dependent resistance, $R(t)$, of a spark gap during breakdown provides information on the power losses in the gap (especially important in high power switches) and provides some clues as to how breakdown initiates and grows. We have described work in determining $R(t)$ in various gases.^(1,2) The range of overvoltage applied to the spark gap has been restricted because of the difficulty in applying the overvoltage without breakdown occurring during the rising edge.

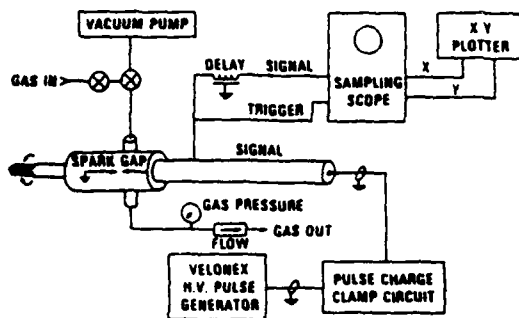


Figure 1. Original apparatus to measure $R(t)$.

The Experiment

Figure 1 shows the original experimental apparatus. The coaxial transmission line is terminated in an integral spark gap. It is pulse charged by a high voltage pulse generator. The pulse charge clamp circuit sharpens the leading edge of the charging pulse by clipping the voltage amplitude at a predetermined value. Breakdown of the spark gap changes the line termination from an open to a short. The time derivative of the current in the transmission line is

*Supported by NSMC Independent Research Program

measured using a small B (time derivative of the magnetic field) probe and a sampling oscilloscope and is recorded on an X-Y plotter. A coaxial transmission line is used because it does not significantly attenuate or radiate microwave frequencies permitting a time resolution of 50ps. The microwave frequencies involved mandate the use of a sampling oscilloscope which in turn requires a highly repeatable signal.

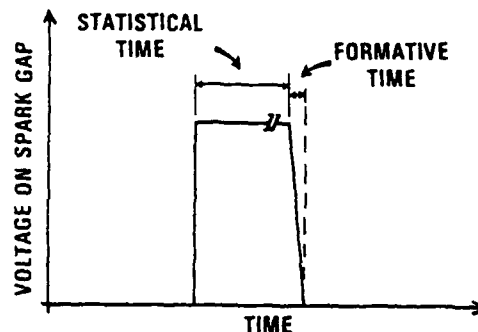


Figure 2. Definition of statistical and formative time.

The idealized voltage on the spark gap as a function of time is shown in Figure 2. We define the mean of the times between application of voltage to the spark gap and breakdown as the statistical time (t_s). It is also known as observational time or switch delay by others. The time between the start of current through the gap and the time when current reaches a constant value is called formative time (t_f).

The times to breakdown that are averaged to find the statistical time are not fixed and in fact, do have a wide range of values. Formative time is more repeatable and in general much shorter than t_s . After the transmission line is charged, and breakdown occurs, the line discharges through the spark gap. The current through the gap is determined principally by: (1) the voltage to which the line was initially charged, (2) the characteristic impedance of the line, (3) the capacitance of the spark gap and (4) the changing gap resistance $R(t)$. The charge voltage and B are measured. From B the time derivative of the current $I(t)$ and $I(t)$ can be calculated. Since the other parameters are fixed, $R(t)$ is easily calculated. Other probes could be substituted for the B probe so long as $I(t)$ is found.

The delay line in the signal path (Figure 1) allows the scope trigger circuits to be activated by the time the signal arrives. The coaxial transmission line has been used for some time³ while the sampling technique is relatively new⁴. The gas handling system allows the gap to be flushed with gas between each breakdown. The X-Y plotter driven by the sampling scope provides a large scale replica of the breakdown signal which is later manually digitized.

Limitations

Some results of this work are given in references

1 and 2. The experiment is limited in the overvoltage that can be applied to the spark gap. The problem encountered is illustrated in Figure 3 which shows the statistical time, t_s , as a function of electric field in the gap for nitrogen.

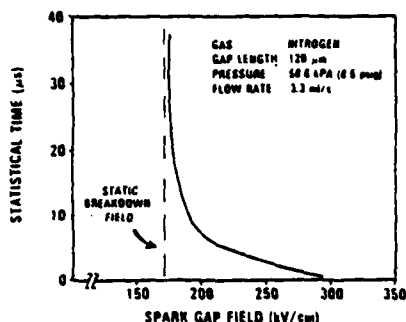


Figure 3. Statistical time as a function of spark gap electric field.

As the electric field decreases, t_s becomes longer and asymptotically approaches the static breakdown field (E_s). For the small nitrogen-filled gap used here, E_s is about 167 kV/cm. Small gaps, as shown, typically have statistical times that vary from tens of microseconds to nanoseconds as the overvoltage is increased. The measurement of formative time becomes more difficult as statistical time becomes less than one microsecond with the original system. Some time is required for the charging pulse to charge the transmission line to its final value. With the high voltage pulse generator and clamping circuit used, this rise time (t_r) is 1 to 2 μs depending on the final charging voltage. When $t_r \approx t_s$, breakdowns frequently occur on the leading edge of the voltage pulse. For the gap described in Figure 3, overvoltages were limited to $E < 2E_s$. This is a severe limitation since spark gap switches are generally highly overvolted.

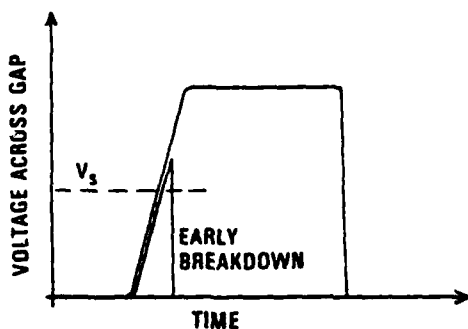


Figure 4. Early breakdown of spark gap compared to normal breakdown.

Two voltage pulses applied to the spark gap are shown in Figure 4 which stresses the rise time of the pulse. One pulse reaches a maximum value and holds that voltage on the gap until breakdown occurs. After the second pulse exceeds the static breakdown voltage (V_s) and before final amplitude is reached, the gap prematurely breaks down. Early breakdown can always occur but is rare if $t_s \gg t_r$.

The effects of early breakdown are unusually harsh in this experiment because a sampling scope is used. The voltage to which the transmission line is charged when breakdown takes place is directly proportional to the current that flows. Figure 5A shows two current waveforms that would flow in a

transmission line charged to two different voltages.

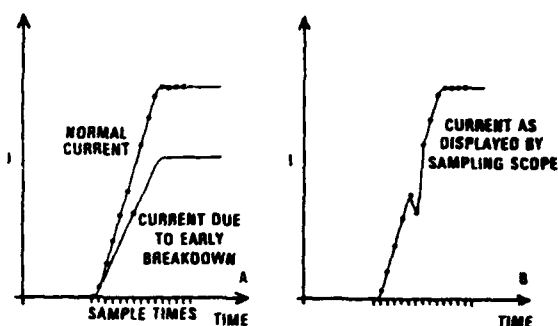


Figure 5. Effects of early breakdown on sampled data.

The normal current flows when the line is charged to the value set by the pulse charge clamping circuit; the lower current results when early breakdown occurs. Thus early breakdown causes current amplitude jitter. Fourteen sample points are represented by circles. If the repetitively charged spark gap breaks down normally six times, once at some early time, and seven times more at the usual voltage, the samples shown would be obtained. The output of the sampling scope would be as shown in Figure 5B. In the actual experiment, sampling is much more frequent but the results are comparable for the same ratio (~10%) of early breakdown. Also, since the ratio of early breakdowns is determined by the nearness of t_s to t_r , changing the number or density of samples taken does effect the results, but does not eliminate the error.

If the time interval between samples is short (and many samples are taken), early breakdowns will have occurred in almost every region on the composite curve. The result is a blur or a very noisy waveform. As the sample interval is increased Figure 5B is approached.

Improvements

The most straightforward way of reducing early breakdowns is to reduce the rise time of the voltage applied to the gap. As t_r becomes smaller compared to t_s , the probability of early breakdown becomes more remote. The t_r , typically 1 μs, provided by the high voltage pulse generator and clamping circuit can be shortened. A goal of having $t_r < 10$ ns was set after some preliminary experimentation showed (see Figure 3) how strongly t_s was dependent on overvoltage. The form of this dependence is also of interest.^(5,6) A second approach is to gather and process the data so as to minimize the effects of a few early breakdowns that statistically do occur. To do this the sampling scope was modified to be computer controlled.

Decreasing Rise Time

The strong dependence of t_s on overvoltage means that a rise time of 10 ns or less is needed to significantly increase the experiment's range. A peaking spark gap is a traditional method of decreasing rise time and is fairly easy to implement. The voltage rise on the peaking spark gap must be considered so the problems described do not now fall on the peaking gap. A hydrogen thyratron is therefore used as a switch to apply voltage to the peaking gap with about 100 ns rise time. This apparatus is illustrated in Figure 6.

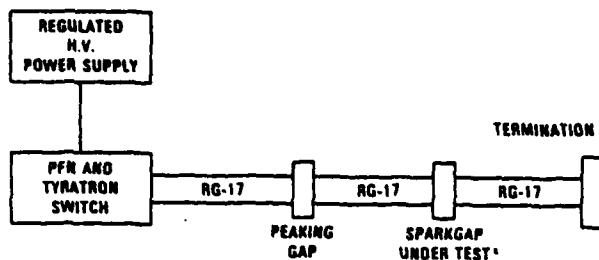


Figure 6. System to reduce risetime

A pulse forming network (PFN), charged by a regulated high voltage power supply, is discharged into a section of RG-17 (now RG-218) coaxial cable. This three-meter cable section is connected to a one-meter section by a peaking spark gap. The one-meter section of cable is connected through the test spark gap to a third piece of RG-17 which is terminated in its characteristic impedance (50Ω). The thyatron launches a voltage pulse with a rise time of less than 100ns into the first section of cable. The spacing and pressure of the peaking spark gap is set so that the gap's t_b is much greater than the 100-ns t_r . (Essentially the overvoltage on this gap is made small). Breakdown of the peaking gap launches a voltage pulse into the middle section of RG-17. The rise time of this pulse is the formative time for breakdown in the peaking gap and is less than 1ns.

Embedding both the peaking spark gap and the test spark gap in the coaxial line provides the microwave frequency response needed to maintain the fast rise time. Using a large cable (diameter = 22.1 mm) provided space to hold-off voltage when the dielectric was removed at the spark gap electrodes.

Data Processing

Regardless of how fast the risetime of the charging pulse is, there is a statistical probability that the spark gap will breakdown early. If $t_r \ll t_b$, the probability of early breakdown is small, but generally not insignificant. Therefore each set of sampled values will likely contain some spurious points. Figure 7A shows the current through the spark gap as a function of time for three breakdowns. The current waveforms are superimposed so the sample times and values can be compared. The effect of the one early breakdown is shown. If several values are averaged at each sample time, the effects of a relatively few early breakdowns can be significantly reduced (Figure 7B).

Since a greater number of breakdowns now need to be observed, a greater number of early breakdowns will be seen. The effect of an early breakdown is, however, less severe at any single time position. Effectively, the error has been spread over the entire waveform. Since the shape of the waveform is more important than the small amplitude error introduced to all points, a more accurate $I(t)$ is obtained. Noise in the measurement system covers the slight ripple introduced. The number of data samples averaged at each sample time depends on the ratio of early breakdowns to all breakdowns. If 1 in 10 breakdowns is early, then 10 should be averaged to sufficiently minimize the error. The ratio of early to normal

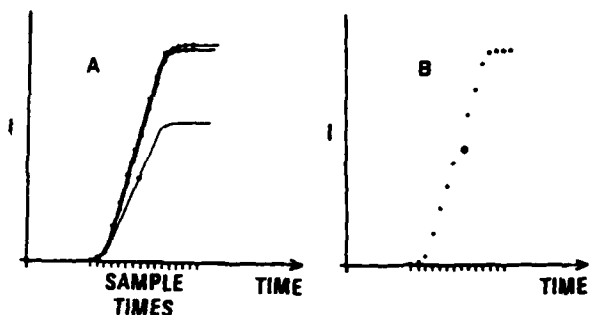


Figure 7. Reducing effect of early breakdown by averaging many waveforms.

breakdowns is related to how close t_b is to t_r , but the functional dependence is not known.

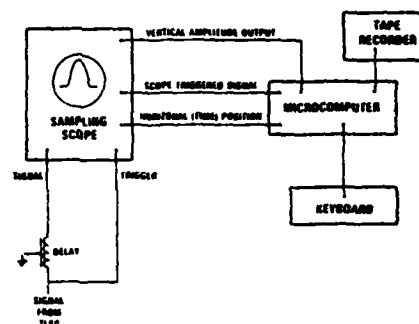


Figure 8. Microcomputer control of sampling oscilloscope.

To implement this averaging scheme a microcomputer is used to control the sampling scope. (Figure 8). The computer determines the sample time for each datum and finds the arithmetic average of the data at this time position. Sample time is simply the time between the triggering of the scope and the time the input signal is sampled. It can also be thought of as the horizontal position, on the scope face, of the sampled signal. By controlling the sample time the computer can collect several samples at each point on the waveform. The number of samples collected is controlled by inputs to the computer. Preliminary work indicates an average of about 10 breakdowns at each time position reduces errors to the system noise level. The scope triggered signal is used by the computer to determine when a sample has been taken.

Since noise about the trigger point makes precise overlaying impossible, the scheme of averaging the data as the waveform is being generated is more accurate than overlaying and averaging several waveforms generated from the sampled data. Effectively, a new source of error is introduced by the overlaying procedure.

The microcomputer and the cassette system used to record data have additional benefits. The on-line analog-to-digital conversion is more precise than the previously used manual system and all data, gas species pressure, etc. can be recorded on the tape. Since the computer, for a given time resolution and number of samples to be averaged, always

requires the same number of breakdowns, the test runs are far more uniform.

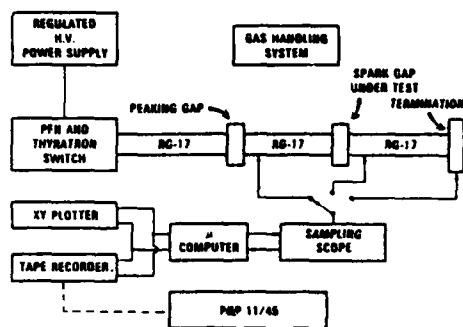


Figure 9. Experimental equipment overview.

Revised Experiment

The overview shown in Figure 9 incorporates changes in three major areas: the pulse charging system, the transmission line and test spark gap, and the data collection system. The rise time of the voltage applied to the test spark gap has been reduced three orders of magnitude, from over 1 μ s to less than 1 ns. A two-step process using first a thyatron and a peaking spark gap accomplishes this.

The faster rise time accentuates some problems. Because the formative time of the peaking gap is the leading edge of the voltage, the leading edge has approximately the same waveform as the expected signal. Care must be taken to separate the two. This is the principal reason for changing from a spark gap that shorts the transmission line to one that connects it to an additional section of transmission line. The signal probes are thus isolated from the charging voltage. The capacitance of the test spark gap passes some current before breakdown but it is small compared to the current after breakdown.

Three types of measurements are used: δ probes, capacitive divider probes, and the attenuated transmitted signal. The δ probes must be very small to have the required frequency response and they are difficult to calibrate. For these reasons capacitive divider probes are built into both the peaking spark gap and the test spark gap to supplement the information from the δ probes. As mentioned above, the final section of transmission line is terminated in its characteristic impedance, but voltage across the load can still be measured by using 50 Ω attenuators.

The introduction of a microcomputer allows better control of the sampling scope as described above and is a data logging system. Aging of the spark gap has a marked effect on its characteristics. The computer allows test runs to be precisely repeatable, down to the number of breakdowns observed. The effects of aging are thus much easier to ascertain.

The gas handling system and data flow have been changed only slightly. Gas must now be supplied to two spark gaps at independent pressures and flow rates. Different gas species will also be used, with dry air normally in the peaking gap.

Data flow is simplified since the manual digitizing of data is now done by the analog-to-digital converters in the microcomputer. Using magnetic tape in cassette form to store data is very convenient and should reduce transcription errors. The data on the cassettes is entered into a PDP-11/45 for further processing. A fast Fourier transform is used to compensate for the frequency dependence of the attenuation found throughout the system. The signal waveform at the test spark gap can thus be reconstructed. From this data the current in the transmission line is found and finally $R(t)$ calculated. The time resolved power and energy losses are then directly available.

References

1. W. K. Cary, Jr., J. A. Mazzie, IEEE Trans. Electron Devices, ED-26, 1422, 1979.
2. W. K. Cary, Jr., D. D. Lindberg, J. W. Rice, IEEE 2nd International Pulsed Power Conference, Digest of Papers, p. 114, 1979.
3. R. C. Fletcher, Phys. Rev., 76, 1501, 1949.
4. T. P. Sorensen, V. M. Ristic, J. Appl. Phys. 48, 114, 1977.
5. E. E. Kunhardt, W. W. Byszewski, Development of Electrical Treakdown in Dense Gases, to be published.
6. K. R. Allen, K. Phillips, Proc. Roy. Soc., A278, 188, 1964.

DESIGN AND PERFORMANCE OF A HIGH REPETITION RATE
SPARK GAP SWITCH AT 50-kW POWER LEVELS*
J. T. Naff, Richard J. Sojka,** and Edward P. Zeehandelaar
Physics International Company
San Leandro, California 94577

Summary

Operation of a pressurized air, vortex-flow spark gap switch is reported for repetition rates greater than 1 kHz for 20-kA current pulses lasting less than 100 ns. Low jitter operation (less than ± 5 ns absolute) has been achieved in a 36-J/pulse switching application.

The design of the spark gap is discussed in terms of electrode and insulator heating, switch recovery, cooling requirements, gas flow geometries, electrode materials, electrode shapes, and erosion.

Switch performance using a 2- Ω , 25-ns double transit time Blumlein pulse forming line at 50 kV and 1850 pulses/s is described. The PFL was capable of delivering 26 J/pulse into a matched load at a maximum voltage of 85 kV. Spark gap erosion and gas heating losses limited switch life and circuit output energy, respectively. During a 16 million shot test the average spark gap erosion was approximately 1 μ g per mC. Measurements of circuit efficiency and flowing gas temperature rise indicated that 25 percent of the energy stored in the PFL dissipated as heat.

Testing indicates that performance can be improved by lowering resistive phase losses and reducing electrode erosion. Continuing work will be reported.

Introduction

In this paper we describe the operation of a gas-insulated vortex-flow spark gap at 50-kW average power levels and at a repetition rate of 1850 pulses/s. Many of the design and engineering problems encountered during the development of this spark gap are described, including electrode erosion, gas heating, and circuit efficiency.

The performance of spark gaps in single-shot pulsed power applications is well known. These devices are capable of high voltage, high peak current, and high di/dt switching performance. They are also adaptable to various geometries (i.e., coaxial gaps, rail gaps, etc.). For high repetition rate operation (> 100 pulses/s), spark gap performance is thought to be limited by spark gap voltage recovery and electrode erosion.

Operation of high repetition rate spark gaps depends on numerous parameters (i.e., gas flow rates and pressure, peak currents, charge transfer, etc.) that are related to the complex time history of the arc physics. Techniques for improving spark gap switch life and efficiency, and suggestions for pinpointing the limits of high repetition rate spark gaps are also discussed.

Switch Design

The tested repetitive spark gap switch uses vortex flow to provide switch voltage

recovery and gas cooling. Air flow in the switch is accomplished with air tangentially injected into the discharge region, as shown in Figure 1. The main advantages of this vortex-flow design are protection of the acrylic insulators due to air flow tangential sweeping, good heat transfer and arc thermal recovery due to vortex turbulence, and a field-free exhaust region in the main electrodes, which is advantageous for switch recovery.

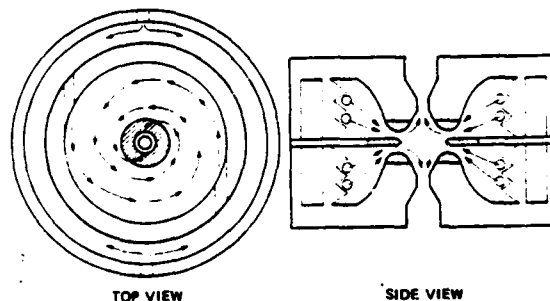


Figure 1 Design of vortex-flow spark gap switch.

The switch consists of two annular electrodes with a thick (approximately 3/4") midplane trigger electrode. A UV illuminator is installed in the thick midplane electrode to ensure low jitter switch operation. The electrode tips are fabricated with K-25 metal, a machinable, copper-infiltrated, tungsten composite manufactured by Metal Works Plancee of Austria. The switch is designed to operate at voltages of 50 kV and pressures as high as 90 psig. Figure 2 shows the fabricated switch that was installed in a low-inductance ground-return casing for operation in the existing test facilities at Physics International Company.

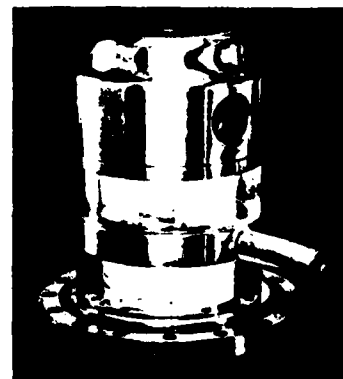


Figure 2 Fabricated spark gap switch.

Testing and Performance

Existing facilities used for spark gap switch testing included the following:

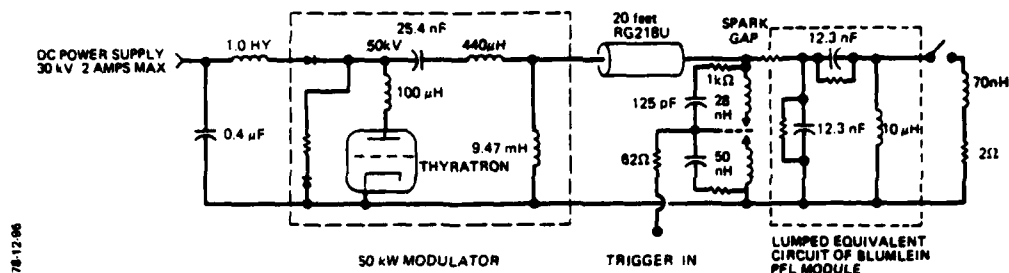


Figure 3 Electrical schematic of modulator and Blumlein PFL test circuit for spark gap switch testing.

- 100-kW power supply and modulator
- Low-impedance Blumlein PFL test circuit
- Peaking spark gap, dummy load, and auxiliary cooling systems
- Spark gap trigger circuit
- Spark gap air flow systems
- Diagnostics for measuring necessary voltages, currents, temperatures, pressures, and flows

The erection of the 2-Ω, 25-ns (double-transit-time) Blumlein PFL circuit shown in Figure 3 was accomplished with the test switch. Detailed operation of this circuit is described elsewhere.² Triggering of the spark gap is accomplished with a 1-kV/ns voltage pulse reaching a peak of 75 kV. A schematic of the spark gap trigger circuit appears in Figure 4.

The spark gap switch was tested at a 1-kHz repetition rate for 11 million shots at the 33-kW power level. The gap was operated at as high as 1850 pulses/s, the repetition rate limit of the trigger circuit. The 1-kHz performance is summarized in Table 1.

Table 1 1-kHz switch performance.

Voltage holdoff	52 kV
Peak current	20 kA
Current pulse duration (half-sine)	98 ns
Total PFL switching inductance	78 nH
Switching delay (trig in to PFL volts out)	48 ns
Delay time jitter	< ± 5 ns abs
Switch energy dissipation (Energy loss/energy stored in PFL)	
Initial	20%
11 million shots	29%
Average erosion rates	
Cathode	0.83 μg/m Cb
Anode	1.0 μg/m Cb

Switch energy dissipation (ED) was determined from the formula

$$ED = \frac{0.32 \times \text{Flow Rate (SCFM)} \times (T_{\text{OUT}} - T_{\text{IN}})}{\text{Repetition Rate}}$$

where the switch inlet and outlet temperatures are in degrees Fahrenheit. Switch energy dissipation increases with the number of shots. The increase of electrode gap spacing caused by erosion in turn increases this energy dissipation. The erosion rates indicated in Figure 5 were arrived at as a result of examination of the electrode tip profiles. The total switching inductance cited in Table 1 includes 48 nH for the spark gap and 30 nH for the transition section between the spark gap and PFL.

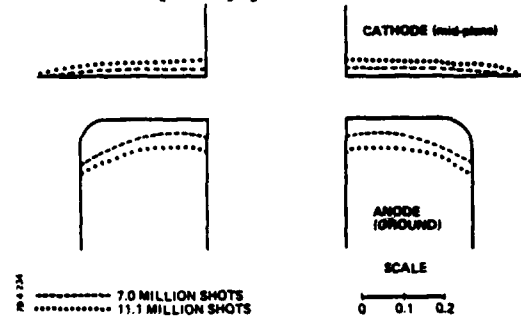


Figure 5 Erosion profiles for the mid-plane cathode and main electrode anode (ground) during an 11.1 million shot test.

The switch performance was judged in terms of the PFL gain, defined by

$$\text{Gain} = \frac{\text{Erected PFL Output Volts}}{\text{PFL Charging Volts}}$$

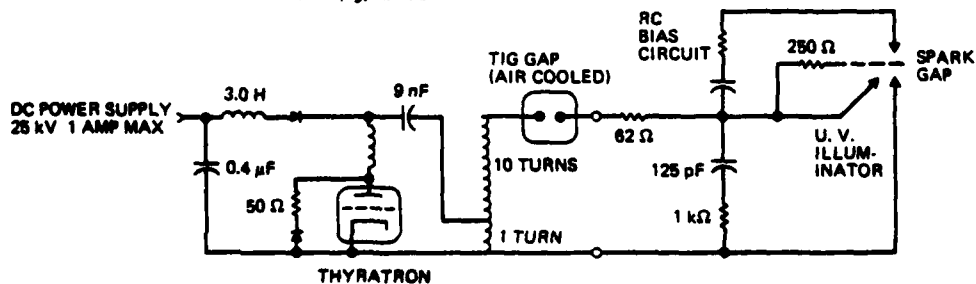


Figure 4 Electrical schematic of spark gap trigger circuit.

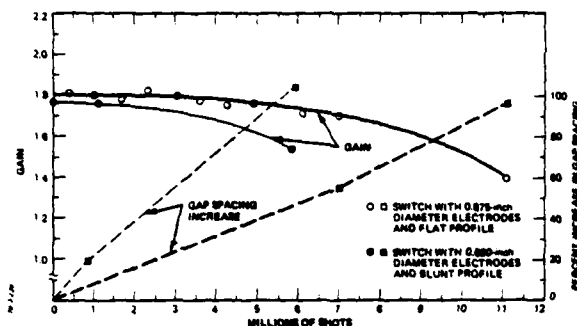


Figure 6 Gap spacing increase and PFL gain performance during 1000-pps testing.

Figure 6 shows the drop-off in gain due to the increase in gap spacing and switch energy dissipation over the 11 million shot life test.

During testing, the switch air flow was increased until negligible prefires were observed on an oscillographic pulse charging waveform.

Spark gap airflow and inlet pressure were adjusted between 77-115 SCFM and 45-90 psig during 1-kHz testing. Typically, the switch inlet pressure was constant at 65 psig for the first 7 million shots. As the gap spacing increased, reduction of the switch pressure was required to maintain a negligible misfire rate. The pressure drop across the switch, shown in Figure 7, was constant over the range of gap spacings encountered (0.085 to 0.200 inch per side).

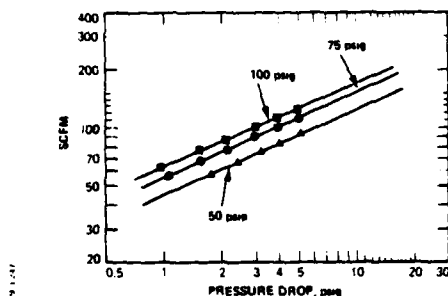


Figure 7 Pressure drop versus air SCFM for spark gap switch.

Technical Results and Issues

The spark gap switch tested is limited by electrode erosion and switch energy dissipation. The erosion rates reported here are larger than those reported previously^{3,4} (10^{-3} g/Cb as compared to 10^{-5} g/Cb). The use of high-speed gas flow could account for this difference. The erosion rates previously reported are primarily for large charge transfers (20 mCb - 10 Cb) and for long current pulse durations (20 μ s - 200 μ s). Gap erosion rates have received little attention in terms of the relatively new high-power switching requirements of greater than 20-kA and less than 100-ns pulses. Besides limiting the gap life, erosion causes a gap

spacing increase which in turn increases gap heat dissipation. This gap increase can be minimized by using larger-diameter electrode tips or servo-controlled movable electrodes to keep the gap spacing constant. Gap lifetime can be increased by a factor of 3 to 5 using a gap design with a smaller initial gap spacing and larger-diameter electrodes. While the physics of spark erosion are still not completely understood, calculations of erosion rates derived from electrode hot spot formations⁵ indicate that electrode cooling can reduce erosion.

A major part of the gap heat dissipation reported here is attributed to resistive phase losses⁶ incurred when a portion of the stored energy is being converted into heat, etc., in the expanding spark channel. For the given PFL switching impedance and spark gap geometry, the resistive phase time constant is 7 ns, and the expected losses are 2 J/pulse. The gas heating measurements and PFL output waveforms indicate a 7-J/pulse dissipation. The experimentally derived heat dissipation consists of resistive phase losses and arc I^2R losses which persist until the arc quenches. Accurate measurements of the time-resolved power flow in the gap must be made to determine the source of these losses. Resistive phase energy dissipation can be reduced by either decreasing gap spacing (i.e., increasing the gap operating field strength), or by providing multichannel switch operation.

No attempt was made to determine the voltage recovery characteristics of the spark gap as a function of airflow. During testing the flow rate was maintained between 15 and 20 CFM. At this flow rate, the interelectrode region is flushed every 0.25 ms. The highest repetition rate attained was 1850 pulses/s at a 61-kW power level. This repetition rate represents a limitation of the spark gap trigger circuitry. The repetition rate limit of this spark gap for these pulsed power levels is still unknown.

Conclusions

Operation of a > 1-kHz repetition rate vortex-flow spark gap at 50-kW power levels has been described. Electrode erosion limits this device in terms of lifetime (11 million shots) and gap heat dissipation caused by gap spacing increases (20-30 percent of the stored PFL energy). Work is continuing to increase the reliability of these gaps for greater than > 20 kA, 50 kV, and less than 100 ns pulses. Currently, a spark gap with water-cooled electrodes is being constructed that could minimize erosion in these devices. In addition, programs underway at Physics International Company are attempting to understand the basic physics of fast-recovery high repetition rate spark gaps, and we are developing techniques for improving their performance in terms of long life and improved circuit operation and efficiency.

References

*Part of this work was supported by the Rocketdyne Division of Rockwell International.

**Present address: GTE-Sylvania, P.O. Box 188, Mountain View, California 94042.

1. T. R. Burkes, et al., "A Critical Analysis and Assessment of High Power Switches, Volume 1," NP30/78, Naval Surface Weapons Laboratory, Chapter IV (September 1978).

2. R. Sojka, High Frequency Spark Gap Switch and PFN Development, PIIR-9-79, Physics International Company (April 1979).

3. R. Petr, D. Barret, and T. R. Burkes, "Spark Gap Erosion Results," Digest of

Technical Papers, 2nd IEEE International Pulsed Power Conference, pp. 308-310 (June 1979).

4. G. S. Belkin and V. Ya. Kiselev, "Electrode Erosion in Pulsed High Current Discharges," Soviet Physics - Technical Physics, Volume 2, pp. 280-283 (1966).

5. F. Llewellyn Jones, "Electrode Erosion by Spark Discharges," Brit. J. of Appl. Phys., Vol. 1, No. 3, pp. 60-65 (1950).

6. J. C. Martin, Switching Notes , No. 10, AWRE (unpublished) (1970).

SPARK GAP ELECTRODE EROSION DATA

D. M. Barrett, R. A. Petr, T. R. Burkes
Electrical Engineering Department
Texas Tech University
Lubbock, Texas 79409

Summary

Electrode erosion has been found to be dramatically affected by the acoustic properties of the electrode material and electrode configuration. This paper describes experimentally derived data generated to demonstrate this phenomena. The tests were conducted at low pressure with cylindrical rod electrodes arranged in a parallel plane geometry. Materials investigated are aluminum, brass, and moly. The electrical parameters are square pulses of 10 μ sec. duration rep-rated at 10 pps. Pulse currents are in the range of 1 Ka. The results indicate that, in some cases, erosion can be affected by approximately an order of magnitude simply by varying the electrode length.

Introduction

In recent years, large pulsed power systems have become increasingly important to both industry and scientific efforts. Although, there have been many advances in electron tubes, thyratrons and solid state switching, the spark gap remains in the spotlight as a candidate as a switch in many applications.

The major limiting factor of a spark gap's life time is directly related to the erosion characteristics of the electrode material. Various investigations⁽¹⁾ have reported that erosion results are often inconsistent. The objective of this investigation is to correlate the erosion characteristics to the acoustical properties of the electrode material. Such a correlation may account for some of the afore mentioned inconsistencies.

In a recent paper⁽²⁾, it was shown that the establishment of an arc on the surface of an electrode will result in an acoustical compression wave being launched into the electrode material. As the wave propagates in the electrode, it will be reflected at interfaces where a significant change in acoustical impedance exists. If the reflected wave appears at the electrode surface while the spot is still molten, a portion of the material may be ejected, which would result in increased erosion. A series of experiments were conducted to verify that erosion is a function of the acoustical properties of the electrode material. The experiments were conducted at low pressure (< 50 microns) with peak currents of one kiloamp. The spark gap was over-volted by a 10 microsecond rectangular pulse, so that the anode and cathode are well defined.

The Test Circuit

The test circuit is shown in Figure 1. A type E pulse forming network that was used in previous studies⁽³⁾ was modified to produce a

10 microsecond pulse with an impedance of 6 ohms. The pulse has a rise and fall time of approximately 750 nanoseconds.

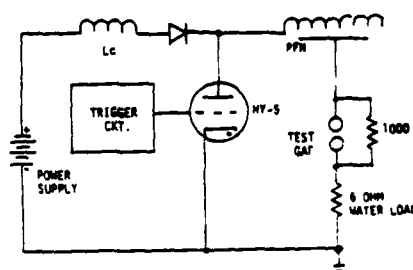


Figure 1. Spark Gap Test Circuit

Electrode Test Fixture

Basically, the test fixture consists of an acrylic cylinder which is held in place between two aluminum end-plates. The electrode samples are held in place by a fixed collet and an adjustable collet that is free to move on an aluminum shank. The gap length between the two sample electrodes may be varied with the use of a micrometer mounted on the exterior of the chamber. The test chamber is vacuum tight and pressures as low as 10 microns may be maintained within the gap. The electrodes are placed in the collets which when tightened, grips the electrodes securely. The cross-section of a collet is shown in figure 2. The gripping action of the collet constitutes a reaction mass which will cause a reflection of the acoustical waves within the electrode.

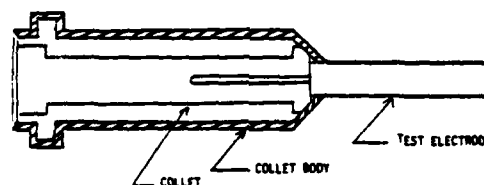


Figure 2. Collet Cross-Section

Experimental Procedure

For the series of test conducted, aluminum, brass and molybdenum were used as the test electrodes. Each electrode consists of a cylindrical rod arranged in a parallel-plane geometry. The ends of the electrodes are machined flat. The electrodes are then ultrasonically cleaned and weighed within one tenth of a milligram.

After an electrode is weighed, it is placed into the collet which clamps the electrode in position. Electrodes of various

lengths are placed in the gap. Each electrode undergoes 75 coulombs of charge transfer, after which the electrode is removed from the gap and weighed again. The gap length was maintained to be equal to the diameter of the electrode sample.

Erosion Results

The erosion results have been normalized with respect to the total charge transfer and are presented in gram per coulomb loss versus length of the electrode. The properties of aluminum, brass and molybdenum that are important to this study are shown in Table I.

Table I. Properties of various materials.

Material	Density	Velocity of Sound
Aluminum	2.7 gm/cm ³	5 mm/ μ s
Brass	8.6 gm/cm ³	3.5 mm/ μ s
Molybdenum	10.1 gm/cm ³	5.4 mm/ μ s

Figures 3 and 4 illustrates the erosion characteristics for the aluminum anode and cathode respectively. It is apparent from these plots that the erosion is a function of the length of the electrode. The rate drops dramatically between 10 and 15 millimeters for both the anode and cathode. Table II indicates how many reflections occur within the 10 microsecond pulse for a given electrode length. It is assumed that a molten spot exits on the surface of the electrode for the duration of the pulse. The erosion characteristics of the electrode correlate very well with the number of reflections calculated.

Table II. Number of reflections for each electrode length aluminum
 $V_T = 5.0$ mm/ μ s.

Electrode length	Number of reflections within a 10 μ s pulse
5 mm	5
10 mm	2
15 mm	1
20 mm	1
25 mm	0
30 mm	0
35 mm	0

Similarly, the erosion rate for brass varies with the length of the electrode as shown in figures 5 and 6. Both the anode and cathode have similar shaped erosion characteristics, although the cathode generally has a higher erosion rate as would be expected when there are multiple reflections within the electrode, a higher erosion rate was indicated as was the case with aluminum.

Figures 7 and 8 are the erosion results for molybdenum electrodes. Both the anode and cathode erosion rates show very little dependance on the length of the electrodes compared to other material. Upon examination of the experimental apparatus it was discovered that the collet did not constitute a

sufficient reaction mass to cause a significant reflection in the molybdenum electrode. As a side note, it was observed that a significant amount of the molybdenum cathode material had been deposited upon the anode.

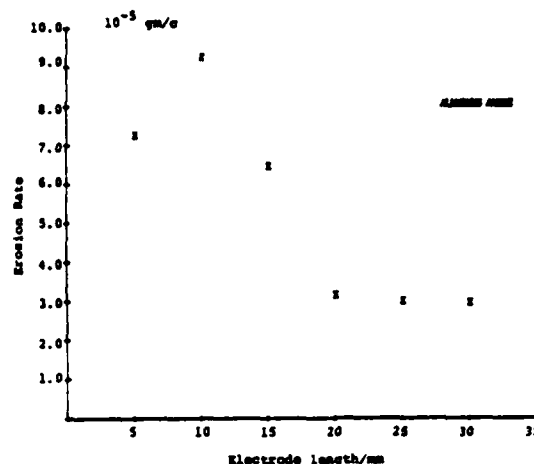


Figure 3. Aluminum Anode

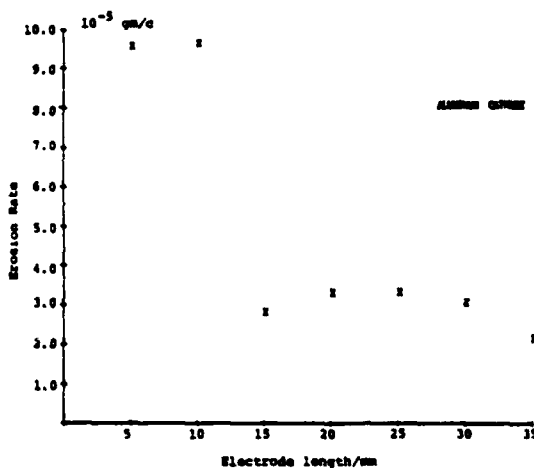


Figure 4. Aluminum Cathode

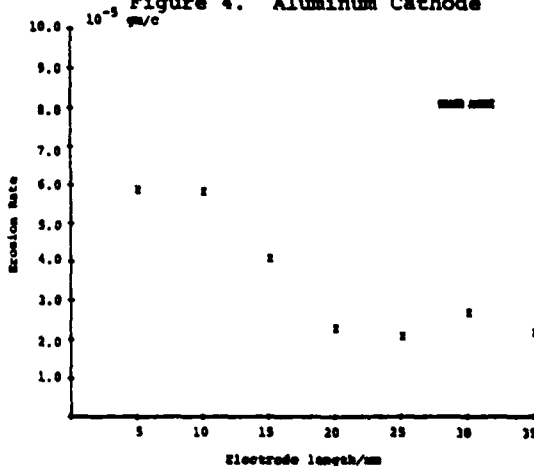


Figure 5. Brass Anode

Conclusions

Although, the experiment described in this paper is relatively simple, the results that have been obtained clearly indicate that the electrode erosion rate is related to the acoustical properties of the material. These results are by no means conclusive, but it is hoped that they will provide incentive for additional research in erosion related to acoustical phenomena. Such research will provide data that can be incorporated into spark gap design in the future.

References

- [1] T. Kubono, J. Appl. Phys., Vol. 49, p. 3863, 1978.
- [2] R. Petr and T. Burkes, "Acoustical phenomena in erosion of spark gap electrodes", accepted for publication in J. Appl. Phys. Letters.
- [3] R. Petr, D. Barrett and T. Burkes, Digest Tech. papers of 2nd IEEE Pulsed Power Conference, Lubbock, Texas, p. 308. June 1979.

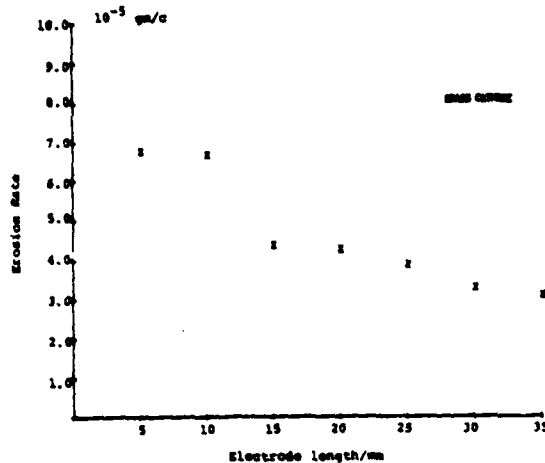


Figure 6. Brass Cathode

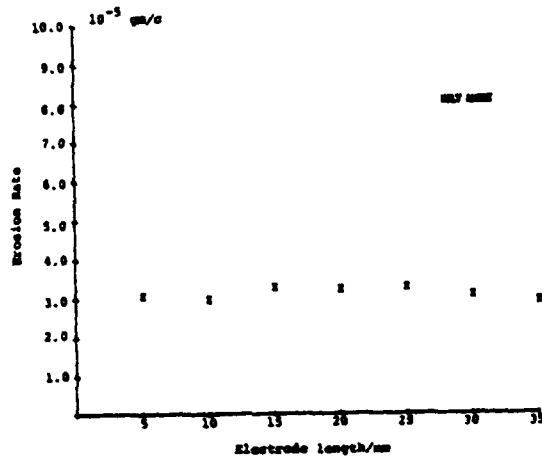


Figure 7. Molybdenum Anode

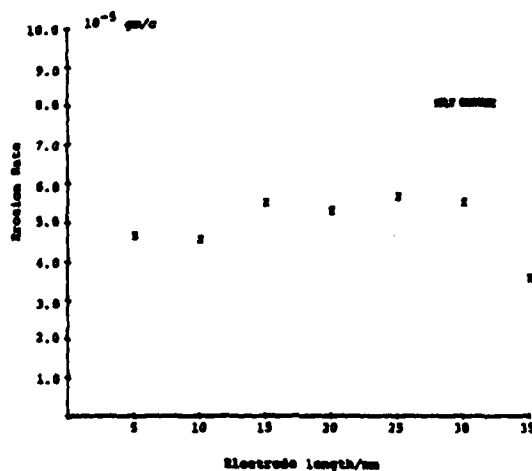


Figure 8. Molybdenum Cathode

LASER-TRIGGERED SWITCH MODIFICATION TO VEBA*

J. R. Bettis,** J. K. Burton, R. K. Parker,

M. Herndon, and A. K. Kinkead

Naval Research Laboratory
Washington, DC

and

A. H. Guenther and E. J. Kobiela

Air Force Weapons Laboratory
Albuquerque, NM

Summary

A high-current relativistic electron accelerator has been modified to permit command output switching. As originally designed, the generator pulse forming network (PFN) had an unbalanced water Blumlein with the output switching provided by a self-closing water switch between the inner and intermediate conductors. The switch region of the Blumlein has been redesigned to replace the self-closing water switch with a laser-triggered gas switch. The switch conversion not only provides a command triggered output capability, but also results in significant improvements in the output waveform. Substantial improvement in the voltage fluctuation during the constant portion of the output waveform and in the shot-to-shot reproducibility of the output voltage were necessitated by the requirements of the free-electron-laser (FEL) experimentation. Switching is accomplished by a Q-switched ruby laser pulse introduced into the spark gap radially. Portions of the beam were diverted by partial reflection (internal to the central element) along two additional radial paths, from the center outward, in order to provide up to three simultaneous switch channels. The radial introduction provides a fail-safe single-channel irradiation along the opposite radius regardless of optical component alignment. Simultaneous discharge of all channels will result in a reduction of switch inductance which will reduce output voltage rise time by as much as 2/3. The designed command triggering jitter of less than ± 5 nsec has been achieved by single channel discharge. Successful operation of the switch has improved output waveform and will allow simultaneous initiation of separate high-voltage high-peak-power events.

*Work supported by ONR and NAVAIR.

**Present Address: U.S. Naval Academy.

Introduction

The Versatile Electron Beam Accelerator (VEBA) located at the Naval Research Lab, Washington is being modified to produce an intense beam free electron laser (FEL). The FEL is to be produced by the interaction of an intense electron beam and a spatially periodic magnetic field. The overlap of these two short (~ 50 nsec) events coupled with a small allowable energy spread in the electrons place the following requirements on the switch for VEBA:

1. Command triggering - so that a signal from one event could be properly delayed and used to trigger the other.
2. Jitter $< \pm 5$ nsec - to ensure maximum overlap, and
3. Multiple Channel Operation - to reduce risetime and ripple in the output voltage of VEBA.

The requirements can most readily be met by a laser-triggered, gas dielectric spark gap, or Laser-Triggered Switch (LTS).

Design Considerations

The overvolted water switch has the advantage of very short risetime. The ripple on the output voltage, however, generates a spread in electron energy which is too great to permit the required interaction necessary to produce laser output. A laser-triggered water switch would have preserved this short risetime but was ruled out because the acoustic shock carried by the water in the switch region would have made the survival of optical components very difficult. The waveform predicted by the TEMP¹ computer code for a single channel laser-triggered switch using a gas dielectric shows acceptable ripple, however, the relatively slow risetime drove the design to multiple channel switching in order to reduce switch inductance.

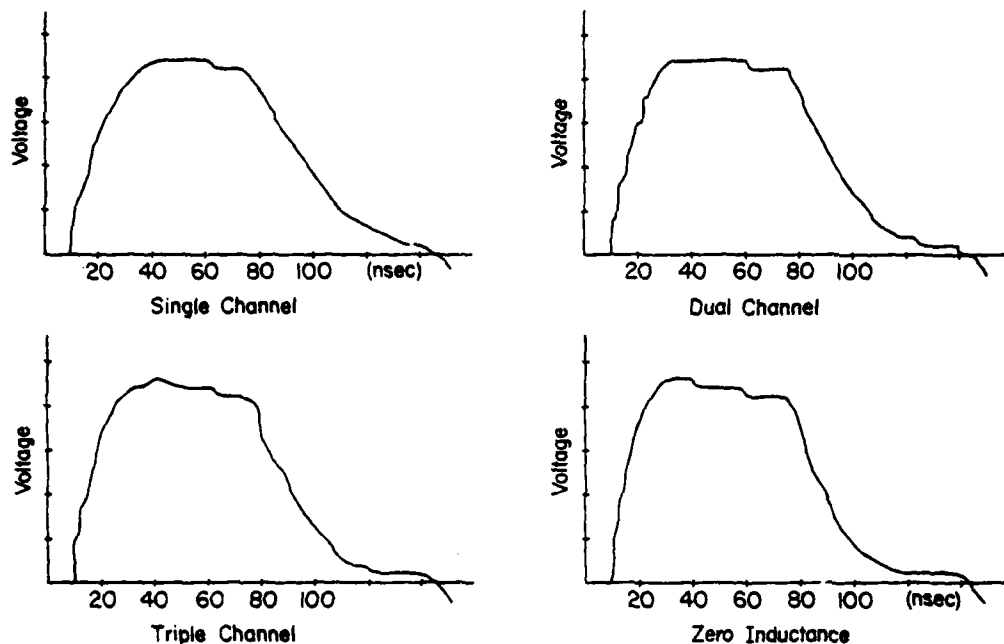


Figure 1

TEMP. Generated Voltage vs. Time Showing Risetime Reduction vs. Number of Channels

Figure 1 displays the TEMP generated waveforms for single, dual, and triple channel switches as well as a zero inductance switch. The machine-limited risetime with a gas-filled switch appears to be about 20 nsec and is obtained for two channels. The LTS was designed to accommodate up to three simultaneous channels to test the predicted limit on risetime and to better assure that at least two channels would be initiated each time.

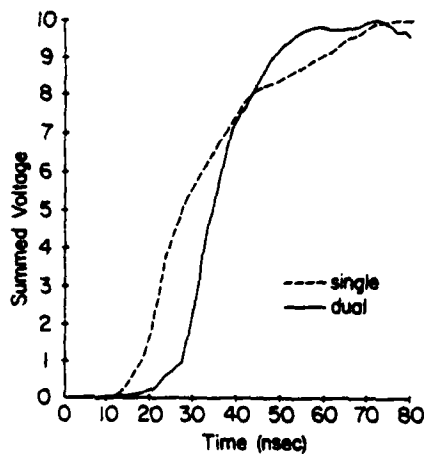


Figure 2

Digitized Traces of Single vs. Dual Channel Voltage Rise.

Unlike the axial switching schemes of most previous work² the configuration of VEBA necessitated a radial introduction of the laser beam as shown in figure 2. The beam splitting and focusing optics were therefore located in the inner electrode so as to focus the multiple laser beams on the intermediate electrode.

Timing was accomplished by initiating the slowest event (laser amplifier flashlamp) which in turn initiated the Marx gaps. A di/dt loop senses Marx erection and the suitably delayed signal triggers the optical shutter (Pockels Cell) of the laser.

Design Details

With the basic design completed the details to be specified included: electrode material and configuration, optics mounts, type of dielectric gas, and laser output requirements.

The electrodes must be easily machinable, resistant to spark erosion, and must produce copious ionization when intercepting the focused laser beam. Previous work³ has shown that stainless steel is a good choice. Because the breakdown arc is initiated at the focus of the laser beam it is possible to increase erosion resistance and ionization production by installing flush mounted tungsten buttons in the host stainless steel electrode. Future plans call for this retrofit. The electrode configuration consisted of a ring affixed to the intermediate cylinder as the target and Rogowski-like contours on the inner cylinder drilled to allow laser egress.

The laser beam is turned into the switching region through a nylon tube which forms the interface between gas and oil dielectrics. The beam is focused by 6" focal length lenses onto the intermediate electrode. A single lens provides for single-channel operation while the addition of a 50% reflecting mirror and second lens produces two switch channels. A 33% mirror and a third lens will complete the three-channel arrangement.

The dielectric gas was a 50:40:10 mixture of N_2 , Ar , and SF_6 . The switching delay varies inversely with the product of the Townsend ionization coefficient, α , and electron drift velocity, v , thus argon is used ($\alpha v \approx 150 \text{ sec}^{-1}$) even though it has a relatively small dielectric strength. Nitrogen ($\alpha v \approx 40 \text{ sec}^{-1}$) and SF_6 ($\alpha v \approx 5 \text{ sec}^{-1}$) give the required dielectric strength. It is possible, of course, to use a pure SF_6 dielectric⁵, but a large increase in laser power is needed to offset the electronegativity of SF_6 .

Based on previous work⁶ it was estimated that a minimum laser power of 100 MW per channel would be required to reliably trigger the 8.9 cm gap at maximum voltage. The laser power required varies inversely with the reduced field, E/p , in the gap. Thus, much more laser power is required to switch 0.75 MV at 108 psi dielectric pressure ($E/p = 15 \text{ v/cm-torr}$) than to switch 0.5 MV at 40 psi dielectric pressure ($E/p = 27 \text{ v/cm-torr}$). These two nominal operating conditions give 1.27 and 0.85 MV output voltages respectively due to transformer action. For preliminary, low-voltage work a laser power of 30 MW was used at a reduced field of about 27 v/cm-torr at self-breakdown.

Results

Single Channel

For a 0.7 MV output the self-breakdown of the spark gap is 0.51 MV. The gap conditions are: 41.5 psia, 8.9 cm spacing, and 800 nsec risetime on the Marx voltage. The reduced field at self-breakdown is 26.7 v/cm-torr. The laser pulse can be inserted anytime during the 800 nsec voltage rise. Table 1 shows the delay and jitter of the LTS versus the time of laser insertion. Note that at the lowest insertion time (430 nsec) the reduced field in the gap is only 14.5 v/cm-torr.

TABLE 1

Insertion Time	Output Voltage	Delay	Jitter
700 nsec	0.66 MV	84 nsec	5.5 nsec
600	0.63	93	2.1
500	0.60	124	20.7
430	0.57	193	45.4

The pressure was increased to 108 psia on the 8.9 cm gap which resulted in self-breakdown voltage of 0.7 MV or an output voltage of 1.2 MV. The gap could not be reliably triggered with the 30 MW laser pulse due to the low value of E/p ($\approx 12.8 \text{ v/cm-torr}$ at 90% of the self-breakdown volt-

age). Laser power was then increased to 115 MW (4.0 joules in 35 nsec) and a limited range of insertion times were used to produce the results in Table 2.

TABLE 2

Insertion Time	Output Voltage	Delay	Jitter
975 nsec	1.1 MV	83 nsec	6.5 nsec
920	1.01	88	9.1
875	1.07	96.5	7.9

The jitter here is worse than in the low-voltage, low-laser power case. This indicates that a minimum laser power of perhaps 150 MW per channel would be a more realistic design parameter.

Dual Channel

The beam splitter and additional lenses were installed for two-channel operation. Laser power was kept at 120 MW nominal, thus a lower switch voltage (higher E/p) was used to increase the reliability of the switching. Previous dual channel switching⁷ revealed that the two channels would share the current and thus reduce the risetime if the synchronization between channels was better than about half the output risetime. The predicted two-channel risetime is 20 nsec which means that the jitter must be better than ± 10 nsec to achieve two-channel operation. Because jitter of less than ± 10 nsec was achieved at $E/p \approx 20\text{--}25 \text{ v/cm-torr}$ with a laser power of 30 MW the prospects for dual channel switching with 60 MW per channel seemed very good.

Figure 3 is a digitized reproduction of a single channel and dual channel switching event. The risetime (10-90%) of the single-channel is

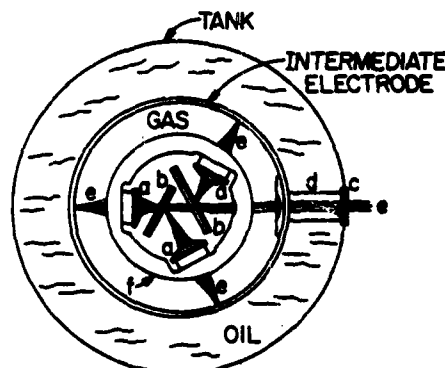


Figure 3

Radial Introduction of Laser Beam

- a. lens
- b. beam splitter
- c. window
- d. nylon tube
- e. laser beam showing focussing
- f. inner electrode

about 40 nsec while that of the dual channel is 20 nsec. Very reliable dual channel switching was produced. In addition, the dual channel LTS produced a flat waveform with less than $\pm 5\%$ ripple for 4 nsec duration.

Conclusions

Laser-triggered switching can be used to initiate multiple channels in a gas insulated, pulse-charged spark gap. Figure plans call for increased laser power to produce three channel switching at the elevated voltages needed for the FEL.

References

1. Burton, J. K., J. J. Condon, M. D. Jevnager, W. H. Lupton, and T. J. O'Connell, IEEE Proc. Fifth Symp. on Engr. Problems of Fusion Research, 1974, pp. 613-618.
2. Guenther, A. H. and J. R. Bettis, J. Phys. D: Appl. Phys., Vol 11, 1978, pp. 1577-1613.
3. Bettis, J. R., and A. H. Guenther, IEEE J. Quantum Electronics, QE-6, 1970, pp. 483-491.
4. Guenther, A. H. and J. R. Bettis, IEEE J. Quantum Electronics, QE-3, 1967, pp. 581-588.
5. Pendleton, W. K. and A. H. Guenther, Rev. Sci. Instr., 36, 1965, pp. 1546-1550.
6. See reference 2, also Guenther, A. H., R. P. Copeland, and J. R. Bettis, Rev. Sci. Instr., 50, Nov. 1979, pp. 1486-1487.
7. Guenther, A. H. and J. R. Bettis, Laser Interaction and Related Plasma Phenomena, 1971, pp. 131-171.

LASER-TRIGGERED RAIL-GAPS

R.S. Taylor, A.J. Alcock and K.E. Leopold
National Research Council of Canada
Division of Physics
Ottawa, K1A 0R6, Canada

ABSTRACT

Low energy pulses of unfocussed, coherent UV radiation have been used for the first time to initiate synchronized low-jitter multichannel breakdown in a gas insulated edge-plane rail-gap.

The test layout consisted of a pulse forming network (PFN) connected through an edge-plane rail-gap to a matched load consisting of a $\sqrt{2}\Omega$ CuSO₄ liquid resistor. A few millijoules of UV radiation produced by a rare gas halide laser was passed through a quartz entrance window and down the rail-gap axis. The gap voltage hold-off capability for μ s charging times of the PFN and for a 2 atm 90% Ar, 10% SF₆ gas mix was typically ~ 40 kV/cm. With laser triggering up to 100 channels per meter have been observed visually while the voltage across the 2 Ω load was fully erected in 10 ns. The jitter between the laser pulse and the voltage pulse across the load was ≤ 5 ns. These results were substantially unaltered when an initially high impedance laser discharge replaced the $\sqrt{2}\Omega$ load.

This technique appears promising as a simple, yet reliable method of obtaining nanosecond synchronization between an external trigger source and one or more low-inductance, high voltage rail-gaps.

INTRODUCTION

In order to switch high voltages from a low impedance pulse forming network into a rare gas halide laser or other similar low impedance loads, a low jitter, low inductance switching device is required. Present switching devices include pressurized surface spark gaps¹ or edge-plane rail-gaps with gas² or liquid³ dielectrics in addition to electrically triggered rail-gaps.⁴ However, for low jitter operation both the surface gap and the edge-plane rail-gap require very rapid charging rates while the electrically triggered rail-gap requires extremely fast high voltage trigger pulses.

A possible alternative to the above devices, especially when synchronization of many gaps is required, is the application of laser-triggered switching. In the past, laser-triggered spark gaps have achieved sub-nanosecond jitter; however, they have been limited to essentially single channel operation.⁵⁻⁸ The use of synchronous triggering and multiple independent gaps offers one approach to low inductance switching, but is considerably more complex than a single multichannel device requiring only one trigger beam.

The experiments described in this paper have demonstrated that an unfocussed beam of moderate intensity UV laser radiation can initiate multichannel breakdown in a low inductance edge-plane rail-gap with nanosecond jitter.

EXPERIMENTAL CONFIGURATION

A schematic diagram of the laser-triggered rail-gap test facility is shown in Fig. 1. The pulse forming network (PFN) consisted of a distilled water dielectric parallel plate transmission line that was pulse charged from a two stage Marx bank. By altering the inductance between the Marx generator and the line, charging times (τ_c) ranging from 0.5 to 3 μ s could be obtained. The PFN, with an inductance and characteristic impedance of 40 nH and 2 Ω , respectively was terminated through the rail-gap in a matched copper sulphate liquid resistive load. Voltage measurements on the PFN and load resistor were obtained with a calibrated copper sulphate resistive divider - high voltage probe⁹ combination with an overall risetime of ~ 1 ns. As shown in Fig. 1, the rail-gap consisted of two 50 cm long brass electrodes, one of circular cross-section, the other shaped in the form of a knife-edge. Electrode separations of 1.5

and 3.7 cms were tested with various gas mixes and over a 1 - 3 atm pressure range. The spark-gap was usually operated for ~ 20 discharges on a static fill. It was then pumped down to a pressure of a few Torr and subsequently refilled with gas.

Rare gas halide lasers¹⁰ operating at 1933 Å (ArF), 2486 Å (KrF) or 3080 Å (XeCl) wavelengths, and providing 50-100 mJ of energy in 10-20 ns duration pulses, as well as a N₂ laser¹¹ (3371 Å) producing 60 mJ, 300 ps duration pulses were used as the coherent UV sources. The beam cross-sections for the rare gas halide and the N₂ laser were 0.5 x 2 cm² and 0.1 x 0.5 cm², respectively. A sample of the incident laser radiation was directed onto a photodiode where it was detected and displayed on a fast risetime storage oscilloscope. The main beam which could be attenuated by calibrated neutral density filters was passed unfocussed through a quartz entrance window and into the interelectrode volume parallel to the knife-edge.

The number of visibly intense channels occurring in the gap was monitored for many discharges to obtain an average value N . Simultaneous monitoring of the laser and voltage pulses permitted measurements of the time delay (τ_d) between the peak of the optical signal and the time at which the voltage across the load reached 90% of its maximum value. Voltage risetimes (τ_r , 10-90% points) and the magnitude of the voltages across the PFN and the resistive load were also measured.

RESULTS AND DISCUSSION

The initial data were obtained with a KrF laser and an electrode spacing of 1.5 cm. Gases such as CO₂, N₂, He, Ne, Ar and SF₆ used alone or in mixes were tested in the switch. For $\tau_c \geq 400$ ns and without laser irradiation switch breakdown occurred in 1-3 channels. However, with KrF irradiation only pure argon or argon diluted with a small percentage of SF₆ (up to 12%) produced reliable multichannel ($N \sim 35m^{-1}$) breakdown well below the self-breakdown voltage. Fig. 2 shows a typical set of laser and voltage pulses obtained using a 2.4 atm 10% SF₆, 90% Ar gas mix. This pressure and gas mix were used for subsequent experiments. The dashed line in Fig. 2 represents the average self-breakdown voltage (V_B) of the gap. The time delay τ_d between the voltage across the 2 Ω load and the optical signal was 10 ns while the voltage risetime across the load was 8 ns. The average jitter in τ_d was ~ 3 ns while the parameter m defined as the ratio of V_B to the minimum voltage on the PFN

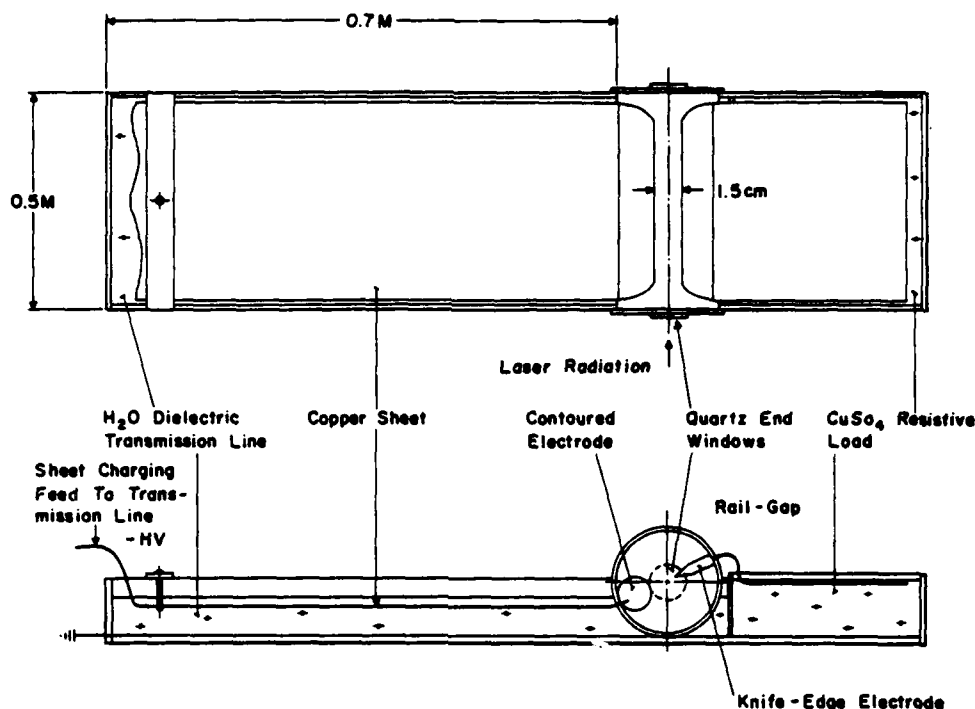


Fig.1 Schematic representation of the laser-triggered rail-gap test bed

for which significant ($N \geq 10$) multichannel breakdown occurred was ~ 2.0 .

The use of longer wavelength XeCl laser radiation produced as many as 75 - 100 channels per metre but at a reduced value of $m = 1.4$, while a shorter wavelength ArF laser produced results similar to those obtained at the KrF wavelength. It was further observed that the performance of the gap was substantially unaltered when the $\sim 2\Omega$ resistive load was replaced by an initially high impedance XeCl laser load.

Fig. 3 shows that N increases dramatically with KrF flux. For large V/V_B ratios the value of N levels off at high laser energy densities; however, for lower ratios considerably more radiation is needed to achieve multichannel gap closure. Nevertheless, the required energy densities can readily be achieved even with a small rare gas halide laser.

A series of more detailed experiments was performed using a 3.7 cm gap separation. With standard operating conditions and $t_d \sim 0.8 \mu s$ the self-breakdown voltage V_B was ~ 140 kV and reliable multichannel breakdown could be obtained for $m = 1.7$.

It was found that the voltage polarity applied to the electrodes was extremely important. Table I outlines some rather preliminary measurements of the self-

breakdown voltage as a function of electrode polarity. Both positive knife-edge configurations broke down at lower voltages than the negative edge configurations in qualitative agreement with the breakdown data observed for point-plane spark-gaps using electronegative gases.¹² Multichannel triggering was only possible when the knife-edge polarity was positive ground. This appears to be consistent with strong space charge effects in the anode region being enhanced by the large field gradients associated with the knife-edge. A positively charged edge might be expected to give similar results; however, as can be seen from Table I this configuration is considerably less useful due to its lower self-breakdown voltage.

Fig. 4 shows that t_d can be reduced by operating at high values of V/V_B . Presumably at lower voltages the avalanche process has not achieved a significant ionization level to launch very rapid streamers. If one makes the rather crude assumption that the time delay represents a streamer propagation time across the gap, then the minimum time delay of Fig. 4 corresponds to a streamer velocity of 1.2×10^8 cm/s. The time delay data for the 1.5 cm gap predicts a similar velocity of 1.5×10^8 cm/s.

Fig. 5 demonstrates that the number of channels levels off with increasing KrF energy density in similar fashion to that shown for the 1.5 cm gap (Fig. 3).

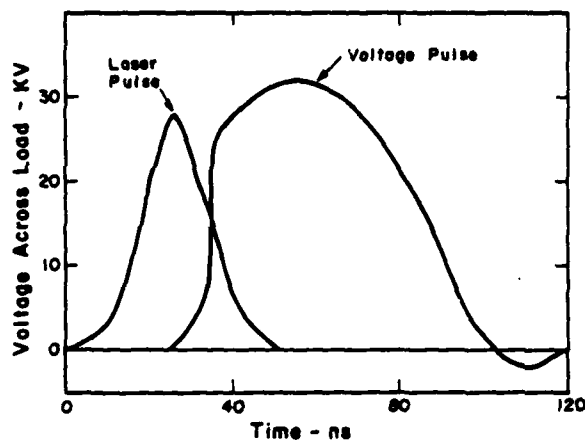
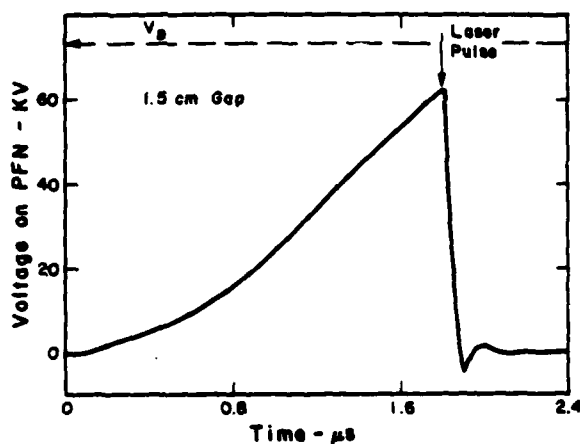


Fig. 2. Top: Voltage on PFN with laser irradiation of gap.
Bottom: Corresponding voltage across the resistive load.

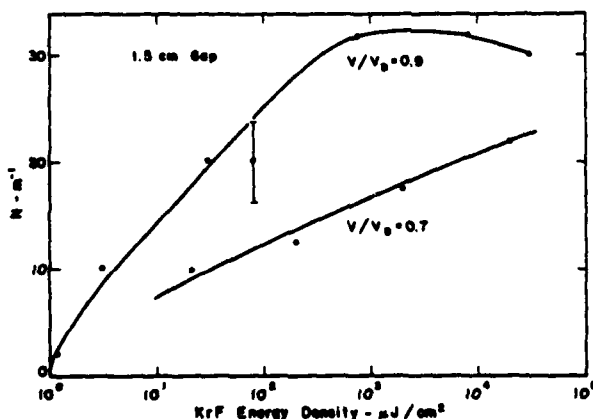


Fig. 3. Number of channels as a function of the KrF energy density. The value of t_c was 1.7 μ s.

This figure also shows that there is a corresponding decrease in the voltage risetime with increasing flux.

TABLE I
Polarity Dependence of
Self-Breakdown Voltage^a

Polarity on Edge	V_B (kV)
+ charged	85
- charged	105 ^b
+ ground	140
- ground	150 ^c

a data were obtained with a 2.4 atm 10% SF_6 , 90% Ar mix, a t_c of 0.8 μ s and with a 3.7 cm gap separation.

b gas pressure was only 1 atm.

c lower limit due to tracking on perspex walls.

Calculations of the resistive and inductive contributions to the voltage risetime were made using the empirical formulae of J.C. Martin.¹³ The calculated risetimes were a factor of two larger than experimentally observed values. However, branching of many channels near the cathode was frequently observed and may account for the discrepancy. On the other hand, calculations of the standard deviation in switch breakdown voltage underestimated the experimental deviation by ~ 2 . Nevertheless, the agreement is still quite reasonable considering the assumptions made in the calculations.

As shown in Fig. 6, increasing the gap pressure resulted in a substantial increase in N and subsequent decrease in the voltage risetime. The data were obtained under constant irradiation conditions and with $V/V_B \sim 0.8$. The self-breakdown voltage scaled as $p^{1/2}$ and, therefore, the ratio of the mean electric field to pressure (E/p) was not constant but decreased as $p^{-1/2}$. The improvement in N with higher pressures, demonstrates the importance of the field strength in obtaining good multichannelling.

GAS ADDITIVES

The possibility of using low ionization potential gas additives in a spark-gap arose from previous work on laser-induced preionization of TE-laser discharges.¹⁴ In those experiments a rare gas halide laser was used to produce sufficiently high electron densities in a TE-laser medium containing a small amount of additive to ensure uniform preionization of the excited volume. Fluorobenzene, for example (I.P. = 9.2 eV), has a strong vibronic absorption near 2500 Å and an intermediate excited state close to the KrF photon energy (5 eV).¹⁵ Efficient two step photoionization is, therefore, possible. It was anticipated that irradiation of the entire interelectrode region of a rail-gap with KrF fluences of ~ 100 mJ/cm² and with fluorobenzene concentrations of a few tenths of 1% would produce electron densities in excess of 10^{11} cm⁻³ in a 15 ns period sufficient to initiate breakdown of

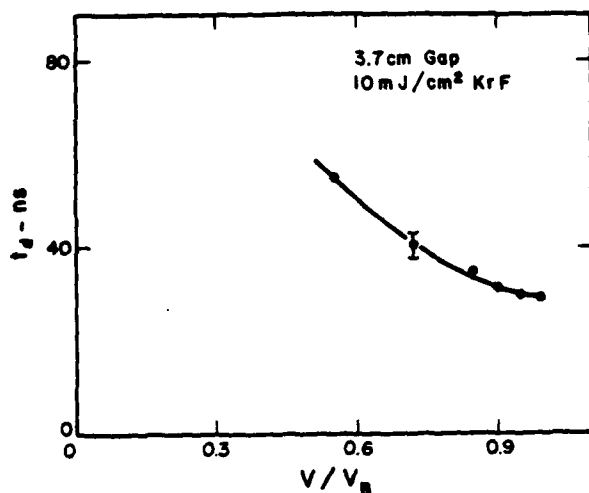


Fig. 4. Time delay as a function of the normalized operating voltage.

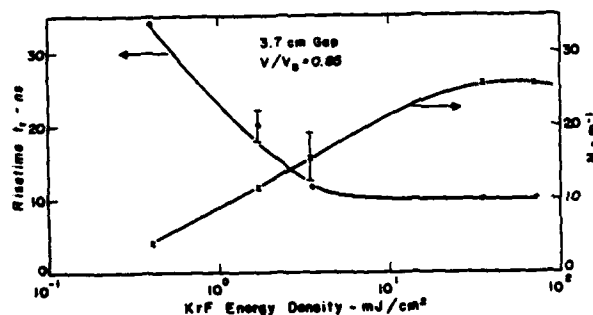


Fig. 5. Risettime of the voltage across the resistive load and number of channels as a function of the KrF flux.

the gap. Indeed, under such conditions breakdown occurred in only 1-3 channels with no temporal correlation with the laser pulse! However, by using a mask to prevent the KrF beam from irradiating the knife-edge region multichannel breakdown over the entire gap was observed. Further experiments to investigate the influence of the spatial distribution of the KrF beam with and without the presence of an additive in the gap were performed. The irradiated regions and important observations are shown in Fig. 7.

Without an additive the knife-edge region (zone 3) must be irradiated in order to achieve satisfactory performance. However, with an additive in the gap, irradiation close to the circular cross-section electrode (zone 1) yielded reliable operation although it required a higher KrF energy than in the previous case. However, as mentioned above, the presence of significant (15 mJ) KrF radiation near the knife-edge resulted in poorer rather than improved performance when an additive was used. Finally, the optimum performance occurred with modest KrF irradiation (1 mJ) of the entire interelectrode gap or even of region (4) slightly offset from the normal channelling region. Previous electron density measurements¹⁴ were used to estimate that high energy irradiation of zone

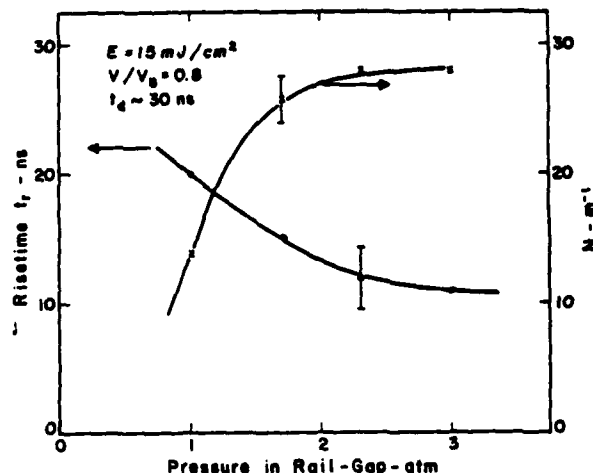


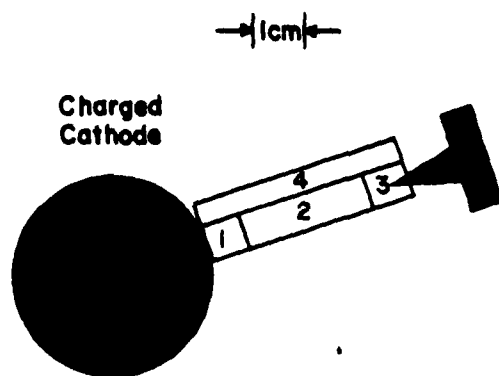
Fig. 6. Risettime of voltage across the resistive load and number of channels as a function of rail-gap pressure.

(3) may have produced $10^9 - 10^{11}$ electrons cm^{-3} while for low flux irradiation $10^6 - 10^8$ electrons cm^{-3} were probably created in the gap. These observations, together with the decrease in N with increasing KrF fluence (no additive case) shown in Fig. 3, imply that a critical electron density ($\sim 10^9 \text{ cm}^{-3}$) must not be exceeded near the knife-edge. A possible physical explanation may be that electron densities $> 10^9 \text{ cm}^{-3}$ result in significant overlap of avalanche heads near the anode leading to a reduction in space charge fields thereby inhibiting streamer formation. This is exactly what one tries to achieve when preionizing a TE-laser.¹⁵ This critical number density may well be a function of V/V_0 and higher additive concentrations and KrF fluences may be tolerated at the lower operating voltages. Improvement in the range of voltages for which multichannel breakdown occurred was indeed observed by using additives.

It should be emphasized that good multichannel switching for long charging times of the PFN could only be obtained when the laser radiation was allowed to enter the switch; that is, the additive alone did not produce the good channelling. Furthermore, for fluorobenzene pressures ≤ 0.1 Torr the addition of an additive did not significantly alter the value of V_0 . It was also determined that the maximum number of multichannel discharges possible with sealed gap operation and the transmission of the KrF radiation through the switch were essentially unaffected by the presence of small quantities of additive. The usefulness of additives was demonstrated in another experiment in which a 60 μJ , 300 ps duration N_2 laser pulse was directed along the edge electrode of the 1.5 cm gap separation rail-gap. In 3 atm of pure argon, with a V_0 of ~ 40 kV only 1 or 2 channels were produced. However, the addition of ≤ 1 Torr of tri-n-propylamine¹⁷ (IP = 7.2 eV) permitted multichannel ($N \sim 25 \text{ m}^{-1}$) triggered switching with a $t_d \sim 10$ ns, $t_r \sim 20$ ns and a jitter ≤ 5 ns.

CONCLUSIONS

In this paper we have demonstrated that unfocused laser radiation in the near UV (1900 \AA - 3400 \AA) of



Rail-Gap Crossection

	KrF Irradiation Zone	t_d (ns)	t_r (ns)	N (m^{-1})
No Additive	1 (10mJ)	100	20	6
	3 (0.5mJ)	30	10	30
~0.1 Torr	1 (3mJ)	30	15	6
	3 (1mJ)	30	10	20
	3 (15mJ)	50	25	5
Fluorobenzene Additive	1+2+3 (1mJ)	30	10	30
	4 (3mJ)	30	10	30

Fig. 7. Effect of flux level and spatial distribution of the laser radiation on switch performance for $V/V_B \sim 0.9$.

modest energy (0.1 - 100 mJ) and pulse durations of 300 ps to 15 ns can produce multichannel breakdown of an edge-plane rail-gap switch with a jitter of a few nanoseconds.

As yet the initiation mechanism of multichannel breakdown is not clear and further experiments using streak photography to understand the spatial and temporal development of the avalanche to streamer process are needed. The initiating electrons may result from photoionization of metastable Ar^* since the cross-sections¹⁸ can be quite substantial at wavelengths in the near UV or by electron photodetachment¹⁹ of SF_6 , SF_5 , F^- etc., or possibly by multiphoton ionization of low ionization potential impurities or gas additives. The fact that the polarity on the knife-edge electrode must be positive seems to rule out electron production at the electrode by means of the photoelectric effect.

Table II summarizes the data obtained with the 1.5 and 3.7 cm gap spacings when using ~ 15 mJ of KrF

Table II
Summary of Important Laser Triggered
Rail-Gap Parameters^a

	Gap Spacing	
	1.5 cm	3.7 cm
V_B (kV)	80	140
I_{PK} (kA)	20	35
t_d (ns)	10	30
t_r (ns)	8	11
N (m^{-1})	35	30
Jitter (ns)	~3	~5
m	2	1.7

^a The data were obtained for a 2.4 atm 10% SF_6 , 90% Ar gas mix, a t_c of 0.8 μs and a $V/V_B \sim 0.8$.

radiation and a small concentration ($\leq 1m$ Torr) of fluorobenzene additive. The important parameters necessary to achieve reliable performance are:

- positive ground polarity on the knife-edge electrode
- ~ 10% SF_6 , 90% Ar gas mix
- 2 - 3 atm gas pressure
- irradiation of the entire interelectrode gap by a laser beam propagating parallel to the electrodes
- use of an additive matched to the lasing wavelength to enhance the ionization yield.

The technique was successfully scaled from a gap separation of 1.5 cm to 3.7 cm and may well be scalable to larger gap spacings. Furthermore, the device should, in principle, be scalable to gap lengths of several meters due to the high transmission of the KrF beam and the availability of low divergence coherent UV sources. However, the increased optical transit time may necessitate the use of several trigger beams. No attempt to operate the device at high repetition rates has been made; however, the availability of commercial UV lasers capable of 150 Hz operation should permit the investigation of high repetition rate switching.

In conclusion, we believe that this technique provides a simple, yet reliable method of triggering many rail-gaps by an external source with nanosecond jitter.

REFERENCES

1. W.J. Sarjeant, R.S. Taylor, A.J. Alcock and K.E. Leopold, IEEE Trans. on Electron Devices, Vol. ED-25, pp 1414-1417, Oct. 1979.

2. J.C. Martin, Proceedings of the Conference on energy storage, compression and switching, pp 3-13, Asti-Torino, Italy, Nov. 5-7, 1974.
3. D.L. Johnson, Proceedings of the Conference on energy, storage, compression and switching, pp 515-520, Asti-Torino, Italy, Nov. 5-7, 1974.
4. G.R. Neil and R.S. Post, Rev. Sci. Instrum., Vol. 49, pp 401 - 403, March 1978.
5. A.H. Guenther and J.R. Bettis, J. Phys. D : Appl. Phys., Vol. 11, pp 1577 - 1613, 1978.
6. W.R. Rapoport, J. Goldhar, J.R. Murray, to appear in IEEE Trans. on Plasma Science in a special issue on "Plasma switches and switch plasmas".
7. L.P. Bradley, T.J. Davies, IEEE J. Quantum Electron. Vol. QE-7, pp 464, Sept. 1971.
8. L.P. Bradley, J. Appl. Phys., Vol. 43, pp 886 - 890, March 1972.
9. W.J. Sarjeant and A.J. Alcock, Rev. Sci. Instrum., Vol. 47, pp 1283, 1976.
10. R.S. Taylor, A.J. Alcock and K.E. Leopold, Opt. Commun., Vol. 31, pp 197 - 202, Nov. 1979.
11. The laser was obtained from Photochemical Research Associates Inc., London, Ontario, Canada.
12. J.C. Martin, "Pressure dependency of the pulse breakdown of gases", AWRE Dielectric Strength Notes, No. 15, Sept. 26, 1967.
13. J.C. Martin, "Multichannel Gaps", AWRE Report, SSWA/JCM/703/27 (1970).
14. R.S. Taylor, A.J. Alcock and K.E. Leopold, accepted for publication in Opt. Letters.
15. P.A. Hackett, D.M. Rayner, C. Willis, E. Weinberg and D. Phillips, "Resonant two photon ionization of benzene, fluorobenzene and m-difluorobenzene", submitted for publication to Chem. Phys. Letts.
16. J.I. Levatter and Shao-Chi Lin, J. Appl. Phys., Vol. 51, pp 210 - 222, Jan. 1980.
17. J.S. Levine and A. Javan, Appl. Phys. Lett., Vol. 22, pp 55 - 57, Jan. 1973.
18. K.J. McCann and M.R. Flannery, Appl. Phys. Lett. Vol. 31, pp 599 - 601, Nov. 1977.
19. F.D.A. Boylett and B.G. Williams, Brit. J. Appl. Phys., Vol. 18, pp 593 - 595, 1967.

UV PREILLUMINATED GAS SWITCHES*

L. P. Bradley, E. L. Orham, I. F. Stowers and J. R. Braucht
Lawrence Livermore National Laboratory
P.O. Box 5508
Livermore, California 94550

Summary

We have designed, built, and characterized uv preilluminated gas switches for a trigger circuit and a low inductance discharge circuit. These switches have been incorporated into a 54X76X150cm pulser module to produce a 1 Ma output current rising at 5×10^{12} amps/sec with 1 ns jitter. Twenty such modules will be used on the Nova Inertial Confinement Fusion Laser System for plasma retropulse shutters.

Introduction

We are developing a compact highly reliable pulser¹ to be used as a system component on the Nova laser. A prototype unit has been built and tested. The pulser contains 8 capacitors connected through 4 rail-gap switches and a coaxial feedthrough to an exploding wire. When charged to 50 kV the pulser applies 1 Ma rising at 5×10^{12} a/sec to the load.

The pulser is shown in perspective in figures 1 and 2, and in crosssection in figure 3. The active portion of the pulser is essentially coaxial with no exposed edges. A guiding philosophy of the design has been to use 10-20 ns components (i.e., capacitors and switches) that are within the state of the art, and to re-engineer them to improve performance and reliability.

A main feature of the pulser is the one piece elastomer insulator^{1,2}. It gaskets against the capacitors and switches to prevent interface tracking. Because of its resistance to corona it requires no additional grading material. It conforms to the conductor surface and maintains contact after each magnetically induced impulse. The silicone elastomer² has a median dielectric strength of 1.12 MV/cm, and exhibits a threshold breakdown strength of 0.61 MV/cm below which extremely long life is obtained.

Circuit

An equivalent circuit of the pulser is shown in figure 4. It consists of a trigger section and a main discharge circuit. In the final application in Nova, the trigger signal will be delivered via fiber optics from the Nova master oscillator. As presently configured, for testing of the prototype pulser, the signal is generated by a logic module. The logic signal fires a Pulsepak 10 A through a transformer to provide a 40 kV trigger signal with 1 ns jitter to the trigger section. This signal simultaneously uv irradiates the trigger gap and applies a

trigger voltage to the trigger electrode. In the final system the trigger circuitry will be totally redundant as required to provide reliability. The voltage generated by the trigger section is likewise applied to the main rail-gap to provide uv and trigger voltage.

In the main discharge circuit, the capacitors, switch, and insulator each contribute 3 ns to the loop inductance. The total loop inductance, including strays, is 10 ns.

Trigger Switch

The trigger switch, shown in figure 5, was constructed several years ago using a Tachisto 501 switch body³. The trigger and illuminator electrodes were retrofitted into the switch body in analogy with the Pulsar SW50K gap^{4,5}. All electrodes are elkonite, a copper-tungsten material. The small gap between the trigger and illuminator electrode breaks first upon receipt of the trigger signal. This electrically bridges the trigger electrode to the illuminator electrode and simultaneously floods the main gap with uv. The trigger electrode is positioned 2/3 of the distance from the high voltage electrode toward the ground electrode. The trigger polarity is selected to break the wide gap first. Thereafter the full gap voltage is placed across the narrower gap breaking it. This trigger approach has been used for over two years in several pulsers, and has exhibited negligible erosion or shift in operating point.

Main Rail-Gap

The main discharge switch, a rectangular assembly, contains four separate rail-gaps in one envelope. Each rail-gap has two 21 cm rails which are graded at the ends and a larger trigger blade spaced 2/3 of the distance from the high voltage electrode toward the ground electrode. The electrodes at present are brass. At each end of the main gap is a pair of elkonite uv illuminator electrodes. A 40-50 kV trigger pulse with 8 ns risetime is simultaneously applied to the trigger blade and through current limiting resistors to the illuminator gaps. Alternatively, the trigger pulse is brought first through the illuminator electrodes where it is sharpened and produces uv, and then on to the trigger electrodes. In either case, the illuminator gap breaks first by virtue of its small space and high field enhancement.

*Work performed under the auspices of the U.S. Department of Energy by Lawrence Livermore Laboratory under Contract NO. W-7405-Eng-48.

The switch body was cast from mica filled epoxy. Internal contours on the epoxy serve to increase the creep path length and most importantly to shadow regions of the insulator from both uv and debris from the main arc. Nonconductive silicone g-rings are hidden from the expanding gases to prevent conductive contaminants from re-entering the gap.

The bottom of the switch is held in compression against the silicone insulator to prevent tracking. As an aside, the capacitors have a thin layer of silicone cast onto the flat face between the rail headers, and are compressed against the elastomer. The capacitors are connected via a compression leaf spring to one side of the switch. The center of the switch is bolted to the center of the coaxial feedthrough. The electrodes are aligned and fixed in position with a jig prior to final switch assembly. One version of the switch contains a transparent plexiglas top to permit observation of streamer channel formation.

The function of the uv preillumination is to produce free electrons and atoms with metastable levels throughout the main gap. A 90:10 mixture of Ar:SF₆ gas is used as the fill gas. The electrons produced by the preillumination help in initiating avalanches and streamers and also cause precise closing of the streamers.^{6,7} The two features of the preillumination are that it reduces jitter and it minimizes increase of jitter with erosion of the trigger blade edge.

The cascade gap, wherein a larger gap is broken first by the trigger voltage and then the smaller half is broken by the gap voltage has been used for many years.^{8,9,10,11,12} We have demonstrated analytically, and confirmed experimentally, that an optimum trigger voltage exists which is slightly below the main gap voltage to produce reliable cascade operation. Clearly a separate region of operation exists for higher trigger voltages^{8,9} which will cause both gaps to close nearly simultaneously. From a system point of view, the cascade region has benefits because of its lower trigger requirement, and we have therefore selected this mode.

We have constructed the pulser and run it for the past several months with no problems. The jitter from the input of the pulser module to the switched current as monitored by the leading edge of magnetic field monitors (B-dot probes) was 1 ns. Additionally, although not required for the inductance of the pulser, uniformly distributed multichannels have occurred. The multichannel operation helps minimize electrode erosion.

Conclusion

In the short term, the pulser has operated perfectly. Toward very long term, reliable operation on Nova we are examining alternate switch gas (Ar:N₂:SF₆) and electrode material (Schwarzkopf K25 copper tungsten, POCO AXF5NC and ACF10W graphites). The goals are to obtain minimum erosion, minimum shift

in operating point, and minimum prefire with age.

Acknowledgements

The authors thank R. Duffus, H. Rien, and R. Sites for their contributions to this work.

References

1. L.P. Bradley, E. L. Orham, I. F. Stowers, and P. Koert, Development of a Plasma Retropulse Shutter for Shiva and Nova, UCRL 52830, Lawrence Livermore Laboratory, (Sept. 26, 1979).
2. L. P. Bradley, E. L. Orham, J. R. Braught, and I. F. Stowers, Elastomer Dielectric for Pulse Power. "Proc. 1980 Conf. on Electrical Insulation and Dielectric Phenomena", Boston (Oct. 29, 1980) to be published.
3. C. Chase, Private Communications.
4. W. Crewson and T. Naff, Private Communication.
5. H. Bacchi and J. C. Pauwek, p. 489, Proc. of the 9th Int. Conference on High Speed Photography, Denver, Aug. 2-7, 1970.
6. L. P. Bradley, "Preionization Control of Streamer Propagation," J. Appl. Phys. 43, 886 (1972).
7. L. P. Bradley and T. J. Davies, "Laser Controlled Switching," IEEE J. Quantum Electronics 7, 464 (1971).
8. W. H. Borkenhagen, R. F. Gribble, L. D. Hansborough, R. K. Linford, J. G. Melton, and W. C. Munnally, Multichannel Spark Gap Technology for Staged Theta-Pinch Machines, p. 676, Proc. 6th Symp. on Engineering Aspects of Fusion Research, San Diego (Nov 18-21, 1975).
9. P. D'A Champney, Some Recent Advances in Three Electrode Field Enhanced Triggered Gas Switches, p. 463, Proc. Int. Conf. on Energy Storage, Compression and Switching, Turino (Nov. 5-7, 1974).
10. P. M. Barnes, J. E. Gruber, T. E. James, The Parallel Operation of Low-Inductance High-Current Spark Gaps Without Transit Time Isolation, J. Sci. Instruments, 44, p. 599, (1967).
11. J. E. Gruber, and T. E. James, Fast Pulse Breakdown of Nonuniform-Field Pressurized-Air Spark Gaps, Proc. IEE, 115, p. 1530 (1968).
12. A. E. Bishop, and G. D. Edwards, Low Inductance 100 kV Switch (Spark Gap) for Starting, Diverting, and Clamping Capacitor Discharges, Proc IEEE 113, p. 1549 (1966).

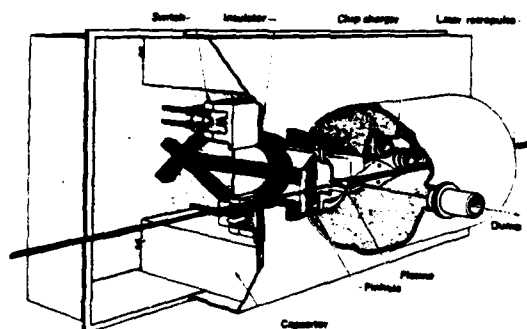


Figure 1 Nova retropulse plasma shutter module. The pulser contains capacitors, switches and insulator. The electrical pulse vaporizes a wire and, with railgun electrodes, propels the plasma across a laser beam path. The plasma protects the laser from light reflected back from the target.

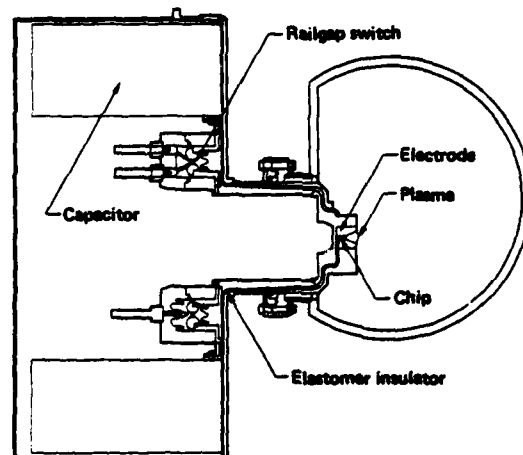


Figure 3 Cross-section of Nova plasma shutter module showing location of capacitors, switches and the elastomer insulator that connects these components to the plasma load.

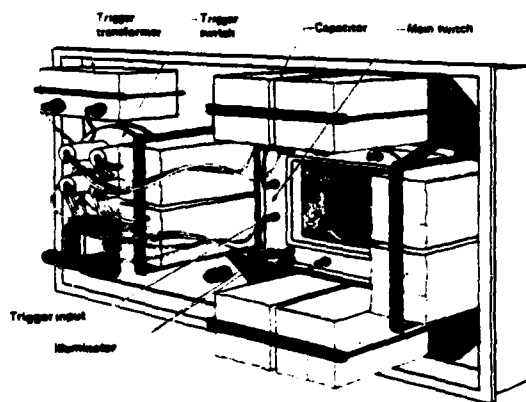


Figure 2 Pulser module showing essentially coaxial arrangement of capacitors and switches. The trigger unit along with all high voltage components are contained in an electromagnetically shielded box.

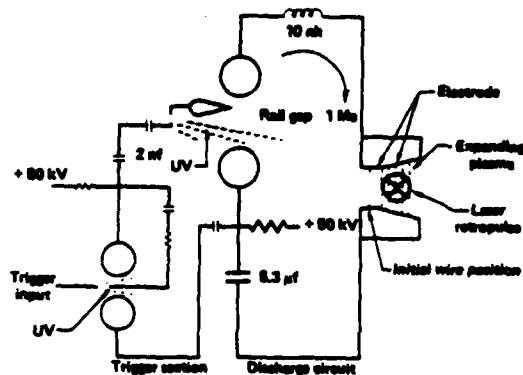


Figure 4 Equivalent circuit of pulser showing main discharge loop from the capacitor to the plasma. The trigger circuit provides both trigger voltage and uv preillumination.

NOTICE

This report was prepared as an account of work sponsored by the United States Government. Neither the United States nor the United States Department of Energy, nor any of their employees, nor any of their contractors, subcontractors, or their employees, makes any warranty, express or implied, or assumes any legal liability or responsibility for the accuracy, completeness or usefulness of any information, apparatus, product or process disclosed, or represents that its use would not infringe privately-owned rights.

Reference to a company or product name does not imply approval or recommendation of the product by the University of California or the U.S. Department of Energy to the exclusion of others that may be suitable.

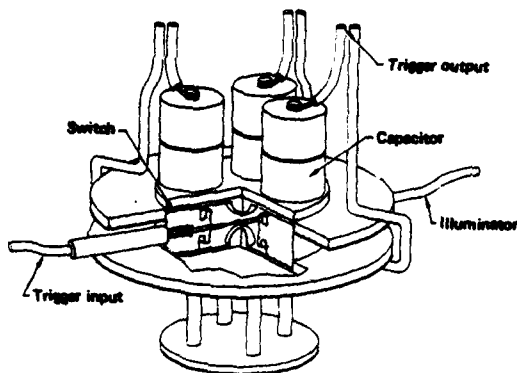


Figure 5 Uv preilluminated trigger switch assembly.

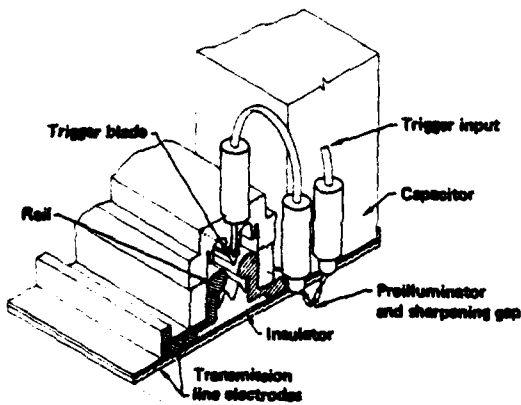


Figure 6 Uv preilluminated rail-gap assembly.

X-RAY TRIGGERED SWITCHING IN SF₆ INSULATED SPARK GAPS*

E. L. Neu

Sandia National Laboratories, Albuquerque, New Mexico 87185

Abstract

Several methods are being investigated for triggering low-jitter pressurized, SF₆-insulated spark gaps operating at 3 MV with the capability of switching hundreds of kilampères. One method, which is located external to the main current carrying plasma channel, uses pulsed x-rays to generate ionization within the working gas volume to initiate low jitter gas breakdown. In this paper, a model of gas breakdown with x-ray ionization is developed and results of two series of experiments are described. One experiment used 35 kV with a 1.83 mm gap and the other used 1 MV with a 7.62 cm gap. Both experiments used a 600 kV Fabreton 706 flash x-ray source to demonstrate the feasibility of using pulsed x-rays as a means of triggering SF₆ insulated gaps with nanosecond jitter.

Introduction

Multimegavolt, SF₆-insulated spark gaps are used in the power compression process of large particle beam accelerators. The switch closure jitter becomes critical when many switches are required to close simultaneously. In large, physically-distributed, multimodule, short-pulse accelerators, such as the 30 TW Particle Beam Fusion Accelerator PBFA, 36 switches must close within a 7 ns time window. Triggers and other gaps with trigger electrodes located in the path of the current carrying plasma suffer erosion of the triggering electrode, which increases the jitter in switch closure time. Electron beams¹ and lasers² may be used to initiate the breakdown process. However these triggers suffer damage to input windows or lenses in switches carrying several hundred kilampères. Illumination of the switch cathode surface with UV radiation reduces the statistical time lag in starting avalanches,³ and UV illumination of the gas volume can control the velocity of the streamer phase in the breakdown process.⁴ This paper presents experimental results using a pulsed x-ray source to liberate electrons from the electrode surfaces. These electrons in turn deposit charge in the insulating gas volume, preionize the gas, and thus control the switching time.

Breakdown Modeling of SF₆ Insulated Gaps

DC Applied Field Case

Electronegative gases, such as SF₆, exhibit an electron capture process which competes with the first Townsend ionization process in a gap with an applied field. Below a critical value of E/P, the ratio of the electric field to the pressure, the attachment process removes electrons from the avalanche faster than they are generated. At 117 volts/cm/mm of Hg in SF₆, the attachment and generation coefficients are equal.⁵ Breakdown can occur at this or any greater value of E/P provided the gap is wide enough to allow the number density at the tip of the avalanche to reach 10¹⁰/cc. This is the Raether condition for conversion of the avalanche to a streamer.⁶ A gap with a non-uniform field distribution has a DC breakdown field given by

$$E_{DC} = 88.7 \left(\frac{P}{P_0} \right) \left(\frac{1}{FEF} \right) \text{ kV/cm} \quad (1)$$

*This work was supported by the U.S. Dept. of Energy, under Contract DE-AC04-76-DP00789.

where FEF is the field enhancement factor for the most highly stressed region in the gap. P/P_0 is the normalized pressure in atmospheres. An avalanche growing into a region where the FEF is decreasing may enter a region with a local value of E/P below 117 volts/cm/mm of Hg. The electron number density will then decrease and the avalanche process will stop. The effect of spatial variation in the FEF over the avalanche growth length, for the gaps discussed in this report, was evaluated by numerical integration of the Townsend growth equation. The non-uniform FEF changed the DC breakdown value, as calculated from Eq. (1), by less than 1 percent. Fields only slightly in excess of those given by Eq. (1) are sufficient in SF₆ to cause the avalanche to reach the Raether criterion in a few nanoseconds while traveling a few tenths of a millimeter.

Pulsed Applied Field Case

The time required for spark gap breakdown in a pulsed field is composed of three time intervals. First, the time required for the appearance of the initial electron to start the avalanche is known as the statistical delay. The initial electron may be pulled from the cathode surface by field emission or the initiating electron may be detached from a negative ion by the applied field.

The second time interval in the spark breakdown process is known as the formative time. During this time interval the initial electron is accelerated by the applied field and generates new free electrons through collisions with gas molecules. The rate of generation is given by the first Townsend coefficient for the gas used in the gap. Electronegative gases have an equivalent coefficient which is made up of attachment and generation coefficients, usually given as a function of E/P. Data on experimentally measured spark formative times in SF₆ by Felsenthal and Proud⁷ have been combined with data on attachment and ionization coefficients by Bhalla and Craggs⁸ to give an equation for the electron drift velocity, in the avalanche phase, as

$$V_d = 2.39 \times 10^7 + 1.49 \times 10^5 \text{ E/P cm/s} \quad (2)$$

where E/P is in volts/cm/mm of Hg.

The time and distance required for an avalanche to reach an electron number density of 10¹⁰/cc have been computed by assuming a uniform field enhancement factor over the avalanche growth length for the time varying fields used in the experiments. The formative times calculated are a few nanoseconds with avalanche growth lengths of from a few tenths of a millimeter to a few millimeters. Exact values are given in the discussion of the experimental results.

The third time interval in the spark breakdown process is the streamer phase. Propagation of ionization fronts across the gap in the streamer phase may reach 10¹⁰ cm/s. Streamer velocity has been shown to be a function of the charge density present in the gas volume⁴ and is proportional to one over the cube root of such existing charge density. The streamer phase is terminated with the appearance of a low impedance plasma channel which then carries the full switched circuit current.

Experimental Results

1.83 mm Gap Experiments

The initial experiment used a DC or pulse charged, SF_6 insulated, 1.83 mm long gap. The brass anode is 5 cm in diameter with 0.5 cm radius of the edges while the cathode is a 3.2 mm thick aluminum sheet. Both electrodes were bead blasted and cleaned before beginning the breakdown experiments.

A DC self-break curve versus pressure for this gap is given in Fig. 1 and agrees with values obtained from Eq. (1) when allowance is made for the short gap length. Since scatter in the breakdown voltage was observed to increase significantly above 25 psia, this pressure was used in all x-ray triggered experiments.

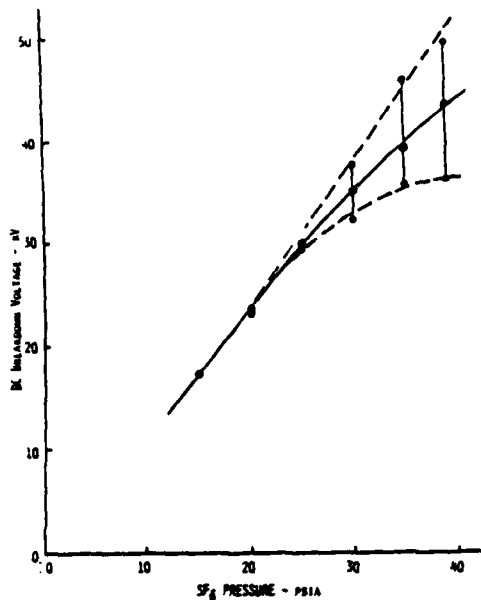


Fig. 1. DC breakdown voltage vs. SF_6 pressure 1.83 mm gap.

The circuit shown in Fig. 2 was used to pulse charge a 0.04 μF capacitor, across which the gap was placed, in 1.1 μs . Breakdown timing information was obtained from a 8-dot coil monitoring gap current and from a resistive voltage monitor mounted across the gap. The output of the 600 kV Febatron was monitored with a PIN diode which was time correlated with the other monitors.

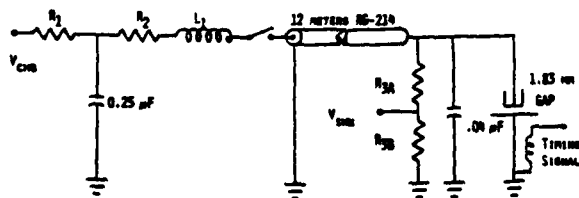


Fig. 2. 1.83 mm pulse test circuit.

The measured DC breakdown voltage of the 1.83 mm gap at 25 psia was 29.5 kV while the minimum pulsed self-breakdown was 56 kV. The calculated formative time for these conditions is 4.5 ns with an avalanche length of 1.83 mm. The overvoltage present in the pulsed breakdown may be due to a long statistical delay. Since the volume of gas between the electrodes is small and since the initiating electron has to appear near the cathode in order to reach the Raether condition within the gap length, a long statistical delay might result.

X-ray breakdown of this gap was initiated with the Febatron source located 5 cm behind the aluminum cathode. A CYLTRAN code simulation for these conditions predicts an ion density in the gap of 4×10^{13} pairs/cc. The timing of the flash x-ray source was adjusted to provide ionization in the gap at 35 kV on the applied voltage waveform. This corresponds to an applied field of 191 kV/cm and an E/P value of 148 volts/cm/mm of Hg which is above the DC breakdown value. The standard deviation in gap closure time, as measured from the time difference between the PIN diode signal and the break in the voltage waveform, was 1.3 ns. The total spread in 12 shots was 3 ns with a delay of approximately 2 ns. The intensity of the source was then reduced 8 to 9 orders of magnitude with shielding blocks. The delay in switch closure increased to 10 ns but nanosecond jitter in the gap closure time was maintained. In this x-ray triggered gap, the Febatron supplies the electrons to initiate the avalanche and the breakdown time is governed by the formative time of the avalanche.

7.62 cm Gap Experiments at 1 MV

The second series of experiments used a modified 3 MV trigatron with conditioned hemispherical stainless steel electrodes spaced 7.62 cm apart. Figure 3 shows a cross sectional view of the gap with 10 percent equipotentials plotted by the electrostatic field solver JASON. The variation in field enhancement factor with axial position is given in Fig. 4.

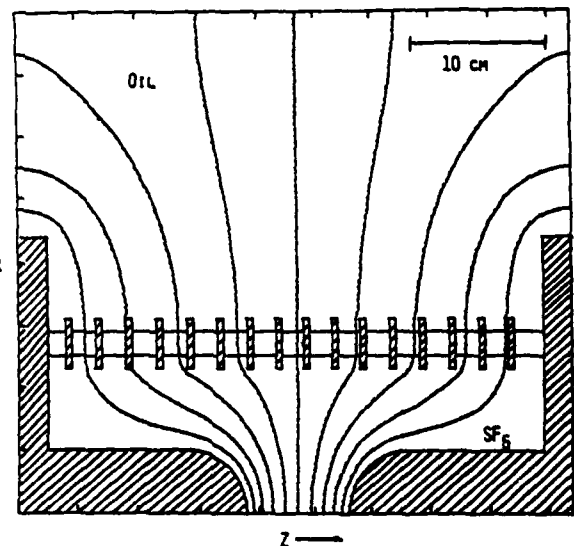


Fig. 3. Modified 3 MV trigatron - 10 percent equipotentials.

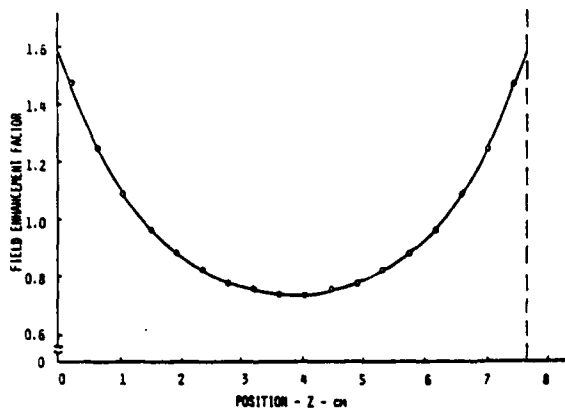
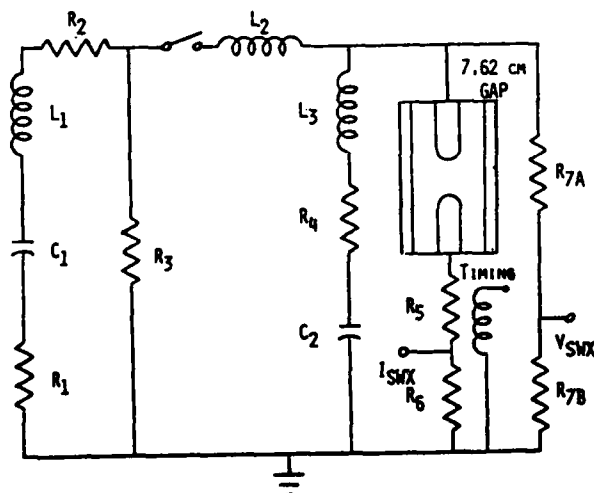


Fig. 4. Field enhancement factor vs. axial gap position, 7.62 cm gap.

The Marx generator and intermediate store capacitor in the Mite accelerator¹⁰ were used to pulse charge the gap to peak voltage in 900 ns using the circuit shown in Fig. 5. The 1.75 Ω load resistor limited peak currents through the switch to 144 kA with an applied voltage of 1.2 MV. The closure of the switch was monitored by a Rogowski loop in the switch ground circuit, and the firing time of the 600 kV Febetron x-ray source was monitored with a PIN diode. Accurate measurements of the time difference between the Rogowski and PIN diode signals was obtained with a CAMAC digital system which has a time resolution of 250 ps. All signals were simultaneously displayed on fast dual beam oscilloscopes. The Febetron source target was physically located 135 cm from the axis of the switch. The dose at the switch axis was approximately 0.75 mr which corresponds to a deposited charge density of 5×10^{10} pairs/cc in the gas volume.



$R_1 = 5.1 \text{ M}\Omega$ CVR, $R_2 = .916 \Omega$, $R_3 = 862 \Omega$, $R_4 = 1.1 \Omega$
 $R_5 = 1.75 \Omega$, $R_6 = 5 \text{ M}\Omega$ CVR, $R_7A, R_7B = 3000:1$ MONITOR
 $C_1 = 41.5 \text{ nF}$, $C_2 = 19.4 \text{ nF}$
 $L_1 = 5.35 \text{ }\mu\text{H}$, $L_2 = 0.2 \text{ }\mu\text{H}$

Fig. 5. Mite switch test circuit.

The pulse-charged self-breakdown curve for this switch is given in Fig. 6 in addition to the calculated DC breakdown curve. The gas pressure in the switch and the Marx charging voltage were adjusted in each case to maintain switch breakdown at 600 to 650 ns into the charging waveform. An operating pressure of 25 psia was selected for x-ray triggering experiments and 17 self-break shots gave an average pulsed self-break voltage of 1.21 MV with a standard deviation of 1.8 percent.

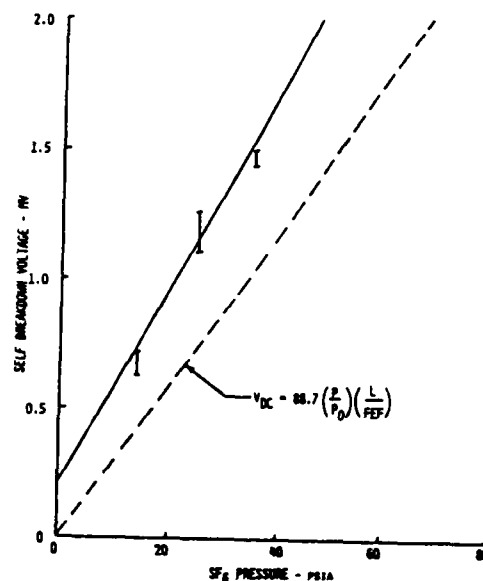


Fig. 6. Self breakdown voltage vs. pressure, 7.62 cm gap.

The first test with the Febetron x-ray source, which had a 3 ns wide output pulse, involved firing the Febetron from 0 to 500 ns before the calculated DC breakdown level was reached on the pulsed waveform. Breakdown was stabilized at 923 kV with a standard deviation of 1.5 percent in 12 shots. Switch closure occurred 80 ns after the voltage exceeded the DC breakdown value and was independent of the time between the x-ray pulse and the DC breakdown point. If net ionization produced by the x-ray source removed any statistical delay in the start of the Townsend avalanche, then the time for the combined avalanche and streamer phases is 80 ns. The avalanche length for this geometry and field enhancement factor is 0.5 mm and the formative time required to reach 10^8 ion pairs/cc is approximately 1.1 ns. Therefore, the streamer transit time is 79 ns, and the average streamer velocity is 9.6×10^7 cm/s. Without the Febetron, the time between the DC breakdown level of 732 kV and the pulsed self-break level of 1.21 MV was 220 ns. If statistical delay is neglected for the moment, then the average streamer velocity without x-ray induced charge is 3.5×10^7 cm/s. This is approximately the same as the electron drift velocity in the avalanche phase for the experimental conditions. The charge deposited by the Febetron increased the average streamer velocity by a factor of 2.7. Experimental results will be given in the next section to show that the statistical delay is in fact negligible for the 7.62 cm gap experiments.

The timing of the Febetron was delayed for the second series of experiments so that the Febetron would deposit charge in the gap after the DC breakdown level but before the streamers would normally have closed the gap. The mean delay between the x-ray induced ionization and gap closure was 55.1 ns with a standard deviation of 10.5 ns which is 1.75 percent of the total switching time. According to the model of switch operation presented in this paper, the streamer in this case starts out from essentially the DC level on the pulsed waveform (because of the short time and distance, in the avalanche phase) and travels at 3.5×10^7 cm/s until the x-rays deposit charge in the switch gas. At this time the streamer velocity increases to 9.6×10^7 cm/s which is maintained until the switch closes. As an example consider the data for shot 5-20-13. The time between the DC breakdown level and the arrival of the additional charge is 90 ns. During this time the streamer, traveling at 3.5×10^7 cm/s, has moved 3.15 cm across the gap. The calculated time for the avalanche to cross the remaining 4.47 cm at 9.6×10^7 cm/s is 46.6 ns which is in good agreement with the measured value of 51.3 ns. These calculations have not included any statistical delay time but from the measurements it is less than a few nanoseconds. Lower breakdown jitter may be possible with higher x-ray doses or increased applied field strengths. It should be pointed out that the standard deviation in the breakdown time or amplitude remained approximately a constant fraction of the total switching time both with and without the extra charge from the Febetron despite the change in streamer velocity. Additional experiments are planned using other field geometries to further study overall switch jitter and streamer velocity modification.

Conclusion

Low jitter, pressurized SF₆ insulated spark gaps capable of operating at voltages of from 2 to 3 MV and currents of several hundred kiloamperes are desired for large, distributed, particle beam accelerators. This report shows that a pulsed x-ray source deposits charge within a switch gap volume without special windows. The injected charge eliminates statistical time lags and modifies streamer velocities. Experimental results for a 1.83 mm gap operating at 33 kV has demonstrated closure time jitter of 1.3 ns. This gap probably operates in a mode dominated by statistical and formative time delays which are subject to improvement by x-ray induced charge deposition. A mildly divergent field gap operating at 1 MV with a spacing of 7.62 cm has demonstrated both x-ray stabilized and x-ray triggered modes of operation. Gap operation, in this case, is dominated by streamer closure time and the charge produced by the x-ray source nearly triples the average streamer velocity. The standard deviation of the gap closure time is approximately 1.5 percent of the total switching time. The measured jitter of this 144 kA switch was 10.5 ns and is not directly suitable for use in large, multiple-switch, accelerators. Additional experiments are underway to understand and reduce this jitter.

Acknowledgments

The author wishes to gratefully acknowledge helpful discussions with J. P. VanDevender and the timely and competent help provided with the experimental research by I. Molina and W. B. S. Moore.

References

1. K. McDonald, M. Newton, E. E. Kunhardt and M. Kristiansen, Proc. of the 2nd IEEE Int'l. Pulsed Power Conf., Lubbock, TX (1979).
2. J. J. Moriarty, H. I. Milde, J. R. Bettis and A. H. Guenther, RSI, Vol. 42, No. 12 (December 1971).
3. P. Felsenthal and J. M. Proud, Phys. Rev. **139**, A1796 (1965).
4. L. P. Bradley, J. Appl. Phys., Vol. 43, No. 3. (March 1972).
5. M. S. Bhatta and J. D. Craggs, Proc. Phys. Soc., **80**, 151 (1962).
6. H. Raether, Electron Avalanches and Breakdown in Gases (Butterworth, London, 1964).
7. L. B. Loeb, Science **148**, No. 3676, 1417 (1965).
8. J. A. Halbleib, Sr. and W. H. VanDevender, CYLTRAN—A Cylindrical Geometry Multimaterial Electron/Photon Monte Carlo Transport Code, SAND74-0030 (March 1975).
9. S. J. Sackett, JASON—A Code for Solving General Electrostatics Problems, UCID-17814 (1978).
10. T. H. Martin, D. L. Johnson and D. H. McDaniel, Proc. of the 2nd Int'l. Topical Conf. on High Power Electron and Ion Beam Res. and Tech., Ithaca, NY, p. 807 (1977).

DEVELOPMENT OF INSTANT-START THYRATRONS

D. Turnquist, T. Lynch, and S.S. Merz
EG&G, Inc., Salem, Massachusetts

N. Reinhardt
Consultant, Lexington, Massachusetts

Abstract

A new family of cold-cathode, instant-start thyratrons is now being developed. Experimental results are discussed for this new series of high power switches, versions of which are now being built as modified EG&G 7620s and HY-5s. Instant-start cathodes used in smaller tubes at up to 500 amps peak and 0.5 amp average have been scaled in accordance with cathode utilization and heat transfer considerations. These cathodes have been tested for their ability to start reliably from cold at full power, and to maintain cathode activity for subsequent cold starts at elevated peak and average currents. Novel reservoirs to ensure adequate hydrogen pressure for cold start and subsequent high power operation have been designed and tested. These results are discussed together with a description of measures taken to minimize weight, size, and complexity in a series of instant-start, 40-kiloamp, 1 megawatt-average-power hydrogen thyratrons now under construction.

Introduction

The hydrogen thyatron was originally developed to serve as a low-loss gas discharge switch having long life and a high repetition rate capability. This was accomplished by using a thermionic cathode and low pressure hydrogen for the gaseous conducting medium.

The hot cathode supplies microsecond pulses at current densities of 10 amperes per square centimeter of space charge-limited emission. The 0.2 to 0.6 torr gas pressure and subsequent plasma density is sufficiently high to give mean free paths less than 2 millimeters and Debye lengths and plasma sheath thicknesses much less than 1 millimeter. As a consequence, the cathode can be folded and compressed into a compact structure with well defined and controlled current distribution, heat load, and thermal characteristics. Life times of these cathodes are determined only by the slow thermal evaporation rates of the emissive material — a process that can take many thousands of hours. An arcing device, such as a spark gap or ignitron, derives its emission from an arc spot in which the energy loss is high and sufficiently concentrated to cause local vaporization of the cathode material. In these arcing devices, the emission mechanism requires a destructive condition, leading to short lifetimes.

While the hydrogen pressure is high enough to provide thin plasma sheaths, it is also low enough to provide high voltage recovery times of a few microseconds when used with inter-electrode spacings of a few millimeters. Hydrogen or deuterium is used because the low ion mass provides

fast de-ionization and completely avoids cathode damage by ion bombardment. In addition, the high voltage holdoff characteristics of these gases are good at low pressures. Finally, reservoir structures can be incorporated into devices to counter-act gas cleanup by the discharge.

Both the cathode and reservoir are operated hot — several hundred degrees Celsius. They require heater power input while in operation or standby, and require minutes for warmup. The problems of supply and disposal of this power, and the warmup wait, have become especially severe with modern requirements for power efficiency, light weight, and warmup times of less than one second.

Efforts to develop cold cathode hydrogen thyratrons have been continuing for nearly 40 years. A recent attempt by Vagin⁽¹⁾ used a trigger discharge current greater than the switched main discharge current in a thyatron-type structure having cold metal electrodes. This device had high time jitter, and was set to be controlled by means of the trigger-cathode discharge. EG&G attempted to duplicate these results,⁽²⁾ but found that the device arced uncontrollably even at current densities of only a few amperes per cm². Further Russian work in this area evolved into a low pressure spark gap,⁽³⁾ that used a hollow cathode, bare metal, high work-function structure which avoided arcing. Difficulty with long, nonreproducible trigger delay times was experienced and extensive cathode conditioning was only partly successful in repressing arcing.

We have now developed a thyatron which overcomes these difficulties. Our initial work produced the plasma-heated thyatron designed to predetermined specifications at a 20 kV, 5 kW average power level.⁽⁴⁾ Work is now in progress to extend this capability to the megawatt average power level. The present development includes large-scale cathodes, an instant-start reservoir structure, and a lightweight, high voltage envelope structure combined within a single device that has the excellent triggering and life characteristics of a standard hydrogen thyatron.

Design Goals

General design goals for the instant-start thyratrons are:

- 1) Ratings and characteristics comparable to conventional thyratrons of equivalent size.
- 2) The ability to start instantly (<1 second) and repeatedly at full power without any warmup wait or standby heater power.
- 3) Grid drive requirements compatible with solid-state circuitry and a power gain of 1000 or more.

4) Service lifetimes of tens or hundreds of high voltage operating hours, free of destructive arcing or other catastrophic degradation as a result of starting or operating.

Specific operating goals for both the original design and the present development are given in Table 1.

Table 1. Specific operating goals.

	Feasibility Demonstration	Instant-Start Megawatt Switch
Peak anode voltage, epv, (kv)	20	40
Peak anode current, ib, (ka)	0.5	40
DC average current, Ib, (Adc)	0.5	50
RMS average current, Ip, (Aac)	16	1400
Pulse repetition rate, PRR, (Hz)	1000	250
Anode delay time drift, Δt_{ad} , (μs)	0.5	0.1
Operating Mode	Continuous	120 sec burst
Life, operating		
(Hrs)	500	12
(Pulses)	1.8×10^9	5×10^6
Weight		
(Pounds)	---	25

To meet the requirements for long life, low jitter, and low delay time variation, it was evident that any cathode that operated in the arc mode had to be avoided. The use of a thermionic oxide-coated cathode was also precluded since any structure light enough to be heated in a second or less would be very susceptible to accidental arc-fault damage. Self-heating of an oxide cathode was not feasible either because when cold the high surface resistance causes high fields that result in damaging arcs. The objective then was to find a practical cold emitter, using available materials having known properties.

A new hydrogen reservoir material or structure was also needed. Conventional designs use titanium hydride operating at several hundred degrees Celsius. Upon cooling, the reservoir absorbs most of the background hydrogen in the tube, leaving the pressure too low to allow the tube to trigger cold. One possible alternative to prevent hydrogen re-absorption upon reservoir cooling was to place a thermally controlled palladium barrier between the reservoir material and the tube interior. Reservoirs of this type are used in some commercial thyratrons where heat generated in the cathode structure is used to warm the reservoir and its palladium shell. Current

investigations of transition metal alloys for hydrogen storage promise a way to develop a reservoir for operation at normal ambient temperatures.

With several potential solutions to the reservoir problem, it was decided to concentrate on a solution to the cathode problem, then pursue the reservoir, and finally incorporate both in a lightweight tube structure. Preliminary work on the cathode has been successfully completed, and experiments are underway to produce a large scale version for megawatt operation, along with the necessary reservoir and envelope.

The Cathode

Cathode Concept

The cathode concept was based on the emission properties of impregnated tungsten used for cold cathodes in xenon flashlamps and spark gaps. This material, a porous tungsten matrix filled with barium aluminate, has emission properties that result from a barium monolayer formed on the surface by suitable activation. The barium aluminate is contained within the bulk of the material, and not applied as a surface coating, as with the oxide cathode. The ten-fold lower surface resistance that results⁽⁵⁾ makes the impregnated cathode more suitable to cold-start operation.

Due to the low resistivity and the low work function of the barium monolayer, heavy pulse currents can be drawn, at least for a short time, without arcing. Some low pressure discharge devices operate with current densities well in excess of 100 amperes/cm². Arcs, if they do occur, do not alter the cathode properties. Not only is the tungsten matrix resistant to arc damage, but arc sputtering uncovers a substrate of the same composition and emission capability as the original surface.

However, during cold emission the barium replacement mechanism — tungsten reduction of the aluminate — followed by migration of free barium to the surface⁽⁶⁾ does not operate. In cold-cathode devices which are deliberately allowed to arc, local intense heating caused by the arc spots allows barium monolayer renewal to take place automatically, maintaining the cathode surface in an active condition. In the thyratron, this option is not available: the cathode cannot be allowed to arc. To maintain cathode activity the surface must be heated by some other means, both to activate it during manufacture, and to bring it to reactivation temperature on each operating cycle.

The discharge-heated cathode concept provides a means to accomplish this in a hydrogen thyratron. The cathode is configured to be heated for initial activation during manufacturing, and to heat itself automatically during operation by dissipation in its structure and surrounding gas discharge. Each time it reaches the activation temperature, it renews itself without the need for external power. Once the operating temperature is achieved, the monolayer is maintained and emission takes place by normal thermionic processes. At shutdown, the monolayer remains to provide emission capability for arc prevention during the next cold start.

Impregnated tungsten has long been used for thyratron cathodes, notably in British practice.

Typically a small slug of material is run hot, emitting its own electrons and replenishing the active material on nearby large-area structures that are also used as emitters. In the discharge-heated cathode, this material is used differently, particularly during the first seconds of operation. The unique ability of the cold material to emit without arcing, for a few moments at least, allows the corners and surfaces of the emitting structure to be heated, thus starting the flow of thermionically emitted electrons.

In applying this concept, several uncertainties were encountered: how much emission could be drawn from the cold material without excessive arcing; would the proposed self-heating be fast enough to prevent such arcing; how would the triggering characteristics be affected during the transition from cold to hot operation; what current distribution was to be expected for a geometrically complex structure arranged for discharge heating; and what the proper geometry was for the cathode itself.

Yet, preliminary experiments showed that sufficient non-destructive and precisely triggerable cold-cathode emission could be obtained from a structure of reasonable size, and tube behavior could be predicted despite the need for many estimations and simplifying assumptions. The goal of an instantly starting thyatron was then soon realized in a practical tube.

Experimental Tube Design

The design goals for the feasibility studies were appropriate to a 2-inch diameter thyatron as the test vehicle. Thyatrons of this size are convenient to build and test to obtain scaling information. Boundary effects, construction, and cost are minimized. Accordingly, a series of tubes was made from parts commonly used for the EG&G HY-10/7620 thyatron, a 20 kV, 5 kW tube. The only major departures from conventional designs were the new cathodes and the thermally isolated reservoirs. The reservoirs are standard assemblies in enclosures attached to the main envelope by tubing. (A typical tube is shown in Figure 1.) The cathode was heated directly via a heavy-duty feed-through during processing and activation. This feature also allowed the tube to be operated in a conventional hot cathode mode for diagnostic purposes. An auxiliary grid supplied pre-trigger ionization. The heat shields and spacings of various electrodes were arranged to prevent long path discharges during cold cathode start-up operation, except to the emitter surface.

Similar tubes are being planned, built, and tested for high power operation using 4.5- and 8-inch diameter envelopes to verify scaling to megawatt average power operation.

Cathode Design

To design a thyatron that met the specifications given in Table 1, the pulsed emission capability of the cathode material when cold had to be established first. The geometry, current density distribution, heat balance, and warmup of the cathode were dependent on these values.

To characterize the material, a variety of tubes were built and tested. Figure 2 shows some of the cathode configurations used.

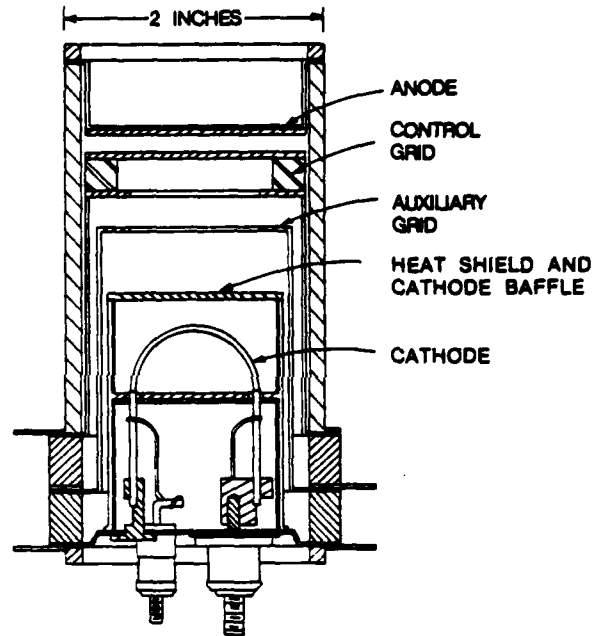


Figure 1. Experimental Instant-Start Thyatron.

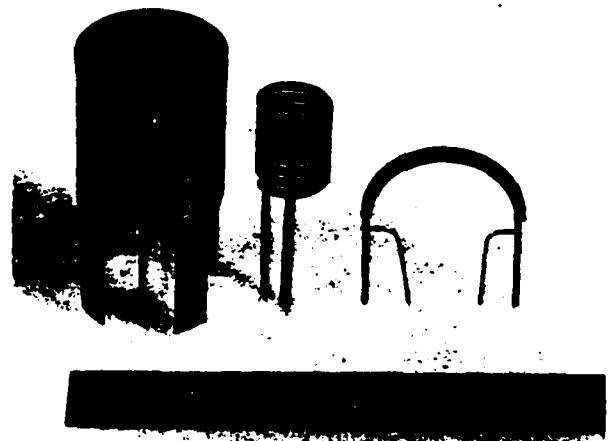


Figure 2. Experimental Cathode Configurations.

Maximum Current Density: The main requirement — that the cathode not arc during cold start and warmup — is most severe at switch-on, when the emission capability of the cold cathode is at a minimum. This factor determines the minimum cathode size for a given tube rating.

A large, planar cathode was first chosen as the most likely to provide a reasonably uniform current distribution. Single, isolated pulses were used to prevent cathode heating. As the pulse current was increased, arcing was readily detected by step discontinuities in the oscilloscope trace of the diode voltage drop.

For this 1-inch diameter cathode, the arc condition for cold operation was 80 amperes/cm². Arcing was evident in about one out of every ten pulses at this current density, occurring about 200 ns after the start of the pulse.

No definite arc limit could be determined for a cold oxide cathode of comparable size. The cathode either arced or failed to conduct on each pulse.

Measurements on cathodes of more complex shape intended for actual use in the experimental tubes yielded higher cold-cathode current density limits. In one case, a single arch cathode similar to that shown in Figure 2, the current limit exceeds 220 amperes/cm² with 10-microsecond pulses.

Current Distribution: Current and power dissipation distribution on the cathode surface of a thyratron has been established as a function of the plasma sheath voltage, plasma column electric field, the internal cathode resistance, and the specific surface resistance of the cathode. Of these, the last is the least well characterized for pulsed hydrogen discharges.

The surface resistivity (R_0) of cold cathodes operated under single pulse conditions was determined from the change in diode voltage drop versus pulse current. We assumed uniform utilization, and made use of the facts that the plasma field is reasonably independent of current,⁽⁷⁾ and that sheath voltages are relatively constant.^(7,8) A cathode of 11.2-cm² area, with an internal cathode resistance of 0.68 ohm was used. Good linearity of voltage drop with peak current was obtained over 260-1240 amperes in 0.4 torr of hydrogen.

The resistivity obtained, $R_0 = 0.11 \text{ ohm-cm}^2$, is in agreement with a reported measurement made in the vacuum of $R_0 = 0.25 \text{ ohm-cm}^2$, for a dispenser cathode,⁽⁵⁾ an emitter similar to the impregnated cathode.

These values are encouragingly low. By comparison, standard oxide cathodes at operating temperature have much higher values of R_0 , typically 2-10 ohm-cm². When cold, the surface resistance becomes extremely high. As a consequence, they suffer disastrous arc damage if pulsed operation is attempted.

Since the current density distribution to be expected in tube service was unknown, and because of the predetermined fixed size of an ideally configured commercially available impregnated tungsten cathode, the current densities of early cathode designs were set at 45 amperes/cm² (a value also thought to be reasonable for the cathode when hot). The cathode, a short helix, was 11.2 cm² in available area.

Cathode Geometry: While arcing was to be avoided, the intent was to run the cathode heavily loaded to minimize warmup time and to ensure that it would run hot. In this, as well as other respects, the short helix was ideal. It was self-shielded to some extent and had a high surface-to-volume ratio, with a heat capacity of only 0.18 cal/°C. A significant feature was the large ratio of conductor length to cross-sectional area. This increased the total internal resistance and easily heated the structure for initial activation or tube diagnostics by passing heater current directly through it. Its inductance was 330 nH — negligible compared to the 10 μH PFN.

The large-length-to-cross-section ratio has been retained in subsequent experiments to provide rapid self-heating. Most of the cathode heating is caused by dissipation in the cathode plasma sheath (sheath voltage, ~20 V, times average current) or in the internal resistance of the tungsten structure. At current densities over 80 amperes/cm², the resistive heating contributed over 50% of the heat input in the designs tested. With a low surface resistivity, its corresponding power dissipation is also low, typically about one tenth the total.

Feasibility Tests and Evaluation

One triode and several tetrode designs, using both planar and helical cathodes, were built and successfully operated under test conditions of 20 kV anode voltage, 1 μs pulse width, 0.5 A dc average current, and a pulse repetition rate of 1000 Hz. Three identical tubes of the type shown in Figure 3 were built and tested using the final helical cathode design. Subsequent tubes (as in Figure 1) were built using a single curved bar of cathode material, and tested in a variety of 1, 5, 7, and 10 microsecond pulse conditions at several hundred amperes peak and several hundred Hz. The same cold-start procedure was used with all tubes.

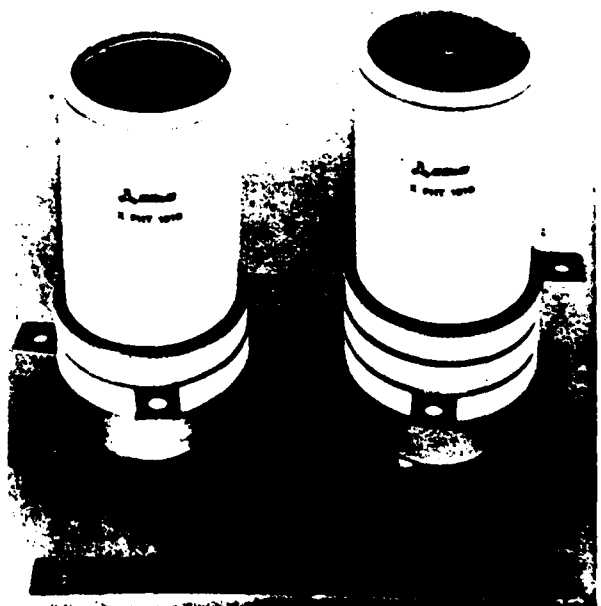


Figure 3. Discharge Heated Thyratrons.

Cold-Start Procedure: The typical cold-start procedure involves warming the appended reservoir to increase hydrogen pressure in the tube, and turning on the auxiliary grid dc power supply so that once the tube is running, a 5 to 20 mA keep-alive current flows. Then the anode supply voltage is increased to yield up to 20 kV on subsequent resonantly charged pulses. The tube is then ready to fire, although the cathode and the tube remain cold.

Then, when a start is desired, the grid driver is snapped on. Each time this is done, the thyatron starts instantly, at full power. All pulses occur at full anode voltage: the tube passes instantly from cold, nonoperating status to full operation.

Startup has been repeated at will scores of times during tests and demonstrations, without inadvertent cathode arcing or tube holdoff failure in any of the experimental tubes.

Triggering Behavior: Most discharge heated thyatron operations have been performed using a 5 to 20 mA keep-alive applied to the auxiliary grid. This allowed routine use of a standard 800 V, 4 a, solid-state driver producing a 0.5 μ s pulse (FWM). This driver was capable of reliably triggering the experimental discharge heated thyatrons, starting cold. With the keep-alive applied, anode delay time was less than 200 ns, with grid breakdown occurring at less than 700 V on the leading edge of the driver pulse.

As the cathode warmed to its full operating temperature, the grid breakdown voltage and the anode delay decreased. When the cathode reached equilibrium, these parameters were almost independent of the auxiliary grid keep-alive current, and the grid signal was indistinguishable from that of the thyatron when operated with externally

supplied cathode heater current (or from that of a conventional, standard thyatron). The anode delay time drift was less than 100 ns for the helical cathode tubes measured over the first 30 seconds after turn on. For the single bar cathodes at current densities of 30 to 210 amperes/cm², delay time drifts were 20 to 180 nanoseconds respectively. In almost all cases the time jitter was less than 5 nanoseconds and often less than 2 nanoseconds.

In any thyatron the anode delay time is reduced as the cathode warms to equilibrium temperature. In conventional tubes several minutes are allowed for this process. In the discharge-heated thyatron, less than 30 seconds is allowed, starting from the first pulse. These stringent specifications were met by a combination of cathode activation, adequate triggering, and use of a cathode having a small heat capacity, able to rapidly assume its final temperature.

Life: A sample of the helical cathode design was evaluated and life tested with the results given in Table 2.

During the life test, the tube was cold-started for a logged total of 47 times. In previous tests, an additional 40 to 50 cold starts were made. Repeated starts at full power from cold did not affect the triggering characteristics: time jitter remained less than 1 ns, and the 0 to 30 second anode delay time drift was less than 100 ns.

Columns 2 and 3, Table 2, show that conventional 2-inch tubes perform similarly under similar severe operating conditions. In the first of these test conditions, the conventional tube ran exceedingly hot and failed catastrophically. The second test produced a range of short operating lifetimes for the five-tube sample involved. Limited data for conventional tube operation in the vicinity of the

Table 2. Helical cathode DHT performance.

Parameter	Symbol	DHT Testing	Hot Cathode Type 7620 Life Tests (Typical)	
Anode Voltage, kv	epy	20	20	14
Peak Current, a	ib	500	240	175
Pulse Width, μ s	tp	1	1	0.42
Pulse Rate, sec ⁻¹	pps	1000	2000	6000
Pulse Rise-Time, ns	tr	200	200	88
Average Current, Adc	Ib	0.5	0.48	0.34
RMS Current, Aac	Ip	15.8	10.7	7.2
Grid Drive:				
Control Grid Voltage, v	egy2	800	180	180
Control Grid Impedance, ohms	Zg2	100	500	500
DC Average, Adc	Igl	0.02	—	—
Time Jitter, ns	tj	<1	<2	<1
Anode Drift:				
Drift, ns	Δt_{ad}	<100	40	<50
Stabilization Time	tas	0-30 sec	2-10 min	2-10
Life, Hours	—	266	412	250-400
Number of Tubes Tested	—	1	1	5

program objectives indicate that the plasma cathode thyatron behaves much like a standard thyatron of equivalent size, and may have a similar intrinsic life.

Testing on later designs, largely confined to producing basic design data, has included some

extended operation at high current densities. Table 3 compares some of the results.

During normal testing the arch cathode tube has exceeded the shot life requirements for high power operation, even though the cathode is very heavily loaded.

Table 3. Comparison of test results.

	Helical Cathode	Arch Cathode	Standard 7620 Oxide Hot Cathode
Cathode Area (cm ²)	11.2	1.46	30
Current Density (a/cm ²)	45	220	8
DC Average Current Density (A _{dc} /cm ²)	0.045	0.452	0.016
RMS Average Current Density (A _{ac} /cm ²)	1.42	9.97	0.358
Pulse Width (μs)	1	10	0.4-1
Life (Hours)	266	>>12	250 to 400
(Shots)	9.6 x 10 ⁸	>>8.6 x 10 ⁶	2.9 x 10 ⁹
Cold Starts	>100		N/A

Scaling to High Power

Using the results obtained with the 2-inch experimental and feasibility models, large scale tubes are being built and tested. Figure 4 shows the cathode configuration for a 10 kiloampere design. The cathode area is 80 cm², giving an average current density of 125 amperes/cm². The envelope and high voltage structure are based on the results of high power burst mode tests performed with conventional hot cathode designs, the HY-5001 and HY-5002.⁽⁹⁾ The complete structure, with an isolated reservoir and pressure gauges, is shown in Figure 5.

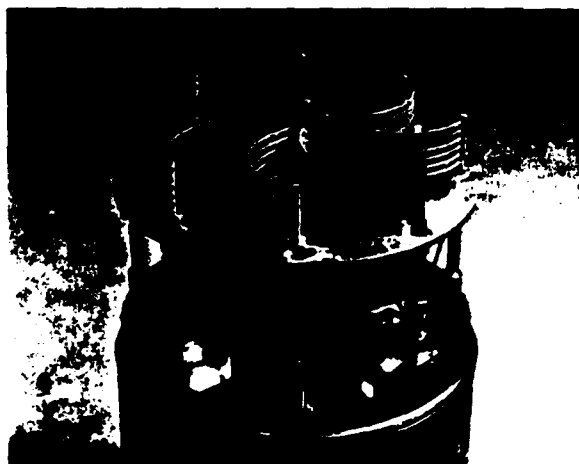


Figure 4. 10-Kiloampere Cathode Configuration.

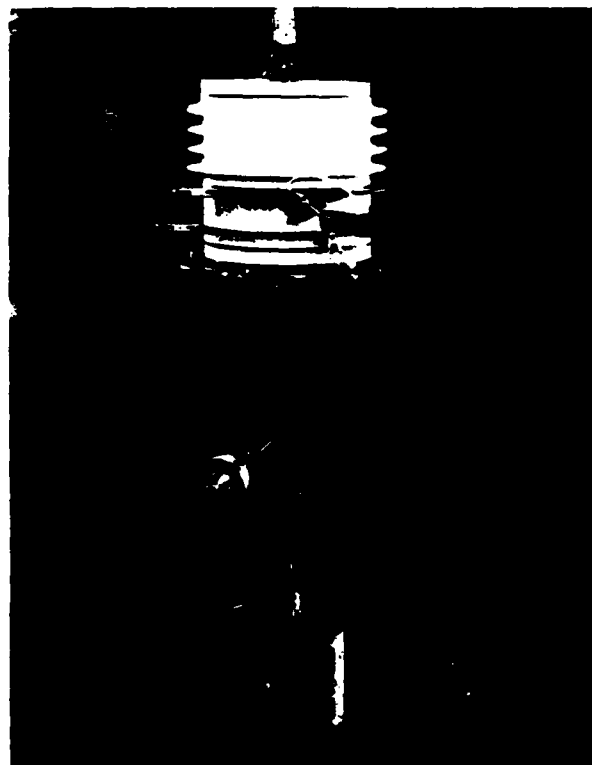


Figure 5. Experimental 10-Kiloampere Tube.

Experiments with configurations of this size are intended to verify design principles and scaling, and to lead directly to cathode designs for 40 kiloampere, megawatt average power bursts.

The Reservoir

In an instant-start tube, the initial non-operating hydrogen or deuterium gas pressure must be maintained at a value that allows tube start. During subsequent operation, the pressure may be stabilized by replenishing any gas buried or consumed by clean-up processes which may take place rapidly during cold-cathode starting. Finally, the fill gas purity must be maintained against possible accelerated outgassing of the cathode and other tube parts during tube operation. For these reasons, simply filling the tube envelope with gas at the proper starting pressure is inadequate. A reservoir is required.

In conventional, hot-cathode thyratrons pressure is maintained by either the usual heated metal-hydride reservoir and auxiliary electrical control circuits, or by the use of an additional heated getter for gas impurities. Since these reservoirs are heated structures, they often require warmup times roughly commensurate with those of hot cathodes. On shutdown, as the reservoirs cool, the titanium or zirconium metal typically used absorbs the gas with which it had been in equilibrium. The tube is left partially exhausted, at a pressure too low to allow instant re-start. A delay for reheating both cathode and reservoir is required, if the tube is to be operated after brief shutdown.

We have been investigating several ways to maintain the desired gas pressure of 0.2 to 0.5 torr in an instant-start tube. One of these is the further development of existing techniques for maintaining hydrogen pressure despite reservoir cooldown, typically by secluding the active material behind a separate palladium or platinum-silver barrier. Heating and gas transfer rates through the barrier are chosen to allow a tube-volume of gas to be locked out of the reservoir during cooldown, thus keeping it available for a subsequent instant startup. Thermal characteristics are also designed to replenish the gas fill through the barrier during tube operation, using heat generated in the cathode.

We are also exploring the behavior of recently developed transition-metal alloys capable of maintaining an equilibrium pressure of hydrogen in the desired pressure range at essentially room-ambient temperatures.

Recent work on metal-alloy hydrides for use in hydrogen energy storage and pressure-buffer applications^(10,11,12) indicates that it is possible to control room temperature equilibrium pressure over several orders of magnitude by suitable substitutions of other metals in the hydride alloy lattice, especially in the system LaNi_5 . We have been working with arc-melted, annealed, and hydrided samples of the system $\text{Zr}(\text{Fe}_x\text{Mg}_{1-x})$ developed by the Magnetic Materials team at Fort Monmouth. They discovered that this material exhibits room temperature hydrogen plateau pressures of 0.1-1 torr for compositions close to equimolar ZrFeV , with pressure adjustable by varying the composition. Large amounts of hydrogen can be stored in suitably activated material and recovery of equilibrium pressure after system evacuation is very rapid.

Using this material, we have made and tested reservoirs which appear promising as replacements for conventional heated reservoirs in the instant-start tube.

Reservoir design using the new complex alloys is a promising route to the desired cold-start reservoir. The dependence of equilibrium pressure upon ambient temperature is such that actual gas densities (important in respect to tube operation) are well maintained. Packaging of reservoir alloys for use in tube activation, prevention of poisoning during operation, and exploration of performance in actual tubes, all remain to be completed. Design of actual reservoirs for use in the instant-start tubes will be strongly affected by the cleanup rates observed in cold starting, a subject now under investigation.

The Envelope and High Voltage Structure

The overall objective of the current development program is to reduce the weight and increase the efficiency of the system which uses the switch. Elimination of heater power supplies is a major step toward meeting this objective, but further improvements in the switch structure are also needed. Current and voltage requirements were realized earlier in the development of high power, hot cathode thyratrons,⁽¹³⁾ resulting in a device weighing about 47 pounds. All of the restrictions imposed on the design of the earlier hot cathode tube still apply, and must be met in a device of half the weight.

Two major steps have been taken to obtain this reduction. First, the ceramic insulator lengths, the corresponding internal supports, and the connecting structures have been shortened. However, operation at relatively high external electric field stresses results; therefore, the tube must be operated in a dielectric medium other than air.

Second, an extensive thermal and mechanical analysis has been conducted to determine minimum size for various parts of the tube. While switching up to a megawatt of average power during a burst, the grid structures each receive over 1 kilowatt; the total tube dissipation is about 8600 watts. By taking advantage of the short-burst length, both the anode and base structures are significantly reduced. Further analysis of stress on the ceramic seals resulted in the ceramic insulator thicknesses being substantially reduced. The overall result is a new 25-pound configuration which is compared with the earlier MAPS-40/HY-7 structure in Figure 6.

Conclusions

By employing the concept of a discharge-heated cathode, the design objectives specified for an instant-start hydrogen thyratron requiring no warmup time and no heater power have been met. Simplifying assumptions facilitated the design of the cathode, and enabled the behavior of experimental tubes to be predicted.

Several 2-inch diameter tubes built from standard parts operated consistently at established test conditions of 20 kV anode voltage, 500- μ a peak current, 1- μ s pulsewidth, and 1000-pps pulse repetition rate. Other experimental tubes demonstrated operation at high current densities with 10 μ s pulsewidths.

Triggering requirements are comparable to those of equivalent hot cathode thyratrons. With an appropriate driver and several milliamperes of keep-alive current, the jitter is less than 1 ns and the anode delay time drift is less than 100 ns.

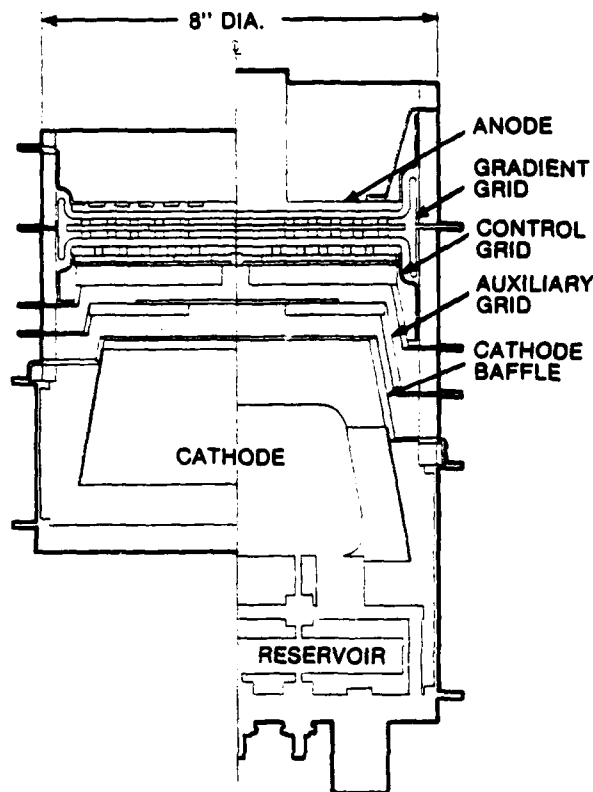


Figure 6. MAPS-40 Thyatron and Lightweight Instant-Start Version.

Use of a relatively low-powered, solid-state driver gives a switched power gain of more than 1000.

A representative tube accumulated 226 hours of life, and further testing on subsequent designs indicates that the discharge-heated thyatron has an intrinsic lifetime at least comparable to standard tubes operated under similarly severe conditions. Feasible instant-start reservoir systems are being investigated, and lightweight, megawatt tube structures are being designed.

Acknowledgments

The cathode concept and initial designs are due in large part to the efforts of Dr. D. Fleischer and much of the recent cathode data have been taken by Mr. U. Hemmer. The low temperature reservoir materials have been suggested and prepared by Dr. A. Tauber and Dr. R. Finnegan of USAERADCOM, Fort Monmouth, New Jersey.

This work in this paper has been supported in part by:

US Air Force (AFAPL), Dayton, Ohio
US Air Force (AFWL), Albuquerque, New Mexico
US Army (ERADCOM), Fort Monmouth, New Jersey

References

1. L.N. Vagin and L.G. Ivleva. "The Autron - A Controlled Plasma-Cathode Gas-Discharge Device," *Priory 1 Tekhnika Eksperimenta* 6 157, 1968.
2. D. Fleischer and D. Turnquist. "Plasma Cathode Thyatron," Final Report, ERADCOM Report Number DELET-TR-77-2704-1, September 1979.
3. Aksenov, et al. "Controlled Gas-Discharge Instrument with a Cold Hollow Cathode," op. cit. 4 184, 1970.
Aksenov, et al. "Low Pressure Spark Gap Switch with Hollow Pilot Electrode," op. cit. 6 218, 1970.
Aksenov, et al. "Controlled Gas-Discharge Device with Cold Hollow Cathode," *Electronic Letters* 7, No. 3, 61, 1971.
Aksenov, et al. "Some Special Operating Features of a Pulsed Gas Discharge Device with a Hollow Trigger Electrode," *Radio Eng. and Electr. Phys.* 16, No. 7, 1192, 1971.
4. D. Fleischer, D. Turnquist, S. Goldberg, and N. Reinhardt. "The Plasma-Heated Thyatron," *IEEE Transactions of Electron Devices*, Vol. ED-26, No. 10, p. 1444, October 1979.
5. A.H.W. Beck. *The Institution of Electrical Engineers*, Paper 2750R, 1958.
6. E.S. Rittner, W.C. Rutledge, and R.H. Ahlert. "Mechanism of the Barium Aluminate Impregnated Cathode," *J. Appl. Phys.*, Vol. 28, pp. 1468-1473, 1957.
7. S. Goldberg and D. Riley. "Research Study on Hydrogen Thyatrons," EG&G, Inc., Wellesley, Mass., Vol. 3, 1957.
8. J.E. Creedon, S. Schneider, and F. Cannata. "Cathode-Grid Phenomena in Hydrogen Thyatrons," in *Proceedings, 7th Symposium on Hydrogen Thyatrons and Modulators*, Fort Monmouth, New Jersey, 1962.
9. J. Creedon, J. McGowan, and A. Buffa. "Adiabatic Mode Operation of Thyatron for Megawatt Average Power Applications," *IEEE Conference Record of 1976, 12th Modulator Symposium*, February 1976.
10. J.H.N. Van Vucht. "Intermetallic Compounds, Background and Results of Twenty Years of Research," *Phillips Technical Review* 36, pp. 136-146, No. 5, 1976.
11. D. Shaltiel, I. Jacob, and D. Davidov. "Hydrogen Absorption and Desorption Properties of AB₂ Laves-Phase Pseudobinary Compounds," *J. Less Common Metals*, 53, pp. 117-131, 1977.
12. R. Finnegan, A. Tauber, and F. Rothwarf. "Hydrogen Reservoir Materials in the System ZrV₂-xFe_xHy (private communication).
13. D. Turnquist, S. Merz, R. Plante, N. Reinhardt, and J. Creedon. "The MAPS-40 Burst Mode 40-kV Megawatt Average Power Hydrogen Thyatron," *IEEE Transactions on Electron Devices*, Vol. ED-26, No. 10, p. 1438, October 1979.

AN ECONOMICAL HIGH CURRENT FAST RECOVERY THYRATRON SYSTEM

T. P. Donaldson, L. J. Kettle, H. Menown,
C. V. Neale, B. P. Newton, R. Sheldrake.

English Electric Valve Co., Ltd, U.K.

Abstract

A requirement arose to charge a number of capacitive loads from a 27 kV source using a sinusoidal wave form composed of a 20 kA, 12 microsec, positive half cycle, followed by a 10 kA, 8 microsec, negative half cycle. A constraint imposed on the system was a recovery time of less than 80 microsec.

A complete switching system to meet the requirement is described. The economic and technical reasons for the choice of three glass tubes in parallel rather than a single ceramic double cathode tube are discussed. Two of the glass tubes operate in forward parallel and the third in reverse parallel. Solutions to the problems of current sharing, reverse triggering and fast recovery are also presented.

Introduction

Financial considerations are of prime importance when considering equipment design. Normally during the development stage it is customary to choose a component which already exists, taking into account both its price and capability.

Seldom are components required in sufficient quantity to enable items to be custom built, but in the case of the Blumlein Charging System for the ATA accelerator at Livermore, thyratrons were needed in much larger quantities than this approach was feasible. (A total of 1200 chassis are required).

It is possible to make a double cathode ceramic tube which, with a single tube, would satisfy the requirement. Such a thyatron however with its features of high average current and ruggedness provides "Overkill" which must be paid for. It was therefore decided to develop an existing glass tube which in the event has produced a solution at approximately half the cost.

The thyratrons are required to switch power via pulse transformers to charge water blumleins which drive the ferrite loaded accelerator cavities. Figure 1 shows the optimum current pulse required to drive the

pulse transformers, along with the current levels specified for testing the tubes, and a decision was made to adopt a multi tube parallel path approach by extrapolating known facts from the tubes driving the ETA. These are the FX2508 and are described in the article (Ref 1) where they are presently operating at 5-6 kA. Thus it was decided that a reasonable approach would be to adopt a three tube triad.

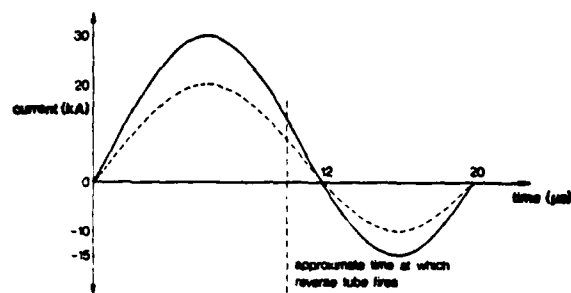


Figure 1.

This doubles the current capability of the forward tubes and an inverse tube added to carry the reverse current component.

The task has proved far from easy and twelve months development has taken place as much development was required on the circuit techniques as on the tube itself and the following circuit was finally adopted. (Fig. 2).

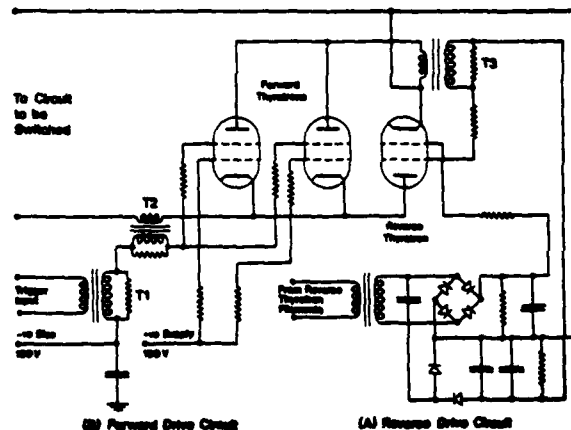


Figure 2.

Circuit Explanation

Two of the tubes in parallel switch 10 kA each and are able to hold off 27 kV when not conducting. The third tube, connected in parallel with the other two but in the reverse

position, switches 10 kA and is able to hold off 27 kV reverse when not conducting. In the single switch chassis shown in Figure 2, each CX1538 tube is primed by a 60 mA DC G1 drive and biased by -140V on G2. Power for the biasing of the tube in the reverse position is derived from its heater filament transformer. The triad, forming the switch chassis, is triggered by a 1 μ sec 500 V pulse applied from T1 to G2 of both forward tubes via the secondary of T2. The effect of T2 which has the full forward current through its primary is to increase the trigger voltage to either of the forward tubes which is late in firing. In practice this has been found to operate very well and current sharing of less than 5% is not difficult to achieve.

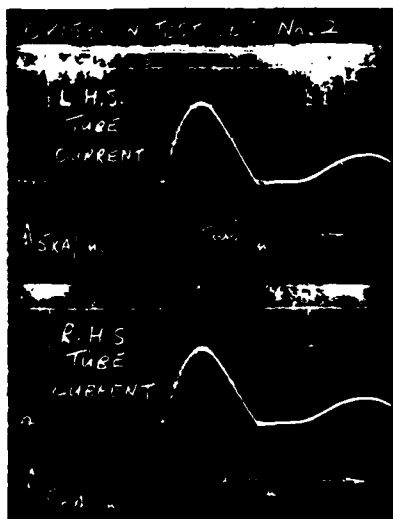


Figure. 3.

T3 provides the trigger to the inverse tube as indicated on the waveform in Fig. 1.

Tube Testing

The system used in the ATA employs over 3,000 tubes in the Blumlein charging system and two types of malfunction can occur, (a) prefire, (b) refire. In the former, the tube fires before it is triggered and in the latter the tube fails to recover.

In both cases the occurrences must be kept to a minimum and consequently a tight prefire/refire spec of 1 in 12000 shots has been applied.

The specification requires that the tubes be tested at current levels which are 50% above operating values, otherwise the test set circuit is as nearly as possible the same as has been previously described. Fig. 4 shows the equipment on which most of the

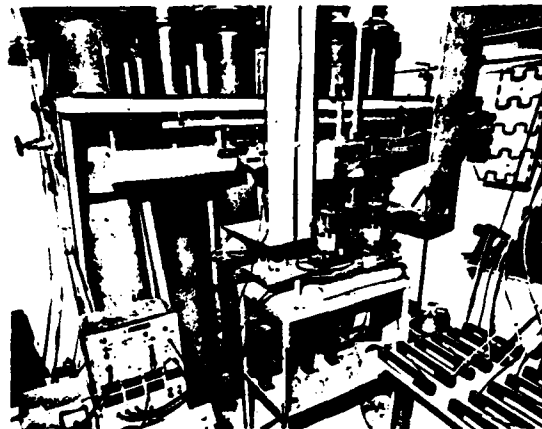


Figure. 4.

original development work was done, whilst Figs. 5 & 6 show an equipment recently built. This latter has been specifically tailored to test tubes to the test waveform shown in Fig. 1 and to operate in the circuit shown in Fig. 2.

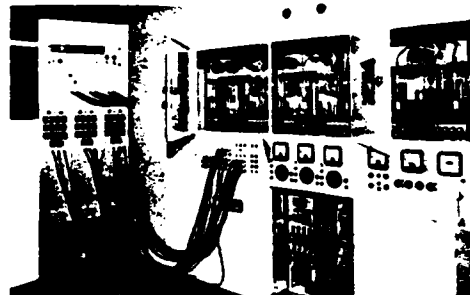


Figure. 5.

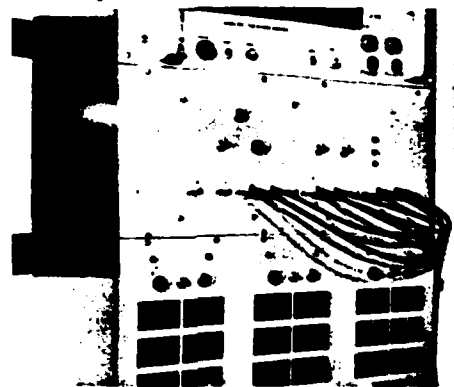


Figure. 6.

References

- (1) Off-Resonance Transformer Charging for 250 kV Water Blumlein. E Cook, L Reginato. Thirteenth Pulse Power Modulator Symposium.

Acknowledgements

The authors wish to thank the Directors of the English Electric Valve Co. Ltd. for permission to publish this paper.

HIGH-POWER TETRODES WITH PYROLYTIC GRAPHITE GRIDS IN SWITCH TUBE SERVICE

B.R. GRAY
Rome Air Development Center (OCTP)
Griffiss AFB, New York

S.G. McNees
EIMAC DIVISION of VARIAN
Palo Alto, California

Summary

The grids in a high vacuum tube are typically small in comparison to the other elements of the device, yet are subjected to an appreciable portion of the total power dissipated in the device. The degree of interaction between the grids and the electron stream flowing from cathode to anode of the tube, determine the total effect the stream has on the grids and of the grid on the electron stream. Electrons intercepted by the grid will produce several effects ranging from (1) stable grid current (2) grid current emission due to thermionic effects (3) grid emission due to secondary electron flow, to (4) deformation due to thermal mechanical mechanisms. An additional form of emission is that of field emission due simply to high electrostatic fields. The grids must also be able to absorb power that is radiated from the hot cathode and not be damaged. Grid performance is highly dependent on material selection, fabrication technique, heat sinking, power loading, etc. This paper describes a program to implement a unique material into the grid structures of a common high power tetrode, the EIMAC 4CW100000E. Modifications to the standard tube are described along with test results for the modified tube. In general higher control grid and screen grid currents are produced because of reduced secondary electrons generated in the tube.

Pyrolytic graphite has properties that set it apart from metallic elements. Among these are (1) high strength at elevated temperatures, (2) higher emissivity, (3) high dimensional stability and (4) low secondary emission.

A description of the idealized graphite form is presented and compared to a typical deposit of pyrolytic graphite. Pyrolytic graphite is formed from a chemical vapor deposition (CVD) process of the thermal decomposition of methane or other hydrocarbon gases.

Introduction

The modern day high vacuum electron tube is capable of exceptionally large power handling ability. Power delivered to a useful load however, must inevitably result in some internal power absorption within the tube. Present tube technology allows upward of one megawatt average power to be absorbed on and in the anode and have heater power input of about 10-30 kilowatts. The same tubes that provide that capability is limited to only 4 and 15 kilowatts of power on the grid and screen respectively.

It would seem that the anode dissipation limits can be readily increased by the proper cooling designs in the water flow system and the filament and/or cathode can be increased as need be to supply

whatever plate current is desired but the grids are caught in the middle, literally. Since the grid must be in the electron stream flow in order to exert controlling forces and since the cross section are very small, it is very difficult to provide an adequate heat sinking of the grid element, particularly in non-focused electron flow designs.

The theoretical power limit of any grid is the point at which either mechanical deformation takes place and/or it becomes hot enough to emit electrons and act as a cathode. Obviously what we seek then is a grid with unlimited power dissipation ability, free from mechanical distortion due to thermal effects and freedom from any emitted electrons because of high temperature.

Grid Problem Areas

A control grid inserted into an electron stream will be affected by the electrons that are intercepted if the grid has a positive potential such that electrons are pulled toward the grid and the energy associated with those electrons is deposited on the grid. When the energy deposited is equal to or greater than the effective work function of the grid material the grid will begin to emit electrons thermionically as if from a cathode.

Another method of grid-electron interaction is for an incoming electron to eject electrons from the atoms of the grid surface. This effect could occur without a detectable temperature increase of the material thus it is a distinctly different mechanism.

An alternate to grid emission by electrons being ejected by impacting electrons on the grid surface is for electrons to be pulled from the grid surface by high field gradients. Field emission is limited to cases where high field gradients exist at the grid surface. Field emission currents generally cannot be decreased by bias voltages on the grid. It is possible that negative grid voltages will increase the field emission current.

A grid in a hot cathode tube must be able to withstand the thermal loading imposed on it by radiated power from the filament-cathode without significant movement. Power dissipated on the grid input circuit likewise must not cause grid movement. Materials with low coefficient of expansion are essential in this along with proper bracing techniques and grid cooling. Only high temperature materials can be used, and special coatings are often used for grid emission control.

PYROLYTIC GRAPHITE

Pyrolytic Graphite (PG) has been called a space age material. This is not exactly the case, however because it was produced in the late 1800s and used for filaments in lamps. In the 1950s much more

Density gm/cm³
Tensile Strength kg/m²
Thermal Conductivity W/cm²/°C/cm 20°C
1000°C
Specific Heat joules/cm³/°C
Total Thermal Expansion 200-1000°C
Total Emissivity 1000°C
Electrical Resistivity ohm cm 20°C
1000°C

Pyrolytic Graphite		Molybdenum	Copper
A B Plane	C Plane		
2.21		10.2	8.89
13·10 ⁶	317·10 ³	100·10 ⁶	15·10 ⁶
3.98	.018	1.6	3.94
1.88	.011	1.1	3.6
2.41		2.66	3.42
.24%	1.6%	.6%	2.1%
.77	.5	.25	.04
4.3·10 ⁻⁴	.67	8·10 ⁻⁶	1.8·10 ⁻⁶
1.6·10 ⁻⁴		2.9·10 ⁻⁵	8.6·10 ⁻⁶

Table 1. Important Physical Constant of Pyrolytic Graphite

research was started as a result of the space program. Many applications have been made of PG since then to use its unique high temperature features. An effort has been made by several companies to exploit PG in electronic tube assemblies. It is not surprising to see why it is attractive as a material in high power tubes if one considers the physical constants in Table 1.

The structure of the graphite form of carbon consists of planar grouping of atoms with very strong bonding between atoms in the same plane but relatively weaker bonding between atoms in adjacent parallel planes. An idealized arrangement of the single crystal graphite lattice is shown in figure 1.

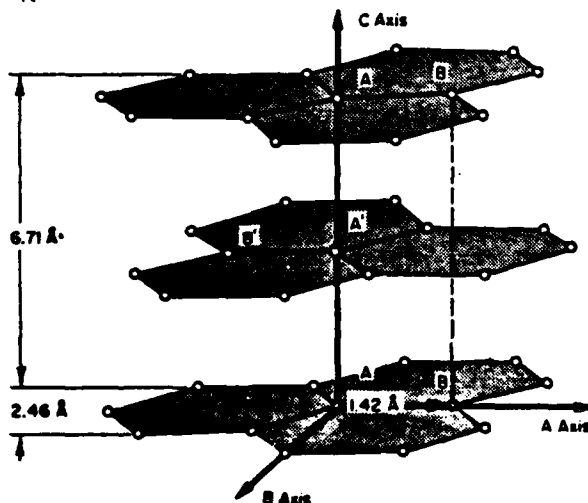


Figure 1. Ideal Crystalline Structure for Graphites

It is important to note here that pyrolytic graphite deposited through the chemical vapor deposition is different from the idealized form. Instead of being perfectly ordered in planes the ordering is quite random with the degree of ordering increasing with the deposition temperature. Deposits formed at 1000°C have a glass-like quality

while those formed at 1800°C have almost perfect ordering in the A-B plane. The ordering in the C direction however is more random. Ordering in the C direction approaches that of single crystal graphite at about 3000°C.

Other factors effecting the quality or type of deposit are (1) the substrate on which the deposit is formed (2) the flow rate and type of gas feeding the furnace (3) the pressure at which the deposit is formed and (4) heat treatment after the deposit is formed.

Furnaces for making the PG blank cups are shown in figure 2 photograph.

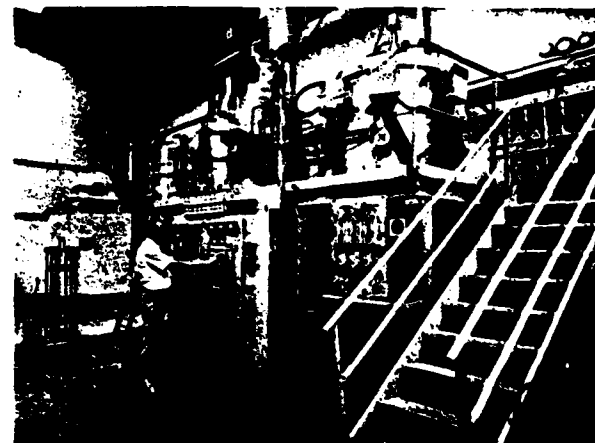


Figure 2 Photo of Furnace Used in Producing Pyrolytic Graphite

Tube Design

The layout of the completed tube is shown in figure 3. Figure 4 is a photograph of the cathode and control grid assembly of the 2097V. The only difference between the two tube types is the density of the filament. All copper parts which were used in the stem of the 4CM100000E were replaced with molybdenum and Kovar. The internal brazes were replaced with heliarc welds. These changes

improved the internal maximum safe operating temperature as well as improving dimensional accuracy. The increased current required for the double density filament presented no problem with this new stem design.

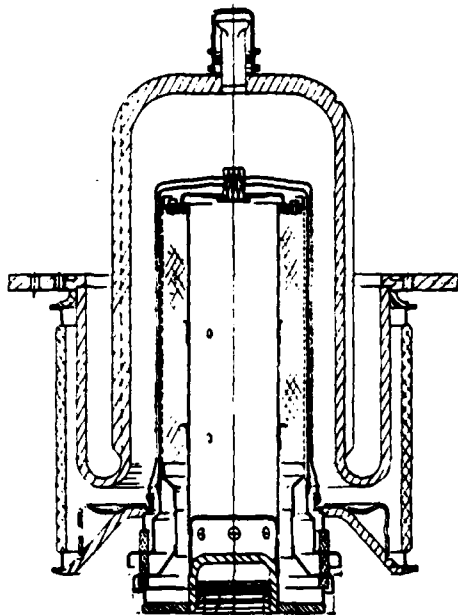


Figure 3. Layout for the Modified Tubes



Figure 4. Photo of the Cathode-Control Grid Assembly for the X2097V Tube

In a power grid tube using a non-focusing geometry the electrical performance is improved by reducing grid bar diameter and increasing the number of grid bars to 120 from 80 used in the

4CW100000E was practical and did not hurt tube rigidity.

The grids are made by first forming a graphite cup on a heated mandrel in the furnace. Thickness of the deposited layer is approximately 0.04cm. Following inspection, abrasive machining by sand blasting is used to form the grid slots and bars with the aid of a mask or template. The cutting action is primarily perpendicular to the deposited layer or radially in the case of a cylindrical blank cup. Grid bars of about 0.02cm in width have been produced in this fashion. It should be possible to produce even finer dimensions than this in thickness and width. Width of the bars for the two tubes of this program however are 0.03cm. The grid slot is approximately 0.254cm while grid cathode spacing is 0.1cm. Equivalent dimensions for the screen grid are such as to give the proper grid-screen alignment. Figure 5 is a photograph of several blank cups and finished grid units.

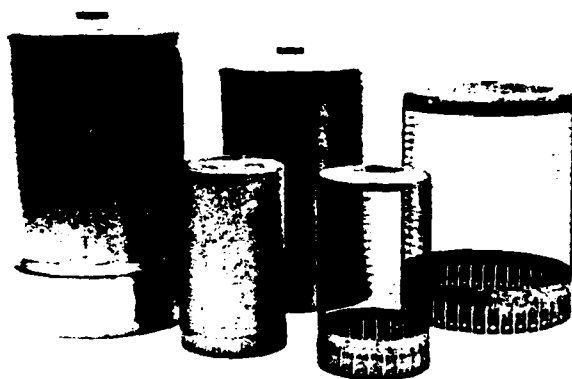


Figure 5. Photo of several grids showing blank grid cups and finished units.

Tube and Circuit Performance

Constant current curves are typically used to show the essential operating features of a gridded tube and it is assumed the electrode voltages shown are equal to the source voltage. While this is adequate for tube characterization, it is not the same as in a real circuit since a useful output is desired. A load of some type and a much higher anode supply voltage is employed in order to develop the useful output. The tube merely serves as a switch to control current flow through the load. The switch however is not an infinite current device responding in a proportional way to changes in load impedance or supply voltage.

Typically for short pulses, where variations in supply voltage during the pulse are held to a low value, it is desired to operate the switch tube at or near saturation with the anode operating at a minimum value. Either control grid or screen grid current and power is the ultimate limiting factor in this type of service. There is an optimum area of performance where the grid dissipation can be minimized simultaneously with anode dissipation.

During the test, at EIMAC and RADC, constant current curves were taken to characterize the tube. These tests proved that a higher grid current is required because of the reduced secondary electrons from the grid. It was also shown that with a high impedance load the supply voltage could be raised to higher values to obtain a minimum anode voltage during the pulse i.e. saturated conditions of 3-5

KV pulse for maximum efficiency.

Attempting to operate with a lower load impedance 200-300 ohms, however resulted in a minimum anode pulse voltage of 10-12KV at saturated anode current. In each case the point of saturation was defined as the level where anode current essentially limited and grid currents began a rapid rise.

Test results tabulated in Table 2 show some of the data points taken at RADC for the X2097U. No data was taken at RADC on the X2097V tube because of tube breakage, however comparison curves for the two tubes shows considerable improvement over the 4CW100000E. Figure 6 shows the difference in the cathode current for the three tubes when operating as diodes; i.e. $E_g = E_s = E_p$. This is in accordance with having a closer grid cathode spacing, 40 additional grid bars in each modified tube and doubling the filament area in the X2097V tube.

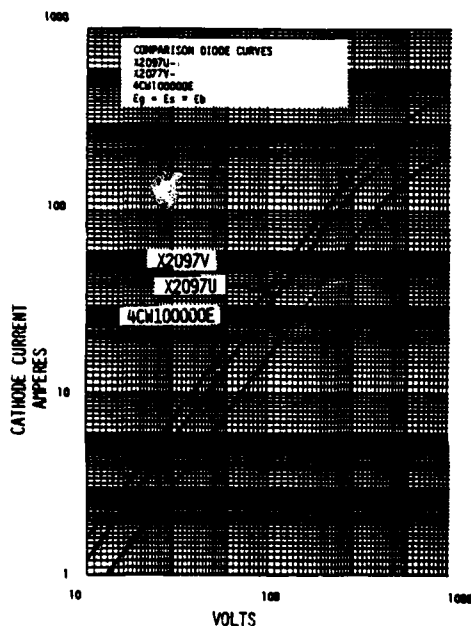


Figure 6. Comparison Diode Curve for the X2097V X2097U and the 4CW100000E

It was observed in the test at RADC and recorded in Table 2 that areas exist in the operating range of the tube where increasing grid currents can exist for either high or low anode pulse voltages if grid voltage is high enough. While it is easy to see that a minimized anode voltage near to or equal to grid voltage will produce high grid currents, it is not as clear that high grid currents can occur with anode voltage much higher than the grid voltage. The case of increasing grid currents at elevated anode voltage is not necessarily restricted to this test. Indeed data sheets for other tubes indicate it will occur, but very rarely is the condition seen because it is a rather inefficient method of operation and also because limited grid power limits prevent observation of the effect in many cases. Some type of series regulator circuit could encounter this condition.

It is also apparent in Table 2 and in the constant current curves; figure 7 thru 11 for the X2097V, X2097U and the 4CW100000E, taken at 2000 and 3000 volts screen voltage; that control grid current for the pyrolytic graphite gridded tubes is significantly higher for equivalent anode voltages and currents. This will be the result of eliminating or sharply reducing the amount of secondary electrons generated at the tube grids. Circuit designers have always used the secondary electrons as a form of free driving power, but with caution. Seems like the elimination of secondary electron is a hollow victory since more actual drive power is required which would only tend to make the grid become hotter. It will be shown later how the loss of secondary electron affects the mutual conductance of the tube.

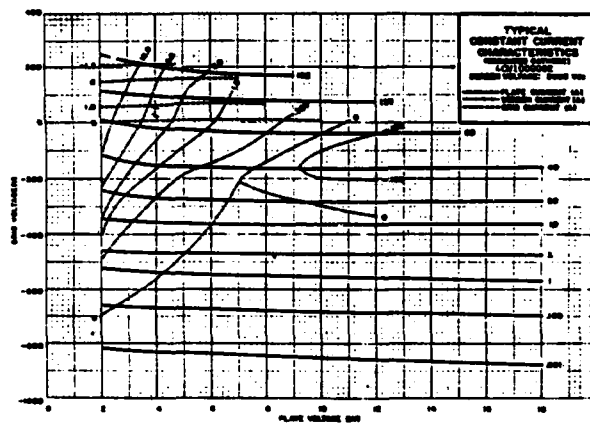


Figure 7. Constant Current Curve for 4CW100000E at 2000 Volt Screen

Ebb KVDC	Ep KV Peak	Ip Amp	eg1 Volts	ig1 Amps	eg2 KV	ig2 Amps	ic Amps	R1 Ohms
20.5	2.0	66	400	55	1.0	34.17	144	280
20.5	2.25	64	180	20	2.0	16.6	98	290
20.5	1.8	66	220	31	2.0	28.3	118	283
20.5	1.8	67.2	180	17	2.5	23.3	100	284
57	5	40	200	34	0.5	3.83	92	1300
58	10	40	200	30	0.2	1.0	72	1200
52	16	140	500	72	2.0	5.9	220	257
52	18	128	400	58	2.0	4.0	200	140
40	12	104	580	80	1.0	36.6	208	268

TABLE 2 Selected Data Points for X2097U Tube Tests

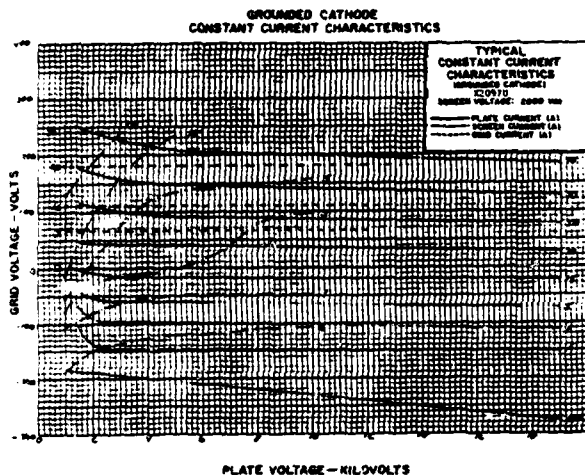


Figure 8. Constant Current Curve for the X2097U at 2000 Volt Screen

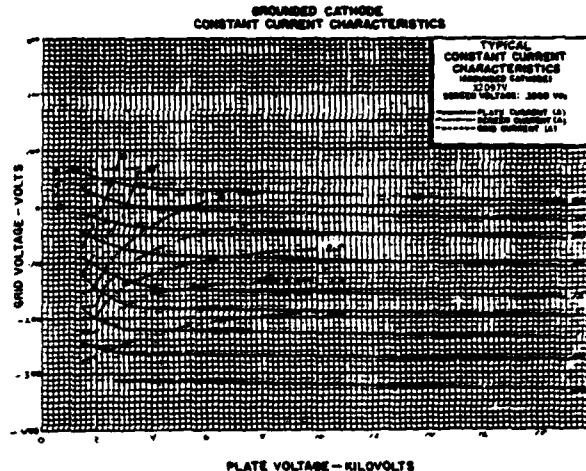


Figure 11. Constant Current Curve for the X2097V at 3000 Volt Screen

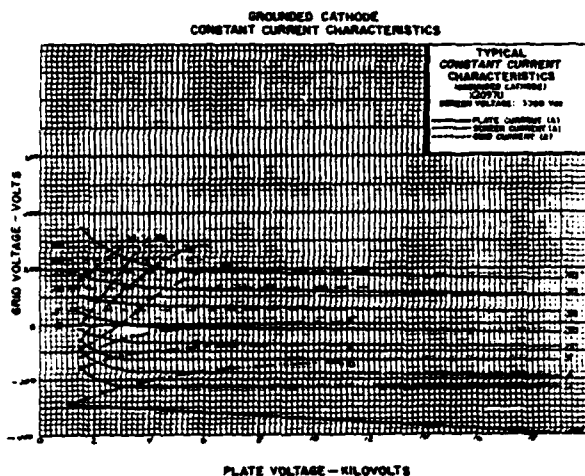


Figure 9. Constant Current Curve for the X2097U at 3000 Volt Screen

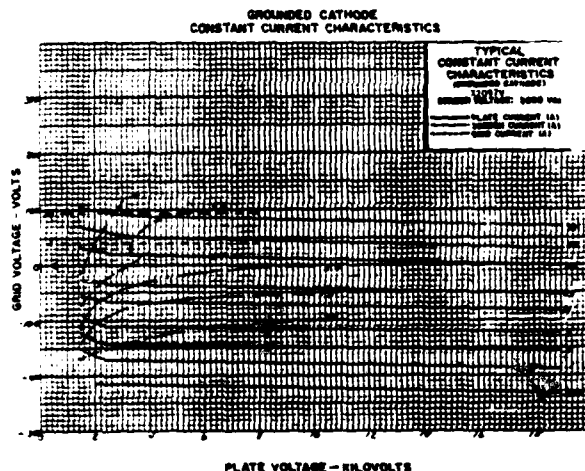


Figure 10. Constant Current Curve for the X2097V at 2000 Volt Screen

Test Modulator

Test modulator for evaluation of the tubes at RADC is shown in figure 12. In the foreground is a high power dummyload while in the background is the tube under test.

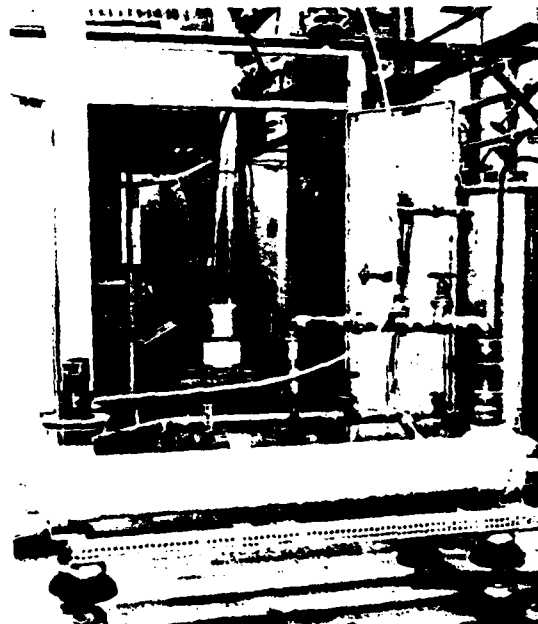


Figure 12. Photo of Test Modulator

The simplified schematic in figure 13 shows the main element of the video pulse circuit. P.S. 1 is a 140 KVDC supply rated at 9 amperes DC controllable from 2KV to the 140KV. The anode load resistor consists of a weak solution of copper sulfate circulated in two 6 foot lengths of 3 inch glass pipe. Heat dissipated in the solution is absorbed in a liquid-liquid heat exchanger cooled by a demineralized water cooling system. The circulating pump for the electrolyte is powered through a 3 phase 1:1 isolating

The bias stages for the driver and the tube under test includes a "Thyrte" voltage variable resistance sized so as to draw negligible current at just under normal bias voltages.

Without a regulating element across the bias supply capacitor the bias supply voltage will vary in response to the average grid current drawn by the tube. This variation will normally be an increase in the negative voltage from normal positive grid current flow. If negative grid current exists, however, the bias supply voltage will attempt to move in a positive direction reducing available bias. While this latter effect is an extreme situation certain peculiar systems can be complicated because of it.

It was noted that essentially the same techniques were necessary for controlling H.F. type oscillations in the tube as is commonly used for typical pulse modulators. Filament bypassing, grid circuits suppressors, shielding, etc. were all necessary.

In principle the fact that pyrolytic graphite has a fairly high resistivity should help provide suppression of spurious signals, particularly in large tubes because it would be in the direct field of the rf voltage. Certain large tetrodes or triodes have dimensions which could conceivably support an oscillation about the tube circumference between grid-cathode-screen-anode. With grids of pyrolytic graphite a lossy element would exist on the boundary of such an oscillating voltage field and tend to provide a loading effect.

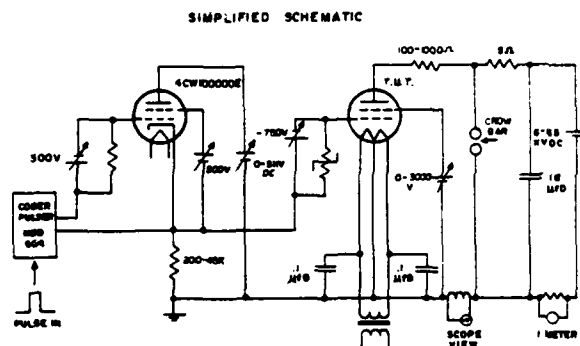


Figure 13. Simplified Schematic of Test Circuits at RADC

Primary Grid Emission

Primary grid emission was measured at the factory by the standard production test employing 60Hz positive half sinusoid power pulses to heat the grid and the negative half cycle to measure the emitted grid currents. Data presented in Figure 14 and 15 show the primary emission current for the modified tubes and the standard 4CW100000E. It is evident that the X2097U tube has a significant reduction in emission current even though closer hot spacings are used and the grid bars are increased. It is also clear that the X2097V tube is receiving much more radiated power from the cathode because of increased radiation from the cathode. It appears that the X2097V tube receives approximately two extra kilowatts of radiated cathode power as compared to the X2097U tube.

The relatively high thermal emissivity, while not that of a black body radiator, is considerably higher than that of tungsten or moly and is extremely helpful in making the grid operate at a lower

temperature with less grid emission.

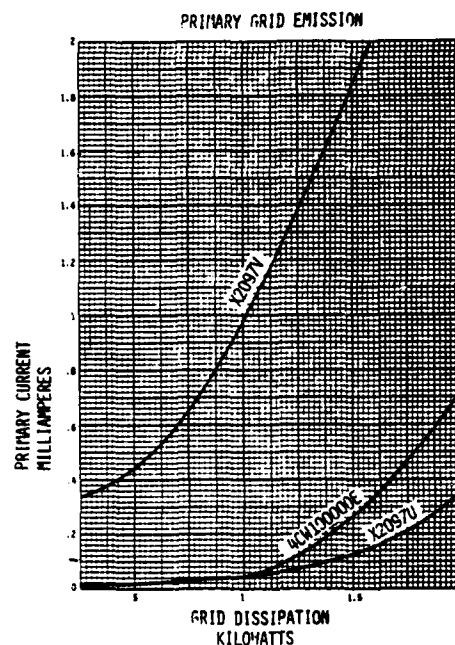


Figure 14. Primary Current Grid Emission for the X2097Y, X2097U and the 4CW100000E Tetrode.

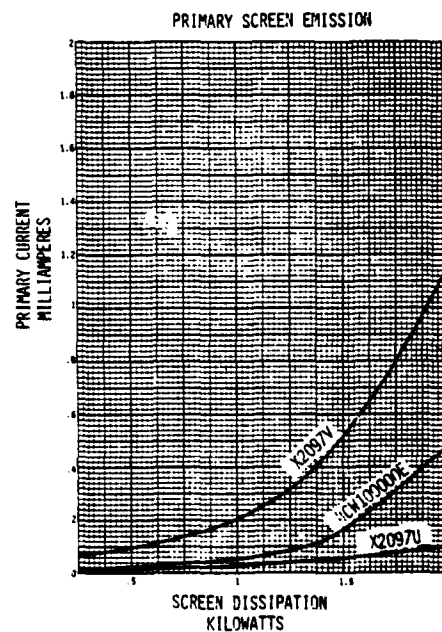


Figure 15. Primary Current Screen Emission for the X2097V, X2097U and the 4CW10000E Tetrode.

Secondary Electron Generation

Electrons emitted as a result of interaction between an atom and an impinging electron are termed secondary electrons as compared to electrons originating from the atom as a result of thermal effects. It is the intentional basis of operation of a large class of devices; photo multiplier tubes, magnetrons, crossed field amplifiers and is also an inadvertent feature of other electron tubes. Usually it is desirable to increase the secondary electron yield in the first class but reduce it in devices where it is not an essential feature. Much research has been done to understand and to emphasize the desired effect.

The susceptibility to secondary electron emission is dependent on several factors. Among these are (1) material density, (2) surface finish (3) temperature and (4) angle of incidence.

Figure 16 is a graph by Harries showing the electron emission yield ratio for a number of common electron tube materials.⁽³⁾ Note that materials that are desirable for many other reasons tend to have the highest yield ratio. Carbon identified in literature as lamp black, soot, or graphite has been used in small receiver type tubes for anodes. Aquadag or colloidal graphite, used in cathode ray tubes has a reasonably low yield. Tungsten, an otherwise desirable and commonly used high temperature metal, has a high secondary emission ratio.

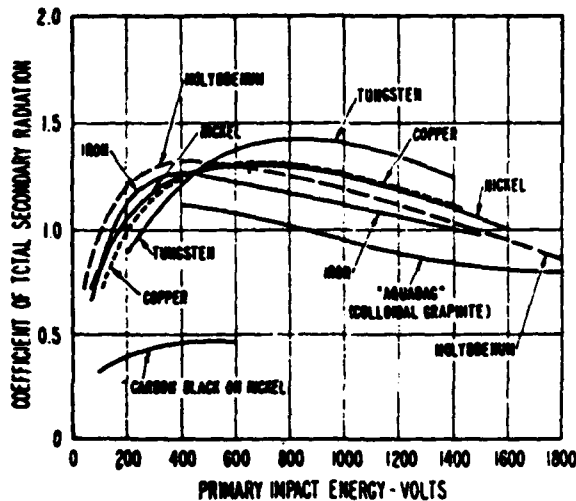


Figure 16. Comparison of Secondary Electron Yield Ratio for Various Materials as a Function of Electron Ratio.

Figure 17 (a and b) will give an insight into why carbon works so well for this application⁽⁴⁾. Shown is a representation of an electron striking a reasonably smooth and dense surface, in (a) and a surface coated with particles forming a matte like surface in (b). The electron striking a hard and smooth surface releases other electrons that can easily escape from the surface of the electrode. A rough surface finish of particles, however, forms a top layer that block the escape path of electrons released from under the surface and tends to absorb the released electrons.

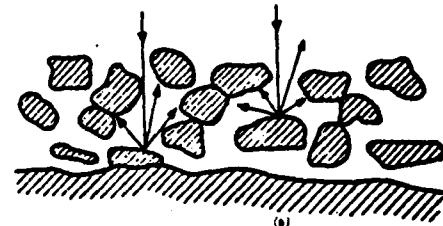
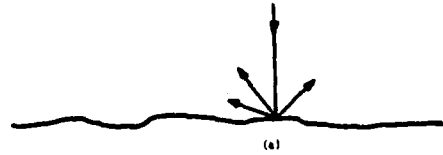


Figure 17(a and b). Showing the Effect of Coating On The Secondary Electron Yield

Figure 18 is a curve by Brüning relating the surface conditions of carbon to the electron yield⁽⁵⁾. This points out clearly that not only is the atomic structure important but also the microscopic arrangement of the elements i.e. loose particles versus smooth surface.

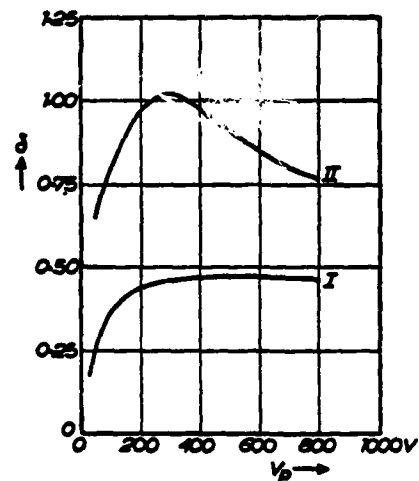


Figure 18. Curves Showing the Difference in Secondary Yield for Carbon as a Result of Surface Conditions

Note in figure 16 the maximum point in the secondary emission ratio as a function of the energy level of the impinging electron. One would logically assume that the total number of secondary electrons freed from the atoms would rise in proportion to the energy level of the received electron. Apparently, as the energy level increases the incoming electron penetrates deeper into the grid material releasing more secondaries from deep within the grids which are reabsorbed before reaching the grid surfaces to produce a measurable electron current. This is a plausible explanation for the well defined region of negative grid current of typical gridded tubes.

The angle of incidence of the incoming electron will also play a prominent role in the emission ratio. It is obvious that maximum energy is extracted from the velocity of the incoming electron if the electron impacts the surface perpendicularly with a greater probability of interaction with the atomic structure. Figure 19 by Muller shows the variations of secondary emission as a function of the incident angle of the impinging electrons. (6)

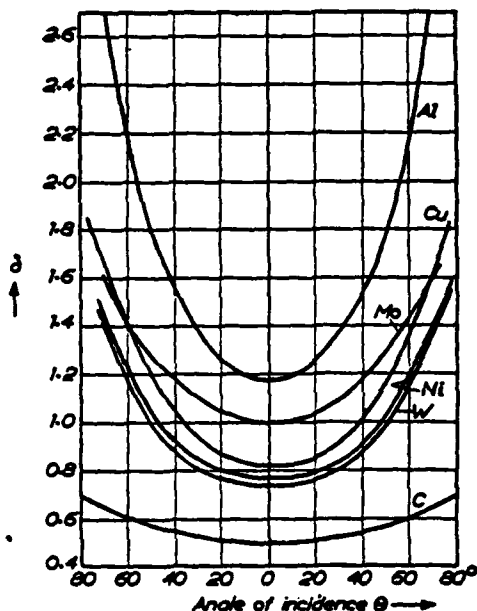


Figure 19. Graph Relating the Incident Angle of Impacting Electrons to the Secondary Electron Yield

Demonstration of Secondary Electron Control

As one of the motives for building the pyrolytic graphite gridded tube was to prevent secondary electron formation at the grids, a reliable method to demonstrate success or failure of the effort was needed.

One can see the effect of secondary electrons far easier than measuring directly. A meter placed in the grid or screen circuit of a tube shows only the algebraic sum of all currents flowing in the circuit. A current flowing in the grid circuit develops a voltage, polarity dependent on the direction of current flows, across the total circuit impedance. A negative grid current, i.e. primary emission or secondary electron flow will produce a positive voltage causing an unstable load for the driver stage. It is customary to place sufficient shunt loading across the grid so that the driver always sees a nearly constant load. The degree of loading thus partly determines the total drive power required plus the stability. To see the effects of impedance, R_1 in figure 13 was varied from 200 ohms to 55000 ohms. The only apparent effect is a degradation of the rise and fall time of grid voltage at negative grid voltages. That no reversal of grid current occurs indicates that secondary electrons have been eliminated or greatly diminished with the pyrolytic graphite grid. This is in marked contrast to a similar test with the standard 4CW100000E.

Increasing the shunt load resistor to little greater than 1000 ohms made operation very unstable, and positive grid drive above 50 volts was impossible. Attempts to provide for a pulse drive voltage capability of 200-400 volts prior to initiating start pulse also produced unstable operation. This indicates a significant reduction in the secondary electron generation. Compare also the characteristic curves in figures 7 thru 11 noting that no negative grid currents appear and that the area where secondary screen appears is much smaller than in the 4CW100000E.

High Voltage Stability and Field Emission

Considering the type machining used and that carbon in some form exists as loose particles, one could become concerned that a messy situation could arise in the form of loose particles or dust. Supporting this worrisome thought is that the tubes tend to not have as high a holdoff voltage as in standard metallic grid designs. This is not a final conclusion yet, because conditioning to higher voltage levels by normal high potential testing has been achieved. The first anode arc might occur at 30 KVDC while the next will occur at slightly higher levels if the energy in the previous arc does not damage the grid structure. Hold off to 65 KVDC has been achieved after only a few arcs.

An unfortunate tube breakage provided an opportunity to observe where arcs had terminated on the grid structure of the X2097V tube. It is not certain the amount of energy deposited on the grid but the mark left by the arc is a slight darkening of the dark gray surface. Due to the high thermal character of pyrolytic graphite, one could expect arc resistance to be a good feature of pyrolytic graphite.

Field emission curves for the two tubes were taken up to a maximum of 80 KVDC between screen and anode. At anode voltage of 50 KV field emission current is 0.5ma for both tubes while at 75KV the U and V version have 5.5ma, and 10 ma respectively.

Conclusion

In this paper a unique grid fabrication material has been described pointing out the strong positive feature along with some of the recognized negative ones and suggested areas of future work for improvements.

Positive Factors:

- (a) High thermal and mechanical stability
- (b) Low secondary electron emission
- (c) High emissivity for better radiation cooling
- (d) Ease of fabrication
- (e) Shows good resistance to arc damage

Negative Factors:

- (a) Can require higher drive power
- (b) Microparticles

Areas of recommended future work:

- (a) New methods of grid slot-bar machining
- (b) Coatings to introduce controlled secondary electron generation to lower drive power requirements.
- (c) Microparticle control.

References

1. S.G. McNeese: Final Rept RADC-TR-79-106 May 1979
2. W.H. Smith, D.H. Leeds; Modern Materials, Vol 7 1970 Academic Press
3. R.I. Sutherland; Care & Feeding of Power Grid Tubes pg 13, 1967, Harries

4. H. Bruining: Philips Technical Review, Vol 3, pg 88
5. H. Bruining; Physics & Application of Secondary Electron Emission; Electronics & Waves, McGraw Hill Book Co, Pg 43, 1954
6. H.Q. Muller; Die Abhangigkeit der Sekundarelektronemission einiger Metalle vom Einfallswinkel des Primaren Kathodenstrahle Z. Physics.

THE 1980 FOURTEENTH PULSE POWER
MODULATOR SYMPOSIUM

Application and Circuit
Considerations of the X2062J and K Switch Tubes

Sterling G. McNees
Eimac Division of Varian
301 Industrial Way
San Carlos, CA 94070

Summary

High voltage power grid switch tubes are used as simple DC off/on devices and, in addition, can control pulse shape and act as a voltage regulator. Two new high voltage, high current, switch tubes have been developed by Eimac for expanding fusion energy programs. The X2062J and X2062K have evolved from basic power grid designs which have been in production for many years at Eimac. Attention to the proper design parameters, proper choice of materials and their processing, plus many hours of high voltage, high current testing at the unique Eimac high voltage test facility have resulted in reliable economical tetrode switches. These new tubes are finding many applications around the world and have served to advance the state of the art in high voltage switching.

The X2062J and K are high-voltage high-current switch tubes (Fig. 1). The X2062J has a voltage rating of 100 KV and the X2062K 130 KV. Both tubes have identical current ratings of 80 Amps. Pulse lengths may vary from 1 μ sec. to several seconds. As a class D switch tube anode dissipation is approximately 2% of the total power load. The X2062J has a 350 KW continuous anode dissipation. The X2062K rating is 750 KW and, for short pulses, over 12 MW. (Table 1). This reserve capability means that the X2062J and K may be used as voltage regulators controlling such things as pulse rise time, load arc protection and recovery and compensating for voltage sag in the power supply.

In this paper, voltage, current, and dissipation, the three design parameters of most interest to the circuit designer, are discussed along with various application problems.

Although voltage hold-off is the first thing which comes to mind when thinking of switch tubes, current is where the tube design begins. The Child Langmuir Law determines the current density and thus the total anode area. The equation is:

$$J = \frac{2.3 \cdot 10^{-6} (V_1^{3/2} + V_2^{3/2})}{X^2} \text{ amps per unit area}$$

V_1 , the anode voltage during current conduction, must be greater than V_2 , the screen voltage, because of anode secondaries. The output spacing X is that distance required for arc-free operation at the rated voltage hold-off.

The word "arc-free" needs some defining. No high voltage tube can be guaranteed "arc-free". Obviously if output spacing is increased the reliability improves but the maximum current density decreases and an engineering compromise is necessary. A good definition of "arc-free" is less than one arc per day, and output spacing is based on this rather illusive definition.

Thus the only way to find out if a tube meets its design voltage requirements is by full power testing. Eimac has had for many years an in-house testing facility capable of 3 MW at 180 KV continuous. This facility permitted pulse testing at full current and voltage. Parameters were so chosen that anode and screen dissipation during the pulse are close to the maximum continuous ratings. This severe testing condition is the only way to ensure that a switch tube will meet the design objectives and give trouble-free service.

For good efficiency at rated current and class D operation, the anode "on voltage" should be about 2% of the "off voltage." The point to be made here is that an efficient tube cannot be a small tube. The X2062J and K are part of a tetrode tube family whose history goes back 15 years. The J and K uses many of the design concepts of these proven performers. The major changes are the anode and output ceramic assemblies. The X2062J and K are rated for 80 Amps or a current density at the anode of 80 ma/cm² for the J and 70 ma/cm² for the K at less than 2 KV plate voltage.

As already implied voltage hold-off is a function of spacing (Fig. 2). It is also a function of shape, temperature, material, and degree of vacuum. Much harder to understand, but nonetheless important, is the crystallography of the materials, their purity, and the amount of absorbed and dissolved gasses. Vacuum arcs differ from typical arcs in that the source of ions comes exclusively from the surfaces and, strangely, mostly from the negative element as positive ions. The arc always originates at the negative element. Although extensively investigated, the fact is that there is not a good understanding as to when and where an arc will occur. However, a body of empirical knowledge is being gathered. It is known that high melting, high work function, and high atomic number, but not radioactive materials, are best for high voltages. An oxide surface like chrome oxide often helps. The surface should be clean and free of organic materials. As techniques improve one is seeing a slow but steady improvement in the usable voltage hold-off for a given spacing, and it is expected that there will be still further improvement in the future.

Anode dissipation is the last of the major design factors. In any water-cooled tube the continuous anode dissipation rating is limited by the maximum heat transfer from the anode wall to the liquid, whereas for short pulses the anode wall acts as a heat sink. Although higher levels of dissipation can be attained; for long life under CW conditions the value of heat transfer at the wall-water interface ranges from 100 W/cm² for low velocity water to about 800 W/cm² for water velocity of over 30 ft/sec. These figures are doubled for the usually quoted value which is the dissipation at the electron beam anode surface. All dissipations above 100 W/cm² involve the generation of some vapor and

the velocity and volume of water determine where this vapor will condense. If the bulk water is less than 70°C this condensing produces sonic waves. These waves, if close to the anode surface, have the effect of causing quick release of the new vapor bubbles from the surface and, thus, improving the heat transfer rate. It should be noted that the transfer of heat from the anode to a dry vapor surface is poor and this is why vapor bubbles must be removed quickly to prevent tube runaway. High velocity water performs this function and is the best way to remove heat from the anode wall.

All of this explanation is fundamental to understanding the various anode dissipation ratings which vary with pulse length. The published anode dissipation rating is for pulse lengths greater than 100 msec and equivalent to the continuous ratings, but for shorter pulses advantage can be taken of heat sinking the energy in the anode wall. For the X2062J the rating goes from 300 KW to 9 MW for a 10µsec. .33 duty. The X2062K, which has a thin wall brazed septum type anode, the rating is 750 KW continuous to 12 MW for a 10µsec. pulse.

Thin walled anodes also are an effective solution to the cycling effects of thermal stress and long-term creep which can cause thick wall anode failures after several hundred hours operation. For long life and freedom from thermal ratcheting problems it is best if the anode operate <350°C. The anode wall should not heat sink more than 1500 joules/cm. and for dissipation longer than 50 msec. the power density should not exceed 750 watts/cm².

The 750 KW continuous and 12 MW short pulse dissipation ratings for the X2062K provide ample range for using the tube as a voltage or current regulator. The ability to control the value of the current makes power grid vacuum tubes unique among high voltage switching devices. It is possible to have a slow rise time at the beginning of a pulse. Fall time may be programmed if it is longer than the natural decay of the load circuit.

The X2062J and K are operated either as a switch in series with load, usually on the high voltage side, or as a shunt tube for voltage regulation (Fig. 3). Regardless of the type of operation in a non-resistive type load there is the likelihood of voltage spikes and ringing in the case of a load arc. These peak voltages must be added to the normal DC voltage, and because of this, in many real applications it may be necessary to operate the tube at well below its actual voltage rating.

There are also some limitations on current and this is due to screen dissipation. The lower the "on current" plate voltage, the higher the screen dissipation, and this point must be taken into consideration and proper trade off made by the circuit designer.

The circuit is simple, but it must be realized that any active device may exhibit unwanted oscillations. The medium gain characteristics of the

this oscillation problem. The circuit designer can further minimize the problem by using a screen bypass capacitor which is effective up through the low UHF frequencies, not driving the grid positive and using a small series resistance in the grid lead. If these steps are taken and an oscillation is still present, then it is best to determine the exact circuit and place a wave trap at the appropriate position. Field experience so far has shown no troublesome problems.

The question of whether to use one large tube or many smaller tubes has, over the years, been answered in different ways with the decision based on performance, reliability, and cost. In the case of high power switch tubes the performance is for the most part independent of size and is little altered whether one tube or several tubes are used. This is true whether the tubes are used in parallel or series or both. The exception is internal oscillations, that is, an oscillation whose circuit is entirely within the tube. In large tubes this can be as low as 400 MHz, and the larger the tube, the more troublesome this type of oscillation. If tubes are used in parallel, decoupling elements may be added which will prevent multi-tube type oscillations, and a cathode resistor of a few ohms will provide a means for equalizing the currents in each tube. For tubes in series a low cost varistor will insure equal voltage drop between tubes.

The question of reliability is a moot point. It is certainly sometimes true that fewer components improve reliability. On the other hand, very large tubes are not as rugged, and the problem of internal oscillations becomes more difficult to solve with the larger sizes.

Thus, the decision to use multiple tubes or not comes down to cost. Up to a point, larger tubes are more cost effective than smaller, but then, because of mechanical problems caused by size, the cost effectiveness reverses and goes down. As tubes get bigger in diameter thermal expansion becomes a major problem and increased length causes severe vibration and stability problems. Where is this point? The X2062K is not far from optimum. Increase the diameter, costs go up sharply. In the case of the X2062J and K the length could be increased 25% before natural mechanical resonance causes problems.

These tubes are currently in operation at Oakridge, the U.S. Naval Research Laboratory, and at Fusion Research facilities in both France and Japan (Fig. 4). They are in the installation phase for Doublet 3, and have been ordered by LLL, the Calhan Lab in the UK, and CNEN Francate in Italy. Oakridge is successfully using both series and parallel arrangements for increased voltage and current demands and will shortly begin operation of a system using both a series and parallel combination of four X2062K's for higher power operation. These devices are presently being used as modulator-regulators for neutral beam sources, gyrotrons and high power klystrons, and are finding homes in many new applications.

TABLE I. TECHNICAL DATA

	X2062J	X2062K
Filament Voltage	12	12 V
Filament Current	660	660 A
Plate Voltage	100 KV	130 KV
Plate On Current @ 0 Egl and 2000 Ec2, Eb	100 A	80 A
Plate Dissipation	300 KW	750 KW
Screen Voltage	2	2 KV
Bias Voltage for <10 ma Ib @ 100 KV	-700	-700 V

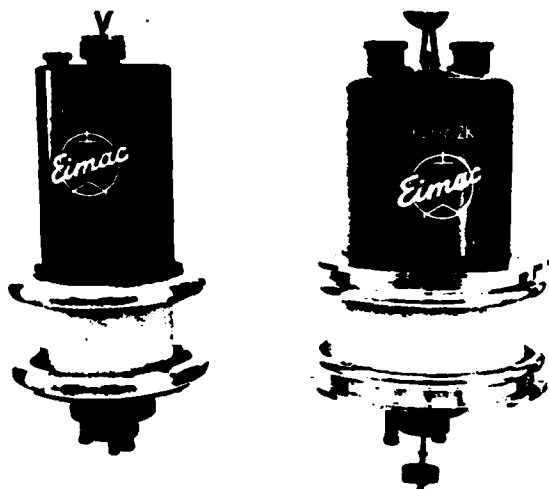


FIG. 1. X2062J on left and X2062K. The J was developed in 1977 and the K in 1978.

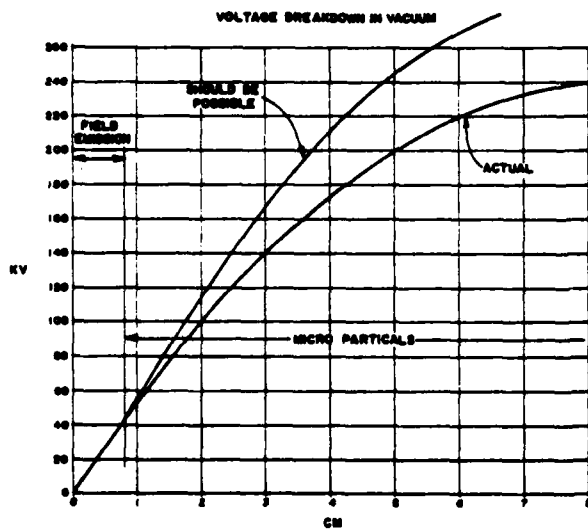
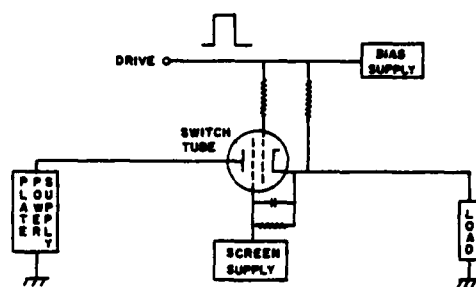
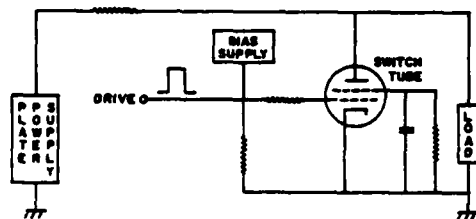


FIG. 2. Voltage hold-off as a function of spacing.



SERIES SWITCH



SHUNT REGULATOR

FIG. 3. Typical switch tube circuits.

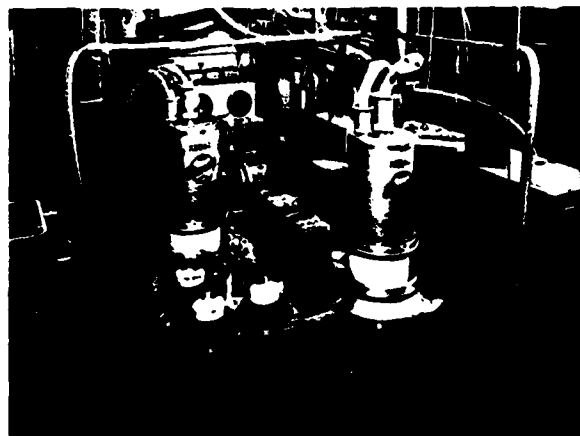


FIG. 4. ONRL 80-kV 100-A modulator using X2062J's in parallel.

DESIGN OF LARGE AREA E-BEAM CONTROLLED SWITCH

L. A. Miles, E. E. Nolting
Naval Surface Weapons Center
White Oak, Silver Spring, Maryland 20910

I. M. Vitkovitsky, Dominic Conte*
Naval Research Laboratory
Washington, D.C. 20375

Abstract

Theoretical analyses of electron beam switch operation suggest that a very fast electron beam initiated switch with closing times of a few nanoseconds and opening times of less than 100 nanoseconds is feasible.¹ A switch with this short recovery time makes high repetition rate operation possible. To experimentally confirm these analyses a test switch has been designed in which a nominal 150 kV, 1 kA electron beam is used to control the switching of a 200 kV, 10 kA Marx capacitor bank. An investigation of the performance parameters of the switch is being conducted and the results are providing data for the development of a repetitive switch capable of rates in excess of 10 kHz.

The basic design of the switch is a modification of that used in electron-excited, high-pressure gas lasers.² One new feature is the use of a cable pulse forming line to shape the electron beam waveform. The cable produces a fast rise time, short duration electron beam pulse that allows observation of the intrinsic properties of the gas dielectric. The electrical and mechanical design stresses low inductance for short beam pulse production. The design must also be compatible with a uniform electron beam-current distribution to avoid local heating which can delay the opening of the switch.

Introduction

In the past few years researchers have worked on a gas switch concept that appears to be applicable to fast, high power repetitive switching.^{3,4,5} In this switch concept an ionizing electron beam is injected into a high pressure gas region which separates two planar electrodes. The electron beam initiates a volume discharge between the electrodes that is maintained as long as the beam is present. Since the volume discharge is not self-sustaining it rapidly extinguishes when the electron beam is removed and the gas regains its dielectric strength.

In addition to its fast recovery and potential for repetitive switching the electron beam controlled switch (EBCS) has the advantage that it is triggerable over a large range of voltages. Experiments show that this type of switch operates well at 50% of its static breakdown voltage. Operating this far below static breakdown virtually eliminates prefires, a feature extremely important in large pulse power devices requiring switch synchronization for maximum output. Furthermore, experiments to date show that jitter is small (~ 8 ns) and fairly constant over the operating voltage range of the EBCS.⁶

The volume discharge generated by the electron beam offers other advantages over the conventional arc dis-

charge of spark gap switches. The most significant advantage of volume discharge is lower inductance. Also, because the volume discharge results in lower switch current density, electrode erosion and mechanical shock associated with the closure are reduced. These two processes are the most important causes of switch life limitation, which is of major importance in high repetition rate switches. The volume discharge also helps designers adapt the switch to many design geometries. Since the switch current occupies the same volume as the electron beam, different geometries can be accommodated by designing the diode to produce the desired beam shape, e.g., annular, cylindrical, rectangular, etc.

Theoretical analyses of electron beam switch operation, including gas chemistry considerations and multipulse operation, have been performed.¹ These calculations have been performed using the CEMAIR air chemistry code which tracks approximately 100 rate equations which can occur in mixtures of nitrogen and oxygen. The analyses suggest that the use of high pressure nitrogen gas ($\sim 1.01 \times 10^6$ Pa = 10 atm), with a small percentage of oxygen, which is an electronegative gas, can result in closing times of a few nanoseconds and opening times of on the order of 100 nanoseconds. While other gases should produce superior switch performance, their chemistry is not nearly as well documented as that of nitrogen and oxygen and so initial experiments will be performed with combinations of these two elements. After a thorough understanding of the physical processes governing EBCS is obtained, other gas dielectrics will be used to optimize switch closing and opening times.

The calculated fast turn on and off times indicate that an EBCS can be used in a repetitive mode at rates $> 10^4$ Hz. Experiments to date have demonstrated much of the phenomenology associated with EBCS. It is the intent of this investigation to study the physical principles controlling single pulse EBCS operation, to compare these findings with the predictions of gas chemistry codes and to establish this method of switching for peak power levels of greater than 2 GW.

This paper presents the design and construction progress on the initial electron beam test switch. A 200 kV, 10 kA, switched source is to be used in these tests. The combination of mechanical and electrical requirements led to a number of hardware design problems. The solution to these problems are presented below.

Electrical Design

For purposes of discussion the electrical design of the EBCS may be divided into two parts: the electron beam generator and the voltage source to be switched.

*Present address: R&D Associates, 1401 Wilson Boulevard, Arlington, Virginia 22209

A detailed schematic diagram of both of these electrical circuits are shown in Figure 1. Figure 2 shows the integrated circuit layout of the EBCS. The NETTWO circuit analysis computer code was used to analyze both the electron beam generator and the high voltage source to determine the best circuit element values. Figure 3 shows selected NETTWO waveforms for these circuits. The electron beam generator and the switched source are discussed separately in the following paragraphs.

Calculations indicate that a cold cathode electron beam gun with a voltage of 150 kV and a current density of 1 A/cm² over a discharge cross section of 1000 cm² should be used to switch the 200 kV, 10 kA Marx capacitor bank.¹ The 1 A/cm² value was used for design purposes, however the current density of the electron beam will be varied to determine the minimum possible current needed to switch the 200 kV voltage source. The cold-cathode design is shown in Figure 4. Since the electron gun is a space-charge limited diode, the Langmuir-Child law was used to determine the anode-cathode spacing needed to obtain the desired current of 1 kA (i.e., 1 A/cm² over 1000 cm²). The geometry of the diode is approximated by one quarter of a cylindrical diode. The expression for the space-charge limited current in this geometry is:

$$i = 1.47 \times 10^{-5} V^{3/2} r_a^{-1} \beta^2 \text{ Amps} \quad (1)$$

where L is the length of the cylinders in centimeters, V is the diode voltage in volts, r_a is the radius of the anode in centimeters, and β^2 is a function of the $\log(r/r_c)^7$ (r_c is the radius of the cathode in centimeters). The diode was modeled in cylindrical geometry by assuming that r is the anode-cathode separation, L the length of the anode (50 cm), and r_c is half the thickness of the cathode blade (.002 cm). This implies that $\beta^2 \approx 1$. In this geometry the electron beam gun anode which is the window that allows transmission of the beam into the switch region, represents about a 90° portion of the 360° cylindrical model anode. Using this model, the anode-cathode separation (r) that will give the required current through the anode window is calculated from equation (1) to be 10.7 cm. In general, the anode-cathode separation decreases at a rate of about 2 cm/usec due to the plasma expanding from the cathode. The current density can therefore change with time as β^2 changes. For a 100 nanosecond pulse this should decrease the current density on the order of 10%.

Electrostatic lenses made from screen wire will be used to focus the electron beam onto the anode window to improve efficiency.³ The anode window is 0.043 mm (1.7 mil) titanium foil. The 150 keV electrons incident on this anode will be transmitted with sufficient energy to penetrate 1.3 cm into the 1.01x10⁶ Pa of nitrogen gas. Anode foil lifetime is effected by electron beam heating and overpressure generated by energy dissipated in the switch gap. This is especially true in repetitive switching where heat removal time is long compared to the burst rate. A titanium foil of this thickness should reliably withstand the >1.1x10⁶ Pa pressure differential and survive for many shots.

Although much of the design of the switch is patterned after electron beam pumped lasers,² the need for rapid turn on and turn off times requires a different electron beam generator than used with lasers. For the initial single switch closure studies, the electron beam generator consists primarily of a transformer connected to two parallel 56n high voltage cables (88nf/line). The high voltage cables connected to the output of the transformer are used as pulse forming lines (PFL) to produce a fast rising, 100 nanosecond pulse for the production of the electron beam. In order to achieve the desired 150 kV electrons with proper current density the impedance of the current-limited diode must be 150Ω. This impedance mismatch of

the PFL to the 150Ω electron-beam diode requires a charge voltage of about 180 kV on the PFL to produce the 150 keV electron. Unfortunately the improperly matched PFL causes voltage reflections due to its incomplete discharge. This ringing may inhibit rapid termination of the electron beam which would interfere with the opening of the switch and thus complicate the study of the gas chemistry. To circumvent this problem an auxiliary switch is used to dump the PFL voltage to ground and quickly interrupt the e-beam. In the NETTWO calculation the switch which is located at the input to the PFL, is closed 66 nanoseconds after firing the electron beam gun. This time corresponds to slightly less than the one way transit time of the PFL (50 ns) plus the turn on delay of the diode. Using this time interval, the switch to ground is closed before the voltage pulse (reflected from the electron-beam gun when it is fired) has reached the beginning of the PFL. Locating the shorting switch at the input to the PFL allows it to be triggered at >90% of peak voltage putting less demand on the operating range of the triggered spark gap. A 100 ns pulse is obtained since the effect of the switch closure requires another 50 ns to reach the diode, at which time the voltage on the cathode reverses and the electron beam shuts off. In order to minimize voltage reflections which might prevent a rapid decrease in the diode voltage, a matching 28Ω resistor is put in series with the shorting switch. The NETTWO calculations predict a maximum voltage of 30 kV on the cathode after the electron beam is switched off which is about 20% of the operating voltage of the diode. The effect of the shorting switch is shown in Figure 5.

Two possibilities for the switched voltage source were investigated. An LC generator⁴ was considered and rejected because its oscillatory voltage would require synchronization of the electron beam to the generator output. A Marx generator was chosen for the high voltage source because it would have only a small voltage change during the period that the electron beam is being generated. Therefore the EBCS would be required to open with approximately the same applied voltage that it closed. The ability to recover while voltage is still being applied to the switch terminal is one of the unique features of the EBCS. Consequently, using a Marx generator would allow testing of this feature. Furthermore, synchronization of the electron beam to the voltage source would be much less critical making timing of events easier.

The Marx generator to be used is composed of four stages of .22 μf, 50 kV capacitors and uses a 20Ω resistor for a load. This resistance will produce the nominal 10 kA desired current density of 10 A/cm². It was shown by the initial NETTWO calculations that the voltage applied across the switch was well above the 200 kilovolts expected from the erected Marx capacitor bank. This was caused by the charging of the open-switch parasitic capacitance. To reduce this voltage a 100 ohm resistor was placed in parallel with the EBCS. This over-voltage might have been sufficient to cause an arc breakdown in the switch gap and thus negatively effect switch performance.

The transformer used to charge the PFL was constructed to the specifications determined by the NETTWO circuit analysis. To achieve the desired transformer output it was found that the required natural frequency of the secondary was 2.3 times that of the primary. To accomplish this a four turn secondary was wound concentrically with a 19-1/2 turn secondary on a 30.5 cm (12 inch) diameter cylinder. The turns are 15.2 cm wide, 0.2 mm (8 mil) copper foil with 6 layers of 0.05 mm mylar as insulation. The 0.3 mm of mylar has sufficient dielectric strength to hold the maximum expected voltage of 10 kV/turn. A coupling coefficient of 0.96 was achieved with this configuration. During

operation a 0.2 μ f capacitor with a 50 kV charge voltage will be used to drive the primary. The natural frequency of the primary is about 150 kHz. Tests performed on the transformer with an open circuited secondary show that this input frequency results in a 3.7 times voltage gain. This is in good agreement with the NETTWO calculations for the open circuit gain. NETTWO predicts a voltage gain of seven for the PFL capacitance as load on the secondary. With this gain, a 26 kV charge of the capacitor would produce the required 150 kV on the electron-beam diode.

Mechanical Design

The mechanical design for the electron beam controlled switch has two competing requirements: (1) a thin window that will allow the electron beam to enter the high pressure ($\sim 1.01 \times 10^6$ Pa) switch gap from the vacuum diode and (2) a structurally strong switch chamber that can withstand the large pressure differential ($\sim 1.14 \times 10^6$ Pa = 165 psi). The design is made more difficult by the large size of the anode window (20 cm by 50 cm). This is much larger than the windows used in previous experiments. The size increase is necessary in order to be more compatible with high power transfer requirements of large pulse power devices. In order to meet the two previously mentioned requirements several of the mechanical design features of electron beam excited lasers have been incorporated. One is the use of a "hibachi" support member that provides a frame across which the thin titanium window is stretched. Calculations were made to determine the size of the openings in the hibachi so that mechanical stresses in the foil were less than 3.79×10^8 Pa. All calculations were made using 2.28×10^6 Pa as the assumed pressure. This value is approximately a factor of two larger than the estimated operating pressure of 1.01×10^6 Pa. The results of these calculations agree with those of Harris² who did some of the initial design work for the NRL electron beam excited lasers. It has been possible to achieve approximately 85% transparency with the hibachi support structure.

The design of the switch chamber is shown in Figure 4. A tradeoff was made in strength, machinability and the required thickness of materials for the structural members. One and a half inch thick, high strength aluminum was chosen as the compromise for the material to be used for the pressure chamber end plates. Because of the large forces ($\sim 2.85 \times 10^5$ N) exerted on the end plates of the switch chamber considerable care had to be taken in their design.

The choice of the rectangular geometry was dictated by the previously existing hardware. Due to the rectangular geometry of the switch it is difficult to make exact estimates of the mechanical stresses. All approximate stress calculations were assumed to underestimate actual stress levels by at least 20% to add to the safety factor. The pressure assumed for the purposes of stress calculations was a factor of two greater than the anticipated initial operating pressure of 1.14×10^6 Pa. This was done to account for the expected pressure increase as the switch is operated. It is estimated that the switch pressure increase should be less than one atmosphere per closure.

The geometry and size of the high pressure chamber make diagnostic measurements difficult. The switch gap is recessed into the structural supports that prohibit direct line of sight of the entire volume discharge. Furthermore, introduction of view ports in the chamber wall weakens the structure. However four small ports have been placed in the chamber to allow for visual observation, spectrograph and laser attenuation measurements. These will be in addition to the current and voltage measurements made of the e-beam and switch.

In the mechanical design of the electron-beam gun a lot of effort went into minimizing the electric fields in critical regions to prevent possible breakdown. Corona rings were used at the edge of the cathode support to prevent the structure arcing to the vacuum chamber walls. Also a 45° angle was used on the cathode insulator which isolates the electron beam cathode voltage from ground. This angle minimizes the likelihood of breakdown along the surface of the dielectric-vacuum interface. The cathode consists of the edge of a single titanium foil since experiments show that one edge gives optimum results. However, the foil holder assembly is designed so that more foils could be used if desired.

Experimental Program

The mechanical design of the switch chamber will be tested by hydrostatic methods to insure its ability to withstand up to 2.03×10^6 Pa of pressure. Water is used for this test since a failure under gas pressure would be potentially much more catastrophic. Initial experiments on the EBCS will be performed to determine the electron beam current density and the parameters that control it. Included in this will be a study of beam uniformity in both the electron beam chamber and in the switch region. Adjustment of the electrostatic lens to optimize current through the anode window will be made at this time. Once the electron beam has been characterized, the switch closure will be considered. The voltage on the switch source and the e-beam gun will be adjusted to obtain uniform volume discharge in the switch.

The various gas chemistry affects will be examined and compared with the CHMAIR calculations. During this study the effect of up to 1% oxygen on the opening and closing times of the switch will be considered. Experimental measurements of formation rates of certain atomic species will be made spectroscopically. Other gas dielectrics will be examined after the EBCS operation is thoroughly understood with nitrogen and oxygen mixtures. Satisfactory agreement between calculation and experiment will give confidence for the design of a repetitively operated EBCS, which is the next phase of this program.

Acknowledgment

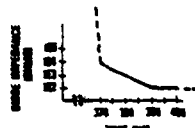
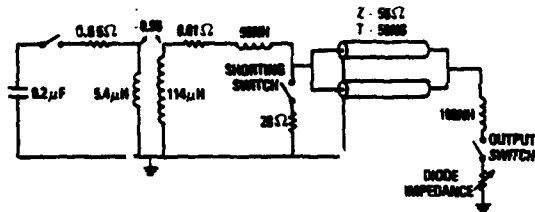
The authors wish to express appreciation to Mr. D. Jenkins and Mr. R. D. Ford of the Naval Research Laboratory for their assistance in the acquisition of materials and coordination of hardware fabrication.

References

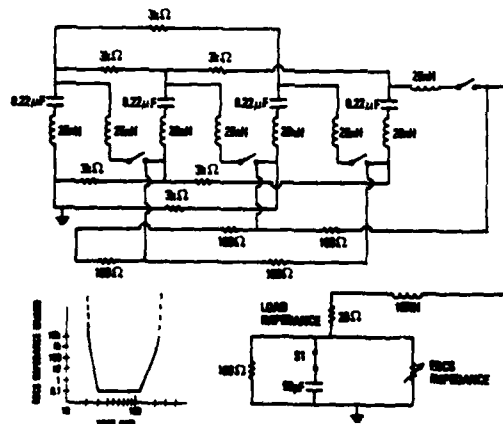
1. R. A. Farnsler, D. Conte, I. M. Vitkovitsky, "Repetitive Electron Beam Controlled Switching," Proceedings 2nd IEEE International Pulse Power Conference, Lubbock, Texas (1979)
2. N. W. Harris, F. O'Neill, and W. T. Whitney, "Compact High-Pressure Electron-Beam-Controlled Laser System," Rev. Sci. Instrum. Vol. 48, No. 8, 1042, August 1977
3. B. M. Kovalchuk and G. A. Masyats, "Rapid Cutoff of High Current in an Electron-Beam-Excited Discharge," Soc. Tech. Phys. Yet. 2,7, 252(1976)
4. J. P. O'Loughlin "PFN Design Interface with E-beam Sustained Gas Discharge" Proceedings International Pulsed Power Conference, Lubbock, Texas (1976)
5. R. O. Hunter, "Electron Beam Controlled Switch," Op. Cit. in Reference 4.
6. A. S. El'chananov, V. G. Emel'yanov, B. M. Koval'chuk, G. A. Masyats, and Yu. F. Potalitsyn, "Nanosecond-range triggering of megavolt switches," Sov. Phys. Tech. Phys., Vol. 20, No. 1, Jul 1975
7. J. D. Ryder, Electronic Engineering Principles, Prentice-Hall Inc., N.Y. 1952

8. Personal communication with W. T. Whitney, NRL, Washington, D.C.
9. R. A. Fitch, V. T. S. Howell, "Novel Principles of Transient High-Voltage Generation," Proc IEE, Vol. III, No. 4, April 1964

This work was supported by Naval Surface Weapons Center/Dahlgren under contract N60921-80-WR-D0075.



(a)



(b)

Figure 1 Schematic diagrams of a) the electron beam generator (.2 μ F capacitor charged to 26 kV) and b) the EBC's Marx voltage source (.22 μ F capacitors charged to 50 kV each). The assumed time histories of the variable impedance diode and EBCS used for the NETTWO calculation are shown in the insets. The 90 pF in b) represents the capacitance of the open EBCS, and switch S1 (which opens when the EBCS closes) is an artifact of the NETTWO program which eliminates this capacitance at the proper time.

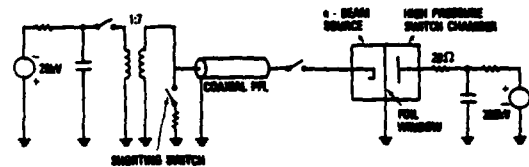
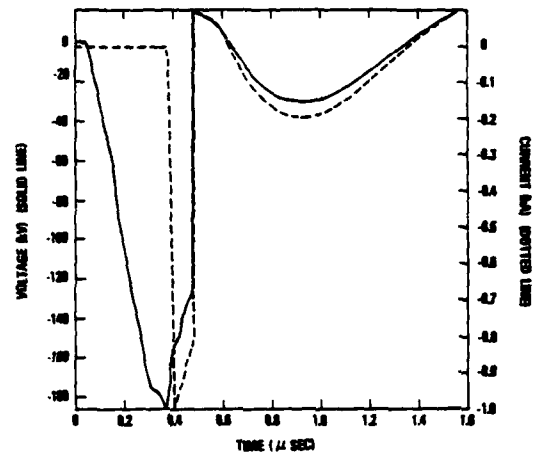
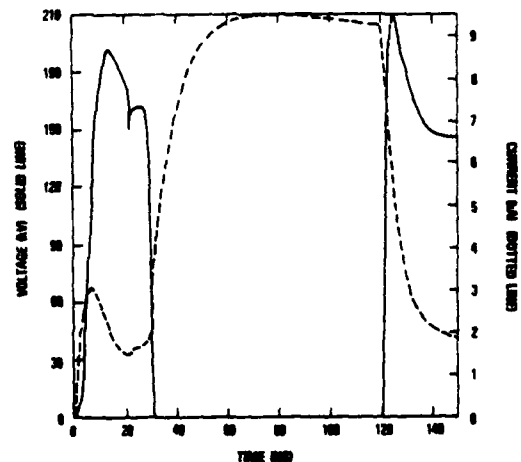


Figure 2 Simplified circuit layout of the complete EBCS.



(a)



(b)

Figure 3 a) NETTWO predictions of the PFL voltage and current waveforms (at the output switch) with shunting switch. b) Calculated current through 20 Ω load and voltage for the EBCS. Time histories of the diode impedance and EBCS impedance are the same as those of Figure 1.

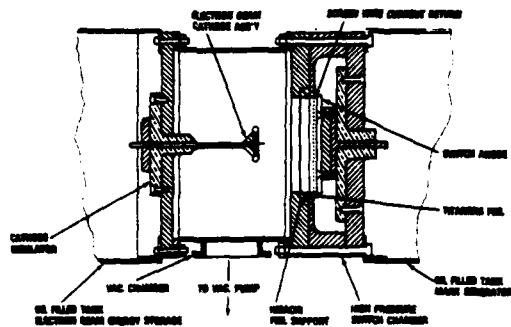


Figure 4 E-beam diode and switch chamber design

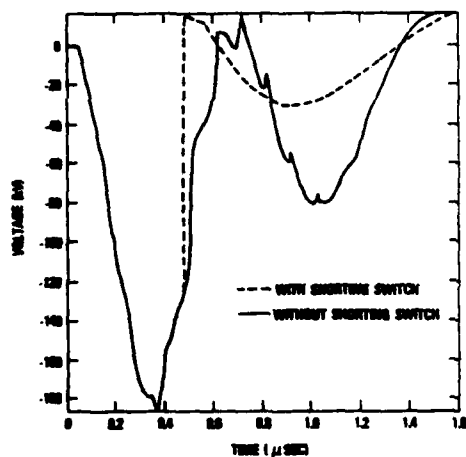


Figure 5 NETTWO voltage waveforms for the output end of the PFL (at the output switch) with and without the shorting switch.

INFLUENCE OF THE DENSITY OF THE SURROUNDING MEDIUM
ON THE
ELECTRICAL BEHAVIOR OF EXPLODING FOILS*

T. L. Berger

Naval Surface Weapons Center
Dahlgren, Virginia 22448

Summary

The opening switch properties of electrically exploded metallic foil fuses are reviewed and discussed. Experimental results are presented which show that the surrounding medium significantly affects most of the fuse properties. The experimental results are discussed in terms of the density and chemical activity of the surrounding medium.

Introduction

In recent years, inductive energy storage has become of considerable interest in pulsed power applications. The primary advantage of inductive energy storage systems is that the magnetic energy density can be very high in comparison with electrostatic energy storage systems (capacitor banks). This high magnetic energy density leads to reductions in the weight, size, and cost of the store. The major disadvantage of inductive energy storage systems is the switch which is required to transfer energy to the load. Unlike an electrostatic store which depends on a closing switch, an inductive store requires an opening switch. In general, it is more difficult to interrupt than to initiate current flow. For this reason, the technology of opening switches lags behind that of closing switches. Consequently, there is a great deal of research and development in the area of opening switches which remains to be done if the advantages of inductive energy storage are to be fully realized.

One of the most popular of the various opening switches, and the subject of this paper, is the exploding metal foil fuse. Fuse action is initiated by dissipation of Joule heat in the foil. When sufficient energy is dissipated in the foil, nonlinear heating due to the temperature coefficient of resistance can cause an explosive transition to the vapor state. Fuse resistance can change by several orders of magnitude thereby disrupting the current which permits energy to be rapidly transferred to the load.

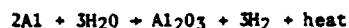
A good opening switch must satisfy several requirements. In addition to efficiency requirements, the switch should be fast, predictable, and able to withstand high voltage. In the case of exploding foil fuses, efficiency is largely determined by the maximum final resistance of the fuse and the energy required to effect this resistance. Predictability means that the time to burst can be determined from circuit parameters and foil properties. Switching speed is the time required for the transition from the conducting to the vaporized state. In order to withstand high voltage, the metallic vapor must be prevented from becoming ionized.

*Supported by NSWC Independent Research.

There are several variables which can affect the switching properties of exploding foils. These include foil material, foil dimensions, initial foil temperature, circuit parameters, and the surrounding medium. These variables are not necessarily independent. For example, time to burst depends on foil dimensions, foil material, and circuit parameters¹. In this paper, we concentrate on the influence of the surrounding medium on the switching properties of exploding foils. The other variables are held constant. Although exploding wires and foils have been the subject of a great deal of study, the effect of the surrounding medium has not received adequate attention in our opinion. Three reasons are present for suspecting that the surrounding medium may significantly affect the switching properties of exploding foil fuses

(1) The state of high resistance is realized when the foil becomes vaporized. According to the vaporization wave hypothesis², a vaporization wave propagates inward from the surface of the conductor. Ahead of the wave, the material is a conductor, and behind the wave, the material is highly resistive vapor. If the vapor is free to expand, relatively long mean free paths and energetic collisions can lead to ionization and electrical breakdown in the outer boundary of the vapor. As pointed out by Maisonnier et al¹, breakdown in the metallic vapor can be prevented by placing the foil in a high pressure gaseous environment or by sandwiching the foil between insulating strips. In this picture, the density of the surrounding medium should be an important factor in the electrical breakdown process.

(2) Logan et al³ have reported temperatures in the neighborhood of 30,000°K for electrically exploded aluminum foils. Due to such high temperatures, the possibility for chemical reactions between the fuse and the surrounding medium must be taken into account. For example, the reaction



has a temperature threshold of about 700°C. Conte et al⁴ have reported experimental results of exploding aluminum foils in water and in hydrogen peroxide. The maximum fuse resistivity in water was reported to be four times higher than could be found in the literature, presumably because of the heat supplied to the fuse and the formation of highly resistive aluminum oxide. The resistivity doubled when the water was replaced with hydrogen peroxide, presumably because hydrogen peroxide is more chemically active than water. Thus, heat transfer and chemical reactions with the surrounding medium may affect fuse performance.

(3) Krivitskii and Litvinenko⁵ have suggested that a pressure increase in the liquid sample will tend to decrease the rate of growth of vapor nuclei. Since the vapor state is the high resistance state, increasing the pressure in the sample is expected to decrease the rate of rise of resistance. In addition to magnetic pressure produced by current flowing through the fuse and hydrostatic pressure exerted by the surrounding medium, shock wave pressure also needs

to be taken into account. As the foil is heated and begins to expand, a shock wave is radiated into the surrounding medium. This shock wave is accompanied by another shock wave which moves into the sample. The intensity of this shock wave depends on the density of the surrounding medium.

In the following, we describe an experimental study of the effects of the surrounding medium on the switching properties of aluminum foils exploded in a number of different gases and liquids. We begin by giving the experimental details. Next we present the results and discuss them. Finally, we draw some conclusions from the work.

Experimental Details

Figure 1 shows the experimental arrangement. The capacitance of the bank is $C = 98 \mu\text{F}$ and the total inductance of the circuit, $L_c + L_p$, is either 492 or 620 nH, where L_p is the inductance between the high voltage measuring point and ground and L_c is the remainder of the total inductance. R_f is the foil resistance, $R_f + R_p$ is the total resistance between the high voltage measuring point and ground, and R_c is the remainder of the total circuit resistance. Voltage is measured with a resistive divider, current is measured with a current viewing resistor, and the time rate of change of the current is measured with a Rogowski coil.

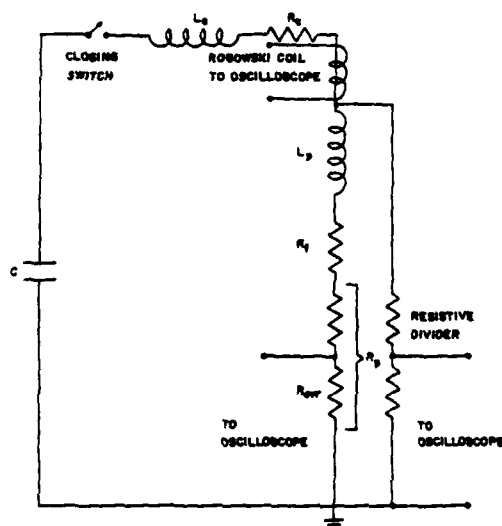


Figure 1. Experimental schematic.

Referring to Figure 1, the measured voltage V is given by

$$V = L_p \frac{di}{dt} + iR_p + iR_f \quad (1)$$

Since V , i , and di/dt are measured, it is necessary to determine L_p and R_p in order to determine the resistance of the foil. L_p and R_p are determined from V , i , and di/dt waveforms obtained when the foil is replaced with a thick copper strap. The dimensions of the strap are the same as the dimensions of the foil except the strap is approximately 20 times thicker than the foil. Thus, there is negligible change in the inductance. The resistance of the strap R_s is much less than 1 mΩ. Assuming

$$R_p \gg R_s, \quad (2)$$

Equation (1) becomes

$$V = L_p \frac{di}{dt} + iR_p \quad (3)$$

Choosing t' such that $di/dt = 0$, and measuring the corresponding values of V and i ,

$$R_p = \frac{V(t')}{i(t')} = 9 \text{ m}\Omega \quad (4)$$

This justifies Equation (2). Substituting $R_p = 9 \text{ m}\Omega$ and the measured values of V , i , and di/dt at another time $t \neq t'$ into Equation (3) gives

$$L_p = 88 \text{ nH} \quad (5)$$

Fuse current, voltage, and the time rate of change of the current were measured for foils exploded in the following media:

Dry Air
50% O₂ 50% N₂
Helium
Argon
Distilled Water
Transformer Oil
30% Hydrogen Peroxide
Carbon Tetrachloride
50% Carbon Tetrachloride
50% Methylene Iodide
Methylene Iodide
Aluminum Oxide

The following results were obtained with an initial capacitor bank voltage of 6kV, bank capacitance 98 μF, and 2.54 cm x 2.54 cm x 0.0023 cm aluminum foil samples.

Experimental Results and Discussion

Time to Burst: Time to burst is insensitive to the surrounding medium and is in good agreement with the simple theory of Maisonnier et al¹. These results may be found in an earlier report by the author⁶.

Peak Electric Field: The effect of the density of the surrounding medium on the peak electric field is shown in Figure 2. The densities for the various gases were determined from the following gas pressures (PSIG). He: 200, 300; Air: 0, 100, 200; 50% O₂ 50% N₂: 0, 25, 100, 200; Argon: 100, 200, 250, 300. This plot shows that the peak electric field tends to increase with gas density, presumably because the effect of increasing the density is to inhibit the expansion of the vapor cloud thereby decreasing the probability of ionization and breakdown in the metallic vapor. It appears that the peak electric field is weakly dependent on gas species. Due to the spread in the data, however, this effect may not be real. Most of the data points in Figure 2 represent average values. For example, the data point for 50% O₂ 50% N₂ at 100 PSIG is an average of 6 shots while the data points for He at 300 PSIG and Ar at 100 PSIG were obtained from only one shot. For a given data point, the average value of a set of measurements differs from the maximum or minimum of the set by as much as 10%.

Under the same experimental conditions, the peak electric field in liquids showed no detectable increase when liquid density was varied from 0.9 to 3.1 gm/cm³.⁶ This may be due to circuit limitations since there appears to be breakdown in the gases but not in the liquids.

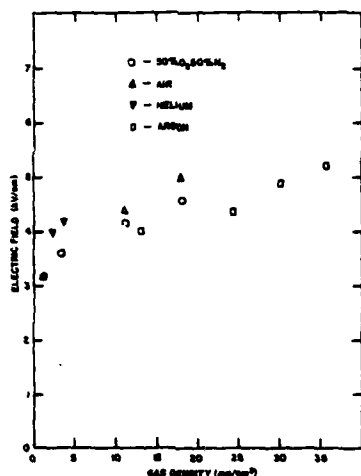


Figure 2. Peak electric field versus density of the surrounding medium for aluminum foils exploded in various gases.

Time Rate of Change of Current: Figure 3 shows that the maximum time rate of change of current increases with the density of the surrounding medium. There is no evidence that maximum di/dt depends on gas species. In liquids, the only measurement made was in distilled water where $di/dt_{max} = 27.4$ kV/ μ sec.

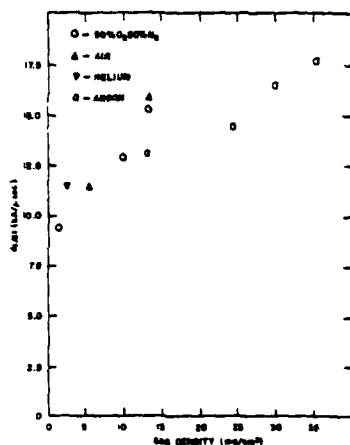


Figure 3. Effect of density of the surrounding medium on the maximum time rate of change of current for aluminum foils exploded in various gases.

Resistance: Figure 4 shows the maximum fuse resistance for foils exploded in various gases at various pressures. As expected the maximum resistance increases with gas density but there is no evidence that gas species is important. The measured value of the maximum resistance in distilled water is $R_{max} = 226$ m Ω .

Time Rate of Change of Voltage: The measured voltage V depends on 3 terms according to Equation (1). Differentiating both sides of Equation (1) with respect to time and assuming L_p and R_p are constants, we have

$$\frac{dv}{dt} = L_p \frac{d^2i}{dt^2} + (R_p + R_f) \frac{di}{dt} + i \frac{dR_f}{dt} \quad (6)$$

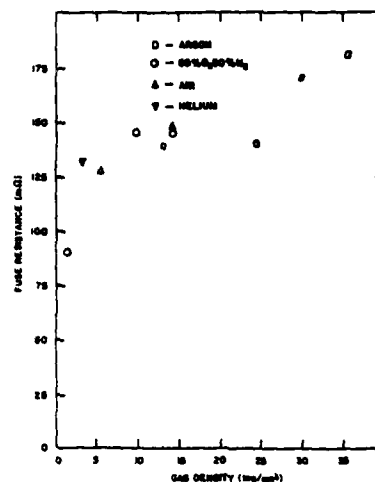


Figure 4. Effect of density of the surrounding medium on maximum fuse resistance for aluminum foils exploded in various gases.

Prior to burst, our data indicate $dv/dt = 10^{10}$ volts/sec, $L_p d^2i/dt^2 = 10^9$ volts/sec, and $(R_p + R_f) di/dt = 10^9$ volts/sec. Thus prior to burst, dv/dt is a rough measure of $i dR_f/dt$. Since the current was found to be about the same in all cases prior to burst, dv/dt is a measure of dR_f/dt , a quantity of considerable interest for switching purposes.

Figure 5 shows part of the voltage waveform at fast sweep speed for a foil exploded in dry air at 150 PSIG. Notice that prior to burst, the time rate of increase of voltage is quite linear. The time rate of change of voltage was measured by simply measuring the slope in the linear region. In some cases, there were significant deviations from linearity which introduced substantial uncertainties in the measurements. For this reason, and also because it was necessary to measure some of the slopes at slow sweep speed (2 μ sec/div), there is considerable scatter in the measurement of dv/dt . There appears to be no significant change in dv/dt when gas species or gas pressure is changed. Similarly, no consistent change in dv/dt is evident when liquid density is changed. In general, however, the data indicate that dv/dt is higher in the gases than in the liquids. For 31 gas shots and 17 liquid shots, we obtain:

$$\langle dv/dt \rangle_{gas} = 57 \text{ kV}/\mu\text{sec},$$

and

$$\langle dv/dt \rangle_{liquid} = 42 \text{ kV}/\mu\text{sec}.$$

Since dv/dt is a rough measure of dR_f/dt , these results support the hypothesis that the internal shock wave prevents the growth of vaporization nuclei and hence reduces the rate of rise of fuse resistance.

Voltage Pulse Width and Current Interruption: The voltage pulse width increases with the density of the surrounding medium. This is most clearly seen in the difference between the full width at half maximum of the voltage pulses obtained for foils exploded in gases and in liquids. Figure 6 shows voltage and current waveforms for a foil exploded in distilled water while Figure 7 shows waveforms for a foil exploded in dry air at 150 PSIG. We have

$$\begin{aligned} \text{FWHM} &= 1.48 \text{ } \mu\text{sec} & \text{liquid} \\ \text{FWHM} &= 0.42 \text{ } \mu\text{sec} & \text{gas} \end{aligned}$$

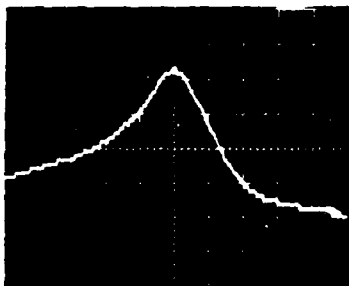


Figure 5. Fuse voltage trace for aluminum foil exploded in air at 150 PSIG. Time increases to the right. Sweep speed is 100 nsec/div. Vertical sensitivity is 2.5 kV/div.

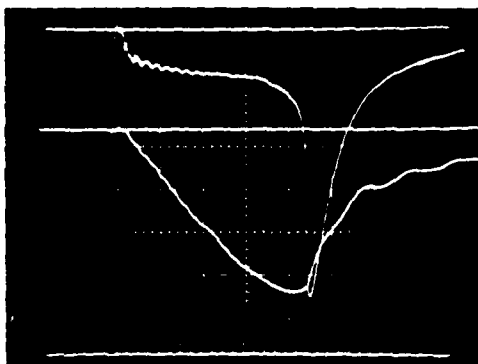


Figure 6. Voltage and current traces for aluminum foil exploded in distilled water. Time increases to the right. Upper trace is fuse voltage and the vertical sensitivity is 2 kV/div. Middle trace is fuse current and the vertical sensitivity is 20 kA/div. The lower trace is time mark trace with time marks 500 nsec apart.

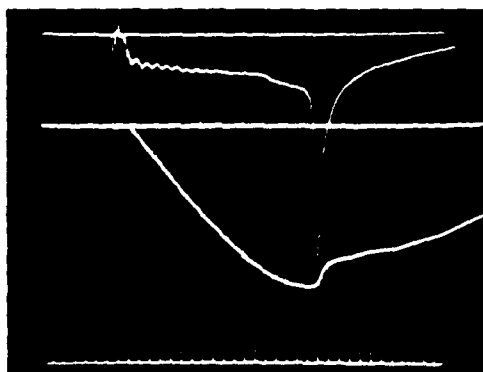


Figure 7. Voltage and current traces for aluminum foil exploded in air at 150 PSIG. Time increases to the right. Upper trace is fuse voltage and the vertical sensitivity is 2 kV/div. Middle trace is fuse current and the vertical sensitivity is 20 kA/div. The lower trace is time mark trace with time marks 500 nsec apart.

which are typical values. Figures 6 and 7 show also that there is much more current interruption in the liquids than in the gases, presumably because of the increased density which prevents breakdown.

Concluding Remarks

In conclusion, our experiments show that the medium surrounding Al foil fuses affects fuse performance significantly. In gases, the peak electric field, resistance, and time rate of change of current all increase with gas density. In liquids, no such changes were observed when the liquid density was increased. This is probably due to the fact that restrike was observed in the gases but not in the liquids. On the average, the time rate of increase of resistance was higher in the gases than in the liquids, presumably because in the denser media, a stronger shock wave enters the fuse material and slows the formation and growth of vapor nuclei. There is no hard evidence that chemical reactions with the surrounding medium affect fuse performance.

Acknowledgement

The author would like to thank R. Dorflein and C. Comford of NSWC for their assistance in the experimental work.

References

1. C. Maisonnier, J. H. Linhart, and C. Gourlan, *Rev. Sci. Instrum.* **37**, 1380 (1966).
2. F. D. Bennett, in "Progress in High Temperature Physics and Chemistry", Carl A. Rouse, Ed., Vol. II, Pergamon Press, Oxford, (1968).
3. J. D. Logan, R. S. Lee, R. C. Weingart, and K. S. Yee, *J. Appl. Phys.* **48**, 621 (1977).
4. D. Conte, M. Friedman and M. Ury, "A Method for Enhancing Exploding Aluminum Foil Fuses for Inductive Storage Switching", Proceedings of the 1st International Pulsed Power Conference, IEEE Cat. No. 76CH 1147-8 Reg. 5, Lubbock, Texas (1976).
5. E. V. Krivitskii and V. P. Litvinenko, *Sov. Phys. Tech. Phys.* **10**, (1976).
6. T. L. Berger, "Effects of Surrounding Medium on the Performance of Exploding Aluminum Foil Fuses," 2nd IEEE Pulsed Power Conference, IEEE Cat. No. 79CH 1505-7, Lubbock, Texas (1979).

THE CROSSATRON SWITCH
A COLD CATHODE DISCHARGE DEVICE WITH GRID CONTROL

Robin J. Harvey

Hughes Research Laboratories
3011 Malibu Canyon Road
Malibu, California 90265

Abstract

The Crossatron switch is a hybrid device being developed for high power, high frequency operation. It uses a crossed-field discharge generated plasma as a source of charge carriers and is grid controlled. The coaxial electrode structures include: an anode, a cathode, a source grid and a control grid. A dc magnetic field (localized to the gap between the source grid and the cathode) is used to sustain a source plasma when that grid is energized. This plasma is an adjustable source of charges analogous to a thermionic emitter with a comparatively negligible thermal inertia. The anode current may be controlled by the source grid current and/or by the control grid potential. This provides for exceptionally short response times and high repetition rate operation. Low power test models have been operated as closing switches to well over 10 kHz at 5 kV and show rise times of 15 ns using anode currents of up to 150 A.

Introduction

The Crossatron is a spinoff from crossed-field closing switch, vacuum tube and gas thyatron technologies. The more recently demonstrated crossed-field closing switch¹⁻⁴ has been shown to have a capability to handle large currents at high voltage. This capability degrades as one attempts to switch at frequencies above 1 kHz or with rise times less than 50 ns. The essential reason is that a crossed-field discharge is required in the spaces between the anode and the cathode potential electrodes in order to conduct current. Such crossed-field discharges have finite response times and require a magnetic field. Furthermore, in order to recharge the anode following each pulse, the magnetic field must be removed.

The switch described in this paper is a candidate for high repetition rate, high peak power operation. It takes advantage of the crossed-field discharge mechanism to generate the charges which are used to close the switch at high speed without requiring a magnetic field in the main electrode gap or a heated cathode. The operating mechanism may be understood by analogy to a thermionic emitter in a vacuum tube. Referring to Fig. 1, the emitter is replaced by a

plasma generated by applying a potential to the source grid in the presence of a fixed magnetic field and a low gas pressure. In the configuration shown, the source grid is pulsed positive and provides an adjustable source of electrons and ions. The charges are held back by the presence of a negatively biased control grid until the source plasma reaches the desired current density (about 5 A/cm²). By raising the control grid potential, the carriers are released to close a conducting path to the anode. The time scale for this closure is shorter than that obtainable by an avalanche discharge in the presence of a magnetic field and is not sensitive to the pressure, unless the anode current exceeds the source current. At relatively low current densities, the anode current may be controlled in a continuous fashion by varying the source grid current or the control grid voltage. At higher densities, the device becomes unstable and will latch into the on-state, and control must be regained by interrupting the anode current.

Experimental Results

A. Three Electrode Tests

The concept of a crossed field switch having a dc magnetic field was first explored using a three-electrode device (Fig. 2). The magnet array is

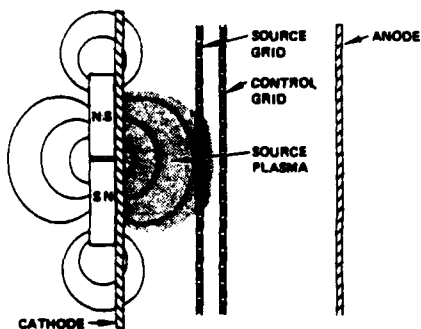


Fig. 1. Coaxial electrode arrangement showing crossed-field discharge generated source plasma.

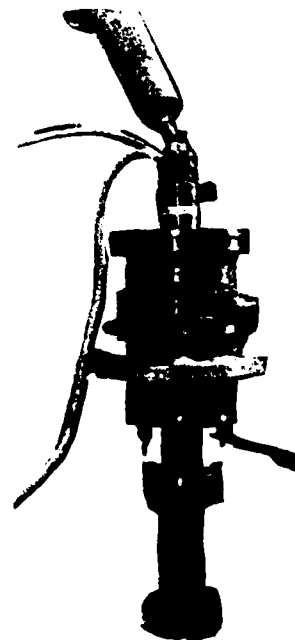


Fig. 2. The Crossatron.

visible on the outside of the tube. The functions of the source and control grids are combined into one electrode supported from below by three small bushings. The outer cathode electrode is 10 cm in diameter, the grid is 9 cm, and the anode (supported from above) is 8 cm. All of these are stainless steel and the grid is perforated sheet stock with a 30% open area. A resonantly charged pulse forming network is used to supply the anode potential and a 200 Ω , 2 kV pulser is used to drive the grid. When the network is adjusted to insure cut-off of the anode current at the end of each pulse, the device runs reliably at frequencies of up to at least 16 kHz. Figure 3 was made at 5 kV and

8771-2

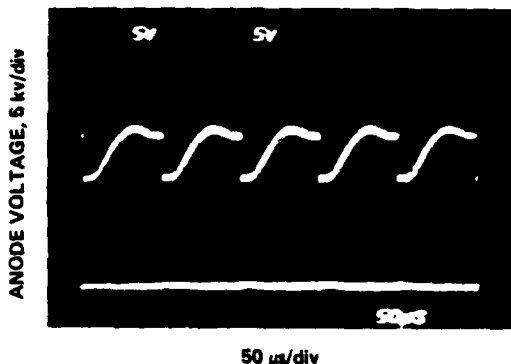


Fig. 3. 10 kHz operation of three electrode device at 5 kV. Peak current 140 A in 200 ns wide pulse. No control grid.

10 kHz with a peak current of 140 A lasting about 200 ns.

In the three-electrode mode of operation, the anode fall time is a function of the trigger pulse rise time. When the external circuit response time is slower than the switch, the source current can regulate itself internally to supply the external circuit. But when the response times are reversed, the initial anode current is divided roughly equally between the cathode and the grid. Then depending upon which of these electrodes is used to return the anode current (i.e., grounded cathode or grounded grid), the other electrode will tend to rise towards anode potential. This, in turn, regulates the anode current at twice the trigger current over a range of anode voltages. In this sense, the tube behaves as a crude amplifier. An example of this is shown in Fig. 4

8771-1

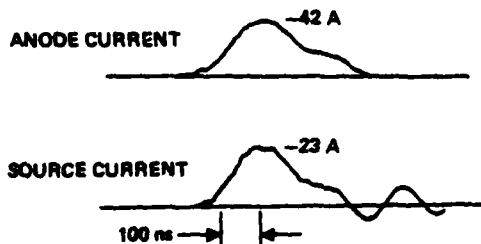


Fig. 4. Amplifier mode showing response of the anode current to the source grid in the absence of a control grid. These pulse shapes are generated over a range of anode voltages from 1 to 4 kV. Ringing in the tail of the source current is capacitive.

using the grounded grid mode. The top trace shows the anode current peaking at 42 A, while the lower trace is the net source current which peaks at 23 A. This situation prevails over a range of initial anode voltages from 1 to at least 4 kV.

B. Four Electrode Tests

In order to isolate the source plasma generation function from the anode current trigger function, a control grid was added to the device and the spacings rearranged to accommodate it. This grid was made from the same stock material as the original source grid. As with the three-electrode device, the anode return current divides amongst the other electrodes. If the source current is reduced below the anode current, the tube behavior becomes unstable. Thus, it is necessary to provide a high source current. This is easily accomplished, since the anode current may be held off by biasing the control grid negative while the source current is increased.

A low level dc keep-alive current (~ 25 mA) is normally maintained in the source plasma to avoid jitter when the main source current is pulsed. Since the source current can have a much longer rise time than the anode circuit, relatively high inductance circuits may be employed to drive the source grid. Figure 5 was made using a 12 μ s wide source grid current reaching about 200 A. The control grid was biased to -300 V and then pulsed to a few hundred volts positive. The oscillogram shows the anode current with the switch (grounded cathode) as a load on an 8 Ω pulse forming network. The upper trace was made at about 1000 V and shows a square pulse with a 20 ns rise time and an amplitude of 50 A. As the voltage is increased, the current rise time is reduced slightly. The measured tube drop was about 700 V, independent of the applied anode voltage or current.

8771-3

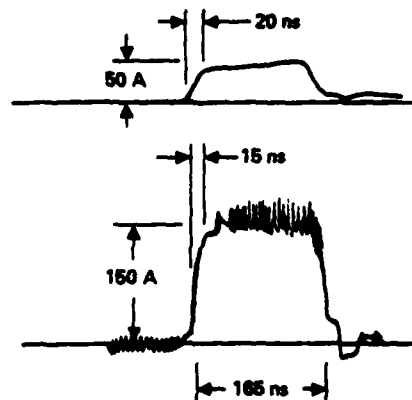


Fig. 5. High frequency response using a negatively biased control grid. Pulse is triggered when source current reaches 200 A. The pulse shape is determined by the network while the amplitude depends on the voltage a) 1000 V b) 2000 V.

Conclusions

The basic operating mechanisms of this cold cathode grid-controlled discharge device appear to be applicable to high frequency, high current, and high voltage, switching, amplification, modulation and regulation systems. The work reported upon here was done at relatively low power and not all of the possible electrode configurations have been considered. But based upon these preliminary results and, upon earlier parallel developments with thyratron and electron tubes, more sophisticated and useful extensions of the technology are likely to follow.

References

1. M. A. Lutz, R. J. Harvey, and H. Alting Mees, IEEE Trans. on Plasma Science PS-4, 2, June 1976.
2. M. A. Lutz, IEEE Trans. on Plasma Science PS-5, 4, p. 24, Dec. 1977.
3. R. J. Harvey, R. W. Holly, and J. E. Creedon, IEEE Pub. No. 76CH1147-8, Proc. 1st Int. Pulsed Power Conf. at Texas Tech. University, Lubbock, Texas, Nov. 9, 1976.
4. R. J. Harvey, "Operational Characteristics of the Crossed Field Closing Switch," IEEE Transactions on Electron Devices, Vol. ED-26 No. 10, p. 1472, Oct. 1979.

10 KHZ VACUUM ARC SWITCH IGNITION*

A. S. Gilmour, Jr. and R. F. Hope III
State University of New York at Buffalo
4232 Ridge Lea Road
Amherst, New York 14226

R. N. Miller
University of Central Florida
7300 Lake Ellenor Drive
Orlando, FL 32809

Summary

The ignition of vacuum arc switches at repetition frequencies up to 10 kHz has been achieved. The ignition technique used was originally described by Gilmour and Lockwood.⁽¹⁾ A current pulse was used to vaporize a conductive film on the insulator between the cathode and the anode. Studies of energy required for arc ignition, as a function of variations in ignitor-cathode configuration, ignition voltage, and ignition pulse length were performed. Switch and circuit configurations required to prevent misfires and to prevent arc-current coupling to the ignition circuit will be discussed. Finally, the ignition circuit will be described along with refinements required for increasing ignition repetition frequencies to the 50 kHz to 100 kHz range.

Introduction

Vacuum arc ignition can be accomplished by any one of several techniques. For example, several millijoules of energy from a pulsed laser can be used to vaporize and ionize material from either the negative or the positive electrode.⁽²⁾ When this plasma bridges the gap between the electrodes, a vacuum arc will occur if sufficient voltage is applied to the electrodes.

A second technique for igniting vacuum arcs is to bring an igniter electrode into contact with the cathode. By passing sufficient current through the contact points, and then withdrawing the igniter electrode, an arc can be initiated. This technique is commonly used in switchgear and is useful when repeated arc ignition is not required.

High-voltage (several thousand volts) breakdown between two electrodes across the surface of an insulator can be used to vaporize one or both electrodes and thus lead to arc ignition. Attempts to use a high voltage pulse to "break down" a vacuum gap (rather than the surface of an insulator) have not produced satisfactory results. This technique has been found to lead to unreliable ignition and there is a strong tendency for arcs to occur where they are not wanted. Finally, substantial energy is dissipated in the ignition circuit.

An arc ignition technique reported⁽³⁾ to be extremely successful employs a titanium hydride igniter. A small current pulse is passed through the igniter causing the release of a small amount of hydrogen. The hydrogen ionizes, leading to an arc.

In the arc ignition technique used with a high degree of success at the State University of New York at Buffalo (SUNYAB)^{1,4} a current pulse is used to

vaporize a portion of a conductive film on the surface of an insulator located between the cathode and an igniter electrode. Possible configurations of the igniter/cathode assembly are shown in Figure 1. The plasma burst resulting from the ignition current pulse fills the interelectrode space. During the ensuing vacuum arc discharge, the conducting film on the insulator is regenerated by the deposition of material from the metallic plasma. The system is thereby prepared for a subsequent ignition pulse.

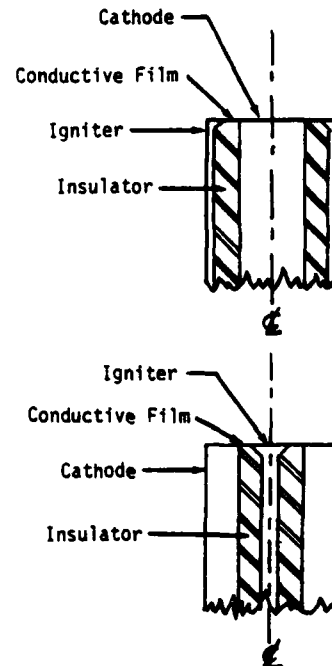


Figure 1. Possible configurations of igniter/cathode assembly in vacuum arc switch.

The primary advantages of the SUNYAB film vaporization ignition technique over other techniques are:

1. No moving electrodes are required.
2. Insulation problems are minimized because a relatively low voltage (few hundred volts at most) is required for ignition.

*Partially supported by the Air Force Aeropropulsion Laboratory through The Southeastern Center for Electrical Engineering Education, Contract F 33615-77-C-2059.

3. Energy supplied by the ignition circuit is used primarily to produce the ignition plasma burst. Thus, ignition energy is minimized. This is particularly important at high repetition frequencies where ignition power is substantial.
4. Automatic cathode positioning is possible.

Electrode Configurations

For efficient arc ignition, the ignition plasma must be permitted to bridge the cathode-anode gap in the most effective manner possible. For example, as is shown in Figure 2, an ignition plasma that is ejected so that a considerable portion of it is intercepted by the anode (anode in position A) readily leads to the establishment of a vacuum arc. If the anode is located at position B, only a small portion of the ignition plasma is intercepted and arc ignition requires a much larger ignition plasma burst and a correspondingly larger ignition energy pulse.

The position of the surface of the cathode relative to the insulator surrounding it also plays a role in determining the ignition energy requirement. As is shown in Figure 3, if the surface of the cathode is above of below the surface of the surrounding insulator, a portion of the ignition plasma may be prevented from expanding in the desired manner toward the anode. If a portion of the plasma is, in effect, trapped near the cathode then additional energy will be required to generate sufficient plasma to ensure reliable arc ignition.

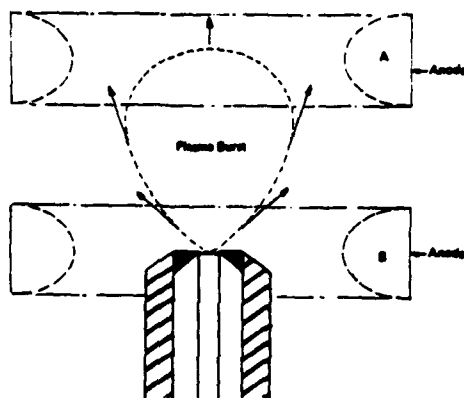
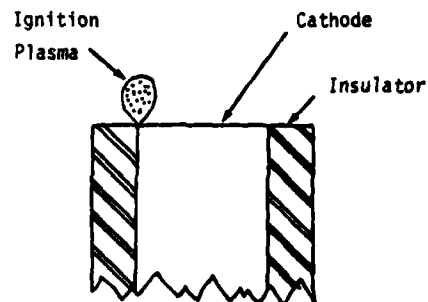
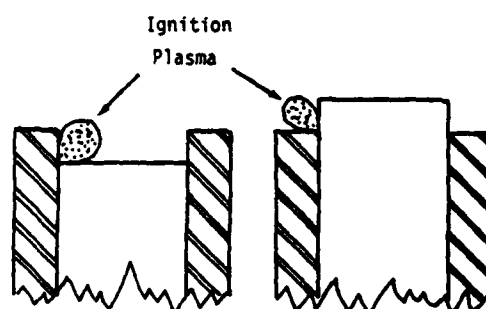


Figure 2. Ignition plasma burst in relation to two possible positions of the anode.

It is extremely important to avoid vacuum gaps between the igniter electrode and the cathode when designing, fabricating and assembling the igniter-cathode components. Even very small gaps (a few thousandths of an inch) greatly increase the ignition voltage and energy requirements. An example of the effect of a vacuum gap (resulting from incorrect component assembly) is shown in Figure 4. The vacuum gap resulted from a tilted igniter electrode as is shown in Figure 5. The reliability of ignition was dependent on ignition voltage, anode voltage and ignition energy. Note that about a joule of ignition energy was required for reliable ignition. This is two orders of



a) Correct



b) Incorrect

Figure 3. Correct and incorrect cathode positioning.

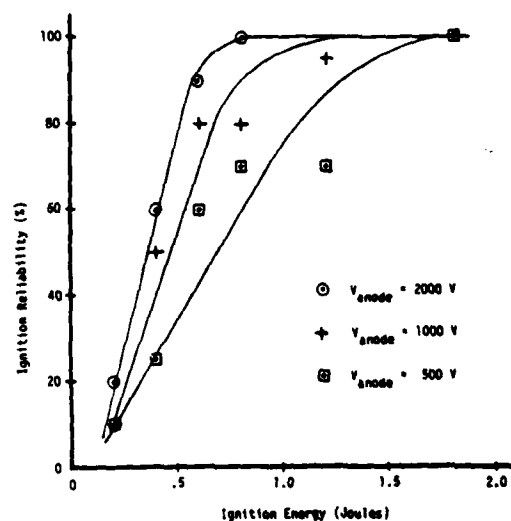


Figure 4. Ignition reliability as functions of ignition energy and anode voltage for an ignition voltage of 2000 V.

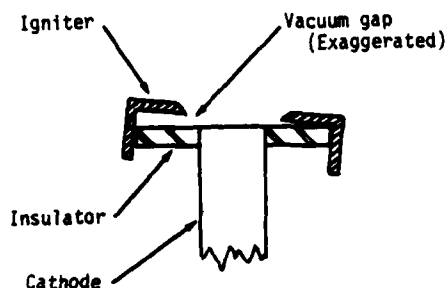


Figure 5. Vacuum gap in igniter/cathode assembly resulting from incorrect component assembly.

magnitude greater than the energy that was required when the vacuum gaps were eliminated.

Recently, to ensure continuity of the ignition film from the igniter to the cathode, a thin film (~ 0.1 micron thick) of cathode material has been sputter deposited on the surface of the igniter insulator prior to final assembly of the cathode and igniter components. Thus film extends well under the igniter electrode. Thus, there is no longer any question about there being electrical contact between the igniter electrode and the film.

When operation for long periods of time is required, it is important to design the igniter electrode so that the surface facing the anode is even with, or recessed below the cathode and insulator surface as is shown in Figure 6. If this is not done, then cathode material will be deposited on the igniter surfaces within line of sight from the cathode. These deposits will gradually increase in thickness and will eventually cause a short circuit from the igniter to the cathode.

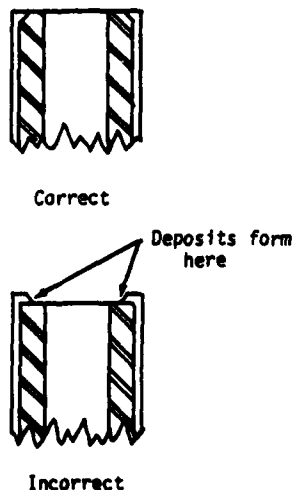


Figure 6. Correct and incorrect igniter-electrode configurations.

Materials

During operation of the vacuum arc switch, erosion of the surfaces of the insulator adjacent to the cathode occurs. Shown in Figure 7 is an aluminum oxide insulator after 1.48×10^7 pulses of operation. Insulator erosion leads primarily to two modes of switch failure. In one, the effective path length between the cathode and igniter increases causing an increase in film resistance. This in turn prevents the ignition circuit from operating properly. In the other mode of switch failure, an automatic mechanism is used to continually feed cathode material into the switch. The tapered underside of the insulator is used to position the cathode. When the insulator becomes sufficiently eroded, the cathode is no longer properly positioned, causing ignition failure. In extreme cases of insulator erosion, the cathode feed mechanism may force the cathode rod through the aperture in the insulator.

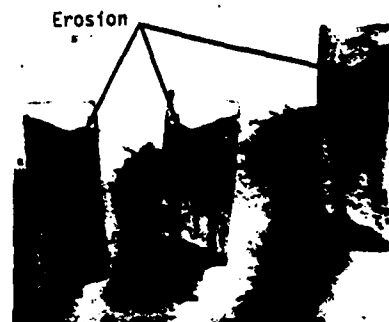


Figure 7. Erosion of aluminum oxide insulator after 1.48×10^7 pulses of operation. Photograph shows insulator broken into three sections. Cathode was automatically fed into tapered side of insulator.

In general, it has been found that the erosion rate is inversely proportional to the hardness of the insulator material. High density aluminum oxide is one of the best materials that has been tested. Boron carbide and diamond are, of course, harder than aluminum oxide; however, arc ignition difficulties have been experienced with these materials. Cathodes fabricated from high boiling temperature materials yield higher insulator erosion rates than do cathodes fabricated from low boiling temperature materials. The use of a large-diameter cathode results in a lower insulator erosion rate than does the use of a small-diameter cathode. On the other hand, it must be realized that the arc tends to remain near the ignition point and so there is a danger with large-area cathodes that erosion will not be uniform. It has been determined that for short pulses, it is the amount of charge in the pulse, not the duration of the pulse, that is important in determining how much of the cathode surface area is consumed. This was shown to be the case by keeping the amount of charge constant while varying the pulsewidth. In this experiment the percentage of the area of the cathode surface that was consumed was constant. That experiment was carried out at a relatively low charge level ($10\text{--}20$) and should be repeated at higher levels.

The energy required for arc ignition is very highly dependent on cathode material. In general, ignition energy is roughly proportional to the product of the boiling temperature and thermal conductivity of the

cathode. A major exception is gold. When comparing gold and copper, it is noted that the products of boiling temperature and thermal conductivity for gold and copper are nearly the same. However, the energy required to ignite an arc on gold is at least two orders of magnitude less than for copper!

For a number of reasons chromium has been found to be a highly desirable cathode material for use in the SUNYAB vacuum arc switches. Its erosion rate (~ 0.05 mg/C) is very low so that its use enhances switch life. It is an excellent gettering material and the vacuum level in a switch containing chromium is found to continually improve as the switch is used.

Fortunately, chromium is also a material that requires only about 5 millijoules for arc ignition when the proper electrode configurations are used.

Electrical Considerations

In its simplest form, the ignition circuit is as shown in Figure 8. After the capacitor, C, has been charged, it is discharged with a switch through the ignition film with the rate of discharge being limited by the inductance of the circuit. Typical ignition-voltage and current waveforms are shown in Figure 9 along with the main switch current waveform

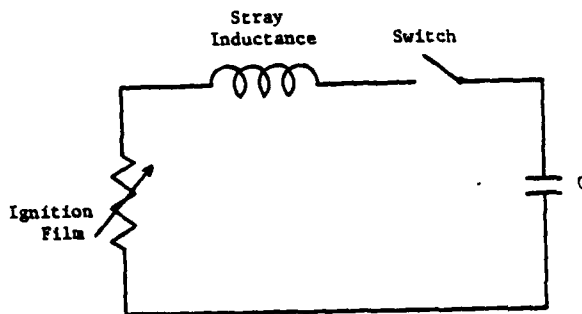


Figure 8. Simplest form of ignition circuit.

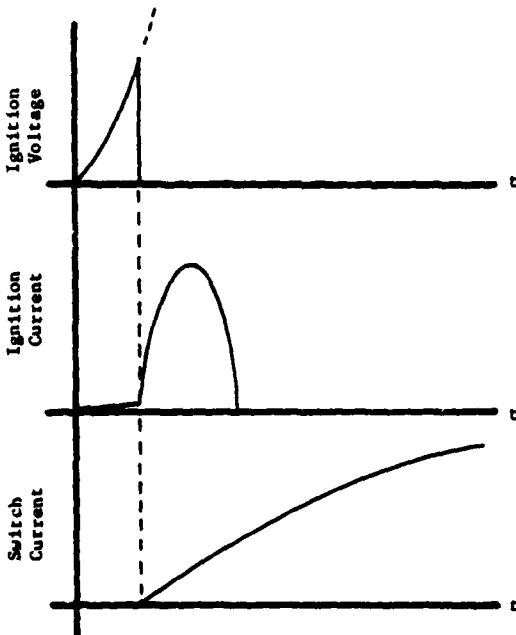


Figure 9. Ignition waveforms.

when the switch is used in an LC circuit such as the series capacitor inverter circuit. The ignition voltage initially increases across the ignition film until film vaporization occurs. Then, very rapidly, as a metallic plasma is formed the effective film resistance drops to a very low value and, simultaneously, the ignition voltage drops. At this point, the ignition current is limited primarily by the inductance of the circuit and so a half-sinusoidal current pulse is generated.

To adapt this basic triggering circuit to the repetitive ignition mode required in the inverter application of the vacuum arc switch dictated several modifications. The resulting triggering circuit, called the pulse power amplifier, is shown in Figure 10 and consists of two identical circuits,

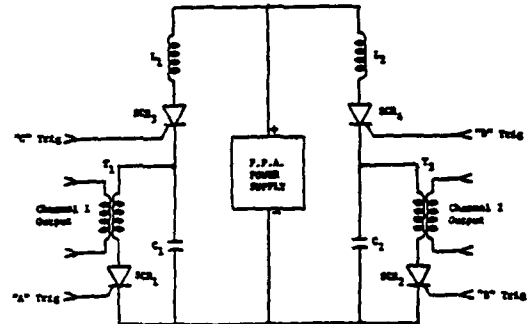


Figure 10. Vacuum arc switch ignition pulse power amplifier.

one for each of the vacuum arc switches employed in the inverter. Looking at the left half of this circuit, SCR₂ controls the initiation of the resonant charging of C₁ through L₁. SCR₁ similarly controls the discharge of C₁ through the pulse transformer, T₁, which couples this resulting ignition pulse to a vacuum arc switch. The addition of T₁ was found to be necessary to isolate the triggering circuit from the relatively high voltages and currents in the inverter circuit. This pulse transformer has a Faraday shield between the primary and secondary windings to reduce coupling through the interwinding capacitance. The operation of the right half of the circuit is identical, and the output of this circuit is used to ignite the other vacuum arc switch.

The basic timing waveforms for the pulse power amplifier are shown in Figure 11. These waveforms were generated as shown in Figure 12. The waveform V₁ is furnished by a pulse generator having controlled output burst capability.

It was reported earlier ⁽⁵⁾ that vacuum arc switches in the inverter circuit would frequently come into conduction without the application of an ignition pulse from the triggering circuit. This problem was eliminated by connecting a 0.02 μ F capacitor between the igniter and cathode electrodes of the vacuum arc switches.

As progress was made in achieving control over the ignition of the vacuum arc switches, efforts began to focus on increasing the ignition rate, thus increasing the duty cycle of the switches. Many consecutive tests have been performed at a duty cycle approaching 50% (which is the maximum

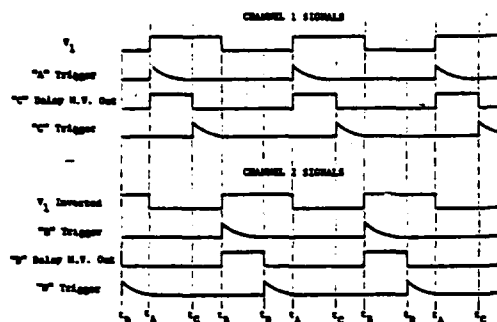


Figure 11. Ignition pulse power amplifier timing waveforms.

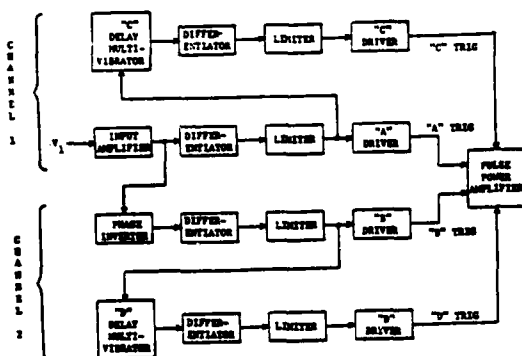


Figure 12. Ignition pulse power amplifier timing circuit block diagram.

permissible by the application) for up to 2000 pulses. No degradation of vacuum arc switch performance was noted during these tests.

In the inverter application, vacuum arc switch current was commutated to zero by the series resonant inverter circuit. This conduction termination was followed by a brief pause to allow that switch to recover before igniting the other switch. As has been described (6), this recovery is essential in the inverter to prevent shorting the dc source. Because of this, an investigation of the recovery rate characteristics of the vacuum arc switch has begun. In this investigation, careful control of the recovery time is important, so a new triggering circuit is being developed to provide this timing. In this circuit the time of the reduction of vacuum arc switch current to zero is detected. A controllable delay then ensues after which a positive anode-to-cathode voltage is reapplied. This sequence will all be controlled by the new timing circuit, and the tests will use the inverter as a test bed for the vacuum arc switches. An additional feature of this new triggering circuit is that it is designed to permit ignition repetition rates up to 100 kHz, making higher frequency testing of the vacuum arc switch possible.

Conclusions

Control of the repetitive ignition of vacuum arc switches has thus been achieved for frequencies up to 10 kHz using a series inverter as a test bed. In achieving this repetitive ignition several different ignition techniques were investigated, with the SUNYAB film vaporization ignition technique proving to be superior. Tests on electrode configurations revealed that care should be taken to eliminate any vacuum gaps between the igniter electrode and cathode and that the anode-facing surfaces of these two electrodes should be even. Aluminum oxide has proved to be a superior material for use as an insulator in the vacuum arc switch, and chromium is very desirable as a cathode material. Electronic control of the repetitive ignition has been achieved.

The series inverter continues to be a good test bed for the investigation of the vacuum arc switch used as a closing switch in a dynamic inter-electrode voltage environment. Tests performed indicate that the vacuum arc switch has higher frequency capability and the limits of this capability are under investigation.

REFERENCES

1. A. S. Gilmour, Jr. and D. L. Lockwood, "Pulsed metallic-plasma generators," *Proc. IEEE*, vol. 60, No. 8, August 1972, pp. 997-991.
2. A. S. Gilmour, Jr. and R. J. Clark, Jr., "Studies on a laser-triggered, high voltage, high vacuum switch tube," *Proc. IIIrd International Symposium on Discharges and Electrical Insulation in Vacuum*, pp. 367-372, September 1968.
3. J. M. Lafferty, "Triggered vacuum gaps," *Proc. IEEE*, vol. 54, pp. 23-32, Jan. 1966.
4. A. S. Gilmour, Jr. and D. L. Lockwood, "The interruption of vacuum arcs at high dc voltages," *IEEE Trans. Electron Devices*, vol. ED-22, No. 4, pp. 173-180, April 1975.
5. R. N. Miller, D. C. Hopkins, C. J. King, A. Pedano, R. Dollinger and A. S. Gilmour, Jr., "A multi-megawatt vacuum arc switched inverter for airborne applications," *Proc. 13th IEEE Pulse Power Modulator Symposium*, State University of New York at Buffalo, Amherst, New York, June 1978.
6. R. N. Miller, R. Dollinger, and A. S. Gilmour, Jr., "High repetition-rate, high power pulse tests of vacuum arc switches," *Proc. 13th IEEE Pulse Power Modulator Symposium*, State University of New York at Buffalo, Amherst, New York, June 1978.

DESIGN OF A TRIGGERED VACUUM GAP FOR CROWBAR OPERATION *

J.E. Thompson, R.G. Fellers, T.S. Sudarshan
and E.T. Warren, Jr.

The University of South Carolina
College of Engineering
Columbia, South Carolina

Summary

Research has been conducted to develop a triggered vacuum gap switch capable of 100 kV, 100 kA, 100 C crowbar operation. An experimental version of the switch has been constructed and consists of two electrodes contained in a bakeable vacuum enclosure. The electrodes have been made of various materials including copper, Elkonite, graphite, brass, and tungsten/copper. The switching action is initiated by using a BaTiO_3 surface flashover trigger located in one electrode. The triggered gap has been operated with vacuum and mercury vapor having a pressure of 1 mTorr. The switch is tested using a 125 kV @ .23 μF and a 510 μF @ 10 kV source for high current, simulated crowbar operation.

Trigger delays have been measured to be on the order of 100 nsec for both vacuum and low pressure gas filled gaps. The delay has been found to be more dependent on trigger energy than trigger voltage. Copper electrodes have been subjected to hundreds of 50 kA discharges with little degradation.

Introduction

A triggered vacuum or low pressure gas switch has been constructed and characterized. The switch has been designed to crowbar a capacitively driven inductive load at peak current and hence minimum voltage. The switch has therefore been designed to be capable of triggering at low voltages, on the order of 1 kV. Other design parameters to be met include a hold-off voltage exceeding 50 kV, inductance of approximately 40 nH, unidirectional current conduction and charge transfer capability of 100 kA and 100 C, respectively, trigger delay of less than 200 ns, and a long lifetime (greater than 10^4 shots). Essentially all of these goal performance parameters have been achieved with the exception of lifetime.

Candidate switches, for the delineated performance parameters, include, in addition to low pressure or vacuum switches, high pressure (1 ATM) spark gaps and ignitrons. High pressure spark gaps, capable of greater than 50 kV hold-off potential, cannot be triggered at low voltages; i.e., the triggerable operating range is relatively small. High pressure gaps are typically capable of transferring charge on the order of only a few Coulombs. Ignitrons can actually meet all of the performance specifications except the high withstand voltage. Ignitrons also suffer from such problems as arc transfer to the wall and trigger amalgamation. These problems shorten ignitron lifetime and ultimately lead to failure.

* Work sponsored by Los Alamos Scientific Laboratory.

Vacuum or low pressure gas (low pressure implies operation to the left of the Paschen minimum) switches have definite advantages for crowbar applications, as compared to high pressure gas switches. The work of other researchers and the results reported here show that switches of this type can hold-off DC and oscillatory voltage on the order of 70 kV and trigger at voltages as low as a few hundred volts with a delay and jitter on the order of 100 ns and 10 ns, respectively. The trigger delay has been observed to decrease as the anode to cathode voltage decreases. This behavior facilitates triggering of parallel gaps which will continue to trigger even though the anode to cathode voltage is reduced by a triggered parallel switch.

It should be noted that the addition of low pressure gas to the vacuum switch has been observed to improve the voltage hold-off and to decrease the trigger delay.

The switch design is capable of holding off maximum DC and oscillatory voltages of 70 kV. The switch delays have been measured to be approximately 100 ns with 10 ns associated jitter. This paper will describe the switch design and construction, describe the excitation sources and experimental arrangement, and present the switch operating characteristics.

Switch Construction

The switch constructed and tested is shown in Figure 1 and consists of two circular disk electrodes separated by a 1 cm gap, a bakeable glass enclosure, and a trigger mechanism located in the lower electrode (the cathode).

The main discharge occurs between the two disk shaped electrodes shown. The electrodes are presently constructed of OFHC copper and are easily removable from the stainless steel supports to facilitate planned life tests with other electrode materials.

The vacuum enclosure or gas containment vessel consists of a 4" diameter pyrex tube and stainless steel flanges. The tube and flanges are joined using a glass to metal seal. All flange connections are made using copper gaskets to permit baking of the entire system. The switch is evacuated or filled with gas through a vacuum port located on the top flange. Both the top and bottom flanges are connected to liquid containment troughs. These troughs are filled with either ice water or acetone and dry ice and provide cooling for the electrodes and support structures.

Electrical connections are made to the switch by attaching six RG-17 coaxial cables to the top flanges. The cables are symmetrically located around the perimeter of the flanges.

The test vessel shown is somewhat long and contributes significantly to the switch inductance. The configuration inductance can be

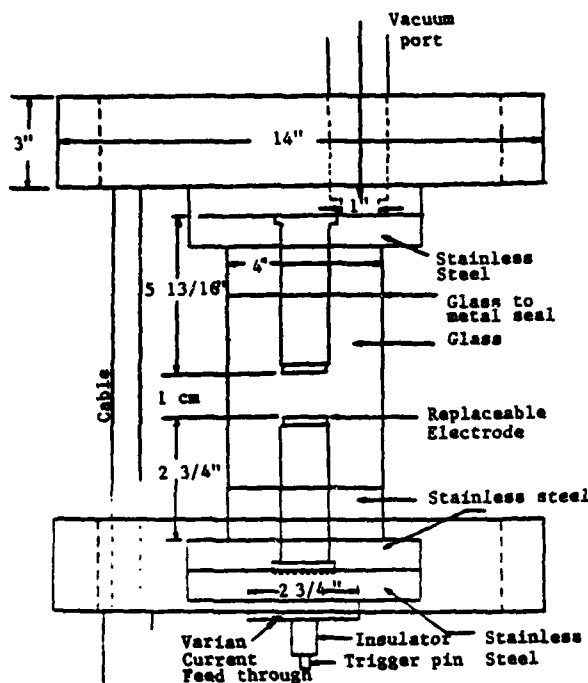


Figure 1. Plasma Triggered Vacuum Gap.

substantially reduced by shortening the containment vessel. The long vessel is presently being used to permit optical diagnostics of the switch discharge. The main discharge is initiated by plasma ejected into the gap from a hole in the bottom electrode. This electrode is consistently used as the cathode. The plasma is produced by a discharge across a BaTiO_3 surface. Details of the trigger mechanism are shown in Figure 2. The trigger consists of a tungsten trigger pin located at the center of a BaTiO_3 disk. The BaTiO_3 disk is tightly fitted into the removable electrode material. A discharge is initiated across the BaTiO_3 surface by applying an approximately 10 kV pulse between the trigger pin and the bottom electrode. Plasma produced by the surface discharge enters the main discharge region through a small hole in the bottom electrode. The lifetime of trigger mechanism of this type has been measured in this work and by others to be greater than 10^4 shots. Data, to be presented, will show that delays on the order of 100 ns can be obtained with this trigger, even at low (≈ 200 V) anode to cathode voltages.

Excitation Sources and Diagnostics

The plasma initiated switch has been tested using various main discharge sources for high voltage, low energy delay measurements, and for high energy, low voltage conduction tests. The surface flashover trigger has been initiated separately using a charged coaxial cable and a capacitor. The switch current and voltage have been measured during these tests. The trigger and main discharge luminosity have been observed using open shutter photography and an image converter camera.

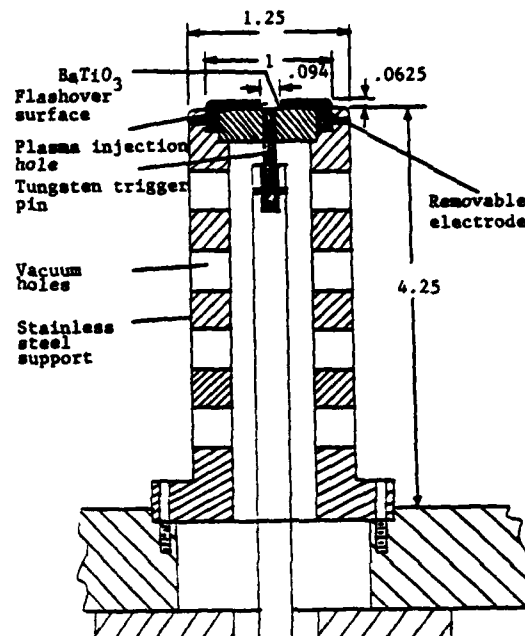


Figure 2. Plasma Trigger Electrode.

High voltage, low energy switch hold-off potential, delay, and jitter measurements were performed using the circuit shown in Figure 3. The circuit consists of a DC charged, .2 μF @ 125 kV capacitor which is connected by six RG-17 cables to the test switch. The inductance values were determined by measuring the ringing frequency of appropriate sections of the circuit.

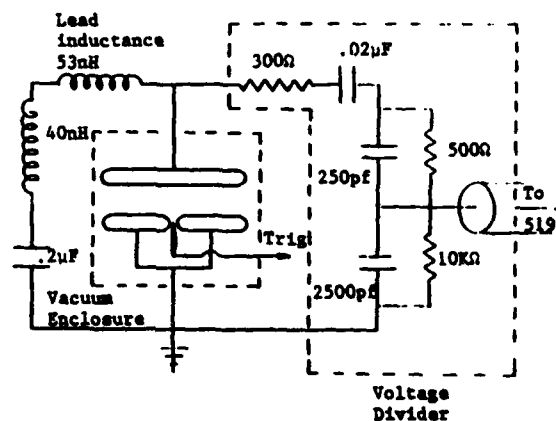


Figure 3. High Voltage Low Energy DC Excitation Source.

High energy discharge tests have been conducted using the circuit of Figure 4. The circuit consists of a 510 μF (three parallel capacitors) @ 10 kV connected through a series ignitron switch to a 4 μH load coil. The test switch is connected to the load coil using six RG-17 cables. The lead and component inductances shown were, again, determined by measuring various ringing frequencies. In operation, currents of up to 100 kA are established in the load coil. The test gap is triggered at the load coil current peak such that current transfers to the test switch. This switching at load coil current maximum requires triggering at the load coil voltage minimum. The test switch discharge current produced by this circuit does not oscillate

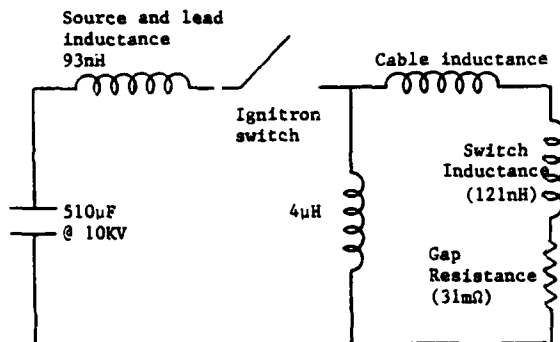


Figure 4. High Energy, Oscillatory Source.

but is overdamped. The identity of the cathode and anode during the main discharge is therefore well established.

Trigger voltage is produced from either a charged coaxial cable or a capacitor. The line source consists of a 70 foot length of RG-8 cable charged to a maximum of 30 kV. The line is discharged by a mechanical switch. The test gap trigger is connected directly to the cable output and provides an open circuit load for the cable. A pulse having an amplitude equal to the DC line charge voltage and a duration of approximately 200 ns is therefore applied to the trigger. The impedance of this source is 50 Ω , the maximum energy stored is 750 mJ, and the risetime is approximately 5 ns.

The capacitive source consists of a .02 μF @ 10 kV capacitor which is discharged, using a spark gap, through a 50 Ω resistor. The test gap trigger is in parallel with the 50 Ω load resistor. The total trigger energy stored by this source is 1 J.

Switch voltage is measured using the compensated divider shown in Figure 3. The divider risetime is approximately 80 ns. The discharge current is measured using a Pearson coil. The trigger voltage is also measured using a low impedance, compensated voltage divider.

Optical measurements have been performed to determine the temporal and spatial variation of the discharge luminosity. Open shutter photography has been used to determine the time integrated spatial distribution of the trigger and main discharge plasma luminosity. An image converter camera,

operating in the framing mode, has been used to determine the temporal behavior of the discharge luminosity. This data is required to determine at what time and current level the main discharge makes the transition from a diffuse discharge to a constricted arc.

Experimental Results

The operating characteristics of the switch shown in Figure 1 have been determined for vacuum operation and low pressure operation using N_2 , Hg, and SF_6 gas. The data have been obtained using bare copper electrodes. Specific characteristics which have been measured include DC hold-off voltage, conduction resistance and inductance, triggered switch delay and jitter, and electrode and trigger lifetime.

Hold-off Voltage Measurements

It is desired to develop a switch which will hold-off at least 50 kV DC. Previous work has established that 100 kV can be maintained across a conditioned 1 mm vacuum gap (stainless steel electrodes). This performance is degraded to approximately 20 to 30 kV after high current conduction by the switch. A larger, 1 cm gap has been more recently used to permit reliable operation at approximately 50 kV. Data, to be subsequently presented, show that shorter switch trigger delays are obtainable for low gas pressure filled gaps as compared to vacuum gaps. Data obtained by other researchers also show that the gap hold-off potential is also greater for low pressure gas filled gaps.¹ Gas filled, either Hg, N_2 , or SF_6 , switch operation is therefore of interest, in addition to evacuated switch operation.

The switch hold-off voltages have been measured for vacuum, N_2 , SF_6 , and Hg operation. It has been found that the 1 cm vacuum gap will hold off greater than 75 kV, and the N_2 filled gap (1 micron pressure) greater than 70 kV. It has similarly been found that the switch, filled with 1 micron of Hg or SF_6 , will hold-off 25 kV and 40 kV respectively. The lower hold-off voltage for Hg is due to long gap breakdown between the two large flanges shown in Figure 1. Long gap breakdown instead of short gap breakdown occurs since operation is to the left of the Paschen minimum. It is expected that the hold-off potential for SF_6 should be superior to N_2 . The relatively low measured value is probably due to errors associated with SF_6 pressure measurement using a thermocouple gauge. The SF_6 pressure is probably higher than the indicated 1 micron.

Switch Conduction Characteristics

The switch inductance and resistance have been measured using the circuits of Figure 3 and 4 respectively. The oscillation frequency of the circuit of Figure 3, with the switch conducting, implies a switch inductance of 121 nH. This rather high inductance is, as previously discussed, due to the long vacuum enclosure necessary for optical diagnostics. The inductance can be reduced to tens of nanohenries by using a shorter insulator between the electrodes.^{2,7} The 121 nH value is therefore not the optimum inductance value.

The conducting switch resistance has been determined by measuring the L/R time associated with the decay time of the crowbarred current in the circuit of Figure 4. A value of 30 m Ω has been measured for a discharge current of 10 kA.

Triggered Switch Delays

Delays associated with switch triggering have been measured using the circuit of Figure 2. Delay data have been obtained for relatively low main gap voltages of up to 6 kV. Low values have been used to simulate crowbar operation for an inductive load current maximum and voltage minimum.

Data have been obtained to determine the affect of trigger voltage, trigger energy, and trigger duration on triggered switch delay. Delay measurements have been obtained by using the charged line and the capacitive trigger sources. The capacitive source stores more energy, has a lower driving impedance, and gives shorter delay times, particularly for vacuum operation.

Delay data have been obtained using vacuum and low pressure fill gas. Delay data obtained with vacuum and gas will be presented as obtained using both trigger sources.

The data have been obtained by measuring the delay between the arrival of the trigger pulse to the switch and the collapse of the switch anode to cathode voltage. The trigger voltage is used to trigger a 519 oscilloscope. The main gap voltage collapse is viewed on the 519 such that the time delay observed from the start of the oscilloscope sweep to the beginning of the voltage collapse is the switch trigger delay.

Vacuum Switch Trigger Delay Measurements: Delay measurements have been obtained using the charged line and the capacitive trigger source. Typical data, representative of results obtained, are shown in Figure 5. Two delays of significance are depicted. The time between the initiation of the scope trace and the beginning of the voltage collapse is defined to be the trigger delay or time to beginning of breakdown, t_{bb} . The delay is relatively independent of external circuit parameters and is indicative of the gap breakdown delays. The voltage is observed to take a non-zero time, t_c , to collapse. This collapse time is dependent not only on the breakdown mechanisms but also upon the circuit inductance.

The vacuum delay data shown in Figure 5 was obtained using a charged line trigger pulser voltage of 5 kV and an anode to cathode trigger voltage of 25 kV. The time to beginning of breakdown and the time to total voltage collapse are seen to be 1.5 μ s and 2.5 μ s, respectively. Similar data have been obtained for main gap voltages, V_g , up to 8 kV and for trigger voltages, V_t , of 10 kV, 15 kV, 20 kV, and 25 kV. These results are summarized by the curves shown in Figure 6. The results show that, for $V_t = 15$ kV, the delays, t_{bb} , are on the order of 1 μ s and are relatively independent of V_g .

Vacuum switch delays, associated with the capacitive trigger source, have also been obtained. These results are summarized in Figure 7. It has been found that a minimum delay of approximately 100 ns exists for $V_g = 200$ volts and $V_t = 10$ kV. Trigger delays decrease as V_t increases. The data further show that for $V_t = 10$ kV, t_{bb} decreases as V_g decreases. This behavior is of course very different than that exhibited by high pressure gaps. Decreasing trigger delay with decreasing gap voltage is very attractive for low voltage, parallel switch, crowbar applications.

It should be further noted that the trigger delays obtained using the higher energy, lower impedance trigger source are shorter than those obtained using the charged line. This implies that higher values of trigger energy decrease the trigger delay. A compromise value of trigger energy must of course be used since increased trigger energy will probably reduce the trigger lifetime.

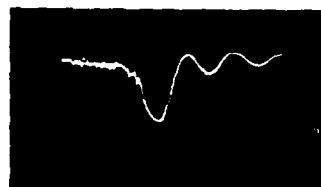


Figure 5. Switch Voltage
500 nsec/cm.

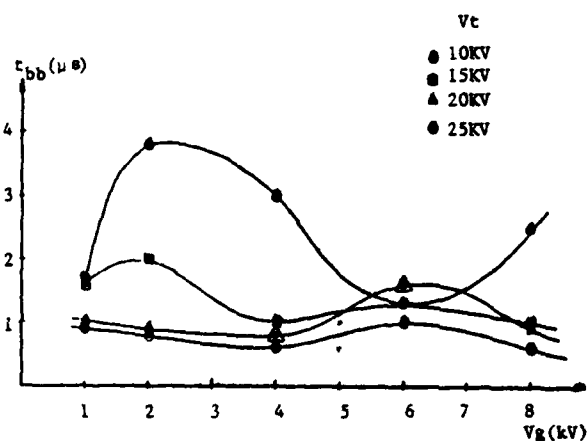


Figure 6. Switching Delays in Vacuum with Charged Line Trigger Source

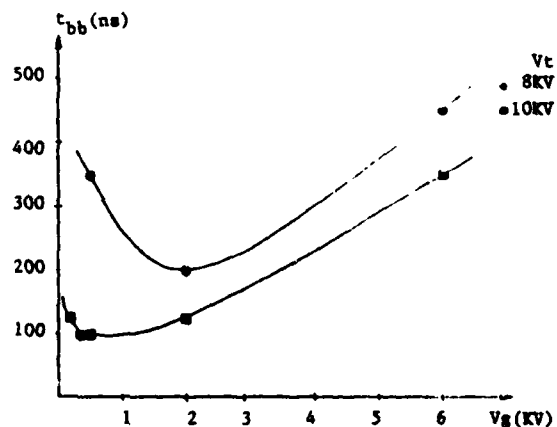


Figure 7. Switching Delays in Vacuum Using Capacitive Discharge Trigger Source.

AD-A119 663

PALISADES INST FOR RESEARCH SERVICES INC NEW YORK
IEEE CONFERENCE RECORD OF 1980 FOURTEENTH PULSE POWER MODULATOR--ETC(U)
1980

F/G 9/5

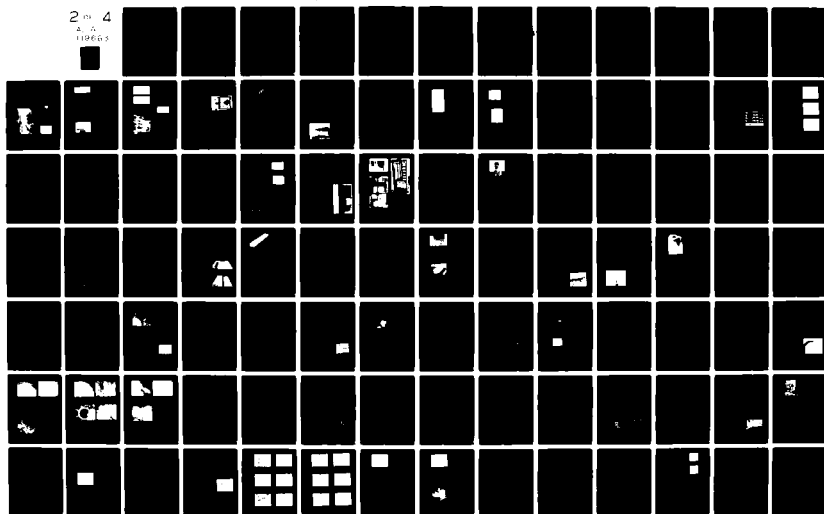
UNCLASSIFIED

80-CH-1573-5-ED

NL

2 of 4

A. A.
11/6/83



Low Pressure Switch Trigger Delays: Switch trigger delays have also been measured for low pressure gas filled operation. Trigger delays have been measured for Hg, N₂, and SF₆ fill pressures of 1 m Torr.

Switch delays measured for 1 mTorr mercury filled switch operation are shown in Figure 8. These data

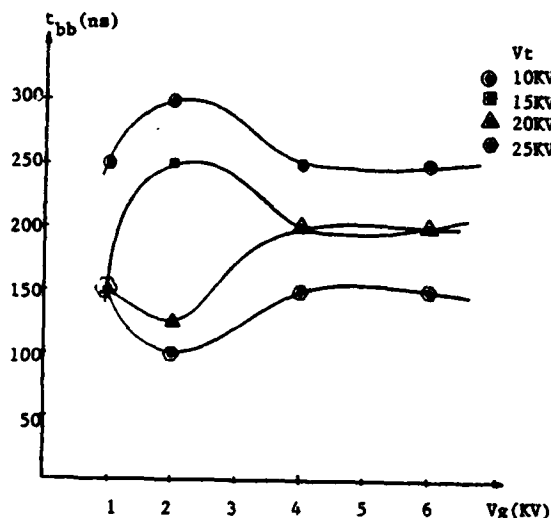


Figure 8. Switching Delays Using 1 micron Hg.

were obtained using the charge line trigger pulser. The data show that t_{bb} is on the order of 150 ns. The delay t_{bb} decreases as V_t increases and is relatively independent of V_g for $V_g > 4$ kV. It should again be noted that, for this low pressure operation, t_{bb} is smaller for lower values of V_g .

Switch delays have also been measured for N₂ gas fill. The results are surveyed in Figure 9. The data

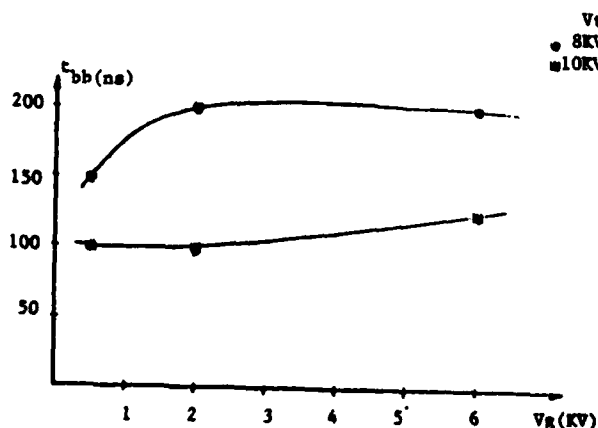


Figure 9. Switching Delay Using 1 micron N₂.

show that t_{bb} is relatively independent of V_g for $V_t = 10$ kV and clearly show that t_{bb} decreases as V_t is increased from 8 kV to 10 kV. The data further show that a delay of 100 ns can be obtained for low values of V_g , appropriate to crowbar switch operation.

The switch operating characteristics have also been determined for low pressure SF₆ operation. The insulating strength of SF₆ is superior to that of N₂. However, the converse has been observed in this work. This is probably due to errors associated with SF₆ pressure measurements. The actually SF₆ pressure is probably higher than the measured values. The delays for an indicated 1 mTorr SF₆ pressure are shown in Figure 10. These data show that t_{bb} monotonically

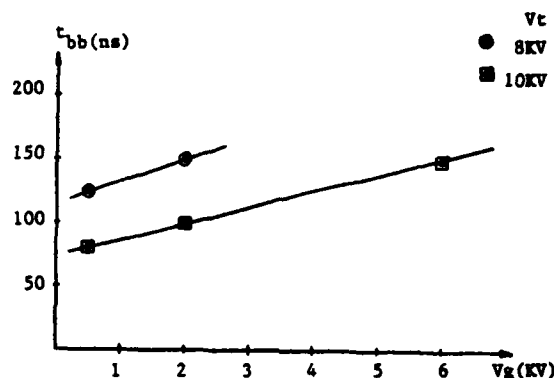


Figure 10. Switching Delays Using 1 micron SF₆.

increases with V_g . An increase in V_t results in a decrease in t_{bb} . A minimum delay of 80 ns has been obtained for $V_t = 10$ kV and $V_g = 500$ V.

Jitter Data: The trigger delays for vacuum, Hg, N₂, and SF₆ have been measured for the plasma injection switch of Figure 1. These delays have been found to be the shortest for the capacitive discharge trigger source and are in the range of 100 ns. The jitter, or uncertainty in trigger time, is also of importance and has been measured for vacuum and various low pressure gases. The data were obtained by superimposing successive switching voltage traces on one photograph. A summary of the data obtained is in Table 1. The

table shows the gas type, pressure, gap voltage, and trigger voltage used and the number of shots taken for each set of parameters. The average delay to beginning of breakdown, $\langle t_{bb} \rangle$, and the standard deviation of the delay Δt_{bb} , have been computed for each group of shots and are listed. The mean delays for $V_g = 500$ V are consistently less than the delays for $V_g = 6$ kV. This again shows that shorter delays exist for main gap voltages appropriate to crowbar applications.

The jitter, Δt_{bb} , is determined by calculating the standard deviation of the measured delays. The jitter is less for $V_g = 500$ V than for $V_g = 6$ kV and is in the range of 10 ns for vacuum and low pressure operation. These low jitter values for low main gap voltages also imply that the low pressure, plasma triggered switch is particularly suitable for crowbar applications.

gas	pressure (Torr)	v_g (V)	number of shots	$\langle t_{bb} \rangle$ (ns)	Δt_{bb} (ns)
Vacuum	8×10^{-7}	500	20	120	9.1
Vacuum	8×10^{-7}	6000	15	365	49.1
N_2	1×10^{-3}	500	10	110	4.7
N_2	1×10^{-3}	6000	10	135	38
SF_6	1×10^{-3}	500	10	113	8.6
SF_6	1×10^{-3}	6000	10	171	25

Table 1. Tabulation of Delay and Jitter (Standard Deviation) of Trigger for Various Gases and Gap Voltage $v_g, v_c = 10kV$.

Switch Lifetime

Data presented thus far have shown the hold-off voltage and trigger delays obtainable with vacuum or low pressure operation. The lifetime of the switch is also important and is being determined using the high energy circuit of Figure 4. Lifetime measurements consist of determining the discharge uniformity, the amount of electrode erosion for high current operation, and trigger lifetime. Data have been obtained for copper electrodes only, to date.

Discharge Uniformity Measurements

A uniform discharge prolongs electrode life. Present work consists of determining under what conditions, and for what discharge current levels, the discharge remains diffuse. Discharge uniformity has been determined using open shutter photography and an image converter camera. Results indicate that the discharge remains uniform for moderate current levels. More recent data imply that the discharge becomes localized in the vicinity of the electrode edges for current levels exceeding 60 kA.

Electrode Erosion

Electrode erosion is the primary factor which limits this switch lifetime. Electrode erosion during high coulomb transfer discharges is currently being investigated using copper electrodes. Hundreds of 50 kA discharges have been applied to the present electrodes. A small amount of electrode erosion has been observed primarily near sharp edges around the electrode disc perimeter. Current work is extending the lifetime measurements to greater than 10^3 shots.

A major problem caused by electrode erosion, in addition to the loss of electrode material and surface degradation, is the condensation of evaporated electrode material onto the containment vessel walls. After a few hundred discharges the glass is no longer transparent. This movement of copper from electrodes to vessel walls is undesirable and will probably ultimately result in degradation of the switch hold-off potential. It is therefore clear that electrode erosion must be reduced, not only to extend electrode lifetime, but also to increase the useful lifetime of electrode surfaces.

Trigger Lifetime

Trigger lifetime presently appears to be no problem. The main discharge has been observed to be away from the central, triggered region and hence does little or no damage to the trigger mechanism. The trigger mechanism is also substantially isolated from the discharge due to the small size of the plasma injection hole. The lifetime of the BaTiO₃ substrate is presently being determined. Several thousand shots have thus far been completed. Previous work by Raju, et. al., also indicates that trigger lifetime is long.⁸

Conclusion

A vacuum or low pressure gas, plasma triggered switch has been designed, constructed, and parameterized. The switch has been tested with vacuum, Hg, N_2 , and SF_6 filling the intergap region. Hold-off voltages have been measured for a 1 cm gap and exceed 50 kV for vacuum and N_2 . The discharge switch inductance and resistance have been measured to be 121 nH and 30 mΩ. Trigger delays have been measured to be on the order of 100 ns with corresponding jitters of 10 ns. The trigger delay has been observed to decrease as the main gap voltage decreases. This is a very attractive feature for crowbar applications. The trigger delay time has further been observed to decrease as the trigger voltage and energy increase. Electrode lifetime and insulator lifetime are currently being investigated. Hundreds of 50 kA shots have been taken with the present set of copper electrodes. Erosion is thus far not severe. Image converter data imply that the discharge remains diffuse for currents up to 60 kA. More than 10^3 trigger discharges have been made. Trigger lifetime is therefore greater than 10^3 shots.

The low pressure switch appears to be well-suited for crowbar applications primarily because gaps with a high withstand voltage can be triggered, with approximately 100 ns of delay, at voltages as low as a few hundred volts. The trigger delay actually decreases as the main gap voltage decreases. Electrode lifetime, particularly for large coulomb transfer operation will be a major problem. Current research is approaching this problem.

References

1. G. M. Aretov, V. I. Vasil'ev, M. I. Pergament, and S. S. Tserevitinov, "Electrical Strength of Vacuum Disc Switches", SPTP, 11, May 1967, p. 1548.
2. S. Kamakshiah and R. S. N. Rau, "Anode Phenomena in Triggered Vacuum Gap", IEEE Trans. on Plasma Science, PS-5, March, 1977, p. 1.
3. K. D. Ware, J. W. Mather, A. Williams, P. Bottoms, and J. Carpenter, "Design and Operation of a Fast High-Voltage Vacuum Switch", Rev. Sci. Instr., 42, April, 1971, p. 512.
4. D. C. Hagerman and A. H. Williams, "High Power Vacuum Spark Gap", Rev. Sci. Instr., 30, March, 1959, p. 182.
5. W. Baker, "High Voltage, Low Inductance Switch for Megampere Pulse Currents", Rev. Sci. Instr., 30, August, 1959, p. 700.
6. J. Mather and A. Williams, "Some Properties of a Graded Vacuum Spark Gap", Rev. Sci. Instr., 31, March, 1960, p. 297.
7. L. Ornstein, C. Hugenholtz, H. Van der Leen, "A Triggered Vacuum Spark-Gap Switch", J. Sci. Instr., 42, 1965, p. 659.
8. G. R. Govinda Raju, R. Hackam, and F. A. Benson, "Firing Characteristics of a Triggered Vacuum Gap Employing a Dielectric Coated with a semi-conducting Layer", JAP, 48, March, 1977, p. 1101.

PHASE STABILITY IMPROVEMENT TECHNIQUES FOR TRANSMITTERS WITH LINE TYPE MODULATORS

Edward M. Piechowiak
WESTINGHOUSE ELECTRIC CORPORATION
MS 709, Box 1897
Baltimore, Maryland 21203

INTRODUCTION

This paper addresses a number of potential sources of phase error which must be controlled within a radar transmitter that uses a line type modulator if superior MTI performance is to be achieved. Among the contributors to phase error which are considered are HVPS ripple, staggered PRF sequence, time jitter, PFN ripple, heater supply, focus coil power supply, and RF drive. Typical phase sensitivities of the microwave tube to the various disturbances are identified and the techniques for minimizing the phase error are described. This information served as the basis for a verification program during which a number of improvements to a test bed transmitter were evaluated to determine the extent of their usefulness. A summary of the test results is given for a transmitter which achieved better than a 64 dB system MTI improvement factor after incorporation of the improvement techniques, an enhancement of well over 20 dB.

This level of performance implies that the moving target to clutter ratio at the processor input divided by the target to clutter ratio at the processor output is better than 64 dB. Since detection of a moving target is accomplished by detection of pulse to pulse phase changes, any undesired phase change in the transmit chain on a pulse to pulse basis will result in reducing the performance of the radar. Figure 1 shows a simplified curve of phase error versus the MTI improvement factor. For a 64 dB MTI improvement factor, the phase error over the number of pulses integrated must be better than 0.034°. The allowable phase error is further modified by the frequency of the disturbance. This is shown by the typical velocity response curve in Figure 2 for the MTI processor. For disturbances which occur at the PRF of the radar there is a benefit of a few dB which allows the phase error to be worse than shown in Figure 1. At one half the PRF, the system must have even more stringent performance. At very low frequencies severe phase errors can be tolerated without compromising system performance.

SOURCES OF PHASE ERRORS

The transmitter that was utilized for the test program employed a cathode pulsed, solenoid focused klystron, the VA963A. Although different tubes and tube types have a broad range of phase sensitivities to various applied voltages and interfaces, the sources of such errors are generally the same. Typical VA963A phase sensitivities are shown in Table 1 along with some of the

sources of phase error.

The most significant source of phase error is generally the cathode voltage applied to the tube by the pulse modulator. The VA963A, as operated for this demonstration, has an electrical phase length of just over 2000 degrees at midband. As the cathode voltage increases and decreases on a pulse to pulse basis, the corresponding increase and decrease in electron beam velocity creates a decrease and increase in apparent electrical length of the tube. This results in a pulse to pulse phase difference which the MTI processor sees as a moving target. An increase in cathode voltage also results in a higher quantity of electrons being emitted which produces an increase in amplitude of the output RF pulse. Generally, any amplitude modulation disturbance is an order of magnitude less significant than the phase change and can therefore be ignored. At higher RF frequencies, the tube appears to be longer by a linear relationship, i.e., 5% higher in operating frequency means 5% longer in length and 5% more sensitivity to the applied cathode voltage.

Traveling wave tubes have longer electrical length than klystrons for the equivalent gain and therefore are more sensitive to voltage variation. Some tube types, crossed field amplifiers for example, show very low phase sensitivity to cathode current but are rather low gain tubes. By the time additional gain stages are provided, it is questionable whether there is any significant overall benefit in utilizing CFA's strictly to achieve additional phase stability because of the phase shift contributed by the additional stages.

Another factor that introduces apparent changes in phase length of the linear beam tube is the focusing solenoid. As the electron beam enters the magnetic field any component of the magnetic field which is perpendicular to electron velocity creates a transverse velocity component of the electrons. Since the energy of the electron is conserved, any transverse velocity component that is added will detract from the axial velocity component, thus causing an apparent increase in electrical length of the tube.

RF drive amplitude variation is another factor which induces phase delay in the klystron amplifier. It is dependent on the tube gain (number of cavities), how close the tube is run to saturation, and the operating frequency of the tube. Since variations in drive power result in extracting more or less energy from the electron beam, there are corresponding changes in the beam velocity which induce phase changes.

Variations in heater voltage on the transmitter tube also affect the MTI performance of the radar. Any changes in cathode temperature will have a significant effect on phase error, but the thermal time constant is much longer than the integration period of the MTI processor which is typically 3 to 4 interpulse periods. More important is the electromagnetic effects which occur on a short time basis when using AC heater voltages. This phenomenon is generally not considered a problem unless system MTI improvement factors of 40-50 dB or more are required.

Finally, one must consider such effects as vibration in the tube with mechanical cavity tuner mechanisms which can physically move under vibration and shock such as might be encountered in airborne and shipboard environments. In addition, physical vibration of coax cables, couplers, and similar components should be considered.

CONTROL OF PHASE ERROR SOURCES

For the demonstration transmitter the technique used for the basic modulator and charging system was similar to that described in previous papers on the ARSR-3 transmitter ^{1,2}. These papers describe the ARSR-3 as a long range search radar built for the Federal Aviation Administration. It uses a VA963A klystron as a final amplifier which is cathode pulsed by a modular solid state modulator.

Figure 3 is the block diagram of the demonstration transmitter. The charging system is shown in the simplified schematic in Figure 4. To maintain tight control of the voltage on the pulse forming network a three phase line rectified input was fed into a transistor switch which dumped a regulated amount of energy into the primary of a charging transformer where energy was stored until the switch was turned off. The stored energy then charged the pulse forming network. Other approaches which could achieve similar electrical performance include multiphase high voltage power supplies with series or shunt regulators and resonant charging systems with De-Q-ing. Since one potential source of error is power supply ripple at multiples of the line frequency, techniques such as multiphase supplies, large filters and line regulators could be used to minimize the effects of line unbalance. However, in most radar systems staggered PRF's are used to eliminate MTI blind speeds and the main ripple component is a function of the stagger sequence. Therefore, more sophisticated regulation is preferred. The large PRF stagger (+30%) in the demonstration system required that techniques such as command charge, and a charging regulator technique be used to minimize the pulse to pulse ripple on the PFN's.

In addition, the increased MTI performance of well over 20 dB better than the baseline transmitter, required that additional regulation capability be included. This was accomplished in the form

of a bleedoff type of regulator across the PFN. Pulse to pulse regulation of 150 millivolts out of approximately 2500V stored on the PFN was achieved with a floating reference. With this regulation approach, the PFN voltage is first regulated to approximately 2.5 volts using the charging regulator to slightly overcharge the PFN. The PFN voltage is then bled down to the desired value with the bleedoff regulator which may be triggered to commence regulation at a fixed time prior to the discharge pulse of the modulator. This type of regulator has also been used in conjunction with an inverter charging modulator described in a paper³ by E.H. Hooper.

As with most line type modulators, the pulse forming network does not have a perfectly flat pulse top, although in the demonstration networks flat top performance was stressed at the expense of rise and fall times. The video pulse bracketed the RF carrier and any time jitter in the modulator trigger amplifier and discharge switch resulted in pulse to pulse variations as shown in Figure 5. Although most of the solid state modulators of the same generic type used in the demonstration transmitter exhibited time jitter of 5 nanoseconds or so, it was found worthwhile to further improve the test bed by providing additional voltage regulators for the trigger amplifier, thus eliminating any time jitter concern.

The phase modulation introduced by the cathode heater supply for the demonstration came from an inverter supply operating at 2 KHz that fed a voltage isolated transformer. The inverter pulse was, therefore, interrupted for a 100 usecond period around the transmit pulse time as shown in Figure 6. This approach is a viable alternative to a regulated DC heater supply, which would require numerous components to be placed at the cathode potential of the klystron. It serves the same function, however, namely minimizing the electromagnetic disturbances generated by the heater on a short term basis. To prevent saturation of the filament transformer by a DC component of current, the pulse width is increased by a 100 usecond period when required to compensate for the "off" time. Other means of controlling heater phase disturbances include synchronizing the inverter frequency with the radar PRF, which could be troublesome when large PRF staggers are required, and operation of the heater at very low frequencies, typically 10 Hz or so, where the disturbance frequency has little effect on the radar MTI.

Focus coil perturbations are readily taken care of by providing a current regulated power supply. The large inductance of the focus coil aids in reducing current ripple. Although permanent magnets have been used on smaller tubes they are not practical for multimegawatt tubes at L-Band.

A solid state amplifier using bipolar transistors was used for the driver in the transmitter. To achieve the required amplitude stability of drive level into the

klystron it was necessary to provide the driver with its own power supply which was isolated from other switched loads. A power supply regulator was physically located in the driver amplifier package to achieve the desired system stability. Semirigid coax cables were substituted for the flexible cables which exhibited phase variation with vibration.

TEST RESULTS

The parameters for the test transmitter are listed in Table 2. The test data was taken using a technique which takes into account, not only the transmitter instabilities, but also those of the frequency source. The output data from the test set was then processed through a computer program that factored in the effects of the MTI system, the clutter residue formula, weighted coefficients, etc. The test set used for stability measurements is shown in the block diagram of Figure 7. Samples can be taken anywhere along the RF amplifier chain to aid in locating sources of phase error. The 15 usecond delay line decorrelates the test sample from the STALO signal to include STALO instabilities into the recorded data as would be the case with real target returns. Adjustment of the phase shifter allows the mixer to be used as either an amplitude or phase detector.

The test technique consisted of taking 64 samples at the same point into the RF pulse on 64 consecutive pulses. The phase errors recorded were then processed with the computer program which simulated the MTI processor shown in Figure 8 this gave, as a result, the MTI improvement factor at a particular point in the pulse after considering all of the data from the 64 samples. This test was repeated at 4 different points in the RF pulse, namely:

- 0.5 useconds from the leading edge,
- 2.5 useconds from the leading edge,
- 3.0 useconds from the trailing edge, and
- 1.5 useconds from the trailing edge.

Two complete sets of data were taken and averaged at each point in the pulse. Data

was repeated at 3 different carrier frequencies; 1260 MHz, 1290 MHz, and 1350 MHz. A summary of the results is shown in Table 3 for both phase and amplitude data. The worst case shown is better than 64 dB MTI improvement factor, a significant improvement over previous hardware designs.

As with most achievements in improving performance, it is only a matter of time before more stringent system requirements demand even further improvements. To determine which areas would have to be addressed in the next generation of stability improvements, a series of additional test were performed. With all of the transmitter improvements installed, a spectrum analyzer was used to determine what discrete spurious lines and what bed level noise existed. Then, after removing one of the improvements at a time, data was taken to determine what change there was in the various noise levels. Repeating this process for various circuit modifications resulted in the data shown in Table 4. As can be seen, the impact is reasonably consistent regardless of the particular improvement be measured. From this data one can conclude that 1) all of these modifications were necessary to achieve the degree of performance measured in the demonstration transmitter and, 2) if any further significant improvement is to be made in system performance, each one of these factors will need to be bettered.

REFERENCES

1. E.H. Hooper and S.R. Bird, "An All Solid-State Modulator for the ARSR-3 Transmitter", Conference Record of 1978, Thirteenth Pulse Power Modulator Symposium, June, 1978, pp. 242-246.
2. C.A. Corson, "Precision Regulated, 20KW, Modulator PFN Charging System", Conference Record of 1978, Thirteenth Pulse Power Modulator Symposium, June, 1978, pp. 34-37.
3. E.H. Hooper, "An All Solid-State, Inverter Charged Modulator with Precision Pulse-to-Pulse Regulation", Fourteenth Pulse Power Modulator Symposium, June, 1980.

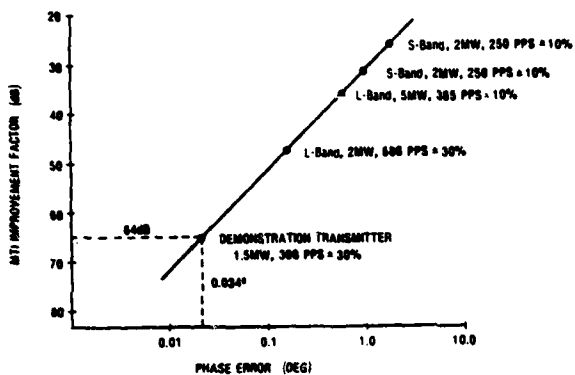


Figure 1. Typical MTI Performance Versus Phase Error

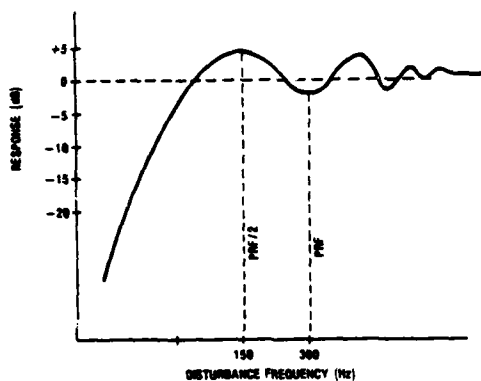


Figure 2. Typical MTI Response Curve

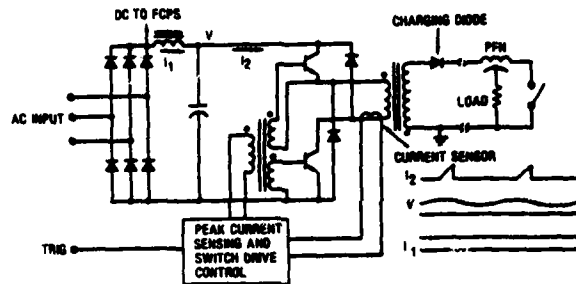


Figure 4. Modulator Charging Power Supply

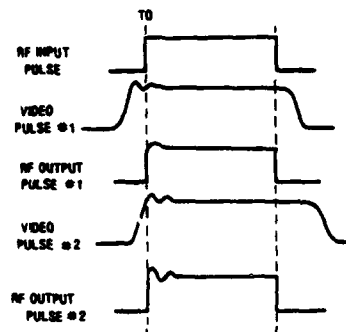


Figure 5. Pulse-to-Pulse Variations in RF Output Due to Time Jitter

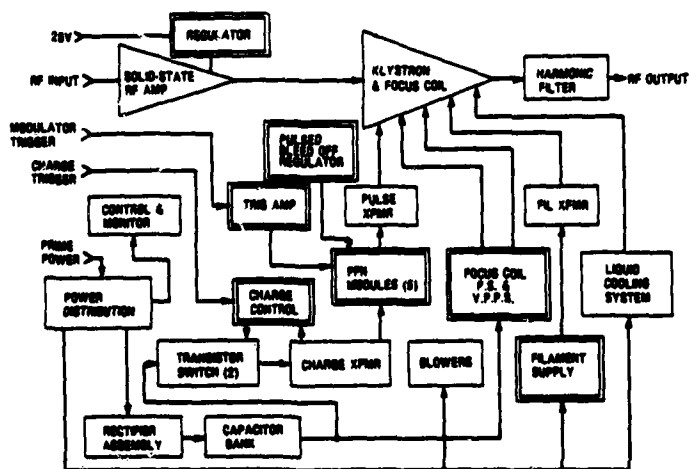


Figure 3. Transmitter Block Diagram

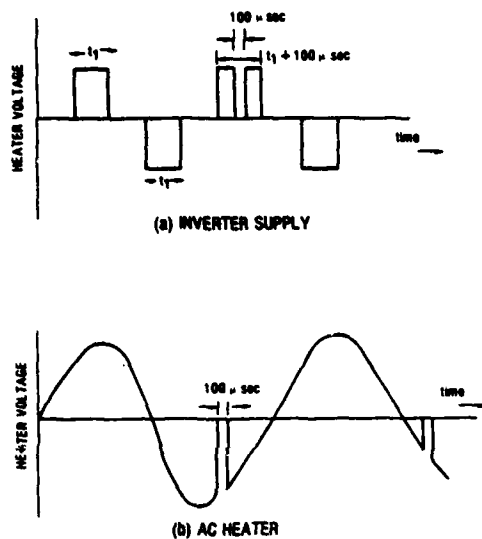


Figure 6. Heater Supply Interrupt Approach

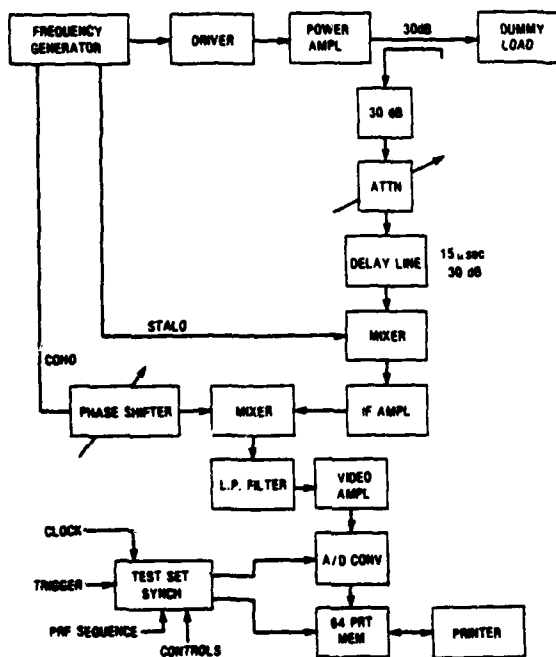


Figure 7. Stability Measurement Technique

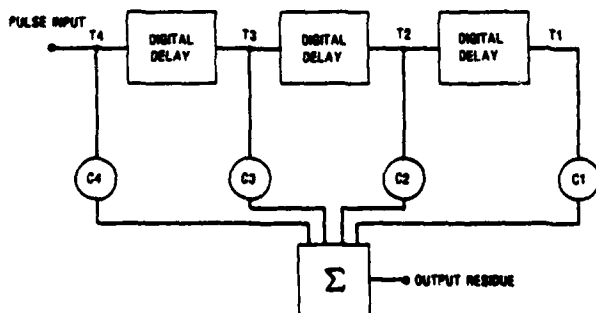


Figure 8. MTI Processor Configuration

SOURCES OF PHASE ERROR

VA963 PHASE SENSITIVITIES

LINE UNBALANCE	} • 7.5°/KV (RELATED TO FREQUENCY)
HIGH VOLTAGE POWER SUPPLY RIPPLE	
PRF STAGGER	
CHARGING CIRCUIT REPEATABILITY	
TIMING JITTER & PRF RIPPLE	
FOCUS COIL POWER SUPPLY RIPPLE	• 3°/1% CURRENT
RF DRIVE	• 10°/dB (NEAR SATURATION)
HEATER	• 10°/V THERMAL
TUBE TYPE	• 0.005°/V DYNAMIC
VIBRATION/TUNERS	

Table 1. Sources of Phase Error and Klystron Phase Sensitivities

• FREQUENCY	1250 - 1350 MHz
• PEAK POWER	1.5 MW
• RF PULSEWIDTH	8.7 μ sec
• VIDEO PULSEWIDTH	9 μ sec
• PULSE REPETITION RATE	300 PPS
• PULSE RATE STAGGER	± 30%
• PRIME POWER	115/120V, 30, 60 Hz

Table 2. Parameters for Test Bed Transmitter

	1250 MHz	1280 MHz	1350 MHz
PHASE DATA			
0.5 μ sec FROM LEADING EDGE	60.90 dB	60.75	61.50
2.5 μ sec FROM LEADING EDGE	60.80	60.84	60.87
3.0 μ sec FROM TRAILING EDGE	64.82	63.86	66.06
1.5 μ sec FROM TRAILING EDGE	61.95	64.13	61.30
PULSE AVERAGE	64.23	65.84	65.01
AMPLITUDE DATA			
1.0 μ sec FROM LEADING EDGE	72.76 dB	77.76	72.87
4.3 μ sec FROM LEADING EDGE	73.66	72.31	64.76
PULSE AVERAGE	73.23	75.06	73.82

Table 3. Results Summary

	CHANGE IN COEFFICIENTS (dB)	CHANGE IN NOISE RED (dB)
BLEEDOFF REGULATOR	9.5	0.5
FILAMENT INTERRUPT	9.0	3.0
REGULATED TRIGGER AMPLIFIER	3.6	0.3
REGULATOR RF DRIVER	0.1	0.3

Table 4. Sensitivity Analysis

MAGNETRON/MODULATOR INTERFACE DESIGN CONSIDERATIONS

N. S. Nicholls

Royal Signals and Radar Establishment
Malvern, United Kingdom

Empirical data on the buildup of oscillation in a typical magnetron with different constant applied cathode voltages was previously described. With some assumptions, this information may be used to calculate, by a step-by-step numerical procedure, the buildup of cathode current with a time-varying cathode voltage. By imposing a relationship between cathode voltage and cathode current, and their time derivatives which is characteristic of the modulator, the behavior of the combined system is obtained. This procedure is applied using two alternative families of idealized modulator designs, both of the PFN and pulse-transformer type but differing in the disposition of capacitance and inductance. Both are constrained by a common requirement of an acceptable current pulse shape. Within each family, the open-circuit dv/dt is progressively increased until a limiting value is found, above which stable oscillation is not established. In one family the output impedance is predominantly inductive during the first thousand or so rf periods while in the other it is predominantly capacitive. The limiting value of dv/dt is much higher for the inductive impedance type of modulator. It is shown that such modulators may be designed which are efficient, economical, and reliable than is possible with a capacitive output impedance. It is expected that longer magnetron life will also be obtainable. From this it is seen that magnetron dv/dt ratings need to be specified which include the effect of modulator impedance characteristics.

AN ALL SOLID-STATE, INVERTER CHARGED MODULATOR WITH PRECISION PULSE-TO-PULSE REGULATION

Edward H. Hooper
Westinghouse Electric Corporation
Command and Control Division
Baltimore, Maryland 21203

Summary

A new all solid state, high power, line-type modulator has been developed for use with tactical radar transmitters. This new modulator offers improved performance, modular construction, and improvements in reliability and maintainability. It employs RBDT switched PFN modules to generate nine microsecond, nine megawatt peak power pulses at an average power of 24KW.

A novel aspect of the modulator is its use of a four-module inverter and regulator system to charge the PFN's to within 0.01% on a pulse-to-pulse basis. The inverter system converts power from low voltage dc to 10 KHz which is transformed and rectified to charge the PFN's in small steps. During most of the PFN charging interval, all four modules operate together at maximum frequency to charge the PFN at maximum rate. As full PFN charge is approached, both inverter frequency and the number of operating inverter modules are reduced to lower the step interval, slow the charging rate, and obtain the required regulation.

This paper describes the modulator and gives performance results obtained in tests with a tactical radar system.

Introduction

A number of radar transmitters have been produced at Westinghouse which include modular, all solid state, line-type modulators. All employ Reverse Blocking Diode Thyristors (RBDT's) in a pulse switching technology which has become well established by its use in such systems as the ADS-4 and ARSR-3.^{1,2}

To complement this pulse technology, more recent work has concentrated on developing complementary charging systems which are modular, all solid state, and incorporate means for precise regulation of Pulse Forming Network (PFN) voltage on a pulse-to-pulse basis.

The most recent of these is a charging system which uses conventional SCR Thyristor switched, half bridge inverter circuit modules and a post charge precision final regulator. This charging system was incorporated in a new modulator, with RBDT switched PFN Modules, to replace the existing modulator in an established tactical radar. The new modulator offers improvements in reliability and maintainability as well as a modulator which operates with much lower voltages than its predecessor.

Operating parameters of the new modulator, which is the subject of this paper, are as follows:

Peak Pulse Power	10 MW
Average Power	24 KW
Pulse Width	9 μ Sec
Pulse Repetition Frequency	258 pps
Output Pulse Voltage	117 KV
Pulse-to-Pulse Regulation	0.01%
Primary Power	208V, 400 Hz
Inverter Input Voltage	280 VDC

The Modulator, along with the VA-145E Twystron which it pulses, are packaged in the 3 ft. by 6 ft. by 6 ft. transmitter compartment of a tactical radar shelter with single door access.

Modulator Description

The modulator comprises modules interconnected as shown in the block diagram in Figure 1. The output pulse is generated by five PFN Modules, each with its own PFN and solid state switch. The five modules are operated together in parallel through a high turns ratio pulse transformer to supply the required video pulse train to the load. The PFN's are recharged by selective operation of the four inverter modules. Control of the modulator is through a central logic unit which processes incoming triggers in response to various fault monitor and control inputs.

The inverter modules are identical, resonantly commutated, half bridge inverter circuits with resonant feedback diodes to limit voltage swing in the inverters during light loading conditions at the beginning of each charge cycle. Each operates as a current source supplying a 7.5 to 10 KHz sinewave through a summing and voltage step up transformer to a bridge rectifier. The full wave rectified output constitutes a charge-rate drive to the PFN's which may be stopped and started as the inverters are turned on and off through inverter trigger gating.

Figure 2 is a photograph of the modulator cabinet assembly as viewed through the transmitter compartment access door. The PFN Modules are in the middle portion of the cabinet to the left with their outputs fed through the "coal chute"

to the high turns ratio pulse transformer in the pressurized SF₆ tank. The four inverter modules are above the PFN Modules. Power supplies and the control logic circuitry are in the lower left portion of the cabinet.

All modules are removable and easily replaceable with identical spare units to minimize down time in the event of a part failure. To expedite fault isolation to the proper module, an LED fault monitor display on the control panel identifies fault categories. A quick check of test points on the modules then identifies the module to be replaced.

Modulator Operation

Operation of the modulator may be described with reference to the waveforms in Figure 3. These waveforms are keyed to the block diagram Figure 1, although their generation is described in detail in subsequent sections of this paper.

The charging cycle begins with all four inverter modules operated in parallel at their maximum frequency of 10 KHz. At this frequency, inverter current, which is frequency dependent and flows through the reflected PFN capacitance load, is high so that maximum charge is transferred to the PFN per inverter cycle and the PFN voltage change or step per cycle is highest. This together with the high cycle repetition rate causes the PFN charging rate to be at its highest.

As the PFN voltage approaches its target value, inverter frequency is dropped to 7.5 KHz. This lowers the charging rate both by reducing inverter currents (and hence the per cycle step level) and the cycle rate.

Next, three of the four inverter modules are shut off to further reduce the step interval. The step interval varies from about 80 volts at the beginning of the charge cycle to about 15 volts during the single inverter module cycles. The inverter triggers are stopped when a sample of PFN voltage crosses a preset reference level so that the PFN voltage is left between five and twenty volts above its long time average pulse-to-pulse operating level. The excess charge is then bled off by a final regulator during a fixed time interval preceding the discharge pulse to bring the PFN voltage at pulse discharge to within 0.1 volt on a pulse-to-pulse basis.

Figures 4 and 5 are waveform photographs of operation of the charging system. Figure 4 is a photograph of the voltage on the common charging bus to the PFN's. Figure 5 shows the top of several charging cycles in which the pulse-to-pulse charge voltage variation and its bleed down to a very uniform voltage at the time of pulse discharge is shown.

The modulator output pulse is generated by simultaneously discharging the PFN's in the five PFN Modules through a high turns ratio pulse transformer into the modulator load. The pulse switches in the PFN Modules

are RBDT assemblies which are impulse triggered by the trigger amplifier. Since the voltage on the PFN's is regulated to within 0.01% on a pulse-to-pulse basis, the modulator output pulse at the pulse transformer primary is likewise regulated, subject to reset variations in the pulse transformer that may occur in stagger mode operation.

PFN Modules

The PFN Modules are similar in circuitry to those used in the ARSR-3 transmitter and have been described previously.² Figure 6 is a simplified schematic of the module and its trigger interface. The five PFN's, one in each module, are charged and regulated by the Inverter charger and regulator through a common charge bus.

During the PFN charging interval, the trigger capacitor is charged from a separate charging system in the Trigger Amplifier. Just prior to pulse discharge the trigger switch is turned on to simultaneously discharge all trigger capacitors each through its own trigger transformer to apply a trigger pulse simultaneously to all PFN module RBDT switches. The RBDT switches are two terminal, thyristor type devices which switch from a nonconducting state over a large conduction area in response to a high dv/dt pulse. Upon switching of all devices in the stack, the PFN's discharge in conventional line type modulator fashion to generate and shape the modulator output pulse.

Figure 7 is a photograph of the PFN module. The PFN occupies the upper portion of the module. The RBDT switch assembly is the stacked assembly at the bottom through which passes the full input air to the module. The module is entirely air cooled.

Inverter Circuit

A half bridge, series loaded, resonantly commutated inverter circuit with diode energy return is used in each of the charging modules. Figure 8 is a simplified schematic of a single charging module circuit with the rectified capacitive load that it sees looking into a PFN. Figure 9 presents theoretical waveforms of the inverter in the neighborhood of a single cycle of circuit operation. Figure 10 shows actual output transformer primary current waveforms both near the beginning and the end of the PFN charging interval.

The two SCR's are triggered and conduct alternately, one for each half cycle of inverter operation. Each SCR conducts for a period of time determined by the resonant circuit that it sees and then is turned off by the backswing that follows. The circuit which each SCR sees is the series loaded resonant circuit identified by the flow path associated with it in Figure 8.

During normal inverter operation, each SCR is triggered while the reverse diode across its complementary SCR is still

conducting in the backswing. The overlap is timed so that the same initial voltage conditions exist in the circuit for each half cycle of operation and such that peak inverter currents (400A) are well within the ratings of the SCR's. As trigger frequency is reduced and the degree of overlap is reduced, inverter current per cycle is then reduced. In effect, lowering inverter frequency reduces inverter currents by effectively moving circuit operation further from circuit resonant frequencies.

The load on the inverter circuits is the capacitance of the PFN's as reflected back through the inverter output rectifier and transformer. Because of the turns ratio, the equivalent capacitance seen by the inverter is much larger than the inverter capacitance so that the output voltage change per cycle is small. Furthermore, because of the rectifier action, the existing PFN voltage at the beginning of the cycle opposes the dc source voltage. The effect on the inverter is then a constant parameter circuit with an equivalent source voltage for each cycle which diminishes from cycle to cycle. The feedback diodes compensate for this source drop during most of the cycle by decreasing the amount of feedback current as the PFN charges.

Inverter currents are thus largely inverter circuit determined. Since these currents are coupled and rectified to charge the PFN's, the action of the inverter system as seen by PFN's is as a charging current source.

Figure 11 is a photograph of an inverter module. The two SCR's in the forward part of the module are liquid cooled in order to minimize heat sink volume and simplify cooling air flow. The overall size of the module is 19 x 20 x 6½ inches.

Final Regulator

The inverter system as implemented in the radar is capable of controlling voltage to within 20 volts out of 3000 volts, or to within 0.33%. A significantly finer regulation can be obtained on a pulse-to-pulse basis by using a bleed off regulator as shown in Figure 12. This regulator regulates to a floating reference which is always slightly below the minimum voltage placed on the PFN's. Under regulating conditions, the transistor is driven to conduct a bleed current which is directly proportional to the error voltage. The result is an exponential decay as illustrated in the waveform in Figure 12.

The final regulator is employed during a fixed time interval of 600 microseconds just preceding the pulse discharge of the PFN. It is off and has no influence during the charging interval.

Figure 13 is a multi-exposure waveform photograph which illustrates the action of the final regulator.

Conclusions

The modulator described in this paper is a significant departure from conventional line-type modulators used with radar transmitters. It has demonstrated very tight pulse-to-pulse regulation and reliable operation. Presently, a number of systems are in the field with good operating reports.

The modular aspects of this modulator, coupled with the existing monitor functions already incorporated plus built in test features under development make this approach highly available with down time limited to that required for module replacement. Related development effort is underway in which faulty modules are dropped automatically and equipment operation maintained without human intervention.

References

- 1) C.A. Corson, "A Modular Modulator for on Air Defense Radar", Conference Record of 1976 Twelfth Modulator Symposium, 1976, pp. 182-186.
- 2) E.H. Hooper and S.R. Bird, "An All Solid-State Modulator for the ARSR-3 Transmitter", Conference Record of 1978 Thirteenth Pulse Power Modulator Symposium, June, 1978, pp. 242-246.

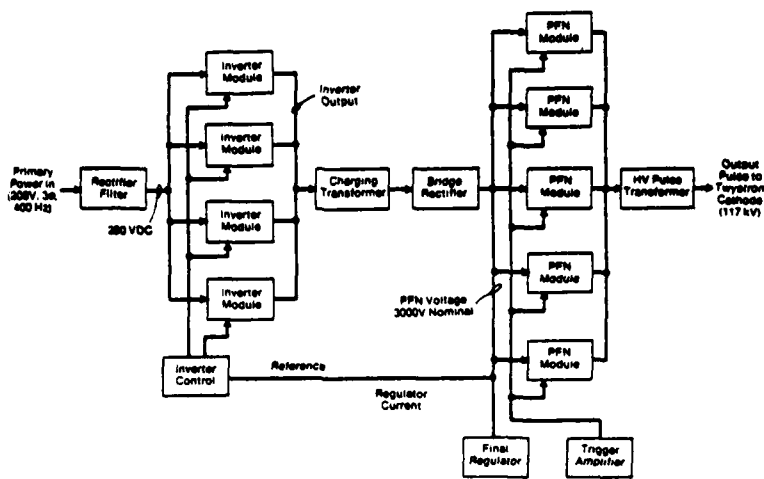


Figure 1. Modulator Block Diagram

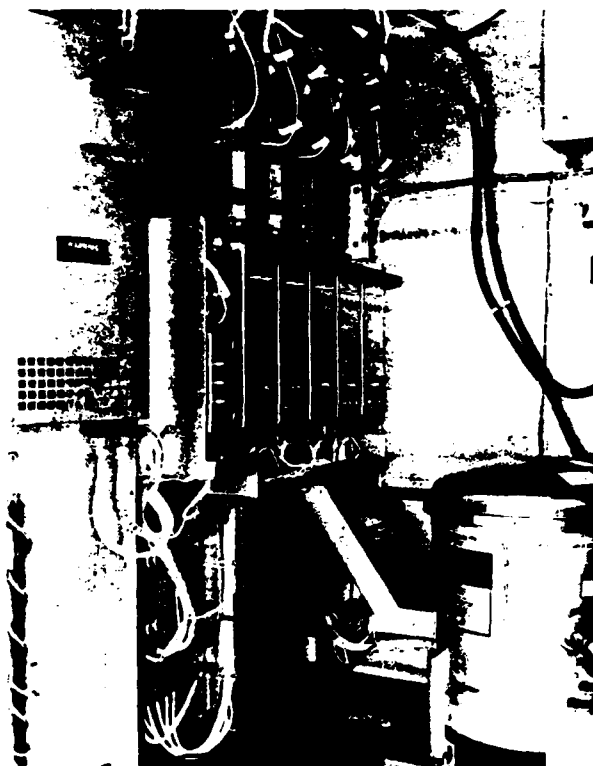


Figure 2. Modulator Assembly

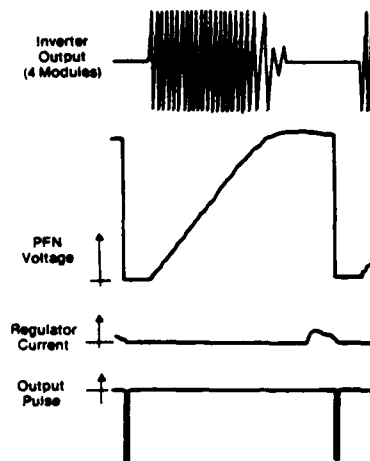


Figure 3. Modulator Waveforms

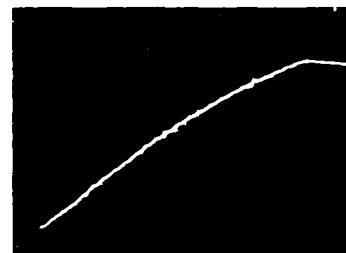


Figure 4. PFN Charging Waveform (Vertical, 1000V/div., Horizontal, 500 Microseconds/div.)

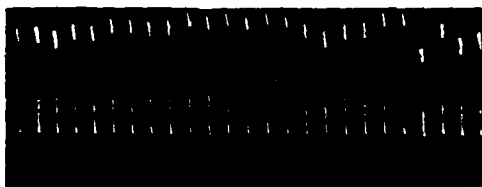


Figure 5. Final Regulator Impact on PFN Voltage (Vertical, 10V/div.; Horizontal 10mSec/div.)

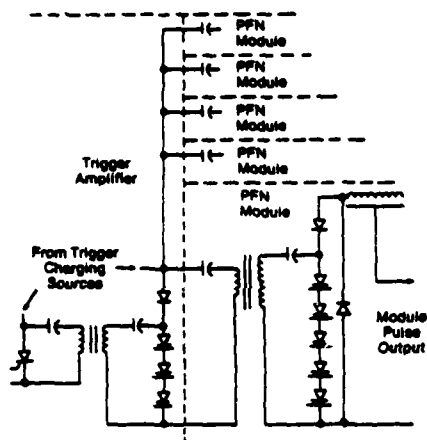


Figure 6. Solid-State Modulator Trigger System

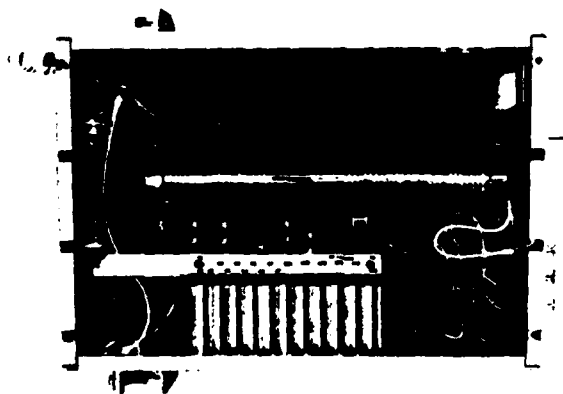


Figure 7. PFN Module

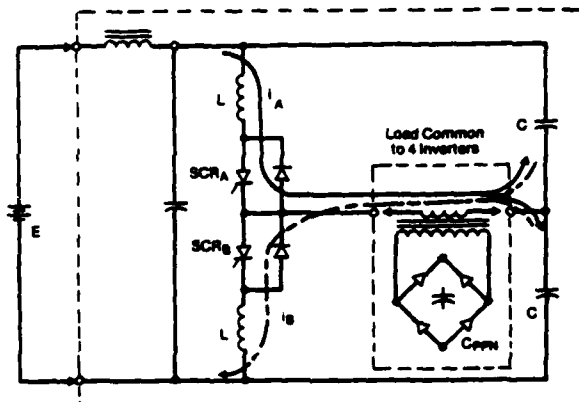


Figure 8. Inverter Circuit for Capacitor Charging

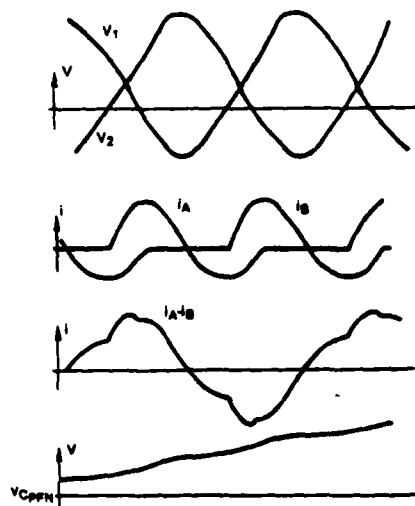


Figure 9. Inverter Waveforms

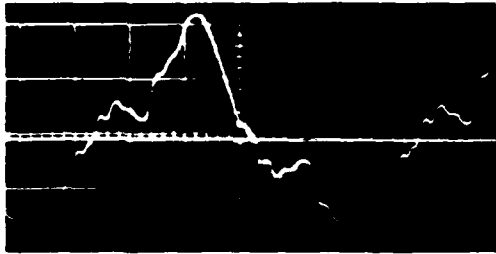


Figure 10. Inverter Output Current Waveforms at the Beginning of the Charge Cycle and at the End of the Charge Cycle. (Vertical, 200A/div.; Horizontal, 20 microseconds/div.)

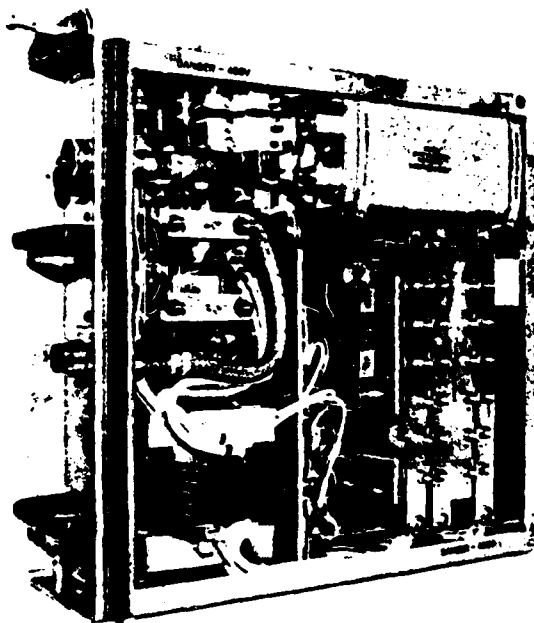


Figure 11. Inverter Module

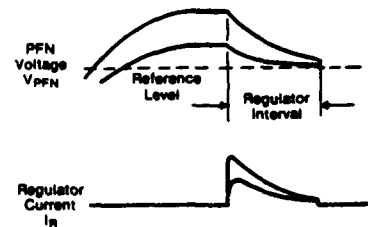
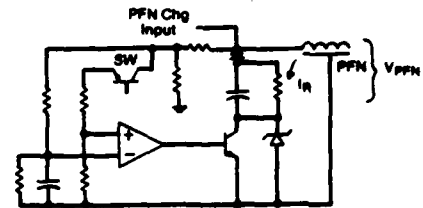


Figure 12. Final Regulator



Figure 13. Top of Regulated PFM Voltage Waveform in Multiple Cycle Exposure Showing Effect of Final Regulator. (Vertical, 10V/div., Horizontal, 200 microsecond/div.)

HIGH EFFICIENCY PULSE POWER SUPPLY FOR A SEMICONDUCTOR LASER ILLUMINATOR

Dr. Richard R. Shurtz, Byong H. Ahn,
Dr. C. W. Trussell, J. E. Miller, and D. J. Horowitz

Night Vision and Electro-Optics Laboratory
Fort Belvoir, Virginia 22060
703-664-5550

Summary

A high efficiency pulse power supply has been developed to drive a low impedance array of injection laser diodes. Pulse forming is achieved using a 0.5Ω delay line with a 140 MHz cut-off frequency which is matched to the array using an exponentially varying impedance transformation. The delay line is resonantly charged by a 28 V DC power supply to 200 V with 90% efficiency and discharged through two banks of seven of SCR's. Since the SCR switch impedance is 14% of the delay line impedance, the discharge efficiency is 88%, for an overall charge-discharge efficiency of 80%. The delay line is constructed using ceramic capacitors soldered to flat copper supports and is divided into four detachable segments each providing 25 nanoseconds of pulse length. Several different impedance matching segments with output impedances between 0.2 and 0.5Ω were tried in order to obtain maximum power transfer to the array. The laser array consists of twenty three 50 mil wide strips of laser material which produce an average light output power of 1/2 watt. The planar stripe geometry diodes, comprising each strip, are driven in parallel. To minimize array inductance, the strips are driven by their own striplines. The array inductance is calculated to be 8 nh. The pulser is constructed in modular form to assure precise control of leakage inductance. The delay line dispersion was measured and is compared with theory. Appropriate design curves are presented. Pulse shapes into both linear and non-linear (diode) loads are shown.

Introduction

An injection laser illuminator was designed and fabricated to provide up to 1/2 watt average power of 0.85 micron radiation for a pulsed-gated viewing application at the Night Vision and Electro-Optics Laboratory. See Figure 1. Because of prime power constraints, the device was required to, and did, achieve a plug-in-the-wall efficiency in excess of 5%.

The central element of the illuminator is a stack of 23 monolithic stripe geometry arrays of GaAlAs injection lasers. The 0.85 micron radiation is collimated to a $1/2^\circ \times 1/2^\circ$ beam using crossed cylindrical lenses. The diodes are driven by an 80% efficient pulser which delivers 90 nanosecond pulses at a repetition rate of up to 16 KHz.

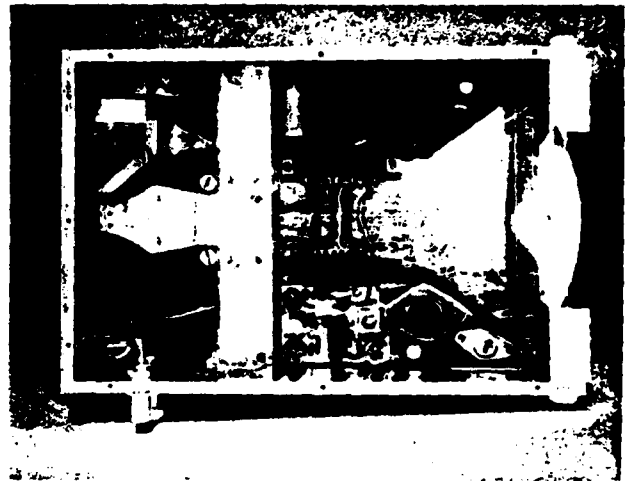


Figure 1. Top view of GaAs laser illuminator including pulser, laser diode load and collimation optics.

In this paper we describe only the key elements of the pulser, that is: the transmission line, the impedance matching circuit, the electronic switch, the charging circuit, and finally, the timing circuit. We discuss the design equations for the transmission line and the critical factors leading to efficient pulser operation.

Key Pulser Components

The Transmission Line

General Theory: We describe a transmission line of the type shown in Figures 2a and b. We know from standard filter design theory that the phase shift, θ , through one section, as shown in Figure 2c, is given by:

$$\theta = \sin^{-1}(\omega/\omega_c); \omega_c = \frac{1}{\sqrt{L_0 C_0}} \quad (1)$$

where: ω_c = the cut-off angular frequency
 L_0 = inductance per segment
 C_0 = capacitance per segment

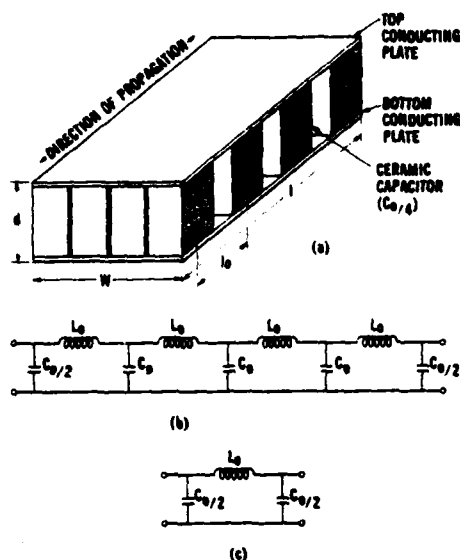


Figure 2. (a) Artists conception of lumped transmission line formed with ceramic capacitors. (b) Equivalent transmission line circuit. (c) Equivalent circuit of a single transmission line section.

To compute the dispersion curve, consider a propagating wave of angular frequency, ω , which has a wavelength which extends N transmission line segments. This wave has phase shift per section, δ , of $2\pi/N$ and a velocity, v , of $N\omega/2\pi$ sections/sec. Using these parameters, in conjunction with equation (1), the delay line dispersion can be expressed parametrically in terms of N as follows:

$$\sqrt{L_0 C_0} v = N \sqrt{L_0 C_0} f = \frac{\sin(2\pi/N)}{2\pi/N}; N \geq 4 \quad (2)$$

where v = velocity in units of segments/sec
 N = number of segments per wavelength
 f = frequency

Equation (2) is plotted in Figure 3. This result will serve as the primary transmission line design curve in the subsequent discussion. The cut-off condition corresponds to $N = 4$ (i.e., $\delta = \pi/2$). Frequencies higher than the cut-off frequency are severely attenuated by the transmission line. The present theory only applies to propagating waves at frequencies below cut-off.

A second result which is needed to design the transmission line is the inductance per unit length of two parallel plates of width, w , and separation, d . This is easily calculated using standard conformal mapping techniques and is given by:

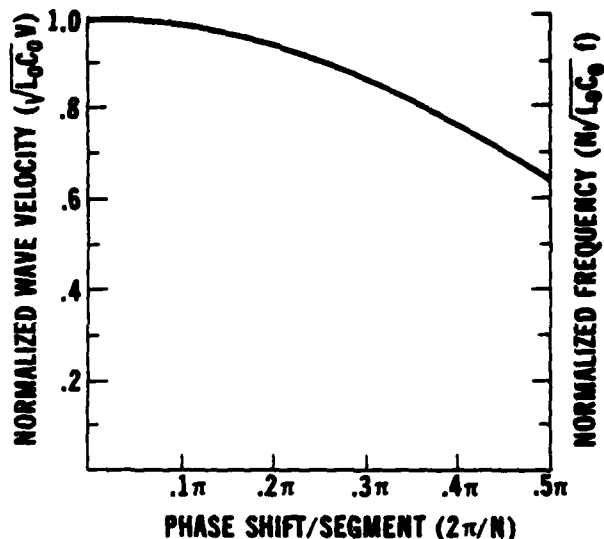


Figure 3. Dispersion curve for a lumped transmission line plotted parametrically in terms of N , the number of sections per wavelength. Normalized axes allow curve to be used for any line.

$$L = \frac{\pi}{2} u_0 / \ln(X_2/X_1) \quad (3)$$

where X_2 and X_1 are roots of the following equation:

$$\frac{-\pi w}{d} = 1 - X_1^2 + 2 \ln X_1 \quad (4)$$

Equation (3) is plotted in Figure 4 for convenience.

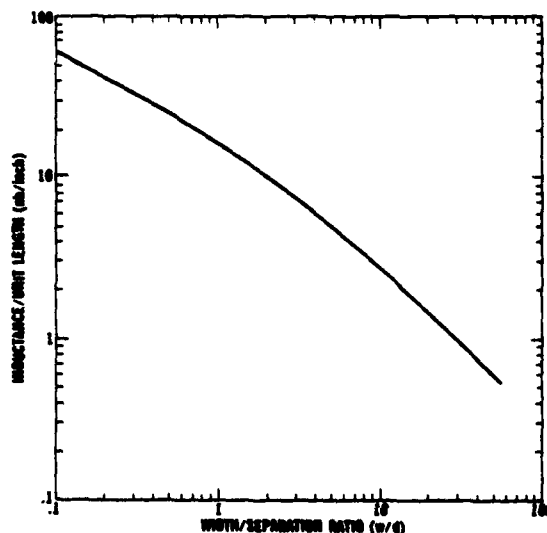


Figure 4. Inductance per unit length of parallel plate transmission line of width, w , and separation, d .

Selected Configurations: The transmission line, fabricated for the laser illuminator, was formed by inserting many rows of high-Q multilayer ceramic capacitors between brass plates of appropriate width, w , separation, d , and length, l . (See Figure 2a). Each capacitor row spans the plate width, w . The center-to-center spacing between the rows determines L_0 , in conjunction with Figure 3. The capacitors do not alter the parallel plate inductance. Key transmission line properties are given by:

$$\begin{aligned} Z &= \sqrt{L_0/C_0} \\ \tau &= 2\sqrt{L_0 C_0} n \\ f_{co} &= 1/2\pi\sqrt{L_0 C_0} \end{aligned} \quad (5)$$

where: Z = transmission line impedance
 τ = discharge pulse width
 n = number of segments in line
 f_{co} = cut-off frequency.

Delay lines with cut-off frequencies as high as 150 MHz and impedances as low as 0.2Ω can be conveniently fabricated.

During the course of this project, two delay lines were constructed using the design parameters previously described. For convenience, both were folded over in a fashion which did not disturb the inductance per unit length. The 140 MHz delay line with its SCR switching array is shown in Figure 5. The key features of each are shown in Table 1. The ten segment line, folded once, has a 38.5 MHz cut-off, a $.54\Omega$ impedance, and an 83 ns discharge pulse. The forty segment line, folded three times, has a 141.5 MHz cut-off, a 0.50Ω impedance, and a 90 ns discharge pulse. The measured and theoretical dispersion curves for each are shown in Figure 6. The capacitors selected for the 10 segment line exhibited a frequency dependent capacitance, explaining the deviation from theory.

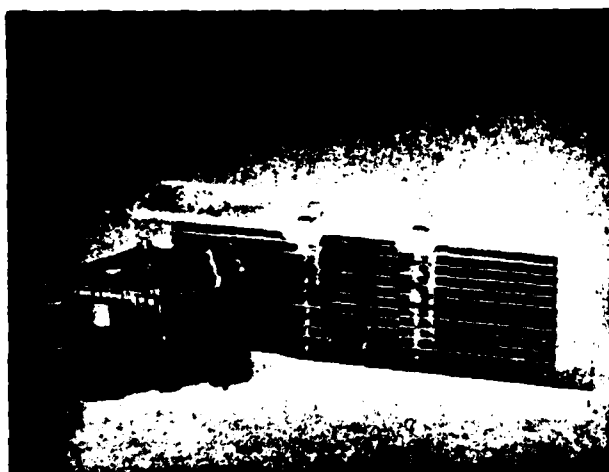


Figure 5. Photograph of the 40 segment delay line with SCR switching board as described in Table 1.

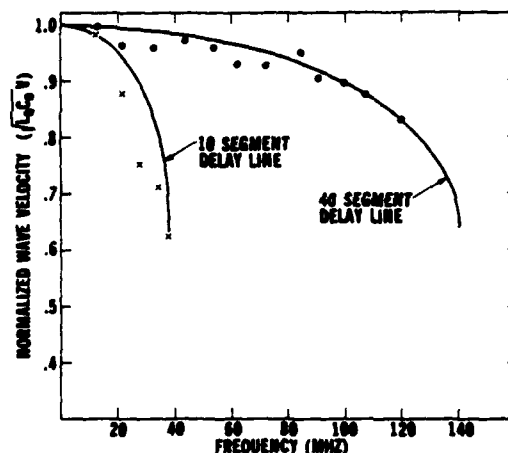


Figure 6. Theoretical and measured dispersion curves for the 10 and 40 segment transmission lines.

TABLE 1

Parameter	Delay Line 1	Delay Line 2
No of Segments	10	40
L_0 (nh)	2.24	.56
C_0 (nf)	7.69*	2.25
f_{co} (MHz)	38.5	141.5
$Z(\Omega)$.54	.50
τ (ns)	83	90
W (cm)	2.50	1.17
d (cm)	1.37	.32
l (cm)	5.6	10
No. of Folds	1	3
No. of Capacitors	20	160
Capacitor Type	NPO	High-Q
Capacitor Nomenclature**	L76/3300	S42/560

*at 1 KHz the value was measured to be 10 nf. This value measured at 10 MHz.

**Johanson Dielectrics, Inc.

The ten segment delay line was used to drive the illuminator described elsewhere. The forty segment delay line was used to drive the illuminator described here.

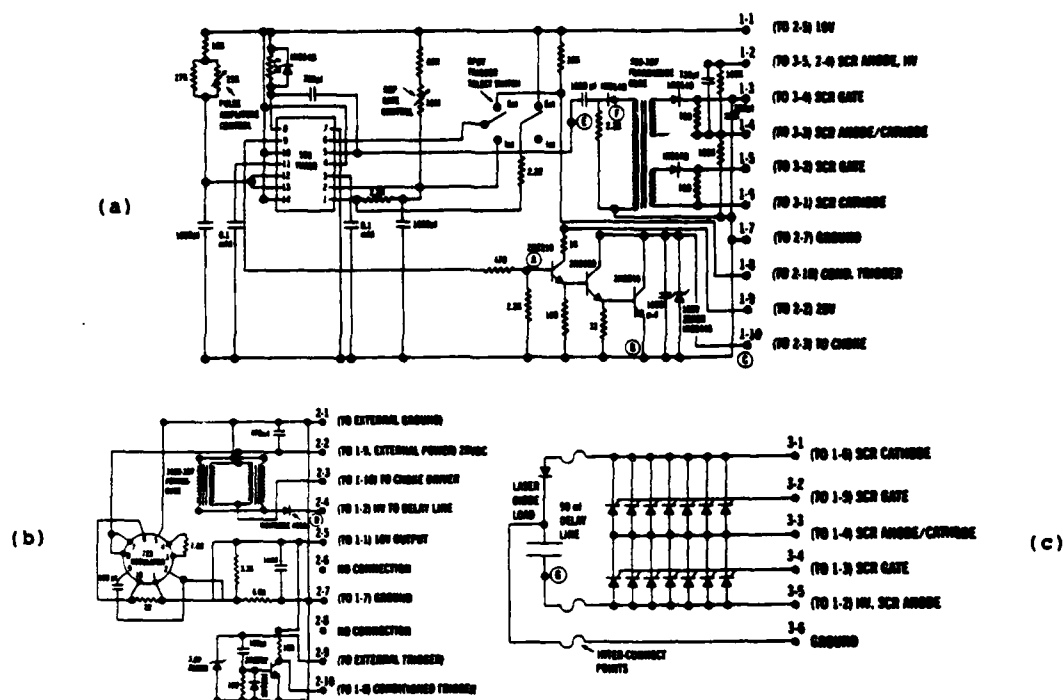


Figure 7. Pulser Circuit Diagrams.
 (a) Timing board including SCR trigger circuits and voltage up-converter choke driver.
 (b) Up-converted choke board including external trigger conditioner and 10V regulated supply.
 (c) SCR switching board including interconnects to load and delay line.

Impedance Transformation: Since the delay line impedance did not always match the load impedance and it was not practical to build a new line for each load, an impedance transformation technique was employed. An exponential impedance transformation was constructed using the transmission line design curves shown previously. The width, w , was increased to reduce the inductance exponentially, while the capacitance per row was increased exponentially. In this fashion, Z was exponentially reduced, while the cut-off frequency remained constant. At 10 MHz, the transformation section is $1/4\lambda$; at cut-off (140 MHz), it is 2λ . Thus at the low frequency end, the segment serves as a quarter-wave matching filter and at higher frequencies as an exponential transformation. A more complete description of this transformation technique is given elsewhere.

The Electronic Switch

The transmission line is charged to a voltage of up to 200 V. The current pulse to the laser diode load is initiated by the sudden conduction of two banks of Unitrode GA301A high speed thyristors (SCR's) which discharge the delay line through the load to ground. See Figure 5.

Each SCR bank has seven SCR's driven in parallel, so that no single SCR carries a current surge in excess of 30 amps. All fourteen SCR's are mounted on a PC board which, when attached to the delay line, provides the three required interconnections shown in Figure 7c. The inductance of the switch, as mounted, is less than 1 nh. The switch on-resistance is $1/7$ the delay line impedance allowing an 88% discharge efficiency.

Each bank has a 100 V stand-off rating so that shunt resistors are needed to equalize the total voltage of the delay line between both SCR banks. Two 330 pf capacitors are used to prevent dv/dt firing during the rapid recharge cycle. See Figure 7a for circuit details. Both banks are triggered by the leading edge of a 5 μ s pulse transmitted through a pulse transformer. The two secondaries and the primary each

have six turns and are mounted in a 905-3B7 Ferroxcube core. The trigger pulses at points E and F in Figure 7(a) can be seen in Figure 8.

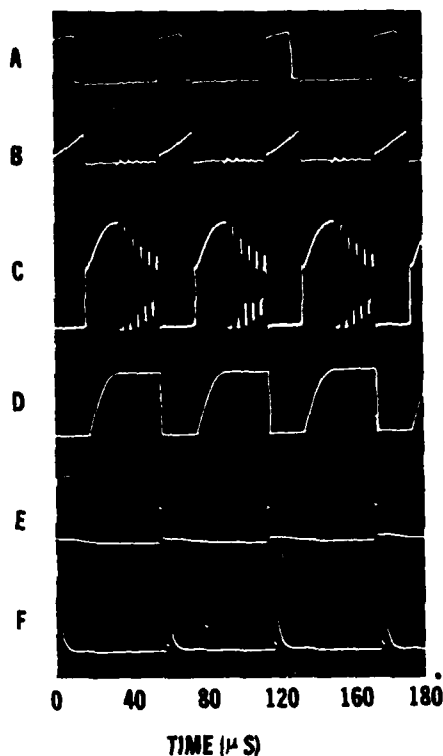


Figure 8. Waveforms at various circuit points.

- (a) 556 IC choke drive output
- (b) Choke primary current during charge-up
- (c) Voltage across power transistor driving choke primary
- (d) Delay line voltage
- (e) 556 IC SCR trigger drive output
- (f) SCR trigger drive voltage at pulse transformer

The Charging Circuit

The delay line is resonantly charged from a 28 VDC input power source to 200 VDC using two 3622-3B7 Ferroxcube transformers driven in parallel. See Figure 7b. The transformers each have a 20 turn primary and 60 turn secondary. Their gap has been adjusted to give an effective core area, A_e , of 400 cm². The primaries are driven by the three transistor amplifier shown in Figure 7a. When the primary current is terminated, the energy stored in the magnetic field is transferred to the delay line. A fast recovery diode prevents the delay line from discharging back through the transformer. Relevant waveforms shown in Figure 8, a through d.

The delay line voltage is determined by the current flowing through the primary when the transistors stop conducting, that is:

$$\frac{1}{2} L_p I_p^2 = \frac{1}{2} C V^2 \quad (6)$$

where L_p = primary inductance
 I_p = peak primary current
 C^p = delay line capacitance
 V = delay line voltage

The transistor on-time is varied to control the delay line voltage. The inductance of the secondary determines the L-C charge time of the delay line, after primary cut-off.

By selecting a high efficiency power transistor and making certain that the ferrite cores did not saturate, a 90% charging efficiency has been achieved.

The Timing Circuit

A 556 dual timer IC⁷ is used for all clocking functions. One timer is used to trigger the SCR's and to establish the repetition rate when an external trigger was not used. The second timer, triggered by the first, controls the primary current to the charging cores. See Figure 7a for circuit details.

External trigger pulses are amplified and inverted as shown in Figure 7b. The 10 VDC needed to drive the 556 IC and the trigger conditioning circuit is derived from the switching regulator circuit, using a 723 IC⁷, also shown in Figure 7b.

Operation of Pulser

The pulser was first evaluated by driving a 0.51 dummy load with an inductance estimated to be less than 1 nh. These results are shown in Figure 9. The top trace shows the voltage across the delay line. Note that the voltage drops to about 100 V as soon as the SCR's discharge and remains nearly constant until the end of the pulse. The SCR switching time appears to be 10-15 ns, which negates some of the high frequency capability of the delay line. In any case, the current through the load exceeds 160 amps for 60 ns of the 90 ns pulse. The overall power conversion efficiency in this case is nearly 80% from 28 VDC to 100 ns pulses.

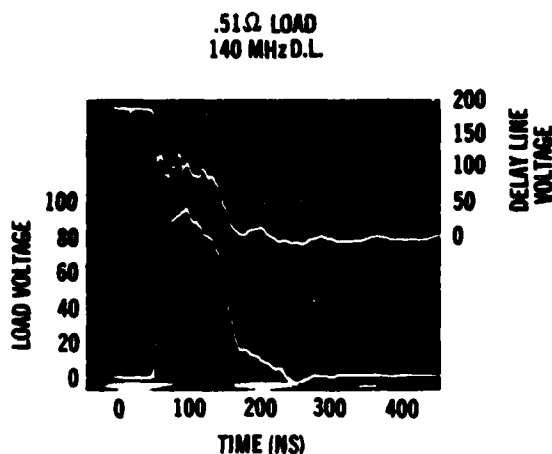


Figure 9. Pulser performance into .51Ω load.
Upper Trace: Voltage across delay line
Lower Trace: Voltage across load

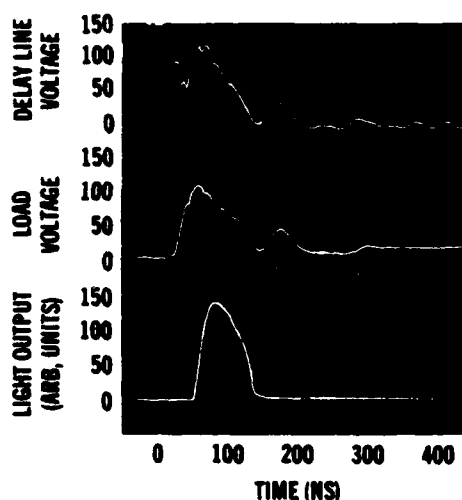


Figure 10. Pulser performance into laser array, with 8-10 nanohenry inductance.
Upper Trace: Voltage across delay line
Middle Trace: Voltage across laser array
Lower Trace: Laser array light output

The pulser was then attached to the laser diode array composed of a stack of 23 stripe geometry diode arrays, each 50 mils wide. The light output pulse from this array is shown in Figure 10. The output pulse does not extend the full 90 ns, presumably because of stray inductance in the array which slowed the current rise time. This inductance is evidenced by the inductive spike seen on the delay line and load voltage just after SCR switching.

The array inductance was minimized by driving each element with its own E-film transmission line and connecting these lines in series using a low inductance connection. Array inductance is estimated to be 8 nh. By reconstructing the connectors attached to each diode stripline, this inductance can be further reduced to 2 nh for an improved pulse shape.

Conclusions

The use of delay lines formed by ceramic capacitors is a flexible and convenient method to form high frequency (150 MHz) transmission lines with impedances less than 1Ω. Resonant charging techniques proved to be the most efficient method to charge the delay line. High speed SCR arrays can provide switching times as fast as 10 ns. The limiting factor in pulse shape ultimately proved to be the stray inductance of the laser diode array. Pulser efficiencies in the 80% range can be obtained.

References

1. H. P. Westman, ed., Reference Data for Radio Engineers, H. W. Sams & Co., Indianapolis, 1968.
2. R. E. Collins, Field Theory of Guided Waves, McGraw Hill, New York, 1960.
3. Understanding Chip Capacitors, Johanson Dielectric, Inc., Burbank, California.
4. B. H. Ahn, R. R. Shurtz, C. W. Trussell, J. E. Miller, "Low Inductance Impedance Transforming Techniques to Drive an Array of Injection Lasers," in these proceedings.
5. Thyristor New Design Ideas, 10-74MB, Unitrode Corp., Watertown, Mass.
6. Linear Ferrite Magnetic Design Manual, Ferroxcube, Sangerties, NY.
7. Fairchild Linear Integrated Circuits Data Book, Fairchild Semiconductor, Mountain View, California.

MULTIPLE OUTPUT MODULATOR FOR MICROWAVE DIODE PULSE POWER GENERATORS

Samuel Levinson
Norden Systems, Inc.
Subsidiary of United Technologies Corporation
Norwalk, Connecticut

ABSTRACT

Microwave Diode Pulse Power Amplifiers are being developed for Radar applications.

To achieve useable gain, peak power, and average power levels, typically over 100 diodes are required in multi-stage, multi-diode cavity amplifier arrangements, wherein each diode is concurrently pulsed at its optimum current level.

A multiple output modulator has been designed (and tested) which provides essentially lossless output current division, a wide range of output pulse widths and duty cycles, a substantial reduction in parts count, and current feed back output control. Fault protection is also provided.

The basic modulator unit is a D.C. coupled differential amplifier with current feedback providing a constant pulse current output in proportion to a control pulse input. A number of independent modulator units are concurrently pulsed to drive a multi-stage Microwave Diode Pulse Power Amplifier. The number of independent modulator units is determined by fault isolation/localization considerations.

The output of each modulator unit is subdivided by a network of balancing transformers to a number of diode loads.

A diode fault is detectable as an out of tolerance imbalance condition between diode loads. This is sensed by an auxiliary winding on the balancing transformers.

Introduction and Summary

This paper discusses the design of a modulator for a multistage microwave pulse power amplifier which employs a large number of IMPATT diodes.

First, the diode characteristics are described to establish modulator output requirements.

Three modulator system design alternatives are evaluated from the viewpoint(s) of efficiency, reliability, and/or redundancy, and size, weight, and cost effectiveness. These alternatives are:

- One modulator per IMPATT diode.
- One large modulator driving all the diodes through series resistors (as required for diode current adjustment).
- A multiplicity of constant current output modulators, each driving a group of IMPATT diodes through balancing coils which divide the current equally among the diodes.

The constant current driver with balance coils provides the highest efficiency with a suitable and controllable compromise between simplification and redundancy. It is also the most size, weight, and cost effective of the various design alternatives considered.

This paper also addresses the trade off between redundancy, reliability, and the number of IMPATT diodes per modulator. Protective circuit design, i.e., fault detection and modulator driver shut down to limit and isolate an IMPATT diode fault is also discussed.

An experimental four IMPATT diode driver with a four unit simulated load, and protective circuit were built and tested. Results indicated good agreement with design concepts and computations.

Background

Solid State microwave IMPATT diode power sources are currently being developed for missile and airborne radar transmitters.

Because of the present limited peak power output of a single diode, power combiners, which sum the power outputs to the desired level, are used.

For a 1Kw multistage RF power amplifier, power combiners with as many as 64 IMPATT diodes and over 100 IMPATT diodes overall are contemplated. A (proposed) design employing 124 IMPATT diodes is shown in Figure 1.

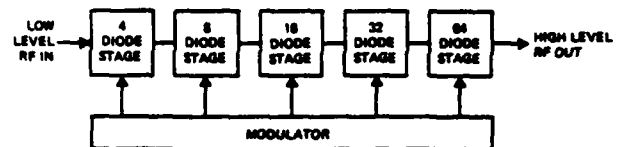


Figure 1. A Solid State Microwave Power Amplifier

For multi-mode operation, the radar transmitter needs a wide range of pulse widths and duty cycles, all of which are reflected in the pulse modulator design requirements.

The RF parameters of the microwave diodes are affected both by the pulse current level and by heating during the pulse. Where the phase-characteristic over the pulse is important, the modulator may be required to provide a non-rectangular output current pulse, shaped to provide the desired RF characteristics. This implies that the modulator should be a current source with a controlled or shaped output pulse for optimum RF performance. Pulse current and voltage waveshapes of interest are shown in Figures 2a, b.

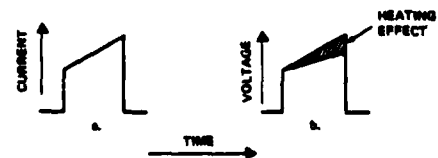


Figure 2. Shaped Modulator Output Pulse Waveforms

Diode to diode variation in the Voltage-Current characteristics, and low dynamic impedance preclude paralleling IMPATT diodes from a common modulator output bus.

The large number of IMPATT diodes requires that the modulator have equally numerous outputs, each with a controlled output current.

To provide one modulator per IMPATT diode is reasonable if only a small number of diodes are involved, but is undesirable from the viewpoint of size, weight, and cost where large numbers of diodes must be pulsed.

A technique of modulator output current division using balance coils has been developed. This allows one modulator to efficiently drive a number of IMPATT diode loads, thereby effecting a reduction in parts count, and with attendant improvements in size, weight and cost effectiveness of the modulator.

The proper application of the balance coil technique to a large multistage IMPATT diode amplifier requires a tradeoff of redundancy versus complexity and cost, to achieve an optimum system design.

Design Factors

Diode Load Characteristics

IMPATT diodes are highly non-linear loads. To the modulator, they appear as reverse biased diodes in series with a resistance.

Typical operation entails a continuous trickle current of about 1 milliampere per diode, which pre-pulse-biases the IMPATT diode to its threshold voltage.

The pulse current, in the order of 1 to 2 amperes per IMPATT diode, raises the voltage across the diode to about twice the threshold.

The IMPATT diode p-n junctions are extremely small and there is a significant temperature change during the pulse. The temperature coefficient of the voltage drop is positive, so the voltage drop across the diode can rise with time during a uniform current pulse input, typically about five percent.

IMPATT diode technology is rapidly changing and new devices with new characteristics, at ever increasing power levels, are the present state of the art.

Modulator Efficiency

Modulator efficiency is determined by the minimum achievable series switch voltage drop and by the standby losses during the interpulse interval.

Standby losses become significant at low duty cycles, and where short pulses with fast rise times are encountered. The standby power consumption of a pulse amplifier increases with gain bandwidth product as required to generate the desired output pulse.

The series switch voltage drop has to be minimized for best power efficiency. Where the current waveform has a peak, (See Figure 2) there is a corresponding load voltage peak. The minimum modulator series voltage drop is at that point. At other points during the pulse, the voltage drop is higher and power efficiency is reduced. Presumably, the

RF performance improvement by current pulse shaping exceeds the reduction in modulator efficiency to yield a net gain in overall system performance.

Redundancy and Reliability

Where numerous IMPATT diodes are used in a power combiner, theoretically, a failure of one diode may only reduce the RF stage power output by the contribution of the one diode, provided the modulator survives and/or limits the effects of the diode failure.

Diode failures usually entail a change in modulator load impedance, and are frequently a short circuit. A short circuit is potentially the most dangerous, particularly where bipolar transistors are used as series switches, due to secondary breakdown vulnerability. Fault sensing, e.g., within one microsecond is required to protect the modulator and/or limit failure effects. This requires one or more comparators and associated circuitry per modulator or per IMPATT diode and is an additional weight, size, and cost item.

Design Alternatives

In a microwave diode pulse power generator, there are, if large power gains and power outputs are to be attained, numerous diodes in many stages. Figure 1 shows one such proposed design with 124 diodes.

The initial design concept was to design one modulator per diode, which might be built as an integrated circuit (hybrid).

This design concept provides redundancy and individual optimal output adjustment, but at the expense of a large multiplicity of parts, with a attendant size, weight, and cost penalties.

Alternative designs, to provide economy, and simplification were investigated.

One alternative is to have a single high power modulator driving all of the IMPATT diodes in parallel.

A single high power modulator is generally more size, weight and cost effective than a multiplicity of smaller units. A single large unit, however, has to feed the numerous IMPATT diodes each with its different threshold voltage and series resistance. Unless the IMPATT diodes are selected to very narrow specification limits, a single modulator output bus will not provide the proper current to a large number of concurrently pulsed diodes. One simple solution is to provide resistors in series with each IMPATT diode. This is shown in Figure 3.

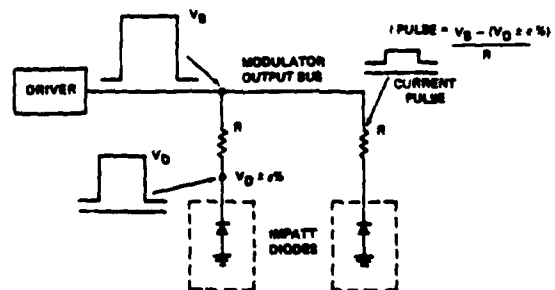


Figure 3. Modulator and Load Voltage Relationships

The series resistors give fault isolation (if fusible resistors are employed) and short circuit current limiting, but lose power due to the minimum resistance and voltage drop necessary to effect load current balance between diodes.

The attainable power efficiency using series resistors depends on the allowable load current variance and the economic cost of procuring IMPATT diodes with corresponding voltage and current tolerances. Up to now, with available diodes, calculations show that the power loss in the series resistors increased the modulator size, and the overall power drain excessively, and negated the size, weight, and cost advantages of simplifying the modulator design down to one unit.

Another alternative system design, which is the subject of this paper, is to use a series of modulators, designed as constant pulse current sources, feeding a set of balance coils which divide the current among a number of IMPATT diode loads.

Balancing coils make it possible to divide the current output of a pulse modulator nearly equally between dissimilar IMPATT diodes, with low cost, and high efficiency.

The balancing coil approach does not give fault isolation so a multiplicity of modulators must be used if a partial or "soft" failure protection mode is to be obtained.

For an RF system with numerous IMPATT diodes, e.g., Figure 1, it appears that the optimum application of the balancing coil technique will use a number of modulators, e.g. 30 to 40 units, feeding IMPATT diodes in groups of 1 to 4.

Output division, and judicious organization of modulator drivers with respect to the RF amplifier stages will reduce the overall number of parts in the system as a whole while protecting overall system function. For example we might use 8 modulator circuits each driving 4 IMPATT diodes, for a 32 IMPATT diode stage, and 16 modulators each driving 4 IMPATT diodes in a 64 diode stage. Figure 4 shows a multistage diode amplifier and multiple modulators each driving an IMPATT diode group.

In the low and intermediate power level stages, where 4, 8, or 16 IMPATT diodes are used, each diode makes a proportionately larger contribution to the total output relative to the 32 or 64 diode output stages.

In the low and intermediate power stages with 8 and/or 16 diodes we might use one driver for each

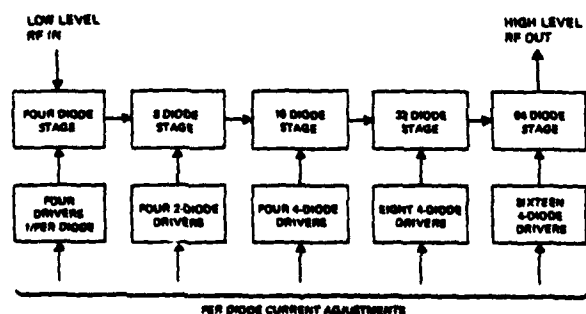


Figure 4. Multistage Diode Amplifier

2 or 4 diodes in 4 x 2 and 4 x 4 arrangements, respectively. In the lowest level stage, with only 4 IMPATT diodes, only one driver per diode should be used, (for redundancy and reliability).

Diode Operating Current

Each stage may use the same diode type. However, the diode operating current in each stage is dictated by the required RF stage gain and power output. All of the IMPATT diodes are pulsed concurrently, during operation.

In order to adjust the diode operating current as required, the modulators have to be grouped in stages corresponding to the RF amplifier stages.

Figure 5 shows a 4:1 balancing coil circuit.

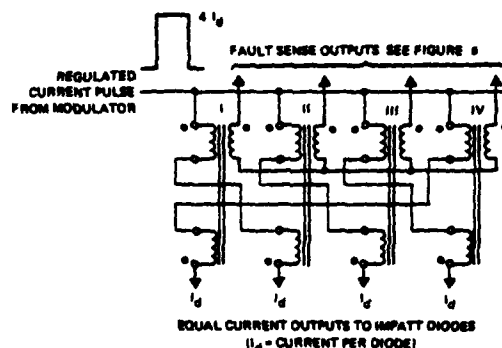


Figure 5. Equal Current Division by Balancing Coils

The balance coil technique is an efficient load combining technique. Whereas, with the series resistor method a significant excess modulator output voltage must be provided for the per diode current balancing process to be effective, in the balance coil technique, the modulator output voltage is the average voltage required by the group of IMPATT diodes, and per diode current equalization is a function of the balance coil inductance.

The inductance of a balance coil is:

$$L = \frac{\Delta E \times \tau}{\Delta I} \quad \text{where}$$

L = Balance Coil inductance,

ΔE = Voltage inequality between loads, Volts

ΔI = Current inequality between loads, Amperes

τ = Pulse width, seconds.

Fault Protection Technique With Balance Coils

It may be assumed that an IMPATT diode will fail either open or short, and it is very improbable that two or more diodes in a group, e.g., a group of 4 IMPATT diodes, will fail the same way at the same time, or that a diode failure entailing only a small shift in the v-i characteristics will occur. Since the action of the balance coils is to generate a voltage to equalize the currents through the various loads, any IMPATT diode failure will result in an excessive voltage across the balance coil terminals. A

third winding on the balance coil can sense the balance coils overvoltage condition, and this can be used to drive a fault sensing circuit. Since there are many balance coils, i.e., one per IMPATT diode, the fault sense outputs can be "OR" connected, as shown in Figure 6 in order that any one diode fault will be detected.

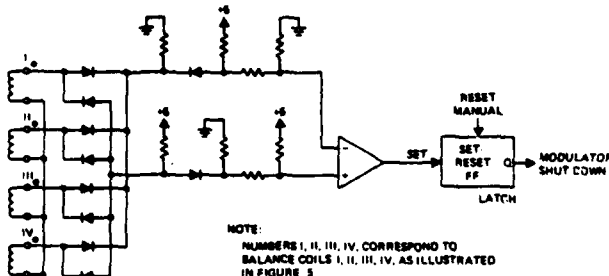


Figure 6. Fault Sensing Technique Using a Third Winding on a Balance Coil

An advantage of the third winding technique is the D.C. isolation of the high power modulator output circuitry and the low power fault detection logic, minimizing EMI problems.

Modulator Driver Design

A direct coupled series modulator driver design is the smallest, lightest, and most efficient, and has the least number of parts. Further, suitable operation at the shortest pulse width and the shortest rise and fall times, guarantees performance at all longer pulse widths, rise times, etc. provided only that the duty cycle capability is available.

In our experimental work to this point, we have developed a direct coupled series modulator design, in the form of a feedback controlled pulse current source. See Figure 7.

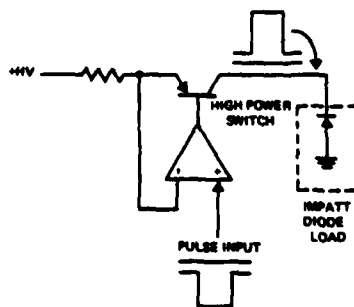


Figure 7. Feedback Controlled Pulse Current Source

The usefulness of the direct coupled series modulator technique depends on the availability of a suitable series transistor with adequate voltage and current ratings, and with the required speed of response. Currently we are able to series modulate a load up to (+) 110 volts at 6 amperes, using a single power MOSFET, as a P channel series switch.

Because the modulator is a current regulator, a short circuit mode IMPATT diode failure does not result in a current increase.

The series power transistor, however, has to absorb and dissipate the power that was supplied to

the IMPATT diode load. Fault detection can be implemented by load voltage sensing.

An open circuit failure is generally harmless. However, a short circuit failure will require prompt modulator shut down to protect the series switching transistor and to protect the rest of the system.

Experimental Work and Results

Experimental circuits have been built and successfully tested to demonstrate:

- Balance Coil Current Equalization
- Pulse Current Regulation
- Fault Detection

Balance Coil Current Equalization

In these tests, four simulated IMPATT diode loads, each consisting of two Zener diodes in series, and a series resistor, were connected through a 4:1 balance coil current divider. Using a current probe, the currents through each simulated IMPATT were observed to be nearly equal. Ordinary, 5% tolerance components were used. A photograph of the experimental set up is shown in Figure 8. The schematic is shown in Figure 9.

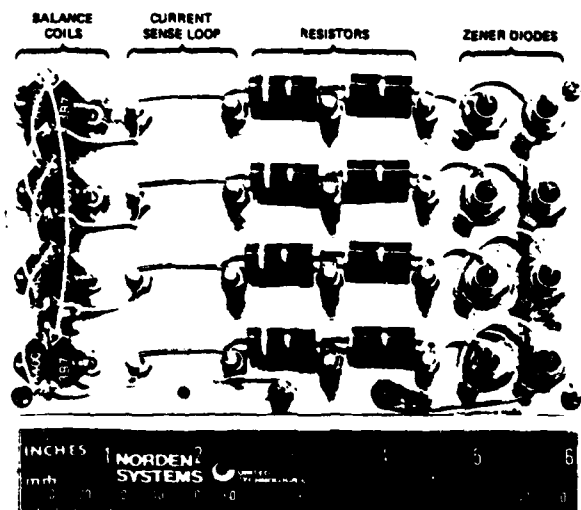


Figure 8. Simulated IMPATT Diode Load

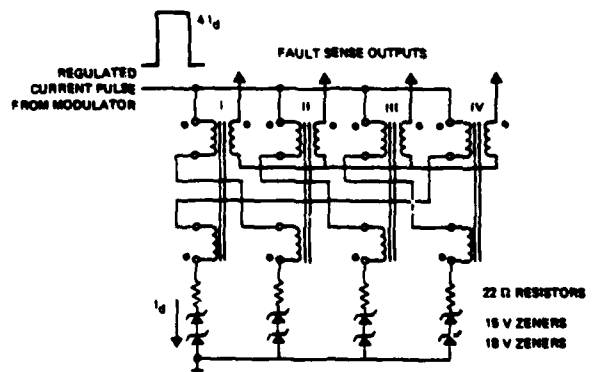


Figure 9. Simulated IMPATT Diode Load Schematic

After the initial observation, a deliberate imbalance was created by short circuiting one of the two series Zener diodes in only one of the four concurrently driven simulated IMPATT diode loads. The current division between the three "good" simulated IMPATT loads, and the "bad" load was then measured.

It was found that the balancing coils maintained current equality and that the voltages on the loads were adjusted by the balance coils, as predicted by design.

Pulse Current Regulation

A pulse current source was designed and implemented first with commercial high speed operational amplifiers, and later with circuitry of our own design. The current-regulator driver consisted of an OP AMP, a current booster, and a power MOSFET.

Operation at pulse widths from 0.2 to 10 μ s and duty cycles to 30% was achieved. Double exposure oscilloscope photographs, (See Figures 10 a, b, c) show the pulse shape, and the pulse train on appropriate time bases. The pulses were into a 3 ohm load.

Fault Detection and Protection

A fault detection circuit was implemented using a third winding on each balance coil to sense the load inequalities. A 4:1 simulated IMPATT diode load was made using, as before, two series Zener diodes and a series resistor. A "bad" diode was simulated by shorting out an 18 volt Zener, as described earlier.

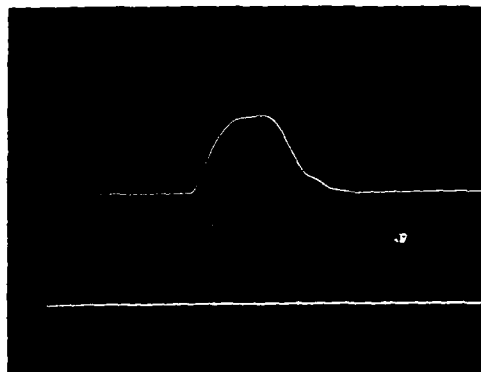
The LM 139 comparator type used has a response delay which precludes operation below 0.5 μ s.

At the 1 μ s pulse width, the protection circuit functioned as designed. Below 1 μ s and especially below 0.5 μ s pulse width the circuit sensitivity to load unbalance decreased, until response ceased. The comparator output was observed and the fault detection signal had a 100 ns rise time after a 500 ns delay. The fault signal from the sense winding of the balance coil followed the pulse without delay but had a high percentage of ringing and distortion, particularly at the shorter pulse widths.

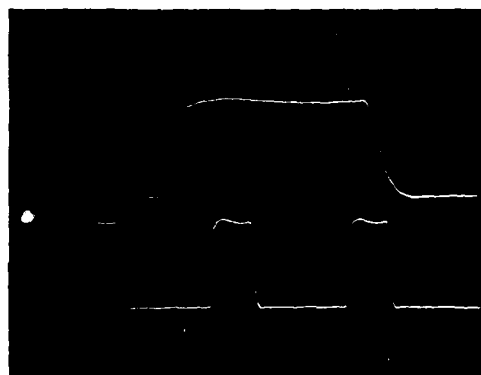
The fault detection circuit used one percent components, and diode temperature compensating techniques in its design. DC measurements indicated the expected voltages within 2-3 percent.

Conclusion

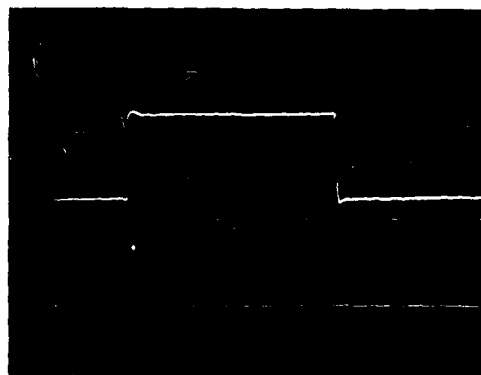
In our experimental work we now have a regulated current pulse source driving a 4:1 current divider and with fault detection. This is virtually a complete building block of a modulator for a Solid State Transmitter.



a. Top - 0.1 μ s/cm-H 20V/cm-V
Bottom - 10 μ s/cm-H 20V/cm-V



b. Top - 0.2 μ s/cm-H 20V/cm-V
Bottom - 1.0 μ s/cm-H 20V/cm-V



c. Top - 2.0 μ s/cm-H 20V/cm-V
Bottom - 50.0 μ s/cm-H 20V/cm-V
10% Duty

Figure 10. Experimental IMPATT Diode Modulator Output Waveshapes

A SWITCHING-CLASS ELF POWER AMPLIFIER

Dr. Bodo Kruger
NAVELEX

Dr. Jimmy Rogers
George Hanna
Continental Electronics Mfg. Co.

William North
GTE Products Inc.

The Extremely Low Frequency Band (ELF) was proposed in the late 1950s for communication with submarines at speed and depth. After experimentation with various antenna types the Beverage antenna, a horizontal antenna with grounds at either end, was chosen. The first proposed ELF communications system was called Sanguine, and was intended to survive a considerable nuclear attack through hardening and redundancy. A full Sanguine system would have had about 100 transmitter sites with a total connected ELF power of several hundred Megawatts. In choosing a power amplifier design, survivability and reliable operation in a nuclear stressed environment were the main criteria followed by maintainability and unmanned remote operability. Various types of solid-state, vacuum-tube and rotating machine amplifiers were considered. The higher thermal mass of vacuum tubes, and their higher tolerance for abuse and impulse-type stresses, characteristic of lightning and high-altitude electromagnetic pulse, compared with solid-state components, plus their "off-the-shelf" status, when compared with rotating machine type amplifiers, made them the choice. The ELF project office was reinforced in this position by the development of two other high-power amplifiers for the Navy: the highly successful tube-type VLF amplifier for the relay airplane TACAMO; and the solid-state (SCR) amplifier built for the Wisconsin ELF test facility. Although this amplifier has performed for 12 years, it has shortcomings which could

not be entirely eliminated in spite of two major efforts to do so. It can deliver full power to a dummy antenna but only half power to the actual antenna. During local thunderstorms the amplifier is likely to blow SCR protective fuses, sometimes as many as 40 at a time.

A complete ELF transmitter, although much smaller in scale than the full Sanguine system, and no longer required to physically survive nuclear attack, consists of multiple power amplifiers, not necessarily at the same geographical location. Each power amplifier must be capable of supplying 650 kW of ELF power to multiple segments of buried-cable dipole antenna, the far ends of which are low-impedance grounded to produce a deep-earth return current loop.

The carrier frequency is 76 Hz. The modulation is MSK frequency-shift keying between "chips" of 72 and 80 Hz. The maximum transition rate between chips is 16/second. The minimum chip length at 72 Hz is 4.5 cycles and at 80 Hz, 5 cycles.

At 76 Hz the nature of the antenna is such that for every ohm of resistance the series inductive reactance is between 4 and 5 ohms. Series capacitance is added to each antenna segment to achieve resonance at 76 Hz.

In addition to the aforementioned requirements the design goals included maximum conversion efficiency, output current constant, regardless of load impedance, and low-inertia control of output amplitude.

To achieve maximum conversion efficiency in a power amplifier there is but one criterion which must be met: the output current of the final amplifier stage or stages must flow only when the voltage drop across the stage or stages is at a minimum. In a conventional high-frequency power amplifier the irreducible value of output stage shunt capacitance has a susceptance which is sufficiently high with respect to the load conductance that it must be shunt resonated at the carrier frequency. The variational voltage across the output stage is thus constrained to be sinusoidal. Maximum efficiency is achieved as the conduction angle of the output stage current is reduced to coincide with the instantaneous minimum of plate voltage. As conduction angle approaches zero, the limit of class C operation, the theoretical conversion efficiency approaches 100%. Unfortunately the ratio of peak-to-average output current approaches infinity at the same time. For this reason most practical high-power high-frequency amplifiers are operated class B, with 180° output current conduction angle and maximum theoretical efficiency of 78.5%. Improvements can be made by the proper phasing of harmonic resonances to rectangularize the voltage waveform, categorized as class D.

At carrier frequencies as low as ELF the susceptance of the final amplifier output capacitance is negligibly low with respect to load conductance. There is no reason, therefore, not to force the final amplifier output voltage to be rectangular, i.e., saturated, with minimum voltage drop, when conduction is required, and cut off when it isn't.

For this particular application the optimum coupling network between amplifier and load to permit this mode of operation is an L/C Tee network. The input inductor of the Tee network provides the low-loss impedance across which the harmonic voltages required of a rectangular waveform may be developed. The low-pass filter characteristic of the Tee network provides harmonic attenuation, augmented, of course, by a series-tuned load, with its Q of 5. Lastly, by making the electrical length, at the fundamental, of the network approximately 90°, it functions as an impedance inverter. The inherently low-impedance, constant-voltage nature of a voltage-saturated output stage appears, at the output of the quarter-wave Tee network, to be a constant-current, high-impedance source.

The current through the network must be continuous and bipolar. The output amplifier, therefore, must be double-ended.

Either push-pull or push-push (totem-pole) final amplifier connections are appropriate. Consideration of output transformer volt-ampere requirements, however, resulted in the selection of the totem-pole arrangement. A simplified schematic diagram of the switching class (class S) ELF power amplifier which resulted from the foregoing design considerations is shown in Figure 1.

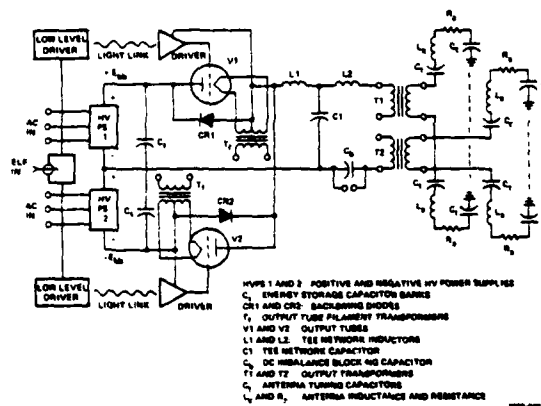


Figure 1. Simplified Schematic Arrangement of ELF Switching Class Power Amplifier

The final amplifier tubes are connected in a "totem-pole" arrangement, characteristic of almost all contemporary high-quality audio-frequency power amplifiers and of the floating-deck type of high-voltage pulse modulator. The use of positive and negative high-voltage power supplies permits the required bi-polar output of the final stage. Each power supply uses a six-phase full-wave rectifier (12-bump) driven from dual delta and wye connected secondary windings to minimize ripple and, more importantly, to minimize distortion of the primary power input current.

The L/C Tee network has a Q of unity. At the carrier frequency of 76 Hz the inductive and capacitive reactance of the elements, normalized to the resistive component of load impedance, are very nearly unity and the phase delay of the network is very nearly 90°. The actual values differ slightly to optimize performance at the two modulation frequencies, 72 and 80 Hz.

The output of the Tee network is transformer coupled to the load, which can consist of one or more series-tuned buried-cable dipole antenna segments. The primary windings of the output transformers are connected in series and the turns ratios of the individual transformers are identical so that constant current is delivered to each load segment regardless of its impedance.

Maximum conversion efficiency and maximum utilization of the output tube plate current and voltage holdoff capability occur when the two tubes are alternately cut off or driven to saturation by successive half-cycles of fundamental-frequency square waves. Even though the grid drive waveforms are rectangular, the plate current is constrained to be nearly sinusoidal by the series tuned nature of the load and output coupling network. The plate current conditions, therefore, are nearly identical with those of conventional class B operation, with 180° conduction angle.

The output tubes are shunted by backswing diodes, to permit reverse current flow, the purpose of which is two-fold. As mentioned earlier, the load and load-coupling network are tuned to the 76 Hz carrier frequency. Modulation, however, is in the form of output at either 72 or 80 Hz. At these two frequencies, and with the nominal antenna Q of 4.4, the plate current either leads or lags the plate voltage by a phase angle of approximately 24°. The voltage and current relationships are shown in Figure 2. Note that current flow onto L1 of the Tee Network in the positive direction can occur only through V1 or CR2 and current in the negative direction can occur only through V2 or CR1. Current through the tubes V1 and V2 discharges the storage capacitors and current through the backswing diodes CR1 and CR2 charge the capacitors, returning energy to the power source.

The Tee network input current shown in Figure 2 lagging the fundamental-frequency component of network input voltage. For a given lead or lag phase angle θ , the peak input current must be $I_i/\cos \theta$ for the same output power as would be produced at unity power factor, where I_i is the in-phase component of current. The average power supply current, over 1 cycle of Tee network input voltage is:

$$I_{AVG} = \frac{I_i}{2\pi \cos \theta} \left[\int_{-\theta}^0 \sin \omega t \, d\omega t + \int_0^{\pi-\theta} \sin \omega t \, d\omega t \right] = \frac{2 \cos \theta I_i}{2\pi \cos \theta} = \frac{I_i}{\pi}$$

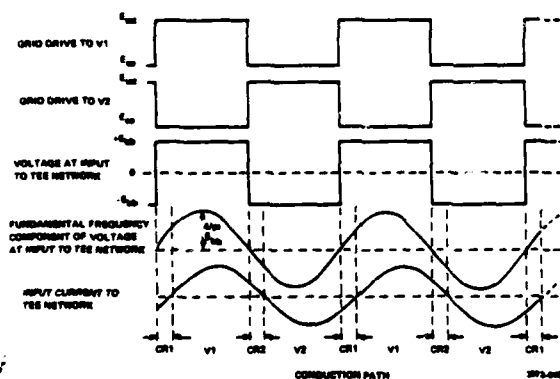


Figure 2. Voltage and Current Relationships in ELF Switching Class Power Amplifier

This is the same value as for a unity power factor load. The peak

value of ELF output voltage is $E_{bh} \times 4/\pi$. The total ELF power developed by both tubes is $4E_{bh}I_i/2\pi = 2E_{bh}I_i/\pi$, which is the same as the total DC input from both power supplies. Thus, with tubes having perfect switch characteristics, the conversion efficiency is 100% regardless of load phase angle. The backswing diodes, in effect, permit the quadrature component of load current to flow out of each power supply through a tube and back through a diode so that the net charge loss due to quadrature current is zero.

Contrasted with class B operation, a load phase angle of θ would cause both the peak and average plate current to rise to $1/\cos \theta$ for the same output power. For the same 24° load phase angle, the plate input would rise by 9.5% and the dissipation in an output tube with zero plate drop at the minimum plate voltage would increase from 27.4% of the useful power output to 39.5%, an increase of 44% in dissipation.

Even though maximum efficiency and tube utilization are achieved with fundamental-frequency square, wave drive, the only means of controlling output amplitude while preserving efficiency require lossless variation of either power supply voltage or ELF output coupling factor, such as with Inductrol or step-regulator type devices. These, however, are not likely to be rapid enough to permit differential amplitude control between the two modulation frequencies when they can alternate as frequently at 16 times per second. Furthermore, the suppression of harmonic content in the output is left entirely to the filter characteristics of the Tee network and the series-tuned antenna, which are shown in Figure 3, for the minimum anticipated antenna Q of 4.

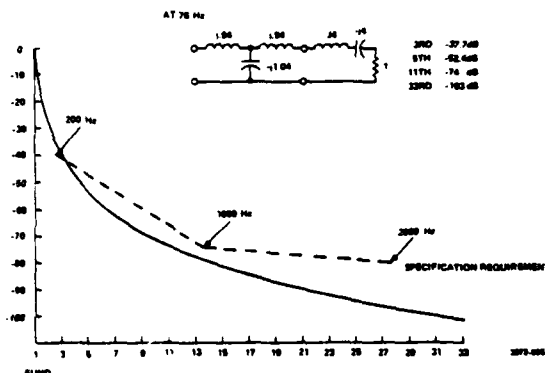


Figure 3. Harmonic Attenuation of Tee Network and Antenna

The solution selected was pulse-width modulation of the input signal. As the sampling rate of the pulse-width modulation increases the lower-order harmonic content of the rectangular voltage waveform diminishes. Successful audio-frequency modulators at high power have been built using pulse-width modulated switching class operation. A typical means of obtaining the proper timing for the pulse-width modulation, where a sampling rate of up to 10 times the highest audio frequency is used, is to superimpose a sawtooth voltage waveform on the input audio signal and measure the width of the sawtooth component as it penetrates a fixed voltage threshold. The output audio envelope, after low time delay filtering, is fed back to the input, predistorting the input audio so that the proper time relationships will be obtained. The ELF power amplifier being described, however, has 90° phase delay between the output of the switching-class final amplifier and the load, precluding negative feedback as a means of assuring the proper pulse-width-modulation timing. Furthermore, there is no audio-analog input to this amplifier, only digital computer commands. It became necessary, therefore, to predict the timing sequence required to produce outputs of the desired frequency and amplitude.

The amplifier was designed to accommodate sampling of the desired output sine wave at intervals as small as every 10°, which, at 80 Hz output, is a sampling rate of 2880/second. The transmitter station computer was asked to determine the proper conduction and cutoff intervals for V1 and V2, for each sample interval, in

accordance with the following expression:

$$\sin \frac{\theta_{ON}}{2} = \frac{1}{4 \sin(\theta_1 + \frac{\theta_S}{2})} \left\{ \cos \theta_1 - \cos(\theta_1 + \theta_S) + \frac{K}{2} \left[\theta_S + \sin \theta_1 \cos \theta_1 - \sin(\theta_1 + \theta_S) \cos(\theta_1 + \theta_S) \right] \right\}$$

θ_1 = angle of fundamental at beginning of sample
 θ_S = length of sample in fundamental-frequency angle
 K = ratio of peak value of fundamental frequency voltage to peak rectangular voltage at input to Tee network

Figure 4 shows the nature of the waveform timing for a sample interval of 10° . The expression given describes the timing relationships for the first-quarter cycle of the desired sinusoid. The computer produces a mirror image for the second-quarter cycle and inverts the first two for the last-half cycle. The angle θ_{ON} is the length of time, expressed as phase angle at the desired frequency, that the uppermost of the two tubes (V1) is driven into conduction. During the time that V1 is cut off, Tee network input current must flow in either CR1, CR2 or V2. When current is in-phase with the ELF voltage it must flow in CR2 during intervals in the first-half cycle that V1 is cut off. The accommodation of pulse-width modulation, therefore, is the second function of the backswing diodes.

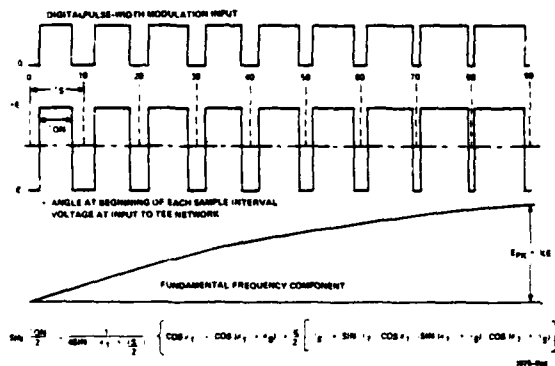


Figure 4. Timing of Pulse-Width Modulation for Sampling Interval of 10 Degrees

As the sine wave output reaches its peak value the off intervals for V1 approach a few microseconds out of a total period of 12.5 milliseconds, minimum. It makes sense, therefore, to consider eliminating the off intervals near the peak altogether, using a larger sample interval there. Furthermore, the other component of output-circuit loss, in addition to the integral of the product of plate current and saturation plate drop of the output tubes, is the switching loss. This loss arises from the charging and discharging of the total capacitance referred to the Tee network input each time a rectangular voltage transition occurs. The energy stored in this capacitance must be dissipated in the output tubes. In the classical floating-deck modulator, which drives a predominantly capacitive load, this is the major component of plate dissipation.

The limiting case of sample interval which still permits amplitude control by means of pulse-width modulation is one-half cycle. The expression for conduction angle is considerably simplified, becoming:

$$\sin \frac{\theta_{ON}}{2} = 1/4 (2 + K) \text{ as shown in Figure 5.}$$

For a modulation K-factor of $4/\pi$ the conduction angle is 180° , which is a fundamental-frequency square wave. For a K-factor of zero, giving zero fundamental-frequency output, the conduction angle is 60° , which is a third harmonic square wave.

Which pulse-width modulation format (the high sampling rate, the minimum sampling rate, or an intermediate compromise) would ultimately prove to be optimum was left to tests performed on an actual power amplifier. The advantage offered by high sampling rate, which is superior lower-order harmonic distortion of the input

voltage to the Tee network is countered by the larger content of higher-order harmonics, increased switching losses, and an upper limit to usable K-factor of unity. Since the ratio of peak-to-average output tube plate current for a given ELF output is $4/K$, tubes with higher peak emission would be required for a given ELF output power when compared with the minimum sampling rate upper limit of K-factor, which is $4/\pi$.

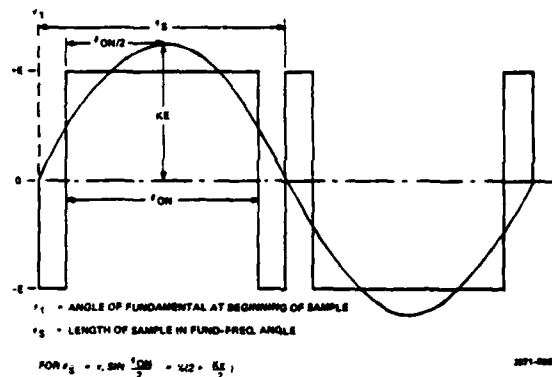


Figure 5. Timing of Pulse-Width Modulation for Sampling Interval of 180 Degrees

The minimum sampling-rate format on the other hand, is all third harmonic at a K-factor of zero, and has low-third harmonic content only for K-factors between 1 and 1.2, as shown in Figure 6.

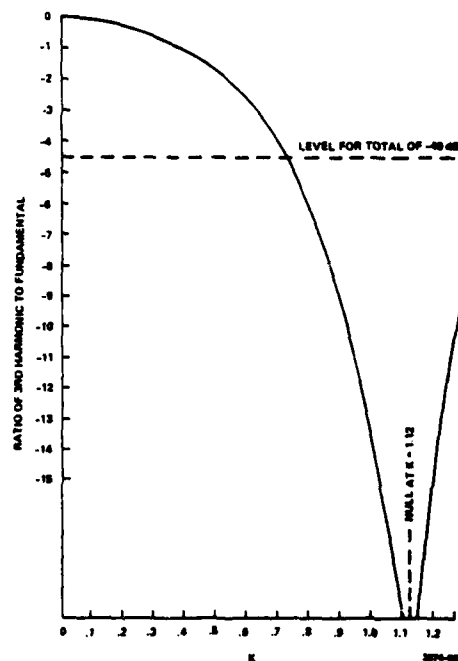


Figure 6. Third Harmonic Tee Network Input Voltage Content as a Function of Pulse-Width Modulation K-Factor

The full-scale ELF power amplifier design is for a rated power output of 650 kW into the resistive component of an antenna series-tuned to 76 Hz, when driven at either 72 or 80 Hz, resulting in a total output of 715 kVa. It is intended to deliver either 100 amperes rms to a total of 65 ohms or 300 amperes to a total of 7.22 ohms, with a nominal PWM input K-factor of 1.15.

The major components of this design are shown in Figure 7.

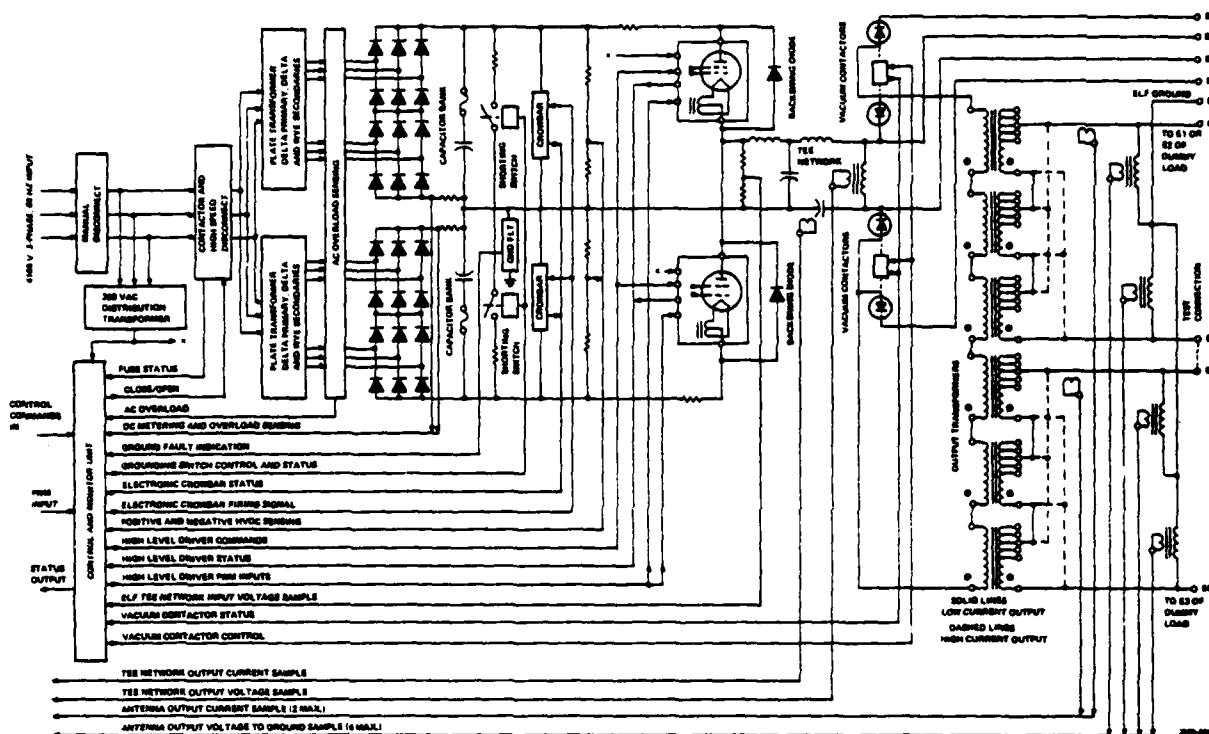


Figure 7. Major Component of 650 kW ELF Switching-Class Amplifier

The output tubes are EIMAC type 8973 (X-2710) tetrodes. The output tube connections and output operating conditions are shown in Figure 8.

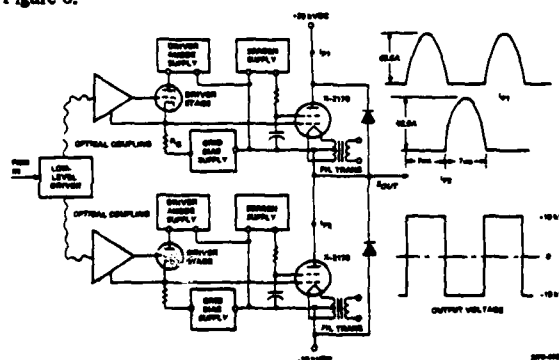


Figure 8. ELF Power Amplifier Output Tube Connections and Operating Conditions

To verify the performance of the design, two scale-model power amplifiers were constructed, each rated at 10 kW power output (12.3 amperes), which duplicated the full-scale design component for component. For output tubes, two pairs of parallel-connected EIMAC 3CX3000 triodes were used. Although the present design of the full-scale amplifier uses the large EIMAC tetrodes, the original design was intended to make use of specially-developed high- μ triodes, with modest plate dissipation capability but disproportionately high grid dissipation rating so as to be optimum for the switching class application, in which high-grid drive

level is desired to minimize the saturated plate drop, which, in turn, results in a minimum of plate dissipation.

The 10 kW power amplifiers were designed and constructed concurrently with high power testing of actual samples of the high- μ triodes, under simulated per-tube operating conditions at the high-power test facility at RADC. Both tubes tested failed prematurely, as a result of grid-cathode stresses. It became obvious that a conservative design called for consideration of tubes with much higher electrical ratings, of which the X-2170 was deemed optimum.

A comparison of the actual circuit component values and operating conditions of the 10 kW power amplifier and the design values for the 650 kW amplifier are listed in Table 1. Figure 9 shows oscilloscope waveforms of signals at various points throughout the amplifier. Figure 9A shows the output current on the same time base with the digital input PWM signal, having a modulation K-factor of 1.15. The output current has a peak-to-peak value of slightly more than 35 amperes, corresponding to just over the 12.3 ampere full-load output current at 10 kW power output. Note the nearly 90° phase difference between output current and PWM input, caused by the delay of the Tee network. Figure 9B shows antenna or output voltage and current on the same time base. Note the difference due to the tuned load being driven off resonance. Figure 9C shows output current with the input PWM changing from 72 to 80 Hz 16 times per second. Figure 9D shows output current when the input PWM changes frequency 4 times per second. Figure 9E shows the output voltage from the totem-pole output stage (input to Tee network) on the same time base as the input PWM. Figure 9F shows the input current in the Tee network and the input PWM. Figure 9G shows current from the positive-polarity high-voltage power supply and input PWM. Current in the negative direction is return current through the backswing diode. Figure 9H shows the 208 Vac mains current in one of the three phases, demonstrating the nearly sinusoidal waveform and the 12 bumps associated with a 6-phase, full-wave rectifier system.

Table 1. Comparison of 10 kW and 650 kW Power Amplifier Characteristics

Rated Power Output	10 kW	650 kW
Rated Output kVA	11 kVA	715 kVA
Load Current at Full Power	12.3 A RMS	99 A RMS
Load Resistive Component	66.3 Ohms	66.3 Ohms
Load Q	4.4	4.4
Plate Supply Voltage	± 4.4 kV	± 20 kV
Plate Supply Average Current	1.3 A.	18.4 A.
Peak Plate Swing	4 kV	19 kV
Nominal PWM K-Factor	1.15	1.15
ELF Fundamental-Frequency Voltage at Input to Tee Network	4.6 kV	21.9 kV
Peak Plate Current	5 A (total)	68.5 A
Tee Network Inductor Value	$L1 = L2 = 1.98H$	$L1 = L2 = 0.67$ Hy
Tee Network Capacitor Value	$C1 = 2 \mu F$	$C1 = 5.9 \mu F$
Tee Network Input Impedance at 72 Hz	925 / 23	315 / 23
Tee Network Input Impedance at 80 Hz	917 / -23	313 / -24
Output Transformer Turns Ratio	3.86	2.24

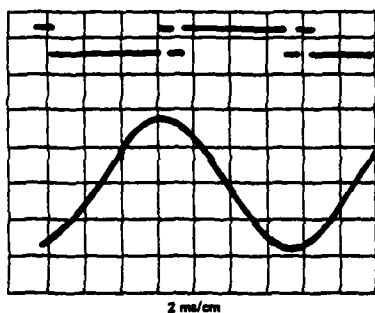


Figure 9A. 2 ms/cm

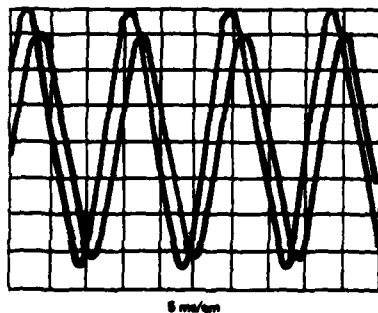


Figure 9B. 5 ms/cm

INPUT PWM

DUMMY ANTENNA
CURRENT, 10A/cm

DUMMY ANTENNA
CURRENT, 5A/cm
DUMMY ANTENNA
VOLTAGE

3001-006

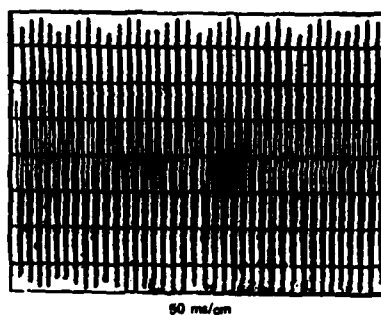


Figure 9C. 50 ms/cm

DUMMY ANTENNA
CURRENT, 5A/cm

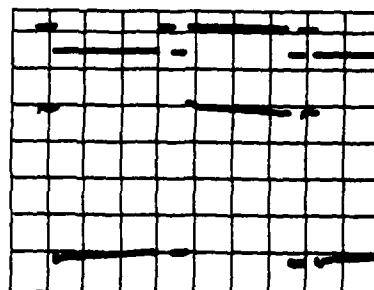


100 ms/cm

Figure 9D. 100 ms/cm

DUMMY ANTENNA
CURRENT, 5A/cm

3001-006

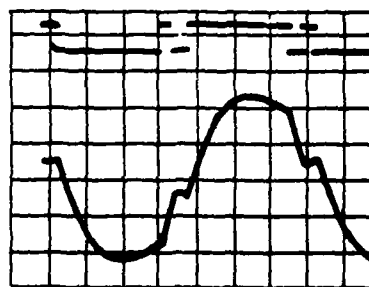


2 ms/cm

Figure 9E. 2 ms/cm

INPUT PWM

INPUT VOLTAGE
TO TEE NETWORK,
2 kV/cm



2 ms/cm

Figure 9F. 2 ms/cm

INPUT PWM

INPUT CURRENT
TO TEE NETWORK,
2 A/cm

3000-006

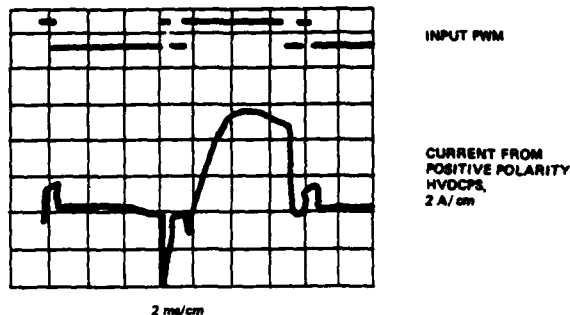


Figure 9G. 2 ms/cm

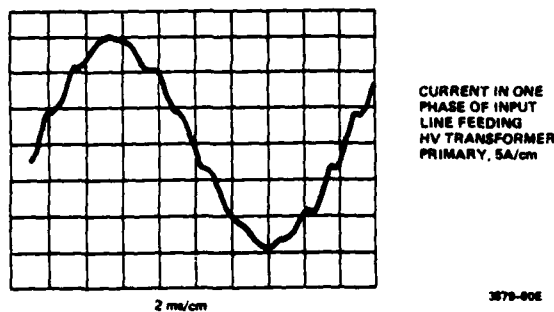


Figure 9H. 2 ms/cm

Figure 10 shows the two side-by-side control units for the two 10 kW power amplifiers, one of which has a panel removed revealing the integrated-circuit card nest. Figure 11 shows the two high-power cabinets, containing the dual high-voltage power supplies, energy storage capacitor banks, crowbars, the totem-pole output stages and drivers and the optically-coupled signal links; the Tee networks and the output transformers. Figure 12 shows the six output transformers, on the lower shelf; the Tee network inductors, on the middle shelf; and the Tee network capacitor bank, near the top. Figure 13 shows the dummy antenna cabinet, with the incremental 50 millihenry antenna-simulation inductors on the floor; the incremental resistors on the right and the antenna tuning capacitors to the left.

The testing program for the 10 kW power amplifiers for the most part verified the theoretical expectations for performance, including transient stresses resulting from rapid frequency changes, harmonic content both of output current and of input current, and behavior of two power amplifiers sharing common-load impedance or mutual coupling.

The major hazard of harmonic content is interference with telephone communication. For this reason one of the requirements of performance was to meet a Telephone-Influence-Factor weighted RMS of total output current and of vector-sum three-phase input current. The requirement is stated as:

$$f = 5000 \text{ Hz} \quad I_n = \text{harmonic current}$$

$$\left[\sum (I_n T_N)^2 \right]^{1/2} = 1090 \text{ A. } T_N = \text{Telephone Influence Factor (TIF)}$$

$$f = 72 \text{ Hz}$$

Measurements, normalized to 99 A full-scale antenna current, as a function of PWM K-factor, gave values of 196 A, 197 A, and 182 A, at K-factors of 0.5, 0.8 and 1.15, respectively, compared with predicted values of 186 A, 176 A and 166 A. Measurements were made using a standard TTS-37B telephone noise measurement set and a capacitive differentiator to produce the 6 dB/octave inductive-coupling factor.

Compared to low sampling-rate PWM the use of high sampling rate PWM produced negligible improvement in telephone interference performance and in some cases even degraded performance. For that reason the lowest sampling rate PWM was adopted as standard.

To measure the degree to which the power amplifier behaved as a constant-current source the dummy antenna was reduced, in approximately 15% steps, from 66.3 ohms to a short circuit. The output current varied from 12.3 to 12.8 amperes, a 4% change.

The PWM input was also varied in K-factor from 0.3 to 1.27 (the limiting case of $4/\pi$, producing a fundamental-frequency square-wave input). The measured values of output current varied essentially linearly as a function of K-factor.

Conversion efficiency of the output stage proved virtually impossible to accurately measure, with some measurements indicating slightly over 100%. It was equally difficult to directly measure the plate losses of the air-cooled output tubes. The overall efficiency of the 10 kW PA, however, was measured to be 76.5%, including all cooling, filament and loss loads. Overall efficiency of the 650 kW PA is expected to be approximately 80%, with a power factor greater than 85%.

The amplifier control unit contained all of the functions to be implemented in the full-scale PA, which included the extensive remote readout of built-in-test equipment indications; automatic reset of crowbar and ELF interrupt functions and lockout if the count of such events exceeded a preset number within a given time interval; and response to digitally-transmitted control signals appropriate for a nominally unmanned installation. All logic functions were executed in TTL digital integrated circuits. It proved difficult and, in some cases, not entirely possible to immunize the TTL logic from internally-generated impulsive noise, such as crowbar firings, relay closures, etc. For this reason the design of the full-scale PA control unit was implemented with zener-diode-coupled, high-noise-immunity 15-volt logic elements.

Tests were performed, at the RADC high-power test facility, with simulated per-tube ELF amplifier operating conditions, on the X-2170 tetrode.

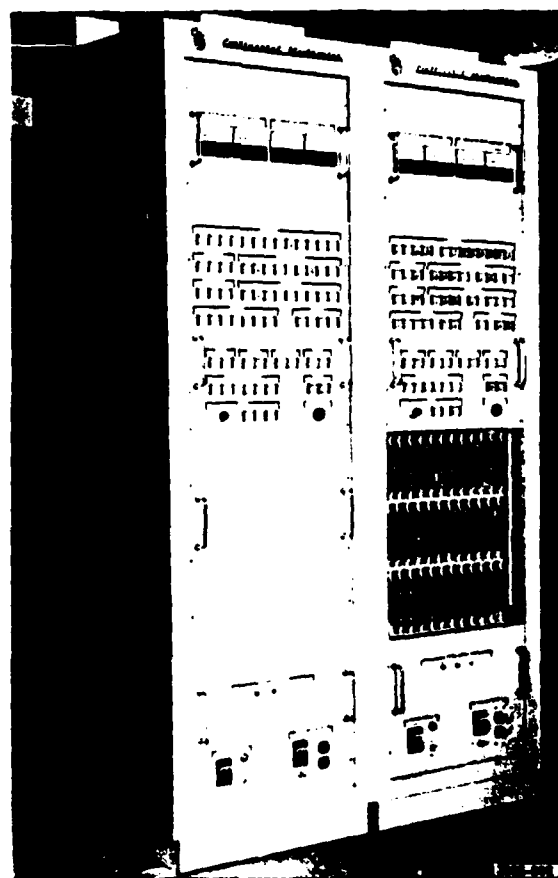


Figure 10. Side-By-Side ELF Power Amplifier Control Units



Figure 11. Overall View of 10 kW ELF Power Amplifiers



Figure 12. Tee Network (upper) and Output Transformers (lower) of 10 kW ELF Power Amplifier

The tests imposed considerable more stress on the RADC facility than they apparently did on the X-2170, which behaved quite serenely. The tests and their ELF amplifier significance are summarized in Table 2.



Figure 13. Tuned Dummy Antenna for 10 kW ELF Power Amplifier

Table 2. X-2170 Tube Evaluation

	TUBE RATING	ELF PA REQUIREMENT	RADC TEST COND.	NOTE
PLATE VOLTAGE	60 kV	40 kV	40 kV (60 kV)	8 HR RUN (DET. TEST)
PEAK PLATE I	400 A	60.5 A	70 A	8 HR RUN
RMS PLATE I	60 A (DC)	34.7 A	30 A	8 HR RUN
PLATE DISSIPATION	600 kW	20 kW	60 kW	30 MIN RUN
SCREEN DISSIPATION	7.5 kW	3.75 kW	4.2 kW	30 MIN RUN
CONT. GRID CURR.	2000 W	60 W	60 W	8 HR RUN
FILAMENT VOLT.	10.5 V. AC	TAPS 10.5-10.5 V	10.5 V	8 HR RUN
LOAD POWER	1000 MW	200 MW	600 MW	8 HR RUN

NO INCIDENT DURING 8-HR HEAT RUN. VACUUM PUMP CURRENTLY STEADILY DIMINISHED THROUGHOUT RUN. RADIATING IMPROVED VACUUM.

207-100

Acknowledgements

The authors would like to express their gratitude to Jimmy Weldon, Ed McBurney, Ed Bently and Gerald Thompson, of Continental Electronics, and Jeff Otto and Bob Linde, of GTE Products, without whose efforts none of this would have happened.

DEVELOPMENT OF HIGH-RELIABILITY, MULTIKILOHERTZ REPETITION-RATE, FAST-DISCHARGE COMPONENTS

G. McDuff, K. Rust, W. J. Sarjeant, and P. Mace
Los Alamos Scientific Laboratory
P. O. Box 1663
Los Alamos, NM 87545

Introduction

A pressing need has arisen for the development of very long-life, energy-transfer system components. As additional applications for fast pulse-power techniques are conceived, especially in laser technology, component specifications become more and more severe. High-repetition rates, high-peak and rms currents, and extremely high reliability are but a few of the difficult constraints. The two basic components in pulsed-power technology are capacitors and switches. In order to develop these high-voltage components, a unique laboratory has been constructed using state-of-the-art diagnostic and shielding techniques.

The laboratory is comprised of three basic systems:

- Charging systems
- Diagnostic systems
- Grounding and shielding systems

The block diagram in Fig. 1 shows the basic system layout. It is important to note that each system may be used separately or in conjunction with the other system blocks.

In the first year of operation, approximately 24 different thyratrons, capacitors, saturable inductors, and current-viewing resistors have been characterized in the facility. A thorough investigation of polypropylene/silicon oil low-loss capacitors has been made and is discussed later.

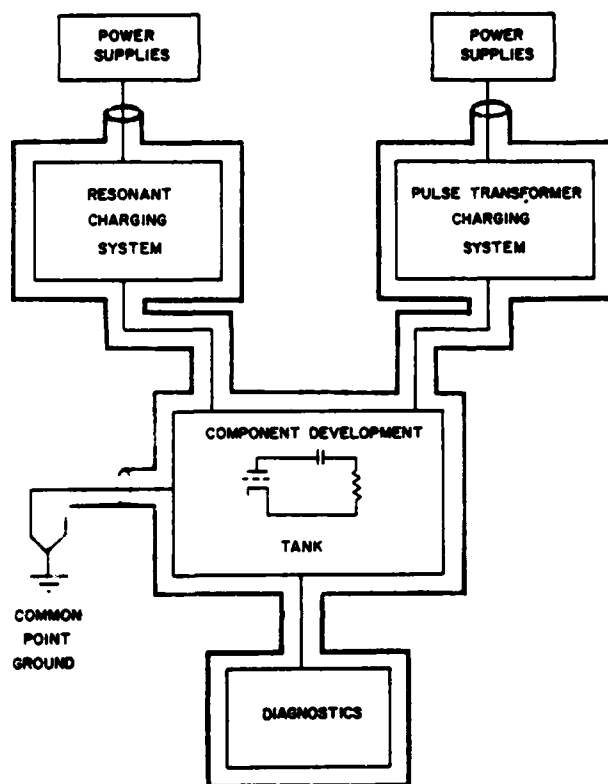
The Charging Systems

Perhaps the most important part of pulsed-power technology is power conditioning. In the component development laboratory, both resonant and pulse transformer charging (command charging) are used to fully characterize the behavior of discharge components.

Linear resonant charge voltages of 5 to 60 kV at repetition rates to 3000 pps are available. With the use of saturating inductors, peak-charge voltages of 75 kV are achieved. Pulse-forming-network (PFN) capacitors up to 4 nF can be charged to 80 kV at 1000-pps repetition rates. At reduced operating parameters, capacitors of several microfarads can be operated in a discharge circuit.

Pulse-transformer charging extends the operating range of the facility to a maximum charge voltage of 120 kV at repetition rates of 5000 pps. Capacitor values up to 15 nF can be charged in 2 to 10 μ s. Wall-plug efficiencies of 85% are achieved with present pulse-transformer charging systems, and efficiencies of greater than 90% are expected in systems under development.

Since the resonant and pulse-transformer charging systems are completely separate, a discharge circuit under investigation can be changed from one to the other in a few minutes.



SYSTEM GROUNDING & SHIELDING

Fig. 1. High-repetition rate component-development laboratory operating system.

Diagnostics

In the field of component development, accurate and reliable diagnostic capabilities are essential. The heart of the laboratory diagnostic center is a computer-controlled two-channel transient digitizer of 500-MHz bandwidth. Pulse-current measurement capabilities of up to 50 kA at 350-MHz bandwidth are incorporated in the experimental area. A recently developed 250-kV dc to 100-MHz passive high-voltage probe and a 100-kV dc to 250-MHz probe complement the current measurement capabilities. With other in-house diagnostic techniques, such as ion microprobe, x-ray topography, and chemical analysis, a complete data base for the physics, chemistry, and metallurgy of components is being established.

A new thyatron current-viewing-resistor mounting flange assembly, shown in Fig. 2, was developed in conjunction with T & M Research, Albuquerque, New Mexico. Low-inductance design (<40 nH) and wide range of resistance values make it suitable for almost any circuit. This new diagnostic tool has been found to be indispensable in thyatron circuits.

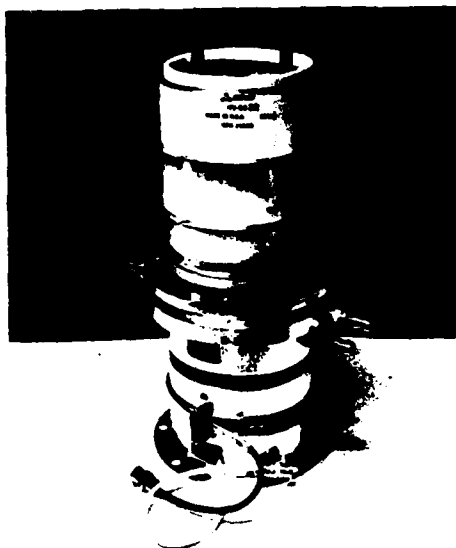


Fig. 2. Thyatron current-viewing resistor/mounting flange assembly.

Capacitors

Along with the development of various high-voltage components, the present area of prime interest is multikilohertz, long-life, low-inductance capacitors. A major program to fully characterize capacitors designed for pulse duty is in progress. The motivation for pulse-capacitor development is threefold.

- To obtain a data base to understand the physics and chemical processes affecting capacitor life.
- To develop low-loss, extremely long-life capacitors $> 10^{12}$ shots.
- To interact with industry in designing capacitors in the range of 1 to 20 nF capable of 10 kA/nF peak current in a 50- to 100-ns discharge.

There are two configurations that meet the low-loss requirements, silicon oil/polypropylene and dry, reconstituted, mica-type capacitors.

The equivalent series resistance (ESR) is of prime importance in determining the loss of the capacitor during the discharge pulse. The ESR measurement was approached from several directions. The conventional method of deriving ESR from a ringing discharge was used along with phase shift, Fourier analysis, and temperature variation measurements. A direct method using circuit theory applied to nonlinear time-varying second-order circuits was also used. Results from all methods indicated an ESR of less than 100 m Ω . A 0.5% accuracy of resolution is the limit of the present laboratory diagnostics. To make high-accuracy ESR measurements at 50-kV, 1-kA pulse levels at which the capacitors operate, a 0.02% resolution of accuracy would be needed. In the polypropylene/silicon oil capacitors, dependence of lifetime on repetition rate has been determined as seen in Fig. 3. The repetition-rate dependence is due to a time-voltage stress relation seen only in high di/dt circuits.

A new in situ method has been devised to detect an imminent failure in polypropylene/silicon oil capacitors using partial-discharge detection techniques. All capacitors of this type tested have failed in the same predictable manner due to the same failure mechanism. The method of capacitor-failure prediction has thus far proved to be 100% reliable.

Thyratrons

High-average power switching is a major area in the field of pulsed power. To meet the requirements of long life, high-repetition rate, and low loss, the thyatron at present is the only viable choice. In addition to the above qualities, thyratrons require less support equipment than high repetition-rate spark gaps and are far more economical to use. Areas of thyatron investigation include efficiency, power and energy flow, and switching characteristics.

One of the major problems to date in fast-discharge, kilohertz repetition-rate spark gap switching is the large losses experienced (20 to 30%) in the switch. In long-life, high-reliability circuitry such losses are totally unacceptable. The thyatron losses during commutation in this fast-discharge circuit have been measured for the first time in this new facility. For stored energies of 1 to 1.2 J, this loss is 2.2% at an 80-ns pulse width and a peak current of 700 A. The losses were observed to decrease rapidly with increasing energy, as expected, so that low-loss switching is feasible with thyratrons, giving long economical life at high switching efficiencies.

New, compact, short-pulse thyratrons are currently under development for 50 to 100 kV multikilohertz operation at current rates of rise in excess of 10^{12} A/s at 10 to 100 kA peak current operation.

System Upgrade

The present component-development laboratory has an average power capability of 50 kW. A second facility, capable of 300-kW continuous average power, is under construction. The new facility is similar in concept to the existing laboratory with many advances in diagnostic capabilities. Two projects planned for the high-power laboratory are development of high-energy density capacitors and PFNs for repetitive pulsed-power laser applications.

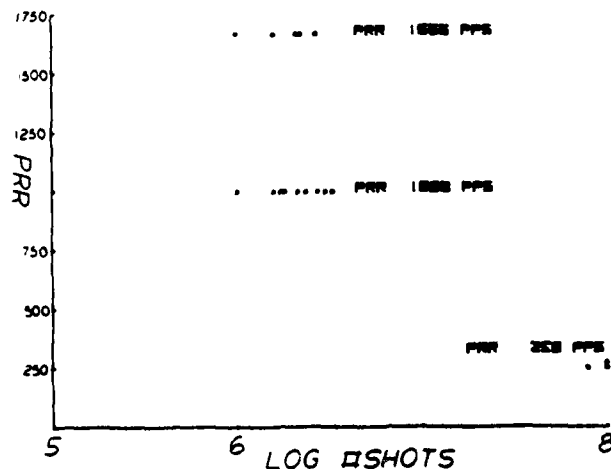


Fig. 3. Lifetime vs pulse repetition rate for silicon oil/polypropylene.

The high-repetition rate component-development laboratory has received much internal support as well as support from industry. Interaction and technology transfer between other national facilities and industry

is encouraged within the Los Alamos Scientific Laboratory and are vital to the advancement of pulse-power technology.

ELECTROMECHANICAL SHOCK IN PULSE POWER COMPONENTS

BY

T. R. Burkes
Electrical Engineering Dept.
P. O. Box 4439
Texas Tech University
Lubbock, Texas 79409

and

W. J. Sarjeant
M. S. 429
Dir. E-4
LASL
Los Alamos, NM 87545

Summary

Most components used in high power pulse generators undergo mechanical shock stresses during the pulse or on its leading edge. As power densities become very high, this shock may lead to anomalous behavior as well as introduce failure modes that may not be immediately obvious. It has been shown that acoustic shock waves traveling within spark gap electrodes can affect electrode erosion by as much as an order of magnitude. Thus, a new point of view is required for component design where shock may be a critical factor. The mechanisms for generation of shock forces, both thermal and electromagnetic, are reviewed and applied to resistors, capacitors, magnetic devices and switches. The mechanisms described are square law effects so that it can be concluded that for high energy pulses, mechanical shock stress will be a critical factor in component survival.

Introduction

In a broad and general way, the mechanisms for the generation of mechanical forces in pulse power components can be ascribed to two mechanisms, thermal shock and forces generated through electrostatic and electromagnetic mechanisms. These forces usually manifest themselves by audible noise generated during the operation of a high power pulse generator. Obviously, something must be moving for the sound to occur and this movement can lead to material fatigue, insulation failure, etc. Also, erratic behavior may be generated by the shock through excitation of mechanical resonances peculiar to a particular component. For instance, jitter in an ignitron may be a function of pulse repetition rate because of ripples produced on the mercury surface due to the high magnetic pressure at the arc spot(s).

Under the transmission of microsecond and shorter pulses of electrical energy through power-conditioning components, very rapid deposition of thermal energies into dielectrics and mechanical connections can cause intense localized heating. Depending upon the thermal damage levels of each material, such heating may cause single-pulse catastrophic damage or multiple-pulse accumulative damage resulting in early failure of the component in the system. In the context of the present discussion, the discharge times of interest ($\leq 10^{-6}$ sec.) apply to numerous laser systems and other pulsed systems of current interest. As the thermal diffusion times for even thin films and very good heat sinks are many microseconds [1], the heating in most components will be nearly adiabatic. This discussion will be qualitative in nature and relate these transient thermal and electromechanical effects in capacitors, resistors, and switches to each other.

Thermal Effects

The primary effect of a fast electrical pulse is to cause a sharp temperature increase in dielectrics (e.g., capacitors) or conductive metal surfaces (e.g., thyatrons and spark gaps). Permanent changes are caused by molecular restructuring of the insulators or by sputter damage to metal surfaces. For fast electrical pulses the thermal analysis presented is of general applicability.

In the study of temperature rises at insulator-to-insulator or conductor-to-gas discharge interfaces, a one-dimensional model is generally appropriate [1] as illustrated in Fig. 1. The Region III to left of Region I has the same properties as Region II in most capacitor winding geometries. For switch thermal transfer cases, Region III is normally a glow discharge or arc with a thermal diffusivity much smaller than D_1 , meaning that thermal transport back into this region may be neglected. Radiation effects from the metallic collector of Region I are not considered. For this microsecond type time scale, the radial thermal diffusion per pulse is negligible, allowing the three-dimensional heat conduction equation to be simplified from

$$\frac{\partial T}{\partial t} = D \nabla^2 T + \frac{D}{K} U_0 \quad (1)$$

to:

$$\frac{\partial T}{\partial t} = D \frac{\partial^2 T}{\partial x^2} + \frac{D}{K} U_0 \quad (2)$$

where T is the temperature in K, t is time in seconds, x is distance in meters, and U is power density in watts per cubic meter. The constant D is the diffusivity in square meter per second and K is the thermal conductivity of the material in watts per second meter-kelvin. Assuming continuity and negligible temperature rise for very large x , then this equation can be solved as there is no radial or azimuthal temperature variation [2]. Starting from an initial temperature of T_0 , if $D_{11} = 0$ then an adiabatic temperature rise takes place in Region I so that

$$T - T_0 = \frac{D_1}{K_1} U_0 t. \quad (3)$$

Thus, this is the maximum temperature rise that can take place and yields a true upper limit, e.g., particularly when thermal diffusion out of Region I takes place slowly.

A second solution to the transient temperature rise is found in the case of depositing thermal energy in Region I, with $D_{11} = 0$ and $D_{11} \rightarrow \infty$. The solution has been obtained by Domingos [2] in his excellent

study of transient effects in resistors and is of general applicability to capacitor and switch heating. Figure 2 plots the relationship between temperature rise for a finite layer for different boundary conditions.

The temperature distribution at several times can be obtained for several pulse lengths. For very short times the rise is significant only in the insulator with the peak temperature as given by Eq. (3). Gradually, the thermal energy diffuses into Regions II and III. For most configurations, $D_{II} = D_{III}$ is of interest and the character of the distributions for several times (1-4) is plotted in Fig. 3. Note that cessation of the electrical pulse, after say 1 μ s for dielectrics of thickness of a few mils, results in cooling of the insulator by diffusion into the outer regions with a time constant $1/D$. This thermal energy gradually diffuses into the substrate environment, such as the metallic (generally aluminous) conductors in a film capacitor or the electrode cooling structure in repetitive switches.

Let us now turn to some examples of transient thermal effects and also some damage situations separate from adiabatic heating wherein the impulse damage has a dominant voltage effect. Temperature distributions in a one-dimensional model of a film resistor have been calculated by Domingos using a finite difference technique. Assuming an initial equilibrium temperature of T_0 , a constant power pulse applied for several pulse durations, the temperature as a function of time is similar to the distribution in Fig. 2. The wings of the distributions illustrate diffusion of thermal energy on a time frame equal to the pulse duration and clearly illustrates the large film temperature rise obtainable for even modest input energies. For example, carbon-film and metal-film resistors suffer damage for input energies from 12 to 200 mJ for 1- μ s pulse duration [2]. This is to be compared to 2.4 J for carbon composition resistors where the thermal heating is of a bulk nature in contrast to the films wherein the vaporization or melting point temperature is readily achieved at much lower energies. As the pulse duration increases it has been observed that the energy threshold for damage rises significantly (10^{-3} J at 10^{-5} s to 10^{-3} J at 10^{-3} s for Allen Bradley carbon-composition resistors) [3]. This may be caused by internal voltage stress-induced breakdown at the higher voltages used at shorter pulse widths [4]. Indeed, the question of accumulated damage with number of pulses has been addressed at some length in the design of high-voltage coaxial attenuators [5]. Previous studies of damage were concerned primarily with large, irreversible (~ 5 -10%) changes in resistance in one single pulse. For electromagnetic-pulse applications this is very useful information for system design. In the development of repetitive pulse systems, it is of more value to assess the accumulative damage with shots and applied voltage. Figure 3 illustrates the per cent resistance change in a 56- Ω , 2-W Allen Bradley carbon-composition resistor as a function of number of pulses, for a lot size of 10 resistors at each voltage level [5]. The pulse width in all cases was 260-ns FWHM. The points are the average for 10 resistors, each resistor being subjected to 1, 10, 100, and 1000 pulses and measured thereafter. The error bars represent the maximum excursions from this average value observed. The dependence of the $\% R/R$ upon number of pulses, N , is obtained from a least-squares fit to the data and if V is the peak pulse voltage in kilovolts

$$\frac{\% R}{R} = \frac{1}{5.0} - 0.22 \ln N. \quad (4)$$

It is presumed that the small, accumulative damage per pulse is caused primarily by superheating at carbon carbon granule interfaces as has been observed by Hinton in crystalline, thick-film resistive structures [4]. This gradual reduction in resistance is of concern in voltage dividers as well as rf circuitry and has prompted a shift to metal film resistors in low-level systems. At higher voltages and powers the problem is considerably more acute, and new structures are required.

Electromagnetic Forces

For most cases, the simplified approach of the description of the force generation mechanisms, i.e. electrostatic and electromagnetic, is justified because of symmetry and the dimensions of components is usually small compared to a wavelength of the excitation current or voltage. In general, the total force generated by an electric or magnetic field can be expressed as

$$f = - \frac{\partial W_f}{\partial x} \quad \left| \begin{array}{l} q = \text{const. (capacitors)} \\ \phi = \text{const. (inductors)} \end{array} \right.$$

where W_f is the total energy stored in the field, x is a dimension and q is the charge on conductors (for electrostatic fields) and ϕ is the magnetic flux (for electromagnetic fields) [6]. In general, forces derived from electromagnetic fields act to change the circuit or component dimensions to increase the total energy stored. For magnetic fields, it can be further said that the magnetically derived forces will act to reduce localized energy density, even though overall energy storage will increase. Electric fields, on the other hand will produce forces that act to increase energy density.

Electrostatic Forces

The force exerted on the dielectric in a capacitor may be expressed as

$$f = \frac{1}{2} V^2 \frac{dC}{dx}$$

where V is the applied voltage, x is a dimension and C is the capacitance expressed as a function of x . Thus, if C is given by

$$C = \frac{\epsilon A}{x}$$

where ϵ is the permittivity, A is the area of the capacitor plates and x is the plate separation. The compressive force exerted on the dielectric is

$$f = - \frac{1}{2} V^2 \frac{\epsilon A}{x^2}$$

This formulation gives a pressure of about .1 lb/in² for an electric field stress of 6 Mvolts/meter in mylar. This mechanical force is exerted by the capacitor plates on the dielectric so that a squeezing action is transmitted to the oil (impregnate) and a pumping action is initiated. Thus, the capacitor vibrates at the pulse repetition frequency. Because of the usual construction of capacitors, this force will be most predominant on the outermost layer. The internal forces will be largely counterbalanced except at localized points such as foil wrinkles.

If the highest dielectric material in a capacitor does not fill the complete volume between the capacitor plates, then a stretching force is exerted on the higher dielectric material in directions to fill the capacitor. This effect can be seen by expressing C as $C = \frac{\epsilon_1 x}{d}$

where d is the plate separation, l is the plate length and x is the dimensional direction in which the dielectric does not fill the area between the plates. Thus, the stretching force is given by

$$f = \frac{1}{2} \epsilon l \frac{d}{dx}$$

From this formulation it can be seen that the higher dielectric materials are attracted to the highest field regions (the foil edges). Further, any high dielectric impurities will be attracted to the high field regions. It also follows that the low dielectric materials will tend to be displaced by the high dielectric materials. If low dielectric materials are suspended in a high dielectric fluid where a significant electric field gradient is present, a churning action may be observed.

Magnetic Forces

Since magnetic fields and thus inductances are inherent in any electrical circuit, a useful formulation for the magnetic forces is given by

$$f = \frac{1}{2} i^2 \frac{dL}{dx}$$

where i is the current and L is the inductance expressed as a function of x . This formulation ignores the nonlinearities of iron. It is none-the-less useful for visualization of the character of magnetically derived forces of electrical circuit components.

Inductance may be expressed functionally as

$$L = \frac{\mu N^2 A}{l}$$

where N = turns,
 μ = permeability,
 l = magnetic path length,
 A = cross sectional area of magnetic path.

clearly, the forces on a current loop are such that the magnetic length tends to shorten and the cross sectional tends to increase. Thus an inductor undergoes an axial compression as well as expansive force. In the event that iron is present, the iron undergoes a compressive force along the magnetic path (magnetostriction) and a very noticeable "thump" is associated with iron core devices used in pulse power systems. This mechanical motion generates losses in pulse transformers, charging inductors, etc. not accounted for by eddy current and hysteresis losses since mechanical work is being done which is not returned to the electrical circuit.

Magnetic fields may become especially intense at circuit configurations such as angle turns or U-shaped bends. Situations involving turns may be depicted by the arc channel and the electrodes of spark gaps. This configuration can exert sufficient force on the electrode to generate acoustic waves into the electrode [7]. Thyatron anode cups represent a case of a U-shaped revolution. At very high di/dt operation, the current will run along the anode skin and considerable force may be exerted on the walls and bottom of the anode cup.

Situations involving concentration of magnetic fields may be more appropriately described by

$$f = \frac{\partial}{\partial x} \left[\int \frac{1}{2} \mu H^2 dv \right]$$

where v is the volume of interest. Manipulation of this equation results in a magnetic pressure [8]

$$P = \frac{1}{2} \mu H^2$$

This pressure may be exerted directly on the surface of conductors causing a considerable shock wave to be developed. (The exact nature of the pressure pulse depends on the circuit configuration and the reader is referred to ref. 8.) Those situations involving geometries where magnetic fields are concentrated can be expected to undergo considerable mechanical stress during the discharge.

Conclusions

Because most materials expand when heated, transient adiabatic heating of pulse power components can lead to extreme internal stresses in pulse power components. When these stresses are combined with those due to electromagnetic forces, especially magnetic effects, various failure mechanisms become clear. A resistive conductor undergoing a rapidly rising, high current pulse may develop surface cracks and pitting due to the sudden shock forces exerted on its outer layer (< one skin depth). The thermal stress in SCRs may be especially severe under pulse loading [9]. Because considerable energy will be deposited in the depletion region upon turn on, this region will expand sufficiently to vibrate the crystal. Repetitive pulsing may then lead to mechanical fatigue.

Electromagnetic and thermal forces may produce sufficient shock for high di/dt operation to over stress insulator/conductor interfaces so that leaks occur. Simple metal-to-metal contacts which are not uniform are forced apart by the uneven current distribution. Thus, pitting and arcing may occur within metal connection so that performance suffers as well as early failure.

Although electrostatic forces are usually weak, they none-the-less can lead to troublesome problems. High dielectric impurities are attracted to the points of highest field stress. For instance, oxides of aluminum do not have high breakdown strength but would be attracted to the highest fields leading to corona and/or breakdown.

As energy densities increase, the consequences of mechanical motion and shock can be expected to introduce early failure modes and anomalous behavior. It should be noted that the mechanisms for the production of shock stresses are square law effects. The application of transient thermal diagnostics to other electrical energy storage and transfer components will become a matter of more concern in the future as repetitive high-average power applications continue to expand. This, along with electromechanical effects, may well turn out to represent a limit to present system scalability and point toward the research and advanced development activities, which will then be required to meet future applications.

References

1. H. Domingos, "Transient Temperature Rise in Film Resistors," Rome Air Development Center Technical Report RADC TR-74-92, April 1974.
2. H. Domingos, "Electro-Thermal Overstress Failure in Microelectronics," Rome Air Development Center Technical Report RADC-TR73-87, April 1973.
3. H. Domingos, "Pulse Power Effects in Discrete Resistors," to be published as a DNA report.
4. J. P. Marton, private communication.
5. W. J. Sarjeant, "A 50-ohm Coaxial High-Voltage Attenuator with 80 Pico-second Rise Time," unpublished.
6. S. Seely, Electromechanical Energy Conversion, McGraw-Hill, 1962.
7. R. Petr and T. R. Burkes, "Acoustic Phenomena in Erosion of Spark Gap Electrodes," Applied Physics Letters, Vol. 36, April, 80.
8. H. Knoepfel, Pulsed High Magnetic Fields, North-Holland Publishing Co., 1970.
9. G. Karady and R. Cassel, "Design Philosophy of 600 MN Pulsed Energy Converters for Toroidal Field Coil of TFTR at Princeton," Proceedings of the Seventh Symp. on Engr. Problems of Fusion Research, Vol. I, Oct. 25, 1977.

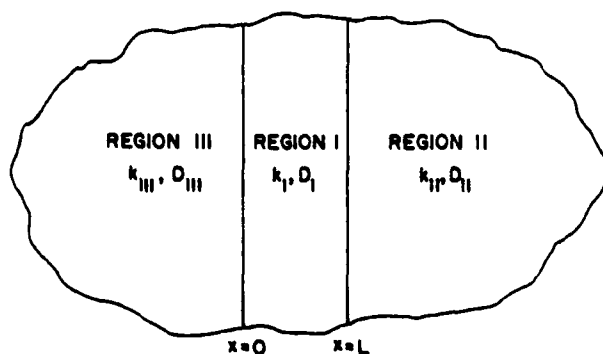


Fig. 1. One-dimensional model of a film resistor. Region I is the resistive film, Region II is the substrate, and Region III is the insulating jacket. (Ref. 2)

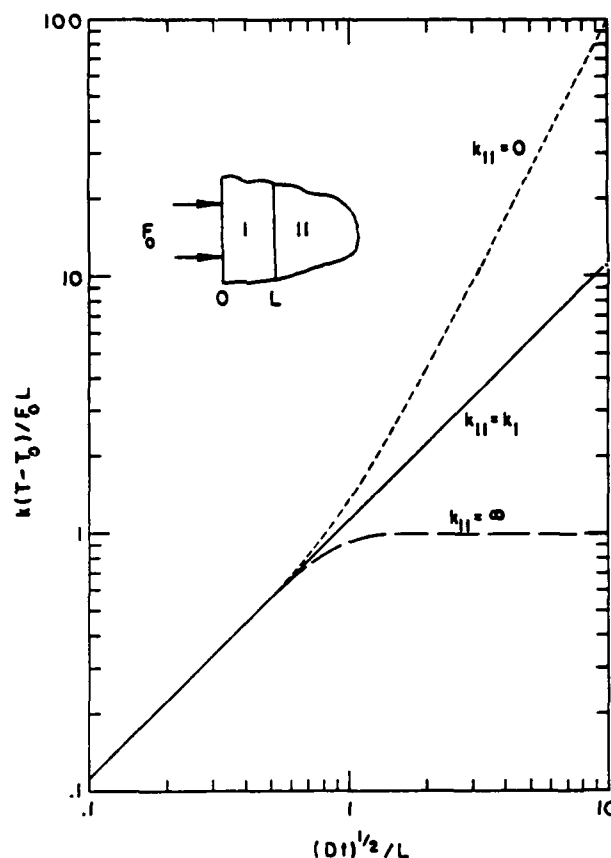


Fig. 2. Peak temperature rise in a finite layer with different boundary conditions. Region II is a perfect insulator in the top curve, a perfect heat sink in the bottom curve, and has the same thermal properties as Region I in the center curve. (Ref. 2)

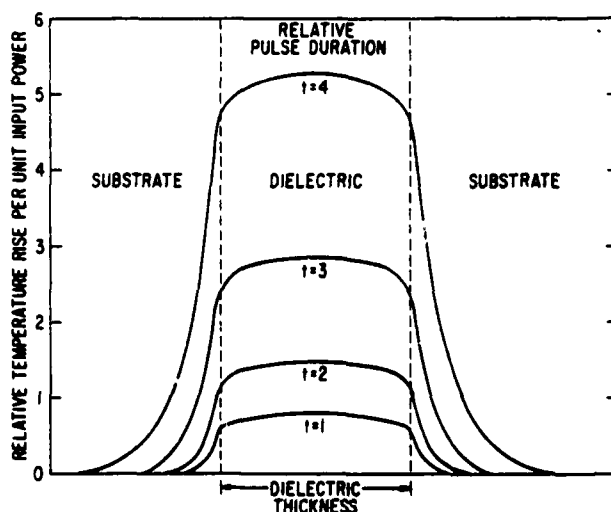


Fig. 3. Illustration of the transient temperature rise per unit input power in a dielectric film surrounded on either side by a thermally high diffusivity substrate. As the pulse duration increases, the thermal effects change from adiabatic heating to significant heat flow during the pulse.

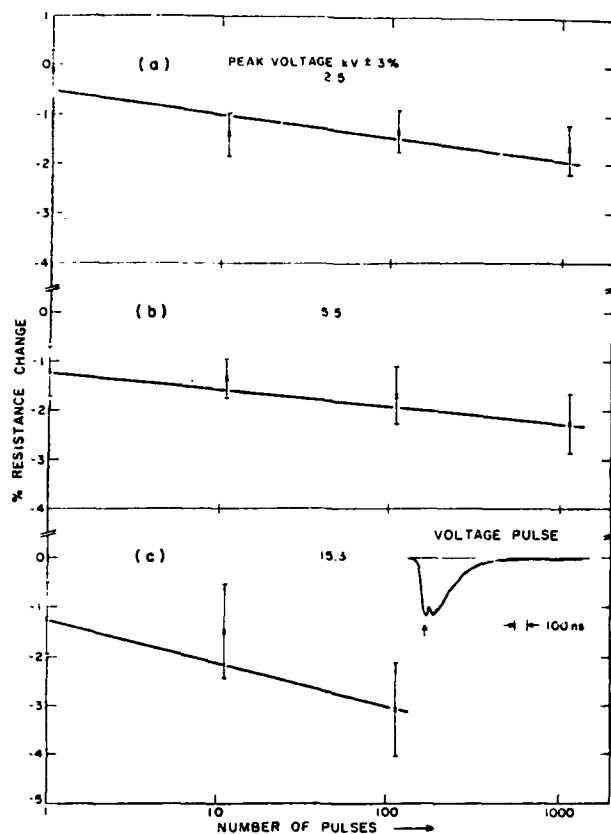


Fig. 4. The per cent resistance change in 56-Ω, 2-W Allen Bradley carbon-composition resistor as a function of number of pulses, for a lot size of 10 resistors at each voltage level.

HYDROSTATIC PRESSURIZATION OF OIL-IMPREGNATED CAPACITORS TO ACHIEVE EXTENDED AC LIFETIMES

W. A. FITZSIMMONS and M. KANG

National Research Group, Inc
P.O. Box 5321 Madison, Wisc. 53705

Abstract

Metal foil, dielectric film, oil impregnated capacitors often develop internal corona near sharp metal edges when under high AC electrical stresses. We have identified at least two distinct types of corona: a relatively non-damaging weak uniform glow; and a very damaging spark-like discharge. Pressurization of the oil impregnation reduces both types of corona, and sufficient pressure will extinguish the spark corona. In situations where dielectric lifetimes would be from 10^3 to 10^6 cycles, pressurization increases the lifetime to in excess of 10^9 cycles with no observed failure. A simple model is discussed that correctly predicts the observed relationship between pressure and voltage for the extinction of the spark discharges. Based upon these results, a prototype pulse forming network has been constructed which meets the requirements of: a) high reliability; b) very low inductance ($< 1 \text{ nH}$); c) low output impedance ($\sim 0.3 \Omega$); d) high heat transfer characteristics; e) single unit packaging; f) reasonable cost.

Experiment

The corona discharges that take place within metal foil, dielectric film, oil filled capacitors was simulated with the experimental arrangement shown in Fig. 1. The insulating film is located between the flat bottom of an aluminum vessel and the end of a one inch diameter aluminum rod that is purposefully machined flat to leave a very sharp circular metal edge which is placed upon the insulation. Full wave AC voltages are applied between the metal electrodes at the frequencies of either 60 or 400 Hz, with voltages as large as 14 kV RMS.

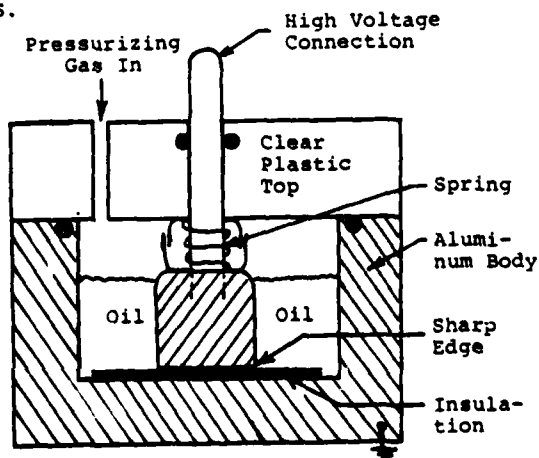


Figure 1: Experimental Arrangement

The experiment proceeds by setting the hydrostatic pressure in the capacitor vessel, and then increasing the AC voltage until spark corona is visually observed. The voltage is then slowly reduced and the voltage at which the corona extinguishes is recorded. Measurement of the somewhat lower corona extinction voltage is preferred since this better represents the maximum operating voltage of a full scale pulse forming network.

Experimental Results

Before discussing the more quantitative aspects of these measurements, it is perhaps best to mention a few qualitative results. Two types of corona have been observed near the sharp edge of the HV electrode. In all cases, damaging spark-like discharges can be observed under appropriate conditions. In the case of transformer oil impregnation however, an additional weak luminous glow was also observed, but this corona does not appear to have any serious damaging effect. When observed with a current probe, the weak glow is a series of closely spaced current spikes that occur during the rising and falling portions of the voltage wave that follow voltage zero crossing. After several hours of pressurization, the color of this weak glow seemed to depend upon the type of gas used to pressurize the system.

A second important observation is that with Mylar (a polyester film) and with no paper next to the sharp edge, the spark-like corona could not be extinguished at any reasonable pressure/voltage condition. Insertion of a layer of drafting paper between the Mylar and the sharp edge resulted in spark corona that was easily extinguished under pressure. On the other hand, Kapton (a polyimide film) with no paper resulted in corona that was also easily extinguished under pressure. Perhaps the difference is due to the fact that Mylar, when heated to relatively modest temperatures, tends to vaporize.

Finally, we observed at least two types of spark-like corona during this experiment. Both occur more or less randomly in time with an "eyeball" frequency that increases rapidly with electrical stress. However at lower stress, the spark corona occurs more or less randomly in position along the sharp edge; where as above a certain threshold, the sparks concentrate at one or a few locations. The second type is extremely damaging, and dielectric failure soon follows. Capacitors that have predictable pulsed lifetimes may be suffering from the low stress type of spark-like corona damage.

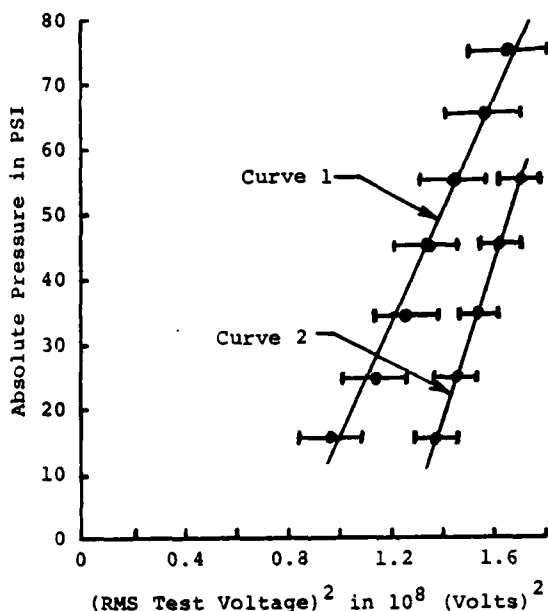


Figure 2: Applied Pressure versus (Voltage)² for the extinction of spark-like corona in test cell. Insulation is one 5 mil sheet of Mylar plus one 2 mil drafting paper next to sharp edge. Curves 1 and 2 refer to transformer oil and Dioctyl phthalate impregnation respectively.

The measured relationship between the applied absolute pressure and the spark corona extinction voltage for the case of one 5 mil sheet of Mylar plus one 2 mil sheet of drafting paper located between the Mylar and the sharp edge electrode is shown in Fig. 2. Curve 1 corresponds to transformer oil impregnation, and Curve 2 refers to Dioctyl phthalate impregnation.¹ Our results indicate that the square of the extinction voltage is proportional to the applied pressure.

Two reasonable assumptions seem to be sufficient to explain the observed relationship between pressure and voltage:

- 1) The spark-like corona is initiated by discharges that take place within oil vapor bubbles, with the bubbles being spontaneously produced during each half cycle of voltage because of the very high local electrostatic energy density in the oil near the metallic sharp edge.
- 2) The electric field in the bubble during and after the initial gas breakdown is zero, or at least very much reduced because of charge transport.

The question of bubble nucleation sites is not addressed because the sequence of the measurements implies many previous corona discharges which would be expected to supply many nucleation sites.

The remaining argument is simply that the electrostatic energy in the oil that is available to produce a bubble of volume V , this would be approximately $\frac{1}{2}\epsilon_0 E^2 V$, must be greater than the thermodynamic energy needed to vaporize the liquid, produce a liquid-vapor interface, support perhaps some heat lost due to heat conduction, and then do the work PV that is required to produce a bubble of volume V at pressure P . The electric fields near sharp edges can easily be in the range of 5000 V/mil, and this corresponds to electrostatic energy densities in the range of $5 \times 10^5 \text{ J/m}^3$. On the other hand, pressures of the order of 5 atmospheres also correspond to energy densities in the range of $5 \times 10^5 \text{ J/m}^3$. Thus for the electrical stresses to be found in typical high voltage pulse forming networks, pressures of several atmospheres are sufficient to extinguish the damaging internal corona. Furthermore, the required pressure would be expected to depend upon the square of the operating voltage as is indicated by our experimental results.

The differences between Curves 1 and 2 in Fig. 2 suggest that perhaps additional properties of the solid and liquid dielectric materials may need to be considered during the selection process. Fluid properties such as heat of vaporization, surface tension, and speed of sound may influence the dynamics of bubble formation and collapse. One of the most important fluid properties that must be determined is the solubility of various gases in the liquid as a function of pressure. Vapor properties such as ion mobilities, Townsend coefficients, and types of gases produced when subject to a discharge may also be important. There is evidence that the amount and perhaps the type of gas generated when the solid dielectric is heated is important. It is clear from this discussion that the simple energy argument proposed to explain the results in Fig. 2 by no means exhausts the subject. In fact more questions have been raised than answered. Nevertheless, we believe that one of the major considerations with respect to the engineering of very high reliability capacitors and high voltage pulse forming networks has been identified.

Longevity Tests

Longevity testing of AC capacitors necessarily requires testing at high frequencies. The results in Fig. 2 were obtained at 60 Hz, and this frequency is much too low for a serious lifetime test. Several comparison measurements were carried out at 400 Hz with the result that approximately twice the pressure is needed to extinguish the spark corona. This effect is not yet understood, although it may represent nothing more than the time for thermal relaxation after a spark discharge. During the course of these measurements, and the arrival of some materials, it was found that Kapton could be used as insulation without requiring an additional paper film to obtain pressure extinguishable corona. This is relatively important because the elimination of the paper greatly simplifies the construction of full scale units.

Having found a second and perhaps more interesting case of pressure extinguishable corona, two longevity tests were undertaken: one to test a Mylar-paper-transformer oil system, and the other to test a Kapton-Dioctyl phthalate system. For both cases, 3 sheets of 5 mil thick plastic insulation were used, the operating frequency was 400 Hz, applied pressure was 60 psig, and the voltage was 14,300 V(rms). Also, in both cases the applied pressure was approximately a factor of two above the corona extinguish pressure. Both tests were carried beyond the goal of 10^9 complete voltage cycles without dielectric failure. Each test required about thirty days of continuous operation. It should be noted that the weak luminous glow corona was present throughout the Mylar-paper-transformer oil experiment.

High Voltage Pulse Forming Network

The success of the longevity tests, in particular the Kapton-Dioctyl phthalate results, convinced us that it was now worth the effort to construct a high repetition rate pulse forming network since it appears that pressurization would be sufficient to achieve long life. In addition, we have found that relatively thick plastic films (5 mil thick instead of perhaps 0.5 mil) can be used; this greatly simplifies construction and also reduces the overall dielectric surface area which seems to us might avoid what could otherwise become a very difficult cleanliness problem.

The electrical design of the pulse forming network is that of two Blumleins arranged to operate in parallel as shown in Fig. 3. This configuration allows the majority of the outside surfaces of the final package to be at ground potential.

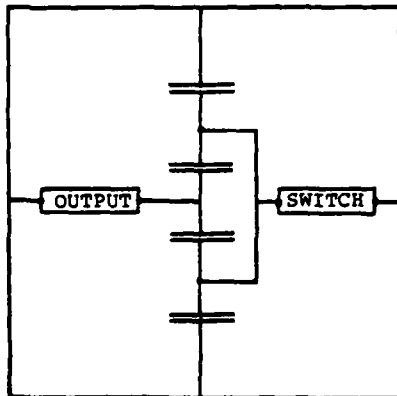


Figure 3: Schematic of "Twin" Blumlein pulse forming network showing electrical location of high voltage switch and output.

The basic design concept is to interdigit the fins of commercially available aluminum (air cooler) fin stock, so that a corrugated sandwich of Kapton sheets and 5 mil thick aluminum foils can be located between the opposing sets of fins, resulting in the appropriate arrangement of electrical surfaces. The insulation between each of the electrical surfaces is three 5 mil Kapton sheets with degassed Dioctyl phthalate impregnation. The aluminum fins, being perpendicular to their common base and penetrating into the pressure chamber, should provide exceptional heat transfer to the outside. Also the arrangement of fins provides the mechanical strength to support the operating pressure of 100 psig, even though the final package has a relatively large flat top and bottom.

Figures 4, 5, and 6, is a sequence of photographs that show this twin Blumlein in various stages of assembly. Fig. 4 shows (going from left to right) the injection molded metal-plastic outer casing, the lower fin stock with the corrugated Kapton-aluminum foil sandwich inserted into the fins, and the bare upper fin stock. Fig. 5 shows the lower fin stock with its plastic-foil sandwich inserted into the outer casing. Fig. 6 is a photograph of the final package.



Figure 4: "Twin" Blumlein in early stage of assembly.

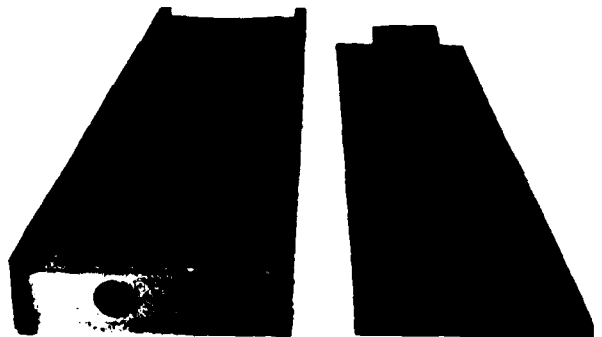


Figure 5: "Twin" Blumlein in final stage of assembly.

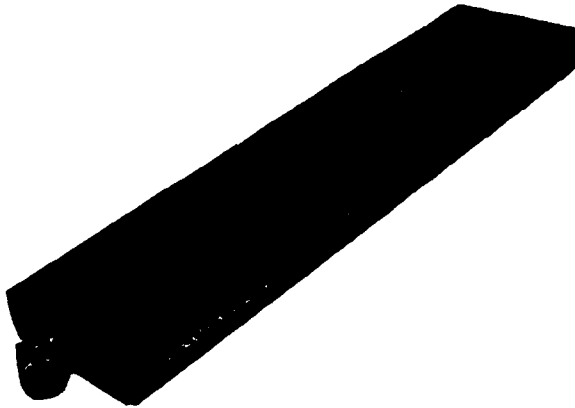


Figure 6: Completed Pressurized "Twin"
Blumlein High Voltage Pulse
Forming Network.

The completely assembled unit measures 23 1/4"
5-3/4" wide, and 1-3/4" thick. The electrical
and pressure characteristics of this PFN are:

Operating Voltage ----- Up to 30 kV so far
Operating Pressure ----- 100 psig
Total Capacitance ----- 50 nF (measured)
Output Capacitance ----- 12.5 nF (measured)
Switch Side Inductance - <1 nH (calculated)
Output Impedance ----- ~0.3 (calculated)
Ultimate Lifetime ----- Not Known
Heat Transfer Rates ---- Not Known
Unit has been operated in thyatron and
spark gap switched laser plasma circuits.

Summary

This paper has described a still incomplete research program intended toward the development of industrial quality high voltage pulse forming networks and pulsed capacitors. The basic objectives are good reliability (that is 10^{10} to 10^{12} cycles before failure), low inductance (<1 nH), low output impedance (0.5 or less), high heat transfer characteristics to accommodate high repetition rates, single unit packaging with serviceability, and reasonable cost. Our investigation of the pressure quenching of the internal corona that occurs in typical PFN structures prompted us to construct a prototype pressurized "Twin" Blumlein PFN in order to demonstrate the possibility of meeting the above requirements. The prototype PFN appears to have been successful, although testing has not been completed, and more materials questions have been raised than answered.

1) The reason for our selection of Dioctyl phthalate along with many other helpful ideas can be found in: Hughes Aircraft Company TECHNICAL REPORT AFAPL-TR-77-40, December 1976, Robert D. Parker.

DEVELOPMENT OF SOLID DIELECTRIC ENERGY STORAGE LINES*

Roger G. Little and Ward Halverson
Spire Corporation
Bedford, Massachusetts 01730

Summary

Materials and techniques for the design and construction of solid dielectric energy storage lines are reviewed, and the development of a 9-ohm line capable of highly repeatable, nearly square 200-kV pulses is described.

Introduction

Energy storage in d.c.-charged, solid dielectric lines is attractive in many applications where highly reproducible, submicrosecond pulses are required. A single spark switch can discharge a charged line into a matched load to produce nearly "square" pulses with very short rise and fall times and no prepulse. Several lines can be stacked and triggered simultaneously or sequentially with very little jitter.

Spire Corporation recently undertook the development of d.c.-charged dielectric lines to form 200-kV pulses with a risetime of less than 15 ns and a duration of 40 ns. A cylindrical line with 9-ohm impedance, charged to 400 kV and discharged into a matched load, was designed to satisfy these requirements. Figure 1 is a conceptual diagram of the solid dielectric line, trigatron spark switch, and field-emission diode to produce a high-power pulsed electron beam. The energy store can be d.c.- or pulse-charged through the high-voltage termination at the end of the line.

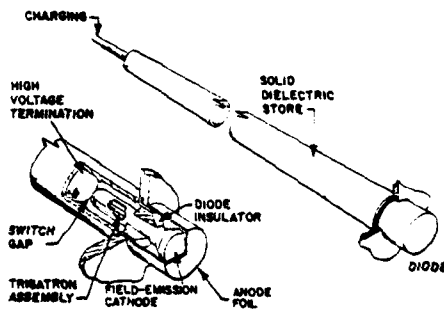


Figure 1. Solid Dielectric Line Driving Field-Emission Diode

In addition to the electrical specifications, a minimum lifetime of 1000 pulses at full charging voltage was set for the charge store. The physical design of a solid dielectric line and the choice of dielectric material are probably the most important considerations for achieving long lifetime and good holdoff from flashover at high-voltage terminations. Requirements for the dielectric material included high intrinsic breakdown strength, a relatively flat dielectric constant and dissipation factor at high frequencies, good resistance to surface flashover, and ease of handling and forming into the configuration of a coaxial transmission line. In this paper we discuss the techniques which ultimately produced a 9-ohm solid dielectric energy store line which achieved or surpassed all the initial design goals.

*Work supported in part by Defense Nuclear Agency.

Lifetime of Pulsed Dielectrics

The lifetime of a dielectric material periodically stressed by pulsed or static electric fields depends on several factors. The principal ones are the maximum working electric field and the waveform of the pulse imposed on the material. Additionally, the volume of stressed material enters weakly in the ultimate breakdown strength of a given sample.⁽¹⁾ These effects can be expressed as a simple, semiempirical formula,

$$L \approx \left(\frac{K_i}{E_{\max} V^{1/10}} \right)^n \quad (1)$$

where L is the shot lifetime, K_i is the intrinsic dielectric strength of 1 cm³ of material, E_{\max} is the maximum working electric field, V is the volume of stressed material in cubic centimeters, and the exponent, n , is typically 7 to 8.^(1,2)

It is evident from Equation (1) that the choice of materials with high dielectric strength and careful design to reduce enhanced field regions are imperative for long lifetime. Furthermore, high temperatures and irradiation by ultraviolet or x-rays must be minimized because of their known tendencies to reduce the breakdown strength of dielectrics.⁽²⁾

A number of materials were tested for use as the dielectric in the energy storage line. Small-sample measurements of the d.c. dielectric strength of the materials were performed in a high-voltage testing facility. Polyurethanes and epoxies were cast around shaped electrodes spaced by a known distance, and sheet materials were compressed between similar electrodes in an oil bath.

Table 1 shows the materials tested, the expected intrinsic dielectric strength from manufacturers' specifications (when available), and the results of the small-sample tests conducted by Spire. The values indicated by the "greater-than" symbols represent the voltage limit which could be placed between the electrodes of the test fixtures. Time limitations of the development program precluded retesting the cast materials with smaller spacing between the electrodes. It appeared from the small-scale tests that the most promising materials for the line were polyurethane, Mylar, and epoxies.

Design Considerations

An engineering analysis of the requirements of the pulser showed that a 8- to 10-ohm line discharging into a matched field-emission diode gave the best performance for the system. A coaxial geometry with a 9-ohm wave impedance and a round-trip travel time of 40 ns was selected for the line. The line was designed to be charged by a small Van de Graaff generator connected through a probe to the center conductor, although a high-voltage electronic power supply could also be used for charging.

The 9-ohm line was designed with an outer diameter of 12.7 cm and an inner cylindrical conductor of 9.7-cm diameter. At a charging voltage of 400 kV, the maximum electric field on the dielectric was 300 kV/cm.

Equation (1) predicts a lifetime greater than 10,000 pulses for a material with an intrinsic dielectric strength of 3 MV/cm. This expected lifetime was considerably greater than the nominal 1000 shots required for the application.

TABLE 1. DIELECTRIC STRENGTHS OF MATERIALS
CONSIDERED FOR 9-ohm LINE

Material	Expected Value (MV/cm)	Measured Value (MV/cm)
Lucite (Polymethyl- methacrylate)	3.3	2.8
Mylar (Polyethylene terephthalate)	3.6	3.4
Polyurethane USC ⁽¹⁾ UEP ⁽²⁾	3.0 —	1.1 3.0
Epoxy DS ⁽³⁾ 5009 E&C ⁽⁴⁾ Stycast 2850 E&C Stycast 1264	— 3.2 2.9	1.4 1.8 3.0

Notes:

- (1) Urethane Systems, Inc., Stockton, California
- (2) Urethane Engineering Products, Inc., Johnston, Rhode Island
- (3) Dielectric Sciences, Inc., Woburn, Massachusetts
- (4) Emerson and Cuming, Inc., Canton, Massachusetts

The high-voltage termination at the diode end of the line was designed to be part of a trigatron spark switch. The interface region where the high-voltage termination, the dielectric material, and the insulating gas around the switch all meet is a "triple-point"; triple-points are well known to suffer from flashover and volume breakdown. Furthermore, ultraviolet radiation, charged particles, and highly reactive chemical compounds are generated in the nearby spark switch.

The design of the switching termination of the line was aided by a computer calculation of the electric field distribution in the critical region of the triple-point. The code FFEARS⁽³⁾ was used to generate the potential plot shown in Figure 2. An important result of the analysis was the design of the wedge-shaped dielectric extension which partially covers the high-voltage termination. This design greatly reduces the potential gradient in the triple-point area; later testing confirmed that dielectric failures were virtually eliminated in this region.

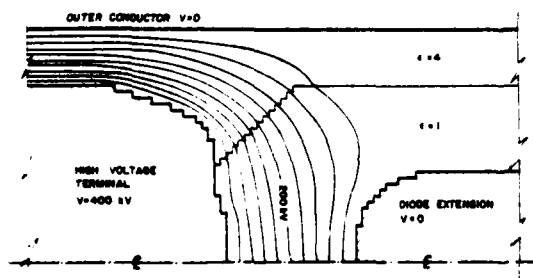


Figure 2. FFEARS Analysis of Region of High-Voltage Termination and Spark Switch

Construction and Testing Program

Mid-scale lines, with lengths of 120 cm and diameters approximately the same as the full-scale lines, were fabricated of the most promising dielectric materials. Polyurethane and epoxies were cast and Mylar sheet was wrapped around cylindrical center conductors. The outer cylindrical electrode of the lines was formed by metallic paint. A Lucite line was made by painting a metallic layer over the inside and outside of prefabricated tubing obtained commercially. The end triple-points at the high-voltage terminations were molded with epoxy to reduce the electric field in these regions.

The mid-scale lines were charged by a Van de Graaff generator and discharged into an 8-ohm dummy load. The charging characteristics, discharge waveshape, and tendency to develop corona discharges and flashover were evaluated in these tests.

Two types of dielectric failure became evident in the testing of mid-scale lines. First, volume punctures developed in the cylindrical dielectric material between the inner and outer conductors of the charged line and other regions of high stress. These breakdowns occurred during both charging and pulsing of the line. The punctures had characteristic multiple breakdown channels in a tree-like pattern. The second type of failure was located in the switch region and occurred after several discharges through the spark switch. The breakdown channel was a direct puncture to the ground plane and was usually displaced several centimeters from the switch termination.

The first type of failure occurred only in the materials which showed low intrinsic dielectric strength in small sample testing. The second type, which was always within the line-of-sight of the spark switch, may have been initiated by surface flashover and damage from the products of the spark. We found that both types of punctures in cast dielectrics and Lucite could be successfully repaired with high-dielectric-strength epoxy.

Full-scale lines of 365-cm length were fabricated of polyurethane, Lucite, and Stycast 1264 and 2850 epoxies. The lines were pressurized in dielectric gas in a vessel which also contained a Van de Graaff generator for charging and a copper sulfate resistor as a dummy load. The lines were repetitively charged and discharged, and the voltage and current waveshapes of the discharge were monitored on high-speed oscilloscopes.

The results of testing the full-scale lines were very similar to those of the mid-scale lines. The polyurethane line developed volume punctures in the cylindrical body of the dielectric. The higher strength Lucite and Stycast 2850 punctured in the switch region after several shots, including a number of flashovers of the high-voltage terminations. The Stycast 1264 epoxy, on the other hand, showed excellent resistance to surface flashover, and the full-scale line cast of this material successfully completed a 1000-shot lifetime test at full charging voltage with no apparent change in the electrical characteristics of the output pulses. A 10 percent - 90 percent risetime of 15 ns and a pulsewidth of 45 ns (FWHM) are typical of the output pulse.

Applications

Since the completion of the development program of the solid dielectric energy store, the 9-ohm line has been used routinely to drive a field-emission diode which produces a high-power pulsed electron beam. The beam has been used to generate x-ray bremsstrahlung, to study electron beam propagation, and to pulse anneal ion implantation damage in semiconductors. The line has been charged and discharged more than 6000 times without failure; most of this operation has been at the full charging potential of 400 kV. Figure 3 is a photograph of the

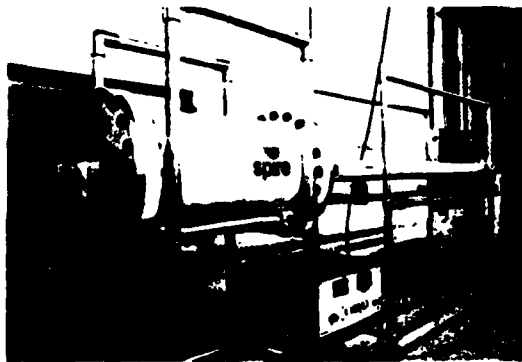


Figure 3. SPI-PULSE 600 Electron Accelerator
Driven by 9-ohm Solid Dielectric Line

high-voltage pulser, designated SPI-PULSE 600, in which the 9-ohm line is the energy store. In this pulser, the line and its Van de Graaff generator (at left) are housed in a 100-psi pressure vessel for the insulating gas used to suppress corona and flashover. The diode assembly is located in a vacuum housing (at right), which is an extension of the pressure vessel.

Spire is using the same dielectric materials and fabrication techniques to build other types of energy storage lines for pulsed electron beams. Figure 4 is a photograph of the solid dielectric energy store of the SPI-PULSE 300 pulser designed for semiconductor processing. This line, when charged to its normal operating potential of 100 kV, will have an almost unlimited lifetime because of the high strength and good resistance to surface flashover of the solid dielectric material used for its construction.



Figure 4. Solid Dielectric Energy Store of
SPI-PULSE 300

We believe that there are many other applications for solid dielectric energy storage lines where inherent simplicity, reliability, and ease of maintenance in a large system are important considerations. Laser drivers, pulsed x-ray generators, and pulse generators for particle beam fusion are only a few of the possible applications for this technology.

References

1. J. C. Martin, "Volume Effect of the Pulse Breakdown Voltage of Plastics", in "Pulsed Electrical Power Dielectric Strength Notes, PEP 5-1", Air Force Weapons Laboratory, Kirkland AFB, NM, Report No. AFWL TR-73-167 (1973).
2. A. S. Denholm et al., "Review of Dielectrics and Switching", Air Force Weapons Laboratory, Kirkland AFB, NM, Report No. AFWL TR-72-88 (1972) Section 6.
3. J. E. Boers, "FFEARS, A Digital Computer Program for the Simulation of Laplace's Equation Including Dielectric Interfaces and Small Ungrounded Electrodes", Sandia Laboratories Report No. SC-RR-71 0377, Albuquerque, NM (1971).

HIGH POWER CAPACITOR TECHNOLOGY*

Robert D. Parker
Technology Support Division
Hughes Aircraft Company, Culver City, California 90230

Abstract

This paper reports the final results of an exploratory development program for capacitors for use as energy stores with a high rate of power transfer. (Previous reports have detailed the advances made with improved winding techniques and constructions.) It was found that very lightweight cases were easily built but very delicate, and that the overall weight of a capacitor is more sensitive to encasement details than has been previously thought; detailed examples are given. A flame treatment process to smooth foil edges resulted in a 5 to 10 percent improvement in capacitor CIV. Two promising techniques for terminating extended foil sections were developed; electron-beam welding in this application was the subject of a patent filing. Tests of two types of 15 kV components in a PFN simulator at 150 to 300 pps, burst duty, demonstrated energy densities between 21J/lb and 77J/lb for the finished capacitors. Tests in a full 6 section type E PFN (20 μ s) confirmed these values, and in addition provided temperature rise data. Over 270,000 shots were run with no failures.

Introduction

For a long time it has been suspected that the presence of folds, wrinkles, tears, and globs of impurities is deleterious to the reliability, life, and energy density of energy storage capacitors¹. Studies of specific insulation systems have proved the role of water² and low resistivity dielectric fluid³ in some types of failures. There have been research studies on new polymeric insulating materials⁴, and on the properties of one or another of the constituents of commonly used systems^{5,6}. However, there is very little published work on detailed efforts to design and produce improved capacitors⁷, the majority of the work describing test results and giving only the vaguest allusion to changes in materials or construction details which contribute to the reported improved test results⁸.

The hypothesis which was tested in the preliminary phase of the program described in this paper was that improvements in reliability, life, and energy density could be made with existing materials simply by making the capacitor structure physically more perfect⁹. From this hypothesis came the technique of winding capacitor sections in an already-flattened configuration using tension control of each web, the use of highly purified dielectric fluids, and the use of computer analyses to determine capacitor performance at the operating point¹⁰.

This paper reports the final phase of this capacitor development program. New techniques were tried in case construction, foil edge modification, and extended foil termination. Three different types of component were designed, fabricated, and tested both in and out of an actual PFN.

PFN Environment

It has been previously shown¹¹ that the details of PFN construction as well as the exact circuit in which the PFN is employed have a profound effect on the

survival of the capacitors used in the PFN. For this reason, and also to ensure the desired pulse shape¹², it is useful to analyze the electrical conditions to which each capacitor is subject.

Specification

One unusual feature of this program was that the capacitors were to be developed and tested to one set of specifications, and then assembled into PFNs and tested to a slightly different set of specifications. The capacitor specifications were:

Voltage:	15 kV
Pulse Width:	20 μ s
Pulse Rate:	300/s
Pulse Train Length:	2×10^4
Time Between Pulse Trains:	2h
Life:	10^6 pulse
% Voltage Reversal:	20

while the PFN specifications were:

Type:	E
Number of Sections:	6
Voltage:	15 kV
Stored Energy:	1.5×10^3 J
Pulse Shape:	Rectangular
Pulse Width:	20 μ s
Pulse Rate:	300/s
Pulse Train Length:	2×10^4
Time Between Pulse Trains:	2h

It quickly is apparent that the PFN specification imposes much more difficult conditions on the capacitors in terms of peak current (and therefore power dissipation) because of the pulse width. The capacitors themselves were to work at a 20 μ s pulse width; in the PFN, they must produce a pair of pulses about 1.5 μ s wide.

Computer Modelling

The capacitor current waveform for both charge and discharge was modelled on a computer, so that the constituent frequency components could be found. These were used to calculate total power loss in the capacitors, since it was possible to measure the equivalent series resistance (ESR) as a function of frequency. The values found are given in Table I for a 20 μ s wide current pulse for each capacitor, and in Table II for a capacitor in a 6-section 20 μ s PFN. A check was made on the computer analysis by comparing computer-generated current waveforms, as in Figure 1, with actual waveforms measured from low voltage model PFNs. Notice in the tables the unsurprising result that the power loss for the short pulse is several times larger than for the long pulse. Power loss depends on the square of the RMS current, which is clearly larger for the short pulse.

*Supported by the U.S. Air Force Aero Propulsion Laboratory under Contract F33615-75-C-2021.

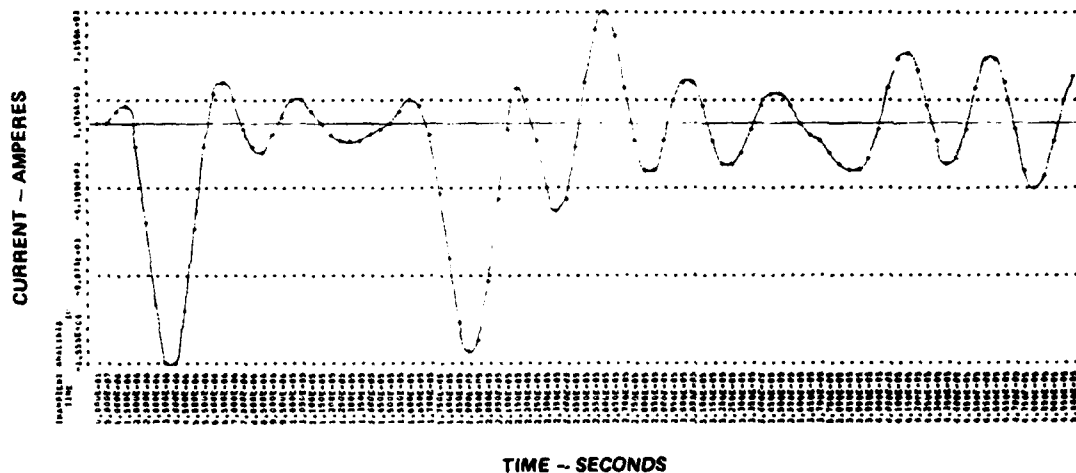
Table I. Capacitor Current Spectrum

	Charge	Discharge					Sum
		Frequency Components					
		f_1	f_2	f_3	f_4	f_5	
Frequency, kHz	0.15	12.5	25	37.5	50	62.5	
Current, A Rms	2.9	26.4	28.2	16.3	8.6	5.3	46.5
Typical Loss, Watts	10	45	41	12	3.2	1.1	114

Notes: a) 300 pps rate assumed, operating into matched resistive load
b) Current values for 1.0 μ F capacitor
c) Power loss for polysulfone/kraft construction

Table II. Capacitor Current Spectrum, 20 μ s PFN Output

	Charge	Discharge					Sum
		Frequency Components					
		f ₁	f ₂	f ₃	f ₄	f ₅	
Frequency, kHz	0.15	75.5	151	226	302	337	
Current, A Rms	2.9	66.7	71.3	41.1	21.8	13.3	117
Typical Loss, Watts	10	173	178	57	16	5.7	506

Figure 1. 20 μ s PFN, Capacitor Current Waveform

The ESR of capacitor sections of various types was laboriously measured, using several different apparatuses at different points in the frequency spectrum. This data is displayed in Figure 2, plotted together with the squares of the currents from Tables I and II. This gives a visual idea of the expected power dissipation, since it is simply the product $I^2 \times \text{ESR}$.

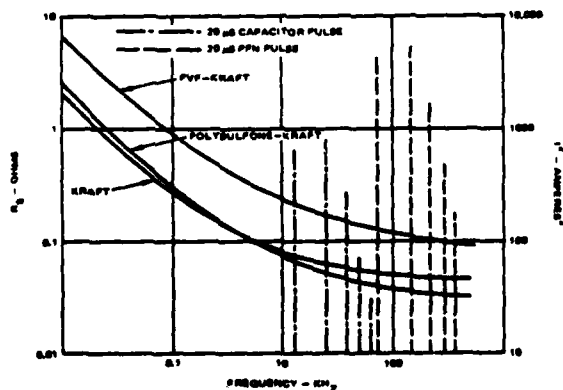


Figure 2. ESR and Harmonic Discharge Current

Foil Edge Investigation

It has been previously suggested that it might be possible to reduce failures at capacitor foil edges by smoothing off the rough projections. If the failures

were reduced, it might then be possible to operate the components at higher energy density. Some preliminary work had been conducted [3], an extension of which is reported here.

A typical sheared edge of a 6 μ m Al capacitor foil is shown in Figure 3, in a scanning electron micrograph (SEM). All experiments were performed on this type of foil. Testing consisted of edge treatment, SEM examination, and corona inception measurement in an oil-filled two plate capacitor designed to provide maximum electrical stress at the treated foil edge.



Figure 3. Sheared Capacitor Foil Edge as Received

Four different processes were evaluated: laser cutting, spark erosion treatment, fine grit blasting, and flame treatment. Of these, the spark cutting and flame treatment were the most successful.

Spark Erosion Treatment

Spark erosion cutting was done on a Charmille machine. This machine is used for removal of broken taps and machining of precision parts such as apertures and blind grooves. A matrix of cutting parameters was established. The control parameters which influence edge shape were cutting tool feed rate and spark energy.

Additional tests were performed on multiple pieces of foil stacked up. Particulate contamination was excessive near the cut edge. This contamination naturally was minimized on the stacked material. Cutting of this type would not be recommended on the winding machine because of the creation of particulate contamination by the process. Rolls of material could be pretreated by spark erosion machining of the entire roll of foil. To efficiently do this, the foil should be supplied on an aluminum core rather than the usual cardboard core.

Flame Treatment

It was speculated that a torch flame could be used to remelt the foil edge to eliminate the sharp points. Initial tests produced non-local heating and distortion because aluminum is such a good heat conductor. Laying the foil on cooled surface solved that problem. A propane torch which had a poor flame control was used. However, it was expected that the rounding could be observed using this torch and, if the technique had any validity, finer methods of control of the torch would be evaluated. The concept of a large heat sink in contact with the foil worked so well that further work on better torches was unnecessary. The basic conclusion was that large variations in flame distance and size will burn off or remelt the edge of the foil away from the heat sink and stop its action where the aluminum foil is well heat sunk. It is expected that a heated air jet would behave equally well, although this was not checked. A typical edge is shown in Figure 4.



Figure 4. Flame-Treated Foil Edge

A torch treatment method would be very easy to build into a conventional capacitor winder. A water cooled metal roller would be necessary in the treatment area.

Corona Testing

A simple fixture employing a five-layer insulation of alternate layers of 0.3 mil kraft and 32 gauge polysulfone was used. The fixture was placed in a pyrex dish and vacuum baked at 105°C for one hour at 30 to 50 microns pressure. It was then filled with processed mineral oil while in the vacuum chamber. The filling was done over a 1/2 hour period. Each fixture filling had a number of preprepared sample stacks consisting of insulation and aluminum foil under the oil surface. These were positioned as shown using tweezers. The samples were not moved above the oil surface during positioning so no air bubbles were trapped.

The corona inception voltage (CIV) of each specimen was measured. It was found that each of the tested treatments improved the CIV over untreated foil, the improvement being in the 5 to 10 percent range.

Case Weight Minimization

In a conventional capacitor of the size considered on this program, the case, case insulation, and terminal are an appreciable fraction of the total capacitor weight. This is illustrated vividly in Table III. Therefore, the development of two different types of lightweight case, metal and plastic, was undertaken. Because of the exploratory nature of this program, and because the exact intended conditions of use are not known and are presumed to be changing, little consideration of the operating environment was given. For example, the stainless steel encased units are very light and hermetically sealed, but they break if dropped and probably would not function well in a variable pressure environment unless the sides were stiffened.

Table III. Weight of Capacitor Parts, Standard Unit

Item	Weight (kg/lb)
2-3 pad bundles	2.63/5.79
Case and terminal	9.5/2.1
Epoxy board	0.29/0.64
Case insulation	0.25/0.56
Oil	1.09/2.4
Total	5.22/11.5

Metal Cases

It was decided to design and fabricate as light a metal case as was possible to assemble. The capacitor chosen for assembly into the case was a very lightweight 250J unit. The case itself is made of 5 mil stainless steel sheet. It is carefully folded into shape and spot welded to hold it together. The seams are then soldered; the soldering is facilitated by a 0.3 mil tin plating. Soldering was chosen over brazing because of the ease of assembly. The fill-port and ground posts are also made lighter than those usually used. The entire case without bushing weighs 75g. A completed capacitor using this case is shown in Figure 5.



Figure 5. Very Lightweight Energy Storage Capacitor

A much larger design was then attempted, to house a 500 joule (1.1 μ F 30 kV) capacitor. A scaled up version of the previous design, this case also had a larger fill port and only one ground post.

Both cases were moderately difficult to assemble, because of the care required in soldering the seams and handling the flimsy cans before the capacitors were assembled into them. The smaller case contained the capacitors well during testing, but the larger case failed catastrophically in two instances. Standard ceramic bushings were used for both cases. However, for airborne operation high voltage connectors could be used, saving approximately 80 percent of the bushing weight of 57g.

Plastic Cases

Three fiberglass containers were designed and fabricated, to test their use as capacitor cases. Cases of this type have 3 main advantages: light weight, high strength, and built-in high voltage terminals. Plastic cases are not, however, considered hermetic, and therefore have not been considered for airborne use.

The case size chosen was 5.48 x 7.13 x 5.0 inches, with 0.875 inch corner radius and 0.05 inch wall thickness. The containers were formed of 6 layers of epoxy-glass prepreg, using a metal tool and the standard vacuum bagging technique. A flat lid was used, and the high voltage connectors consisted of studs molded into the lid.

One case was used for a distension test. It was found that a pressure difference of 5 psig produced distension sufficient to accommodate the volume change expected from a capacitor assembly over the range -50°C to +90°C. The strength of the container was substantially in excess of 10 psig.

Another case was used for electrical testing. A 10 section 3 μ F capacitor was assembled into it, and oil impregnated. Electrical tests revealed no problems with the terminations. However, temperature

cycling revealed a slight oil seepage through the resin/glass composite. It was concluded that this effect could be eliminated with a gel coat applied to the interior of the case.

Extended Foil Termination

Conventional tab-type terminations work well in PFNs with pulse widths above 20 μ s, but detailed analyses show that an extended foil construction is necessary to achieve a low ESR if the pulse width is 10 μ s or below. Required inductance should not influence termination choice, as it has been shown that very low inductance tab-type constructions are possible¹⁴.

Selection of Techniques

As customarily practiced in the capacitor manufacturing industry, an extended foil termination is made by smearing solder on the foil protruding from the end of the section. This technique is at best uncontrolled and subject to wide variation in contact resistance and therefore failure rate. Therefore, other methods not usually applied to extended-foil terminations where foil is used were investigated as well.

Four techniques were examined:

- Commercial soldering.
- Oxy-acetylene welding in nitrogen.
- Flame-spray of metal.
- Electron beam welded strips.

The commercial technique was investigated to determine if the process could be made well controlled and repeatable. The oxy-acetylene welding was tried to see if a carefully controlled bead could be obtained. The flame spray technique is customarily used on commercial metallized film capacitors, and Hughes had recently developed techniques to produce uniform repeatable low resistance terminations. The electron beam welding was the technique thought to have the most promise, inasmuch as it can be very precisely controlled.

Contact Resistance Tests

In order to test the efficacy of various techniques, test specimens for the measurement of contact resistance were made. Both the commercial solder technique and the gas welding produced sloppy, poorly controlled joints which were obviously high in conductive particle residue. Some problems with the solder wetting the foil were encountered. However, an aluminum solder¹⁵ was not tried, because of an esthetic reluctance to use the necessary extremely corrosive flux.

For the flame spray tests, two different materials were used in the spray:

- Babbitt only
- Aluminum with babbitt on the top.

For the electron beam work, straps 0.016 inch (0.04 cm) of alloy 2024 were welded to the sample ends. Samples of both flame spray types and the electron beam weld were temperature cycled. The DC contact resistance of all specimens was acceptably low, and no changes were observed after temperature cycling. Microsectioning revealed some particulate penetration for the flame spray, and a very clean electron beam termination.

Pulse Testing

Capacitor sections terminated with flame spray and with electron-beam welding were assembled and pulse tested. The sections were 2.2 μF , 7.5 kV nominal, similar to the sections used in the 15 kV capacitors. Tests revealed satisfactory flame-spray performance, but the electron-beam units failed. Dissection showed that the welding had slit the insulation, a problem which could be solved by closer process control. A patent application has been filed on the electron beam technique.

Conclusions

The really intriguing development uncovered in this work is the use of electron beam welding to terminate extended foil capacitors. The connections were very good, but further process development would be necessary to eliminate the dielectric cutting observed in these specimens. The termination is mechanically fragile, but very clean.

The flame-sprayed babbitt terminations are acceptable and uniform, but have an inherent problem with particulate contamination.

Complete Capacitors

Two of the types of capacitors that were fabricated and tested have been briefly described elsewhere¹⁶, and are described in this section. These components were designed for high repetition rate operation, and differ in the impregnant, the electrical stress, and the energy density.

The heavier of the two components was designed directly from the results of the pad tests, and was placed in a conservative, well-constructed metal box such as is normally used on military-type components of that size. The lighter component utilized a different impregnant and field balance, and was encased in a very lightweight stainless steel case, which was designed as part of the case weight minimization study. Basic constructions are given in Table IV. The third capacitor type was a higher energy extended foil version of the lightweight component; its fabrication and test are described elsewhere¹⁷.

Table IV. Capacitor Construction Details

	Standard	Lightweight
Stored Energy	250 J	250 J
No. Sections-Series	3	2
No. Strings-Parallel	2	2
Dielectric Fluid	Mineral oil	DOP
No. Dielectric Layers	5	5
Margins	0.375	0.25
Termination	tab	tab

It was determined by a series of indirect measurements that the thickness of the oil layers in these components was 1.0 μm for each pair of surfaces. Thus, a component with 5 solid dielectric layers also contained about 6.0 μm of fluid. This is approximately 32 percent less fluid than is normally found in an oil-filled capacitor. The extreme thinness and uniformity of the fluid layers is thought to be partially responsible for the high layer operating fields and uniform degradation found experimentally.

Field balance calculations were performed for both components using the results determined in the preceding paragraph. These calculations are summarized in Table V.

Table V. Electric Field Balance

	Standard	Lightweight
Average Stress	3750 V/mil	4460 V/mil
Layer Stress Paper	1904 V/mil	3430 V/mil
Plastic	2918 V/mil	5256 V/mil
Oil	4113 V/mil	2761 V/mil

The weights of the individual parts of each component are shown in Table VI.

Table VI. Capacitor Weights

	Standard	Lightweight
Sections (wet)	3.126 kg	1.126 kg
Case	892 g	96 g
Terminal	57 g	57 g
Case Insulation	546 g	102 g
Extra Oil	599 g	101 g
Totals	5.22 kg	1.482 kg
Specific Weight	20.88 g/J	5.93 g/J
True Energy Density	0.087 J/cm ³	0.265 J/cm ³
"Energy Density"	21.7 J/lb	76.5 J/lb

Capacitor Tests

Two different types of tests were run. All capacitors were tested in a single-capacitor test bay, and then PFNs were assembled according to the specification given in the second section and tested with a large power supply and load.

Experimental Details

The test bay used to test one capacitor at a time to the 20 μs width requirement has been previously described¹⁰. Four modifications were needed to test the 2.2 μF 15 kV capacitors (instead of the 1.1 μF 7.5 kV pads previously tested). A new larger power supply was designed and built; this was capable of 0 to 8.5 kV at 11A. It was designed to operate from 3 phase 400 Hz power, to avoid harmonic resonances of 60 Hz at higher repetition rates. The load resistors¹⁸ were changed to a new value. The overload cut-outs, clipping circuits, and current metering circuits were all adjusted to the higher value. Finally, the thyatron was changed from an HY-5 to an HY-5001 to handle the increased current.

Single Capacitor Test Results

The plan of test as prescribed by the statement of work was more of a proof-of-design (POD) test than a developmental test. Inasmuch as it was felt that this work was still in the developmental stage, a developmental type test was used.

The summary of testing for the standard component is given in Table VII. Serial 2 was a demonstration unit, and serial 15 is a 5-tab-per-foil experimental model. Temperature rise data was taken by attaching

a thermocouple to the center of the capacitor end. The case temperature rise was 3 to 5°C at the end of the burst, and 25°C 25 minutes after the burst. Components which were "screened" were checked for infant mortality only. It was required to assemble the PFNs from these components.

Table VII. Pulse Test Summary, Standard Units

Serial Number	Total Shots (1000s)	Voltage (kV)	Notes
1	233	15.0	OK
2	Not tested		
3	220	15.0	OK
4	223	15.0	OK
5	11	6.5	Failed
6	113	12.5	Shorted
7	107	15.1	OK
8	32	4.0	Failed
9	36	7.5	OK*
10	51	7.5	OK*
11	52	7.5	OK*
12	31	7.5	OK*
13	50	7.5	OK*
14	51	7.5	OK*
15	-	7.5	Failed

Capacitors screened for use in PFN.
Duty was 130 pps for 1 minute, 2 hours between bursts, or equivalent.

The summary of testing for the lightweight parts is given in Table VIII. Temperature measurements showed a 30°C rise after the burst.

Table VIII. Pulse Test Summary
Lightweight Units

Serial Number	Total Shots (1000s)	Voltage kV	Notes
1	32	15.0	Failed
2	146	13.5	Failed
3	187	14.0	OK
4	49	7.5	OK*
5	156	14.0	OK
6	176	14.0	OK
7	51	7.5	OK*
8	51	7.5	OK*
9	67	7.5	OK*
10	51	7.5	OK*
11	50	7.5	OK*
12	51	7.5	OK*

*Capacitor screened for pulse forming network.

Of the twenty-six components tested, there were six failures - four standard and two lightweight. Of the standard units, two were bulk or random dielectric failure, one was edge failure, and one (S/N 015) was a tab failure ascribed to a manufacturing defect. Both lightweight failures were at the foil edge. No case rupture or fluid leakage occurred on failure.

PFN Test Experimental Details

The PFN tests were accomplished at the High Power Laboratory of the Rome Air Development Center, Griffiss AFB, New York. A standard line-type modulator circuit was employed, and the equipment from the large test bay was used¹⁹. An exposed copper coil was used for the PFN inductance, and was designed so that either the standard or the lightweight capacitors could be tested. The actual measured pulse width, zero-to-zero, was 24 μ s.

Test Results

Throughout the testing, triggering problems were encountered with the switch tubes, so that occasionally the exact test profile desired could not be run.

The initial tests were run on standard components for the purpose of checking the waveshape. The observed pulse was rectangular. The minimum charge time was determined by the power supply and charging reactor.

A summary of the test data using the standard capacitors is given in Table IX. The capacitors performed well in this service. During the testing, the case temperature of C₆, the most highly stressed unit, was monitored. It was noted that C₆ was noticeably warmer than the other five capacitors. Referring to Table IX, runs 10 to 13 were accomplished in a period of about 8 minutes. The maximum case temperature of C₆ occurred 47 minutes after the test, and was 12°C larger than the starting temperature. The peak current at 15 kV was 9600A.

Table IX. Standard Capacitor PFN
Testing Summary

Run Number	Rate	Voltage (kV)	Total Shots
1	100	6	60,000
2	125	7	75,000
3	125	3	15,000
4	125	7	5,625
5	125	10	7,500
6	125	13	7,500
7	5	15	1,200
8	30	15	5,400
9	>200	15	4,500
10	>200	15	15,000
11	3	15	360
12	33	15	1,650
13	125	15	15,000

Because of the time pressure, and because the Project Monitor expressed the desire to have at least 6 good lightweight units, it was decided to replace C₆ in the standard line with a lightweight capacitor, S/N 12, rather than use all 6 lightweight units. This component was instrumented for case temperature measurement, and four additional runs were made. This data is shown in Table X. The component got quite warm, but performed well. Temperature data is shown in Table XI.

Table X. PFN Data with 1 Lightweight
Capacitor

Run	Rate	Voltage (kV)	Total Shots
14	50	10	9,000
15	50	13	4,500
16	50	15.0	9,900
17	>200	15.0	16,500
18	50	15.0	18,000

Table XI. C₆ Case Temperature Data

Run	T _{initial} (°C)	T _{final} (°C)	T _{max} /Time
14	26	32	41/13 min
15	41	43	49/10 min
16/17	36	51	66/10 min

Note: T_{max}/time means the maximum case temperature (°C) at how long after the run.

Conclusion

The capacitor development program reported herein, and in previous reports¹⁰, has shown that the basic hypothesis of improving energy density and reliability over commercially-built components by making capacitors more mechanically perfect is a fruitful one. Moreover, in the process of developing a pulse-discharge capacitor technology, numerous improvements applicable to other types of capacitors as well have been made.

A complete, detailed final report¹⁷ has been prepared on this work.

Acknowledgement

The author is grateful to Michael P. Dougherty, the Air Force Project Monitor, and Richard Verga, both of the Aero Propulsion Laboratory, for their continued support. Bobby R. Gray of the High Power Laboratory, Rome Air Development Center, performed the PFN tests and furnished the test bay and much valuable advice.

References

- Boicourt, Grenfell P., "Problems in the Design and Manufacture of Energy Storage Capacitors", Los Alamos Scientific Laboratory Report LA-4142-MS, January 1970.
- Boicourt, Grenfell P., "The Diagnosis of Under-Drying in Paper Castor Oil Capacitors", Los Alamos Scientific Laboratory Report LA-UR-75-2128, 1975.
- Shaw, David G., "AC Conduction in Impregnated Polymer Insulating Systems", IEEE Trans. Elec. Insul. Vol. EI-10, June 1975.
- Buckingham, K. A., and Reddish, W., "Low-Loss Polypropylene for Electrical Purposes", Proc. IEE, Vol. 114, November 1967.
- Bartnikas, R., "Dielectric Loss in Insulating Liquids", IEEE Trans. Elec. Insul., Vol. EI-2, April 1967.
- Hakim, Raymond, "The Effect of Oxidation on the Dielectric Properties of an Insulating Oil", IEEE Trans. Elec. Insul., Vol. EI-7, December 1972.
- Loescher, D. H., "High Voltage Failure of Mylar Energy Storage Capacitors", Sandia Laboratories Technical Report, SAND75-0440, 1975.
- Creedon, John E. and Fitch, Richard A., "A Half-Megawatt Pulse Forming Network", Proc. IEEE International Pulsed Power Conference, 1976.
- Parker, Robert D., "Energy Storage Capacitors of Very High Energy Density", IEEE Trans. Parts, Hybrids, and Packaging, Vol. PHP-13, June 1977.
- Parker, Robert D., "Interim Report-Capacitors for Aircraft High Power", Air Force Aero Propulsion Laboratory Technical Report AFAPL-TR-77-40, September 1977.
- Dailey, C. L. and White, C. W., "Capacitors for Aircraft High Power", Air Force Aero Propulsion Laboratory Technical Report AFAPL-TR-74-79, July 1974.
- Masten, L. and Burkes, T. R., "Constant Current PFN", Proc. IEEE International Pulsed Power Conference, 1976.
- Parker, Robert D., "Effect of Foil Edge Modifications and Configurational Changes on Energy Storage Capacitor Weight", IEEE Trans. Parts, Hybrids, and Packaging, Vol. PHP-13, September 1977.
- Loescher, Douglas H. and Sidnell, Norman A., "Film Capacitors with Low Internal Inductance", IEEE Trans. Parts, Hybrids, and Packaging, Vol. PHP-13, December 1977.
- Dailey, C. L. and White, C. W., "PFN Characterization and Life Test", Air Force Aero Propulsion Laboratory Technical Report AFAPL-TR-75-69, January 1976.
- Parker, Robert D., "Application of PFN Capacitors in High Power Systems", Proc. IEEE 2nd International Pulsed Power Conference, 1979.
- Parker, Robert D., "Capacitors for Aircraft High Power", Air Force Aero Propulsion Laboratory Technical Report AFWAL-TR-80-2037, January 1980.
- Gourlay, Robert D., "A Compact Low-Inductance Load for Pulse Tests", Proc. IEEE International Pulsed Power Conference, 1976.
- Gray, Bobby R., "Long Pulse Switching of High Power Tetrodes", Proc. 1976 Twelfth Modulator Symposium, 1976.

LOW INDUCTANCE IMPEDANCE TRANSFORMING TECHNIQUES FOR INJECTION LASER ARRAYS

Byong H. Ahn, Dr. Richard R. Shurtz,
Dr. C. W. Trussell and J. E. Miller

Night Vision and Electro-Optics Laboratory
Fort Belvoir, Virginia 22060

Summary

Two impedance transformation techniques are described. The first technique exponentially varies the impedance up to a factor of 5 using a lumped transmission line circuit with a 140 MHz cut-off frequency. The second technique uses an integral laser array-transformer with the semiconductor laser material mounted directly into the single turn secondary. The transformer produces a 144 to 1 impedance transformation with only 18 nanohenry leakage inductance and generates an 83 nanosecond, 1500 ampere pulse through the laser array for a peak light output power of 600 watts when driven by a 0.5Ω impedance, 41.5 nanosecond delay line charged to 200V.

Introduction

During the course of a laser illuminator development program conducted at the Night Vision and Electro-Optics Laboratory, several injection laser array configurations evolved, each with its own electrical (i.e., impedance, inductance, capacitance) characteristics. Because it was desirable to drive these arrays with a common pulse forming network, a method to impedance match the delay line to various non-linear laser diode loads was sought.

Two original configurations to perform this task were developed and fabricated. The first was a lumped transmission line formed by ceramic capacitors in which the impedance was exponentially tapered from the delay line (0.5Ω) to the load ($<0.5\Omega$). The second was a low inductance pulse transformer (12:1) with the laser diodes mounted directly in the single turn secondary.

The overall pulser block diagram is shown in Figure 1.

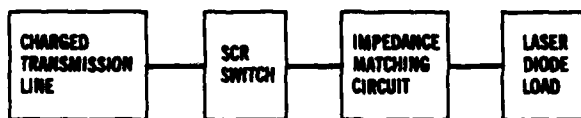


Figure 1. Block Diagram of Pulser

The transmission line is resonantly charged to 200V and discharged through the load to ground by a double bank of SCR's. The transmission line used with the transformer

produces a pulse length of 83 ns and has a cut-off frequency of 38.5 MHz. The one used with the taper has a 90 ns pulse length and a 140 MHz cut-off frequency. The design curves for the characteristics of the transmission lines are described elsewhere in these proceedings.⁽¹⁾ In this paper we discuss only the impedance matching circuit approaches.

Discharge Pulse Shape

The discharge pulse shape of a transmission line coupled to loads representing three matching conditions is shown in Figure 2.⁽²⁾

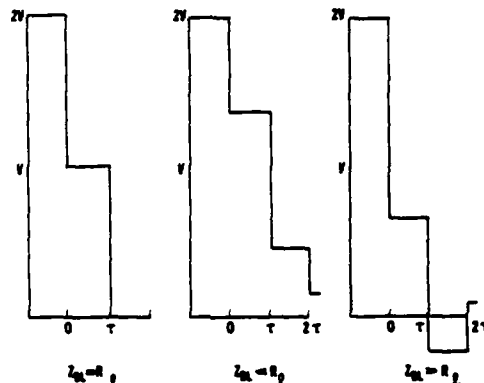


Figure 2. Voltage Discharge Pulse Shapes

In each case, the delay line is charged to 2V, is discharged at time zero, and has a discharge time of τ . In the impedance matched case, the voltage at switch-time drops to 1/2 the delay line charge voltage and remains constant for time τ . All power is transferred to the load during time τ . In each of the mismatch cases, multiple reflections spread the energy transfer over several periods of discharge and result in less power transfer during this 0 to τ time period. We evaluated both matching circuits using measurements of this type.

The Exponentially Varied Transmission Line

The transmission line was formed by soldering ceramic chip capacitors between the conductors of a parallel plate transmission line. The impedance is transformed exponentially between end points. A photograph of one such circuit is shown in

Figure 3. This section transforms the impedance from 0.5Ω to 0.3Ω , while maintaining a 140 MHz cut-off frequency.



Figure 3. Impedance Transformer

The exponential transformation technique is desirable because it can provide broad band matching over the entire band of operation. However, this transmission line must be longer than one wavelength for the exponential character to be seen by the wave. Under normal conditions, such a length is not practical since it would at least be equal to the delay line length. In order to circumvent this limitation, the transition was fabricated to be $\frac{1}{4}\lambda$ at 10 MHz, the key frequency for a 50 ns pulse and $2\frac{1}{4}\lambda$ at 140 MHz, the cut-off frequency. Thus the transition served as a $\frac{1}{4}$ wave matching filter at the lower frequencies and an exponential taper at the higher frequencies, yielding a reasonably broad band performance range.

The impedance of the line is transformed exponentially as:

$$Z = Z_0 e^{-\delta x} \quad (1)$$

where: δ = transformation constant
 x = distance
 Z_0 = impedance at $x=0$

Since the cut-off frequency must be maintained constant over the entire length, both L and C must be varied exponentially as seen below:

$$\begin{aligned} \omega_{co} &= 1/\sqrt{LC} \\ Z &= \sqrt{L/C} \end{aligned} \quad (2)$$

where: ω_{co} = angular cut-off frequency
 $L_{co} = L_0 e^{-\delta x}$ = inductance per unit length
 $C = C_0 e^{+\delta x}$ = capacitance per unit length
 Z = impedance

The product of L and C is independent of x and the ratio varies exponentially as desired. Table 1 shows the design specifications of the transition shown in Figure 3. The total transition length is 1" and the plate separation is 0.1".

Table 1. Transmission Line Design From 0.52Ω to 0.30Ω

Element X	Z(Ω)	L(nh)	W (inch)	C(nf)
0	0.520	0.610	0.440	2.256
1	0.489	0.574	0.473	2.400
2	0.460	0.540	0.506	2.552
3	0.433	0.508	0.550	2.709
4	0.407	0.478	0.583	2.886
5	0.383	0.449	0.627	3.061
6	0.360	0.423	0.671	3.264
7	0.339	0.398	0.726	3.463
8	0.319	0.374	0.770	3.675
9	0.300	0.352	0.836	3.911

The curves which were used to design this transformation are given elsewhere in the proceedings. Pulse shapes of a 0.5Ω transmission line into a 0.3Ω load are shown in Figure 4, both with and without the transformation. The pulse shape improvement is due to the improved high frequency impedance match. The low frequency match for the 90 ns pulses apparently did not improve.

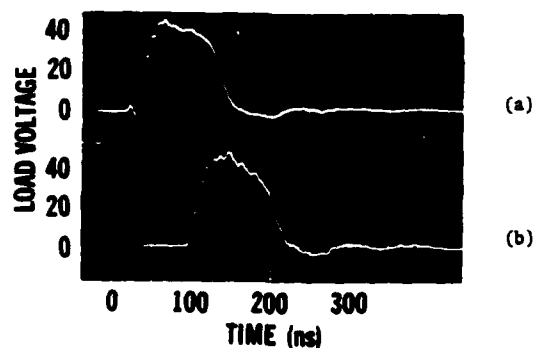


Figure 4. Voltage Across 0.3Ω Load With (a) and Without (b) Impedance Transformation Section

For loads with an impedance below 0.1Ω , the exponential taper was not a practical approach. In this low impedance regime, a pulse transformer with a 12:1 turns ratio was used.

The Pulse Transformer

Theory

The equivalent circuit⁽⁴⁾ of the transformer is shown in Figure 5.

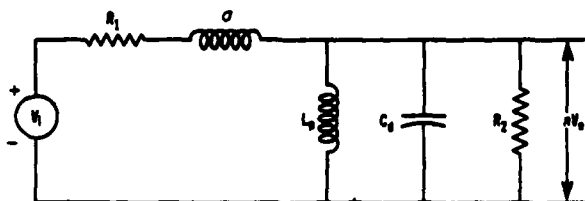


Figure 5. Equivalent Circuit of the Transformer

R_1 is the total source impedance on the primary side, σ the total leakage inductance (series inductance), L_p the total shunt inductance (magnetizing inductance), C_1 the total shunt capacitance, and R_2 the total impedance of the load and the secondary winding as reflected to the primary circuit. Since the turns-ratio of the primary to the secondary is n to 1, the impedance of the secondary is increased by n^2 at the primary input.

$$R_2 = n^2 (R_L + R_{SW}) \quad (3)$$

where R_L and R_{SW} are the load impedance and the secondary winding resistance at the secondary, respectively.

The magnetizing inductance, L_p , is expressed as (see Figure 6):

$$L_p = \mu A N_p^2 / \ell \quad (4)$$

where μ = magnetic permeability of the core

A = cross section of the core

N_p = primary turns

ℓ = flux path length

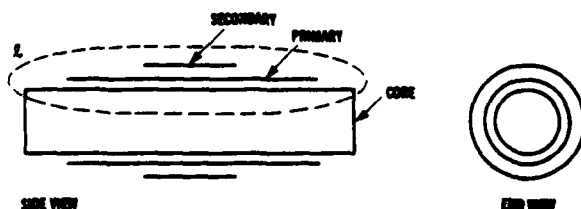


Figure 6. Primary Inductance

The leakage inductance, σ , is the total series inductance and a measure of the magnetic flux which is not coupled to the secondary. It can be expressed in terms of the geometric configuration of the transformer and can be derived from magnetic energy considerations. It is expressed as:

$$\sigma = \mu_0 N_p^2 V / \lambda^2 \quad (5)$$

where V = volume between the secondary and the primary windings
 λ = width of the winding

This is an indication of the energy stored between the windings and it is unrelated to the magnetic permeability of the core.

The leakage inductance can also be expressed in terms of σ , the geometric parameters of the transformer.

$$\sigma = F \mu_0 N_p^2 \ell (d + d_m/3) / \lambda \quad (6)$$

where F = distribution factor
 ℓ = mean path length
 λ = width of the winding
 d = separation between the secondary and the primary windings
 d_m = total thickness of the metal windings (primary and secondary)

We have empirically derived an equation similar to Equation 6, and will experimentally show the dependence of the primary and leakage inductance on the geometric parameters of the transformer in later sections.

Equation 5 indicates the key parameters needed to design a ferrite transformer for maximum power transfer to the load:

- 1) Minimum number of primary turns.
- 2) Minimum volume between the primary and the secondary windings.
- 3) Maximum width of the windings in conjunction with available laser diode array.

In addition, ease of laser mounting, efficient removal of heat from the laser, and impedance match must be considered.

Empirical Design Parameters

We obtained an empirical formula for σ using an 8 mm diameter ferrite core and varying the thickness of the primary winding metal. The width of the winding was 1 cm, the number of primary turns was 10, and the thickness of the Mylar insulator was 0.15 mil. The thickness of the Al foil, the primary winding, was varied from 0.3 mil to 0.8 mil. Figure 7 shows the empirical fit of the equation.

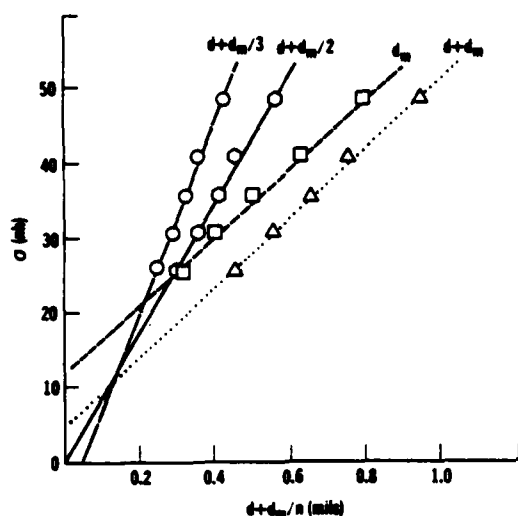


Figure 7. Empirical Fit of σ

For each thickness of the foil, σ was measured and plotted as a function of $d'+d_m/3$, $d'+d_m/2$, d_m and $d'+d_m$ where d' is the thickness of the Mylar and d_m the thickness of the foil. The best fit, assumed to intercept the origin, was found to be:

$$\sigma = 1.09 \mu_0 L_p^3 \left(d + \frac{d_m}{3} \right) \quad (7)$$

This equation is similar to Equation 6 because $d_m = N_p d'$ and $d = N_p d'$.

In addition, we measured inductances for two different ferrite cores and compared the results with Equation 7. These results are summarized in Table 2.

Table 2. Inductances for Different Ferrites

Ferrite	CM 2050	CN 5005
μ_p	100	1400
diameter	0.4"	0.4"
Al thickness	0.006"	0.006"
L_p (without cover)	3.9 μ h	4.2 μ h
L_p (with cover)	15.7 μ h	35.2 μ h
σ^p (measured)	0.049 μ h	0.048 μ h
σ (calculated)*	0.046 μ h	0.046 μ h

*used Equation 7.

The coupling coefficient, K , is approximately 0.9984 using a relationship $\sigma = 2L_p(1-K)$.

The important observations are as follows:

- 1) Magnetic permeability increases L_p .
- 2) Ferrite cover increases L_p .
- 3) σ does not depend upon the ferrite property.

The various geometric parameters in Equation 7 play important roles. Figure 8 shows that minimizing the insulator metal

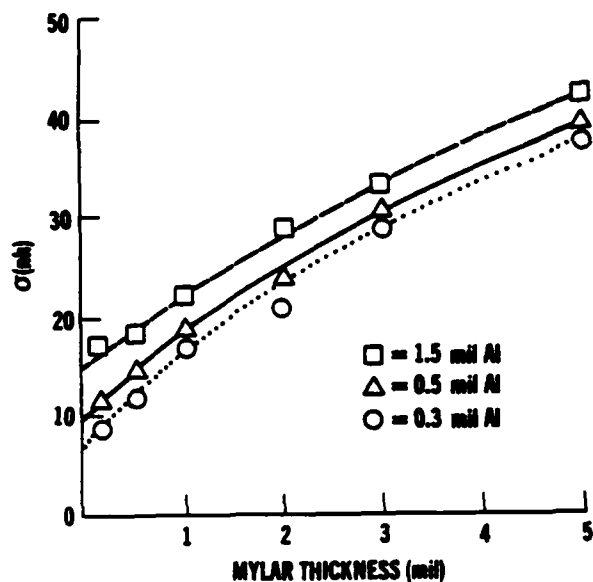


Figure 8. Leakage Inductance vs Metal and Insulation Thickness ($n = 5$)

thicknesses significantly reduces the leakage inductance. The minimum inductance is obtained for 0.3 mil Al foil and 0.25 mil Mylar.

Later, for the sake of rigidity and ease of winding, we used a 0.5 mil thick Cu foil for the windings.

Measurement of Inductance

Leakage inductance and primary inductance are measured using the same resonance technique. If the secondary is open, the technique measures the primary inductance, L_p . If the secondary is shorted, it measures the leakage inductance. Figure 9 shows the equivalent circuit to measure the leakage inductance.

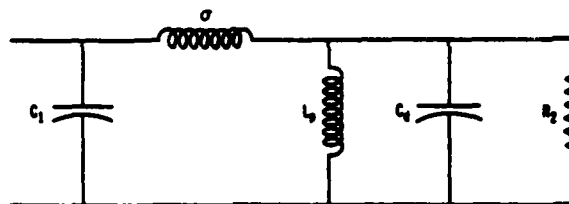


Figure 9. Equivalent Circuit to Measure the Inductance

C_1 is a discrete capacitor shunting the primary input. C_2 is the total shunt capacitance. The resonant frequency, f_1 , is obtained for a given C_1 . Another resonant frequency, f_2 , is obtained for another capacitor C_2 .

$$f_1 = \frac{1}{2\pi\sqrt{C_1 + C_2}} \quad (8)$$

$$f_2 = \frac{1}{2\pi\sqrt{\sigma(C_2 + C_d)}} \quad (9)$$

Eliminating C_d from Equations 8 and 9 and replacing f_1 with $1/\tau_1$ and f_2 with $1/\tau_2$, the leakage inductance is expressed as:

$$\sigma = \frac{(\tau_1 + \tau_2)(\tau_1 - \tau_2)}{(2\pi)^2 (C_2 - C_1)} \quad (10)$$

where τ_1 and τ_2 are the respective periods of oscillation.

A rectangular pulse is injected into the transformer and the output is monitored on an oscilloscope at the same point. The ringing period of oscillation is measured for two different shunt capacitors and inserted into Equation 10 to obtain the inductance value.

Estimating the Required Input Impedance

Figure 10 demonstrates the technique used to determine the array impedance at the operating current. This information is used to either adjust the turns ratio or the input impedance of the transmission line. For the example shown in Figure 10, the effective resistance of the secondary is 0.003Ω. At the primary input for the ten-turn transformer, it becomes 0.3Ω. Required voltage at the primary inputs is 45 volts and required current is 150 amperes.

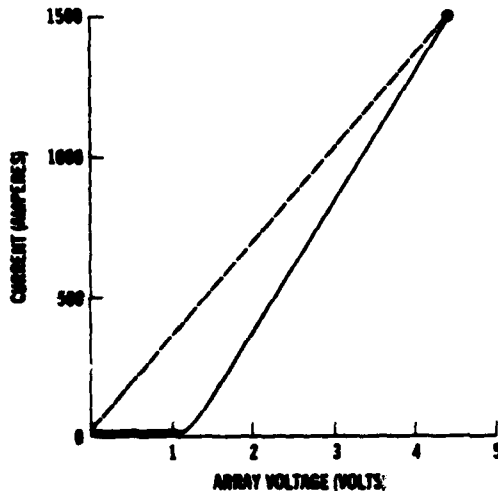


Figure 10. I-V Curve of the Laser Array

The Final Transformer Configuration

The final transformer design was obtained by using 0.5 mil copper sheet for the primary and the secondary windings with 1/4 mil thick Mylar insulation, wound on a 2 mm ferrite core. The number of primary turns ranged from 8 to 12 depending on the array impedance at the operating voltage.

After the primary was concentrically wound and glued, the secondary was tightly wrapped around it. Its outputs are pressed to the H-film made of copper with Kapton

to make electrical contacts to the array. The laser array diodes are soldered to the copper heat sink with their p-side down (see Figure 11). The n-side of the diodes are soldered to a two mil gold foil. The other end of the foil is soldered to the H-film, thus completing the circuit. All the pressure-contacted surfaces are In-tinned.

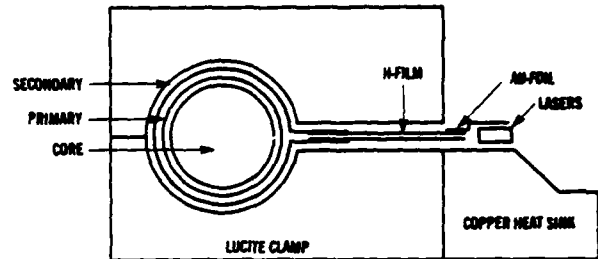


Figure 11. Transformer-Laser Array Schematic

Figure 12 shows the scope traces of the primary voltage and the laser array light output. From the picture it can be deduced that the load impedance is less than that of the transmission line as discussed earlier. The light output actually coincides with the peak of the secondary voltage. Secondary voltage is actually delayed by 30 nanoseconds from the primary voltage. Peak light output is 600 watts and peak secondary current is estimated to be 1500 amps, based on diode quantum efficiency.

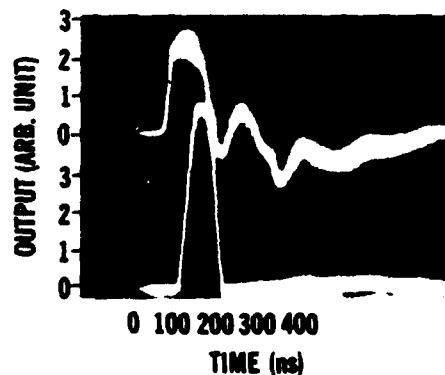


Figure 12. Primary Voltage (Upper Trace) and Light Output (Lower Trace)

Figure 13 shows the components of the prototype transformer-laser array. Shown are the transformer, the SCR banks, and the delay line.

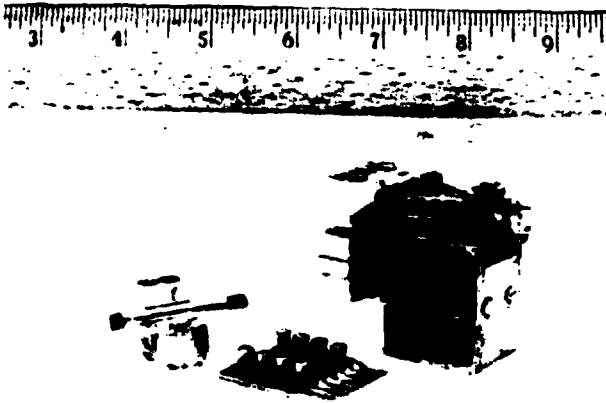


Figure 13. Transformer-Laser Array Components

Conclusion

Two impedance matching techniques have been successfully developed for driving semiconductor laser diode arrays. For intermediate impedance loads, an exponentially impedance tapered delay line has been fabricated. It successfully transforms the high frequency pulse components. However, the transformation is too abrupt to affect

the low frequency components. For very low impedance laser array loads, we have constructed a low inductance pulse transformer. The transformer leakage inductance is 18 nh for 12 primary turns. An array driven by the transformer has produced a 600 watt peak optical output with a pulse width of 83 ns at a repetition rate of 10 KHz. The transformer technique is excellent in principle to drive many diodes in parallel if the input impedance is properly matched.

References

- (1) R. R. Shurtz, B. H. Ahn, C. W. Trussell, J. E. Miller, and D. J. Horowitz, "High Efficiency Pulse Power Supply for a Semiconductor Laser Illuminator," in these proceedings.
- (2) G. N. Glasoe and J. V. Lebacqz, "Pulse Generators," p. 178, Massachusetts Institute of Technology Radiation Laboratory Series, Vol. 5, McGraw-Hill Book Company, Inc., New York, 1948.
- (3) A. B. Bronwell and R. E. Beam, "Theory and Application of Microwaves," p. 200, McGraw-Hill Book Company, Inc., New York, 1947.
- (4) J. Millman and H. Taub, "Pulse, Digital, and Switching Waveforms," p. 69, McGraw-Hill Book Company, Inc., New York, 1965.
- (5) M.I.T. Electrical Engineering Staff, "Magnetic Circuits and Transformers," pp. 359-362, John Wiley & Sons, Inc., New York, 1943.
- (6) J. Millman and H. Taub, "Pulse, Digital, and Switching Waveforms," p. 67, McGraw-Hill Book Company, Inc., New York, 1965.
- (7) J. Millman and H. Taub, "Pulse, Digital, and Switching Waveforms," p. 71, McGraw-Hill Book Company, Inc., New York, 1965.

THE ELECTRICAL PERFORMANCE OF WATER UNDER LONG DURATION STRESS*

by
D. B. Fenneman
R. J. Gripshover
Naval Surface Weapons Center, Dahlgren, VA. 22448

Summary

The performance of water capacitor systems electrically stressed for periods exceeding 100μsec is reviewed and analyzed. Experimental results are presented which demonstrate that the breakdown strength of water-filled lines under such long term stress is independent of stress time and best described as a threshold phenomenon. The study indicates that very long time charging of water lines is possible, with acceptable loss, provided the water is continuously deionized and cooled.

Background

Water, with its high dielectric constant and benign handling properties is commonly used as the intermediate energy storage medium of pulsed power devices, serving to collect electrical energy over a long period of time and subsequently discharging it quickly into the load. Power amplification is measured by the ratio of charging time to discharge time, hence there is benefit in making the charging time as long as possible. Another benefit of long time charging is that it opens up the possibility of using new kinds of sources, such as the compulstator and brushless rotary flux compressor (BRFC) to charge the line; thereby eliminating the need for primary energy storage capacitors. To benefit from such new devices, it will be necessary for the water to collect and store energy for periods exceeding 100μsec. This is more than an order of magnitude longer than the 5-10μsec typical of present devices, and is a region which has received little or no detailed experimental study. It is the purpose of this paper to review the expected performance of water filled lines and present results of experimental studies of achievable performance in the long time domain. It will be shown that water purity and temperature assume crucial importance.

Electrical Properties of Water

Two properties of water which define its performance in a circuit element are: the relative dielectric constant, ϵ , and the conductivity, σ (or alternatively the resistivity, $\rho = 1/\sigma$). From these two parameters a third, termed the intrinsic time constant, τ , can be constructed

$$\tau = \frac{\epsilon_0 \epsilon}{\sigma} \quad (1)$$

ϵ_0 is the permittivity of free space (8.854×10^{-12} F/m). Physically, τ is manifested as the time a capacitor, filled with material of dielectric constant ϵ and conductivity σ , initially charged to voltage V_0 , takes to decay to voltage V_0/e ; i.e.:

$$V(t) = V_0 e^{-t/\tau} \quad (2)$$

This behavior is independent of the size or geometry of the capacitor and makes τ a useful parameter to

relate the fundamental properties of a dielectric to its circuit performance.

The large dielectric permittivity of water is due to its being a naturally polar molecule which in the liquid phase has strong interaction energy between neighboring molecules. It is thus expected that ϵ should be temperature dependent due to thermal smearing of the interaction potential. This is indeed the case, as the formula from the Handbook [1] (with $T' = T - 25$) displays:

$$\epsilon(T') = 78.54 \left[1 - 4.579 \times 10^{-3} T' + 1.19 \times 10^{-5} T'^2 - 2.8 \times 10^{-8} T'^3 \right] \quad (3)$$

This equation displays a variation of 11% in ϵ as T changes from 0 to 25 C.

The conductivity of water arises from three sources: impurity ions, ions from thermal dissociation, and a frequency dependent conductivity, which are additive:

$$\sigma = \sigma_{\text{imp}} + \sigma_{\text{dis}} + \sigma(\omega) \quad (4)$$

The last source is a consequence of the finite time it takes the molecules to realign in a changing field, and can be equivalently expressed as the imaginary part of a complex dielectric constant. This source is well described by Debye Theory [2]:

$$\sigma(\omega) = \frac{\epsilon_0 \epsilon \omega^2 \tau_d}{1 + \omega^2 \tau_d^2} \quad (5)$$

τ_d is the Debye relaxation time, about 10^{-11} sec for water. This contribution is therefore negligible, e.g.: $\sigma(10^6) < 10^{-10}$ S/cm. (1 Siemen = 10^9 OHM $^{-1}$).

The other sources, impurities and dissociation products, contribute conductivities which may be computed as the number of carriers per unit volume, n , times the charge of each carrier, q , times the mobility, μ .

$$\begin{aligned} \sigma_{\text{imp}} &= n_{\text{imp}} q_{\text{imp}} (\mu_{\text{imp}}^+ + \mu_{\text{imp}}^-) \\ \sigma_{\text{dis}} &= n_{\text{dis}} q_{\text{dis}} (\mu_{\text{dis}}^+ + \mu_{\text{dis}}^-) \end{aligned} \quad (6)$$

The mobilities of all ions in aqueous solution are temperature dependent, but unlike electronic conduction in metals, ionic mobilities increase with increasing temperature [3]. The situation can be likened to the case of a ball bearing falling faster to the bottom of a bucket filled with marbles if the bucket is agitated. The increase of mobility with temperature is linear in the region 0-25C.

$$\mu = \mu_0 (1 + aT) \quad (7)$$

Representative values are:

$$N_3^+ : \mu_0 = 2.69 \times 10^{-3}, a = 3.84 \times 10^{-2}$$

$$Cl^- : \mu_0 = 4.26 \times 10^{-3}, a = 3.34 \times 10^{-2}$$

$$H_3O^+ : \mu_0 = 2.49 \times 10^{-3}, a = 1.83 \times 10^{-2}$$

$$OH^- : \mu_0 = 1.09 \times 10^{-3}, a = 3.32 \times 10^{-2}$$

with μ_0 in cm²/volt-sec and a in C $^{-1}$.

*Supported by NSWC Independent Research

Impurity carrier densities and their temperature dependence are hard to predict. Modern mixed bed deionizers will very efficiently scrub ionic impurities to only a few parts per billion on one pass. This, coupled with the fact that the mobilities of the products of dissociation (OH^- and H_3O^+) are 5 to 10 times higher than the mobilities of common impurity ions (e.g., Na^+ , Cl^-) infers that in a well designed water conditioning system, the dominant contribution to conductivity comes from the dissociation reaction:



Carrier densities from this reaction are exponentially temperature dependent and may be expressed as

$$\eta_{\text{dis}} = \eta_{\text{OH}^-} = \eta_{\text{H}_3\text{O}^+} = 10^{A+BT+CT^2} \quad (8)$$

The table in [1] for the ionization constant of water, $K_w(T)$ yields (for η in ions/cm³)

$$\begin{aligned} A &= 13.3082 \\ B &= 2.1475 \times 10^{-2} \\ C &= -1.03 \times 10^{-4} \end{aligned}$$

This empirical fit gives values to 3 places for $0 \leq T \leq 20$. For $T=25^\circ\text{C}$ it is good to 5%, for higher values it rapidly loses accuracy. The temperature dependence of ϵ , σ , ρ , and τ for absolutely pure water are displayed in Figure 1.

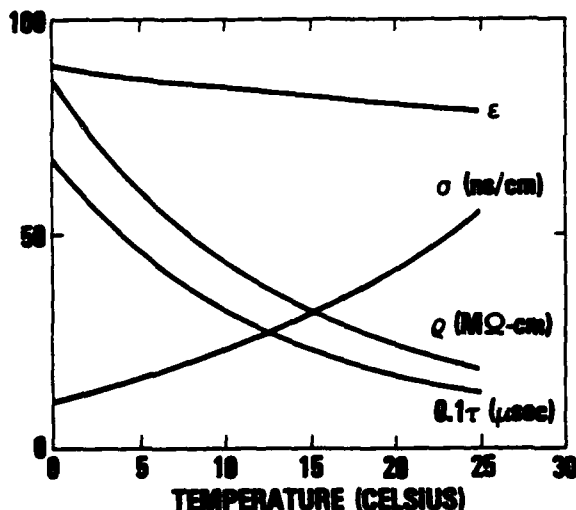


Figure 1.
Variation of electrical properties of absolute pure water with temperature, one atmosphere pressure.

As shown in this figure, the variation of intrinsic time constant τ is especially dramatic, dropping fivefold from 670μsec at 0°C to 128μsec at 25°C. The impact of this variation is of crucial importance when considering long term charging.

Charging Time

From the point of view of the load, the water line is a transmission line with distributed inductance and capacitance, but from the point of view of

the source, it models as a capacitor. When considering long charging times, the energy loss from ohmic heating due to non-zero conductivity of the water dielectric should be taken into account. Consider charging a water capacitor with a voltage waveform

$$V(t) = V_f \cdot f(t) \quad (9)$$

where V_f and t_f are the final voltage and time and

$$f(0) = 0$$

$$f(t_f) = 1.$$

Then the ratio of ohmic heating loss to energy stored is:

$$\frac{E_{\text{ohmic}}}{E_{\text{stored}}} = \frac{\frac{1}{R} \int_0^{t_f} V^2(t) dt}{\frac{1}{2} C V_f^2}, \text{ letting } t' = t/t_f \text{ gives}$$

$$= \alpha \frac{t_f}{\tau} \quad (10)$$

This result is independent of the size or geometry of the capacitor. α is a dimensionless coefficient which depends only on the functional form of the charging waveform. Values of α for common charging cycles and typical charging losses are displayed in Table 1. The table clearly indicates for charging times in excess of 100μsec high water purity and cooling become mandatory.

WAVEFORM	$f(t)$	HEATING LOSS ENERGY STORED	% LOSS FOR $t_f = 100 \mu\text{sec}$ $T = 25^\circ\text{C}$	$T = 0^\circ\text{C}$
LINEAR RAMP	$V_f t$	$\frac{1}{3} \frac{t_f}{\tau}$	62%	10%
RESONANT	$1 - \cos \frac{\pi t}{2t_f}$	$\frac{16}{15} \frac{t_f}{\tau}$	37%	7%
DUAL RESONANT	$\frac{1}{2} (\cos \frac{2\pi t}{t_f} - \cos \frac{\pi t}{t_f})$	$\frac{1}{2} \frac{t_f}{\tau}$	70%	10%
EXPONENTIAL	$\frac{1 - e^{-\frac{2t}{t_f}}}{1 - e^{-1}}$	$\frac{20}{9} \frac{t_f}{\tau}$	70%	10%
S.A.F.C.	NUMERICAL APPROX	$\frac{20}{9} \frac{t_f}{\tau}$	62%	6%

*THEORETICAL MINIMUM - ABSOLUTELY PURE WATER

TABLE 1. WATER CHARGING LOSS

Parenthetically, a point must be discussed. Ohmic heating during the charging cycle increases the conductivity which in turn increases the ohmic heating and so on. Fortunately, due to the high specific heat of water, this effect is negligible for single pulse devices. For burst mode operation it may be of importance, and for repetitively pulsed, continuous duty devices it is certainly an important consideration. This underscores the need for continuously flowing systems.

Electrical Strength Experiments

It remains to discuss one final property: the electrical strength. At present there is no theory to predict the breakdown behavior reliably. Long term electrical stress tests of very pure water have been completed at NSWC. The experimental apparatus and testing procedure are described in more detail in [8] and [9]. The facility, consisting of a Marx bank, water capacitor test cell and water conditioning

system is sketched in Figure 2. The time constant of the Marx generator, $R_M C_M$, is 20 μ sec. In order to do long duration stress studies, the water capacitor must be isolated from the Marx generator. The electrical circuit of the previous work was modified by placing a diode in series with the water capacitor to prevent its discharging. The modified circuit and sample experimental voltage waveforms are shown in Figure 3. Two copper sulphate voltage probes were necessary; a 70k Ω probe on the Marx side of the diode and a 1M Ω probe on the water capacitor side.

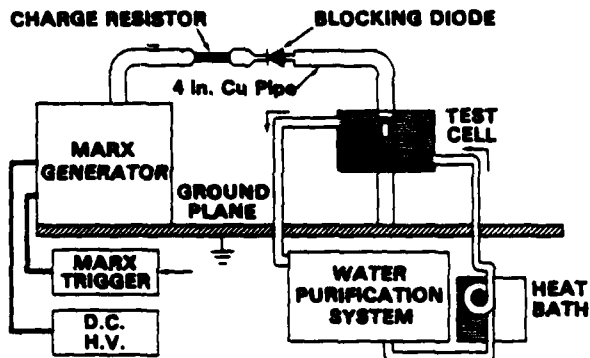


Figure 2. Experimental arrangement.

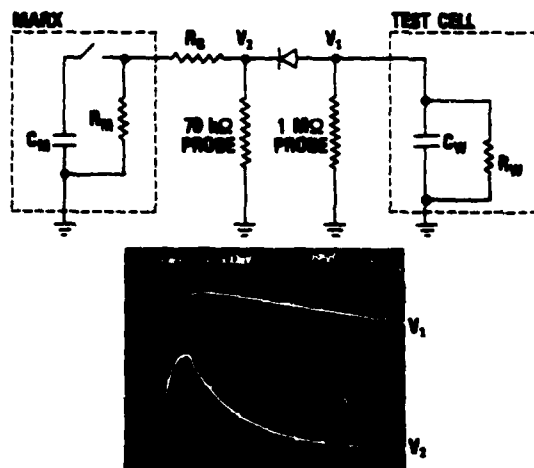


Figure 3. Electrical Circuit and Experimental waveforms. C_M , Marx capacitance = 22nF; R_M , Marx internal resistance, = 900 Ω ; R_C , charge resistor, = 5 k Ω ; C_W , water capacitance, = 1nF; R_W , water resistance, >300k Ω .

Since the 70k Ω probe has better frequency response, it gives a more accurate voltage measurement. However, this probe would load the water capacitor excessively. A higher impedance probe is needed for long stress times. With the 1M Ω probe, the experimentally observed decay time can be used to calculate the water intrinsic time constant from

$$\tau = \frac{\tau_{exp}}{1 - \frac{\tau_{exp}}{R_C C_W}} \quad (11)$$

One purpose of the research was to establish that the water conditioning system could sufficiently purify water, as demanded by the considerations

of the previous section, to produce stress times in excess of 100 μ sec. The water resistivity is continually monitored by Barnstead purity meters, but since they have built in temperature compensation and are always pinned above 18.3M Ω -cm during experiments, they are of little use. Measurement of the logarithmic decrement of the experimental voltage wave form is a direct measure of the intrinsic time constant. Results are shown in Figure 4.

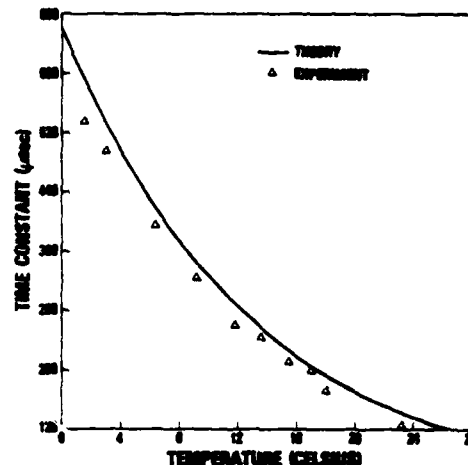
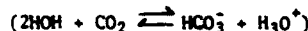


Figure 4. Experimental measure of intrinsic time constant.

The close agreement between theory and experiment indicates that in our system dissociative conductivity dominates. It is important to emphasize the fact that purity of this magnitude requires continuous deionizing. Tests have shown that resistivity will decay from 18.3M Ω -cm (25C value of pure water) to 5M Ω -cm in a half hour if the deionizer is bypassed. In this same regard, deseration is also important to remove carbon dioxide, another source of ions:



An important research area would be to pinpoint the carriers causing this decay and their source (e.g., metal ions).

The electrical breakdown strength is measured in terms of "breakdown probability". Simply stated, if n tests with identical waveforms, characterized by E_{max} (the maximum field experienced) and b (\bar{C}_n) of them suffer breakdown; the ratio b/n is called the breakdown probability. The results of over 400 tests are presented in Figure 5. Each point represents $n > 10$ tests. The points for effective stress times (defined as the time for which $E > .63E_{max}$) of 65 μ sec and 250 μ sec are seen to overlap to within experimental variation. These stress times are obtained by changing water temperature from 2C to 23C. The points for 11 μ sec effective stress times are obtained by removing the blocking diode and allowing the charge on the water capacitor to bleed through R_C and R_W (refer to Fig. 3). The data shows only a slight improvement (~10%) in breakdown strength with reduction of effective stress times by a factor of 25.

The results shown in Figure 5 are valid only for the 81 cm² parallel plate geometry used in the tests. However, it should be expected that, whatever the proper area scaling, the trend shown by these experiments would still hold.

Conclusions

This study indicates very long time charging of

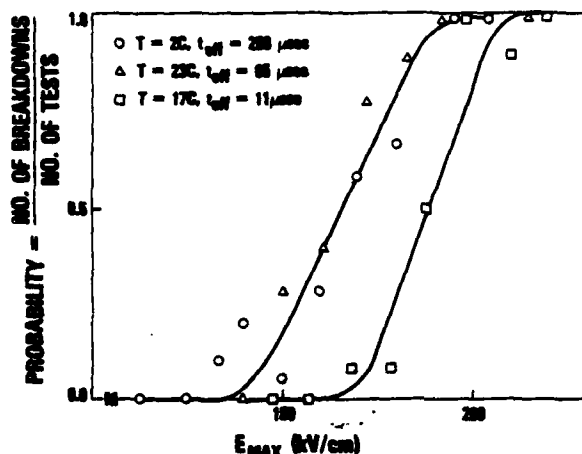


Figure 5.
Breakdown probability vs. maximum applied field.
Bead blasted planar stainless steel electrodes,
81 cm² area. Gap spacing .5cm.

water lines is possible with acceptable losses provided the water is continually deionized and cooled.

With the completion of this work a fairly complete picture of the temporal dependence of the electrical strength of water emerges, though precise values may be in dispute due to differences in experimental techniques and definitions, the view is quite simple. For short times (20ns-200ns) the electrical strength decreases with increasing effective stress times approximately as t_{eff}^{-4} .

For $t_{eff} \approx 1\mu s$ the decrease is as $t_{eff}^{-.33}$; for

$t_{eff} \approx 5\mu s$ the decrease is as $t_{eff}^{-.16}$ [7]. The temporal dependence becoming weaker as stress time increases, approaching a time independent threshold value between 11 and 65 μs . The threshold value is not absolutely sharp but has a statistical variation, the sources of which remain undefined. The behavior of the electrical strength of water is thus qualitatively similar to the behavior in the low dielectric constant insulating oils [8]. The main difference is that the "kink" or "knee" (i.e., the transition from temporal dependence to temporal independence) is less sharp.

Acknowledgement

The authors gratefully acknowledge the enthusiastic and skillful work of L. W. Hardesty and K. Chilton who constructed the apparatus and assisted in the testing.

References

1. R. C. Weast "Handbook of Chemistry and Physics" 58th Ed. CRC Press, Cleveland 1977, p.D152.
2. H. Frohlich "Theory of Dielectrics" Oxford Press London. 1968.
3. M. Eigen and L. DeMaeyer "Self-Dissociation and Protonic Charge Transport in Water and Ice" Proc. R. Soc. A 247 505(1958).
4. D. B. Fenneman and R. J. Gripshover "Electrical Breakdown in Water in the Microsecond Regime" Digest of Technical Papers, 2nd IEEE International Pulsed Power Conference, Lubbock, Texas, June 1979 IEEE Catalog No. 79 CH1505-7.
5. D. B. Fenneman and R. J. Gripshover "Experiments on Electrical Breakdown in Water in the Microsecond Regime" IEEE Trans. on Plasma Science, Sept 1980.
6. J. P. VanDevender "Short Pulse Electrical Breakdown Strength of H₂O" Proceedings International Pulsed Power Conference, Lubbock, Texas, Nov 1976 IEEE Catalog Number 76CH 1147-8 Reg 5.
7. A. R. Miller, "Low Impedance Capacitors Using Pressurized Water as a Dielectric" Proceedings of the 5th Symposium on Engineering Problems of Fusion Research p 471, IEEE New York 1974.
8. T. J. Gallagher "Simple Dielectric Liquids" P. 122, Clarendon Press, Oxford, 1975.

EXPERIMENTS ON
WATER CAPACITOR ELECTRODE CONDITIONING
BY ION BOMBARDMENT*

by

V. H. Gehman and D. B. Fenneman
Naval Surface Weapons Center
Dahlgren, Virginia 22448

Summary

Experiments are described which test the conditioning effect of ion bombardment on the electrical strength of water capacitors. Ions are produced in the normal glow of an argon discharge and impact the electrode surfaces with energies up to 250 eV. Conditioning duration is controlled so that each lattice site is bombarded on the average at least 50 times. After conditioning, the test cell is filled with water and the treated electrodes used as plates of a water capacitor (81 cm² area, 1 cm separation). The parameter due to Martin ($E_{max} \epsilon_{eff}^{1/3}$) is used as an index to judge the effect of conditioning on the electrical strength of the water dielectric capacitor. The lack of a strong effect indicates that surface microinhomogeneities do not contribute significantly to the breakdown process. The surface morphology of the discharge conditioning and the spark cratering is discussed and illustrated with photo micrographs.

Introduction

The energy density of a capacitor is proportional to the square of the applied electric field. For compactness of design, the field should be as high as possible. However, the electrical stress is limited by the ability of the capacitor to resist electrical breakdown. It is well established that the breakdown process originates at the water-metal interface, rather than in the bulk volume of the water dielectric.

The process of the subsequent development of the spark across the water to complete the breakdown has received experimental attention.¹ But the process which first produces the primordial surface plasma initiating the breakdown is not understood.² Nor is the role of surface properties clear. Achieving higher breakdown fields will require knowledge of the influence of such properties as microinhomogeneities due to oxide patches, dielectric occlusions, microwhiskers and so on. This paper describes experimental studies to assess the role of the surface microstructure by treating the surface with ion bombardment from the normal glow of an argon discharge. Surface treatment of this kind is not new, Witcomb³ for example investigated this method for cleaning stainless steel substrates of superconducting A.C. power cables. Argon was selected, not only for its availability and chemical inertness but because its atomic weight is near that of metal lattice atoms, assuring good momentum exchange compared to helium or neon.

Apparatus and Method

The apparatus used for the evaluation of the ion bombardment process has been described in previous papers.^{4,5} Hence, only a brief description will be given. A schematic of the system can be seen in Figure 2 of the previous paper, the blocking diode was not employed in the present work.

The water conditioning system maintains high water purity, deaeration, constant temperature and provides a non-turbulent flow of this water into and away from the test cell. The water resistivity is always greater than 18 M Ω -cm. Constant temperature is maintained by the heat exchanger and is monitored with thermistor temperature probes. Deaeration is achieved by pulling a vacuum on a column of the water with a mechanical pump via a cold trap consisting of an alcohol-dry ice slurry.

The electrical system consists of a ten stage Marx generator capable of 500 kV maximum, several resistor probes and the electronics and oscilloscope necessary to record the voltage across the water capacitor. The erection time of the Marx is on the order of a couple of hundred nanoseconds. Negative potential was applied to the top electrode (bottom electrode at ground potential) through a copper sulfate charging resistor. The voltage is measured using a copper sulfate dividing resistor and its time dependent form is

$$V(t) = 0.71V_0(e^{-t/\omega_1} - e^{-t/\omega_2}) \quad (1)$$

where V_0 = Erected Marx Voltage

$$1/\omega_1 = R_{MARX} C_{MARX} = 20 \mu s$$

$$1/\omega_2 = R_{CHARGE} (C_{WATER} + C_{STRAY}) = 2 \mu s.$$

A new test cell was constructed so that both plasma conditioning and water breakdown tests could be performed without moving the electrodes from the breakdown test configuration and without exposing them to the atmosphere. The plasma conditioning system is shown in Figure 1. The new test cell is a plexiglass cylinder with stainless steel end caps. The end caps are sealed against the plexiglass with an O-ring fitting and access is provided through valves in the end cap for high purity water and the conditioning gas. The cylinder internal dimensions are 8 inches diameter by 12 inches in height. Parallel orientation electrodes are centered in the cylinder. A movable, small mesh, stainless steel screen eliminated the transfer of impurities from the cylinder wall to the electrodes by conditioning plasma-wall interactions.

*Sponsored by NSWC Independent Research Program

ELECTRODE CONDITIONING APPARATUS

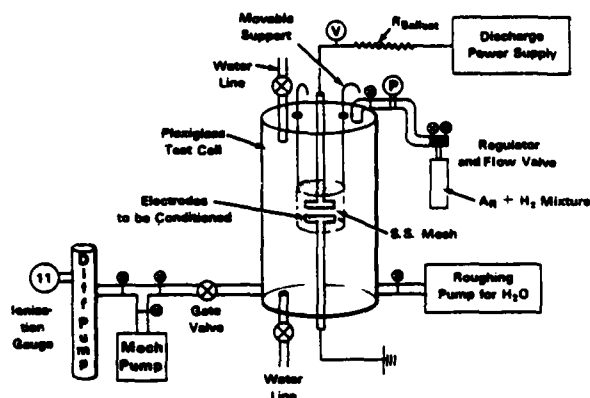


Figure 1. Schematic of the plasma conditioning apparatus for the water capacitor electrodes.

The strategy for the experiments, which is summarized in Table I, was: prepare a set of electrodes, run a series of breakdown tests as a control, resurface and prepare the electrodes again, plasma condition and then run another set of breakdown tests to determine the effect of the plasma conditioning as compared to the control tests.

TABLE I: SUMMARY OF EXPERIMENTAL PROCEDURE

EXPERIMENT	ELECTRODE		COMMENT
	MATERIAL	SURFACE	
I A	304 S.S.	BEAD BLASTED	CONTROL
I B	304 S.S.	BEAD BLASTED	PLASMA-CONDITIONED
II A	ELECTROLYTIC CU	BEAD BLASTED	CONTROL — "FRESH" CU
II B	ELECTROLYTIC CU	BEAD BLASTED	CONTROL — "AGED" CU
II C	ELECTROLYTIC CU	BEAD BLASTED	PLASMA-CONDITIONED FRESH CU
III A	304 S.S.	POLISHED	CONTROL
III B	304 S.S.	POLISHED	PLASMA-CONDITIONED

Two different surface preparations were used: bead blasted and polished. Bead blasted refers to glass bead blasting (Zero-Blast-N-Peen, size 801, MIL-G-9954A). The scale of surface irregularity induced on the electrode surface was on the order of the individual glass beads, about 125 μm . This surfacing

technique has been used previously^{4,5} because it yields a reproducible, well characterized surface. Polished refers to a stepped mechanical polish technique utilizing grinding wheels of 320, 400, then 600 grit followed by alumina particle polishing with 1.0, 0.3 and 0.05 μm alumina particles. This surface was not totally reproducible as stray scratches could cause sharp, unpredicted gradients in the contour of the electrode. This surface was chosen for study in the hope that the flatter contour would yield better breakdown behavior.

The adjectives "fresh" and "aged" used in conjunction with copper electrodes refers to a behavior found in copper only. Copper electrodes exposed to the water in the test cell for a short time (1/2 day) had less favorable breakdown characteristics than copper electrodes immersed in water for some time (approximately 1 week). During this time, a very thin oxide discoloration develops. The copper electrodes used in the plasma conditioning experiments were "fresh".

Conditioning time, gas pressure and other plasma conditioning parameters were chosen for each set of experiments to produce an electrode surface with a required minimum average number of ion bombardments per atomic lattice site of at least 50. In all cases the plasma had a stable, homogeneous glow over the entire electrode breakdown surface. The plasma characteristics were those of a normal glow as defined by Brown⁶ which was then used to determine cathode fall and the plasma parameters. The characteristic curve of the plasma is plotted in Figure 2.

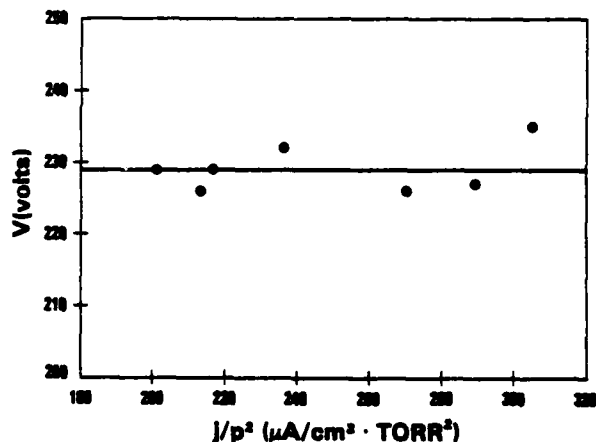


Figure 2. Graphical presentation of the conditioning plasma parameters. Note that the potential drop across the plasma is independent of j/p^2 .

A summary of the calculated effects for the three sets of conditioning treatments is shown in Table II.

TABLE II: PROCEDURAL PARAMETERS AND CALCULATED PROPERTIES FOR PLASMA CONDITIONED ELECTRODES

	I B	II C	III B
GAS	95% A. 5% H ₂	ARGON	ARGON
MEAN PRESSURE	0.570 TORR	0.570 TORR	0.785 TORR
CONDITIONING TIME/ ELECTRODE	18 hr	20 hr	20 hr
MEAN CURRENT ON BREAKDOWN SURFACE	~4.4 mA	~10.5 mA	~10.0 mA
MEAN NUMBER OF A ⁺ BOMBARDMENTS/ ATOMIC LATTICE SITE	50	134	128
MEAN A ⁺ KINETIC ENERGY/BOMBARDMENT	0.83 eV	0.83 eV	0.83 eV
LARGEST PROBABLE A ⁺ KINETIC ENERGY/ CONDITIONING	3.3 eV	4.1 eV	4.0 eV

The figure of merit used to judge the breakdown behavior for a system of electrodes was developed from the work of J. C. Martin.⁷ The figure of merit M is given by

$$M = E_{\max} t_{\text{eff}}^{1/3} A^{-1/10} \quad (2)$$

where E_{\max} is the maximum electric field in the water, t_{eff} is the effective time - defined as the interval during which the field exceeds $0.63 E_{\max}$ - and A is the surface area of the electrodes which experiences 90% or more of the field. A was measured on the electrode while E_{\max} and t_{eff} were determined from the voltage trace. This figure of merit was chosen so we could relate results of these experiments to previous work done on water breakdown at NSWC. Defined this way, M is based on tests which always broke down.

Breakdown Results

The numerical results for the three sets of experiments are tabulated in Table III. The figure of merit, M, for plasma conditioned electrodes is always found to be slightly less than for untreated electrodes; the decrease is much less than one standard deviation. A decrease in the statistical variation of M was observed for the conditioned electrodes.

Each sequence consisted of at least 40 tests for statistics considerations. The conditioning treatments were symmetric for each electrode with an average argon ion energy around 0.8 eV. The current density on the electrodes was found to decrease as plasma conditioning continued so a model based on electron emission from the electrodes does not explain the breakdown behavior in this study. The long conditioning times, number of ion bombardments and energy of the argon ions (which was sufficient to raise the energy state of individual iron atoms to the point of melting) assured the destruction of microinhomogeneities (i.e., microwhiskers, etc). So this mechanism is not viable as an explanation for the breakdown behavior found in this study either.

TABLE III: RESULTS OF PLASMA CONDITIONING OF ELECTRODES

EXPERIMENT	MEAN MARTIN'S NUMBER <M>	$\frac{\sigma(M)}{M} \times 100\%$	NUMBER OF TESTS
I A	0.574	14.8%	41
I B	0.549	12.6%	48
II A	0.441	10.0%	116
II B	0.540	8.1%	50
II C	0.432	7.6%	43
III A	0.504	15.9%	40
III B	0.480	15.2%	40

The post test observations of the electrode surfaces were quite informative. The crater distribution on the bead blasted surface of both the copper and stainless steel electrodes was found to be relatively random in spatial distribution (see Figure 3). This observation supports previous consideration that spark cratering does not create a sufficient disturbance in the bead blasted contour to constitute a weakest link for the next breakdown occurrence. (The total energy dissipated in a breakdown is ~10 Joules). However, the crater distribution on the polished surface is not random (see Figure 4) which indicates that solitary surface inhomogeneities are worse than a uniformly inhomogeneous surface.



Figure 3. Photograph of a bead-blasted, stainless steel electrode after water breakdown tests. Note the spatial randomness of the craters.



Figure 4. Photograph of a polished, stainless steel electrode after water breakdown tests. Note the grouping of the spark craters.

Spark Crater Morphology

Due to the difficulty in observing grain boundaries and other structural features on bead blasted surfaces, only the polished stainless steel electrodes were examined. These electrodes were examined before and after plasma conditioning and before and after spark cratering. An etch-like effect was observed near the spark craters which decreases away from the craters. The micrograph in Figure 5 reveals the grain boundaries and twins within the grains made visible by the slight electrolytic etch effect of dissociated water near the crater. Mechanical twins, as defined by Reed-Hill,⁸ are a mode of plastic deformation - a result of applied stress. The atoms within the twins are realigned into the original crystal structure but with a different orientation than the other atoms within the grain. The twins visible in Figure 5 and at higher magnification in Figure 6 are the result of the mechanical shock of crater formation radiating out from the site of the spark crater.

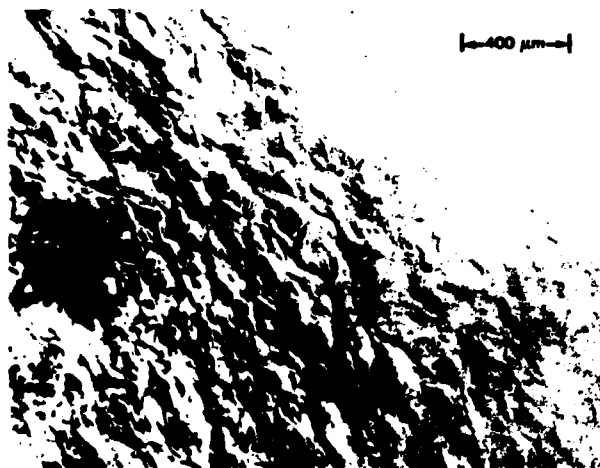


Figure 5. Micrograph of a polished stainless steel electrode after breakdown tests. Note that the surface structure is visible only in the region near the crater.

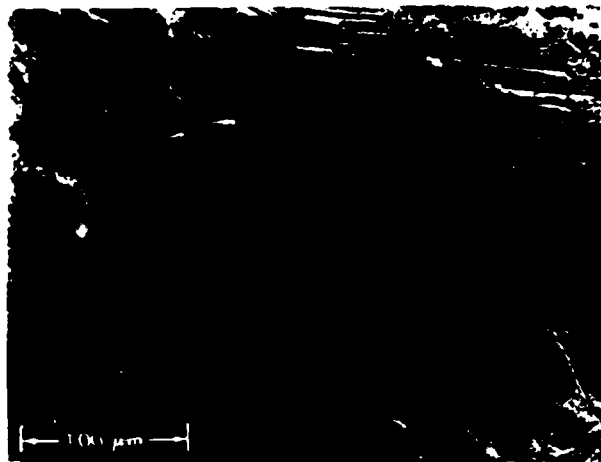


Figure 6. Higher magnification micrograph of the austenitic grains. The smallest division of the reticle is 0.0005 inches in this and all other micrographs.

A range of grain size was noted - some of the smaller grains were photographed at 800X in Figure 7. Figure 7 also shows that the twins do not cross the grain boundaries. The average grain size is ASTM #6 - an expected value for this stainless steel (see Figure 8).

The micrograph shown in Figure 9 depicts a sharp ridge formed between two spark craters. The light source is located at the left edge of the micrograph and the shadow from the ridge can clearly be seen. These ridge formations were observed in several locations on the polished electrodes and may be the reason for the disparity in spark rate grouping seen in Figure 4 as opposed to Figure 3. The field enhancement along the ridge may lead to preferred breakdown sites near craters as opposed to random breakdown on the electrode surface. This clearly demonstrates the large stresses to which the metal is subjected upon crater formation.

Another interesting feature disclosed in the microscopic examination is the presence of solidified melt near craters on the positive electrode and the lack of such an indication on the negative electrode see Figures 10, 11 and 12. This is consistent with the observation that the breakdown process begins at the anode where a spark erupts in a relatively gradual manner and impacts suddenly into the cathode (top electrode). The possibility that melt formation does occur on the top electrode and is not observed because the liquid metal fell on the bottom electrode is unlikely since metal droplets, as the solitary example in Figure 13, are not found in sufficient quantities to support this mechanism.



Figure 7. Very high magnification micrograph of the austenitic grains. Note the twins within each grain.

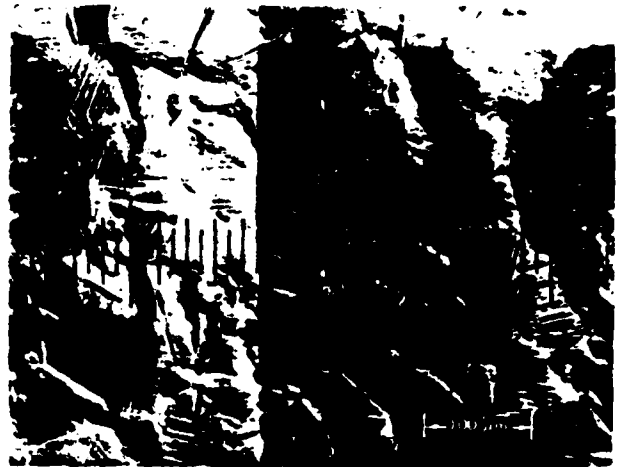


Figure 9. Micrograph of the sharp ridge formed between two craters.



Figure 8. ASTM grain size overlay micrograph. Grain size of the 304 stainless steel is approximately #6.



Figure 10. Micrograph of the anode electrode showing crater grouping and solidified melt.



Figure 11. Higher magnification micrograph of the anode electrode revealing the approximate sizes of the crater and the solidified melt.

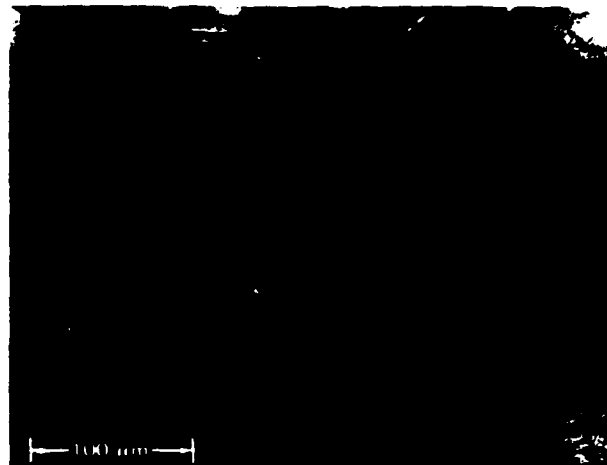


Figure 13. Micrograph of an isolated melt droplet on the bottom electrode (anode). Only one other feature like this was observed.

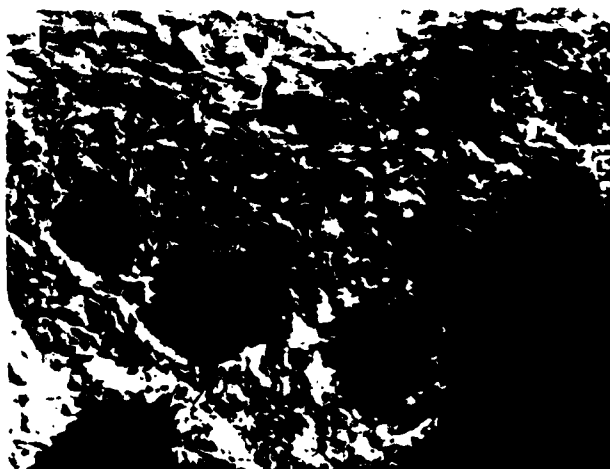


Figure 12. Micrograph of the cathode electrode revealing the lack of solidified melt.

Discussion

The argon ion bombardment of electrodes did not produce a beneficial effect on the water breakdown characteristics. The figure of merit for conditioned electrodes was actually slightly less than that for non-conditioned electrodes, but the difference was well within one standard deviation. The statistical scatter for the conditioned electrodes was slightly less than that of non-conditioned electrodes but the reason for this result remains unclear. The plasma conditioning did decrease the electron emissivity by approximately a factor of 2; hence, if surface work function were a significant parameter of the breakdown process we would have expected a beneficial rather than degrading effect from conditioning.

The metallography of the craters yielded some very interesting observations. The large degree of twinning in the austenitic grains and the sharp ridges found on the electrode surfaces suggests heavy stressing of the metal during crater formation and a mechanism to explain the grouping of spark craters on the polished electrodes (i.e., field enhancement along the ridges). Also there were indications that the breakdown started from the anode and proceeded to the cathode.

Finally, the argon ion bombardment probably removed the passivating layer of chromium oxide, thus allowing metal ions from the anode to participate in the breakdown process.

Suggestions for Future Work

Further investigation of the influence of the electrode surface on the breakdown process is required. Particular attention should be devoted to potential effectiveness of protective oxide layers - their mechanical and electrical properties being of prime importance. Specifically copper oxide on copper electrodes - because of the semiconducting nature of copper oxide - and chromium oxide on stainless steel elec-

trodes - because of its favorable protective, mechanical property - should be investigated. Both films also have the advantage of being easily reformed after degradation of an initial layer.

Since the mechanism of breakdown initiation still is not known it is possible that different ion bombardment conditions could be useful to clean electrode surfaces or produce a beneficial surface reaction (i.e. ion implantation alloying). But the lack of any beneficial results in this study raise doubts as to the probability of success for such treatments.

Acknowledgement

The authors would like gratefully to acknowledge the skill and care of K. Chilton and L. W. Hardesty who constructed the apparatus and assisted in the testing.

The authors would also like to acknowledge the metallurgical expertise of R. Lowry who assisted in the interpretation of the surface morphology.

References

1. A. P. Alkaimov, V. V. Vorob'ev, V. F. Klimkin, A. G. Ponomarenko, R. I. Soloukhin, "The Development of Electrical Discharge in Water", Sov Phys - Doklady Vol 15 #10 p 959 April (1971).
2. E. V. Yanshin, I. T. Ovchinnikov, Yu. N. Vershinin, "Mechanism of the Pulsed Electrical Breakdown of Water", Sov Phys 19 2 (1974) p 95.
3. M. J. Witcomb, "The Development of Ion Bombardment Surface Structures on Stainless Steel", Jour of Materials Science 9 (1974) pp 551-563.
4. D. B. Fenneman and R. J. Gripshover, "Electrical Breakdown in Water in the Microsecond Regime", Digest of Technical Papers, 2nd IEEE International Pulsed Power Conference, Lubbock, Texas, June 1979 IEEE Catalog No. 79 CH1505-7.
5. D. B. Fenneman and R. J. Gripshover, "Experiments on Electrical Breakdown in Water in the Microsecond Regime", IEEE Trans. on Plasma Science, Sep 1980.
6. Brown, Sanborn C., Basic Data of Plasma Physics, 1966, 2nd Edition, The M.I.T. Press, Cambridge, Mass. 1967.
7. T. H. Martin, "Pulsed Power for Fusion", Proceedings International Pulsed Power Conference, Lubbock, Texas, Nov. 1976, IEEE Catalog Number 76 CH1147-8 Reg 5.
8. Reed-Hill, Robert E., Physical Metallurgy Principles, 2nd Edition, D. Van Nostrand Company, New York, 1973.

REPETITIVE MEGAMP PER MICROSECOND di/dt PULSERS FOR DRIVING SUB-OHM TRANSMISSION LINE NEUTRINO PARTICLE DETECTORS

G. J. Krausse, C. G. Dalton, and J. Sarjeant
University of California
Los Alamos Scientific Laboratory
Los Alamos, New Mexico 87545

Summary

With the advent of low-cost honeycomb extrusions of polypropylene sheets, transmission line flash chambers have become highly attractive candidates for large particle detector arrays. This has brought about the need for repetitive pulse systems that must provide exceptionally high peak currents, low levels of spurious radiation, high reliability, and shot life in excess of 10^7 . Each module of 10 flash chambers requires a peak current of 20 kA with a current di/dt greater than 1 MA/ μ s. The pulser output must develop ≈ 7 kV across a load of 0.5Ω with a pulse width of 500 ns. The complete system will require 40 pulsers run in parallel for a combined current output of 1.4 MA peak with a system di/dt of 40 MA/ μ s. The repetition rate will be up to 2 Hz. This paper describes the development of such a system, its unique voltage and current diagnostics, and the impact of the physical limitations of present component technology on lifetime, reliability, maintainability, and pulse fidelity.

Introduction

In an article published in *Nuclear Instruments and Methods*, Volume 158, page 289 (1979), a system was discussed which allowed rapid data collection from particle detectors known as "flash chambers." A flash chamber consists of a noble gas mixture confined between two conducting plates in a dielectric container. The conducting plates are pulsed to a high-voltage level in coincidence with the passing of a charged particle and a plasma is then formed in the dielectric container. At this point, the data may be extracted optically or, in some cases, electrically. Until recently, data collection from flash chambers was a slow and tedious process because a photographic method was employed. Complexity of construction and high cost have also curtailed the use of these novel detectors, but with the advent now of low-cost honeycomb extrusions of polypropylene sheets, flash chambers (Fig. 1) have become very attractive components for large particle detector arrays. The flash chamber readout system developed at LASL can output data at a rate $>2.5 \times 10^6$ bits per interrogation. The period of one interrogation is less than 0.01 s as compared to the previous optical system outputs of several hundred bits requiring seconds or minutes to accumulate. It is clear that this new readout method will be of considerable utility.

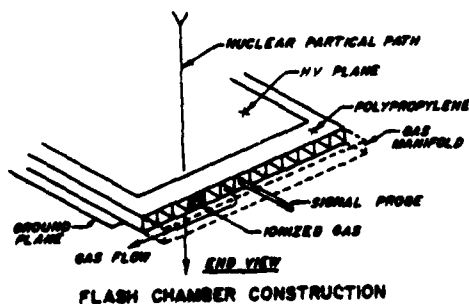
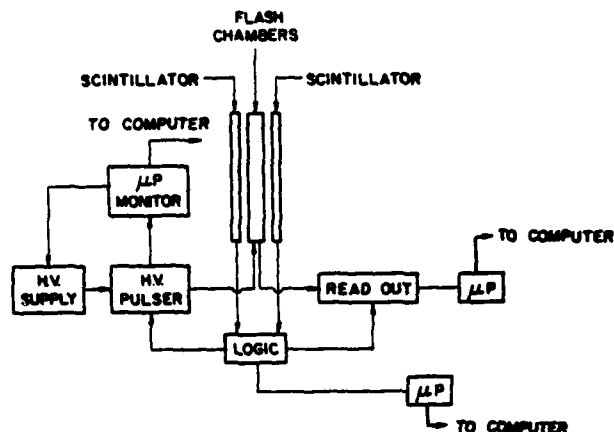


Fig. 1.

At that point in the system development, however, it was dependent on substantial technology base developments in the high-voltage pulse power driver.

Figure 2 shows a simplified, overall block diagram of the instrumentation system. In this system, the flash chamber readout, high-voltage pulser, and the voltage monitors are the major areas of development. The high-voltage pulser is the focal point of this report. This pulser can be divided into four separate areas: the load, energy storage, load-to-pulser interface, and switch. These areas will be discussed in this order.



EXPERIMENTAL CONFIGURATION

Fig. 2.

The Load: The flash chambers for this system are $3\frac{1}{2}$ m by $3\frac{1}{2}$ m with a thickness of 5 mm, and are clad on both sides with 0.05 mm of aluminum foil, forming a parallel plate capacitor with a capacity of 20 nF. Since these chambers have dimensions comparable to the pulse rise and fall times, they cannot be treated as conventional transmission lines. Instead, they are being analyzed more as distributed capacitive and inductive elements than a true transmission line. In order to have a point of reference, the impedance of a chamber was measured and found to be $\approx 5 \Omega$, and the transit time was measured to be 10 ns. The above parameters constitute the predominant characteristics of the flash chamber as an electrical load. In the planned experiment, there will be 400 flash chambers and each pulser will have to drive a module consisting of 10 chambers. This means a load of 0.5Ω and 200 nF for each pulser.

Energy Storage: For high resolution and peak efficiency, the flash chamber requires a rectangular high-voltage pulse with a duration dependent on the chamber's physical size (in our case, 500 ns and a source impedance of 5Ω). A pulse-forming network (PFN), was used to meet these needs. In the first stages of PFN design, computer modeling was used to arrive at a prototype design. This prototype PFN was then tested under load

conditions and adjusted to compensate for distributed parameters not included in the modeling program. Since high-peak currents and low inductance are required in conjunction with a lifetime of 10^7 shots (MTBF, 90% confidence level), capacitor selection was nontrivial. Figure 3 shows the data from which capacitors for the PFN were selected. Although the Axel capacitors seem the most likely candidate, budgetary restraints required a more cost-effective choice. Considering the lifetime cost and ESR data, the emphasis has been placed upon the development of a PFN utilizing mylar capacitor manufactured by Condenser Products.

MANUFACTURE	TYPE	SHOT LIFE	ESR	COST (SINGLE UNIT)
AXEL	MP-5AW	10^6	86 Ω	\$72.00
CONDENSER	MSB-103			
PRODUCTS	-15 MX	10^7	232 Ω	\$8.00
MURATA	DHS	10^4	41 Ω	\$6.00
SPRAUGE	720C	10^5	2.05 Ω	\$6.00

ALL CAPACITOR WERE 10WV UNITS

CAPACITOR DATA

Fig. 3.

Load-to-Pulser Interface: In transmitting the power from the switch and PFN assembly to the chambers, the characteristics of both strip-line and coaxial transmission lines have been assessed. Coaxial lines have yielded the best results so far and seem to be the most cost-effective. Figure 4 illustrates the pulser-to-load interface geometry. The pulse is fed to the module via ten bundles of coaxial cable, each bundle consisting of six 31- Ω cables in parallel. Each module is fed evenly along one edge and is terminated along the edge opposite the feed.

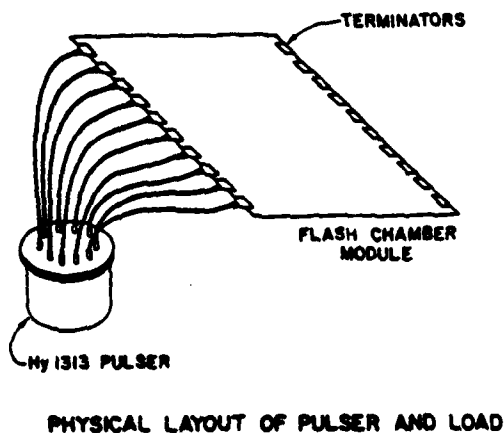
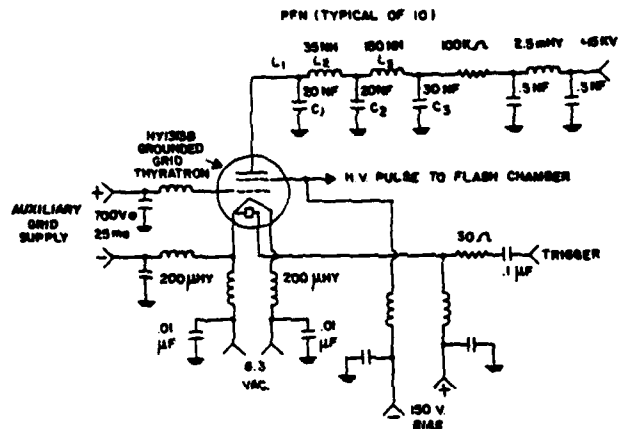


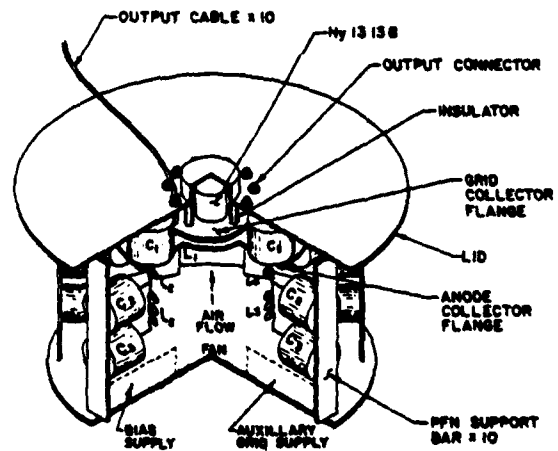
Fig. 4.

The Switch: After an extensive market study and vendor interactions, an EG&G thyatron was chosen for initial prototyping. The choice of a thyatron over a spark gap was based on the low spurious noise requirement and a $>10^7$ shot life. EG&G has developed a new grounded grid thyatron, the HY-1313B, for our specific application. Figure 5 shows the HY-1313B pulser schematic and Fig. 6 shows the physical layout. The thyatron is mounted upside down in order to reduce the output lead length as much as possible. Ten PFNs surround the HY-1313B in a folded wagon-wheel arrangement. This geometry allows very close placement of the first mesh of the PFN while conserving space by folding meshes two and three. To date we have tested the HY-1313B to a peak current of 20×10^3 A at the 10% to 90% points into a 0.5- Ω , 200-nF load and were able to obtain a current rise time of 16 ns (this means a di/dt of 1.25 MA/us) (Fig. 7) and a maximum peak current of 32×10^3 A with a voltage rise time of 50 ns (Fig. 8).



HIGH VOLTAGE PULSER

Fig. 5.



HY-1313B PULSER PHYSICAL LAYOUT

Fig. 6.

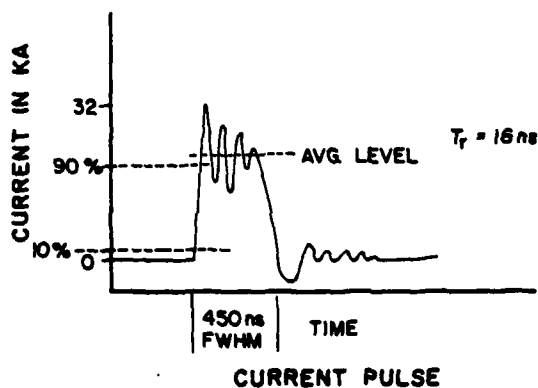


Fig. 7.

Conclusion

Considering shot life, cost, and ESR, the Condensor Products capacitors are being used for further testing of the PFN. The HY-1313B, at the present stage of testing, has successfully driven 100% of the load and looks acceptable at this time. It appears that several changes could improve system performance--a further compression of component density in the vicinity of the HY-1313B, and use of the lower ESR Axel capacitors.

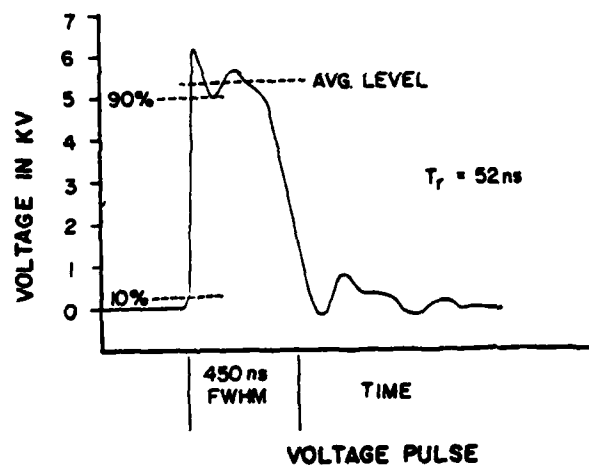


Fig. 8.

Both could have a significant effect on current rise time. In addition, use of a ferrite toroid surrounding the thyatron to improve switching time might also be beneficial.

A MODULATOR FOR CATHODE-PULSED MILLIMETER WAVE EXTENDED INTERACTION OSCILLATORS WITH FINE CONTROL OF PULSE SHAPE

by

D. S. Ladd, G. W. Ewell, and J. C. Butterworth

Georgia Institute of Technology
Engineering Experiment Station
Atlanta, Georgia 30332

Introduction

This paper describes the requirements, design, and operation of a modulator for a series of pulsed Extended Interaction Oscillators (EIO's) operating at 95, 140, and 220 GHz. Important system requirements were an extremely flat top pulse to minimize frequency modulation during the transmitter pulse, coupled with the fast rise and fall times required for the high range resolution system. These requirements were met by developing a non-saturating, hard-tube modulator that provides pulse widths of 20 to 200 ns adjustable in increments of 10 ns. This modulator permitted pulsing of the EIO cathode with less than 50 V departure from a flat top for the approximately 15 KV cathode pulse.

The operation of the EIO's and the specific characteristics which lead to the generation of modulator requirements are briefly discussed. Next, the design and fabrication of the modulator are described in some detail, with particular emphasis on techniques used to obtain fine grain pulse shaping. Finally, performance of the modulator-EIO combination is reviewed, with emphasis on how RF performance is affected by tube-modulator interaction.

Cathode-Pulsed Extended Interaction Oscillators^{1,2,3,4}

The Extended Interaction Oscillator (EIO) is a source of high peak power at millimeter wave (mmw) frequencies. The EIO is a linear beam device in which an electron beam is formed by a pulsed gun. After being focussed, the beam passes through a slow wave structure, coupling energy into the RF field. Unlike a magnetron, most of the electrons pass through the interaction region to a collector so that the beam energy is dissipated away from the delicate RF structure. Also, the cathode of the EIO is removed from the interaction region permitting a substantial increase in size to obtain low current densities. This gives the EIO an average power capability that is much higher than mmw magnetrons and a typical tube life greater than 1000 hours. The operation of 80 GHz magnetrons to obtain comparable lifetimes has required the detection of arcs in the magnetron and shutting down the modulator before the magnetron suffers severe damage.

The operating characteristics of several pulsed EIO's are given in Table I. The beam voltage, or cathode voltage (V_K), is typically -21 KV. The cathode is negative with respect to the anode. The anode voltage (V_A), varies with tube power and frequency. The EIO can be operated by DC biasing the anode and cathode at V_A and pulsing the cathode to V_K or by pulsing both the anode and cathode from ground to their operating voltages.

TABLE I
CHARACTERISTICS OF SOME PULSED MILLIMETER WAVE EIO's

Tube Type	Mechanical Tuning Range (GHz)	Peak Output (Watts)	Cathode Voltage (KV)	Anode Voltage (KV)	Electronic Tuning Range (MHz)
VKV 2043	92.7-96.8	950-1770	-21	-9.0	300-400
VKT 2019	139.7-140.3	270	-20	-12.4	370
VKV 2029	225.3	70	-21.3	-13.1	400

The pulse behavior of the EIO differs from the biased diode nature of the magnetron in that the EIO behaves like an almost resistive load (being a space charge limited diode for which $I_K = K(V_{AK})^{3/2}$). Also, the peak cathode current of the EIO is about one tenth the peak current of a comparable magnetron. To provide fast pulse rise and fall times, however, the modulator must be capable of supplying many times this current to charge and discharge the cathode stray capacity.

Figure 1 shows the variation of output power and frequency with beam voltage for constant beam current in a typical 95 GHz EIO. Note that no RF is produced until V_K reaches about 80% of the voltage at the peak power point. The EIO operating frequency increases with V_K at a rate of about 120 KHz/Volt, at the peak power point. This rate has varied 50% with mechanical tuning position for some tubes. One 95 GHz EIO had a 660 MHz electronic tuning range over a 1 dB power variation.

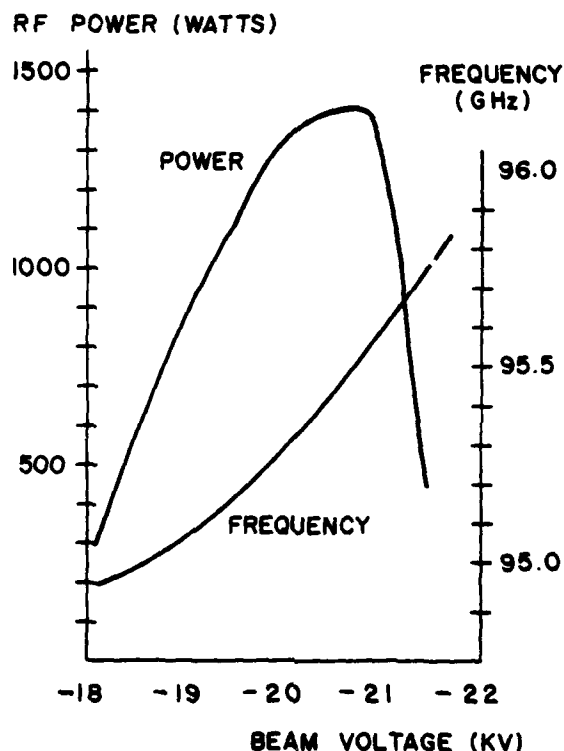


Figure 1. EIO Power and Frequency vs. Voltage

Transmitter Requirements⁶

The minimization of frequency variations during the RF pulse requires that the cathode voltage pulse be flat. The degree of flatness depends on the amount of FM acceptable and the frequency-voltage pushing factor for the EIO. To investigate injection locking of the EIO for a coherent transmitter, it was decided that the cathode pulse should be flat within 50 volts out of 21 KV (13 KV pulse, 8 KVDC) for a 95 GHz EIO. A series of modulators allowing precision manual control of the output voltage pulse shape were developed to provide a high degree of pulse stability. System requirements called for a pulse width variable from 40 ns to 200 ns with 10% to 90% rise and fall times of 20 ns. The 50 V flatness should be at least 150 ns out of 200 ns. The development of these modulators for 95 GHz, 140 GHz and 220 GHz pulsed EIO's was sponsored by the U.S. Army under contracts DAAG39-78-R-9061 (Harry Diamond Labs), DAAK40-78-C-0158 (MICOM) and DAAK70-79-C-0108 (Night Vision Lab).

The EIO Pulse Modulator

Block Diagram

The block diagram of the EIO pulse modulator is shown in Figure 2. When triggered by a TTL pulse, the incrementally adjustable pulse shaper generates a pulse that can be shaped in 10 ns increments. This pulse is then amplified by a linear 15 KV hard tube pulse amplifier. The pulse shaping is required to compensate for the inherent non-linearities of a high voltage non-saturated hard tube modulator. The output of the pulse amplifier is coupled to the cathode of the EIO to produce the RF pulse. The collector peak current I_c , which is proportional to the cathode pulse voltage, is monitored by a peak detector. The voltage from the peak detector is used to regulate the output pulse amplitude through the pulse amplifier control operational amplifier. The operational amplifier feeds a stabilization voltage to the pulse shaper which corrects the pulse amplitude.

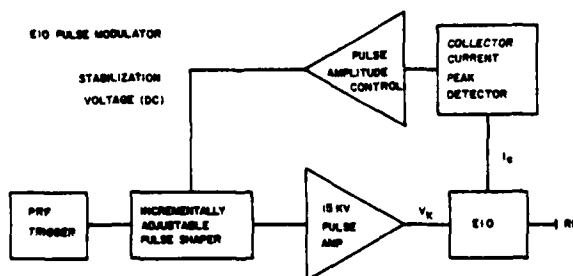


Figure 2. Block Diagram of the EIO Modulator

Pulse Shaper

Precision manual control of the output pulse shape was achieved in the incrementally adjustable pulse shaper. A simplified diagram of the pulse shaper is shown in Figure 3. The circuit design is a hybrid of digital and analog devices resulting in control of the pulse shape in 10 ns increments.

A negative going TTL pulse that is longer than the desired output pulse is inverted through a 74S140 that drives two 100 ns 10 tap delay lines in series. Each tap of the delay line is buffered through an 8T93, which is a Schottky inverter with FET inputs, thus reducing the

loading of the delay line. Figure 4 shows the logic used to generate a 10 ns pulse from one section of the pulse logic circuit. The buffered delay line pulse is NANDed with the inversion of the pulse from the previous tap to produce a 10 ns pulse at the output of each NAND gate. The leading edge of the pulse is delayed 10 ns from the leading edge of the previous pulse. Thus, the output from each of the 20 NAND gates is successively pulsed low for 10 ns over a 200 ns period. Each pulse causes current to flow through the 1K potentiometer and 300 ohm resistors from the emitter of Q_2 and also through X_1 into the emitter of Q_1 . The transistors act as current sources for the 50 pf integrating capacitor. During the 10 ns pulse, the 50 pf capacitor is charged or discharged by the differential current through Q_1 and Q_2 , which is set by adjustment of the 1K potentiometer. At any 10 ns increment, the voltage is determined by the net change from the previous increments. Adjusting a particular potentiometer will not affect the portion of the pulse ahead of its position, but will change the remainder of the pulse after its position.

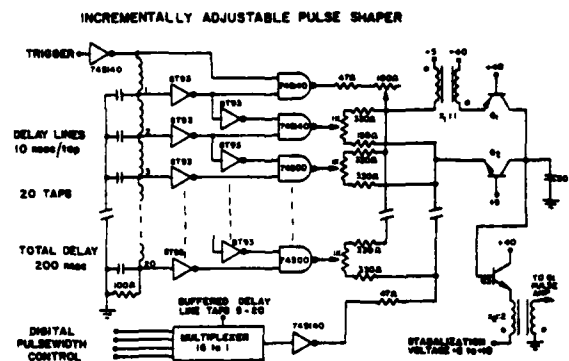


Figure 3. Simplified Schematic of the Incrementally Adjustable Pulse Shaper

High current drivers (74S140) and lower resistor values are used at the start of the pulse to produce a fast rise time. The first 74S140 charges only through Q_1 , and the second is capable of sinking greater discharge than charge current to produce a leading edge spike. The pulse is terminated by dumping the charge through Q_2 and a 47 ohm resistor by pulsing the last 74S140 low for a period equal to the length of the delay line input pulse. The termination time is selected by multiplexing 16 of the buffered delay line taps. The pulse width can thus be digitally controlled on a pulse to pulse basis.

The voltage across the 50 pf capacitor is buffered by an emitter follower Q_3 and then stepped up by a 1:2 transformer, X_2 . The amplitude of the pulse is controlled by reverse biasing the base emitter junction of Q_3 through the primary of X_2 with the stabilization voltage from the pulse amplitude control operational amplifier.

Figure 5 shows three examples of pulse shapes illustrating the degree of pulse shape control. The third pulse is the general shape required to drive the pulse amplifier. The spike on the leading edge gives a fast rise time, the positive ramp compensates for droops in coupling capacitors or transformers.

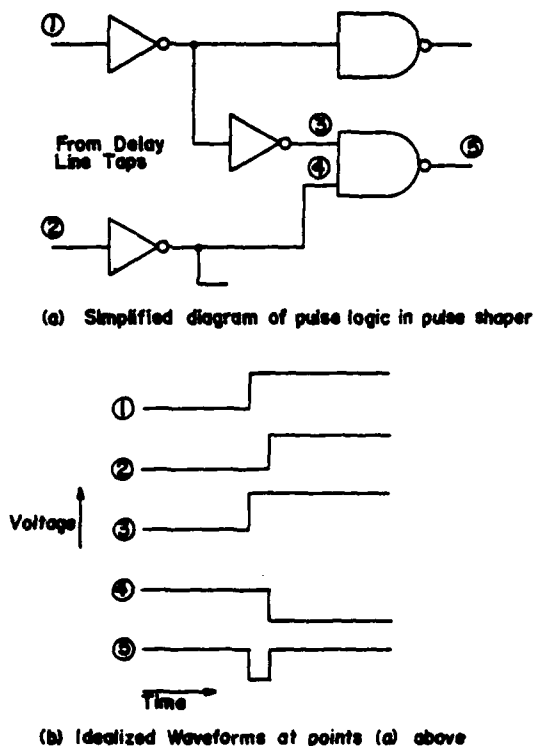


Figure 4. Generation of 10 ns Pulses

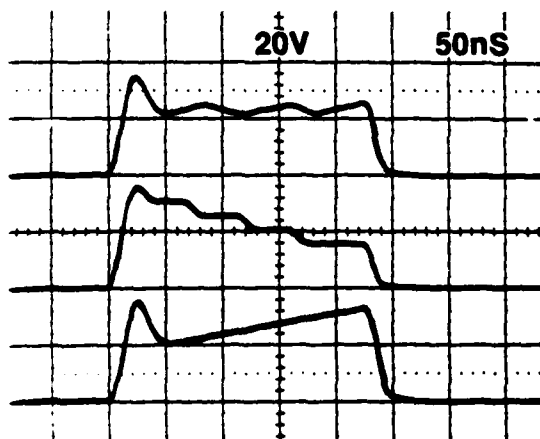


Figure 5. Examples of Pulse Shapes at Output of Pulse Shaper

The Pulse Amplifier

The output of the pulse shaper is amplified by a 15 KV linear pulse amplifier as shown in Figure 6. The pulse amplifier can be divided into the output stage, which is the X2172F, and a driver stage consisting of three 5687's in two transformer coupled stages. The pulse is amplified

with minimal distortion through the driver to the grid of the X2172F. The high gain, limited current and stray capacity in the output stage cause pulse distortion; the pulse shaper compensates for this distortion. A low value plate load resistor for the X2172F is used to rapidly charge the EIO and modulator stray capacity at the end of the pulse. Unfortunately, this makes the transmitter inefficient; the modulator peak output power is 57.4 KW to obtain an RF peak power of 1.5 KW. The output pulse is coupled by a capacitor to the EIO cathode. The EIO heater supply is isolated through a bifilar choke.

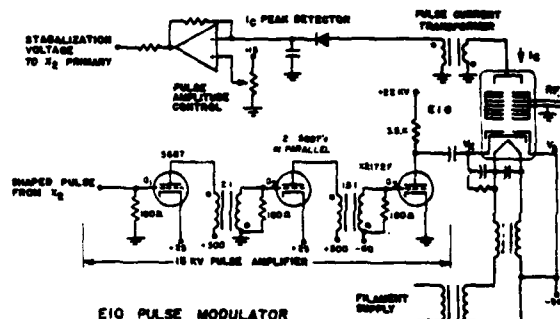


Figure 6. Simplified Schematic of the EIO Pulse Modulator

The Amplitude Control Feedback Loop

Long term instabilities in the gain of the pulse amplifier are mitigated by using a closed loop feedback circuit that detects the peak value of the collector current I_C and feeding the voltage from the peak detector to a high gain operational amplifier that is referenced to a stable voltage source. Variation of the reference voltage controls the pulse amplitude. The stabilization voltage is fed to the emitter follower of the pulse shaper through X_2 . The peak current in the EIO is actively held constant for any pulse shape. This complicates the response of the modulator to an adjustment of a particular pulse shaper potentiometer. Some adjustment experience is required before the desired pulse shape is obtained.

Modulator Performance

Figure 7 shows the RF pulse, cathode voltage pulse (V_K) and collector current pulse (I_C) obtained by modulating a 95 GHz EIO. The absence of ringing on current pulse was achieved by grounding the body of the EIO directly to the shield around the modulator. The capacity between the EIO cathode and the EIO body, with the anode shielded, was measured to be 6 pf. For fast rise times, this coupling will resonate with the inductance of the body ground lead causing pickup in the collector current viewing circuit. The entire modulator must be properly shielded, since peak currents in the modulator during the leading edge are about 14 Amperes, or 20 times that of the collect current. The control of the RF pulse width is shown by the multiple exposure in Figure 8.

Measurement of Pulse Flatness

The measurement of the desired voltage pulse flatness requires about 0.1% resolution in the pulse viewing system. This resolution could not be achieved with a Tektronix P6015 high voltage probe and 7603 oscilloscope. Although they demonstrated that the modulator was capable of being adjusted to give the desired flatness, there was no way of calibrating the probe within 0.1% with available equipment. The true measure

of modulator performance is the amount of frequency deviation during the pulse. The system for which this modulator was developed will use a real time frequency discriminator in a fast phase lock loop, but this device was not available. As an alternative, a TRG Precision Frequency Meter, a TRG Precision Attenuator, and a diode detector were used to demonstrate the pulse flatness. First, the frequency meter was used to measure the change of RF frequency with anode voltage for a 95 GHz EIO. This was measured to be 75 KHz/volt over a 1000 volt operating range where the power varied by about 0.2 dB. The response of the frequency meter in fixed position to changes in V_A and, thus, frequency was measured. Figure 9 is the plot of frequency meter absorption vs frequency at 95.0 GHz. The maximum slope is 0.19 dB/MHz, allowing the pulse frequency deviation to be displayed on the oscilloscope with a linear response over 20 MHz and a resolution of at least 1 MHz

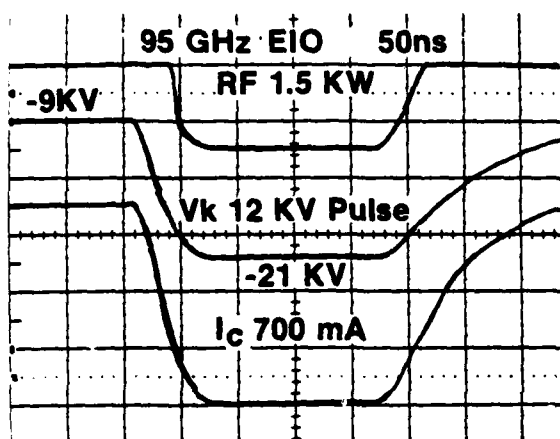


Figure 7. EIO RF, Cathode Voltage and Collector Current Pulses

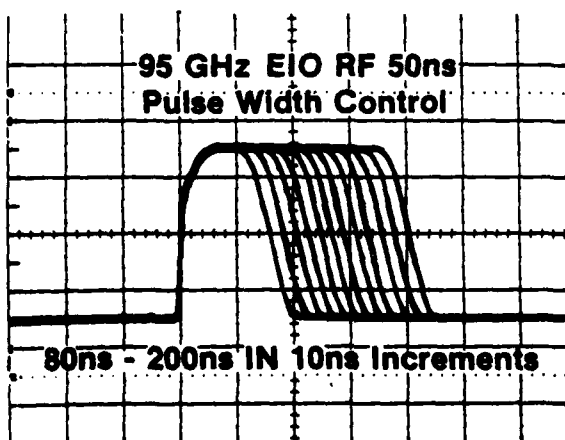


Figure 8. Multiple Exposure of RF Pulse Widths

FREQUENCY METER RESONANCE AT 95 GHz

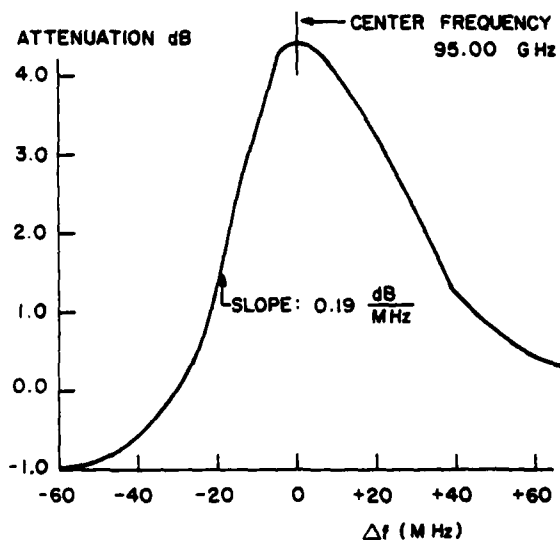


Figure 9. Variation of Absorption with Frequency for Frequency Meter in Fixed Position

Figure 10 shows the "dip" of the frequency meter for four, 100 volt steps in V_A . This corresponds to a change in frequency of 7.5 MHz per step. The combined slope and ripple over the central 130 ns is on the order of one fifth of a step, showing that the frequency deviation is about 1.5 MHz and the pulse flatness is about 20 volts, or better than 0.1% of the beam voltage.

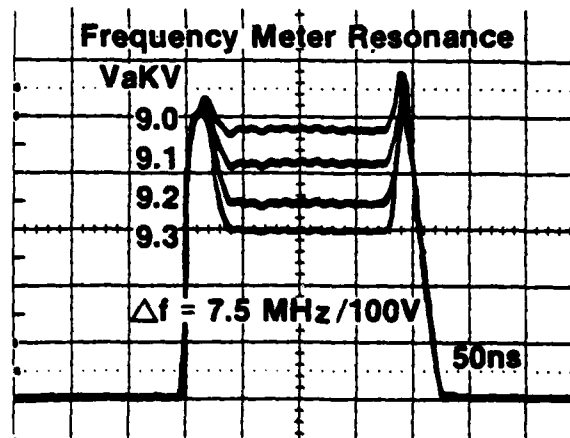


Figure 10. Demonstration of Pulse Flatness Using Frequency Meter Resonance and Variation of Anode Voltage

Although the stability of the modulator was very good for pulse amplitude and short term pulse shape, the pulse shape would change with modulator temperature as a result of the non-linear response of the pulse amplifier to the corrections in the amplitude of the output of the pulse shaper.

Further Development and Applications

Methods of supplying high peak currents during the rise and fall times must be developed to improve the efficiency of this modulator. This could be done by letting the modulator pulse only the high impedance and stray capacity of the EIO until the end of the pulse, then introducing a low impedance by using a tailbiter tube or a saturable choke to discharge the stray capacity.

Long term pulse shape stability can be achieved by incrementally sampling I_C to generate many error voltages that could then be used to correct the appropriate increment in the pulse shaper in addition to, or in lieu of, manual control.

In addition to the generation of fixed frequency pulses, this modulator can be used to modulate the frequency for clutter reduction and pulse compression. Since the pulse shaping is done at low voltage, the incrementally adjustable pulse shaper followed by a suitable pulse amplifier would make an excellent modulator for pulsed IMPATT and Gunn diodes where pulse shaping is presently being done by a linear ramp modulator or tuning a PFN in a line type modulator.

References

1. G. W. Ewell, Radar Transmitters, To be published by McGraw-Hill Book Company 1980.
2. G. W. Ewell, D. S. Ladd and J. C. Butterworth, "High Power Millimeter Wave Radar Transmitters," To be published in Microwave Journal, June 1980.
3. "Introduction to Extended Interaction Oscillators," published by Varian Associates of Canada, Ltd., Georgetown, Ontario, Canada.
4. J. A. Scheer and N. C. Currie, "Advanced Millimeter Wave RF Technology," Proceedings Western Regional Electronic Warfare Technical Meeting, Southwestern Crow Club, White Sands Missile Range, N.M., April 1980, p. 3.
5. Personal Communication with Gordon Selby, EMI Wells Somerset, England.
6. R. W. McMillan, et. al., "Near Millimeter Wave Radar Technology," Phase I Interim Technical Report, Contract No. DAAK70-79-C-0108, U.S. Army ERADCOM, NVL, pp. 20-38.

THREE PULSE WIDTH SOLID STATE MAGNETIC SWITCHING MODULATOR FOR THE AN/SPS-67 RADAR

Steven T. Adams
Raffee Mgrdechian (Axel Electronics)
Norden Systems, Inc.
Subsidiary of United Technologies Corporation
Norwalk, Connecticut

ABSTRACT

A new transmitter/modulator has been developed for the AN/SPS-67 radar, a modernized version of the AN/SPS-10 shipboard radar system*. The transmitter is smaller, lighter and more reliable than the unit it is replacing, and is compatible with reduced background noise clutter, improved moving target detection, and accurate target acquisition.

The AN/SPS-67 transmitter/modulator utilizing a 210 kW, G-band tunable Varian Magnetron, SFD-341, incorporates the following features.

- Three discrete pulse widths: 0.1 μ s, 0.25 μ s, and 1.0 μ s.
- Magnetron cathode voltage tail biting, producing a cathode voltage fall time that is close to the voltage rise time. This feature is designed into the single output pulse transformer.
- Magnetron cathode voltage backswing clipping to reduce post pulse spurious voltages.
- An all solid state modulator design which provides pulse width channel isolation without the use of mechanical relays.
- Magnetic switch core flux reset without dc bias.
- Control of energy to storage capacitors with pulse to pulse regulation.
- Command control of storage capacitor charging and selection.

Performance data on the new transmitter is presented together with initial field test results.

INTRODUCTION & SUMMARY

The AN/SPS-67 System is a high performance, high reliability surface surveillance radar system, which incorporates advanced modern radar technology. The AN/SPS-67 modulator is a modularized, all solid state, magnetic pulser, which provides the required video-pulse to the magnetron. System requirements as related to the transmitter modulator are as follows:

Pulse Width

- Long: 1.0 \pm 0.1 μ s
- Medium: 0.25 \pm 0.02 μ s
- Short: 0.10 \pm 0.01 μ s
- Peak Power: 190 to 285 kW measured at magnetron

The work reported in this paper was performed under Contract #N00024-77-C-7057 with Naval Sea Systems Command, Washington, D.C.

e. Pulse Repetition Frequency (PRF):

Long Range: 1200 pulses per second (p/s) with $\pm 5\%$ stagger.

Medium Pulse: 1200 p/s with $\pm 5\%$ stagger.

Short Pulse: 2400 p/s with $\pm 5\%$ stagger.

Minimum Range: (with 50 feet of waveguide)

- Long Pulse Mode 300 yards, or less, from antenna (1 square meter target)
- Medium Pulse Mode 200 yards, or less, from antenna (1 square meter target)
- Short Pulse Mode 75 yards, or less from antenna (1 square meter target)

Range Accuracy:

- Long Pulse Mode ± 300 feet or less
- Medium Pulse Mode ± 100 feet or less
- Short Pulse Mode ± 37.5 feet or less

Range Resolution:

- Long Pulse Mode 200 yards or less
- Medium Pulse Mode 190 feet or less
- Short Pulse Mode 75 feet or less

The transmitter/modulator, along with the receiver is housed in a cabinet assembly shown in Figure 1.

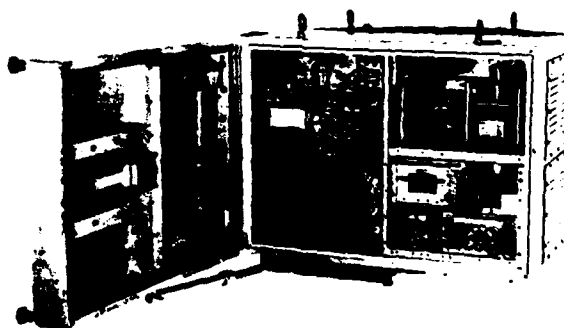


Figure 1. Transmitter/Modulator Cabinet

Figure 2 is a close-up view of the transmitter portion of the cabinet. The coaxial magnetron is mounted on the top portion of the picture. The oil filled modula-



Figure 2. Transmitter Portion of Cabinet

tor is directly under the magnetron in order to minimize lead inductance and keep high-voltage connections as short as possible. The low voltage pulser containing the energy storage capacitors, charge, discharge, select SCRs, and control circuitry are mounted in the assembly on the left side of the photograph. The D'Qing transformer and associated circuitry are mounted in the assembly mounted directly under the low voltage pulser.

Any of the four assemblies can readily be replaced in the field in case of failure.

Figure 3 is a block diagram of the transmitter/modulator. The modulator utilizes three pulse forming networks, and three saturable step-up transformers, one for each pulse width. A single step-up pulse transformer is used to provide the proper voltage pulse to the cathode of the magnetron. The pulse forming networks are charged at 12,000 volts by transferring the energy of the corresponding energy storage capacitor. Selection of pulse width is accomplished within two pulse repetition intervals, by in-

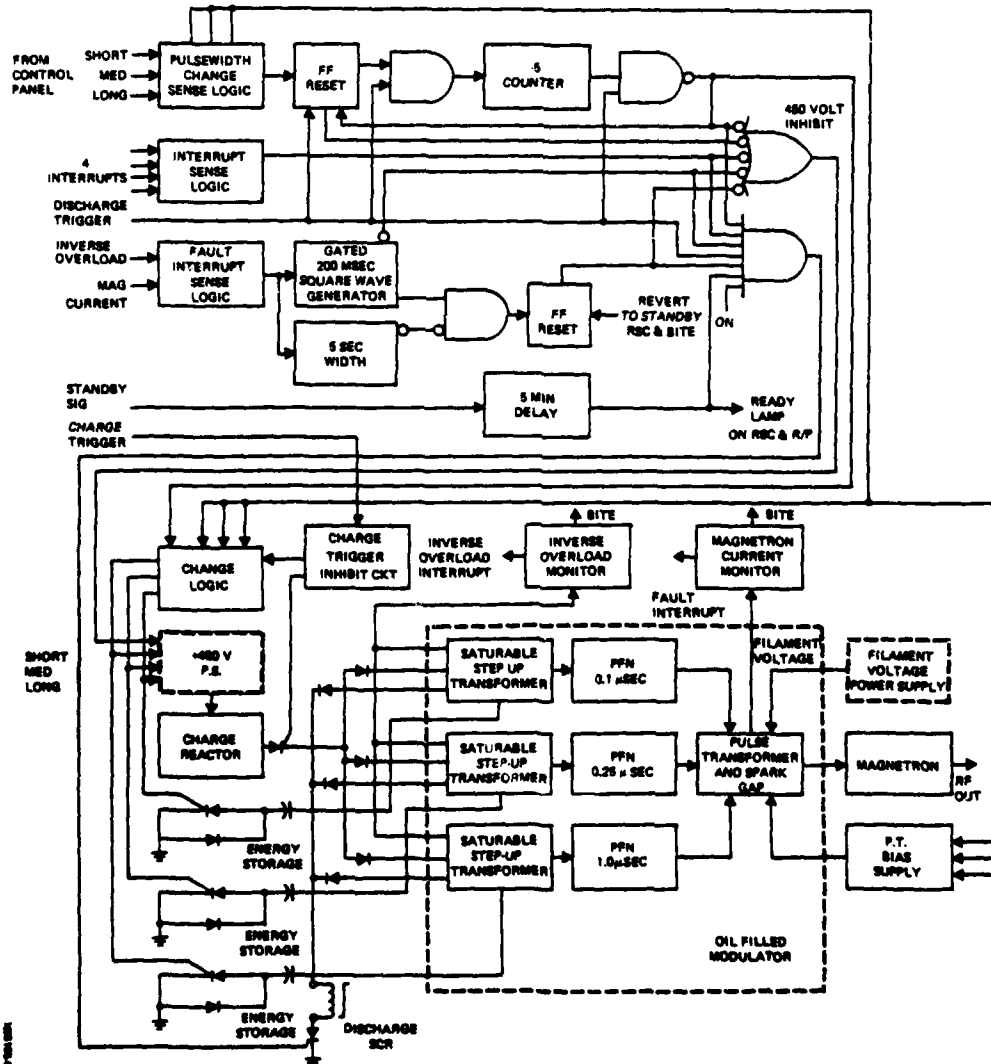


Figure 3. Block Diagram of Transmitter/Modulator

hibiting the charge SCR and selecting the desired pulse width by activating the appropriate select SCR. A pulse-to-pulse D'Qing charging circuit is used to regulate the energy to the energy storage capacitors. Single charge and discharge SCRs are used. Control circuitry is provided for shut-down sequence in the event an inhibit condition occurs on either magnetron over current inhibit or power supply overcurrent inhibit. Upon momentary excitation of either of these signals, the 450 V power supply is turned off for 100 milliseconds and at the same time the charge control pulses are inhibited for 110 milliseconds. Occurrence of four or more of these inhibit intervals within any one second period, causes the transmitter-modulator to revert to reset condition.

A computer analysis of the 1.0 μ s pulser circuit using the CDC SYSCAP II was performed prior to breadboarding stage. The computer simulation allowed detailed analysis of the complex nonlinear transient problem. Design parameters are determined, and system performance characteristics such as magnetron current and voltage waveshapes and power losses were established.

Figure 4 is an equivalent circuit for the charging and the discharging of the 1 μ s pulse forming network.

T_1 is given as using core material as defined below, with 4 turns on the primary from node 1 to node 21 and primary resistance of 4 m Ω , and with 60 turns on the secondary from node 26 to node 0 and secondary resistance of 75 m Ω . Core parameters are as follows: core area, $A = 4.84 \text{ cm}^2$; core length, $= 30.91 \text{ cm}$; Saturated flux density, $B_s = 14.9 \text{ kG}$ and magnetizing force, $H_s = 6$. Oersteds; end of rotation $B_m = 4.7 \text{ kG}$ and $H_m = 3$; residual $B_r = 14.2 \text{ kG}$; magnetizing force at $B = 0$, $H_c = 1.41$; knee $b_k = 13.2 \text{ kG}$ and $H_k = -.5$; air gap, $A_g = 0$; time constant, $\tau_c = 40 \text{ ns}$; and initial $B_i = -14.2 \text{ kG}$. Figure 5 shows these parameter values along with a plot of the resulting computed B-H curve using the Pheno model. The parameters were determined from the Orthondol data sheet shown in Figure 6 and the hysteresis power loss expected for the charging of the PFN, $P_1 = 60 \text{ W}$ which occurs in approximately 10 μ s. Figure 7 is a computer plot of the storage capacitor current, and Figure 8 is a photograph of the 1.0 μ s storage capacitor current of the finished unit.

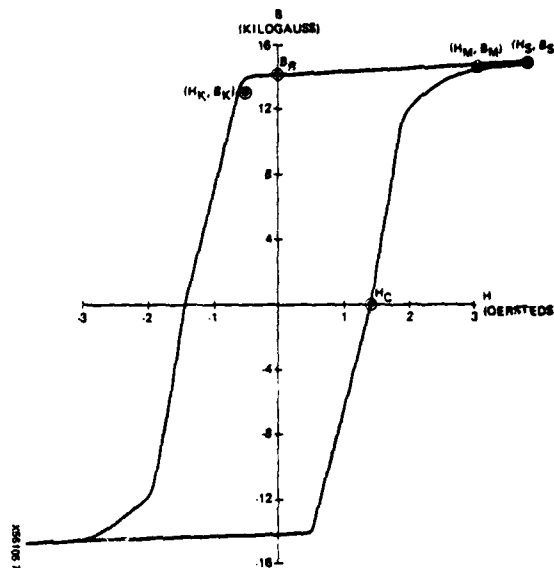


Figure 5. Calculated B-H Curve, 50 kHz

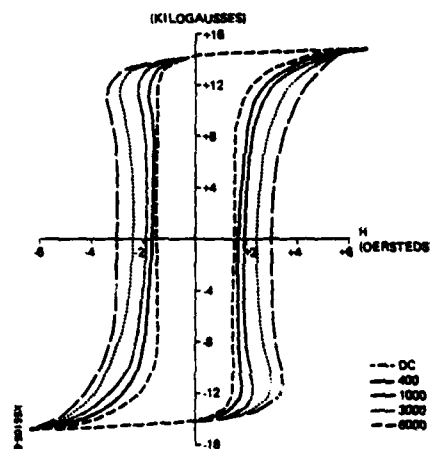


Figure 6. Hysteresis Loops for Orthondol

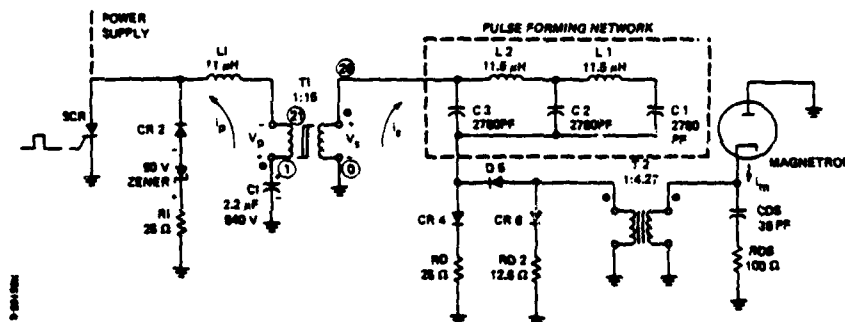


Figure 4. Equivalent Pulser Circuit for Charge and Discharge of 1 μ s Pulse Forming Network

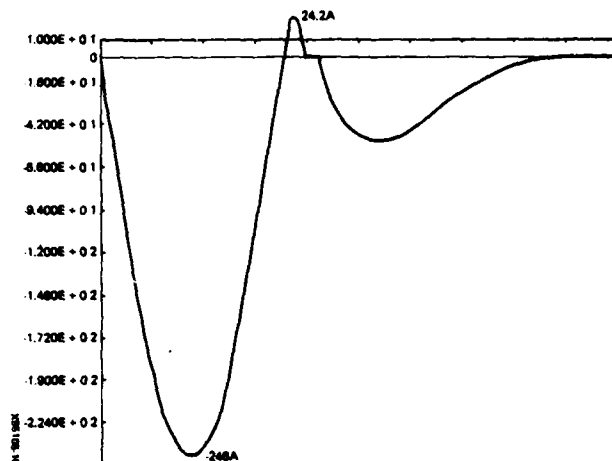


Figure 7. Storage Cap Current

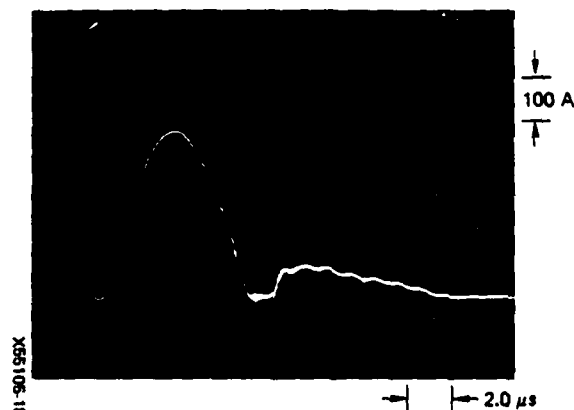


Figure 8. 1.0 μ s Storage Capacitor Current

LOW VOLTAGE PULSER DESCRIPTION

Figure 9 depicts the charging and discharging paths of the three energy storage capacitors C1, C2, C3 for the three pulse widths required by the system. Pulse width selection is accomplished by energizing the appropriate silicon control rectifier SCR1, SCR2, or SCR3. Pulse width channel isolation for the charge cycle is provided by steering diodes CR4, CR5, and CR6. SR1, SR2, and SR3 is the primary winding of the step-up saturable transformers for each of the pulse widths. The charge cycle is initiated when the command charge SCR5 is gated on, charge path is indicated by the solid arrows. During the charge cycle the saturable transformer of the selected mode is reset by the charging current. Discharge is initiated when the discharge SCR4 is gated on. Diodes CR7, CR8, and CR9 provide a ground return to the storage capacitors, and steering diodes CR1, CR2, and CR3 provide pulse width channel isolation. Discharge path is indicated by the dashed arrows. SR4 is a hold-off saturable reactor which helps to reduce turn-on dissipation in the discharge SCR4.

Diode CR10 and R1 comprise the inverse network.

Figure 10 depicts the charging of the energy storage capacitors of 2 modes (0.1 μ s and 0.25 μ s).

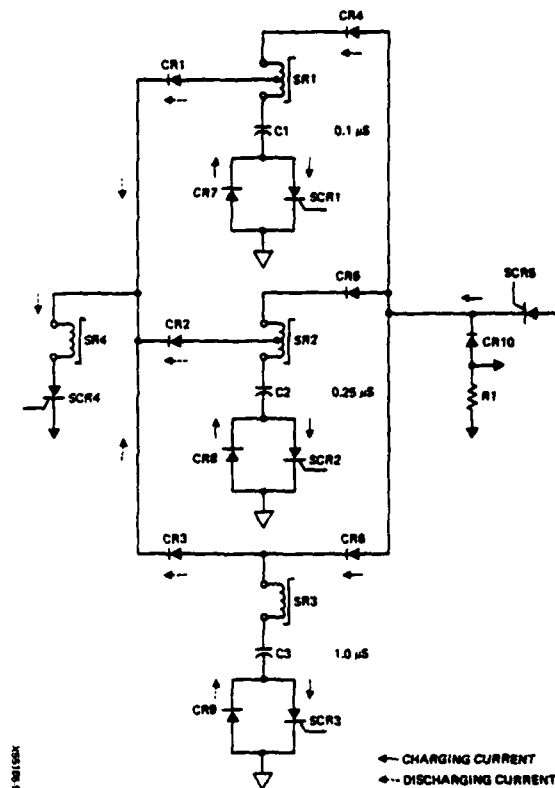


Figure 9. Charging and Discharging Currents of Energy Storage Capacitors

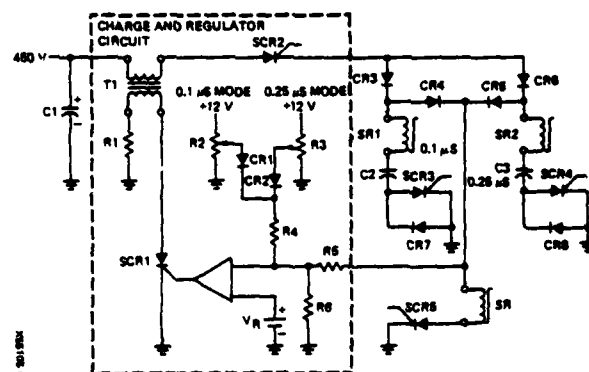


Figure 10. Charge and Regulator Circuit

Energy from C1 is transferred to the selected energy storage capacitor through the primary winding of T₁ when SCR2 is gated on. The amount of energy stored in the energy storage capacitor is regulated by sensing the voltage level on the energy storage capacitor. The sensing is accomplished with a resistive voltage divider network R5 and R6. The level of the sensing voltage is compared to a reference voltage V_R, and when the sensing voltage exceeds that of the reference, SCR1 is gated on, thereby connecting the secondary winding of T₁ across R1 which lowers the Q_{ing} of T₁ and removes the remaining energy stored in the

inductance of the primary winding. The level of regulation is set by either R2 or R3 depending on mode selection.

MODULATOR DESCRIPTION

Specifications

- 210 kW at G-band from a coaxial magnetron.
- Three discrete pulse widths: 0.1 μ s @ 2400 pps; 0.25 μ s @ 1200 pps; 1.0 μ s @ 1200 pps.
- Magnetron cathode voltage tail biting, producing a cathode fall time that is close to the voltage rise time.
- Magnetron cathode voltage backswing clipping to reduce post pulse spurious voltages.
- An all solid state modulator design with pulse width channel isolation, without the use of mechanical relays.
- Small size and light weight.

Considerations

To achieve small size and light weight while accomplishing tail biting and backswing clipping, a novel approach was considered whereby the pulse transformer would act as transformer and switch into saturation at the end of the cathode current pulse to discharge the energy remaining stored in the stray capacitance. In this manner, additional parts or circuitry which would increase the size and weight of the modulator, would not be required.

In order for the PT to pass a 0.1 μ s pulse and a 1.0 μ s pulse, special consideration was required for the core selection. The open circuit inductance of the PT had to be high enough to sustain the wide pulse, while the leakage inductance has to be low in order to pass the 0.1 μ s pulse. The turns ratio had to be selected to achieve good coupling, yet not so low as to require large or bulky components in the HV PFN, the saturable reactor switches or the circuit diodes.

The circuit developed for the HV modulator is shown in Figure 11. SR1, SR2, and SR3 are the switching reactors for the 0.1 μ s, 0.25 μ s and the 1.0 μ s mode respectively. SR1 and SR2 charge the low voltage storage capacitor through the upper (charge) terminal and discharge through the lower (discharge) terminal. This was required to reset the cores of these two channels. SR3 did not require the additional ampere turns for core reset.

The low voltage power supply was established to be 450 V at low input line voltage condition. This voltage was selected to allow for the use of a single chip silicon controlled rectifier with voltage derating to transfer energy from the low voltage storage capacitor to the PFN. The pulse transformer output voltage and current were required to be 24000 V peak at 20 A. The pulse transformer and saturable reactor turns ratios were selected to convert the 450 Vdc to 24000 V peak at 20 A.

The magnetron filament requirement is 11 A at 9.5V rms and is supplied through the filament transformer T2. T3 is a pulse current viewing transformer. E1 is a spark gap and CR7 a backswing clipping diode. CR1, CR2, and CR3 are charging diodes and CR4, CR5, and CR6 are channel isolating diodes. PFN1,

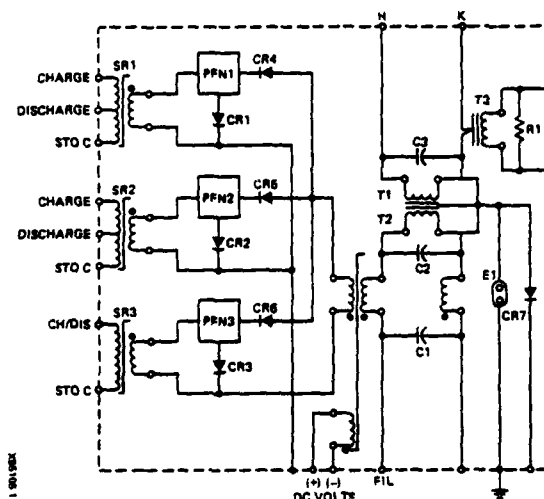


Figure 11. HV Modulator Circuit

PFN2, and PFN3 are the pulse forming networks of the 0.1 μ s, 0.25 μ s and the 1.0 μ s modes respectively.

Operating Principles

The low voltage storage capacitor is charged from the low voltage power supply through a charging transformer, which is used for regulating (by D'Qing) of the charging circuit when a preset storage capacitor voltage is achieved. The operating mode is selected by energizing an SCR, giving a return path to the PS Ground, from the storage capacitor.

Command charge is initiated by energizing the gate of an SCR. The principle discussed above is described in greater detail elsewhere in this paper. Figure 12 is a simplified schematic of a single operating mode up to the charging of the PFN in the high voltage section.

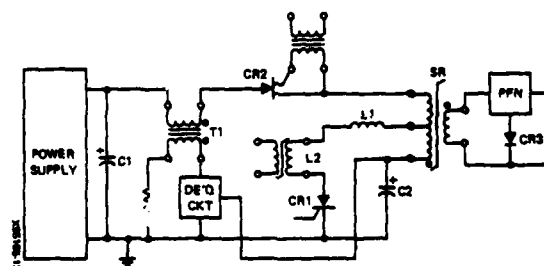


Figure 12. Low Voltage Storage Capacitor

C2 of Figure 12 is called the low voltage storage capacitor. To charge C2 a command is given to CR2 gate which allows current to flow from C1 to C2. The charging circuit operation is discussed elsewhere in this paper in greater detail. We shall now consider C2 as charged to the preset voltage. The SR core will be at negative residual flux after the charging of C2. Because a good switching action is required from the SR, the core must have a square hysteresis loop. An uncut nickle alloy core was selected. When a trigger is applied to CR1, of Figure 13, the storage capacitor C2 discharges through the primary winding of the SR. The SR acts as a step up transformer during the dis-

charge period of the storage capacitor that is charging the PFN in the SR Secondary, see Figure 13.

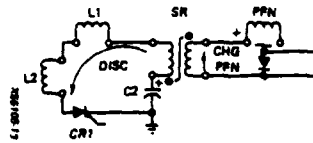


Figure 13. Energy Storage Capacitor Discharge Circuit

After the PFN has been charged and the volt-second capability of the SR has been reached, the SR switches from a high inductance state to a low inductance state represented as the saturated inductance of the SR. At this juncture of operation the PFN discharges. The SR saturated inductance with the pulse transformer leakage inductance, referred to the primary of the pulse transformer, are considered as part of the pulse forming network coil inductance in the design of the PFN. The PFN discharge circuit is shown in Figure 14.

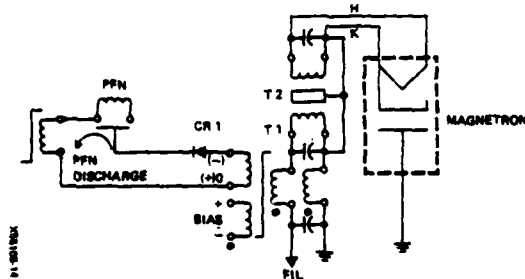


Figure 14. The PFN Discharge Circuit

The pulse transformer for this modulator is also to be used as a cathode voltage tail biter to reduce magnetron noise generation and improve radar performance. The manner of achieving this was by utilizing a core with a square hysteresis loop.

The core flux would go from negative saturation for the widest pulse to be transmitted, and biased appropriately for any other desired pulse width.

Pulse Transformer

Figure 15 depicts the hysteresis loop and flux swings for the various pulse widths of the pulse transformer when properly biased.

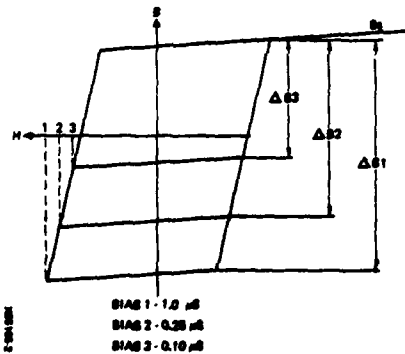


Figure 15. Hysteresis Loop and Flux Swings for Pulse Widths of Pulse Transformer

Figure 16 shows a simplified PT Winding (a) during PFN discharge, and (b) during the distributed capacitance energy discharge. The flux directions are noted and follow Figure 15.

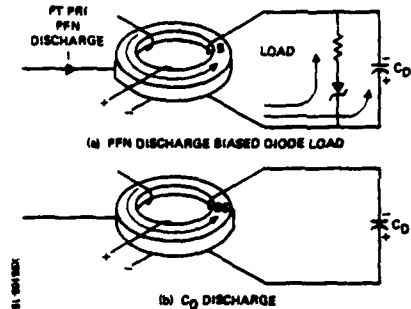


Figure 16. Simplified PT diagram

One should take note when B_S (Figure 15) is reached, the inductance of the pulse transformer is reduced allowing C_D to discharge faster. Figure 17 (b) shows the 1.0 μs cathode voltage with the core fully biased so it will not saturate and Figure 17 (a) shows a biased core cathode voltage fall time. The method described allows for continuous control of the fall time. Figure 18 (a, b, and c) shows three biasing conditions minimum, average and maximum.

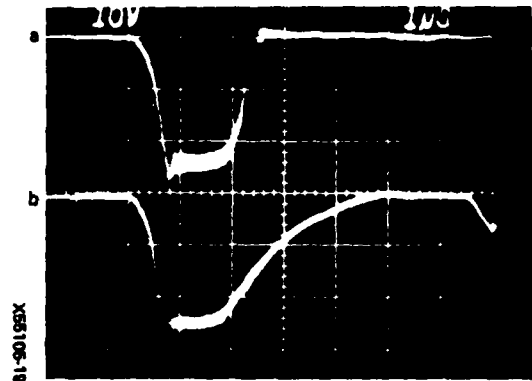


Figure 17. 1.0 μs Cathode Voltage Pulse
a. (top figure): biased for core saturation
b. (bottom figure): biased for no saturation

Figure 19 and 20 repeat the biased and unbiased condition for the 0.25 μs cathode voltage. Figure 21 shows the 0.1 μs cathode voltage (a) biased for saturation (b) biased out of saturation.

The following, Figures 22 thru 27, show the RF Envelope with the cathode voltage in saturation and not saturated for the three operating modes. Note the RF envelopes remain unchanged.

Figures 28, 29 and 30 show the RF detected pulse of the 0.1 μs , 0.25 μs and 1.0 μs mode respectively.

Channel Isolation

Channel isolation is achieved by separating the charging and the discharge circuits of each channel with the use of CR1, CR2, CR3, CR4, CR5, and CR6,

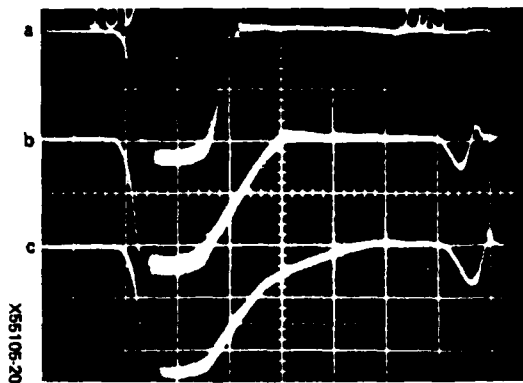


Figure 18. 1.0 μ s Cathode Voltage Pulse
a. (top): minimum bias
b. (middle): average bias
c. (bottom): maximum bias

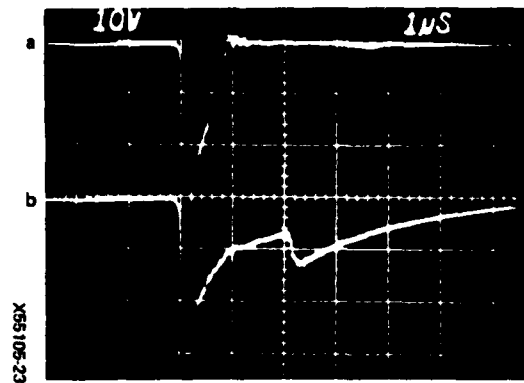


Figure 21. 0.1 μ s Cathode Voltage Pulse
a. (top): biased for saturation
b. (bottom): biased out of saturation

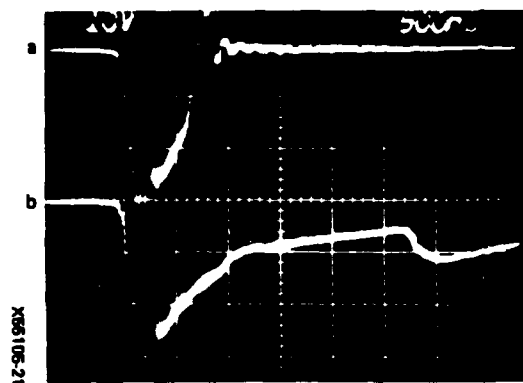


Figure 19. 0.25 μ s Cathode Voltage Pulse
a. (top): biased for core saturation
b. (bottom): biased for no saturation

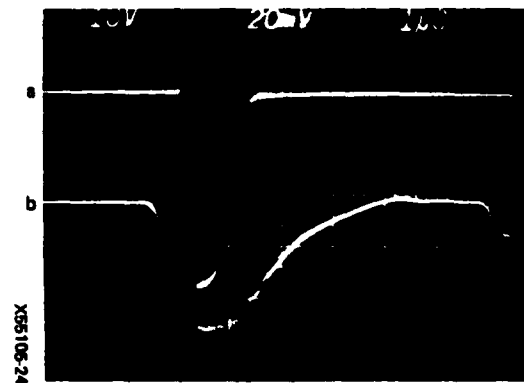


Figure 22. 1.0 μ s Mode
a. (top): RF Envelope
b. (bottom): Cathode Voltage Unsaturated Core

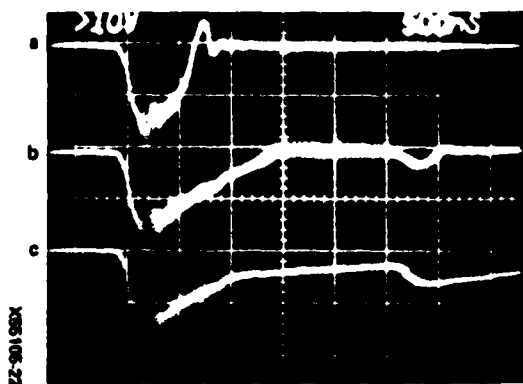


Figure 20. 0.25 μ s Cathode Voltage Pulse
a. (top): minimum bias
b. (middle): average bias
c. (bottom): maximum bias



Figure 23. 1.0 μ s Mode
a. (top): RF Envelope
b. (bottom): Cathode Voltage Saturated Core

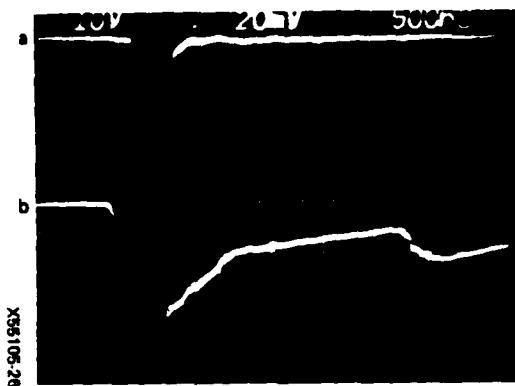


Figure 24. 0.25 μ s Mode
a. (top): RF Envelope
b. (bottom): Cathode Voltage Unsaturated Core

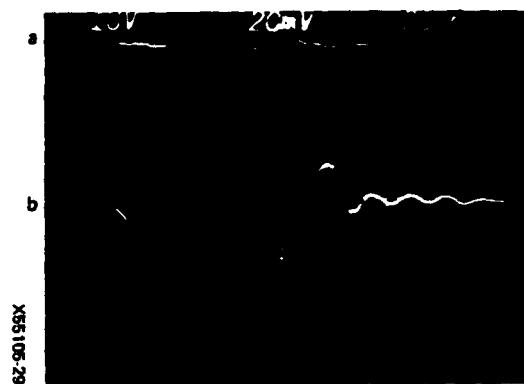


Figure 27. 0.1 μ s Mode
a. (top): RF Envelope
b. (bottom): Cathode Voltage Saturated Core

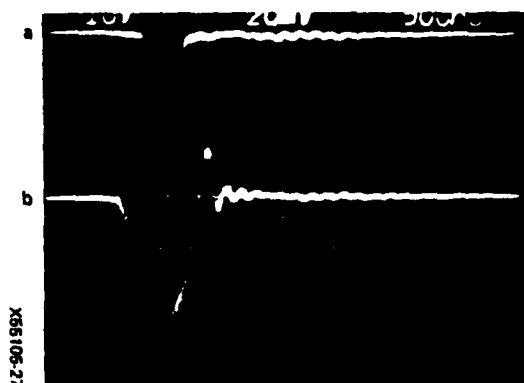


Figure 25. 0.25 μ s Mode
a. (top): RF Envelope
b. (bottom): Cathode Voltage Saturated Core



Figure 28. 0.1 μ s Mode RF Envelope. 0.1 μ s per cm

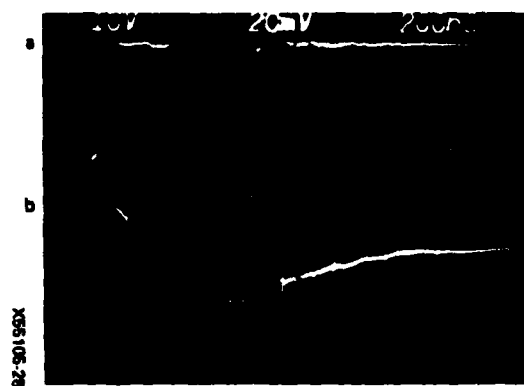


Figure 26. 0.1 μ s Mode
a. (top): RF Envelope
b. (bottom): Cathode Voltage Unsaturated Core



Figure 29. 0.25 μ s Mode RF Envelope. 0.1 μ s per cm

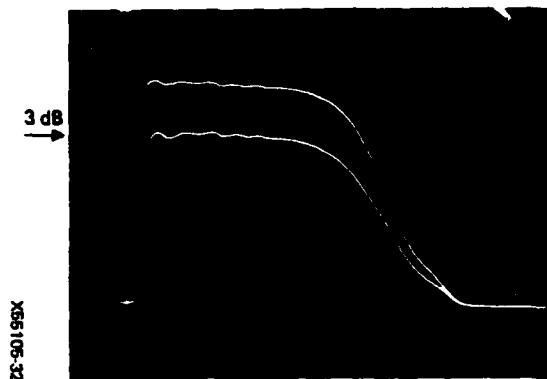


Figure 30. 1.0 μ s Mode RF Envelope. 0.2 μ s per cm

(see Figure 11). The dots on the secondary of SR1, SR2, and SR3 indicate the positive charge voltage end. Channel selection is made by selecting the desired low voltage storage capacitor to be charged. The selection operation is described elsewhere in this paper. Channels stay isolated by charging each PFN through its own charging diode depending upon which storage capacitor is being discharged. After SR saturation, the PFN discharge path is isolated from the unused channels by the use of CR4, CR5, and CR6. To understand the circuit isolation consider the simplified circuit of Figure 31.

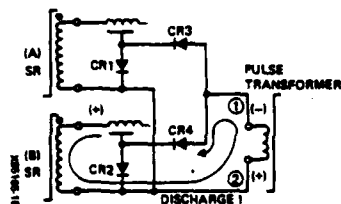


Figure 31. Channel Isolation

Initially the PFN of channel (b) is charged positively. When SR of channel (b) saturates current flows as indicated developing a voltage on the primary of the pulse transformer, as noted. The discharge current flows through CR4 to complete the channel (b) discharge loop, while CR1 and CR3 of channel (a) are back biased, placing them in the off condition. A similar operation takes place if channel (a) were energized. This principle can be applied to any number of channels desired.

Backswing Clipping

Figure 31 shows diodes CR3 and CR1 across the primary of the pulse transformer in parallel with CR4 and CR2. These diodes will clamp any positive voltage being developed at terminal 1 of the pulse transformer. Terminal 1 will want to go (+) as the voltage fall time is decreased and without backswing clipper diodes would in fact develop a (+) voltage at 1. It is desirable to keep this positive developing voltage low to prevent poor magnetron function. This method of diode connections has provided two results: channel isolation and backswing voltage clipping at terminal 1.

Pulse Forming Network

Consideration must be given to the circuit inductances in the design of the pulse forming network i.e.,

the saturated inductance of the SR, the leakage inductance of the pulse transformer and any loop inductances. These parameters are the limiting factors for narrow pulse width generation.

Figure 32 shows PFN during the discharge condition with the PT equivalent circuit. The PFN is an E type line where C1, C2, and C3 are usually equal and the coil is generally a solenoid. In considering the design of the PFN attention must be given to the value for the input inductance $L1 = L1A + L1B + \text{LOOP INDUCTANCE}$. This value $L1$ limits the narrowest pulse width attainable from the modulator. PFN design is discussed in the literature and its not considered here. The reader is referred to previous articles (1) (2) by the author regarding other design details.

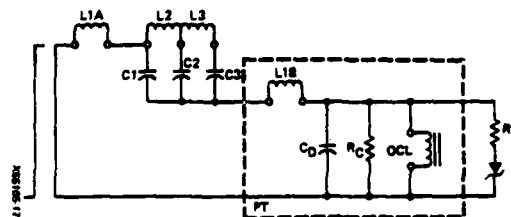


Figure 32. PFN During Discharge Condition

The Saturable Switch

To achieve good switching the SR core must have a square hysteresis loop. This generally requires an uncut nickel alloy core. Figure 33 shows the typical operating cycle for the SR core. The operation starts at the negative residual flux having been set there by the low voltage storage capacitor charging current.

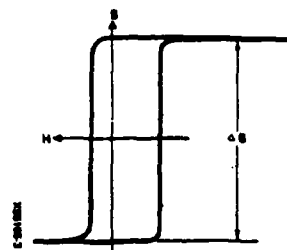


Figure 33. Typical Operating Cycle for SR Core

The flux rises in the positive direction as current flows into the polarity dots shown on the SRs, (see Figure 11). Before an appropriate SR core choice can be made the following must be considered, at a minimum, and limits established.

- Determine the value of the SR saturated core inductance desired.
- Determine the time desired to charge the HV PFN.
- Determine the peak charging voltage of the PFN.

From the values determined above the volt-seconds required can be established and a choice of core made.

Figure 34 indicates the relationship between SR voltage, to PT voltage and magnetron current.

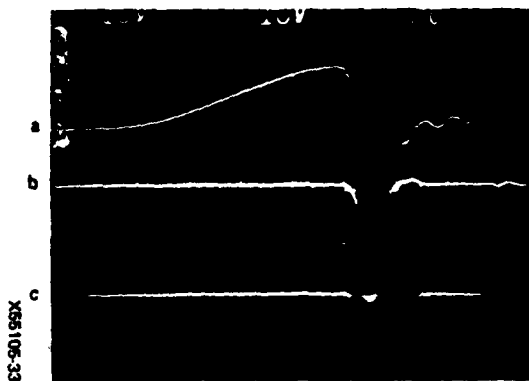


Figure 34. Relationship Between SR Voltage, to PT Voltage + Magnetron Current
 a. (top): SR3 Secondary Voltage
 b. (middle): Magnetron Cathode Current
 c. (bottom): Pulse Transformer Cathode Voltage

Size and Weight

The HV Magnetic Switch Modulator shown schematically in Figure 11 is in a metal, vacuum oil filled, stainless steel housing with cooling fins, oil expansion bellows and appropriate bushings for terminals. The parts shown schematically in Figure 11 are all in the housing whose body dimensions are 8 inches wide by 12 inches long and 5 3/4 inches high. The bushings, bellows and mounting provisions extend beyond the stated body dimensions. To achieve this small size, heliarc welds are used for sealing to avoid massive and bulky O-ring type seals which would have added to the size and weight, or unreliable solder sealing of seams. The modulator may be serviced by any qualified source if the need arises. This provision was incorporated in to the design of the housing. The complete assembly weighs 48 lbs. The modulator is shown in Figure 35.

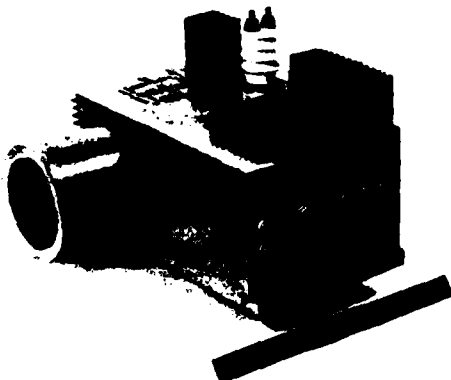


Figure 35. The Modulator

Transmitter/Modulator Performance

The transmitter/modulator has performed well in various tests over the past year. These include environmental tests in accordance with MIL-E-16400. Environmental tests were completed successfully in the Fall of 1979. These tests consisted of subjecting the system to operation from 0°C to 50°C, 5 day test at 95% relative humidity with temperature cycling between 30°C and 50°C. Vibration per MIL-STD-167-1, 5 to 33 Hz, and high impact medium weight shock per MIL-S-901C. Reliability tests were conducted; required MTBF for the radar system is 600 hours, demonstrated MTBF was 795 hours. Total test time for the reliability demonstration was 1,113 hours during which there were no failures in the transmitter/modulator. One system was installed aboard the U.S.S. Marvin Shields for technical and operational evaluation. A failure occurred in the low voltage pulser. One of the steering diodes failed by shorting between anode and ground. In investigating the failure, it was found that the failure was caused by an insulating washer which was installed incorrectly. Total technical evaluation transmitting time was 755 hours. There were no failures during operational evaluation of 2,862 transmitting hours.

Efficiency of the modulator from the dc power supply (450 V) to pulse energy supplied to the magnetron is 65%, 45%, and 20% for the 1.0 μ s, 0.25 μ s and 0.1 μ s mode respectively.

Conclusions

We have demonstrated an all Solid State Magnetic Switching Transmitter/Modulator that is smaller, lighter, and more reliable than the unit it is replacing, and is capable of delivering a 0.1 μ s, 0.25 μ s and a 1.0 μ s pulses with channel isolation. The pulses are passed through a single pulse transformer that is capable, with proper bias current, of reducing the cathode voltage fall time and improve minimum radar range performance.

Acknowledgements

The authors wish to acknowledge the support of Mr. Aldo Bartolomei of NAVSEA during the development of the AN/SPS-67 and are grateful for the cooperation of many people in the ultimate development of the transmitter/modulator. Many vendors were called upon to provide parts to difficult specifications. We also wish to thank E.P. Schweitz, S.S. Brody, Dr. Vincent Bello of Norden Systems, Inc., and Manny Matnick of Axel Electronics, Inc. for their technical assistance.

Bibliography

1. Magnetic Switch Modulator, Raffee Mgrdechian, Conference Record of 1976 Twelfth Modulator Symposium, pp 187-189.
2. Solid State Pulse Modulator, Raffee Mgrdechian, Conference Record of 1976 Twelfth Modulator Symposium, pp 201-205.

GENERATION OF NANOSECOND PULSES WITH A THYRATRON SWITCH

M. Weiner, W. Beattie
US Army Electronics Technology and Devices Laboratory, ER-11M
Fort Monmouth, New Jersey 07703

Summary

Pulses 4 to 10 nanoseconds (ns) wide and 1 to 4 kilovolts (kV) in amplitude were achieved with a four element thyatron switch. The loads tested were a parallel combination of capacitance (20 to 50 picofarads (pF)) and resistance (50 to 100 ohms). Shape and amplitude of the pulse were dominated by parasitic circuit elements in both the thyatron and load. Coaxial return structures surrounding the thyatron were used to minimize inductance. Energy storage was incorporated into the design, thus eliminating the need for lumped capacitors. Results show that a thyatron switch may be suitable for generating narrow pulses 4 to 10 ns wide for modulation of millimeter (mm) wavelength high-power transmitting tubes.

Introduction

Narrow pulse modulation of mm wave tubes will enable future radar systems to achieve improved pattern recognition. The required modulation characteristics are typically: pulsewidths less than 4 ns, pulse repetition rates greater than 20 kilohertz (kHz), and pulse amplitudes of 2 to 15 kV (the particular voltage will depend on the tube type). For the long term future, such modulators will most likely rely on solid-state devices such as avalanche transistors,¹ or possibly pulse sharpening devices.² Since the ultimate risetime capability of the solid-state devices is in the subnanosecond range, mm wave systems with extremely good resolution are foreseen. Until such devices are developed, however, an interim solution for obtaining narrow pulse modulation appears feasible using conventional thyatrons. Thyatrons satisfy both the voltage and pulse repetition rate requirements, but the risetime capability is marginal. This naturally limits the ability of the thyatron to produce the necessary narrow pulse.

This report describes an experimental investigation aimed at optimizing the risetime of a commercially available thyatron. Thyatrons with coaxial return structures to reduce inductance effects were able to produce kilovolt pulses as narrow as 4 ns. The experimental apparatus and the measurement results are described, and application of the pulser circuit to particular mm wavelength tubes is given.

Experiment

Tube Type

A tetrode thyatron, EEV model CX1164, was chosen for the experiment. Comparison with a triode thyatron having similar ratings shows the tetrode type generally performs better with respect to jitter and anode delay time drift. With this tube a direct current biased keep-alive grid, close to the cathode, provides a continuous source of ionization. A pulse delivered to the control grid, biased negatively, performs the triggering function. Separate control of the heater and reservoir voltages is provided, thus giving experimental flexibility. The tube operates with a maximum peak voltage of 12 kV and a peak current of 350 amperes.

Test Circuit and Apparatus

A thyatron circuit with a coaxial return was employed for the initial tests (Fig. 1). Energy storage was in the form of a 50 ohm cable. Current in the keep-alive grid was 150 milliamperes. The control grid was biased negatively to 125 volts. A trigger pulse 600 volts in amplitude and 1 microsecond wide was superimposed on the bias. The trigger was produced by a Cober pulser, model 605P, which has an internal impedance of 200 ohms. A low inductance capacitor, 100 pF, was inserted between the control grid and ground, which helped to isolate the discharge circuit from inductance effects caused by the grid leads. Operation was at a pulse repetition rate of 50 hertz (Hz). Unless otherwise specified, reservoir and heater voltages were operated at 6.3 and 7.0 volts respectively.

In an effort to minimize inductance in the tube, the outer conductor of the coaxial line was connected to the circular return shield surrounding the thyatron (Fig. 1). The load resistors were connected in symmetrical fashion between the shield and the grounded base plate, which was tied to the cathode. For most measurements a total of three 2 watt resistors, in parallel, was employed. The number of such resistors represented a compromise between connecting too many in parallel (increasing stray capacitance) and connecting too few (causing load inductance to increase).

Single pulse waveforms were captured using a Tektronix 7834 storage scope. For the most part the waveforms were obtained with a voltage probe having subnanosecond risetime capability.³ Current transformers such as the Tektronix CT-1 also were used in the initial stages of the investigation. The nanosecond waveforms obtained with the current transformer must be interpreted with caution, however, since any stray capacitance present contributes to the total current seen by the transformer.

Measurements were obtained using two types of energy storage: (a) short 50 ohm coaxial line, approximately 30 centimeters (cm) long, and (b) energy storage derived from capacitive coupling between anode and outer shield with no coaxial line present (charging resistor connected directly to anode). In the case of (a), pulsewidths of approximately 10 ns were routinely obtained, with rise and falltimes of 3 to 4 ns. For 30 cm cables (and longer) the pulse characteristics were still more or less determined by the cable itself. Reducing the cable length below 30 cm, however, resulted in a situation where the pulse characteristics were determined primarily by the thyatron. Accordingly the pulse was dominated by the tube inductance and was badly mismatched to the load impedance. As a result the delivered pulse was small in amplitude. When the cable was removed entirely the pulse amplitude was less than 10 percent of the source voltage for a 50 ohm load. Nevertheless, removal of the cable reduced the pulsewidth to approximately 5 ns. The potential for narrow kilovolt pulses existed, therefore, provided the

thyatron anode to shield capacitance could be increased in the proper manner. Such capacitance may be increased in two ways. The usual technique is to simply add low inductance, lumped capacitance between the anode and the shield. This technique was tried briefly but was abandoned in favor of the second technique, which gave better results. The second method for adding capacitance involved construction of a partial inner shield connected to the anode (Fig. 2). Mylar dielectric was added between inner and outer shields to increase capacitance. The capacitance added in this way is in close proximity with the region occupied by the tube, which should help reduce the effects of the tube inductance. In some respects the structure resembles a short section of transmission line which incorporates the tube inductance. The resemblance is mostly superficial, however, as may be noted from the following facts. First, the thyatron and the surrounding structure is not uniform along its length. Second, the same inner shield that adds to the capacitance also partially isolates the tube from the capacitive effects needed to neutralize the tube inductance. Nevertheless, regardless of explanation, the best pulse characteristics were obtained with the aforementioned structure. This structure exhibited less ringing, greater repeatability, generally faster risetime, and greater pulse amplitude (for a given anode to outer shield capacitance). The structure, by doing away with discrete lumped capacitors, also eliminates potential capacitor failures. It should be mentioned that one property of this structure has not yet been examined, namely, the effect of inner shield depth for a given amount of capacitance. This would help cast light on those effects which are peculiar to this structure.

Experimental Results

The following measurement results are confined to the structure shown in Figure 2. Certain capacitance measurements are important to note. The capacitance between the anode and the outer shield was 40 pF. Stray capacitance between the base plate and the shield, including the stray capacitance of the carbon resistors, was 19 pF. The amount of stray is thus quite significant when one considers that the source capacitance is only 40 pF. In this experiment, therefore, there are no purely resistive loads. Measurements were obtained both with and without additional external capacitance shunting the load. As with the carbon resistors, the capacitance was distributed symmetrically about the shield.

The output pulse amplitude as a function of source voltage is shown in Figure 3 for several cases of interest. The two uppermost curves represent 50 and 100 ohm load resistances with only stray capacitance present. As anticipated smaller voltage transfer occurs at 50 ohms. The remaining curve shows the amplitude for a 50 ohm load with an additional 30 pF shunting the load. The amplitude is further reduced since there is insufficient energy in the delivered pulse to charge the increased capacitance quickly.

Figure 4 shows the pulsewidth (at 50 percent point) as a function of source voltage for the same cases of interest. Note that with only the stray capacitance present the pulsewidth for the 100 ohm resistance exceeds that for the 50 ohm. This is anticipated since the RC time constant is larger. Thus a longer time is needed for the stray capacitance to charge up, as well as to discharge. Also, note that for the same resistance of 50 ohms the addition of shunt capacitance widens the pulsewidth,

as expected.

Figure 5a shows a photograph of the output waveform for the 50 ohm load, with only the stray capacitance present. Note that some pulse top flatness (approximately 2 ns wide) may be ascribed to the pulse. Generally, the pulses were more square at the lower voltages. For example, the same pulse top at 4 kV was about 3 ns. The degree of pulse flatness was significantly enhanced by increasing the heater voltage (pulse characteristics were much less affected by keep-alive grid current and reservoir voltage). Aside from pulse flatness the heater voltage also had a strong impact on pulse amplitude. For example, with a constant source voltage of 6 kV the pulse amplitude across a 100 ohm load was 2168 volts at 6.0 volts, and increased to 2835 volts at 7.3 volts. This effect is attributed to a voltage drop in the cathode coating which is temperature dependent. Dissipation in the cathode is more prominent for low average power operation, a condition which prevailed during the experiment.

Figure 5b shows the waveform under the same conditions of Figure 5a but with an additional 30 pF across the load. Note the obvious fact that the pulse top has disappeared as a result of the increased risetime and falltime.

Application To Millimeter Wave Tubes

The present pulser has direct application to mm wave tubes. They include: extended interaction oscillators and amplifiers (EIO and EIA), magnetrons, and traveling-wave-tubes (TWT). In all these tubes the impedance is similar: roughly 10 to 50 pF capacitance (the exact value dependent on the amount of stray) shunted by a fairly large resistance. The resistance is several thousand ohms in the case of the EIO, EIA, and TWT. For the magnetron the resistance is much lower - on the order of several hundred ohms.

By shunting the tube with an external resistance substantially smaller than the tube resistance, no pull-down circuit is required since the shunt quickly discharges the tube capacitance. Energy is dissipated in the added shunt (with a concurrent lowering of efficiency), but this is a penalty one must pay in order to obtain narrow pulse modulation in a simple manner. It should be noted that by adding the 50 ohm shunt to the tube, the impedance level is entirely compatible with the thyatron pulser investigated here. The loads studied provide a reasonably good simulation of the tube impedance (including 50 ohm shunt) since both the resistive and capacitive elements are similar.

The modulator will first be tested with a 95 gigahertz (GHz) magnetron, EEV model M5163, operating at peak voltage of 10 kV. As mentioned previously the tube load is a parallel combination of capacitance and a resistance of several hundred ohms. The equivalent resistance, however, is in series with a biased diode, i.e., no substantial current is drawn from the magnetron until a threshold is achieved, roughly 80 percent of the peak voltage. This type of load lends itself to pedestal pulsing techniques. Under present plans the magnetron will be pedestal pulsed, in which the pedestal will be an 8 kV pulse, about 50 ns wide. The pedestal will be produced by either a magnetic modulator, hard tube, or possibly another thyatron. The narrow pulse (or "sliver"), produced by the shielded thyatron, will be superimposed on the pedestal to give the required 10 kV (Fig. 6).

Conclusions

A tetrode thyatron has been shown to be feasible for narrow pulse modulation of mm wavelength tubes. By properly shielding the thyatron to reduce inductance, kilovolt pulses with pulsewidths as narrow as 4 ns were achieved. Because of the relatively small pulse energies involved it was possible to construct the pulse capacitance as part of the shield design. This eliminated lumped storage capacitors from the discharge circuit, thus simplifying the design. The shielded thyatron also produced pulses with less ringing and generally faster risetime. The present pulser, tested with capacitively shunted loads of 50 and 100 ohms, will be used to modulate a 95 GHz magnetron. For this purpose pedestal pulsing techniques will be employed.

References

1. J. Stover, N. Komatsu, A. Nieto, "Nanosecond Pulsers For MM Wave Tubes," Third Interim Report, Contract DAAB07-78-C-2991, Feb. 1980.
2. M. Weiner, "Pulse Sharpening In Ferrite Transmission Lines," Digest of 2nd IEEE International Pulsed Power Conference, pp. 91-95, June 1979.
3. W. J. Sargeant, A. J. Alcock, "Voltage Probe System With Subnanosecond Risetime," Review of Scientific Instruments, Volume 47, pp. 1283-1287, Oct. 1976.

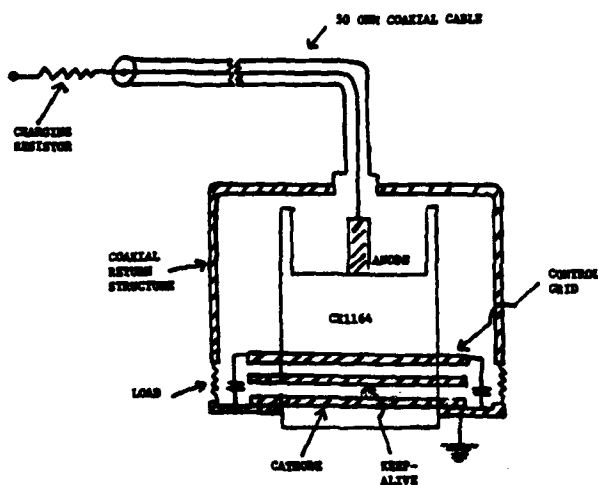


Figure 1. Thyatron With Coaxial Return Structure. Storage In 50 Ohm Coaxial Cable

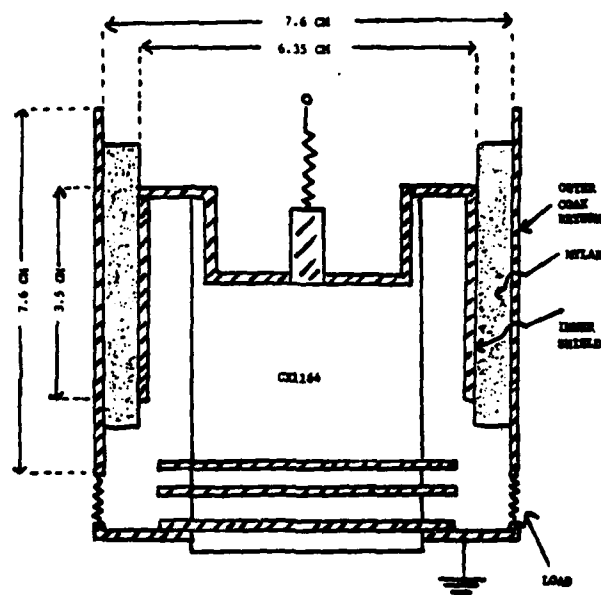


Figure 2. Thyatron With Coaxial Return But With Energy Storage Between Return Structure And Inner Shield (Not to Scale)

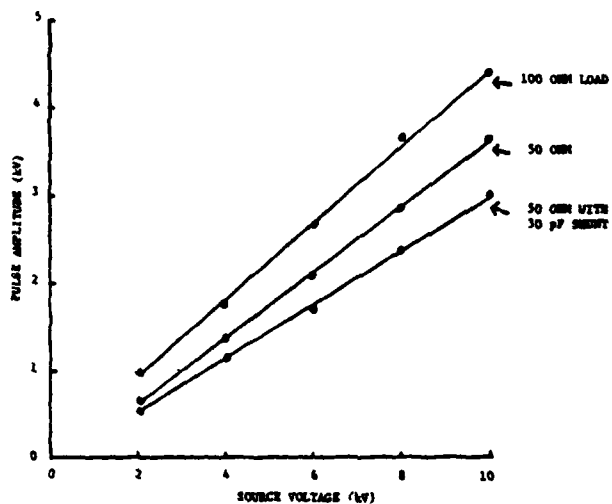


Figure 3. Pulse Amplitude Versus Source Voltage For Various Loads



Figure 5A. Voltage Waveform For 50 Ohm Load.
Source Voltage: 8 kV



Figure 5B. Waveform Under Same Conditions As In Figure 5A But With Additional 30 pF Across Load

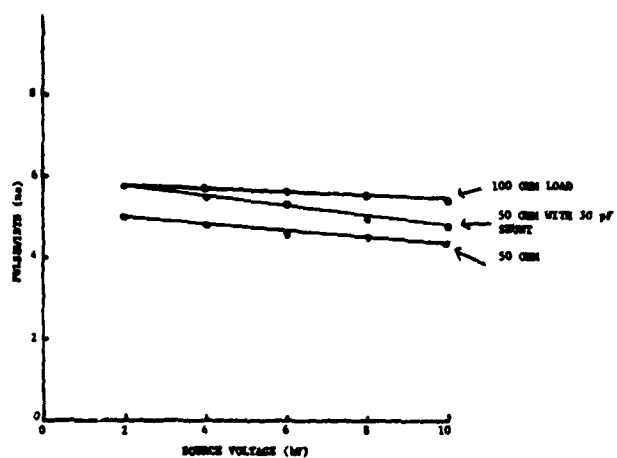


Figure 4. Pulsewidth Versus Source Voltage For Various Loads

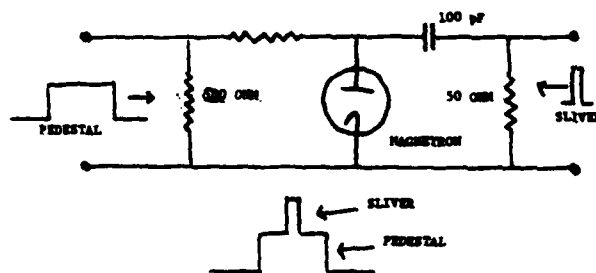


Figure 6. Pedestal Pulser Circuit

DESIGN ISSUES AND ENGINEERING TECHNIQUES FOR REPETITIVELY PULSED SYSTEMS

J. J. Moriarty and G. K. Simcox
Raytheon Company
Missile Systems Division
Bedford, MA 01730

Abstract

Reliability and equipment life are major issues for emerging repetitive pulse systems. The present technology base of switching, dielectrics and power conditioning is examined to determine how these issues may be addressed with a minimum of new development expenditures.

Beyond this, it is foreseen that new developments, particularly in solid-state/magnetic components and circuitry will be necessary to meet the more severe equipment requirements.

Design Issues and Engineering Techniques for Repetitively Pulsed Systems

The achievement of performance reliability is a prime goal for all repetitively pulsed systems. This reliability must be pertinent to the life and mission of the equipment, ranging from the exceptional demands of power plant duty to the limited expectations of experimental equipment.

In some cases there are a number of constraints which bear upon the design effort needed to reach the necessary performance and reliability. Some of these are size, weight, environmental factors, maintenance cycle and cost. A combination of these can seriously strain the available technology.

A subjective ordering of systems by degree of difficulty with contributing design constraints is given in Table 1. The majority of these systems which require pulsed power drivers have been conceived within the past 10 years; and as they emerge from single-shot feasibility studies, the repetitive pulse specifications must be addressed. The total pulsed technology base is neither strong nor adequate in the sense that these demands have been anticipated and, under the circumstances, requires the most effective deployment of existing and developing pulsed power techniques.

Most subsystems and components which have been used or which have a developmental potential for pulsed power have parameter ranges and characteristics which make them uniquely suitable for certain duties. The intention here is to examine energy storage, switches and power conditioning techniques from the viewpoint of exploiting this uniqueness while maintaining the priority of total system considerations during the system engineering phase.

System Engineering

In this phase it is essential to negotiate a specification which takes into account the difficulty factors of all the subsystems. For example, in E-beam pumped lasers, the specification of <10 percent rise and <20 percent fall times for the pulse to reduce anode foil design problems will have a serious influence on the pulse generator reliability and costs. Further, imbalances in specification may exclude the consideration of some desirable technology options.

It is here that the relative difficulties of dielectrics and switching are evaluated and the degree of modularity is determined. It is here also, whenever size and weight are design constraints, that the demands of the pulse generator dielectric upon the overall power-conditioning are determined.

Dielectrics

The literature of solid, liquid, gas and vacuum dielectrics is extensive for ac, dc and single pulse stresses. However, very little information exists in an organized form for the nanosecond-microsecond repetitive stresses of interest here. This is not surprising since quite elaborate test-beds are required for these dielectric studies. Leaving aside the gas medium which is simple, and vacuum which is not, the use of liquid and solid media is most interesting for repetitive systems.

TABLE 1
SELECTION GUIDE FOR DIELECTRICS AND SWITCHES

System (Order of Difficulty)	Particular Constraints	Dielectrics			Switches			
		Liquid Normal Process	Liquid Special Process	Solid	Spark-Gap		Thyratron	Solid- State Magnetic
					3 Elect	2 Elect		
1. Space	Size, Weight, Unattended			X			?	X
2. Industrial	Cost, Efficiency		X	X		X	X	X
3. Mobile (Mil)	Size, Weight	X		X	X	X	X	
4. Static (Mil)			X	X	X	X	X	
5. Experimental		X			X	X	X	

The technology of single pulse systems has been based on the use of water or oil in pulse-forming lines (PFLs) and advantage has been taken of the increased energy densities obtainable by charging these PFLs in $\leq 1.0 \mu\text{sec}$ ($\sim 10\text{J}/\ell$ for oil, $\sim 100\text{J}/\ell$ for water). ⁽¹⁾⁽²⁾ This mode has promoted the development of fast charging generators, such as the low impedance Marx, (1-2 $\mu\text{H}/\text{MV}$)

With repetitive stresses the initiation of streamers in the liquid media must be avoided, as the rationale for fast charging technology weakens and there is a stronger case for using slower charging generators which have potentials for promoting more reliable and simpler power conditioning systems.

Deionized water is a special and important case. If longer charging times are to be used, then the resistivity must be increased to give acceptable generator efficiency. ⁽³⁾ This can be accomplished by cooling the water ⁽⁴⁾⁽⁵⁾ to raise operating resistivities of $\sim 10\text{ M}\Omega\text{-cm}$ by factors of 4 or 5.

Although high energy densities in PFLs are of great interest, consistency of dielectric performance will demand quality control of the media with respect to contaminants, gas content, temperature and pressure. With respect to the latter, it is probably more important to exploit the advantages of modest hydrostatic pressure levels ⁽⁶⁾ than to use high pressures for significant increases of breakdown stress. ⁽⁷⁾

Solid dielectric PFLs provide a high level of insensitivity to charge time and give the prospect of obtaining most reliable operation when coupled with developing rotating or solid-state prime power and power conditioning devices. ⁽⁸⁾ Since solid dielectric is not self-healing, the corona inception levels of these PFL assemblies should be kept well above the equipment operating level. Unlike other dielectric systems, however, no dielectric processing ancillaries would be required.

Recommendations for dielectric usage are given in Table 1.

Switches

Switch technology is recognized as the crucial part of repetitive pulsed power systems. With simplification, it can be said that there are three sets of parameters for closing switch duty:

μsec range:	up to 500 kV, up to 100 Hz
nsec range:	up to 250 kV, 100 to 1000 Hz
nsec range:	more than 1 MV, 10 to 100 Hz

At present, there are two switch types to use as yardsticks of practicability, the flowing-gas spark-gap and the thyatron, either separately or in synergistic combination.

The gas spark-gap has exceptional di/dt and peak power capabilities ⁽⁹⁾ but its characteristics of life and pulse repetition have not been adequately explored. It is known that repetition rates in the kilohertz range are possible with 10^6 - 10^7 shot life at 10-100 kilowatt average power levels. The choice of spark-gaps is reasonable when high peak powers and di/dt values are required, but is speculative when industrial types of duty are involved.

In the megavolt-nanosecond pulse range, the spark-gap is the only switch available and the system engineering should reflect this as the major issue.

At present it is important to apply the peak power and di/dt properties of the spark-gap as widely as possible. To this end, the two-electrode spark-gap used in the over-volted, peaking mode is useful. Because of the lower resistive phase losses in the over-volted mode and consequent lower gas flow rates, the electrode erosion rates have been observed to be approximately an order of magnitude less than those for triggered, three-electrode gaps. With this potential for longer life the spark-gap can supplement the di/dt performance of a thyatron main switch of sub-megavolt potentials in the nanosecond range at pulse repetition frequencies up to a few kilohertz.

The ceramic, hydrogen/deuterium thyatron is generally capable of multikilohertz operation with good reliability for thousands of hours. However, for present use its voltage is limited to $< 100\text{ kV}$ with di/dt levels of $\leq 10^{11}\text{ A/sec}$.

This situation is rapidly changing with development efforts to raise the di/dt, peak and average power bursts. ⁽¹¹⁾ The scaling laws for these devices are now reasonably understood and there are near-term expectations for multikilovolt, 10^{12} A/sec operation at very high peak and average power. The limits are seen to be set by practical ceramic diameters. The thyatron is therefore a major developing candidate for all but the highest voltage, repetitive duties.

Consideration of the extreme requirements of a space-based system gives emphasis to what would be desirable in most land-based systems. It is unlikely that spark-gaps could be used in space; the auxiliaries alone would be undesirable. Thyatrons might be possible, particularly the cold cathode version. Ultimately the choice would be for "passive" devices, free of random events.

Assemblies of light-activated SCRs have an excellent potential, provided that the reliability of the light source can be as high as that for the device itself. Interests other than pulsed power are likely to advance this technology.

The publications of Melville (1950) ⁽¹²⁾ and Katayev (1963) ⁽¹³⁾ provide the basis not only for new switch developments but for new pulse generator concepts which are entirely compatible with highly reliable systems.

The principles of operation of the Melville line are illustrated in Figures 1a and 1b. A thyristor switches a first capacitive energy store to a number of π -network sections, each containing a series, saturable reactor branch. By successfully reducing the volt-seconds and saturated inductance of the branches, the discharge current is incrementally compressed to shorter durations and higher peak currents. Voltage transformations are possible within the chain by converting to shunt saturable transformer branches. This lumped circuit, nonlinear, artificial line technology has its pulse shaping limits imposed by the "sequences" of the core material B-H loop and the minimum saturated inductances which can be obtained.

Katayev recognizes the pulse forming limitations of lumped circuits and rigorously analyses the pulse sharpening characteristics of ferrite loaded transmission lines, which are essentially the distributed component versions of the Melville line.

The progression from lumped to distributed component configuration is seen by Katayev to be a two stage process of pulse generation and pulse sharpening and it would seem profitable to develop this technology in both its forms.

AD-A119 663

PALISADES INST FOR RESEARCH SERVICES INC NEW YORK

F/G 9/5

IEEE CONFERENCE RECORD OF 1980 FOURTEENTH PULSE POWER MODULATOR--ETC(U)

1980

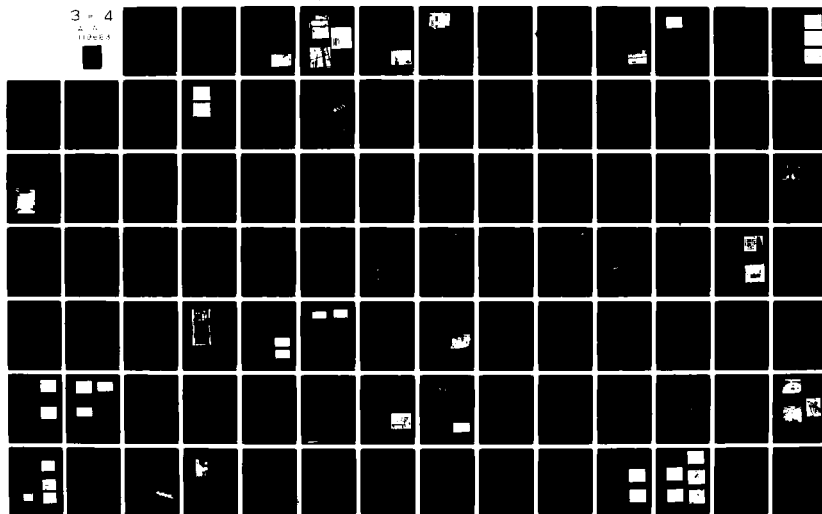
UNCLASSIFIED

80-CH-1573-5-ED

NL

3 - 4

2 - 5
1 - 6



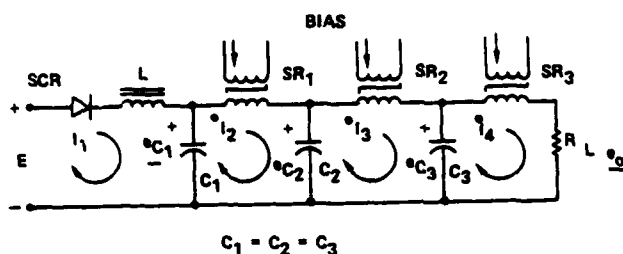
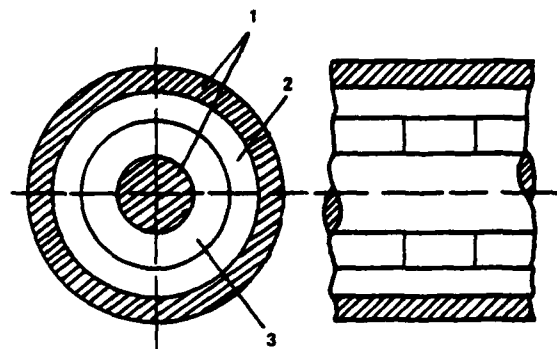


FIG 1a LUMPED COMPONENT-MELVILLE LINE



- 1 - INTERNAL AND EXTERNAL CONDUCTORS
- 2 - DIELECTRIC LAYER
- 3 - FERRITE LAYER CONSISTING OF RINGS THREADED OVER THE INNER CONDUCTOR

FIG 1b - DISTRIBUTED COMPONENT-FERRITE LINE

Figure 1. Magnetic Pulse Generation and Sharpening

A suggested listing of the potential and fields of application for the various switch types is given in Table 1.

Power Conditioning

The scope of power conditioning can have various definitions; here it is defined as that equipment required to charge the first pulsed energy store from a prime power source. This has been trivial for single-shot systems but with the average power needs of repetitive systems in the range 10^3 - 10^6 watts, it is now important. Since this importance is not limited to power levels, power conditioning must be a part of the system design philosophy aimed at reliability and life. The nuances of dielectrics and switching point to simpler, "slower" systems for maximum reliability. Of course, the "speed" of the ultimate stage is determined by the load.

The simplest possible scheme would be one in which the prime power source changes the final energy via a magnetic voltage transformation. This is seen as a developing possibility for the compensated pulsed alternator⁽⁵⁾ if the final energy store is suitable for 50-100 μ sec charging time.

If there is a dc source, the application of high frequency, solid-state inverter or chopper circuits⁽¹⁰⁾ for directly charging the energy store has a number of merits. The use of 10-25 kHz circuit frequencies leads to a reduction of magnetic component sizes and weights; since the energy is transmitted in small increments the potential fault conditions are less severe; by comparator control of the SCR switch triggering, the voltage of the energy store can be controlled to fine limits even with significant variations of the prime source voltage. The effective use of this technology requires charging periods in the order of a millisecond.

If significant energy storage is required at the prime power source, then inductive storage will have its usual advantages. For repetitive systems, the

usual concepts of the opening switch are not appropriate - it is required to extract energy in discrete quantities. Here again, modern inverter technology can be applied. In this mode, the inductive store current is not interrupted but diverted to secondary circuits which "capture" the energy incrementally for transfer to the following power conditioning circuits. These techniques were investigated as potential power supplies for fusion reactor field coils⁽¹¹⁾ and may be revised to meet the requirements of future pulsed power systems.

Conclusions

In the near-term, it is possible to move towards resolutions of the reliability and life issues by the impartial melding of components and techniques.

In the first place, the load pulse specification should be no more severe than necessary, for this determines the ultimate switching duty. The dielectric choice and treatment should promote the use of slower, more reliable power conditioning methods, particularly the high-frequency, solid-state inverter techniques. By means of creative systems engineering with the present pulsed-power technology base, it is possible that all but the most severe industrial and space requirements can be met.

For the longer term, the development of solid-state and magnetic circuitry seems inevitable.

References

- 1) Pulsed Electrical Power Dielectric Strength Notes, PEP 5-1, Vol. 1, Notes 1-23, AFWL, TR 72-167, AFWL, April 1979
- 2) J. Benford et al, "A Unified Pulsed Power Development Plan for Inertial Confinement Fusion", Physics International Final Report, Sandia Document No. 06-9626, 1979

- 3) A. G. Stewart, Private Communication, April 1980
- 4) R. Sojka and G. Simcox, "Development of High Repetition Rate Pulsed Power Generators", second IEEE International Pulsed Power Conference p. 217, 1979
- 5) M. A. Pichot et al, "The Design, Assembly, and Testing of a Desk Model Compensated Pulsed Alternator", second IEEE International Pulsed Power Conference, p. 398, 1979
- 6) T. Burkes, "A Critical Analysis and Assessment of High Power Switches" NSWC Report, NP 30/78, September 1978
- 7) D. Turnquist, "Thyratron Development for High Repetition Rate Gas Lasers", International Conference on Lasers, Orlando, Florida, 1979
- 8) W. S. Melville, "The Use of Saturable Reactors" Proc. IEEE, Vol. 98, PT3, pp 135-207, 1951
- 9) I. G. Katayev, "Electromagnetic Shock Waves" ILLIFFE Books Ltd., London, 1966
- 10) P. W. Clarke, "Self-Commutated Thyristor DC-DC Converter", IEEE Trans. on Magnetics, Vol. MAGB, No. 1, March 1970
- 11) E. Simon and G. Bronner, "An Inductive Energy Storage System", IEEE Trans. on Nuclear Science, pp. 33-40, October 1967

DESIGN OF A 250-kW, 1-kHz LASER PULSER SYSTEM*

David B. Cummings and Boris Yen

Physics International Company
2700 Merced St.
San Leandro, California 94577

Summary

The design and operation of a modulator/pulser system for powering a high-power laser is described. Starting with a 30-kV, 360-kW dc power supply, there are three resonant stages with energy transferred in 350 μ s, 5 μ s, and 85 ns. The first two stages are switched with thyratrons. The output stage consists of eight parallel water Blumlein networks each switched by a spark gap switch. The output voltage is 50 to 85 kV. Jitter of $\sigma < 5$ ns is required.

The 1-percent voltage regulation needed to achieve this jitter specification is accomplished with a thyatron in the grounded secondary of a 2:1 transformer. The regulation must accommodate a snap start from 1 to 10^3 Hz. Extensive fault detection and transient protection are used to guard against a variety of possible faults and interactions. Single-point grounding and double shielding are used to reduce sensitivity to a noisy environment and to contain generated noise.

The Blumlein trigger system is charged by the second stage and fired with a ninth spark gap switch. It also provides bias for the eight Blumlein switches.

Introduction

This pulser system was designed to meet the rather exacting needs of a high-power laser. Table 1 summarizes the principal specifications.

Table 1 Laser pulser system specifications.

• Pulse Amplitude (peak)	85 kV max, 50 kV min
• Voltage Risetime	< 85 ns
• Pulse Polarity	Positive
• Fast Energy	144 joules in 50 ns
• Total Energy	222 joules/pulse
• Average Power	< 222 kW into laser
• Jitter	$\sigma < 5$ ns
• Load	0.25 Ω
• Repetition Rate	1 to 1 kHz (variable) for 10 minutes with snap start capability

Variation of Blumlein charge voltage contributes directly to jitter. In turn, the stringent jitter specification over the wide range of frequencies with a snap start leads to a requirement for modulator voltage regulation of better than 1 percent.

Design Approach

The laser is large and requires a very-low-impedance driver (0.25 ohm). The voltage has to rise rapidly. Therefore, eight par-

allel triaxial water Blumlein modules (2 ohms each) are connected directly to the laser electrodes. Four Blumlein modules are placed on each side in an array much like a V-8 automobile engine. The voltage must rise rapidly (1 kV/ns) which, in these low impedance circuits, demands very low inductance switches with rapid turn-on. These requirements, of course, lead to a high dI/dt (8×10^{11} amps/s per switch). No thyatron offered the necessary combination of parameters. Therefore, an air-blown spark gap switch, described in a companion paper presented earlier in the symposium, was developed. These spark gaps switch the Blumlein modules which constitute the output stage of this pulser system.

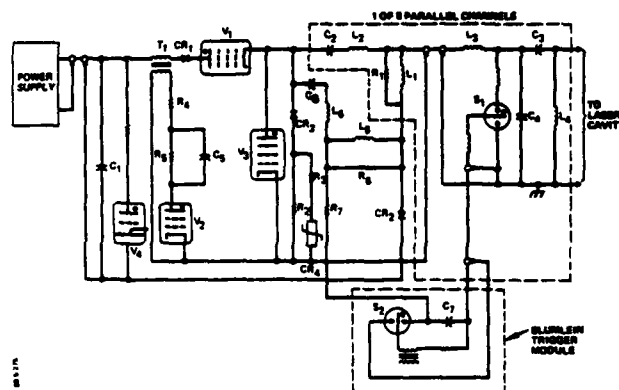


Figure 1 Simplified circuit diagram of pulser system.

A modulator in turn charges up the Blumlein modules. For the simplified system circuit diagram, see Figure 1. Briefly, the modulator (see Figure 2) starts with an external 30-kV, 12-amp dc power supply feeding an internal filter capacitor (see Figure 3). The



Figure 2 Modulator (left) with 360-kW power supply.



Figure 3 Modulator out of tank showing filter capacitors in front of transactor with ignitron and mechanical crowbars; regulator circuit V_2 is to left.

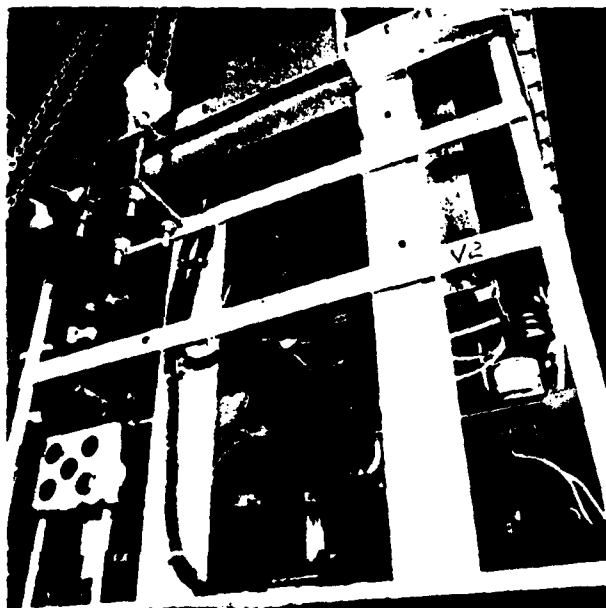


Figure 4 Command charge floating deck (V_1) on left and regulator circuit (V_2) on right.

first resonant stage charges the intermediate store capacitors, C_2 , (eight in parallel) to 48 kV through a transactor (transformer/reactor), L_1 , and smaller parallel isolating inductors, L_1 and L_2 , and damping resistors, R_1 . Command firing is through a floating deck hydrogen thyatron, V_1 , (see Figure 4) with series diodes, CR_1 , to help provide a gentle recovery. Ground return diodes, CR_2 , isolate the power supply ground from the second stage pulse. The ringup time is a maximum of 350 μ s; it is followed by a hold period of 350 μ s to provide the voltage regulating thyatron, V_2 , in the secondary of the transactor, with ample time to recover.

The second resonant stage discharges the eight intermediate store capacitors, C_2 , with the firing of thyatron V_3 (see Figure 5).

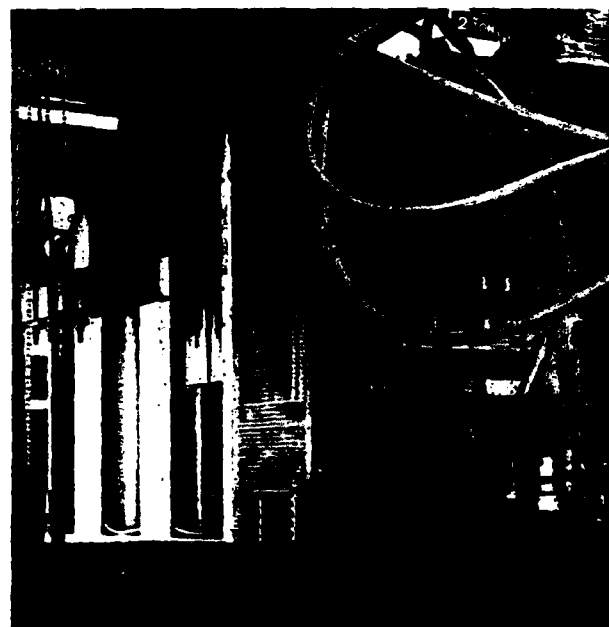


Figure 5 Enclosed output stage (V_3) of modulator with Blumlein trigger module and transactor behind.

Each channel goes through a coaxial cable to its associated Blumlein module. Equal inductances, L_2 and L_3 , at each end of the cable keep its voltage near 24 kV, halving the cable voltage requirements. A reverse shunt diode, CR_3 , protects V_3 from reverse current. In series with CR_3 is a damping resistor, R_2 , for damping oscillations in normal operation, and a metal oxide varistor (MOV) network, CR_4 and R_3 , to limit the reverse voltage on V_3 in the event of a Blumlein module no-fire, prefire, or breakdown. The Blumlein module is shown in simplified form as the capacitances of the inner C_3 and outer C_4 coaxial lines. The inner circuit is completed through an inductor, L_4 , within the Blumlein. With 10 megohm-cm water the RC decay time of the Blumlein modules is 70 μ s, so the ringup time is chosen to be 5 μ s. This charge time allows uniform voltage distribution on the Blumlein.

The Blumlein module and switch design are shown in a simplified form in Figure 6. This is described in more detail in the previously cited paper.

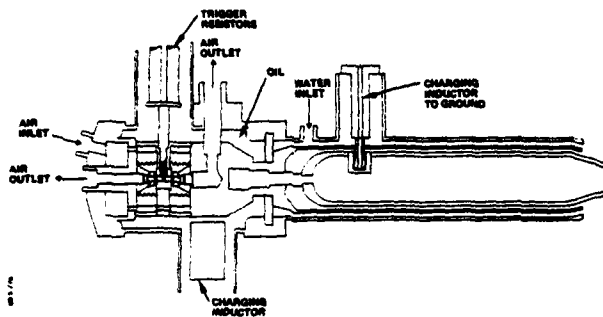


Figure 6 Simplified diagram of water Blumlein module with switch.

Control and Regulation

In order to avoid damage to the various parts of the pulser system, a fault detector system is used. It is designed to sense a variety of faults and to display which faults occurred first. These faults include the following:

1. Intermediate store short
2. V_1 and V_3 latchup
3. V_1 or V_3 no-fire
4. V_2 arc back
5. Charge voltage too high or too low
6. No output
7. Blumlein trigger no-fire or prefire

The responses range in severity as follows:

1. Skip one pulse
2. Skip three pulses
3. Turn off high voltage
4. Fast crowbar

The fourth response is experienced only for a direct charging fault. An ignitron, V_4 , is used to quickly remove voltage from the thyratrons. This action puts a short circuit on the power supply, which in turn protects itself by opening its contactor. A mechanical crowbar switch is then activated for additional safety.

The charging voltage on the intermediate store capacitors is regulated by firing V_2 shortly before the peak of the $1-\cos$ wave. The phase back angle is 32° for steady operation with the nominal input voltage. The design range is from 20° for a steady operation at 5 percent low input voltage to 51° for snap start at 5 percent high input voltage. The oil-cooled resistors are sized to accommodate this latter power level (60 kW) until power supply regulation and adjustment can take place. The value of resistance necessary to ensure transfer of current from the transactor primary to secondary also yields an excessive L/R decay time. Consequently, V_2 might still be carrying current when V_1 next fires. Therefore, a slightly underdamped RLC circuit (R_4 , R_5 , C_5) is used to ensure that the current in V_2 goes to zero promptly, and to provide a small negative anode voltage when it does. With a negative grid bias, deionization is certain.

Since there is stray inductance in the transactor primary the energy stored there

when V_1 fires must transfer to the intermediate store rather than the transactor secondary. Therefore, the voltage control circuit must anticipate the ultimate charge voltage and fire V_2 somewhat early. This correction is a function of the firing angle.

Trigger Circuits

The three thyratrons and the crowbar ignitron are all fired with external thyatron trigger circuits. Each is coupled through an isolation pulse transformer.

The Blumlein Trigger Module is mounted within the modulator tank. It has eight parallel outputs going to the eight Blumlein switches, S_1 . The Blumlein trigger output is switched with a ninth blown spark gap switch, S_2 , identical to the eight in the Blumlein modules.

A small intermediate trigger store capacitor, C_6 , is also charged (through L_5 and R_6) in parallel with the other eight. It is discharged through L_6 and R_7 with the same half period (5 μ s) as its neighbors; however, it transfers its charge into the series combination of the trigger capacitance, C_7 , and the parallel trigger cables' capacitance. By picking the proper cable length the proper Blumlein switch trigger bias is provided.

Test Setup

A test facility built at Physics International consists of two Blumlein modules arranged in a V-2 configuration (see Figure 7). The dummy load consists of a self-breaking blown spark gap and series salt solution resistor simulating the breakdown, resistance, and inductance of $1/4$ of the laser. In order to test all channels of the modulator, a coaxial water load was built in an industrial coffee urn with a soft drink cylinder for the center conductor (see Figure 8). Initially, all eight channels are tested into this dummy load. Later, two output cables were transferred to the V-2 setup for final tests. The channels are not all identical, but the two types of load proved to be compatible.

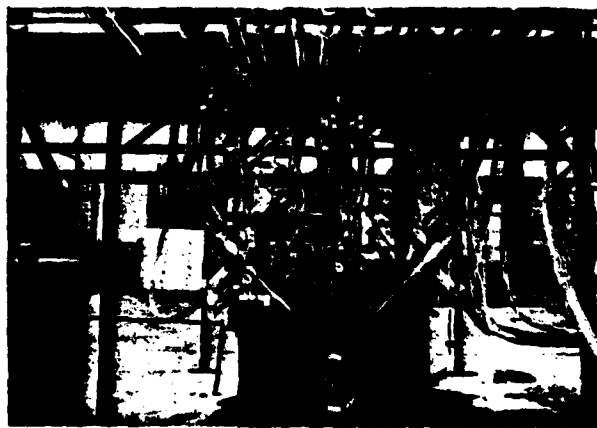


Figure 7 Two Blumlein modules in V-2 test load with oil, air, and water manifolds plus charging and trigger inputs.

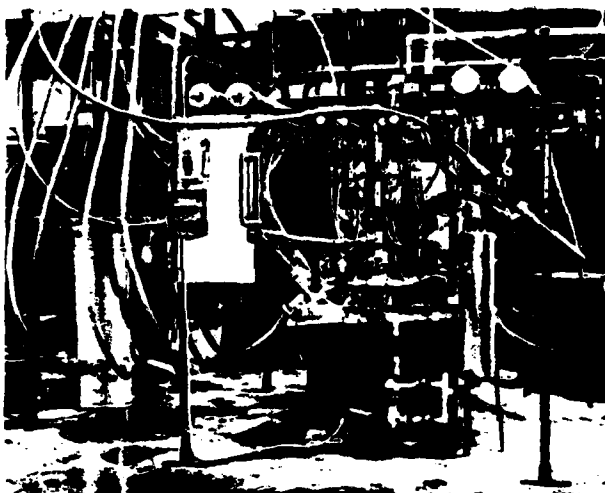


Figure 8 Coaxial water load on left and back of V-2 test load on right.

Test Results

The full system has been operated in preliminary tests at up to 1 kHz with dc input voltages from 19 to 26 kV. This level of operation corresponds to a maximum output voltage over 40 kV. These preliminary tests indicate that the circuit will perform as expected. The initial jitter was less than 5 ns rms. Testing is continuing.

The voltage and current waveforms correspond well to those predicted in computer runs. The command charge tube (V_1) anode rings slightly negative for 10-15 μ s, as predicted. The tube, an HY-5432, recovers faster than expected and winks out at normal reservoir voltages. At higher reservoir voltages it fires when the output tube (V_2) fires. This combination requires more control grid capacitance to prevent double pulsing, and a larger bias resistor to slow recovery, which in turn requires a parallel diode to allow triggering. These were the principal modulator circuit design changes. Various signal level changes were also required for the fault detector circuit. Lastly, the output capacitors were changed to units with a lower stress level to prolong life.

Shielding

This pulser system, which must operate in a high-noise environment, also is itself a potential source of noise. Therefore, pains must be taken to control noise.

The whole pulser system floats within an outer shield. The pulser system and outer shield are tied together only at the ends of

the eight coaxial output cables and the eight coaxial trigger cables. Each of these sixteen cables has an added outer braid which is isolated everywhere except at the load end. Even there, separate joints are made to reduce leakage. The ground is made at the laser cavity so that there are 16 symmetrical "single point grounds." This design accomplishes the desired goal.

Because there is no connection to the modulator tank, no deliberate current flows across the lid joint, which has an RF gasket. The same arrangement continues into the power supply tank. The power is carried on a coaxial cable isolated inside an external braid.

All controls are within shielded enclosures. Control cables are shielded and run through outer braids. Two-conductor cables are filtered at the point where they enter the modulator tank. All transformers to the thyratrons are double shielded. This design also reduces coupling to the floating deck modulator tube, V_1 .

The Blumlein module joints are the greatest potential source of noise. The currents at these joints are the highest in the system, and the risetime the shortest. In addition, it was not feasible to double-shield. Consequently, crushed soft metal gaskets are used on all current-carrying joints to ensure low contact resistance and therefore low leakage.

Conclusions

Preliminary results of testing on this high-power laser pulser confirm the design approach, and the indication is that the design will satisfy the system specifications.

Acknowledgements

The contributions of the following colleagues are gratefully recognized. Gordon Simcox originated the system design, with Tom Naff, Rich Sojka, and Ed Zeehandelaar developing the Blumlein modules and switches. Other contributors were Stan Mercer, Claude Sink, Allan Ball, Pius Chao, Neil Ouye, Ron Shaw, Cliff Wagner, Larry Travillian, Rick Melton, Jim Hauck, Bruce Blucker, Mike Helms, and Charlie Wolff. Gene Mankinen and Doug Johnson provided the program management. Lastly, Stan Lyons made it sing.

References

- * Work done under subcontract to Rocketdyne Corporation.
- 1 "Design and Performance of a High Repetition Rate Spark Gap Switch at 50-kW Power Levels," J. T. Naff, R. J. Sojka, and E. P. Zeehandelaar.

HIGH REPETITION RATE THYRATRON MARX BANK

Stodore P. Ewanizky
US Army Electronics Technology and Devices Laboratory, ERADCOM
Fort Monmouth, New Jersey 07703

Summary

Next generation application of Marx Banks to power high energy lasers and electron beams will require circuits capable of repetitive operation ranging up to kilohertz (kHz) frequencies. This requirement poses severe difficulties for the traditional Marx switching component, the spark-gap. To obtain a low pre-fire probability on this device will require extraordinary research and development (R&D) efforts, and likely produce circuits and configurations that are much less compact than their single-shot counterparts. Consequently, this investigation was initiated to study the particular problem areas that would be encountered by using thyratrons, as an alternative concept, for switching elements in a repetitively pulsed Marx generator.

Relatively high repetition rates, low voltage trigger requirements, and high reliability are well known characteristics of thyatron devices. The major problem area encountered in an experimental circuit, using a conventional thyatron type, was reduction of total anode delay time during the transition period from a parallel to series connection. Results of the investigation are promising and identify inherent design and construction criteria that will be directed to the development of a Marx compatible thyatron.

Introduction

Marx generators have found wide application as a technique for the production of high voltage, high energy, fast risetime pulses. The essence of the Marx principle is to charge a number of capacitive storage elements in parallel and then, through transient switching techniques, connect (or "erect") the elements in series, thus producing an effective multiplication of source voltage.

Although the circuit was originally described by Erwin Marx¹ in 1925, the greatest development in terms of waveform duration and flexibility has occurred within the last one or two decades. To this time, virtually all circuits have been limited to single-shot operation because of the limitations of spark gaps, typically used as the switching elements in high voltage applications. Development of a high rep-rate spark gap is a present technological barrier problem.

In response to the recognized need for a Marx generator capable of high rep-rate operation, this program was initiated to investigate and develop appropriate Marx circuitry using modern thyratrons as the switching elements. Because of the relatively high voltage trigger requirements of spark gaps, Marx circuitry developed for these devices has concentrated on achieving a balance between hold-off reliability and triggering schemes that produce an orderly erection mode, so that predictable output pulses may be realized. High rep-rate capability, low voltage trigger requirements, and high

reliability are well known thyatron characteristics when used in a conventional manner. However, it was anticipated that particular problem areas would arise with the use of thyratrons in a Marx circuit that would demand particular solutions, perhaps different than those that are presented with spark gaps.

This paper describes the results obtained with a four-stage Marx Bank, using conventional 8613 thyratrons and pulse-forming-networks (PFNs) as the storage elements. The circuit was found to produce efficient voltage multiplication, delivering 32 kilovolts (kV), 1 microsecond (μ s) pulses at rep-rates up to 500 hertz (Hz), with an 8 kV direct current (dc) supply. It was found that both external and internal arcing, partly due to conventional tube construction, was the most important factor in limiting the maximum input voltage. However, the circuit reliably operated over a relatively wide range, down to thyatron voltage minimum.

Based on the experimental results, a circuit more appropriate for thyatron operation is presented, which promises to eliminate the particular problems identified by the investigation.

Circuit Design Considerations

A wide variety of Marx circuits exists, both in research and development and industrial application, but analysis of operation and description of them is scant in the open literature. R. A. Fitch² has commented on this situation and presented a description and brief analysis of a number of circuits, beginning with the so-called, "Erwin" Marx, to ingenious modifications dubbed "Martin" and "Maxwell" Marx circuits, all using either two-or-three-electrode spark gaps. Developmental modifications of the original Marx circuit, the "Erwin" Marx, derives trigger voltages for later stages by coupling back to earlier stages via resistive or reactive elements. The "Martin" Marx does the same, but utilizes three-electrode spark gaps which have lower trigger voltage requirements. The elegant "Maxwell" Marx derives its triggering and erection mode by a simultaneously erecting a smaller Marx control circuit, which ascends in parallel with the major circuit that actually produces the energetic pulse. All of these circuits are basically concerned with producing high voltage triggers for each stage, increasing hold-off reliability and operating range, and ensuring a fast and orderly erection mode (minimizing spurious transients). The problem areas that these circuits are attacking arise first from inherent spark gap characteristics, and secondly from the dense component packaging that tends to produce complex interstage coupling parasitic to the explicit circuit.

The particular considerations which affect circuit design for spark gaps are not necessarily appropriate for thyratrons. First, thyatron trigger requirements are typically satisfied by low voltage pulses of only a few hundred volts. Consequently, the more sophisticated schemes deriving trigger voltage by back-coupling are not necessary. This thyatron characteristic, alone, allows simpler circuitry and wide voltage range operation and would be expected to enhance reliability. A second major difference

from spark gaps is the relatively long switching time of thyratrons in response to an applied trigger. Once triggered, a spark-gap Marx circuit will erect at a speed determined by interstage capacitance³ (determined to a large degree by component configuration and arrangement). Switching time of a spark-gap may be only the order of a nanosecond (ns). In contrast, switching time, or anode delay time, of thyratrons depends primarily on internal gas pressure (approximately fixed) and conduction length of the tube. Even with high anode potential and fast-rise grid trigger pulses, ionization of the total conduction length and production of a low impedance plasma involves processes that typically have 100-200 ns duration. Thus, the erection of a thyatron Marx circuit can be expected to proceed relatively slowly and be limited by the switching time per stage.

The practical circuit adopted for this investigation is shown in Figure 1. Only the lowest stage is triggered by a conventional trigger generator. The erection mode can be explained in a manner similar to the triggering of series-connected thyratrons in conventional circuits. When the first stage is triggered for example, the first PFN attempts to discharge through the choke L, dropping the second tube cathode to negative anode potential, effectively doubling the anode to cathode voltage. However, due to the capacitive voltage divider formed, in each tube, by the anode-grid and grid-cathode internal capacitance, the grid becomes positive with respect to cathode and triggers the tube. The grid resistor for each tube provides a path for deionization and recovery between pulses. (It was found that its value is not critical beyond approximately 25 kilohms, but it forms a secondary purpose of limiting grid current and thus should not be very small in value).

The inductors, L, were chosen as interstage decoupling elements, instead of resistors, in the interests of circuit efficiency and ease of fabrication. In their design, it is necessary that their value be such that the oscillation period of each inductor and the capacitance of its associated PFN is much longer than the total erection and pulse discharge time. This automatically ensures small circulation currents and power loss during the total erection time.⁴

The anode voltage, E_{py} , is approximately twice the dc supply voltage, E_{bb} , and is derived from the resonant charging circuit. This supply voltage increase offsets the voltage decrease obtained in using PFN's as storage elements⁵ (peak discharge voltage for an impedance-matched PFN is the network voltage, $E_n = E_{py}/2$). PFN's were used instead of capacitors to alleviate analysis of waveforms and potential problems with load mismatch. In this regard, note that the series-connected PFN's are simply matched by providing a load resistance, R_L , equal in value to the sum of PFN impedances in the circuit. In actual practice, a slight negative mismatch is used to aid tube recovery - standard practice for line-type thyatron pulsers. An interesting alternative to the erection of PFN elements is to erect capacitors as part of a single PFN configuration.⁶

Returning to Figure 1, the iterative structure of the circuit may be easily discerned. Each stage consists of a thyatron, a PFN, and two chokes. The chokes serve as both a reactive load during the circuit erection (as described before) and isolation after erection when the pulse is being delivered to the load.

Experimental Results

Figure 2 shows a photograph of the actual experimental circuit. The PFN's in the background each consist of five 0.0025 microfarads (μF) pulse capacitors with external inductors to form an E^* configuration, giving 1 μs pulses, with 50 ohm characteristic impedance. The isolating chokes were wound on linear ferrite cores, giving 1.6 millihenry (mH) inductance. The low capacitance filament chokes seen in the foreground were necessary to isolate the thyatron cathodes during operation (conventional transformer primary to secondary capacitance would shunt the signal to ground). An appropriate resistive load (seen at the right in the photograph) was constructed with low-inductance, tubular, carborundum resistors.

The circuit as constructed, and as shown in Figure 1, delivers negative pulses to the load. Figure 3 shows a typical current pulse obtained with the circuit operating at repetition rates up to 500 Hz, and 8 kV dc supply voltage. The four-stage circuit produced efficient voltage multiplication, evidenced by the 1 μs PFN output pulse, corresponding to 32 kV peak load voltage. Wide voltage flexibility was easily obtained, with reliable erection occurring for supply voltages greater than only a few hundred volts.

Although the circuit operated satisfactorily at low voltages, problems with external and internal arcing were frequently experienced with E_{bb} approximately 8 kV and limited maximum anode voltage to E_{py} approximately 16 kV. Arcing occurred between grid and cathode socket pins and connections, and also between electrode leads internal to the tubes. Problems were also experienced with arcing between secondary and primary windings of the filament transformers of the elevated stages. These external and internal breakdowns generally caused one or more of the tubes to go into constant conduction, halting operation. A radiological survey conducted during circuit operation determined that X-ray emission was detectable especially from the last tube, for voltages of E_{py} approximately 12 kV. At certain times, however, X-ray emission was detected, even from the first tube, for lower anode voltage. This spurious operation causing abnormal X-ray emission was symptomized by audible microphonics, noisy output pulses and strong electro-magnetic interference. Effective X-ray protection was obtained by simply placing a tubular lead shield around each tube, particularly shielding the grid-anode space.

The cause for spurious arcing at higher voltages can be traced to the progressively increasing anode-to-cathode and grid-to-cathode potentials that are momentarily experienced by each tube as the erection phase proceeds. When the (n-1)th tube fires and conducts, the nth tube will have an anode voltage of $+E_{py}$ and a transient negative cathode voltage of $(n-1)E_{py}$, corresponding to a net anode-cathode potential of nE_{py} . It is easily seen that this net transient voltage can substantially exceed the 20 kV dc hold-off rating of the 8613 thyatron in only a few stages, with only moderate values of supply voltage. This transient over-voltage persists across each successive stage until it attains a low impedance state.

Measurements showed that the total anode delay from stage to stage was almost constant at 80 - 100 ns, over a wide range of E_{py} . The erection speed is obviously limited by the ionization time of each thyatron. It is believed that the X-ray emission observed is generated during this period before the thyratrons

achieved a low-impedance state. Due to the high current demands of the transient overvoltages, high-impedance discharge may occur between the thyatron elements, causing both X-ray emission and the symptomatic, audible microphonics. Sustained operation would certainly cause cathode destruction, deposition of (cathode) low work-function material on the grid, and subsequent grid emission.

Conclusions

(a) Within the limits discovered by the experimentation, a thyatron Marx circuit has been shown to be an efficient means for production of high voltage pulses at high repetition rates.

Unlike spark-gap circuits, repetition rate is not the factor limiting performance with thyatrons. It is, instead, the spurious arcing produced by the inherent, transient overvoltages during the period that each successive thyatron requires to reach a low-impedance state. Thus, the progressively increasing overvoltage, beneficial for a spark-gap switched Marx generator, is counterproductive when thyatrons are used.

(b) Cognizant of these problems and their cause (i.e., progressively increasing overvoltages), a modified form of the circuit was devised which promises to eliminate them and be more appropriate for thyatron use.

Figure 4 shows the circuit (omitting trigger and supply circuitry). Comparison with Figure 1 shows that the major modification is the positional interchange of the thyatrons and PFN's. It is seen that this circuit configuration will produce a positive, rather than negative pulse output. But more importantly for thyatron purposes, no progressive overvoltage occurs at each stage during the erection phase. After the previous tube has fired, the n th tube sees positive voltages on both its cathode and anode. The cathode voltage becomes $(n-1)E_{py}$ and the anode voltage nE_{py} , for a net anode-to-cathode potential of only E_{py} for any tube in the string. This would be a poor circuit for spark-gap switches, where overvoltage is necessary, but should be most appropriate for thyatrons where overvoltages produce serious problems and limitations.

c. Future work in this program, considering the points in (a) and (b), should proceed with modern, developmental, low-inductance thyatrons to shorten anode-fall times, or perhaps discharge heated thyatrons to eliminate filament supplies (especially if ambient-temperature, parasitic reservoirs reach mature development). The modified circuit in (b) should eliminate overvoltage problems with the thyatrons and would only require development of an appropriate triggering scheme. It is not anticipated that this point will present any difficult problem, since thyatron trigger requirements are relatively easily satisfied. In fact, initial experiments with the (b) circuit were successfully carried out at low voltages and triggers for each stage were simply derived from a small secondary winding around the cathode choke of the previous stage.

References

1. E. Marx, "Versuche über die Prüfung Von Isolatoren Mit Spannungstößen," *Elektro-Technische Zeitschrift*, Vol. 450, p. 652, 1925.
2. R. A. Fitch, "Marx - and Marx-Like-High Voltage Generators," *IEEE Trans. Nuclear Sci.*, Vol. NS-18, No. 4, p. 190, Aug. 1971.

3. Op. Cit. #1.

4. M.I.T. Radiation Laboratory Series, Pulse Generators, Vol. 5, (McGraw-Hill, sect. 11.8), 1948.

5. D. B. Cummings, "Conversion of a Marx Generator to a Type-A Pulse Forming Network," *IEEE Conference Record of the Twelfth Modulator Symposium*, New York City, Feb 4-5, 1976.

6. Op. Cit. #5.

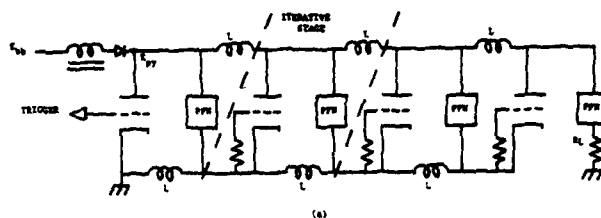


Figure 1a. Practical thyatron Marx circuit. Type 8613 thyatrons used, R_L = load resistance, L = isolating chokes.

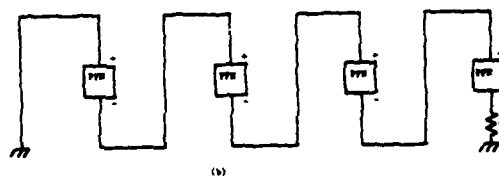


Figure 1b. Effective pulse circuit and polarities after erection phase has been completed.

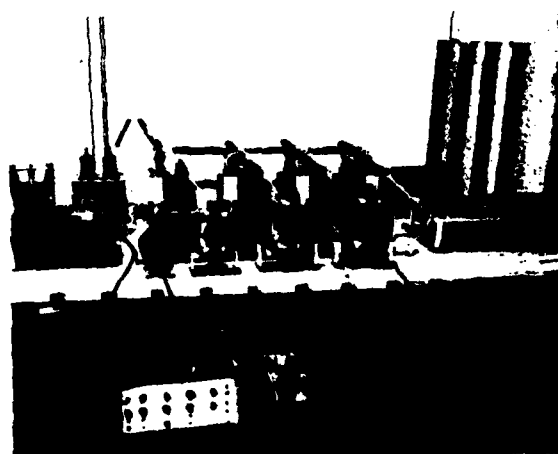


Figure 2. Experimental Marx-Bank setup. First stage, triggered at left, proceeds to last stage feeding load resistors at right.

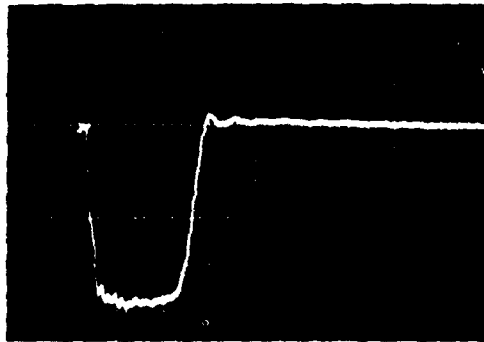


Figure 3. Typical output current pulses. Matching load resistance equals the sum of characteristic PFN impedances.

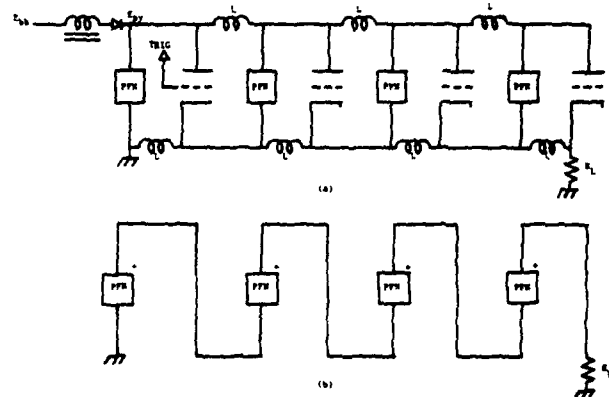


Figure 4a. Modified thyatron Marx circuit.

Figure 4b. Erected state with positive output polarity.

DEVELOPMENT OF A 50 Hz, 250 kV, 500 ns, 500 KW AVERAGE POWER PULSER*

Malcolm T. Buttram

Sandia National Laboratories, Albuquerque, New Mexico 87185

Summary

This paper describes the development of a 50 Hz research pulser with per shot specifications of 250 kV, 500 ns FWHM, 10 kJ. It is designed for burst mode service. The pulser is a two element Guillemin Type C pulse forming network with two parallel Marx generators serving as the first element and a single Marx generator serving as the second element. This paper will consider the two Marx generators of the first element only and will outline the important ongoing developmental areas.

Each generator has a 500 kV output voltage and stores 5 kJ. Two units in parallel are required to achieve the low inductance for a 10 kJ, 500 ns output pulse. Each Marx generator has 8 capacitor stages and four spark gap switches. The switches are cylindrical sulfur hexafluoride insulated trigatrons with vortex purge gas flow. Initial observations are that very little gas flow is required for 50 Hz operation at 50 kV across the switch and 20 kA peak current in a 50 shot burst.

The first switch of one Marx generator is triggered. The first switch of the second Marx is triggered by the breakdown of the first switch of the first Marx. The trigger pins in the second gaps are capacitively coupled to ground. The trigger pins of final gaps are capacitively coupled to earlier stages. For a single generator the delay from triggering of the first gap to full Marx generator erection is 100 to 150 ns. Parallel operation of the two Marx generators is achieved for at least 85 percent of all shots. To increase this to 100 percent may require a better triggering system. Present limitations on the operation of the device come from solid dielectric failure and variation of spark gap self breakdown thresholds.

Introduction

This paper describes the design and development to date of a 250 kV, 500 ns, 50 Hz burst mode pulser. The device is a prototype of a larger system to be constructed from the modules developed in the prototype program. Each module is a 500 kV, 5 kJ Marx generator with sufficiently low inductance for 500 ns output. Several of these Marx generators operated in parallel would form the first stage of a Guillemin Type C¹ pulse forming network (PFN). Subsequent stages would also be 500 kV Marx generators but with substantially lower stored energy. The prototype consists of two of the 500 kV, 5 kJ Marx generators.

The choice of such a system was dictated largely by the need to produce a 500 ns pulse with devices of minimal complexity which could be operated in parallel for higher energy per pulse. A 500 ns pulse length is rather short for a PFN and rather long for a distributed pulse forming line (PFL). For example a water PFL for this application would be 8.3 meters long. Long (> 1 μs) water lines produce acceptable pulses²; however, they are bulky and they require a difficult output switch development program. Both the bulk and switch problems can be avoided by going to a PFN.

*This work was supported by the U.S. Dept. of Energy, under Contract DE-AC04-76-DP00789.

A PFN followed by a step up transformer is not attractive for this regime. The load impedance per module is 6.25 Ω. Assuming the PFN is charged to a reasonable voltage of 100 kV, the transformer voltage gain is 5 and the PFN impedance is 0.25 Ω. For a reasonable output pulse (rise and fall times 100 ns) the transformer coupling constant would have to exceed 0.97. The 50 kV transformer primary switch would operate at 50 Hz, 200 kA and have an inductance less than 50 nH. Four switches to be operated in parallel could be designed for this latter function; however, the coupling requirement is a formidable constraint.

The final option considered is a 250 kV PFN constructed from 500 kV Marx generators. This is most easily done in the Guillemin Type C configuration of Fig. 1a which of all the Guillemin networks has the lowest inductance, a pivotal consideration in the design of a pulse length (inductance) limited device. Contrast, for example, the Type A configuration of Fig. 1b which has often been used to produce microsecond pulses at several hundred kilovolts. In the Type A the first stage (L₁, C₁) is initially uncharged, the subsequent stages, which are initially charged, are used to shape the discharge. As indicated by Table I the inductance of the first stage Marx generator is 244 nH which is small for a 500 kV device. The first stage C PFN is 791 nH. Furthermore, the inductance of later stages increases for the Type C circuit and decreases in the Type A.

TABLE I

Parameters of the First Three Stages of Guillemin Networks for 500 ns, 6.25 Ω Output

	Type C	Type A
L ₁	791 nH	244 nH
C ₁	32 nF	37 nF
L ₂	844 nH	279 nH
C ₂	3 nF	19 nF
L ₃	1147 nH	63 nH
C ₃	1 nF	21 nF

Design

A Marx module is shown schematically in Fig. 2. Eight 0.3 μf capacitors, each charged to 62.5 kV for 500 kV operation, are arranged in two opposed rows of four each. The space between the rows is approximately 4 cm which is also the spacing between the high voltage and ground connections of the generator. This arrangement minimizes the generator inductance by allowing the Marx current to pass over the top of the capacitors at as close a spacing as is consistent with high voltage insulation (in transformer oil) requirements. Figure 3 illustrates the importance of properly positioning this current path. Figure 3a shows the current waveform when a single capacitor is shorted with a 10 cm wide strap across the top, i.e., via the shortest path between its tabs. (The "top" of the capacitor is by definition the end close to the tabs, the abutted ends in the Fig. 2.) The resistance and inductance calculated for this waveform are given in Table II together with values from Fig. 3b and 3c which are for short circuits where the strap runs along the side and bottom of the capacitor respectively. For a Guillemin

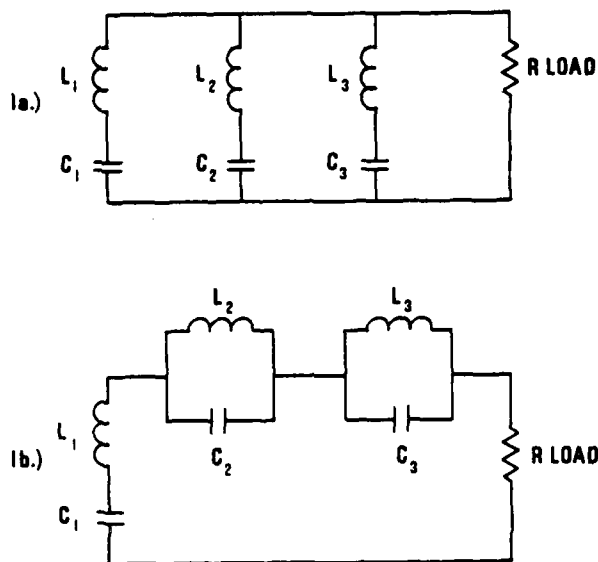


Fig. 1. Guillemin networks.
a. Type C.
b. Type A.

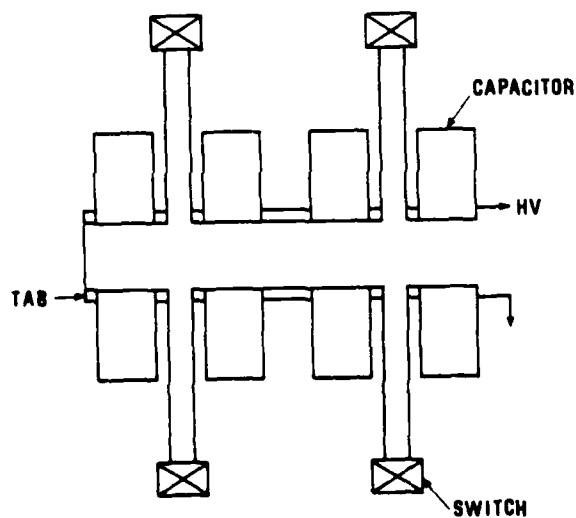
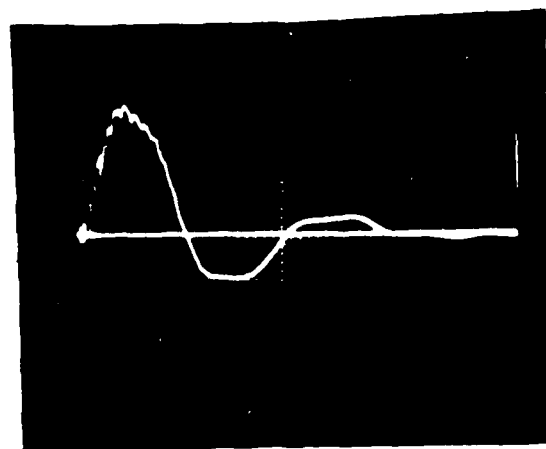
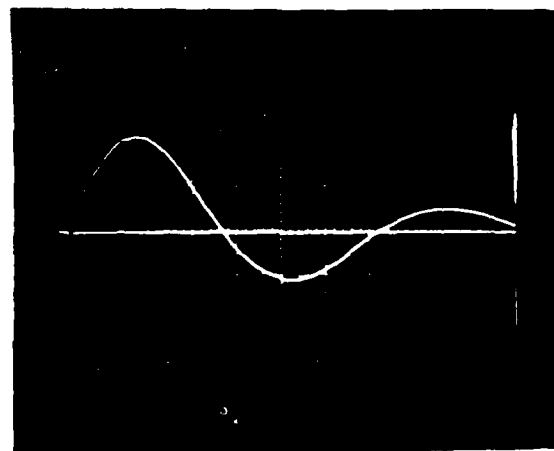


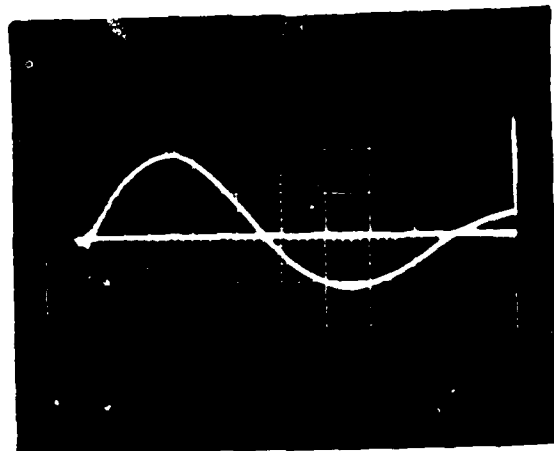
Fig. 2. Schematic of one Marx generator unit illustrating the geometry.



(a)



(b)



(c)

Fig. 3. Short circuit ringing current waveforms from a single capacitor charged to 1 kV.
a. Top strap.
b. Side strap.
c. Bottom strap.
(200 μ s/div, 1 kA/div)

TABLE II

Inductance and Resistance for a Single Marx Capacitor ($C = 0.3 \mu\text{F}$, $L = 25 \text{ nH}$ nominal) for Various Shorting Strap Locations

Strap Location	L	R
Top	66 nH	0.25 Ω
Side	162 nH	0.32 Ω
Bottom	253 nH	0.5 Ω

Type C PFN, the output pulse duration is half the ringing period of the first element. If half the ringing period of a single capacitor exceeds 500 ns, the total Marx generator half period will exceed 500 ns. Therefore the configuration of Fig. 3a, which is the only one with a half period less than 500 ns, is the only acceptable configuration. Figure 3c corresponds to a Marx configuration in which the capacitor bottoms are abutted. This arrangement while geometrically more convenient from the point of view of switch attachment is unusable because of its added inductance. Note that the capacitor has an internal resistance in the range of 0.3 Ω . The series combination of eight capacitors has a measured resistance of 2 to 2.5 Ω which causes a significant loss when the load is 6.25 Ω .

The switches in this geometry are mounted approximately 36 cm from the capacitor tabs as shown in Fig. 2. The transmission line between the tabs and switch is 1.3 cm thick and 10 cm wide. The thickness may have to be increased as will be discussed below. A switch is shown diagrammatically in Fig. 4. All four switches are trigatrons with rather large area trigger electrodes. A re-entrant geometry (cylindrical electrode coaxial with cylindrical housing) was chosen to permit an enhanced length of flashover surface to be inserted as illustrated by the dashed lines in the figure. In practice this was found unnecessary to +75 kV charge and lip on the insulator is provided for mechanical positioning only.

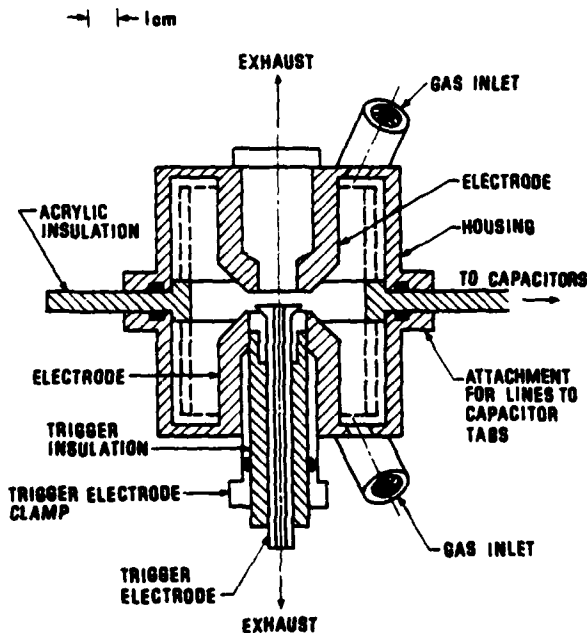


Fig. 4. Schematic cross-section of a Marx switch.

The total inductance of the generator, exclusive of load connections is made of the four parts listed in Table III. The central transmission line (area between the rows) and the tab-to-switch connections are modeled as parallel plate transmission lines 61 cm x 3.8 cm x 20 cm wide and 36 cm x 10 cm x 1.3 cm wide respectively. The switch is modeled as concentric cylinders plus the spark inductance. The capacitor inductance is from Table II, row 1. The computed inductance is 708 nH and the measured inductance is 730 nH which is compatible with the Guillemin Type C requirement of Table I.

TABLE III

Calculated Inductance for Various Marx Generator Parts

Source	Inductance per Element	Total Addition to Marx Inductance
Central transmission line	144 nH	144 nH
Tab-to-switch connection	56	224
Switch	19	76
Capacitors	66	264
Total		708

Switches

A switch is shown in Fig. 4. It is a cylindrical unit with 7 cm ID and 3.8 cm electrodes. Sulfur hexafluoride insulation is used. The switch is purged by injecting gas with a rotary motion as shown in the figure and exhausting through the center of the trigger pin and the opposite electrode. The trigger pin is epoxied into an acrylic sleeve which is held within one of the electrodes by an "O"-ring clamp. The two halves of the switch and the insulator are held together by an external clamp not shown in the figure. The necessity to align and seal the switch without the benefit of bolts through the insulator (which are prone to surface flashover) led to the decision to use a trigatron rather than a mid-plane spark gap. In retrospect, a three element gap could have been fabricated by encapsulating the gap in epoxy (exclusive of holes for electrode removal). The encapsulant would serve as a pressure seal. The spark gaps may be reconfigured to a mid plane of this type in the future. As built, the spark gaps may be operated safely to 100 psig with a typical working pressure being less than 70 psig.

The spark gaps are weakly purged. Extensive studies of the free (unpurged) recovery of spark gaps in air and SF_6 indicate that at least 80 percent of the dielectric strength is recovered within 20 ms^{6,7} even for substantial discharge currents and long pulse durations (> 200 kA, > 1 μs). Experiments with the RTF-I pulser⁸ demonstrate that 20 kA discharges will quench at a 40 Hz repetition rate with no spark gap purging. This process can not continue indefinitely as the gap requires some cooling and with no gas flow will ultimately become hot enough to melt its insulation. Initial experiments indicate that for +30 kV, 20 kA operation the present gaps will quench for a 50 shot burst at 50 Hz with negligible gas flow (less than 3 SCFM per switch). There is some concern whether this is still true at +62.5 kV, 40 kA. The situation is confused somewhat by the failure of the spark gaps to maintain a well defined self-break threshold even under single shot conditions. Figure 5 shows the cumulative probability of breakdown as a function of voltage below the maximum observed breakdown voltage V_{max} for a single switch in a single

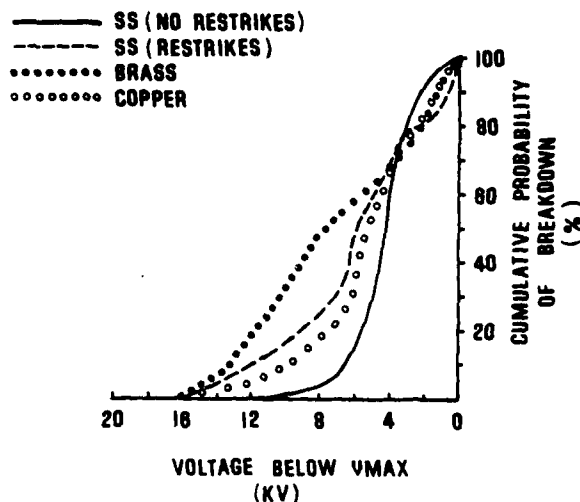


Fig. 5. Cumulative probability of breakdown for various electrode materials as a function of voltage below peak breakdown voltage (V_{max}).

shot mode. V_{max} is in the range 50 to 60 kV. Typical data samples of 40 to 60 shots show a measurable breakdown probability to 16 kV below V_{max} (almost 70 percent of self-break) for copper and brass electrodes. For a system with 8 spark gaps, a 5 percent chance of one gap failing translates to a 34 percent chance of a prefire on a given shot. This has been documented and attributed to changes in the electrode surface for discharges in air using copper and stainless steel electrodes.^{9,10} In the data of Ref. 9 the breakdown spread is somewhat less for stainless steel than for copper and the same is true for the data of Fig. 5. (The stainless steel no-restrikes curve applies.) The situation is complicated by aging effects as indicated by the stainless steel-with restrikes curve. In the no restrikes case each breakdown was a single shot, in the restrikes case each breakdown led to multiple arcs and more severe surface damage. In the latter case the cumulative breakdown probability with stainless steel is similar to the copper data (without restrikes). A study of this process is in progress.

Assembly

The entire prototype assembly is contained in a $1.2 \times 1.2 \times 0.9$ m³ tank of transformer oil together with trigger, trigger power supply, and monitors. The generators are mounted so that the plane of Fig. 2 is the horizontal, with one generator atop the other, separated by 3 cm of acrylic insulation. The trigger is a small air core transformer with a typical output of 100 kV. The triggered electrode is positive and the trigatron gap breaks down on the positive swing of the trigger pulse. The Marx generators are charged resistively through two 4 to 10 K Ω flowing water resistors from a ± 80 kV, 2 MW power supply.

Operation - One Marx Generator

A schematic for one Marx generator including a typical trigger connection scheme is shown in Fig. 6. The first gap is triggered, the trigger electrode of the second is capacitively coupled to ground, and the triggers of the remaining switches are capacitively coupled to earlier stages. Stacks of barium titanate

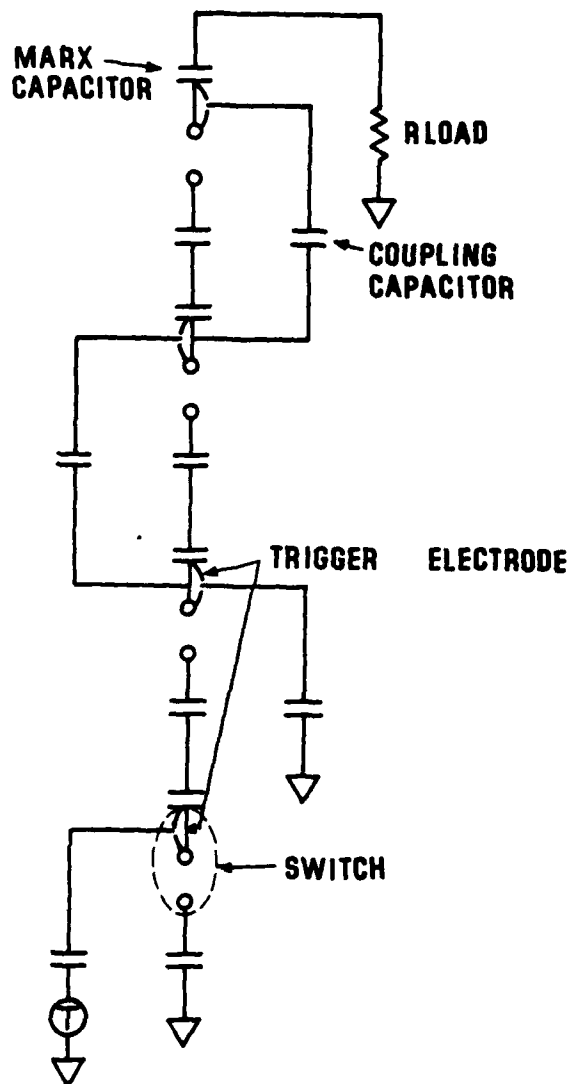


Fig. 6. Schematic of one Marx generator showing trigger coupling.

capacitors are used for these couplings. The spark gaps, particularly the second, do not trigger as reliably if resistors are substituted for these coupling capacitors. With this configuration when the first gap fires the entire Marx generator erects with > 95 percent probability. For 0.64 cm spacing the first gap triggers reliably to at least 70 percent of self-break with the triggering electrode flush with surrounding electrode. For larger gap spacings the trigger must be inserted into the gap, the greater the insertion the greater the triggering range. Typically for a 1 cm gap an insertion of 1.5 mm is appropriate and the gap will trigger from ± 40 kV charge voltage upward. The triggering range extends below 60 percent of self-breakdown from 50 kV upward. Total delay increases with decreasing percent of self-break but is generally in the range of 100-200 ns. For operation below ± 30 kV charge, the Marx operates to 50 Hz in a 1 second burst without problems. Above 50 kV stable operation has been achieved to 10 Hz but is limited by

the ill defined self-break threshold previously discussed and by occasional failure of the solid insulation. This latter failure occurs invariably in gap 3. The spark gap firing sequence is 1, 2, 4, 3 so that gap 3 briefly supports some fraction of the total generator voltage (certainly more than twice the charge voltage). When spark gap 3 fires a 200 MHz standing wave pattern with a node at the switch and a maximum at the tab end is setup in the transmission line leading to the capacitor tabs. This breaks the insulation at the open end of the line. The failure is probably due to cumulative damage as several hundred or thousand shots are typically required to get a failure. An attempt is underway to decrease the overvoltage of gap 3 by decreasing Marx erection time. That failing the insulation thickness must be increased with a corresponding increase in inductance.

Operation - Two Marx Generators

Parallel operation of two generators has been achieved with capacitive coupling between corresponding trigger electrodes of the two generators. Thus as the triggered generator erects, it triggers the spark gaps of the second Marx generator. This coupling scheme is illustrated in Fig. 7. The left generator is triggered as indicated by the trigger generator shown in the figure. The coupling of the remaining trigger electrodes of the left Marx generator is as in Fig. 6. The trigger electrodes of the right generator are coupled to the corresponding main (not trigger) electrodes of the left Marx through barium titanate capacitor strings. With this scheme the trigger electrodes of the right Marx generator fire when the left Marx erects. This does not automatically cause the right Marx generator to erect.¹¹ If, for example, all the gaps of the left Marx have closed but none have closed in the right generator then the left generator will raise the output end of the right generator to 500 kV. It does so by providing current to charge the capacitance of the right generator spark gaps to a value such that the sum of the capacitor and spark gap voltages is 500 kV. Obviously this leaves the spark gaps with no voltage so that the right generator appears to have erected even though the spark gaps have not closed. The time to charge the right Marx as governed by the inductance of the generators (2×700 nH) and the spark gap capacitances (100 pF/8) is 13 ns. This process will almost certainly interfere with erection of the right Marx generator independent of the number of its gaps which may have broken down prior to complete erection of the left generator. In the present system this problem is avoided because the first Marx generator to erect is substantially loaded down by the load resistance. It charges the second Marx to perhaps 250 kV. If two spark gaps of the second Marx have closed the remaining gaps have sufficient voltage to close. Figure 8a shows typical output waveforms from two Marx generators into an overmatched load. The voltage (upper trace) is 420 kV. The current (lower trace) of 24 kA is from the lower generator only. Total current is 48 kA. Load impedance is 8.8Ω .

Figure 8b shows a misfire in which the triggered generator erects, deposits its energy into the load and the second generator erects afterward. The probability of such a misfire increases as the spark gaps are operated farther from self-break with a consequently longer erection delay. In a typical 10 kJ operating regime the misfire probability is less than 15 percent; reducing this to 1 percent level may require an improved trigger system.

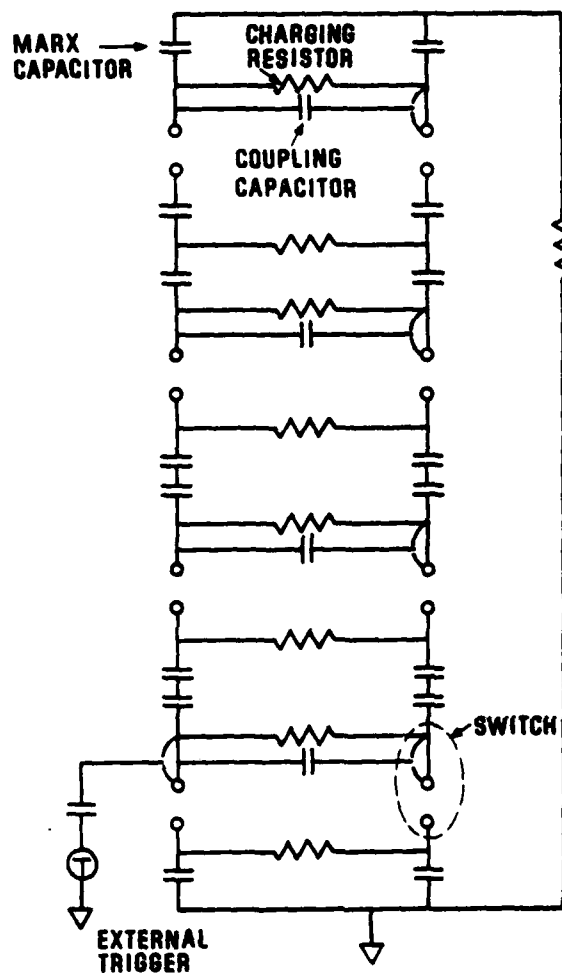
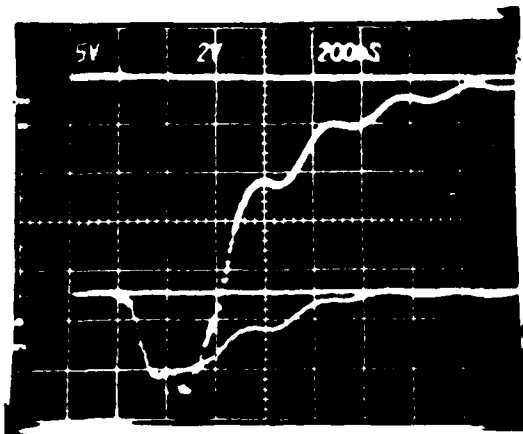
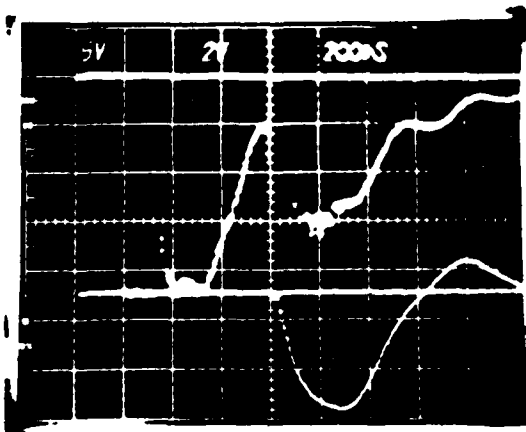


Fig. 7. Schematic of two parallel Marx generators illustrating the cross-coupling scheme used for triggering.



(a)



(b)

Fig. 8. Waveforms from two Marx generators into a resistive water load. Upper trace, voltage (64 kV/div), lower trace current from the untriggered generator (20 kA/div).
a. Proper operation.
b. Misfire.

Conclusions

Data demonstrate that the Marx generator based Gullemin Type C PFN described in this paper is capable of delivering 10 kJ of pulsed energy to a load in 500 ns at 250 kV. The desired repetition frequency can be achieved at half voltage but substantial work remains to be done to achieve full repetition rate at full voltage. Problems encountered include the failure of solid dielectric insulation due to Marx generator erection transients and a failure of the spark gaps to maintain a stable self-break threshold.

Acknowledgments

The author wishes to thank K. R. Prestwich for his assistance in all phases of this effort. W. Crowe and J. P. Corley have done the bulk of the mechanical assembly and have contributed to many other aspects of the project.

References

1. Glasoe and Lebacqz, Pulse Generators, MIT Radiation Laboratory Series, McGraw Hill, NY, 1948.
2. J. J. Ramirez, Sandia National Laboratories, private communication.
3. C. V. Duncan and L. P. Bradley, Proc. of the Int'l. Pulsed Power Conf., Lubbock, TX, 1976, Paper ID-3.
4. J. J. Ramirez, K. R. Prestwich, R. S. Clark and M. T. Buttram, Proc. of the 2nd Int'l. Topical Conf. on High Power Electron and Ion Beam Research and Technology, Ithaca, NY, 1977, Vol. II, p. 891.
5. J. C. Martin, AWRE Report SSWA/JCM/1065/25, unpublished.
6. R. J. Churchill, A. B. Parker and J. D. Craggs, J. of Electronics and Control, 11, 17 (1961).
7. J. A. Philosophos and M. B. Robinson, Insulation/Circuits, April, 1979, p. 48.
8. M. T. Buttram and G. J. Rohwein, Proc. of the 2nd Int'l. Topical Conf. on High Power Electron and Ion Beam Research and Technology, Ithaca, NY, 1977, Vol. II, p. 845.
9. V. A. Aurutskii, Sov. Phys. Tech. Phys. 18, 389 (1973).
10. V. A. Aurutskii, G. M. Göncharenko and E. M. Prokhorov, Sov. Phys. Tech. Phys., 18 386 (1973).
11. T. H. Martin, Sandia National Laboratories, private communication.

STRIP-LINE MULTICHANNEL-SURFACE-SPARK-GAP-TYPE MARX GENERATOR FOR FAST DISCHARGE LASERS

M. Obara, S. Suzuki, Y. Ishibashi, and T. Fujioaka

Department of Electrical Engineering, Keio University,
3-14-1, Hiyoshi, Kohoku-ku, Yokohama-shi, Japan
044(63)1141

Summary

Design and construction of a novel low impedance strip-line-type Marx generator using multichannel surface-spark-gaps for fast discharge lasers are described. This type of Marx generator can supply a fast-rise current pulse to low resistive loads, and is simple, compact and scalable. As it contains PFN function, quasi-rectangular output waveform can be generated. Theoretical study of the output performance has been carried out by numerically solving its circuit equation of the Marx generator. Theoretical results were compared with the experimental results. Its application to the fast discharge excitation of the N_2 and HF lasers and practical characteristic limitation of this type of Marx generator are also discussed.

Introduction

Fast discharge excitation is necessary to initiate N_2 , HF, and rare-gas halide lasers. All discharge rare-gas halide lasers with a UV preionization show a limited stable glow discharge time no longer than 35-40 ns.¹ At the peak of discharge current pulse, dynamic impedance of the discharge plasma is estimated to be less than 1 Ω for ordinary discharge devices. Additionally, the rise-rate of the applied discharge voltage should be greater than 10^6 kV/s for obtaining spatially uniform initiation of the discharge, and electrical power input on the order of 1 MW/cm² is required to produce a sufficient laser gain.² These requirements are also necessary for N_2 and HF lasers.

As the excitation techniques satisfying the above requirements, the L-C inversion,³ Blumlein circuit,⁴ and pulse-charged PFN⁵ have been successfully utilized. Except the pulse-charged PFN, the L-C and Blumlein devices have been used only for small-scale lasers. The pulse-charged PFN exciter can operate with low overall electrical efficiency.

A new excitation scheme for fast discharge lasers has been developed, which is capable of delivering the

power as much as possible into the discharge volume prior to the onset of discharge instabilities. This simple and compact laser exciter consists of a low-impedance, strip-line-type Marx generator with multichannel surface-spark-gaps⁶ and contains the PFN function.⁷

We want to report the design of the strip-line-type Marx generator using multichannel surface gaps for fast discharge lasers, and to report the theoretical analysis of the equivalent electrical circuit by computer simulation. The output power characteristics were compared between the strip-line type Marx generator and the conventional type Marx generator without any additional stray capacitance. Finally we will discuss the discharge excitation of the N_2 and HF chemical lasers by this type of Marx generator.

Modification of a Marx Generator

As Marx generators can easily produce high voltage output pulse by increasing the number of stages of the Marx capacitor and have scalability, they have been utilized widely as a driver for an e-beam accelerator and an x-ray generator for many years. Generally speaking, since the Marx generator has a high output impedance because of its large inductance, a high and short current pulse cannot be generated by a conventional Marx generator without any additional low impedance PFN. Then, its overall electrical efficiency decreases when a PFN is used additionally. Internal inductance of a conventional Marx generator consists of the residual inductance in Marx capacitors, the channel inductance of spark-gap switches and the inductance derived from the structure of the Marx generator. A low inductance capacitor such as ceramic ($BaTiO_3$, or $SrTiO_3$ series) capacitors is suited to diminish the residual inductance in capacitors used. One of the methods to reduce the channel inductance of the spark-gap switch is to supplant a standard spark-

gap switch by a multichannel spark gap switch (rail gap or surface gap switches). As for the structural inductance, it is known that coaxial and strip-line configurations are suitable for realizing a low-impedance circuit. We have previously clarified that these types of Marx generator contain the PFW function, resulting in producing a quasi-rectangular output waveform.⁷

In case of the coaxial-type Marx generator using a standard spark-gap switch, decrease in the impedance was found to depend mainly on the channel inductance of the gap switch used, which limits the minimum inductance of this Marx generator.

Theoretical Analysis

A simplified view of a strip-line-type 4 stage Marx generator with multichannel-surface-spark-gap switches is shown in Figs. 1 and 2.

The equivalent circuit of the strip-line, multichannel-spark-gap-type exciter is shown in Fig. 3. This low-impedance Marx generator has multichannel surface-spark-gaps and stray capacitor C_s on a copper-clad glass-epoxy-laminated board ($\epsilon_s=4$, $t=3.2\text{mm}$, $S=100 \times 100 \text{ cm}^2$) providing the function of the PFW. The Marx generator consists of 4 modules and can store an electrical energy of 50 J at a charging voltage of 20 kV. The discharge was fired by a triggered spark gap, pressurized at up to 3 atm with a dry N_2 gas. A triggered spark gap and the first-stage Marx capacitor C_m were connected with eight coaxial-cables ($10\text{C}2\text{V}$, $Z_0=75 \Omega$) to keep the propagation time of a voltage wave equal. Ceramic capacitors which have virtually little residual inductance, were used as a Marx capacitor C_m . Each energy storage capacitor was composed of 23 ceramic capacitors (62.1 nF in total capacitance) distributed in parallel as closely as possible. Each stray capacitor C_s was made by a copper-clad glass-epoxy-laminated board itself. In initial experiments, each surface-gap was fired in air, utilizing the multichannel arc discharge on an etched laminated board. The length of each surface discharge electrode was 80 cm, the discharge distance being 3 cm.

The output performance of this type of Marx generator shown in Figs. 1, 2 and 3 was analyzed numerically by the computer simulation code. This code has been previously reported.⁷ This system is called Model B in Table 1. The output characteristics of this Marx generator is compared to the Marx generator without stray capacitance C_s (Model A in Table 1). The equivalent electrical circuit of the conventional Marx

generator is shown in Fig. 4. The electrical parameters used in this analysis are listed in Table 1.

In this analysis, the multichannel-gap switch is assumed to consist of the channel inductance and the resistance. Since the output voltage waveform of the Marx generator varies with the resistance of the resistive load, we introduce a normalized load resistance α defined by

$$\alpha = \frac{R_L}{2n} \sqrt{C_m / L}, \quad n = 4$$

where α indicate the ratio of the load resistor R_L to $2 \sqrt{L_c / C_m / n}$ which is the resistance at which critical damping occurs in a simple RLC series resonance circuit. We also introduce a parameter σ_r

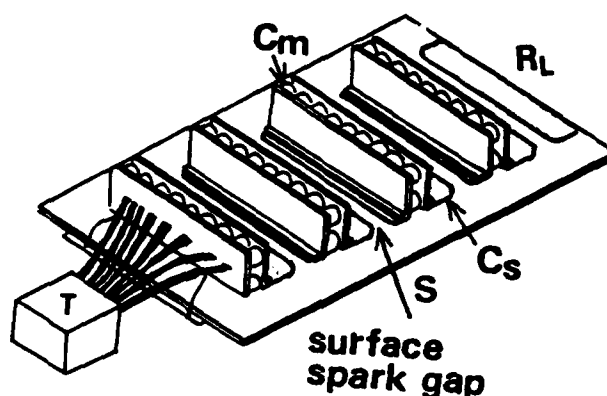


Fig. 1 Simplified view of a strip-line-type 4-stage Marx generator. Not to scale. C_m : Marx capacitor, C_s : Stray capacitance, T: Triggered spark gap, R_L : Load.

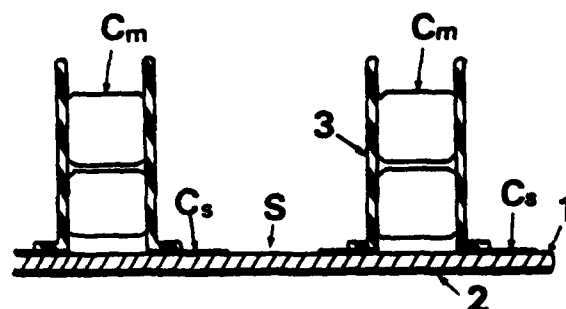


Fig. 2 Cross-sectional view of the strip-line, multichannel-surface-gap-type Marx generator (Partial). 1: Copper-clad glass-epoxy-laminated board, 2: Copper plates, 3: Al plate, S: Surface gap.

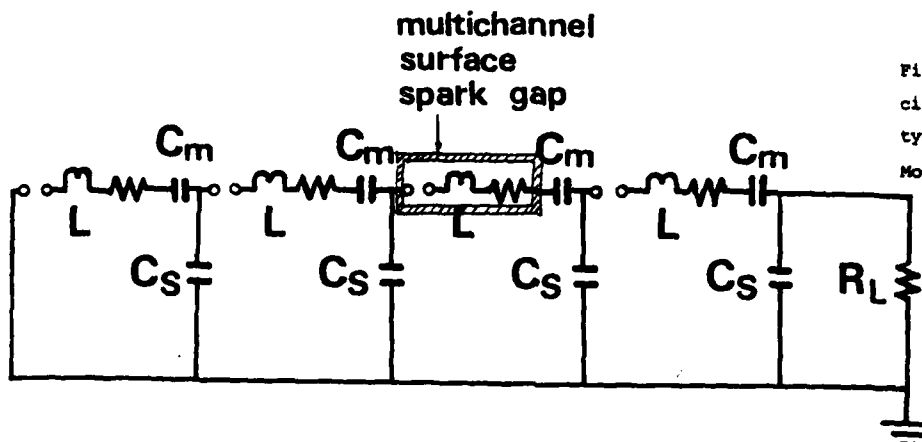


Fig.3 Equivalent electrical circuit of the strip-line-type, 4-stage Marx generator. Model B.

Table 1 Electrical parameters used in this analysis.

	Model A	Model B	Model C *
NM	4	4	12
V_C	30 kV	30 kV	30 kV
C_m	62.1 nF	62.1 nF	62.1 nF
L	10 nH	10 nH	10 nH
	15	15	15
	20	20	20
	25	25	25
	30	30	30
C_s	0	$\sigma_T=2, 9.58 \text{ nF}$ 3, 4.26 4, 2.39 5, 1.53 6, 1.06 7, 0.78 8, 0.60	$\sigma_T=4, 0.27 \text{ nF}$ 5, 0.17
R_L	α	$L=10$ $L=15$ $L=20$ $L=25$ $L=30 \text{ nH}$ $L=20 *$	
	0.2	0.64 Ω 0.79 Ω 0.91 Ω 1.02 Ω 1.11 Ω 2.73 Ω	
	0.4	1.28 1.57 1.82 2.03 2.22 5.45	
	0.6	1.93 2.36 2.72 3.05 3.33 8.17	
	0.8	2.57 3.14 3.63 4.06 4.45 10.90	
	1.0	3.21 3.93 4.54 5.08 5.56 13.62	
	1.2	3.85 4.72 5.45 6.09 6.67 16.34	

NM: Marx Stage
 V_C : Charging Voltage
 C_m : Marx Capacitance
 L : Inductance
 C_s : Stray Capacitance
 R_L : Load Resistance

* The results of Model C are not presented here.

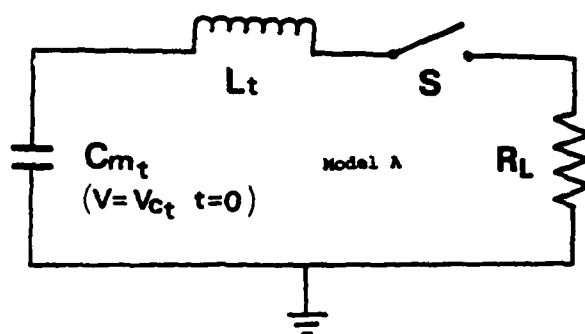


Fig.4 Equivalent electrical circuit of the Marx generator without stray capacitance C_s . L_t : Total inductance, R_L : Load resistance, C_{mt} : Total Marx capacitance, S: Gap switch.

defined by

$$\sigma_T = \frac{\pi}{n} \sqrt{C_m / C_s}, \quad (n=4)$$

which is determined by the Marx capacitance C_m and the stray capacitance C_s .

The output-voltage waveforms calculated by this analysis using the normalized parameter α are shown in Fig. 5. Here $\sigma_T = 5$ is assumed. Dependence of the voltage waveforms on parameter σ_T is shown in Fig. 6. In Fig. 6, α is assumed to be 1. Peak-power dependence on α and σ_T are shown in Figs. 7, and 8, respectively. According to the results obtained, in order to produce the highest peak power the parameters $\alpha = 1.0$ and $\sigma_T = 5.5$ were found to be optimum.

In Model A, the theoretical results are shown in Figs. 9 and 10. In this analysis, the stray capacitance is assumed to be negligible. In this case,

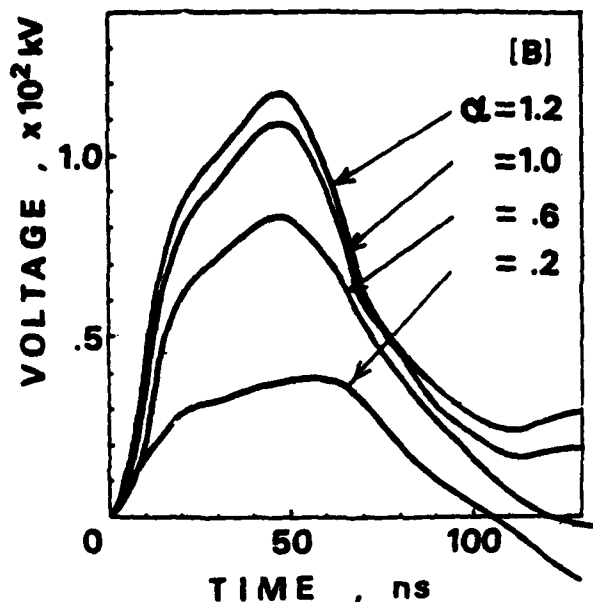


Fig.5 Dependence of voltage waveforms on parameter α .
 $\sigma_T = 5$. $L = 20$ nH. Model B.

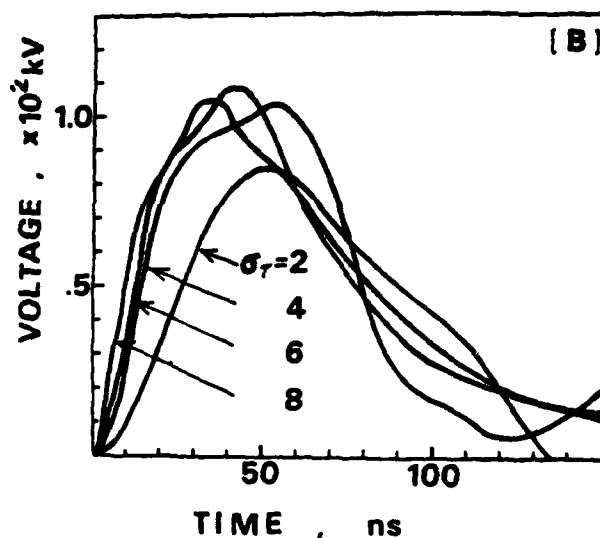


Fig.6 Dependence of voltage waveforms on parameter σ_T .
 $\alpha = 1.0$. $L = 20$ nH. Model B.

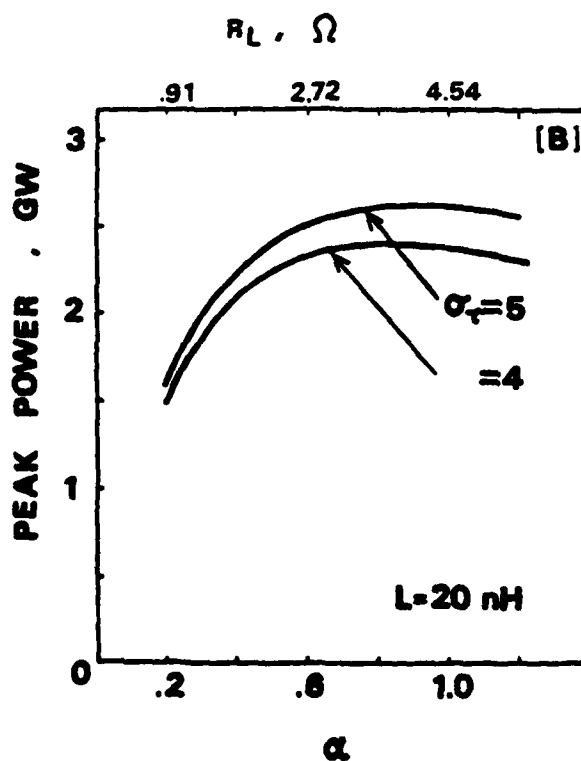


Fig.7 Dependence of peak-power on parameter α .
 $L = 20$ nH. Model B.

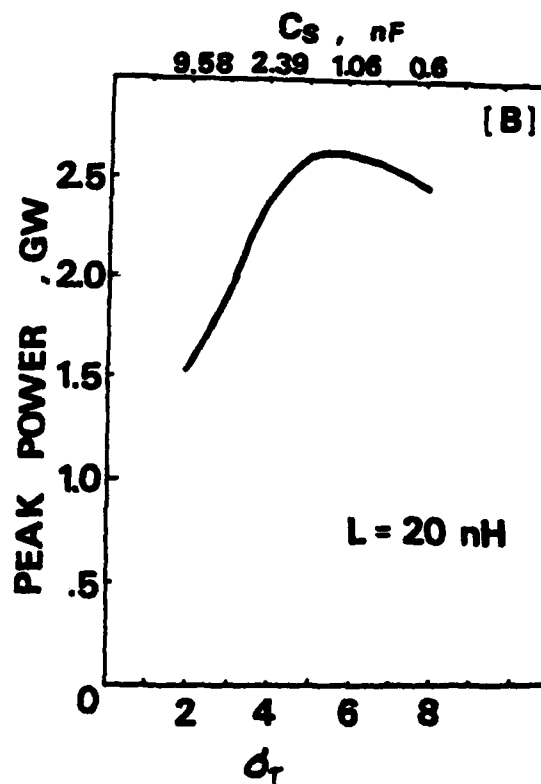


Fig.8 Dependence of peak-power on parameter σ_T . $\alpha = 1.0$
 $L = 20$ nH. Model B.

the peak power was maximized at $\alpha = 0.6$.

The peak powers were compared between the strip-line type Marx generator (Model B) and the ordinary type Marx generator without stray capacitance C_s (Model A) in Fig. 11. As easily be seen in Fig. 11, the peak power of Model B is always larger than Model A against all values of the inductance. Therefore the stray capacitance was found to play an important role for delivering high peak power to the resistive load.

Operating Characteristics of the Marx Generator

The channel number of the surface gap is plotted against the number of the stage in Fig. 12. As the charging voltage increases, the channel number increases. The channel number increases sharply with the stage number. Figure 13 shows the output waveforms at $R_L = 2 \Omega$. As the charging voltage increases, the output waveform rises sharply due to the increase in the channel number, resulting in the decrease in the channel inductance.

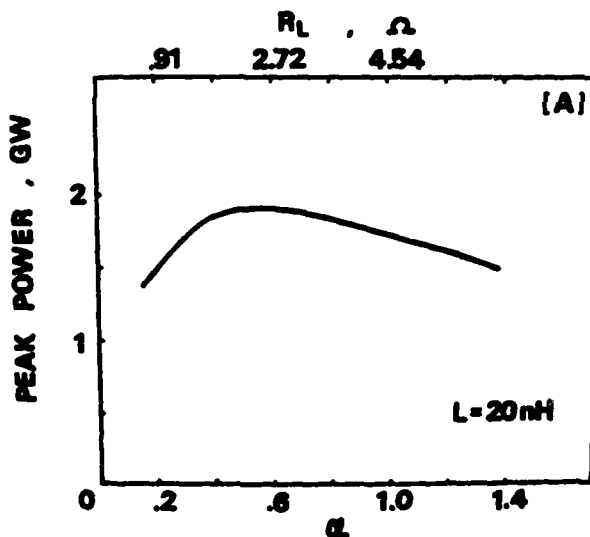


Fig.9 Dependence of peak-power on parameter α .
 $L = 20 \text{ nH}$. Model A.

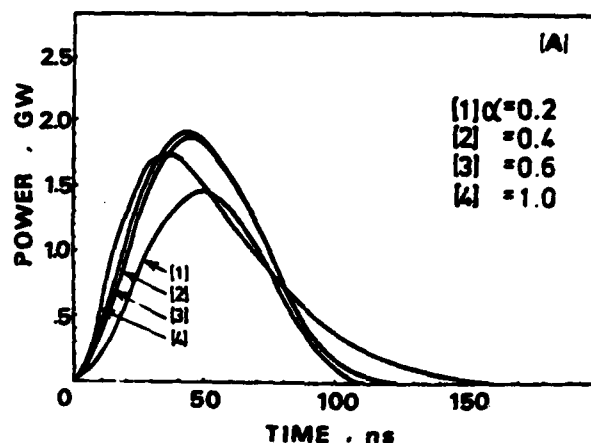


Fig.10 Dependence of power waveforms on parameter α .
 $L = 20 \text{ nH}$. Model A.

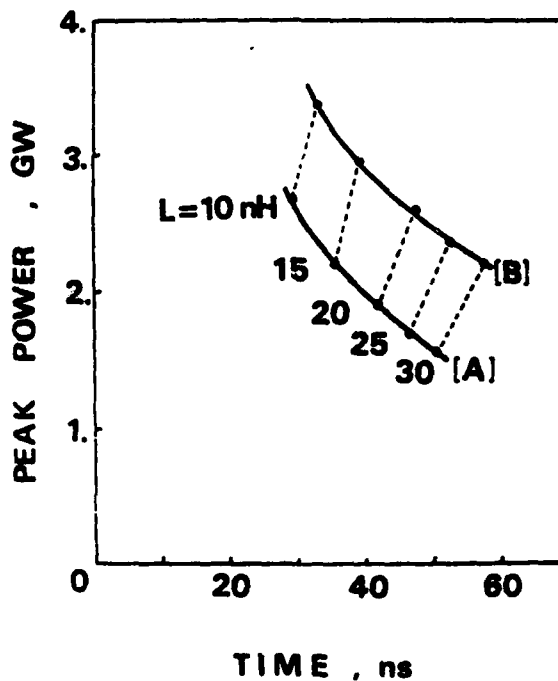


Fig.11 Dependence of peak-power on inductance.
A: $\alpha = 0.6$, B: $\alpha = 1.0$, $C_T = 5$.

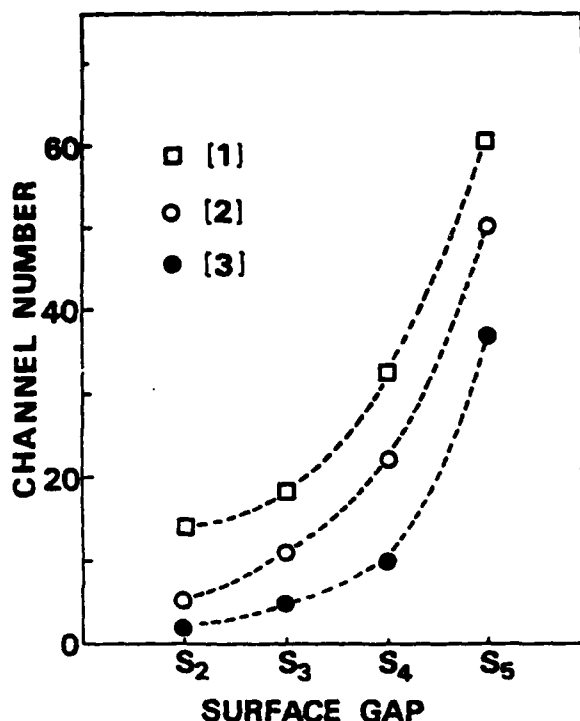


Fig.12 Channel number of surface spark gaps ($d= 30$ mm in air). 1: $V_C = 20$ kV 2: $V_C = 17.5$ kV 3: $V_C = 15$ kV.

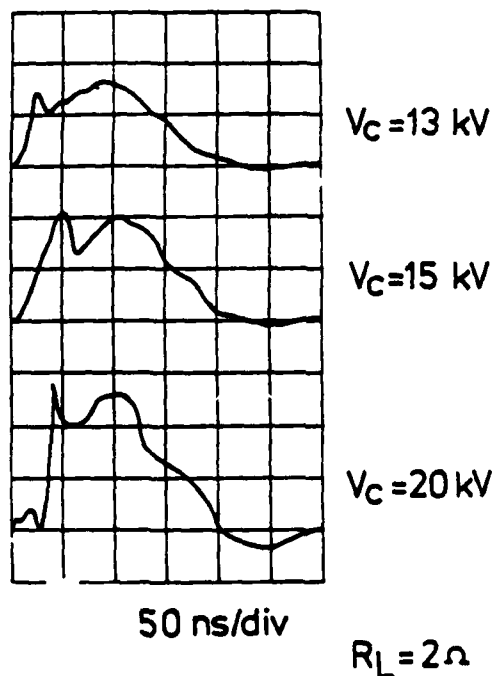


Fig.13 Output voltage waveforms. $R_L = 2 \Omega$.

Excitation of Gas Lasers by This Marx Generator

The fast discharge gas lasers of N_2 and HF were excited by this type of Marx generator. The laser chamber of lucite was used for both N_2 and HF lasers, which was fitted with a CaF_2 laser window at each end. A pair of 90-cm long stainless-steel electrodes were rounded smoothly at both corners to eliminate field enhancement. The discharge volume was $1^w \times 2^h \times 90^l$ (180 cm^3). The laser device had two 1-mm dia. pre-ionization wires placed at the both sides of the cathode which were connected to the anode through two 0.7-nF ceramic capacitors. The electrical connection between the laser electrodes and the Marx generator was made to reduce the inductance as far as possible.

For an N_2 laser, an ASE (Amplified Spontaneous Emission) output was measured when an aluminum-coated mirror was used as a total reflector. The laser energy was measured with a Gentec ED-200 joulemeter. The maximum N_2 laser energy was obtained at a charging voltage of 19 kV and at 60 Torr. The N_2 laser energy and an electrical efficiency at 60 Torr are plotted in Fig. 14 as a function of charging voltage and stored energy. The laser spot size of an N_2 laser was measured to be about $1^w \times 2^h \text{ cm}^2$. The laser pulse shape was detected with a fast biplanar phototube (Hamamatsu TV, R617-02). Signals were recorded with a Tektronix 7904 oscilloscope. The N_2 laser pulse shape is shown in Fig. 15. The pulse width of 20 ns (FWHM) was obtained at a charging voltage of 18 kV and at 60 Torr.

The lifetime of the upper laser level ($C^3\Pi_u$ state) of N_2 (~ 40 ns) is two orders of magnitude shorter than the lower laser level ($B^3\Pi_g$ state)⁸. To efficiently excite an N_2 laser, a fast voltage risetime in the 10-20 ns range, low-loss and low-inductance spark-gap switches, and a low-impedance transmission line are necessary, which means that a fast power pulse shorter than the lifetime of the upper laser level should be applied. According to the result of the N_2 laser performance, the low-impedance Marx generator ($Z_0 = \sim 1-2 \Omega$) newly developed was demonstrated to have a fast voltage risetime (~ 10 ns), and to efficiently excite the N_2 laser.

An HF laser was also initiated by this low-impedance Marx generator to clarify the exciter performance. For an HF laser, the H donor was C_2H_6 and the F donor being SF_6 . The C_2H_6 and SF_6 were premixed and were then introduced from two inlets located at both ends of the laser chamber and exhausted from its center by a

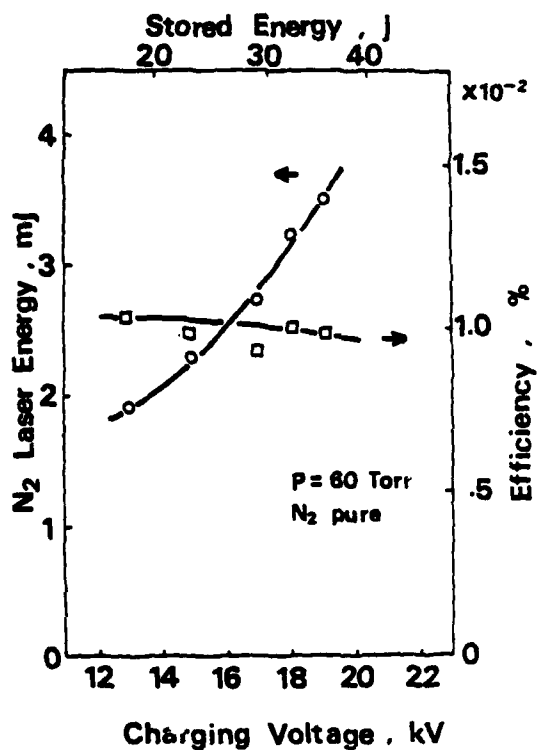


Fig. 14 Plots of N₂ laser energy and electrical efficiency against charging voltage.

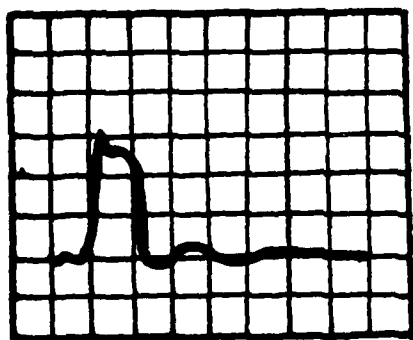


Fig. 15 N₂ laser waveform. Pressure is 60 Torr.
 $V_c = 18$ kV. Horizontal: 20 ns/div.

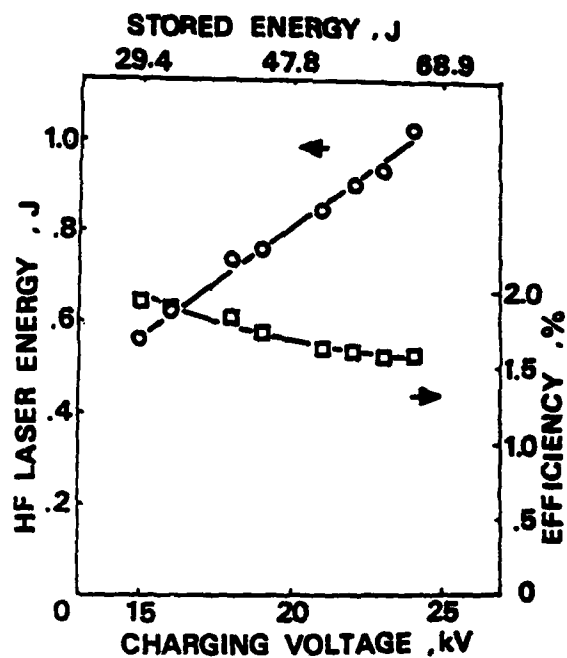


Fig. 16 Plots of HF laser energy and electrical efficiency against charging voltage. Pressure is 120 Torr (SF₆/C₂H₆).



Fig. 17 HF laser waveform. P = 120 Torr, C₂H₆/SF₆ = 2/25. $V_c = 20$ kV. Horizontal: 100 ns/div.

mechanical vacuum pump. An ASE output of an HF laser was measured with a Gentec ED-500 joulemeter when an Au mirror ($R = 8 \text{ m}$, concave) was used as a total reflector. The ASE output of an HF laser is plotted in Fig. 16 as a function of charging voltage and stored energy. As can easily be seen in Fig. 16, the laser energy and the electrical efficiency trade off with each other. The maximum laser output of 1 J (5.6 J/l) was obtained with a 120 Torr mixture of $\text{C}_2\text{H}_6/\text{SF}_6 = 1/25$. The HF laser pulse shape was detected with a photon drag detector. Figure 17 shows a typical HF laser pulse shape when the mixture of $\text{C}_2\text{H}_6/\text{SF}_6 = 1/25$ was at 120 Torr.

Pulsed discharge-initiated HF lasers have been found to efficiently lase when initiated by a low-impedance discharge circuit.⁹ For HF chemical lasers, it is well known that the input energy density and the electrical efficiency trade off with each other. In this case, under the large energy loading of $\sim 380 \text{ J/l}$ an electrical efficiency of 1.5 % and an output energy density of 5.6 J/l was obtained using a low-impedance Marx generator as an initiator.

In summary, a fast discharge laser exciter has been newly developed, which consists of a low-impedance, strip-line-type Marx generator. Using this Marx generator N_2 and HF lasers have been efficiently excited.

Acknowledgement

The authors would like to acknowledge the contributions by C. Takeuchi and I. Kariya.

References

1. R.C.Sze and P.B.Scott, *Rev. Sci. Instrum.* 49, 772 (1978).
2. G.Eden, R.Burnham, L.F.Champagne, T.Donohue and N.Djeu, *IEEE Spectrum* 16, 50 (April 1979).
3. R.Burnham and N.Djeu, *Appl. Phys. Lett.* 29, 707 (1976).
4. S.Sumida, M.Obara and T.Fujioka, *Appl. Phys. Lett.* 33, 913 (1978).
5. W.J.Sarjeant, A.J.Alcock and K.E.Leopold, *IEEE J. Quant. Electron.* QE-14, 177 (1978).
6. *ibid.*, 2nd IEEE International Pulsed Power Conf. June 12-14, 1979, Lubbock TX.
7. M. Obara, Y.Sakato, C.H.Lee, T.Hashimoto and T. Fujioka, 2nd International Pulsed Power Conf. June 12-14, 1979, Lubbock, TX.
8. B.W.Woodward, V.J.Ehler and W.C.Lineberger, *Rev. Sci. Instrum.* 44, 882 (1973).
9. K.Midorikawa, S.Sumida, Y.Sato, M.Obara and T.Fujioka, *IEEE J. Quant. Electron.* QE-15, 19 (1979).

A LOW-INDUCTANCE, 300 KJ, 1.2 MV, MARX GENERATOR
FOR THE LASL-ANTARES LASER FACILITY

J. Harrison, H. Kent, T. Olson, G. Santanaria, and R. White
Maxwell Laboratories, Inc.
San Diego, California 92123

Summary

The final amplifiers of LASL's ANTARES Laser are to be driven by 300 kJ Marx generators. A modular Marx has been designed to meet the requirements of 3 μ H, <20 ns rms jitter, and high reliability. The development progressed through four key stages: a study of inductance as a function of geometry; an analysis of jitter for various triggering systems; a full-scale model of the Marx to verify inductance; and a high-voltage integrity analysis. The final design comprises 10 stages, each having six 2.8 μ F capacitors charged symmetrically to 120 kV, and one 3-electrode spark gap developed by LASL. The open-circuit voltage is 1200 kV, normal load voltage is 550 kV. The capacitors hang from the tank lid on nylon straps. The spark gaps are mounted on the outside of the capacitor modules to give easy access for maintenance. The generator has been successfully fired 2000 times into a (nominal) load impedance of 2.5 Ω , and 20 times into an 0.25 Ω load representing flashover conditions in the load. The measured inductance is 2.3 μ H, and the rms jitter is \sim 10 ns.

Introduction

The discharge of the final amplifiers in the LASL ANTARES CO₂ laser system will each be driven by four 300 kJ, 1.2 MV Marx generators. The complete ANTARES system is designed to have six final amplifiers, so a total of 24 of these Marx generators are required for the system.

Synchronized and reliable performance of these high voltage, high energy drivers is essential for the predictable performance of the entire laser system. Consequently, when developing the final amplifier specifications, LASL gave close considerations to their performance specifications. A low Marx inductance of 3 μ H, and a design goal of 2.5 μ H was specified to maximize the rate of power delivery. This is important to minimize the time available for build-up of undesirable laser oscillations. LASL also specified a maximum jitter for each Marx driver of 20 ns standard deviation. However, there was a design goal of 10 ns, to minimize the imbalances in the power delivery since imbalances can excite laser oscillations. These two requirements were combined with the requirement of a very low Marx generator prefire and non fire rate which was to be demonstrated in a 2000 shot test of a prototype system.

This paper describes the Marx generator designed to meet these requirements, and also describes the design analysis undertaken to ensure that the Marx would achieve or exceed the specified performance and the prototype tests undertaken to confirm the design.

Description of Marx Generator

Figure 1 shows the prototype Marx generator removed from its oil tank. The Marx has ten stages mounted in two 5 stage rows, one above the other. Figure 2 shows a plan view of a row. The major current path is from the grounded end of the upper row, along this row to the back of the Marx where it drops to the bottom row and returns to the output and adjacent to the ground connection. The output end of the Marx is connected to 6 cables through a 0.25 Ω resistor. The resistor is provided to damp the Marx discharge under laser or cable fault conditions.

It will be seen from Figure 2 that the current path zig-zags down each row. The capacitor assemblies carry the current across the rows, and are connected to adjacent capacitor assemblies by gas plasma switches mounted on the outside of the assembly. The capacitor assemblies at the ends of the rows have three parallel 2.8 μ F, 60 kV capacitors, and those in the middle stages have two of these parallel sets connected in series. The capacitor sets are charged alternatively to +60 kV and -60 kV. The capacitors in each capacitor assembly are mounted in a formed sheet metal housing. This housing provides the connection for the Marx discharge current, eliminating any possibility of arcing between capacitor cases, in addition to supporting the capacitors.

The capacitor housings of the top row of capacitors are hung from the lid of the Marx tank by nylon straps, and the capacitors in the lower row are hung from the top row capacitors, also using nylon straps. The final generators will be serviced by lifting the Marx from its tank using an overhead crane.

The prototype had a removable end plate so that it could either be lifted out of its tank, or it could be lifted high enough to prevent interference with the top flange of the tank, then wheeled out through the open end of the tank. A special service fixture was used for this end removal.

A major feature of this Marx design is the accessibility of the switches and the charge and trigger resistors when the generator is removed from its tank. This ready access makes it easy to service these components or to remove them for capacitor maintenance. A special dolly with a lift table is used to remove capacitors, which can be supported on the dolly while the strap bolts are removed, then wheeled out of the assembly. This capacitor removal operation is also very simple.

Switches

The Marx switches are three electrode gas plasma switches with a central electrode with a field distortion edge at the mid plane of the switch. The switch, shown in Figure 3, was developed by LASL. It has high density copper-filled, sintered tungsten main electrodes, which proved to have superior wear characteristics compared to less fully filled sintered tungsten. Cylindrical blue nylon insulators are used between the main electrodes and the ring support of the central electrode. The ends of the switch are clamped together by Permali "Superstuds®." The switch cavity dielectric is pressurized, synthetic air.

The static breakdown/gas pressure characteristic of the switch has been measured by LASL over a voltage range of 50 kV to 300 kV. The Marx is operated at a static breakdown/operating voltage ratio of 2 to minimize the prefire rate.

Triggering

The specified jitter in the erection time of the Marx was 20 ns standard deviation, with a design goal of 10 ns. There are two features that make this a non-trivial requirement. These are the breakdown ratio of 2 used for the switches, and the high capacitive coupling between adjacent stages.

The trigger system adopted to meet these requirements is shown in Figure 4. Erection is initiated by simultaneously triggering the first four switches with a pulse from a 280 kV trigger Marx generator. This trigger Marx is hung from the lid of the Marx tank, and is resistively coupled to the mid-plane electrodes of the switches. Passive triggering is provided for the stages to 10 switches by coupling their mid-plane electrodes to the capacitor case 2 1/2 stages lower in the voltage chain. This connection generates a voltage differential of 300 kV between the low voltage electrode and the mid-plane electrode when the earlier stages erect. This voltage excursion is five times the voltage level between these electrodes at the time of charge completion.

The behavior of the system after this first half of these later gaps closed was computer simulated. It was found that the voltage exceeded three times the charge voltage with the generator output open circuited, and 3 1/2 times the charge voltage when feeding a 6 Ω load. The simulations indicated that the time from closure of the first four switches to completion of erection is ~ 100 ns. This suggested that the design goal of 10 ns jitter might be attainable.

Calculation of Inductance

The inductance of the Marx was of vital importance to LASL, so it was important to make an accurate inductance calculation before construction started. The principle which formed the basis for this calculation is that an upper bound for the inductance of any structure can be obtained by assuming that the current flows only in a limited part of the circuit, and then choosing a flow path that has an inductance that is calculable. The calculated inductance will then be close to the actual inductance if most of the current flows through the selected path.

The ANTARES Marx generator proved to be highly amenable to this type of treatment since most of the current flow was through current paths that had calculable inductances. The complete analysis will not be presented here. However, the method used to calculate the inductance of the stages in the middle of the Marx will be presented as an example.

Figure 5(a) schematically shows, in phantom, two adjacent capacitors in the upper row of the Marx, the two capacitors immediately below these top capacitors and the interconnecting switch for both capacitor pairs. The selected current path is shown in full lines in this figure, and is repeated in Figure 5(b) with the phantom lines of the remainder of the circuit omitted. It will be seen that the chosen path was two triangular parallel plates between the two capacitors in each row, and rectangular, parallel plate conductors between the rows. One side of one of the triangular planes is connected to the adjacent side of the adjacent plate through the capacitor bushings and the switch. The inductance of this geometry can readily be calculated using:

parallel plane formulae for the parallel plate sections

cylinder over plane formulae for the switch section.

This leaves a small volume between the capacitors and the switch section. The inductance of this volume was calculated by assuming that the current flowed in three, parallel, triangular paths forming a transition from the three capacitor terminals to the common switch volume.

After the calculation was complete, an estimate was made of the possible error due to omitted conductors. The complete calculation yielded bounds of 2.1 and 2.3 μH for the total inductance. The geometry of the final Marx was altered slightly from that of the model, adding 0.1 to 0.2 μH to the inductance.

This calculated inductance was checked by constructing a full-scale model of the Marx generator and yielded an inductance figure of 2.5 μH .

The inductance of the prototype Marx generator was calculated to be 2.3 μH from an oscilloscope trace of the ring out of a short circuit test shot. This value is in the mid to low range of the calculated inductance when adjusted for the changes in the geometry from that used in the inductance calculation.

Prototype Tests

The prototype Marx generator shown in Figure 1 has successfully completed a test program to demonstrate its reliability, electromechanical integrity, inductance and jitter. The test series included 2000 full voltage shots fired at a shot rate of one per two minutes into a dummy load designed to closely simulate the amplifier load. Two groups of ten full-voltage short circuit shots were introduced into the dummy load series after 500 and 1500 test shots. The dummy load resistors were replaced by solid aluminum conductors during these tests. An additional voltage integrity test series was introduced into the test series after 1000 dummy load shots. The load impedance was raised from 2.5 Ω to 4.4 Ω for this test. This increased the peak voltage on the generator to 750 kV (vs. 550 kV for the dummy load shots).

The waveforms of the dummy load, short circuit and voltage integrity tests are shown in Figure 6. It will be seen that the waveforms of the first two are underdamped sinusoids with reversals of 5% and 75% respectively, and the waveform of the last is a critically damped sinusoid. The inductance and resistance of the Marx has been calculated from the ringing frequency, 161 kHz, and current reversal of the short circuit shots. The calculation gives a figure of 2.3 μH for the inductance, and 0.46 Ω for the resistance. The inductance figure agrees well with the calculated inductance range of 2.1 to 2.3 μH , especially after adjustment for the geometry changes between the model used in the calculation and the final implementation of the design. The resistance value includes the 0.25 Ω resistance of the series damping resistance, giving a series resistance value of 0.21 Ω for the Marx components and connections.

Jitter was monitored throughout the tests using an HP5370A timer/counter and Tektronix 454 oscilloscope mounted in a screen room, as shown in Figure 7. A double-Faraday shielded B-dot loop, mounted in the current return conductor generated a signal coincident with erection of the Marx. The B-dot signal and a time mark, in the form of a -0.7 V step, coincident with the triggering of the counter stop channel (but delayed 50 ns) were added and viewed on the scope. The time mark serves to verify that the counter is not triggered by spurious electromagnetic interference. The time delay between the trigger pulse and the B-dot signal were recorded for all the test shots. Figure 8 shows the delay distribution for a group of 100 consecutive shots fired at the full ± 60 kV charge (120 kV total). The total delay is 608 ns mean, 6.83 ns standard deviation. Approximately 200 ns of the mean delay is due to cable transit times in the test facility.

Test runs of 100 shots conducted at lower charge voltages showed somewhat longer delays; however, the jitter was lower than the goal of 10 ns standard deviation in all cases.

Seven system prefires were experienced prior to completion of the first 1500 dummy load shots. The instrumentation used for these tests did not discriminate between trigger system and main Marx prefires. After the first 1500 shots, the gap air pressure was varied to check whether the ratio of static breakdown/operating pressure of two was the best operating point. It was found that the prefire rate was unacceptably high at lower pressures and that the jitter increased greatly when the pressure was raised. Pressure changes of 3 psi were sufficient to produce significant degradation in the Marx performance. It therefore appears that the initial pressure of 47 psig is the optimum operating pressure.

During the latter portion of the test program, the system was instrumented with a fiber-optic coupled prefire sequence detector. The unit, by detecting the firing sequence of the trigger generator, trigger Marx or main Marx made it possible to determine the source of prefires. During this latter test sequence prefires were observed only in the trigger Marx.

The LASL-designed switches proved to be conservatively rated for normal duty. Only a slight roughening of the surface, as shown in Figure 10, occurred. In normal operation, degradation and yellowing of the air lines was observed. A chemical analysis of the

deposits indicated that some tungsten particles and aliphatic chemical hydrocarbons were present.

During the second short circuit test series, a switch insulator tracked and the resulting pressure burst the switch cavity. A careful inspection of the switch revealed no obvious causes. A later inspection of other switches showed some evidence of switch insulator degradation. Because of the insulator degradation and switch failure, the switches should be cleaned every 500 shots. The switches had 1500 dummy load shots before the failure occurred.

The prototype Marx was refurbished after completion of the test series, and will be used, together with three additional Marx generators, to drive the first laser amplifier to characterize its performance.

Conclusion

This paper has described the precision erection, low inductance, Marx generator designed for energizing the final amplifiers of the LASL ANTIARES CO₂ laser system. The design was based on careful calculation of the expected performance, and these calculations agreed well with the performance of the prototype unit.

The exhaustive tests on the prototype have confirmed the reliability of the unit, and the ease of assembly and disassembly of the design has been fully demonstrated during assembly, disassembly and maintenance of the prototype.

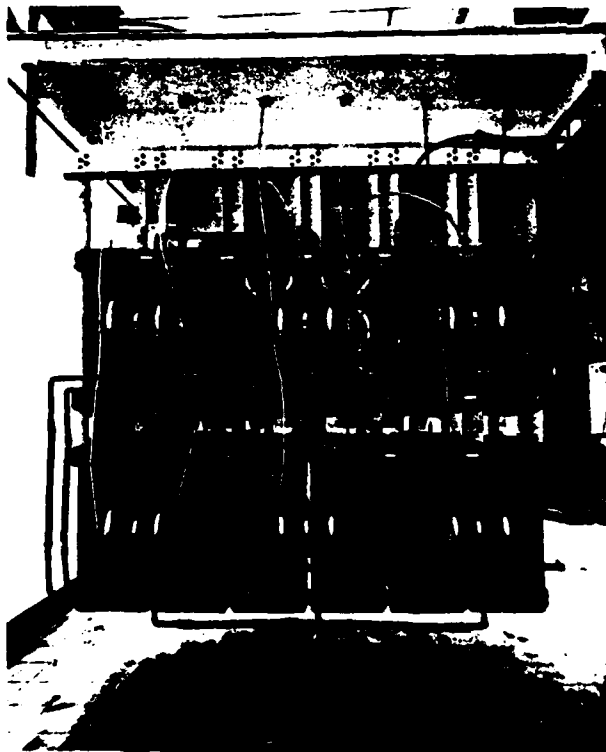


Figure 1. Marx generator removed from tank

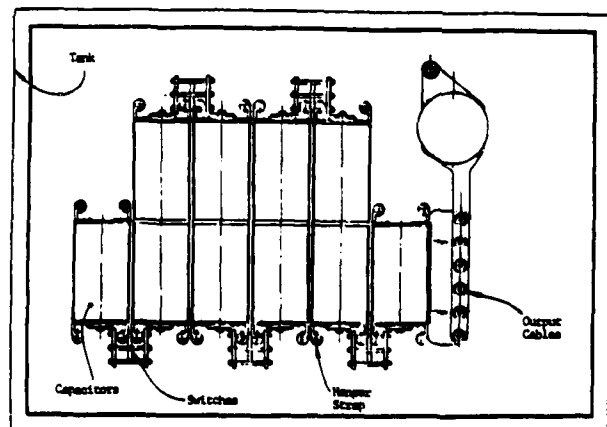


Figure 2. Plan view of a Marx row

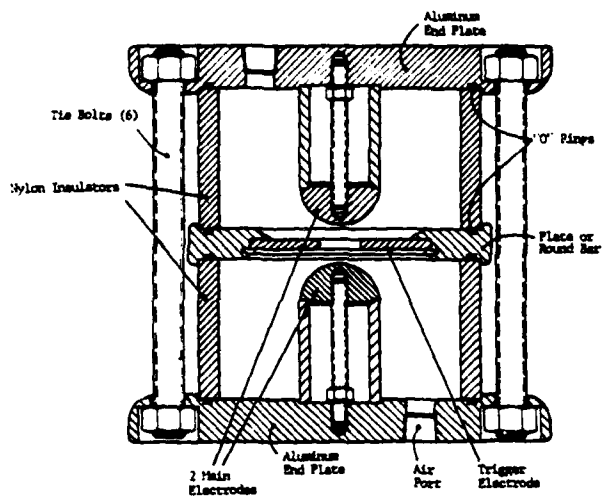
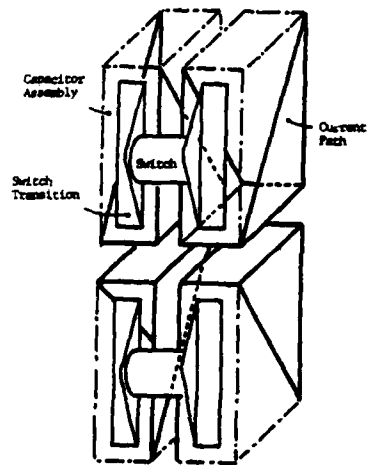
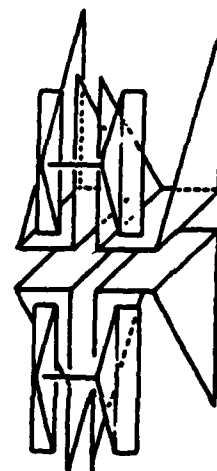


Figure 3. Cross section of Marx switch



(a) Showing capacitor assemblies and switch in phantom



(b) Conduction path only

Figure 5. Sketch of two interconnected capacitor assemblies in top and bottom row showing conduction path (full lines) used in inductance calculation

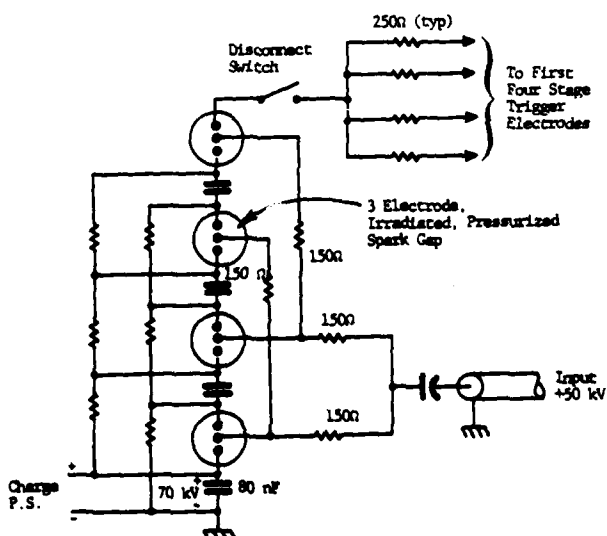


Figure 4. Schematic diagram of trigger system

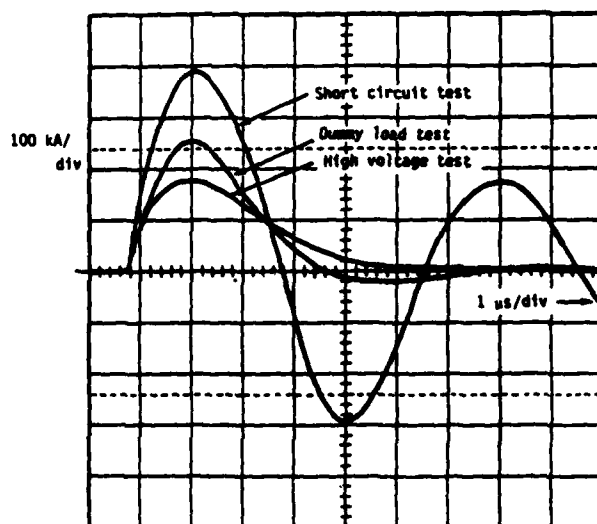


Figure 6. Current waveforms of the three test configurations

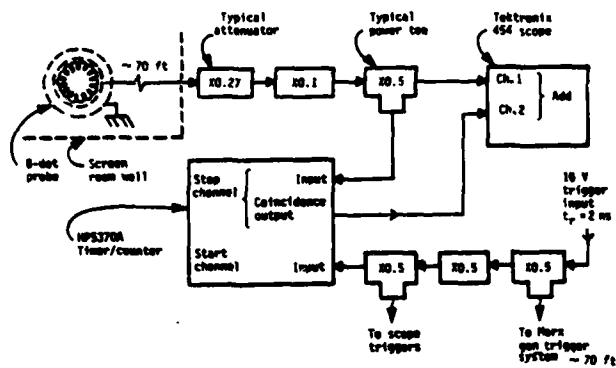


Figure 7. Block diagram of instrumentation system

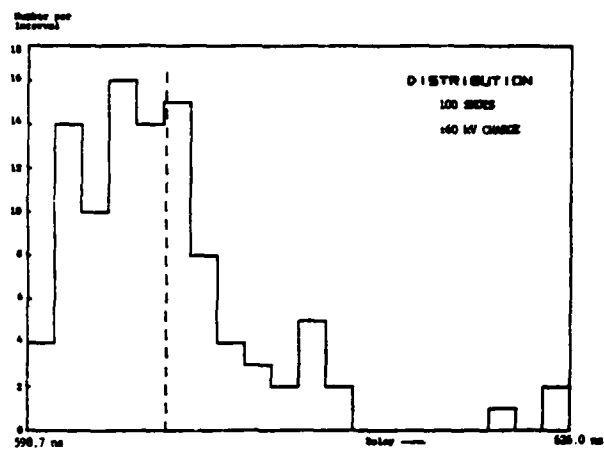


Figure 8. Histogram of delay variation for 100 consecutive shots

IMPLICATIONS OF ELECTRON TRAJECTORIES FOR DESIGN OF MAGNETICALLY INSULATED DIODES*

J. P. Shannon and F. S. Felber
Maxwell Laboratories, Inc.
San Diego, California 92123

Summary

High-voltage diodes, in which electric fields exceed the breakdown value, depend upon insulation by self-generated magnetic fields to inhibit electrons from crossing the vacuum diode gap. Nevertheless, electrons appear to cross diode gaps that should be insulated. This paper presents analytic, relativistic single-particle solutions describing the motion of electrons in the time-dependent, crossed electric and magnetic fields of diodes of different geometry. The solutions indicate that grad B drift may cause a loss of magnetic insulation.

The $\vec{E} \times \vec{B}$ drift drives electrons towards the load on equipotential planes roughly parallel to the anode and cathode surfaces. The much slower grad B drift drives electrons parallel to the axis of symmetry of a converging diode toward the anode surface. The net effect is a slow drift of electrons across the diode gap as they move rapidly towards the load. Because single particle motion has many of the qualitative features of collective motion, we expect that single particle collisions of electrons with the anode are indicative of a loss of magnetic insulation.

Introduction

This paper presents the first analytic, relativistic single-particle solutions describing the motion of electrons in the time-dependent, crossed electric and magnetic fields of non-planar diodes. The solutions indicate that grad B drift may cause a loss of magnetic insulation.

Magnetically insulated diodes can deliver megampere currents to a load or to produce relativistic electron beams. High-voltage diodes, in which electric fields exceed the breakdown value, depend upon insulation by self-generated magnetic fields to inhibit electrons from crossing the vacuum diode gap. Experiments at Maxwell Laboratories and elsewhere have shown that electrons appear to cross diode gaps that should be insulated.

Collective particle effects or resonant wave-particle effects in a diode gap may be important in determining the efficacy of magnetic insulation. However, it is essential to understand the motion of a single electron in the time-dependent fields of a diode to develop an understanding of how well magnetic insulation will work in diodes of different configurations and different time-dependent fields. Because single particle motion has many of the qualitative features of collective motion, we expect that single particle collisions of electrons with the anode are indicative of a failure of magnetic insulation. Moreover, if a sheath of electrons develops at the cathode surface, electrons that cross the gap are likely to come from the outer surface of the sheath, where single-particle solutions should be valid.

In the next section, we derive time-dependent electric and magnetic fields in vacuum diode gaps of three different geometries: disc-feed, biconical, and bispherical. After a discussion of relativistic drifts and adiabatic constants in the following section, analytic solutions of single-particle electron motion in the time-dependent fields of the diode geometries are presented.

Time-Dependent Diode Fields

Because we wish to examine only single-particle motion, we ignore self-fields of particles in the diode gap, and seek vacuum solutions of Maxwell's equations, neglecting displacement currents. We choose the time-dependence of the fields to model the triangular voltage waveforms and parabolic current waveforms of large electron generators. The three diode geometries of interest -- disc-feed, biconical, and bispherical -- have certain features in common. Each is azimuthally symmetric about an axis on which the load is located. Each carries current I towards the load on the anode and away from the load on the cathode. In each diode gap the magnetic field is purely azimuthal and the electric field has no azimuthal component. Each diode gap is much smaller than the overall diode dimensions. The three diode geometries are schematically illustrated in Figure 1.

Disc-Feed

The vacuum fields in this geometry that satisfy the boundary conditions of vanishing tangential electric field and vanishing normal magnetic field on the surface, including the surface of the cylindrical load at $r = a$, are in cylindrical coordinates:

$$\vec{E} = -\frac{2\vec{I}\hat{z}}{c^2} \ln\left(\frac{r}{a}\right) \begin{cases} t \\ 2t_1 - t \end{cases} \begin{matrix} (0 \leq t \leq t_1) \\ (t_1 \leq t) \end{matrix} \quad (1a)$$

$$\vec{B} = -\frac{\vec{I}\hat{\phi}}{cr} \begin{cases} t^2 \\ 4t_1t - t^2 - 2t_1^2 \end{cases} \begin{matrix} (0 \leq t \leq t_1) \\ (t_1 \leq t) \end{matrix} \quad (1b)$$

In these and following equations, \vec{I} is a constant.

Biconical

The vacuum fields satisfying the boundary conditions in this geometry ($\pi - \alpha - \beta < \theta < \pi - \beta$) in spherical coordinates are:

$$\vec{E} = -\frac{2\vec{I}\hat{\theta}}{c^2 \sin\theta} \begin{cases} t \\ 2t_1 - t \end{cases} \begin{matrix} (0 \leq t \leq t_1) \\ (t_1 \leq t) \end{matrix} \quad (2a)$$

$$\vec{B} = -\frac{\vec{I}\hat{\phi}}{cr \sin\theta} \begin{cases} t^2 \\ 4t_1t - t^2 - 2t_1^2 \end{cases} \begin{matrix} (0 \leq t \leq t_1) \\ (t_1 \leq t) \end{matrix} \quad (2b)$$

*Supported by Defense Nuclear Agency.

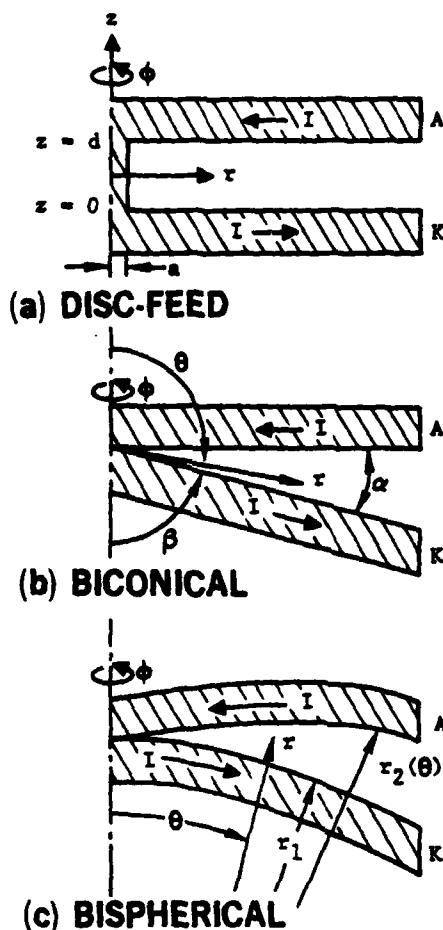


Figure 1. Schematic of diode geometries.

Bispherical

In this geometry the spherical cathode surface is at radius r_1 and the curved anode surface at r_2 is given by

$$\frac{r_2 - r_1}{r_2} + \ln \left[\frac{k_1 r_2}{r_2 - r_1} \left(\tan \frac{\theta}{2} \right)^{1/k} \right] = 0$$

or

$$r_2 = r_1 \left[1 + k_1 \left(\tan \frac{\theta}{2} \right)^{1/k} \right]$$

in which k and k_1 are constants. This surface was chosen to allow the radial electric field to be independent of θ , yet satisfy boundary conditions. In the diode of the DNA BLACKJACK 5 electron generator at Maxwell Laboratories, the constants have the values $k = 4.374$ and $k_1 = 0.0181$. The vacuum fields in spherical coordinates are:

$$\vec{E} = -\frac{2\vec{I}}{c^2} \left[\frac{r_1^2}{r^2} \hat{r} + \frac{1}{\sin \theta} \left(1 - \frac{r_1}{r} \right) \hat{\theta} \right] \times \begin{cases} t & (0 \leq t \leq t_1) \\ (2t_1 - t) & (t_1 \leq t) \end{cases} \quad (3a)$$

$$\vec{B} = \frac{\vec{I} \hat{\phi}}{cr \sin \theta} \begin{cases} t & (0 \leq t \leq t_1) \\ (4t_1 t - t^2 - 2t_1^2) & (t_1 \leq t) \end{cases} \quad (3b)$$

Equations of Motion, Relativistic Drifts and Invariants

The equations of motion of an electron in spherical coordinates are

$$\begin{aligned} \dot{v}_r &= \frac{v_\theta^2}{r} - \frac{e}{m\gamma} \left[E_r + \frac{v_\theta}{c} B_\phi - \frac{v_r}{c^2} \right. \\ &\quad \left. \times (v_r E_r + v_\theta E_\theta) \right] \\ \dot{v}_\theta &= \frac{-v_r v_\theta}{r} - \frac{e}{m\gamma} \left[E_\theta - \frac{v_r}{c} B_\phi - \frac{v_\theta}{c^2} \right. \\ &\quad \left. \times (v_r E_r + v_\theta E_\theta) \right] \end{aligned} \quad (4)$$

where

$$\gamma \equiv \left[1 - (v_r^2 + v_\theta^2)/c^2 \right]^{-1/2}$$

From Eqs. (4) we also find

$$\dot{\gamma} = \frac{-e}{mc^2} (\vec{v} \cdot \vec{E})$$

Because ϕ is an ignorable coordinate, azimuthal motion may be neglected.

When $|\vec{B}| > |\vec{E}|$ in the diode gap, electrons execute Larmor orbits in the plane of the cross section of the gap while drifting towards the load and towards the anode surface. For all three diode geometries, the electron drift is the sum of a rapid $\vec{E} \times \vec{B}$ drift along equipotential surfaces towards the load and a slower grad B drift in the \hat{z} direction toward the anode surface. If the equations of motion (4) are integrated directly, the time step must be much less than a Larmor period. Because each electron trajectory contains very many Larmor orbits, this method of solution is time-consuming. Analyzing electron drifts instead is much quicker and provides a better understanding of the electron motion.

To understand the electron motion analytically, we must derive expressions describing relativistic adiabatic invariants and drifts. We need expressions for the relativistic $\vec{E} \times \vec{B}$ drift, for the relativistic grad B drift, and for the adiabatic change of relativistic perpendicular energy with changing magnetic field.

If \vec{B} is perpendicular to \vec{E} and $|\vec{B}| > |\vec{E}|$, then \vec{E} may be transformed away by a Lorentz transformation to a reference frame moving with velocity.

$$\vec{v}_E = \frac{\vec{E} \times \vec{B}}{B^2} c.$$

In the transformed frame

$$\vec{E}' = 0$$

$$\vec{B}' = \vec{B} (1 - E^2/B^2)^{1/2}$$

In the local transformed frame in the diode gap, an electron experiences a time- and space-dependent magnetic field but no electric field. After we consider the effect of the spatial dependence of \vec{B} on the electron motion, we will consider the effect of the time dependence.

Suppose that the scale length of \vec{B} , which is $B/|\nabla B|$, is much greater than the relativistic Larmor radius

$$a_c = \gamma \frac{mcv}{eB}. \quad (5)$$

Then the grad B drift velocity is

$$\vec{v}_D = \frac{\omega_c a_c^2}{2B^2} \vec{B} \times \nabla B \quad (6)$$

in which the relativistic cyclotron frequency is

$$\omega_c = -eB/mc\gamma. \quad (7)$$

If the local magnetic field is changing in time, then so is ω_c and a_c . The time dependence of these quantities is calculated next, supposing that $\omega_c \gg (\partial B/\partial t)/B$.

The change in the energy of an electron over one orbit is

$$\begin{aligned} \Delta(\gamma mc^2) &= -e \oint \vec{E} \cdot d\vec{l} = \frac{-e}{c} \frac{\partial}{\partial t} \int_S \vec{B} \cdot d\vec{a} \quad (8) \\ &\approx \frac{-e}{c} \pi a_c^2 \frac{\partial B}{\partial t} \end{aligned}$$

The change in the magnetic field over one orbit is

$$\Delta B = \frac{2\pi}{\omega_c} \frac{\partial B}{\partial t} \quad (9)$$

Combining Eqs. (5) and (7) - (9), we find

$$\Delta \left(\frac{\gamma^2 v^2}{B} \right) = 0 \quad (10)$$

Thus the quantity $\gamma^2 v^2/B$ is a relativistic adiabatic invariant similar to the nonrelativistic invariant $\mu = w_\perp/B$. Eq. (10) may also be written as

$$\Delta (\pi a_c^2 B) = 0$$

which is the same whether the motion is relativistic or nonrelativistic. It implies that the number of flux lines passing through a Larmor orbit remains constant.

Analytic Solution

Because the Larmor period is very much less than the transit time of an electron in the diode gap, and because the integration time step in a numerical solution must be very much less than a Larmor period, the numerical solution can require integration over $10^4 - 10^5$ time steps. In this section we present an analytic solution, accurate to within a couple of percent, that determines the relativistic electron trajectory by integration over only about 10^2 time steps.

The analytic solution proceeds as follows. The electron motion is initiated after $|\vec{B}|$ has grown larger than $|\vec{E}|$ and after the Larmor orbit has become much smaller than gradient scale lengths in \vec{B} . The \vec{E} field is transformed away locally by a Lorentz transformation to the $\vec{E} \times \vec{B}$ drift frame moving in a direction along equipotential surfaces towards the load. Because the $\vec{E} \times \vec{B}$ drift velocity is relativistic, all initial thermal velocities that electrons may have are overwhelmed and may be neglected. The $\vec{E} \times \vec{B}$ drift velocity is also much greater than the grad B drift velocity, so that the perpendicular energy "imparted" to the electron at its initiation at a particular point and time by transformation to the $\vec{E} \times \vec{B}$ drift frame fixes the value of the adiabatic invariant $\gamma^2 v^2/B$ over the entire trajectory of the electron. Primes denote quantities evaluated in the $\vec{E} \times \vec{B}$ drift frame.

We illustrate this method of solution by applying it to the case of linearly increasing B in a bispherical diode. In general, diode gaps are thin compared to the dimensions of the diode, so that the $\vec{E} \times \vec{B}$ drift velocity is approximately constant over the width of gap. In a bispherical diode, therefore, $\theta(t)$ can be written in closed form to good approximation by integrating the zeroth order $\vec{E} \times \vec{B}$ drift velocity

$$\begin{aligned} \vec{v}_E &= \frac{-kr_1^2 \sin \theta}{rt} \hat{\theta} - \frac{(r - r_1)}{t} \hat{r} \\ &\approx \frac{-kr_1 \sin \theta}{t} \hat{\theta} \end{aligned}$$

to obtain

$$\theta = 2 \tan^{-1} \left[\left(\frac{t_0}{t} \right)^k \tan \frac{\theta_0}{2} \right] \quad (11)$$

A subscript zero denotes quantities evaluated at time t_0 , the start of the electron motion.

The initial perpendicular velocity in the transformed frame is approximately

$$v'_0 = \frac{kr_1 \sin \theta_0}{t_0}$$

Then the radial motion is found by integrating the radial components of the $\vec{E} \times \vec{B}$ and grad B drift velocities. The grad B drift velocity in the transformed frame is

$$\vec{v}'_D = \frac{b}{\gamma} (\text{ctn} \theta \hat{r} - \hat{\theta})$$

in which $b \equiv mc\gamma^{-2}v'^{-2}/2e\hbar B'$ is invariant according to Eq. (10). The radial position of the electron is therefore

$$r(t) = r_0 + \int_0^t dt \left(\frac{b}{\gamma} \text{ctn} \theta - \frac{r - r_1}{t} \right) \quad (12)$$

The adiabatic invariant determines γ' in terms of $B'(\theta, t)$, which may be simplified to

$$\gamma' = \left\{ 1 + \left(\frac{\gamma'_0 v'_0}{c} \right)^2 \left[\left(\frac{ct}{kr_1 \sin \theta} \right)^2 - 1 \right] \right\}^{\frac{1}{2}} \quad (13)$$

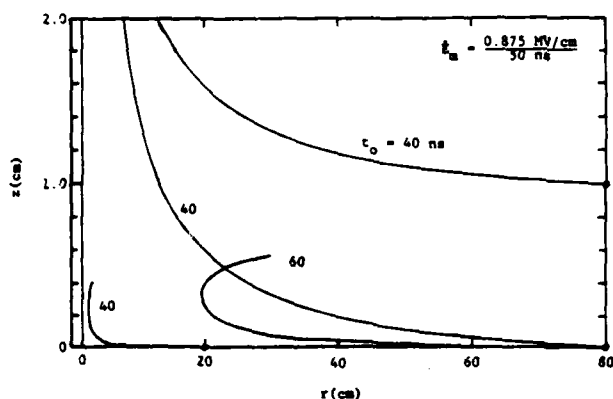


Figure 2. Electron trajectories in disc-feed diode (not drawn to scale). Electrons launched at indicated times t_0 move upwards towards anode in fields given by Eq. (1). Trajectories terminate at anode or at $t = 125$ ns.

for use in Eq. (12). Equations (11) - (13) determine the trajectory of the electron for all time t with any initial conditions t_0, r_0, θ_0 .

Examples of electron trajectories in disc-feed and bispherical diodes for the time-dependent fields of Eqs. (1) and (3) are shown in Figs. 2 and 3 respectively.

In these figures we have supposed a maximum electric field at the diode gap openings of 0.875 MV/cm, which produces maximum potentials of 1.75 MV. The field rises linearly to its maximum value from zero at $t = t_1 = 50$ ns, and decays linearly to opposite polarity until $t = 125$ ns, passing through zero at $t = 100$ ns. We have chosen $I = 2$ kA/ns² so that the peak current through the load is 5 MA at $t = 100$ ns. At $t = 125$ ns, flashover of the diode typically occurs in experiments, so we terminate the calculation there. Only those electrons emitted from the cathode surface before about $t = 60$ ns strike the anode before the end of the pulse. Some electrons that exist or are produced in the gap after 60 ns may strike the anode before the end of the pulse.

The electron positions calculated analytically as a function of time agree with the numerical results to within a couple of percent. The integration can be performed backward as well by selecting a final electron position and time and an initial time. The value of t_0 fixes the adiabatic invariant for the integration. Then one may answer such questions as where an electron came from

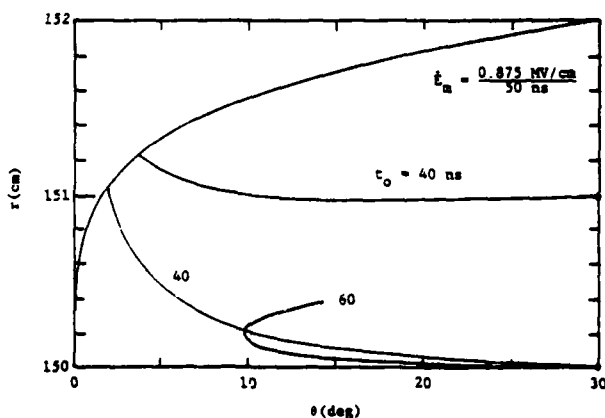


Figure 3. Electron trajectories in bispherical diode (not drawn to scale). Fields given by Eq. (3).

that struck the anode at a particular position at time t . Or one may determine a volume having the property that every electron within the volume during a given time period will strike the anode at a distance greater than a given distance from the axis.

Conclusions

We have presented a method for analytically calculating trajectories of single, relativistic electrons in the time-dependent electromagnetic fields of diodes of non-planar geometry. The method was used to calculate electron trajectories in fields resembling those in the diode of the DNA BLACKJACK 5 electron generator. The calculations show that although the grad B drift causes electrons in the diode gaps to drift

towards the anode surfaces, only those electrons emitted from the cathode surface at early times (before about the peak of the voltage waveform), or produced near the anode at later times, strike the anode surface before flashover of the diode ends the pulse. Because the analytic method allows rapid calculation of electron trajectories, we can determine the volume within the diode gaps from which the electrons producing given leakage currents must be coming. Assuming that single particle motion adequately describes the electron dynamics, we can then compare observed leakage currents with the predictions of the model. Until these further calculations are performed, we can only conclude that grad B drift may be responsible for the loss of some magnetic insulation in the time-dependent fields of diodes.

TERAWATT POWER DIVISION AND COMBINATION USING SELF-MAGNETICALLY INSULATED TRANSMISSION LINES*

J. T. Crow and G. D. Peterson

Sandia National Laboratories, Albuquerque, New Mexico 87185

Abstract

Self-magnetically insulated transmission lines are necessary for the efficient transport of the terawatt pulses used in electron and ion accelerators. For some applications it is desirable to divide one transmission line into two, or to combine outputs of two or more lines into one, by means of self-magnetically insulated convolutes.

Tests have been made on a coaxial-to-triaxial convolute in which connections between negative inner and outer lines are made by pins passing through holes in the intermediate positive conductor. Measurements in the 2 MV, 400 kA, 40 ns pulse Mite facility indicate virtually 100 percent current transport through the convolute and the ability to vary the division of current between the inner and outer lines of the triax by choice of inner line impedance. These measurements, and results obtained with this convolute connected to the ion diode for which it was designed, will be presented.

Introduction

Transmission lines which use self-magnetic insulation can transport high voltage, high energy, short duration pulses over distances of several meters with energy propagation efficiencies greater than 90 percent.¹ In these lines, electrons field-emitted from the negative side of the line are prevented from reaching the positive side by the magnetic field of the current flow in the line. These electrons have a net velocity parallel to the energy flow along the transmission line, and carry a significant part of the line current. Stability and containment of this electron flow is one of the major considerations in designing a low loss magnetically insulated line.

Sandia National Laboratories Particle Beam Accelerator PBFA I² has 36 radially-converging, magnetically-insulated, triplate lines. Each of these lines incorporates a tapered section at the output which changes the configuration from triplate to coaxial. One ion diode³ proposed for PBFA I requires a triaxial feed, so that the power appearing at the coaxial outputs of the lines must be divided into triaxial outputs. Tests of a coaxial-to-triaxial convolute with an electron beam diode, and preliminary tests with the ion diode have been very encouraging.

Coaxial to Triaxial Convolute

Physical Description

The configuration tested is shown in cross section in Fig. 1. The coaxial feed with a positive centerline is on the left. The negative outer housing is connected to the center rod by four pins (two shown) passing through circular holes in the positive line. A planar anode-cathode, electron beam load used for testing is shown on the right. The load impedance is varied by adjusting the A-K gap.

*This work was supported by the U.S. Dept. of Energy, under Contract DE-AC04-76-DP00789.

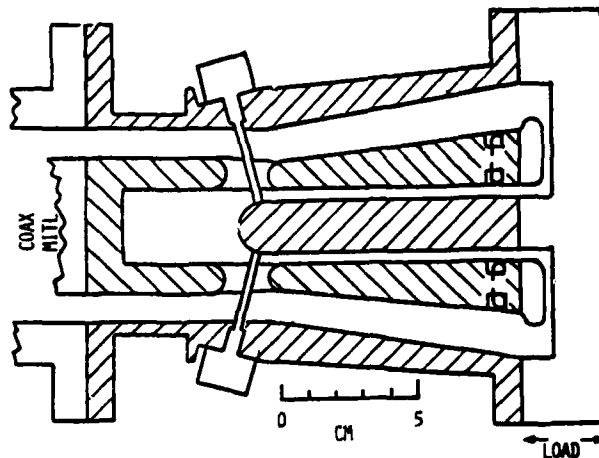


Fig. 1. Coax-to-triax convolute.

The impedance of the coaxial line is 20 Ω . The dimensions of the triaxial section were chosen so that each leg has a constant 25 Ω impedance. In later tests, the diameter of the center rod was reduced from 1.84 cm to 1.32 cm, raising the inner line impedance to 45 Ω in order to test the effect on current division.

Current measurements in the triax section were made with B-dot loops shown schematically in Fig. 1. Other current monitors were located along the transmission line so that current transport efficiency could be determined.

Losses in this design could arise from two sources. One was the abruptness of the transition which might cause instabilities in the electron flow.¹ The other was that consideration of the magnetic fields produced by the current flows in the triax sections and down the connecting pins show that there is a line of zero B field 5 mm to 8 mm toward the load from each pin in the outer half of the triax line. Zero magnetic field implies a loss of magnetic insulation in these regions. In addition, the field gradients on either side of these regions are such that electrons would drift from the negative toward the positive electrode. The losses due to these effects were found to be negligible.

Testing of the coax-to-triax convolute has been done on the Sandia Laboratories Mite facility,¹ and preliminary testing with the ion diode has been done on Hydramite.⁴ Each of these accelerators provides 40 ns pulses of 2 MV and 400 kA into a magnetically insulated transmission line that is essentially identical to those of PBFA I.

Test Results

Figure 2 shows the current transport efficiency obtained in shots on Mite with various A-K load gaps. The measurement accuracy is approximately ± 10 percent. Figure 3 shows the percentage of the total current carried by the outer line of the triax. The current transport efficiency is the total current measured by the B-dot monitors near the load divided by the current measured at the Mite line output.

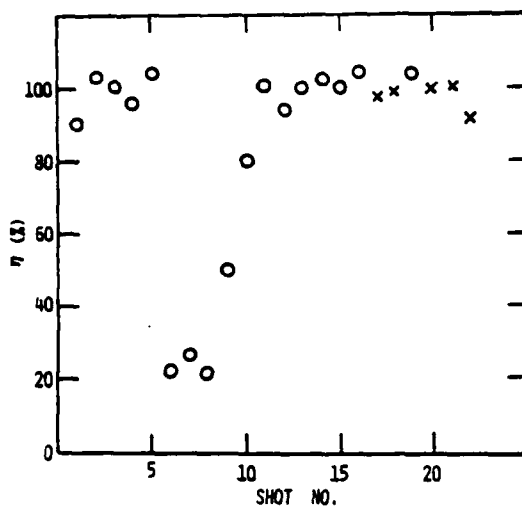


Fig. 2. Current transport efficiency.

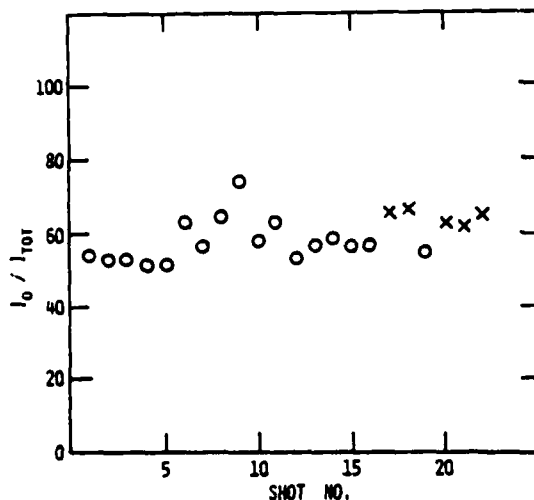


Fig. 3. Ratio of current in outer half of triax line to total current.

The low efficiency of shots 6, 7 and 8 were caused by a combination of poor current contacts and misalignment. These problems were corrected over the next few shots with a return to near 100 percent current transport. The losses in the low efficiency shots were located primarily near the junctions of the center rod and the connecting pins, as evidenced by damage to the positive line in this region.

The current division was approximately 55/45 outer to inner (except for the low efficiency shots) with the 1.84 cm center rod. Using the 1.32 cm center rod (crosses in Figs. 2 and 3) produced current divisions centering on 63/35, still with approximately 100 percent current transport.

The impedances of the loads tested on Mite were calculated by using the transmission line current with a short circuit load (I_{SC}), the current input to the convolute (I_N), and the load current (I_L) in

$$Z_L = Z_0 (I_{SC} - I_N) / I_L$$

where $Z_0 = 7.5 \Omega$ is the geometric impedance of the Mite triplate line. The load impedances ranged from a fraction of an ohm to 2.9Ω . Since the matched output impedance of the magnetically insulated line was $0.63 Z_0$ or 4.8Ω , the Mite line was undermatched in these tests.

Using calculated load impedances and measured I_L , the values of $I_L^2 Z_L$ were calculated for shots with $Z_L > 0.3 \Omega$ and are plotted in Fig. 4.

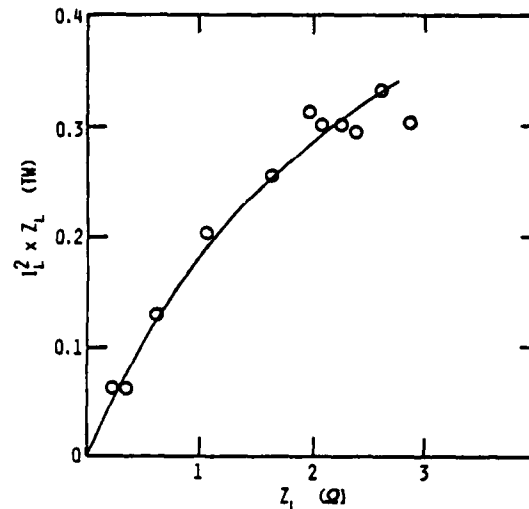


Fig. 4. Power to load vs. load impedance.

Testing on Hydramite

A particularly severe test of a self-magnetically insulated transition is operation into a high impedance load, since high impedance implies little current flow, low magnetic field, and poor magnetic insulation. The ion diode for which this convolute was designed has an externally applied magnetic field which retards electron transport across the diode A-K gaps, especially during the early part of the pulse.

If a loss region is established in the magnetically insulated line during the early, high impedance phase of a pulse, the loss region can become a low impedance load in parallel with the ion diode. Although the zero-B regions near the connecting pins did not produce loss with low impedance loads, they might cause losses with the ion diode because of the initial high impedance phase on the latter experiment.

While the results are preliminary, since testing is not complete, to date there has been negligible loss in the coax-triax convolute in operation with the ion diode.

Combination of Power Flows

Separation of a coaxial magnetically insulated line into a triaxial pair using a pin-hole convolute has been successful, and it is reasonable to expect that power combination using the same technique would also work well. A design is being developed for testing in the near future on the Proto II facility at

Sandia Laboratories in which a triple disk feed is convoluted into a double disk line using pins passing through holes in the positive center plate.⁵ The magnetic zeroes and adverse gradients will be similar in location and magnitude to the tested coax-triax convolute and should have negligible loss in the proposed configuration.

Conclusions

A coaxial-to-triaxial pin-hole magnetically insulated convolute has been tested and found capable of operating with negligible loss with electron beam diode loads of zero to 3 Ω .

The convolute has been tested with an ion diode load, and preliminary data indicate negligible loss. The pin-hole convolute concept appears applicable to power combination as well as division.

Experiments with magnetically insulated transmission lines have been essentially one dimensional configurations. The tests of the coax-triax convolute, which have been successful in spite of potential loss mechanisms inherent in the three-dimensional transition, indicate that considerable latitude may exist in designing magnetically insulated devices.

References

1. J. P. VanDevender, J. Appl. Phys., 50, 3928 (1979).
2. T. H. Martin, G. W. Barr, J. P. VanDevender, R. A. White and D. L. Johnson, 14th Pulse Power Modulator Symposium, Orlando, FL, June 3-5, 1980.
3. D. J. Johnson, Sandia National Laboratories, Albuquerque, NM, private communication.
4. J. S. Seamen and J. T. Crow, Particle Beam Fusion Progress Report, December-June 1979, Sandia National Laboratories, Albuquerque, NM.
5. D. H. McDaniel, Sandia National Laboratories, Albuquerque, NM, and I. D. Smith, ISI, Alameda, CA, private communication.

SIMULATION OF POWER FLOW IN MAGNETICALLY INSULATED CONVOLUTES FOR PULSED MODULAR ACCELERATORS*

D. B. Seidel, B. C. Goplen,[†] and J. P. VanDevender
Sandia National Laboratories
Albuquerque, New Mexico 87185

Summary

Recent advances in the technology of magnetic insulation have led to the design of a new class of high power modular accelerators such as PBFA I which is nearing completion at Sandia National Laboratory. In this accelerator, power is fed inward along 36 radially converging, magnetically insulated transmission line (MITL) modules. In many applications, these 36 modules must be recombined into a central magnetically insulated convolute. This recombination can have a significant effect upon magnetic insulation, primarily due to the inevitable lack of simultaneity between power pulses in the 36 MITL modules.

In this paper, two distinct simulation approaches for magnetic insulation are developed which can be used to address the question of nonsimultaneity. First, a two-dimensional model for a two-module system is simulated using a fully electromagnetic, two-dimensional, time-dependent particle code. Next, a nonlinear equivalent circuit approach is used to compare with the direct simulation for the two module case. The latter approach is then extended to a more interesting three-dimensional geometry with several MITL modules.

The equivalent circuit approach relies upon several assumptions, and the validity of these assumptions is difficult to gauge. However, it is easily extended to many three-dimensional geometries of interest for which the particle code is impractical. Thus, the comparison of the two techniques on the two-dimensional model is very useful as a measure of the validity of the more flexible equivalent circuit approach. In fact, it is found that the simulations are in very good agreement, and consequently our confidence in equivalent circuit approaches is significantly increased.

The simulations performed to date show that nonsimultaneity in pulse arrival time does somewhat degrade accelerator performance. However, in no case has this effect been shown to be catastrophic.

Introduction

Several models have been developed for the treatment of self-magnetically insulated transmission lines. Analytic, one-dimensional models have been obtained which model steady-state insulated flow¹⁻⁴ and the transition region between space-charge limited leakage from cathode to anode and insulated flow.⁵

When the pulse length is short relative to the transmission line's length, it becomes important to consider a time dependent analysis. Toward this end, an equivalent circuit approach has been developed⁶ for a long coaxial line with azimuthal symmetry. The technique uses nonlinear conductance to model leakage between cathode and anode. For the same uniform, coaxial geometry, a self-consistent solution has been obtained using a two-dimensional time-dependent particle code. More recently, the equivalent circuit approach has been extended to treat three-dimensional transmission line structures⁷ (that is, the line is no longer

coaxial or one-dimensional planar and can be driven in a nonuniform or nonsimultaneous manner). Although the equivalent circuit approach is not strictly valid at relativistic voltages,⁸ it has been shown to compare very well to the self-consistent solution for the case of a uniform coaxial line.^{6,7} A similar comparison will be made in this paper for a much more general nonuniform transmission line structure.

Simulation Models

Particle-in-Cell Code

A particle-in-cell (PIC) computer code can be applied to treat the electron flow in a MITL. Here, we have used an extensively modified version⁹ of the MAD2¹⁰ computer code. This code contains a fully dynamic solution of Maxwell's equations in two dimensions and relativistic three-dimensional particle kinematics with the full Lorentz force.

To solve Maxwell's equations, the volume of interest is divided into discrete cells, and two electric and one magnetic field components are associated with each cell. Discrete particles are used to simulate the electron flow and provide a self-consistent source for the field solution. The relativistic equations of motion are solved for each particle in the electromagnetic field. In turn, the particle motion provides a current density source for the solution of the electromagnetic field. Numerically, the formalism is time-reversible and for uniform spatial gridding, it is accurate to second order in time and spatial step size. Particles are introduced to the system by emission from the cathode surface. The charge of each particle is determined by assuming space-charge-limited emission and enforcing Gauss' Law for cells immediately adjacent to the cathode. Similarly, particles encountering metal boundaries are removed from the system.

Equivalent Circuit Model

An equivalent circuit (EC) model^{6,8} has also been applied to the MITL problem. Although this technique certainly requires more assumptions and approximations than the self-consistent PIC code, its merit lies in its relatively low computational cost and its extensibility to more complex structures (e.g., three-dimensional structures).

Simply stated, this approach considers only TEM (principle-mode) propagation and consequently the field distribution between the cathode and anode is determined by the corresponding electrostatic and magnetostatic fields. It is further assumed that the A-K (anode-cathode) gap is slowly-varying along the transmission line (i.e., slowly varying relative to the gap length and the electron gyroradius; for magnetic insulation, these two lengths will be comparable). Consequently, the static fields can be assumed to be locally one-dimensional.

With these assumptions, Maxwell's equations are integrated across the A-K gap and then differenced in the remaining two dimensions. The equations for each cell of the resulting two-dimensional mesh can be

*This work is supported by the U. S. Department of Energy.

[†]Mission Research Corporation, 5503 Cherokee Ave., Alexandria, VA 22312.

identified as Kirchoff's voltage and current equations for the circuit shown in Fig. 1. V , I_x , and I_y are the line voltage and orthogonal components of the line current, respectively. Line inductances and capacitance L_x , L_y , and C are dependent only upon line geometry and are defined by the comparison of Kirchoff's equations and the integrated, differenced Maxwell's equations.

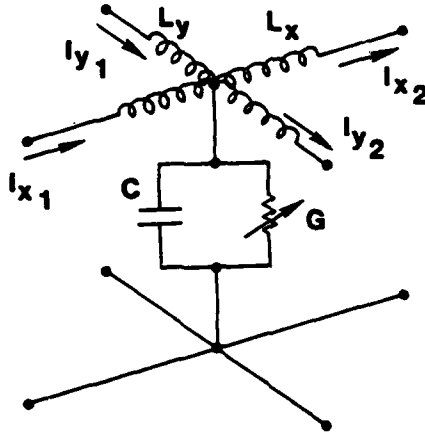


Fig. 1. Equivalent circuit representation of one transmission line cell.

The conductance G represents the electron leakage current between the plates of the MITL. This electron current (and hence G) will vary nonlinearly with both voltage and magnetic field (line current). Here, we take G to have the form

$$G = P_{cl} H_r(\gamma) f(I, I_c) v^{1/2}$$

where P_{cl} is the pervance for space-charge-limited¹¹ electron flow in the absence of a magnetic field, H_r is the relativistic correction factor,¹² $\gamma = 1 + eV/mc^2$ and f is a function which varies from 1 to 0 as the current is increased from 0 to some critical current I_c for which the line will completely self-insulate. Note that P_{cl} for each cell is dependent only upon the transmission line geometry in that cell. The shape of the weighting function f is taken from Ref. 5. The value of I_c is voltage dependent and is found using a saturated parapotential model below .823 MV and an unsaturated boundary current model above .823 MV which has been shown¹³ to be in excellent agreement with measured values of the critical current required for magnetic insulation.

Once the inductances, capacitance, and pervance for each cell are determined, the resulting circuit for the mesh of cells can be analysed using the circuit analysis code SCEPTRE.¹⁴

Simulation Results

Perhaps the simplest case of a multi-module transmission system is the two-module system consisting of a length of transmission line which is excited at each end and has a load somewhere in between. The specific example we consider here is the coaxial system shown in Fig. 2. The outer radius (r_o) varies along the line to follow the impedance variation of a single PBFA MITL. The central region (where $r_o = 8.4$ cm) is the location of an externally magnetically insulated ion diode. The structure is axially symmetric about the

center of the diode region. The structure is excited by two power pulses, one from each end. By delaying one pulse in time, nonsimultaneity effects can be simulated.

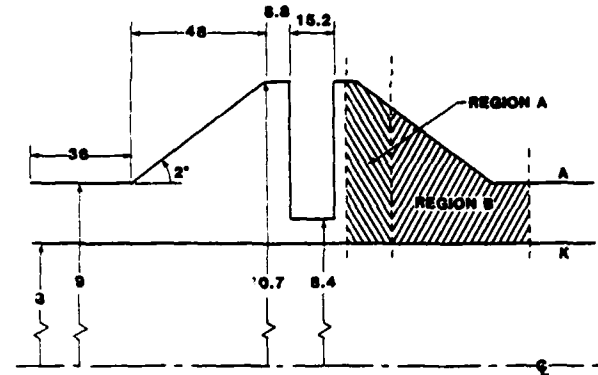


Fig. 2. Coaxial geometry for two-module convolute simulations. (Lengths are in centimeters.)

With the exception of the diode region, the particle field interactions in the PIC simulation are modeled self-consistently. In the diode region, it is assumed that a large externally applied magnetic field confines the electron sheath very near the cathode; consequently, the simulation simply suppresses electron emission over this portion of the cathode. It is further assumed that a space-charged-limited ion current flows from anode to cathode in the gap. This current density, computed at each time step of the simulation from the AK gap spacing and voltage, is then included as an impressed current source in the field solution algorithm. This method should be adequate since the ions are not relativistic and their trajectories will not be significantly deflected by the magnetic field.

In the results that follow, the lines will be driven by a trapezoidal voltage pulse with a peak voltage of 2.4 MV, rise and fall times of 1 ns and 10 ns, respectively, and a total pulse length of 40 ns. The input to the line at the right is delayed in time 3 ns.

Fig. 3 shows plots of particle motion over one time step ($\Delta t = 2.5$ ps) of the PIC simulation, at 4 ns and 7 ns into the simulation. In Fig. 3a, we see that the pulses are propagating down the lines with a lossy front. Behind this front, the line is seen to insulate, and an electron sheath is formed above the cathode. At 7 ns into the simulation (Fig. 3b) the two wave fronts meet to the right of the diode region, as evidenced by the substantial leakage current at that point. In addition, on the left-hand side, we see evidence of particles with nonzero canonical momentum (see Ref. 4). These particles undergo a change in canonical momentum as they enter the tapered transition (since $\partial/\partial x \neq 0$), and their inner radial turning points move off the cathode surface. This results in a sheath of trapped particles which do not encounter either electrode for several gyro-periods.

An example of the time history of the leakage current between electrodes is shown in Figs. 4a and 4b which show the current lost to the anode in regions A and B (see Fig. 2) respectively. For the PIC code, this current is computed by summing all the charge destroyed at the anode of each region over 1 ns time intervals, then dividing by 1 ns to obtain the average current. Also shown in Fig. 4 are comparable results

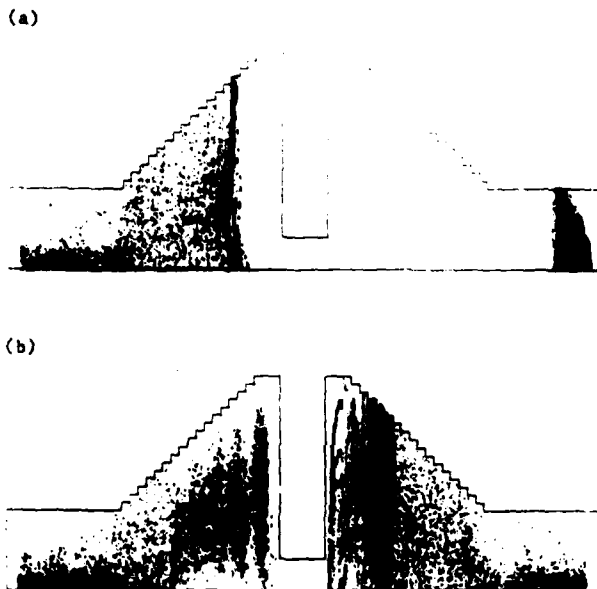


Fig 3. Particle motion over one time step (a) at $t = 4$ ns; (b) at $t = 7$ ns.

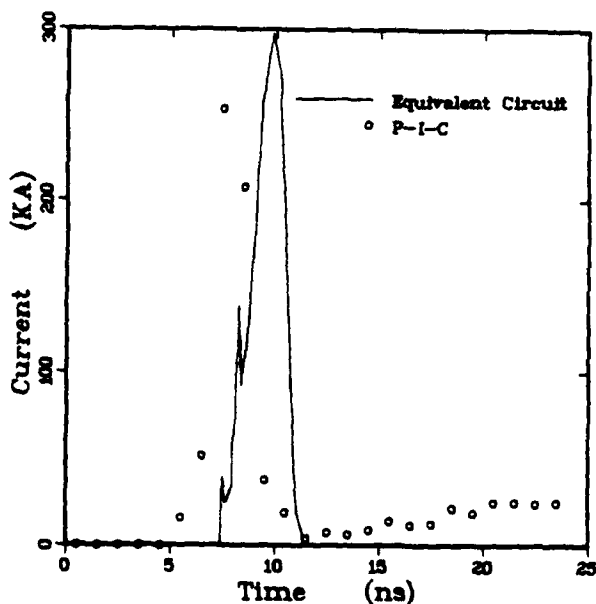


Fig. 4a Electron loss current from PIC and EC simulations over Region A.

from the EC solution for this geometry. In Fig. 4a, we see that region A is well insulated, except for the first few nanoseconds after the two voltage pulses meet. Note that the agreement between solutions is fairly good, with the exception that the velocity of the lossy wavefront is slightly slower for the EC solution. We believe that this minor difference is caused by a slight overestimate of the early time leakage current in the EC solution which impedes the propagation of the wavefront.

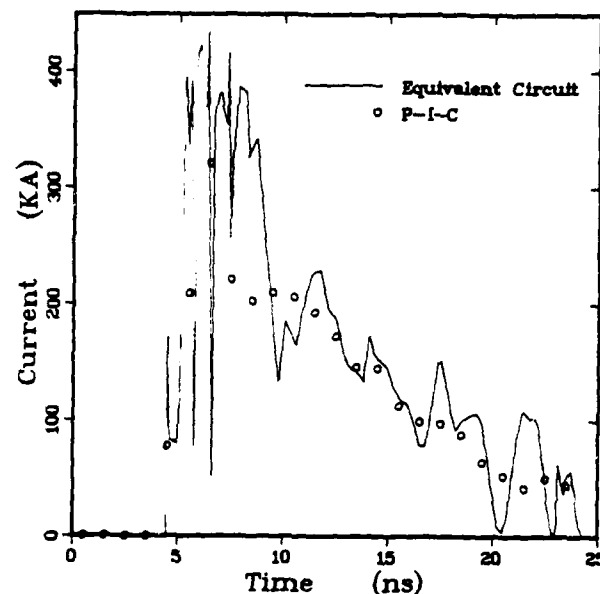


Fig. 4b. Electron loss current from PIC and EC simulations over Region B.

Fig. 4b shows a similar comparison for the leakage current over region B. Here, both simulations predict a leakage which persists for several nanoseconds above 100 kA. This leakage occurs primarily in the vicinity of the transition between the uniform and tapered portions of the line. The oscillatory nature of the EC simulation is due to the nature of the model. Each equivalent circuit cell has an associated resonance, or, thought of in a different way, these are high frequency effects associated with the finite mesh size.

Obviously, the quasi-TEM assumptions of the equivalent circuit approach are severely taxed by the annular shank of the diode between $r = 8.4$ cm and $r = 10.7$ cm. In the PIC simulation, substantial leakage current flows to this shank. The EC model has no mechanism to treat this electron current. Consequently, one can think of the total diode current for the PIC simulation as the sum of the ion current and this leakage to the shank. Fig. 5 shows a plot of the diode current. The PIC ion current is somewhat lower than the EC diode current, whereas the PIC total current is almost the same as the EC diode current (except, again, a slightly slower wavefront velocity is seen for the EC solution). This is not at all surprising, since the system should try to operate at some self-limiting current, and consequently the total load current in both simulations should be that self-limiting current.

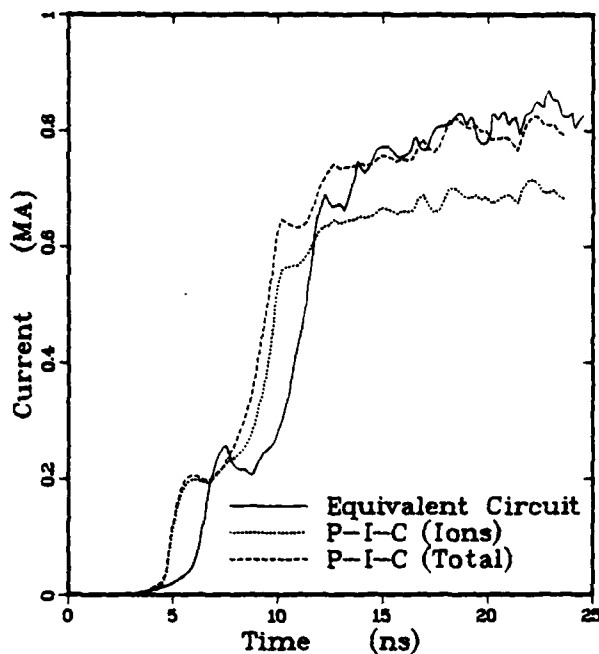


Fig. 5. Ion diode current from PIC and EC simulations.

In order to gauge the effects of the nonsimultaneity on the efficiency of energy transport on this "two-module convolute" structure, the simulations were also performed for other delay times (including zero) between the two input pulses. It was found that out of 53 KJ available to a matched load of 7.1 ohms, 39 and 37 KJ were delivered to the diode for 0 and 3 ns delay times, respectively. In this case, the problem of simultaneity would appear to be secondary to that of matching the machine to the convolute and diode.

Three-Dimensional EC Simulation Results

Encouraged by the overall agreement of the two-dimensional PIC and EC simulations, we have extended the EC simulations to more relevant three-dimensional problems. As an example, we show here the results of a 6-module convolute model for the PBFA I accelerator with an externally magnetically insulated radial ion diode. This structure is shown schematically in Fig. 6.

Six independent radially converging MITL are connected to a central disc triplate convolute structure at 50 cm radius. This convolute, which has a uniform electrode spacing of 3.5 mm, feeds the diode at 20 cm radius. For simulation purposes, the last 80 cm of each of the six MITL are modeled using 2 EC cells, and the convolute is divided into 18 EC cells (see Fig. 6). The ion diode is assumed to have space-charge-limited ion flow, i.e., $I = V^{3/2}$, and the proportionality constant is chosen such that the diode impedance is matched to the self-limited impedance at a diode voltage of 2 MV.

Fig. 7a plots energy lost to leakage in the MITLs and convolute, the energy delivered to the ion diode, and the energy available to a matched load when all six

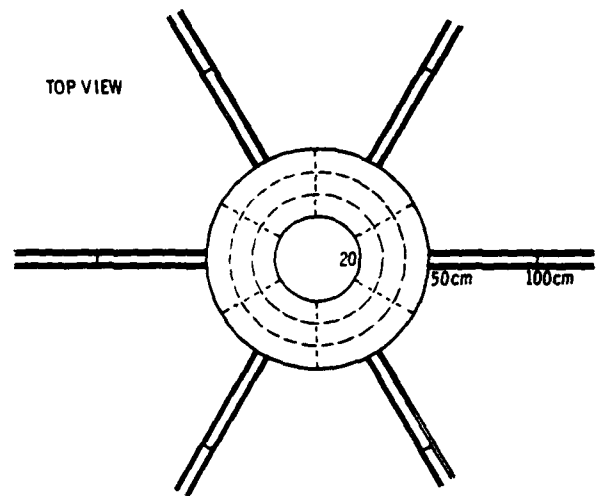


Fig. 6. Top view of 6-line PBFA I model.

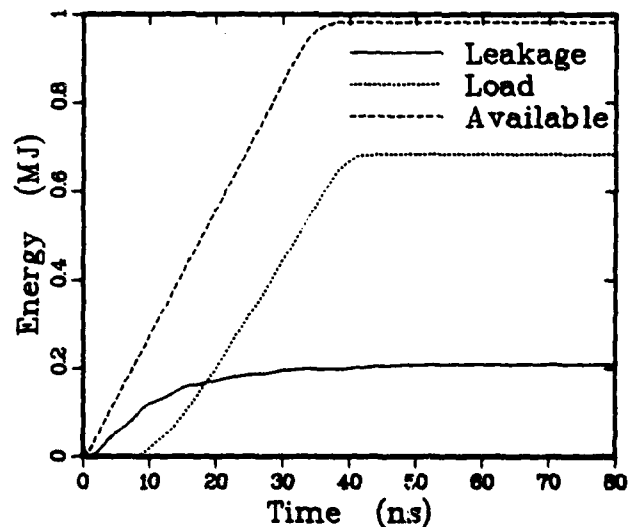


Fig. 7a. Distribution of available energy for simultaneously driven PBFA I model.

MITL's are simultaneously pulsed. Fig. 7b shows a similar comparison for a nonsimultaneous excitation for which the pulse delay times for the six lines are the expected values of a normal distribution with a standard deviation of 3 ns (first-to-last delay of 7.6 ns).¹⁵ These expected values were then randomly distributed among the six lines. We see that 71 and 54 percent of the available energy is delivered to the load for the simultaneous and nonsimultaneous simulations, respectively. Correspondingly, 21 and 32 percent of the available energy is lost to electron leakage in the MITLs and convolute. As can be seen from the diode current in Fig. 8, this loss of energy efficiency is due primarily to the early time loss of current.

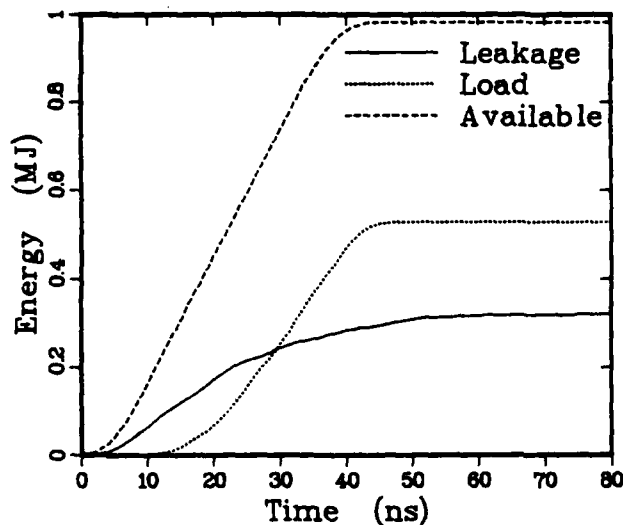


Fig. 7b. Distribution of available energy for non-simultaneously driven PBFA I model.

In addition to the examples presented here, the three-dimensional EC approach has also been used to model a plasma-filled ion diode (AMPFION)¹⁶ on the PBFA I accelerator and for z-pinch on the PROTO II accelerator. In fact, for each of these simulations, the effects of nonsimultaneity were even less significant than for the radial ion diode presented here, probably due to the low early-time impedance of the load for each of these other cases.

Conclusions

Two techniques have been developed which treat time-dependent magnetic insulation in complex structures. Results obtained using particle-in-cell (PIC) and equivalent circuit (EC) simulation techniques have been compared for a relatively complex two-dimensional transmission structure. Based upon the agreement between these two methods, the EC approach has been extended with a fair degree of confidence to three-dimensional structures.

Results using both simulation techniques in two and three dimensions indicate that while nonsimultaneity in modular accelerators does have a detrimental effect upon the efficiency of the accelerator, this effect is certainly not catastrophic in any of the examples that we have considered to date.

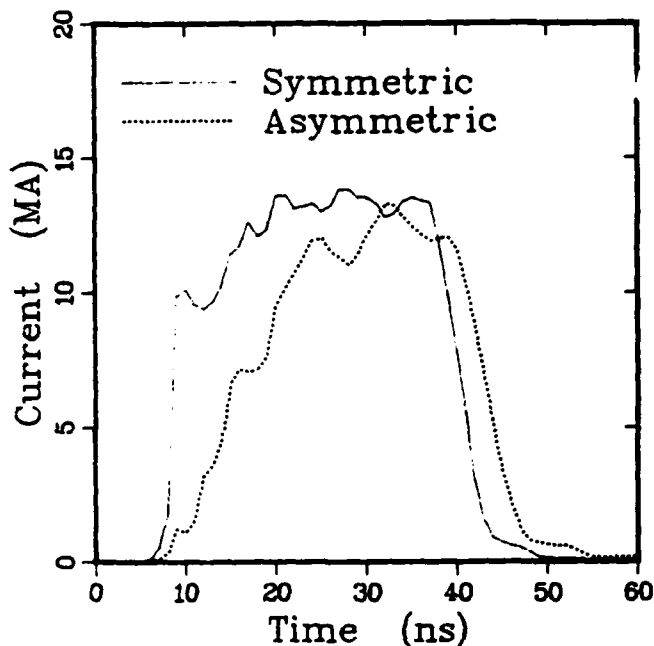


Fig. 8. Diode current for PBFA I model.

References

1. R. V. Lovelace and E. Ott, *Phys. Fluids* **17**, 1263 (1974).
2. A. Ron, A. A. Mondelli, and N. Rostoker, *IEEE Plasma Sci. PS-1*, 85 (1973).
3. J. Creedon, *J. Appl. Phys.* **46**, 2946 (1975).
4. C. W. Mandel, Jr., *J. Appl. Phys.* **50**, 3830 (1979).
5. K. D. Bergeron and J. W. Poukey, *Appl. Phys. Lett.* **27**, 58 (1975).
6. K. D. Bergeron, *J. Appl. Phys.* **48**, 3065 (1977).
7. J. W. Poukey and K. D. Bergeron, *Appl. Phys. Lett.* **32**, 8 (1978).
8. D. B. Seidel, J. P. VanDevender, D. H. McDaniel, and D. L. Johnson, 21st Annual Meeting of Division of Plasma Physics of the American Physical Society, Boston, MA, 1979 (unpublished).
9. B. Goplen, R. E. Clark, and S. J. Flint, Mission Research Corp. Report No. MRC/WDC-R-001, 1979.
10. B. Goplen, R. E. Clark, and B. Fishbine, Air Force Weapons Laboratory Report No. AFWL-TR-77-26, 1977.
11. C. D. Child, *Phys. Rev.* **32**, 492 (1911); I. Langmuir, *Phys. Rev.* **2**, 450 (1913).
12. J. E. Boers and D. Kalleher, *J. Appl. Phys.* **40**, 2409 (1969).
13. S. Shope, J. W. Poukey, K. D. Bergeron, D. H. McDaniel, A. J. Toepfer, and J. P. VanDevender, *J. Appl. Phys.* **49**, 3675 (1978).
14. J. C. Bowers and S. R. Sedore, *SCPTRE: A Computer Program for Circuit and System Analysis* (Prentice Hall, Englewood Cliffs, NJ, 1971).
15. D. L. Johnson, Sandia National Laboratory, private communication.
16. C. W. Mandel, Jr., 1980 IEEE International Conference on Plasma Science, Madison, Wisconsin, 1980 (unpublished).

MEASUREMENT OF FAST RISETIME MEGAMPERE CURRENTS BY QUARTZ GAUGE*
 R. R. Williams, D. H. McDaniel and R. W. Stinnett
 Sandia National Laboratories, Albuquerque, New Mexico 87185

Abstract

Quartz gauges have been used on the Sandia National Laboratories Proto II accelerator to measure current in the magnetically insulated transmission line at the 11 TW power level. The accelerator delivers 3.5 MA at 2×10^{14} A/s in a 40 ns pulse to a 0.0127 m diameter aluminum liner to produce a high density plasma. At this radius and dI/dt levels, the B-dot monitors no longer function for the measurement of load current because the monitor suffers electrical breakdown. Quartz pressure gauges mounted at a radius of 0.0086 m have successfully measured the magnetic pressure due to the load current with nanosecond temporal resolution.

The quartz gauge is mounted 5×10^{-4} m under the electrode surface and hence the current carrying surface is not perturbed by the gauge itself. The surface material is chosen so that its yield strength is greater than the pressure exerted by the magnetic field. Hence, the pressure pulse is not affected by the material properties of the wall as it propagates to the quartz gauge. For this case, only the piezoelectric and material properties of the quartz are needed to infer pressure from the gauge output. The current output in amperes from the quartz gauge is given in terms of the stress- σ in Pascals, transit time through the gauge- t_0 in seconds and the gauge area- A in m^2 by the equation¹

$$I = (2.011 \times 10^{-12} + 1.1 \times 10^{-22} \sigma) \sigma A / t_0.$$

Measurements can be extended to current and pressure levels where the yield strength of the wall material is exceeded, but the analysis of the gauge signal is more complicated. Gauge design requirements and experimental results will be discussed.

Introduction

The Proto II accelerator, at Sandia National Laboratories, delivers a power of 11 TW and a current rate of change of dI/dt of 4×10^{14} A/s. The power flows down a self-magnetically insulated transmission line to a 1.2×10^{-2} m diameter aluminum liner on the axis of the accelerator. This liner produces a high density plasma. The rate of change in the magnetic induction at the surface of the liner is $dB/dt = 6 \times 10^9$ T/s. At this level of dB/dt measurements of current in the magnetically insulated transmission line can not be made using conventional B-dot techniques. Figure 1 shows a conventional method of using a "grooved B-dot" for measuring current. A 50 Ω coaxial cable measures the voltage across the groove induced by the changing magnetic flux within the groove. We have found that at 2 MV/m the current no longer flows along the surface of the groove but bridges the gap and causes not only loss of the electrical signal in the 50 Ω cable but the breakdown of the magnetically insulated transmission line. The breakdown level was determined by varying the groove dimension and radial position and observing when the signal was lost. The electric field across the groove is given by

$$E = \frac{L_g}{\Delta r} \frac{dI}{dt} \quad (1)$$

*This work was supported by the U.S. Dept. of Energy, under Contract DE-AC04-76-DPO0789.

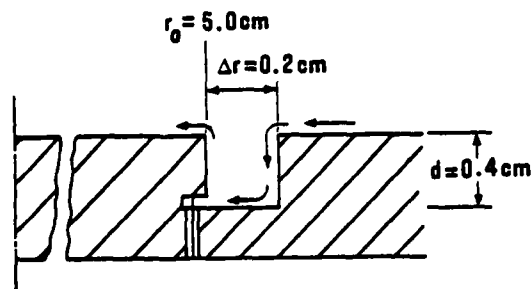


Fig. 1. A typical grooved B-dot current measuring configuration.

where Δr is the width and L_g is the inductance of the groove. The inductance of the groove is given by

$$L_g = 2 \times 10^{-7} d \ln(1 + \Delta r/r) \quad (2)$$

where d is the depth of the groove and r is its radial position. By expanding the log term to first order with $\Delta r \ll r$ we have

$$L_g = 2 \times 10^{-7} d \Delta r / r \quad (3)$$

Substituting this into (1), we find

$$E = \frac{2 \times 10^{-7}}{r} d \frac{dI}{dt} \quad (4)$$

Hence, with the criterion that $E \leq 2 \times 10^6$ V/m we have

$$\frac{d}{r} \leq \frac{10^{13}}{dI/dt} \quad (5)$$

To measure the current at $r = 10^{-2}$ m, which is close to the load of the magnetically insulated transmission line, the depth of the groove for a dI/dt of 2×10^{14} A/s would have to be less than 5×10^{-4} m. Hence, the difficulty of this type of current measurement is apparent. At slightly higher dI/dt 's these grooves cause breakdown within the magnetically insulated transmission lines. We have also determined experimentally that 3.2×10^{-3} m diameter holes in the transmission line containing individual B-dot loops lead to magnetic insulation breakdown.

Magnetic Pressure Measurement

A measurement technique is needed which monitors the current in the transmission line and which does not perturb the conductor's front surface. The current flowing in a radial transmission line has an associated mechanical pressure.

$$P = B^2 / 2\mu_0 = \mu_0 I^2 / 8\pi^2 r^2 \quad (6)$$

A quartz pressure gauge, if placed behind the electrode surface of the transmission line, can directly monitor this pressure. This configuration, shown in Fig. 2,

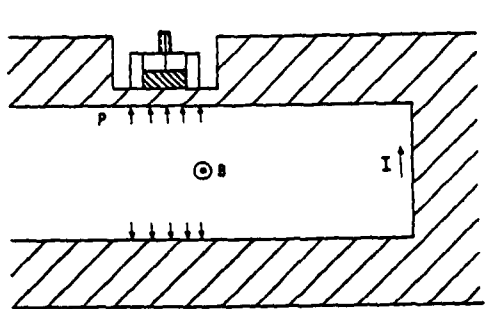


Fig. 2. The configuration for measuring the magnetic pressure due to the current flow.

allows the front surface of the transmission line conductor to be completely free of perturbations provided the gauge is a few times deeper than the electrical skin depth.

Shock pressure measurement in materials is an extensively documented technology.² A typical pressure measurement assembly, shown in Fig. 3, consists of a circular piezoelectric quartz disk bonded to a section of metal. The single crystal quartz is gold plated on opposing flat surfaces. The top surface has two separate electrodes. The inner electrode collects charge from an area designed to see a one dimensional stress wave and connects to a 50 ohm coax cable for instrumentation. The outer electrode forms a guard ring and is electrically loaded to pass the same current per-unit area as the center electrode (Fig. 3). This electrode is needed to minimize edge effects due to the finite gauge size.

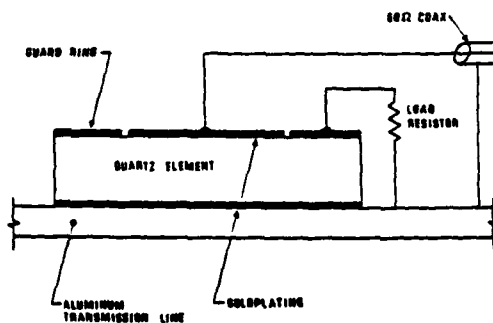


Fig. 3. The quartz gauge pressure measurement assembly.

When a plane pressure wave is applied to the front surface of the piezoelectric quartz element, a current I_g immediately flows in to the load resistors according to the equation⁴

$$I_g = (2.01 \times 10^{-12} + 1.1 \times 10^{-22} \sigma) \sigma A / \epsilon_0 \quad (7)$$

Where ϵ_0 is the transit time of the pressure wave through the gauge in seconds, A is the area in square meters, σ is the pressure in Pascals and I_g is the gauge current in amperes. The current continues to flow until the pressure wave reaches the back surface of the gauge. This equation is valid for pressures up to 3.0×10^7 Pascals. The pressure wave travels at a

velocity of 5.7×10^3 m/s. Hence the useful recording time of the gauge is the gauge thickness divided by this velocity. During this transit time of the pressure wave through the gauge the output current of the gauge follows the input pressure with a nanosecond response time. At the same time that the pressure wave propagates through the quartz, a relief wave propagates inward at a 45° angle from the edge of the gauge. The portion of the gauge affected by the relief wave is covered by the guard ring, and hence the relief wave is not seen by the instrumented electrode.

The sensitivity of the gauge can be controlled by changing of the material stack impedance in front of the gauge. The pressure P_Q in the quartz gauge behind the metal surface is related to the pressure P_M in the metal, and the shock impedances of the quartz and metal Z_Q and Z_M , respectively, by

$$P_Q = (2Z_Q P_M) / (Z_Q + Z_M) \quad (8)$$

By using metals with a higher yield strength than the applied pressure, this measurement technique can be extended to higher pressures without resorting to a more complicated analysis than that given by equation 1.

Gauge Mounting Considerations

Since the quartz gauge requires a uniform pressure pulse to be incident on its front surface, the mechanical tolerances of the surface finish and thickness are very important. At a material velocity of 6×10^3 m/s a difference of material thickness in front of the gauge of 2.54×10^{-5} m corresponds to a difference in arrival time of 4×10^{-9} seconds. When one is trying to resolve current risetimes on the nanosecond time scales, mechanical tolerances are obviously very important. Hence the quartz gauges are mounted on flat surfaces that are parallel to the current carrying surface. The geometry in which the gauge is used must allow spatially uniform (5 percent) pressure over the gauge front. Gauge bonding to the surface is usually done with pressure cured epoxy. Surface finishes are typically 2.5×10^{-8} meters. The mounting procedure should not perturb the flatness of the surface. Another concern of magnetically insulated transmission line gauges is that the anode material in front of the gauge has to be sufficiently thick to stop electrons crossing the vacuum gap. If these electrons penetrate into the gauge a signal resembling that of a Faraday cup will be obtained.

Experimental Results

Initial experiments used four 6.35×10^{-3} m diameter quartz gauges with two located at 0.0254 m radius and two located at 0.0508 m radius. These gauges are 5×10^{-4} m thick which allows a recording time of 100 ns. Figure 4 shows the gauge output signals as a function of time for a Proto II test. The signals rise to peak pressures of 1.5×10^8 Pascals for the gauges at 0.0254 m radius and a pressure of 5×10^7 Pascals for the gauges at 0.0508 m radius in 20 ns. The abrupt signal fall occurs at the end of the gauge recording time. The pressure between these two positions did not vary as r^{-2} and indicates that current losses occurred between these two positions. The losses were verified by Faraday cup measurements. A comparison between the current measured at 0.72 m using B-dot loops to the current measured at the 0.0508 m radius is shown in Fig. 5. The rise times agree with an indicated current loss at peak current between these two positions.

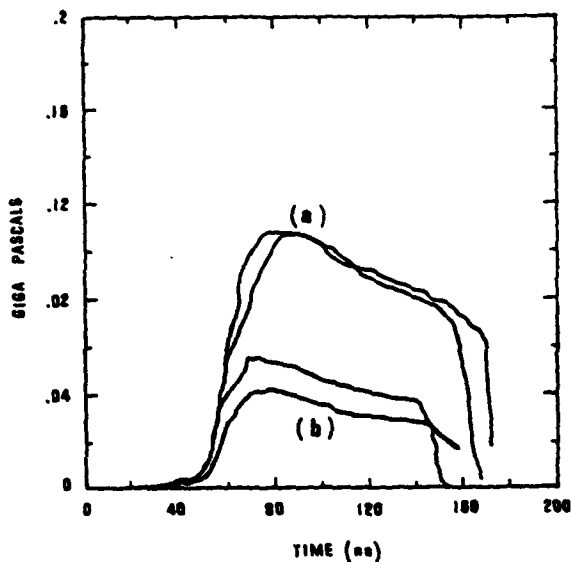


Fig. 4. Quartz gauge traces for a radius of (a) 2.54×10^{-2} m and (b) 5.08×10^{-2} m.

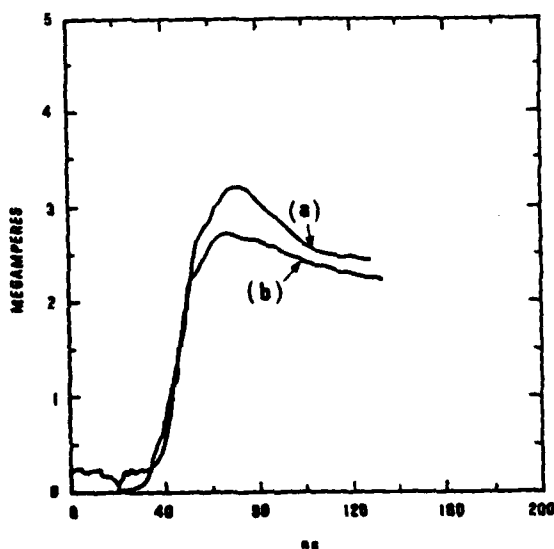


Fig. 5. A comparison between the quartz gauge signal and the B-dot signal.
a. B-dot located at $r = 0.72$ m.
b. Quartz gauge located at $r = 5.08 \times 10^{-2}$ m.

A quartz gauge was mounted to measure the current flowing in the load at a radius of 8.35×10^{-3} m. This quartz gauge had a diameter of 2.8×10^{-3} m and a thickness of 5×10^{-4} m. The experimental results are shown in Fig. 6. A peak pressure of 2.5×10^9 Pascals, which corresponds to a current of 3.5 MA in the load was measured. The quartz gauge current waveform is consistent with the measured liner dynamics and the assembled plasma properties.

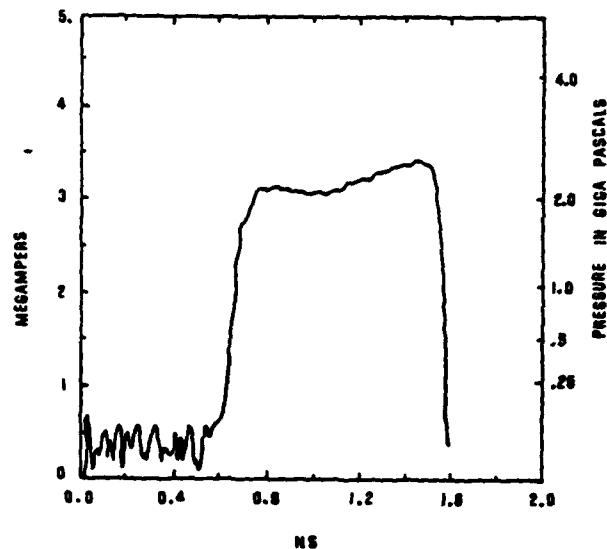


Fig. 6. Current and pressure as measured by the 2.8×10^{-3} m diameter quartz gauge at a radius of 8.35×10^{-3} m.

Conclusions

Quartz gauges have successfully measured magnetic pressure due to a large load current at a small radius. These gauges may be attached to a current carrying conductor without producing electrode surface perturbations. Care in design of the electromechanical assembly is necessary, but using quartz gauges is no more difficult than the more conventional current measuring technique. The gauge has nanosecond frequency response. This technique is extendable to higher current by using hydrodynamic codes to analyze the pressures.

References

1. Lee Davison and R. A. Graham, Physics Reports, A Review Section of Physics Letters, Vol. 55, No. 4, October 1979.
2. R. A. Graham, F. W. Neilson and W. B. Benedick, J. of Appl. Phys., Vol. 36, No. 5, 1773-1783, May 1965.

A HIGH-PRECISION PULSE-FORMING-NETWORK VOLTAGE REGULATOR

R. Sunderland
Marconi Radar Systems, Ltd
Chelmsford, United Kingdom

and

N. S. Nicholls
Royal Signals and Radar Establishment
Malvern, United Kingdom

Summary

Charging regulator circuits of the "de-Q" type may be used to eliminate PFN voltage fluctuations arising from variations in supply voltage and residual voltage on the PFN after the pulse. By closing a regulator switch, excess energy in the charging choke is diverted into a dump. In the system described, the diverted power is returned in series with the incoming supply. This makes possible the use of a thyristor as the divertor switch. Such a system is subject to errors due to regulator switch delay and to the effect of leakage inductance when a secondary winding on the choke is employed. For high precision such errors must be compensated. This means that a decision to close the regulator switch must be taken on the basis of a prediction of the voltage which will be attained when charging of the PFN ceases. The high-speed arithmetic operations required for the prediction are quite complicated and various approximations to the ideal system are therefore examined. A small circuit addition is described which avoids the conflict of factors arising in the choice of a dc dump voltage and also eliminates dump voltage variation as a factor in the prediction problem.

Introduction

Fluctuations of the peak charge voltage on the pulse forming network (PFN) of a modulator employing D.C. resonant charging may arise from HT D.C. supply voltage fluctuations and also from variation in the residual voltage on the PFN at the commencement of charging. The latter may arise from instability of the point at which the modulator switch tube ceases to conduct the ringing in the discharge circuit after the pulse. One way to stabilise the peak charge voltage of the PFN which can cover disturbances from both the above sources is to terminate the charging process when the desired PFN voltage has been attained; by closing an auxiliary switch, the charging current is diverted into a dump (fig 1(a)) leaving the PFN isolated by a reverse-biased diode (fig 1(b)). Note the definition of clip-angle and the clipping circuit conduction angle β shown in fig 1(b). ω is the angular resonant frequency of the charging choke and the PFN capacitance. The auxiliary switch and dump may be coupled to the choke by means of a secondary winding, an arrangement which provides electrical isolation of the dump circuit and allows free choice of the dump circuit voltage but at the expense of

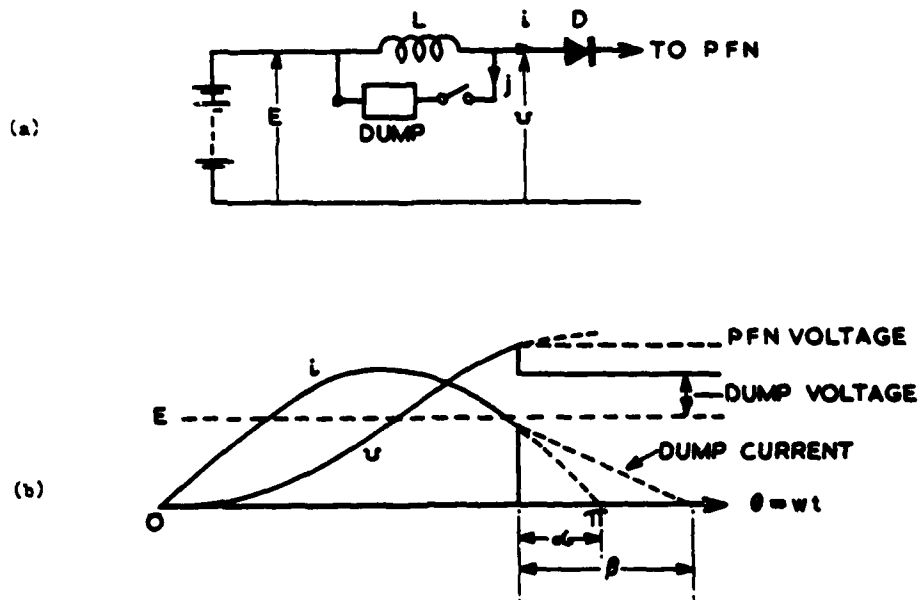


Fig 1.

(a) Basic Regulator Circuit

(b) Idealized waveforms

introducing leakage inductance into the circuit. The effective dump voltage (referred to the choke main winding) may be time dependent but must always be less than the difference between the desired PFN charge voltage and the supply voltage in order to keep the diode reverse biased after clipping commences. It should be large enough to absorb the surplus energy stored in the charging choke before the modulator pulse occurs, since otherwise the recovery conditions for the modulator switch will be adversely affected. A wide variety of circuits is possible, the main difference being associated with the realization of the dump. In this paper we shall be concerned with a charging regulator for a high average power thyratron modulator with a peak PFN voltage of 30 kV in which the diverted energy is returned to the HT supply. The simplest circuits of this class involve a secondary winding on the choke. The recovered power may be returned in parallel with the incoming supply (fig 2(a)) or in series with it (fig 2(b)). Because the circuit of fig 2(a) involves voltages greater than the peak PFN voltage both within the choke and across the diverting switch (in inverse), and because the high impedance auxiliary winding on the choke is prone to a severe ringing problem, the circuit of fig 2(b) was chosen.

A drawback of this circuit is that an increase in the incoming supply voltage causes increased charge diversion which increases voltage on the dump capacitor, thus adding to the total HT supply voltage. A practicable method of overcoming this self-defeating tendency of the circuit is to make the dump capacitor (C of fig 2(b)) sufficiently large to prevent significant changes in its voltage occurring before corrective action can be taken elsewhere in the circuit. For instance, in an MTI radar transmitter, where some slow drift in the peak charge voltage may be allowable, the target PFN voltage may be slowly modified to return the mean clip angle to a fixed value. Alternatively or additionally, the incoming HT supply voltage may be corrected fairly rapidly by means of a phase-controlled rectifier.

The design constraints inherent in the circuit will first be analysed. This will be followed by a discussion of errors and their compensation.

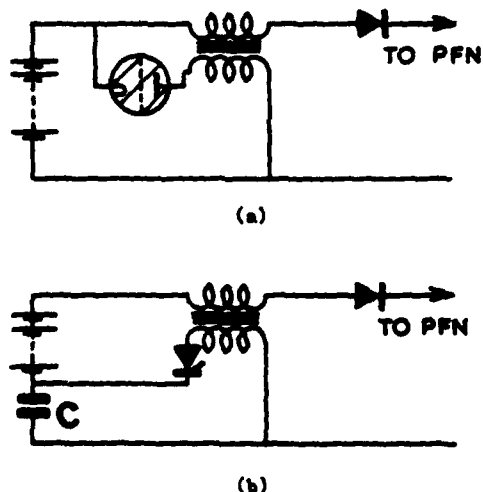


Fig. 2 Energy recovery circuits
(a) Parallel (b) Series

Simplified analysis of the circuit

Although the circuit is amenable to accurate numerical analysis by computer, understanding of the design constraints is perhaps most readily obtained from an approximate algebraic treatment. Initially we shall neglect the effects of leakage inductance in the choke, thyristor delay, residual PFN voltage, potential divider distortion and circuit losses. The complete supply and charging circuit is shown in fig 3. (The diode D2 is only involved in start-up).

Average clipping angle

During charging of the PFN the instantaneous PFN voltage and charging current are given by:-

$$v = E(1 - \cos \omega t) \quad (1)$$

$$i = \frac{E}{\omega L} \sin \omega t \quad (2)$$

(see fig 1)

Where E is the total HT voltage which is equal to the sum of the supply voltage and the voltage across the dump capacitor.

L is the self inductance of the charging-choke main winding

ω is the resonant angular frequency of L with the capacitance of the PFN.

When $\theta = \pi - \alpha$ the thyristor is fired and charging of the PFN ceases, leaving it at a voltage V given by:-

$$V = E(1 + \cos \alpha) \quad (3)$$

α is varied so as to keep V constant in spite of variations of E .

The HT voltage E will be assumed constant during any one charging cycle, but at a value which may be different from its average value E_0 . Let:-

$$E = E_0(1 + \delta) \quad (4)$$

where δ may take positive or negative values. We shall assume that the absolute value of δ to be accommodated during normal operation does not exceed some limit ϵ

$$|\delta| \leq \epsilon \quad (5)$$

Thus we are for simplicity assuming that the average value of E lies mid-way between the limits within which stabilisation is to be provided. In order that stabilisation shall be maintained at the lowest extreme of HT voltage:-

$$V \leq 2E_0(1 - \epsilon)$$

whence, using eqn. 3, the lowest permissible value of the clipping angle at average HT voltage, α_0 , is given by:-

$$V = 2E_0(1 - \epsilon) = E_0(1 + \cos \alpha_0) \quad (6)$$

Hence:-

$$\alpha_0 \geq \cos^{-1}(1 - 2\epsilon) \quad (7)$$

Increasing α_0 above the minimum value increases the average power diverted by the clipping circuit and hence the ratings of and losses in the diverting components. We shall find it useful later to refer to an "optimum" system in which α_0 takes its minimum allowable value.

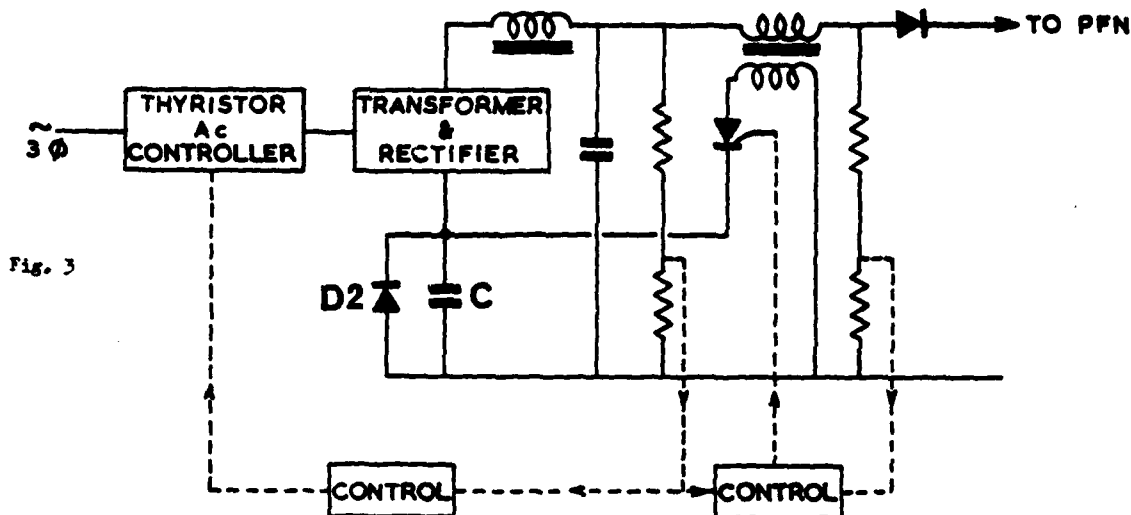


Fig. 3

The dump capacitor voltage

It will be assumed that the dump capacitor is large and that its voltage U therefore constant. U is determined by the conditions in the circuit at average RT voltage.

Since C is in series with the incoming supply, the charge delivered to the PFN during charging must, on the average, be equal to the charge returned to C during diversion. The average charge delivered to the PFN per cycle is given by:-

$$Q = \int_0^{\frac{\pi - \alpha_0}{\omega}} i \, dt = \frac{E_0}{\omega L} \int_0^{\frac{\pi - \alpha_0}{\omega}} \sin \omega t \, dt$$

$$\therefore Q = \frac{E_0}{\omega L} (1 + \cos \alpha_0) \quad (8)$$

To obtain the average charge per cycle returned to C during diversion, we may use the clipping energy balance. The energy diverted from L per cycle

$$J = \frac{1}{2} L i_1^2$$

where i_1 is the charging current at clipping. Substituting for i_1 from eqn (2) gives:-

$$J = \frac{E_0^2 \sin^2 \alpha_0}{2 \omega^2 L} \quad (9)$$

This must be equal to the energy absorbed by C .

$$J = QU \quad (10)$$

From eqns 8, 9 and 10.

$$U = \frac{E_0}{2} (1 - \cos \alpha_0) \quad (11)$$

Note that this is independent of the turns ratio of the choke.

For the "optimum" system postulated above $\cos \alpha_0 = 1 - 2\epsilon$ giving

$$U = \epsilon E_0 \quad (12)$$

This is the minimum possible value of U . For $\alpha_0 > (\alpha_0)_{\min}$, U will be greater.

The turns ratio of the choke

Let N be the ratio main winding turns/secondary winding turns on the choke. There is an upper limit to N dictated by the requirement that there must always be forward voltage on the thyristor at the instant of clipping. This condition may be written:-

$$\frac{V - E}{N} > U \quad \text{or} \quad N < \frac{V - E}{U}$$

This is most stringent when E has its maximum value. Putting $E = E_0 (1 + \epsilon)$ and substituting for V from eqn (6) and U from eqn (11) gives

$$N < \frac{2(\cos \alpha_0 - \epsilon)}{1 - \cos \alpha_0} \quad (13)$$

For an "optimum" system we obtain, by substituting from eqn 7:-

$$N < \frac{1 - 3\epsilon}{\epsilon} \quad (14)$$

Decreasing N below this maximum figure will increase the inverse voltage rating required for the thyristor and also prolong the secondary current, so that for our "optimum" design we shall take the equal sign in eqn 14.

The inverse voltage on the thyristor

The inverse voltage on the thyristor X , which occurs immediately after the discharge of the PFN, is given by:-

$$X = \frac{E}{N} + U$$

Taking the value of U from eqn (11) and putting in the maximum value of E :-

$$\frac{X_{\max}}{E} = \frac{1 + \epsilon}{N} + \frac{1}{2} (1 - \cos \alpha_0) \quad (15)$$

For the "optimum" design, by substitution for N from eqn (14), α_0 from eqn (7) and E_0 from eqn (6) we obtain:-

$$\frac{X_{\max}}{V} = \frac{\epsilon}{1 - 3\epsilon} \quad (16)$$

Duration of secondary current

The maximum duration of the secondary current is given by:-

$$\beta/\omega = \frac{Li_1}{NU}$$

The greatest value of i_1 and therefore of β occurs when $E = E_{\max}$. Then, using eqns 2 and 3

$$\beta_{\max} = \frac{E_0(1+E)}{NU} \sqrt{1 - \left(\frac{V}{E_0(1+E)} - 1\right)^2} \quad (17)$$

For the "optimum" system this, using eqns (8), (12) and (14) reduces to

$$\max = \frac{2\sqrt{2E(1-E)}}{1-3E} \quad (18)$$

Summary of the preceding results

The significance of what has been derived in this section is perhaps made clearest by table 1 which gives the main design parameters normalized to the peak PFN voltage V for a series of "optimum" systems, designed to accommodate increasing HT voltage fluctuations.

Table 1

%	N	E_0/V	α , degrees	U/V %	X/V %	$(\beta - \alpha)$ max. degrees
2	47	0.510	16	1.0	2.1	1
4	22	0.521	23	2.1	4.5	4
6	13.7	0.532	28	3.2	7.3	8
8	9.5	0.543	33	4.3	10.5	13
10	7.0	0.556	37	5.6	14.3	20

In a real system N would have to be reduced and α , would have to be increased slightly to allow for leakage inductance and other factors. There would be consequent increase in E_0 , U , X and $(\beta - \alpha)$.

Errors and their compensation

Error due to thyristor firing delay

The excess PFN voltage ΔV due to a thyristor firing delay τ is given by

$$\Delta V = \tau \left(\frac{dv}{dt}\right) \quad (19)$$

where the suffix denotes that the value at the instant of clipping is to be used. Substituting from eqn (1) gives:-

$$\Delta V = \omega \tau E \sin \alpha$$

from eqn (3)

$$= \omega \tau \sqrt{\frac{2E}{V}} - 1 \quad (20)$$

In an "optimum" system as previously defined and which has no residual PFN voltage after the pulse, $V = 2E$ at the lower limit of E and therefore $\Delta V = 0$ in this condition. The differential error

is therefore equal to the maximum overcharge, which occurs at E_{\max} and is obtained from eqn (2). Putting $E/V = \frac{1+E}{2(1-E)}$:-

$$\text{Max fractional error} = \frac{\Delta V}{V} = \omega \tau \sqrt{\frac{2E}{1-E}} \quad (21)$$

In the system under consideration ($\omega = 400\text{W}$, $E = .02$) and for $\tau = 2$ microseconds eqn (21) gave an error of about 5 parts in 10^4 . From eqn (19) it is evident that the correcting signal required to cancel this error may be obtained by differentiating the PFN voltage. For instance, if the top (high-voltage) limb of the potential divider used to monitor the charging voltage has a resistance R , it is only necessary to connect across it a capacitor K such that $KR = \tau$ in order to achieve compensation. Alternatively, a separate differentiator may be used, and this could be connected to the secondary of the choke if desired.

Another possible way to compensate for thyristor delay is based on measurement of instantaneous charging current, since:-

$$\left(\frac{dv}{dt}\right) = \omega^2 Li_1 \quad (22)$$

with the restriction that the PFN capacitance (and hence ω) must be kept constant.

The effectiveness of compensation possible depends on the constancy of τ . Almost an order of magnitude reduction of the error seems to be obtainable.

Although compensation based on E appears possible, using eqn (20), it should be noted that, apart from the inconvenient processing which it would involve, it would give no compensation for the effect of residual voltage on the PFN after the pulse. This has been explicitly excluded in the derivation of eqn (1). Compensation based on eqns (19) or (22) is free from this objection.

Error due to leakage inductance

Due to leakage inductance between the windings on the choke, charging will continue for a short time after the thyristor is fired, leading to a small over-voltage on the PFN. Since this overvoltage is affected by the supply voltage, the dump voltage and any residual PFN voltage, changes in any of these will affect the final PFN voltage. This is usually the most serious source of error before correction is applied. On the other hand, since the leakage inductance is a very stable characteristic, accurate compensation for its effect is in principle possible.

For an approximate analysis we shall assume that the voltage across the leakage inductance is constant during the overlap period and therefore the currents change linearly with time (see fig 4).

The voltage across the leakage inductance referred to the main winding is equal to $V - (E + NU)$ (see fig 1). From this we may write down the expression for the overlap angle γ :-

$$\gamma = \frac{\omega DLi_1}{V - E - NU} \quad (23)$$

where D is the ratio leakage inductance/self-inductance of the choke.

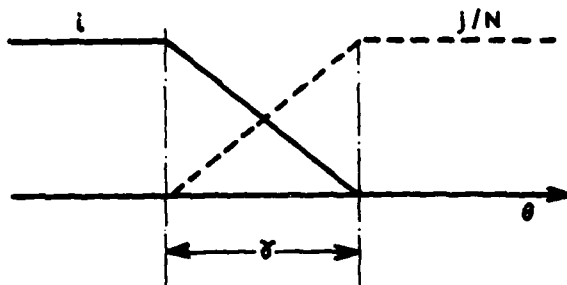


Fig. 4 Currents during overlap

$$\begin{aligned} \text{Hence:- } \Delta V &= \frac{\omega L \gamma i_1}{2} \\ &= \frac{D \omega^2 L^2 i_1^2}{2(V-E-NU)} \end{aligned} \quad (24)$$

In an "optimum" system as previously defined, the denominator of this expression goes to zero at the upper limit of HT supply voltage. Thus the overlap and the consequent overcharge of the PFN will apparently become infinitely large. Though this is a false result deriving from the constant commutating voltage approximation, it does indicate that unacceptable overcharge will occur. One solution to this is to use a value for N somewhat lower than the maximum allowed. For instance, we might make N some fraction K of the maximum value allowed by eqn (14). Then for an otherwise "optimum" system, the differential error becomes:-

Max fractional error

$$\frac{\Delta V}{V} = \frac{2D\epsilon}{(1-K)(1-3\epsilon)} \quad (25)$$

For typical values $D = .02$, $\epsilon = .02$, $K = 0.5$ this gives $\frac{\Delta V}{V} = 1.7 \times 10^{-3}$ which indicates the degree of compensation required. Unfortunately, inspection of eqn (24) reveals that the correction required depends on both i_1^2 , E and U . The latter, although ideally constant, fluctuates somewhat in a real system because C cannot be made extremely large. Thus the task of rapidly computing a correction before each firing of the thyristor is a complex one. It may be somewhat simplified at the expense of a small increase in losses by adding a relatively small extra capacitor connected to C by a diode and arranged to be discharged before each diversion (see fig 5). The value of this capacitor should be just sufficient to ensure that the overlap is finished before the diode conducts. This eliminates U in the denominator of eqn (24), thus reducing ΔV and, which is more important, eliminates its fluctuations from the calculation of the correction.

As in the previous section $\left(\frac{dv}{dt}\right)_2$ is equivalent to i_1 in accordance with eqn (22), provided that the PFN capacitance is kept constant.

If i_1 is expressed in terms of E, assuming zero or constant residual PFN voltage after the pulse, the right hand side of eqn (24) becomes very nearly linear in E, making correction quite simple. This is illustrated in fig (6) which shows the normalized fractional overcharge as a function of normalized

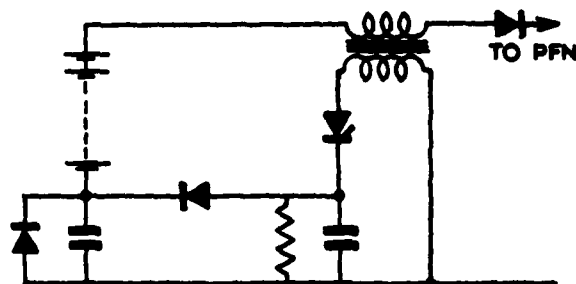


Fig 5. Circuit with added capacitor to reduce error due to leakage inductance

supply voltage (full lines). It is calculated from eqn (24) assuming zero residual voltage and the "optimum" (i.e. minimum) value of ϵ , allowable for each value of ϵ . The choke turns ratio is fixed at $N = 10$. The dashed line shows the locus of E_0/V . It is apparent that for this value of N, operation is not practicable for ϵ greater than about .06. However, it is usually not possible to assume that fluctuations in residual voltage will never occur. Then it is necessary to derive the correction from eqn (24). The i_1^2 term is the most significant. One way in which the squaring process has been accomplished successfully is by using the charging current to linearly control a variable time delay in the thyristor firing circuit.

Transient and Fault Conditions

Start up

If the modulator is started up with C discharged, β will be greatly increased during the first cycle. This follows from eqn (17) since U will be zero at the commencement of diversion. The effect is illustrated in fig (7) which shows the waveforms during a start-up with constant H.T. voltage. This was calculated for $C = 500 \times$ PFN capacitance and with $N = 10$. If current is still flowing in the secondary circuit when the next pulse occurs, the recovery of the modulator switch-tube may be endangered. Two remedies are available - the use of a priming supply to pre-charge C and delay of the second modulator pulse until the secondary current has ceased.

Reduction in the resonant period of the charging choke and PFN relative to the repetition period obviously helps, but is usually limited by the recovery requirements modulator thyatron.

Modulator switch prefire

If the main modulator switch-tube pre-fires whilst charging is in progress, and recovers, an abnormally large diversion of energy into the dump capacitor will follow. The dump capacitor must have sufficient capacitance to absorb one or more of such abnormal diversions without its voltage rising to a level which would prevent clipping at the normal PFN voltage. Otherwise there is a danger that this sequence may repeat itself due to the abnormal PFN voltage which would be reached.

Conclusions

It has been established that a stability in the region of 1 part in 10^4 can be attained in a high power thyatron modulator, using a charging regulator

circuit which adds very little to the cost and size of the equipment. The scheme requires the use of a rapidly controllable HT supply (such as a phase-controlled rectifier) and some rather complex control circuits to provide error correction on an open-loop basis.

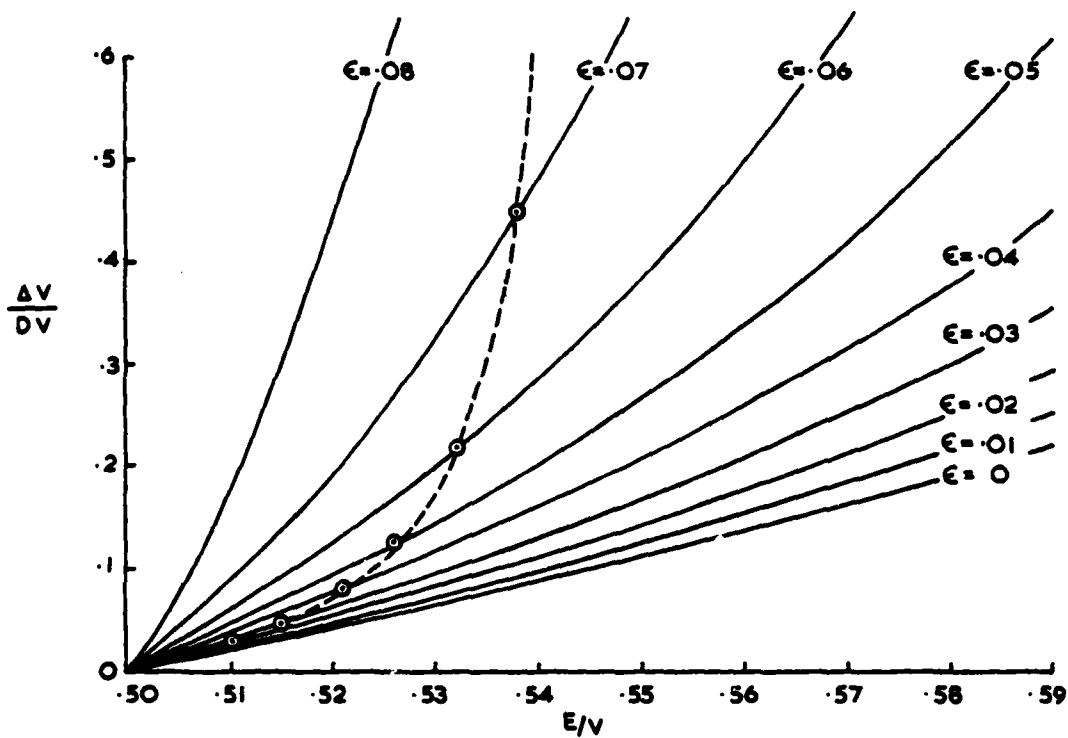


Fig 6. Normalized P.F.N. overcharge due to leakage inductance versus normalized H.T. supply voltage for various values of E

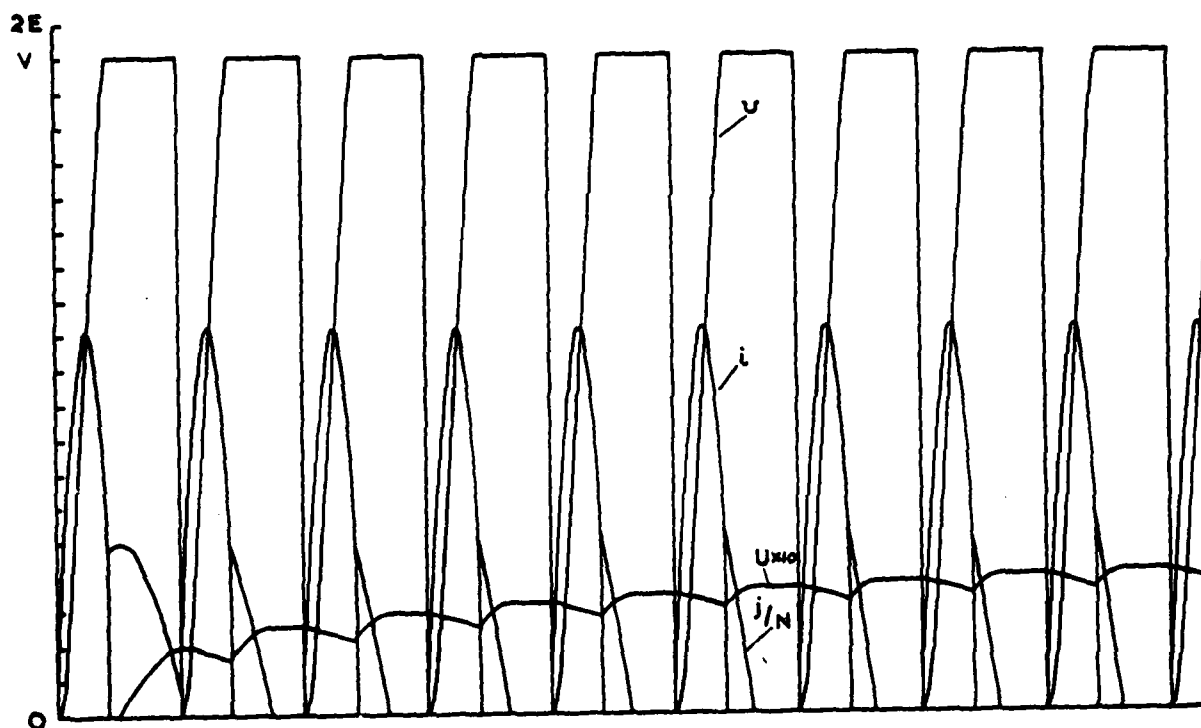


Fig. 7 Waveforms during start-up with $N = 10$ and Dump capacitance C / P.F.N. capacitance = 500

8 MVA MODULATOR/REGULATOR FOR NEUTRAL BEAMS*

Douglas B. Ramsen, Jr., and Trevor H. Overett
General Atomic Company
San Diego, California

Summary

This paper describes very generally the modulator/regulator (Mod/Reg) being built for Transrex by Systems, Science and Software for use on the neutral beam power supplies that Transrex is building for General Atomic Company to power the neutral beam heating systems that will be used on the Doublet III fusion device.

The Mod/Reg is required to provide an 80 kV, 100 A pulse for a second every 90 sec. The voltage is to be regulated to 3%, and in case of fault the pulse must be interrupted within 10 μ sec. An additional requirement was that the total system have very low capacity such that the total energy stored would be less than 15 joules. This is a restriction imposed by the source designer to prevent destroying the source in case of an arc within the source.

General Description

The Mod/Reg (illustrated in simplified form in Fig. 1) is contained within a metal enclosure 12 ft long by 7 ft wide by 10 ft high (Fig. 2). The enclosure is divided into two parts: (1) the high voltage section and (2) the control and power input compartments. These parts of the Mod/Reg are separated by a conducting wall for EMI reduction and protection of system controls.

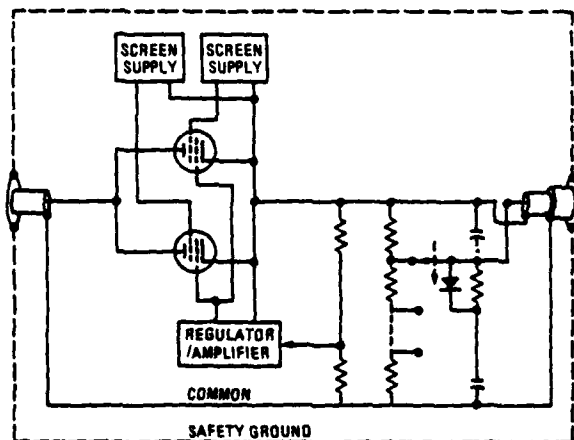


Fig. 1. Mod/Reg basic approach

The power input and controls compartments are located at one narrow end of the overall enclosure (Fig. 2). Double doors provide access to 480 V power input components contained therein. The water cooling manifolds for the X2062K tetrodes are also contained within this compartment, but a splash shield separates the water system from the 480 V system.

The controls section of the system is located adjacent to the 480 V and water manifold compartment. Standard chassis strips are provided for mounting of the circuit breaker panel and control chassis.

The controls section is separated from the 480 V power compartment by a conducting wall. Thus, the controls compartment is shielded both from the high voltage and 480 V power components of the system.

*Work supported by Department of Energy, Contract DE-AT03-76ET51018.

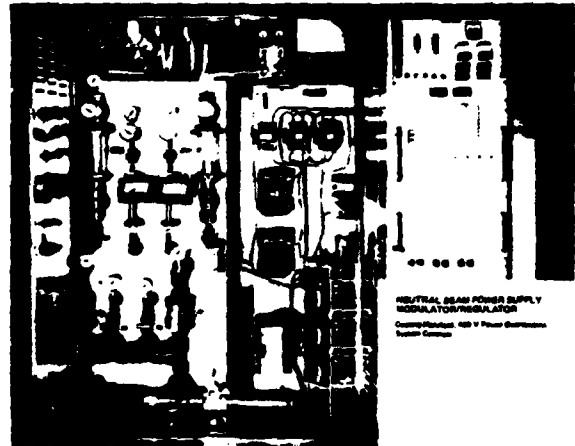


Fig. 2. Mod/Reg enclosure

The high voltage section of the Mod/Reg enclosure is equipped with six large doors, three on each side (Fig. 3). The high voltage deck is shown in Fig. 3.

All high voltage subsystems and components within the enclosure are ambient air insulated, with two exceptions. The high power tetrodes are housed within dielectric enclosures containing SF_6 gas at atmospheric pressure for electrical insulation of the tube insulators. The dielectric enclosures are connected by gas lines to a regulated source of SF_6 gas, although under normal conditions no flow is required. Also, the input

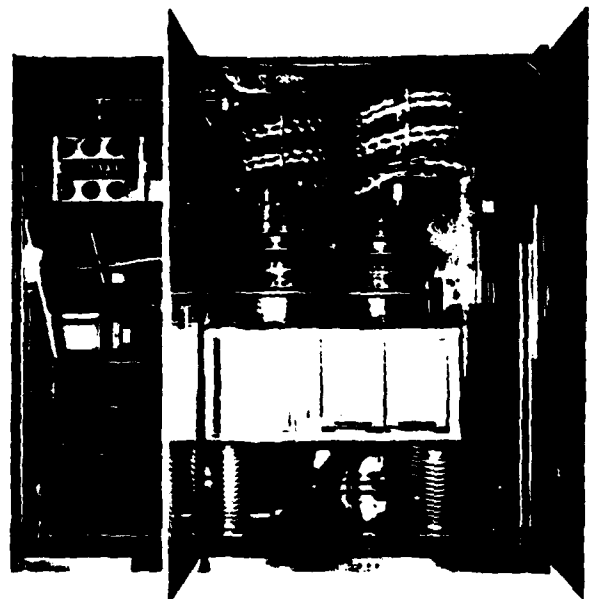


Fig. 3. High voltage section of Mod/Reg enclosure

and gradient grid voltage monitors, which are purchased assemblies, contain SF_6 gas for insulation of the resistive and capacitive elements from which the monitors are fabricated. The monitors are sealed units and require no replenishment of gas.

The principal electrical subsystems which comprise the Mod/Reg (Fig. 1) are described in more detail in the following paragraphs, beginning with the 480 V three-phase input.

480 V Three-Phase Input

Five wire, 480 V three-phase power input to the Mod/Reg enters the enclosure top at the control compartment end of the cabinet. Conduit is provided for the wire run from the top to the control section where the input power connections are made at a terminal board.

Power (120 Vac one-phase) is also supplied to each Mod/Reg for convenience outlets and lights within the high voltage section of the enclosure.

Transformers, associated circuit breakers, and fuses are provided in the power distribution system to supply 120 Vac and 24 Vac for ground-based control and interlock circuitry.

Isolation Transformer

The Mod/Reg isolation transformer is an air-insulated design. This approach, in contrast to oil-insulated designs, was taken specifically to minimize the stray capacity from the secondary windings to the primary and ground.

The transformer, manufactured by Stangenes Industries, Mountain View, California, is illustrated schematically in Fig. 4. The input to each of the three phases is nominally 277 V supplied from a 480 V (line-line) system. Each secondary of the isolation transformer contains two windings. The 120 V secondaries from each phase are combined to form a three-phase 208 V supply to power the X2062K screen power supplies. Two phases each contain 12 V center tapped windings, and these supply filament power to the two X2062Ks. The secondary winding of the third phase contains a center tapped 240 V winding which provides general deck power requirements, including the regulator/amplifier and its associated power supply.

Two shields are provided over each of the three windings which comprise the transformer primary, and these shields are connected by low inductance copper straps to the cores and frame (safety ground). The shields are 0.010 in. thick copper sheet and are wrapped around and completely cover the primary windings. The two shields over each primary winding are separated from each other by means of sheet plastic insulation.

The transformer secondary windings are contained within relatively thick copper shields which are electrically "smooth" to minimize corona. The secondary shields are electrically connected to the high voltage deck.

The stray capacity from the secondary shields to ground with the unit installed is approximately 180 pF.

Current limiting reactors and shorting contactors are provided in series with the tube filament windings to limit filament in-rush current to an acceptable value. These reactors also provide the means for reducing tube filament power when the Mod/Regs are in a standby condition. Thus, as a result, tube filament life can be significantly extended.

Water Cooling System

The system for distribution and monitoring of X2062K cooling water is located within the control compartment of the enclosure. The system provides valving, temperature, pressure, and flow monitors for control and measurement of relevant parameters and for protection of the tubes.

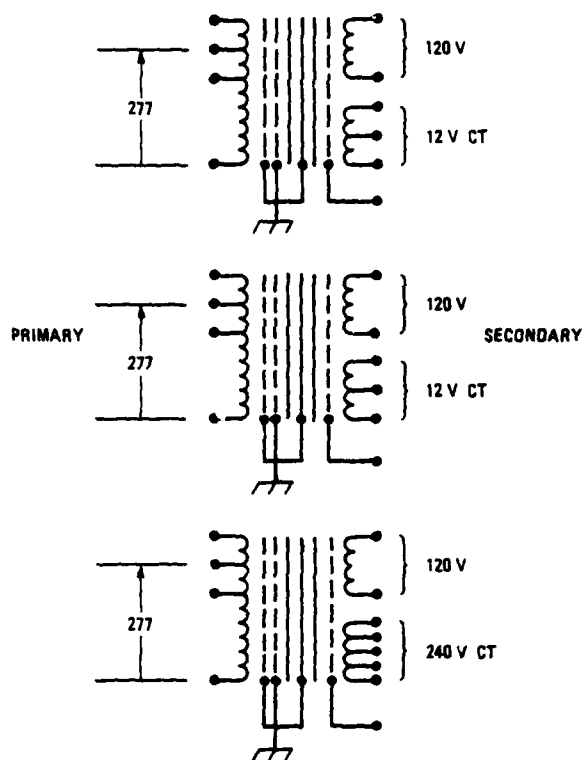


Fig. 4. Isolation power transformer

High Voltage Deck

The high voltage deck, which contains the high voltage series tubes and supporting equipment, is located within the high voltage section of the enclosure. The deck is 64 in. long by 52 in. wide by 30 in. high. It is supported on standard station post insulators; the 21 in. spacing between the bottom of the deck and the common conductor (ground) is more than adequate to safely sustain the 80 kV output voltage.

The spacing between the deck sides and the enclosure walls is about 15 in.; this spacing is also quite safe electrically. The deck has successfully sustained hipot testing, in situ, to 150 kV dc.

X2062K Screen Power Supplies

Screen power for the two X2062K high power tetrodes is supplied from two separate power supplies on the high voltage deck.

Screen supply input power is derived from the previously described high voltage isolation power transformer by way of a three-phase SCR controller. The SCR controller is used as a fast switch to turn off the screen supplies in the event of a series tube fault. In addition, the input to one screen power supply is equipped with a variable transformer which provides the capability for independent adjustment of screen voltages for the two X2062Ks.

The screen power supply transformers are three-phase units equipped with two secondary windings. The secondaries are delta and wye connected and when rectified and connected in series provide a low ripple 12 pulse dc output voltage. The dc output is capacitively filtered to provide low source impedance against the transient screen power demands that exist during turn-on of the series tubes.

One ampere bleeders are also provided at the output of each screen supply to offer, in conjunction with the large filter capacity, a low impedance path for the negative current "islands" which exist in the operating characteristics of the high power tetrodes.

Screen supply output voltage is nominally 1100 Vdc, and each supply is capable of supplying 3 A continuously.

The screen power supplies are contained within modular chassis installed into one side of the high voltage deck. The chassis are equipped with slides for ease of access or replacement if necessary.

X2062K High Power Tetrodes

The Mod/Reg is a conventional series regulator circuit. Its function is to regulate the flow of power to the neutral beam source (NBS) and to protect both the NBS and primary power subsystem in the event of a load fault.

In operation at maximum output conditions, the series tubes must pass 108 A* and regulate the output voltage (80 kV) to within 3%. The output pulse current risetime and maximum pulse width are 50 μ sec (10%-90%) and 1 sec, respectively. In the event of a load fault, the series tubes must reduce the current to near zero as rapidly as possible, in a time less than 10 μ sec.

The voltage regulation range of the series tubes is limited at one extreme by the maximum plate dissipation that can be sustained and is limited at the other extreme by screen dissipation. Tests conducted at EIMAC have clearly demonstrated the capability of each X2062K tetrode to continuously sustain a plate dissipation of 750 kW. Thus, for 54 A per tube, the maximum tube drop is 13.9 kV.

The maximum screen dissipation for the X2062K is 3500 W, and thus for a screen voltage of 1100 V, the minimum tube drop (to result in a screen current less than about 3.2 A) is approximately 3.5 kV. Therefore, the resulting total series tube regulation range at full output voltage and current conditions is 10.4 kV.

The grids of the X2062Ks are driven in parallel from a common driver circuit. Screen voltage is adjusted such that the required maximum output current (108 A) is achieved for a grid voltage of 50 V. Diode clamping is provided to assure this condition. Spark gap protection is provided at the grids for protection of the driver in the event of a tube fault.

Separate screen supplies are provided for the X2062Ks, as previously described, to permit independent screen voltage adjustment. This approach is used to assure equal output current sharing, for equal grid drive, between the tubes.**

X2062K screen protection circuitry (illustrated in Fig. 5) is provided for protection of the X2062Ks as well as for protection of the screen supplies themselves. If a tube fault occurs, the large SCR associated with the screen circuit crowbars the screen voltage. Nearly simultaneously, additional circuitry detects the fault condition and interrupts screen input power.

X2062K filament power (12 Vac, 660 A) is provided from the previously described isolation transformer secondary. High frequency bypasses are provided from each side of the directly heated cathode to the output connection. Filament current and voltage monitoring are provided.

* The NBS load current is 100 A, but the series tubes must pass an additional 8 A to supply the gradient grid resistive divider.

** Screen voltage adjustment is a "one time" adjustment performed during initial system testing. However, the cathode current of each X2062K is monitored to assess current sharing on a shot-to-shot basis.

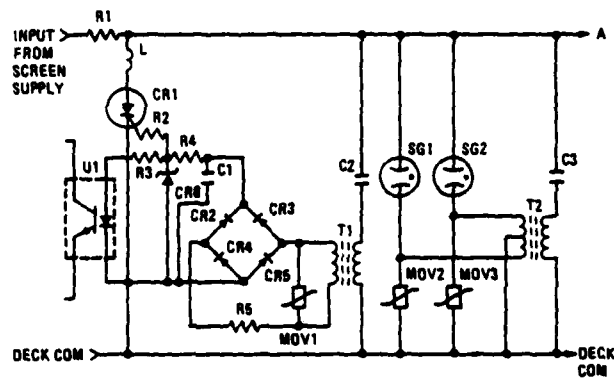


Fig. 5. X2062K screen protection

Regulator/Amplifier

The regulator/amplifier employs a feedback loop and is closed at the high voltage deck by means of a highly stable resistive divider monitor which samples the Mod/Reg output voltage. The reference signal which sets the Mod/Reg required output voltage is transmitted to the deck by means of an optically coupled data link.

The regulator/amplifier circuit is illustrated in simplified block diagram form in Fig. 6.

The series tube grid driver consists of three basic elements: (1) an error amplifier circuit, (2) a transistor amplifier stage, and (3) a cascade drive stage employing two vacuum tubes.

The error amplifier consists of high quality differential amplifiers which compare the feedback signal with the reference signal. The output is buffered to drive the following stage.

The transistor stage amplifies the error output signal from a nominal 10 V level to a level required to drive the final amplifier stage.

The tube stage employs two EIMAC 4CX1000Ks in a cascade configuration. The output stage voltage "swing" is 800 V and its output impedance is low ($\approx 50 \Omega$). A low impedance output driver is required to drive the X2062K's grid capacity for fast blocking of the Mod/Reg output. Based upon an assessment of the stray capacity, the series tube is capable of blocking the output in about 2 μ sec.

The regulator/amplifier system has been the subject of considerable testing in support of the present Mod/Reg systems. Detailed analyses have been performed to define the stage gain and frequency response necessary to achieve overall regulation requirements in conjunction with stable operation. Testing of the amplifier

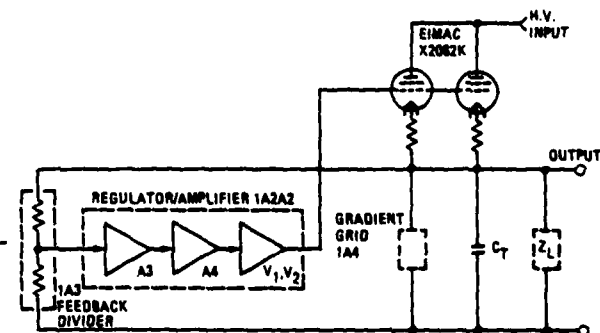


Fig. 6. Mod/Reg amplifier feedback system

system through the driver stage and the results of analysis demonstrate that the required regulation and fast block characteristics of the regulator/amplifier system can be successfully achieved in a system that is stable.

Gradient Grid Circuit

The gradient grid resistive divider consists of 200 50 Ω wire wound resistors (Ohmveve Co.) connected in series. The mass of wire contained in each resistor is 14 g. The peak temperature rise of each element is approximately 600°C. Even at 600°C, the wire which comprises each element is well below the fusion temperature for the material (1210°C).

Air cooling of the gradient grid resistor assembly is proposed to extend its power dissipation capability through a water cooled heat exchanger at the top of the enclosure to minimize the heat load "dumped" into the building that houses the Mod/Regs.

The remaining components which comprise the gradient grid circuit, resistors, capacitors, diodes, and the resistive divider tap changing mechanism are identical to those used in the present units.

Controls and Monitoring

The principal feature of the controls is that multiple-parallel optically coupled data link channels provide continuous monitoring of "on-deck" functions at ground level. The analog links use a voltage to frequency conversion for transmission of the data via optically coupled "light-pipes." This information, upon receipt, is re-converted from frequency to voltage before interfacing with the control system. Analog channel bandwidth is 30 kHz (0 to 30 kHz) and is sufficiently broad for satisfactory reproduction of the input analog signals.

The digital transmission links, i.e., links which provide "on-off" information or fast command functions, are identical to the described analog channels except that V/F and F/V conversion is not employed. In this case the data channel upper 3 db point is 250 kHz, consistent with the need for fast response in some cases.

The second principal feature of the control system is the use of a microcomputer for integration, coordination, and control of the Mod/Reg. The microcomputer is physically located at ground level (safety ground) and accepts inputs from the high voltage "deck" (via the optically coupled data links) and from the ground-based subsystems and components.

The microcomputer coordinates and controls the startup, normal operation, and shutdown of the Mod/Reg. The computer also drives a display panel to visually indicate the Mod/Reg status, as well as to accept and execute commands from the Mod/Reg and the local control system.

The primary mission of the microcomputer is to protect the high voltage tetrodes and critical circuitry and to protect personnel. In these vital tasks the computer is assisted by fast-acting hardwired circuitry in critical areas to ensure personnel and high-voltage circuitry protection even in the case where the computer might not be fast enough to act alone.

An Intel 8080A microprocessor is the brain of the computer that, along with a "programmable-read-only-memory," allows for flexibility. Should modification in control, size, or capability of the Mod/Reg become desirable in the future, the present control circuitry could still be used and the additional functions implemented by simply revising the computer "program" and adding minimal extra circuitry.

Control of the Mod/Reg is accomplished through the use of status, interlock, and control lines. The computer constantly monitors the status of items such as filament and plate water flow to the high voltage tubes, water temperatures, fans, ground hooks, and doors. It also monitors the currents, voltages, and power dissipations that are the key to the operational status of the high voltage tetrodes and associated power supplies and circuitry.

When the status of an item meets certain minimum requirements, it "makes up" an interlock. These interlocks are grouped by function in the computer and called "chains," e.g., Filaments, Safety, Cooling, Screen Supply Enable, and Ready. All of the interlocks within a chain must be in the proper condition before the chain is made up. The chains themselves are interlocks and must be completed before the Mod/Reg can operate.

80 kV, 100 A MODULATOR/REGULATOR CONTROLS

Harlan Aslin and Robert Hartline
Systems, Science and Software
P.O. Box 4803
Hayward, CA 94540

Summary

Neutral beam injectors for plasma heating augmentation in magnetic confinement fusion experiments require the controlled flow of high electrical power. Modulator/regulators (Mod/Regs) control the flow of this power and serve to protect the injector in the event of injector short circuit. This paper describes the control systems of a series Mod/Reg for the General Atomic Co. Doublet III neutral beam injection power supply system. The overall control system incorporates a microcomputer which coordinates and controls the start-up, normal operation, and shutdown of the Mod/Reg. Analog data transmission between ground based controls and controls at high voltage are provided by means of optically coupled data links. Transmission link bandwidth is dc to 30 kHz. Mod/Reg output voltage regulation is provided through the use of two parallel high power, high voltage tetrodes (EIMAC X2062K) configured in a series regulator circuit. A closed loop feedback control system regulates the output voltage to better than 1% with a closed frequency response equal to 250 kHz. The regulator circuit, upon command, reduces Mod/Reg output current to zero within five microseconds.

Introduction

Neutral beam injectors for plasma heating augmentation in magnetic confinement fusion experiments require the controlled flow of high electrical power. Modulator/regulators (Mod/Regs) control the flow of this power and serve to protect the injectors in the event of injector short circuits. The design and fabrication of the Mod/Regs for the General Atomic Co. (GA) Doublet III neutral beam power supply system (NBPSS) was undertaken by S-Cubed* in March, 1978 under subcontract to the Transrex Division of Gulton Industries. The general design of the Mod/Reg in satisfaction of the specified electrical output requirements (GA Specification No. 3-4410.ITS) is the subject of a companion paper¹, and is not presented here. The subjects of the present paper are the Mod/Reg controls. Specifically, the closed loop output voltage control system and overall system controls are discussed in the following paragraphs.

System Controls

The Mod/Reg control system provides all controls, interlocks, and monitors required for operation of the system from the customer's local control system. It incorporates a microcomputer which coordinates and controls the start-up, normal operation, and shut-down of the Mod/Reg. The computer also drives a display panel for visual indication of Mod/Reg status, as well as to accept and execute commands from the Mod/Reg and the local control system (Fig. 1).

* S-Cubed was aided in this endeavor by Mr. Arnold Feldman and Mr. David Snell of Scientec Engineering Co.

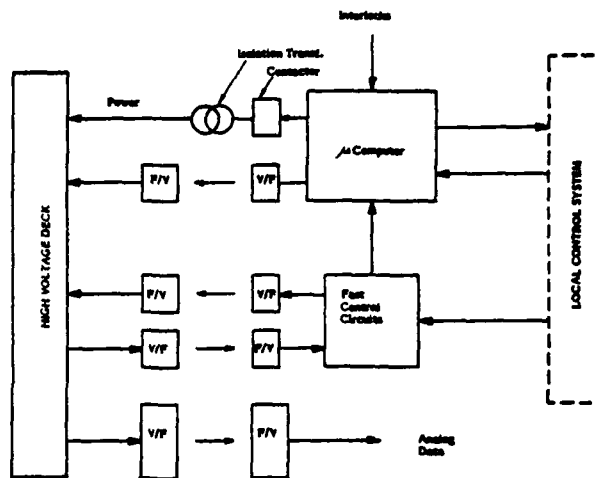


Fig. 1 Computer Control System

The principal function of the microcomputer is to protect the high voltage series tetrodes and critical circuitry and to protect personnel. In these tasks computer control is augmented by fast acting hardwired circuitry in critical areas to assure personnel and high-voltage circuitry protection in cases where the computer might not be fast enough to act alone.

An Intel 8080A microprocessor, in conjunction with a "programmable-read-only memory", provides considerable control system adaptability. Should modification in control, size or capability of the Mod/Reg become desirable in the future, the present control circuitry could still be used and the additional functions implemented by simply revising the computer "program" and adding minimal extra circuitry.

Control of the Mod/Reg is accomplished through the use of status, interlock, and control lines. The computer constantly monitors the status of items such as filament and plate water flow to the high voltage tubes, water temperature, fans, ground hooks and doors. It also monitors the currents, voltages, and power dissipations that are the key to the operational status of the high voltage tetrodes and associated power supplies and circuitry.

When the status of an item meets certain minimum requirements it "makes-up" an interlock. These interlocks are grouped by function in the computer and are called "chains", e.g., Filaments, Safety, Cooling, Screen Supply Enable, and Ready (Fig. 2). All of the interlocks within a chain must be in the proper condition before the chain is made-up. The chains themselves are interlocked and must be completed before the Mod/Reg can operate.

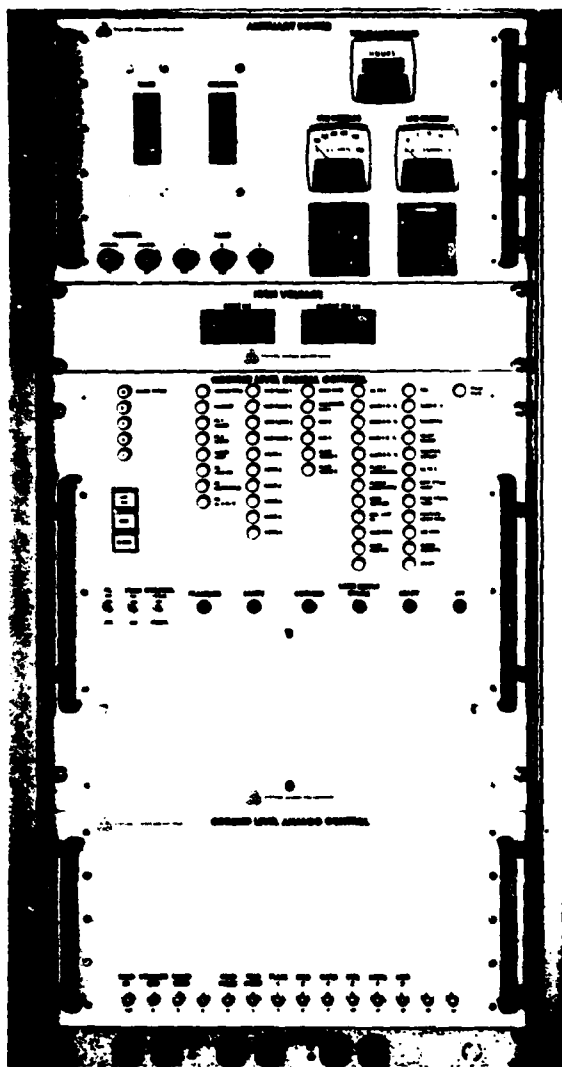


Fig. 2 Ground Level Controls

An internal "watchdog" timer is incorporated in the computer system to guard against computer malfunction. The computer is required to trigger the "watchdog" every several milliseconds. If it should fail to do so the Mod/Reg is immediately shut down. The "watchdog" cycle time is typically 3 ms.

The computer, through the program, is given a complete set of contingencies for orderly system start-up or shut-down. When it detects specified fault conditions it automatically takes proper action including indicating where the fault occurred. Depending on the program and type of fault or "broken" interlock the computer can either return the Mod/Reg to operational status or wait for human assistance and reset.

The computer and its associated circuits are contained within the Ground Level Digital Control chassis inside a shielded compartment (Fig. 2). All wires entering the compartment are filtered to provide a very high degree of noise immunity without using optically isolated input/output channels.

The control system provides analog output signals, available at the front panel of a Ground Level Analog Control chassis for convenient assessment of system performance. The analog signals are transmitted across the high voltage (HV) interface by means of optically coupled data links which are the subject of the following paragraphs.

Analog Data Link

Analog data links were developed by S-Cubed to satisfy the requirements (S-Cubed's) for accurate, stable (particularly dc stability), modest bandwidth (dc to 30 kHz) data transmission across the HV interface.

The data link approach adopted by S-Cubed is illustrated in simplified form in Fig. 3. A voltage-to-frequency converter (V/F) is biased at its input to produce an output frequency of 200 kHz corresponding to an input voltage equal to zero volts. An input voltage in the range of 0 to 10 volts provides a corresponding frequency change from 200 kHz to 250 kHz. The resulting frequency modulated signal drives a light emitting diode (≈ 900 nm wavelength) which is coupled to a length of infrared transmitting, plastic waveguide. A photo detector receives the frequency modulated light signal and through the use of a frequency-to-voltage converter (F/V) and filter (to remove the carrier frequency) provides a 0 to 10 volt output signal. Data link bandwidth is 0 to 30 kHz and long term accuracy and stability is better than 3% over a temperature range from 10°C to 40°C.

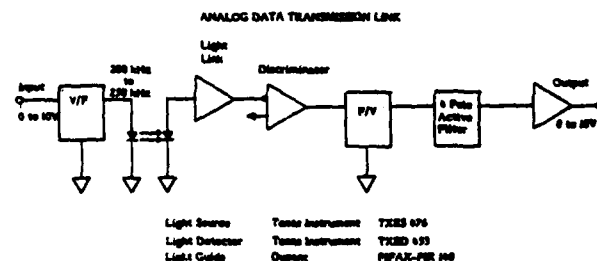


Fig. 3 Analog Data Link

Output Voltage Regulator

The Mod/Reg output voltage regulator control system is illustrated schematically, in simplified form, in Fig. 4. The series regulator circuit comprises two parallel EIMAC X2062K high power, high voltage tetrodes, their associated driving amplifiers, a feedback voltage divider, and a reference signal.

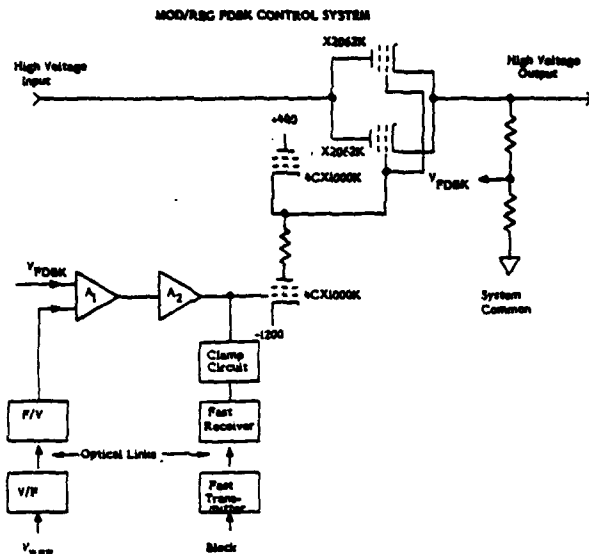


Fig. 4 Regulator Control System

The X2062K tetrodes are driven in parallel from a common driver amplifier stage. Equal X2062K tetrode output current sharing against the effects of unequal tube characteristics is achieved by means of separate, adjustable (one time adjustment) screen voltage power supplies.

The X2062K's driver amplifier consists of two 4CX1000K tetrodes connected in cascode mode (Fig. 4). Driver amplifier supply voltages are +400 V and -1200 V with respect to deck common; the negative supply voltage is determined by the X2062K grid voltage required for cut-off (~800 V).

Fast turn-off of the output current, in the event of a load short circuit, is provided by means of a clamp circuit which is coupled directly to the X2062K grid driver stage for speed (Fig. 4). The clamp circuit drives the lower 4CX1000K of the cascode pair hard into conduction which pulls the X2062K grids rapidly down to cut-off bias.

The X2062K driver stage is driven at its input by means of a modest gain transistor amplifier. The transistor amplifier is turn driven from a low level error amplifier.

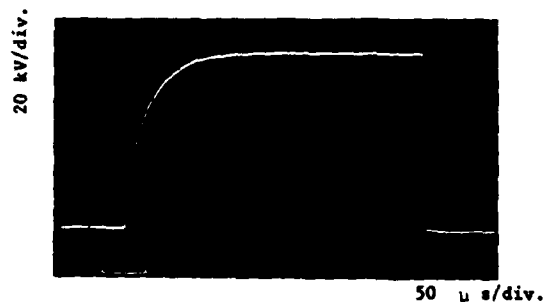
The feedback loop is closed at HV deck level; this decision was based principally upon speed-of-response considerations. The feedback signal is derived from a stable, compensated output voltage resistive divider (Fig. 4). Divider attenuation is about 10,000/1. The reference signal is coupled to the deck by means of an optically coupled data link channel previously described in this paper. The reference voltage is variable in the range from 3 V to 8 V corresponding to the required Mod/Reg output voltage range of 30 kV to 80 kV.

Performance of the feedback control system is illustrated in Fig. 5 and Fig. 4 for the condition where the Mod/Reg is driven from a capacitor bank (1.8 μ F) which droops considerably over the output pulse width. Output voltage and current, in Fig. 5 and Fig. 4 are 80 kV and 110 A respectively.

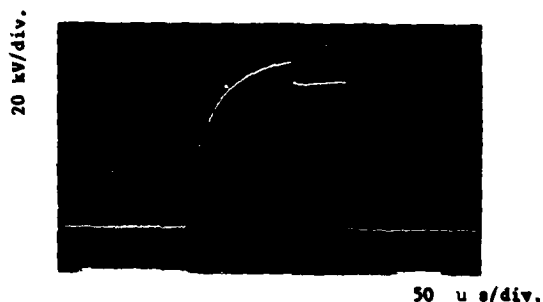
Fig. 5a illustrates the capability of the feedback control system to regulate against a variable input voltage. The capacitor bank initial charge voltage was 110 kV in this case and drooped to about 85 kV over the pulse duration.

Fig. 5b illustrates an output pulse of shorter duration, but in this case a step is applied to the reference voltage during the pulse. The amplitude of the step is about 14% of the reference amplitude. The effect of the step input upon the output pulse waveform is shown in Fig. 6a on an expanded sweep. Based upon assessment of the output waveform the closed loop response of the regulator, for the particular load conditions, is about 250 kHz.

Fig. 6b illustrates the end of the pulse of Fig. 5b, again on an expanded sweep. The pulse is terminated in the same manner whether it be a normal termination or "block". Thus, Fig. 6b illustrates the speed with which the output current is "turned-off" in response to a "block" command. The block command signal delay time, measured from receipt of the signal at the ground based control system, associated with propagation and electronics delays, is about two microseconds. Thus, the total time for blocking, including the fixed delay, is less than five microseconds.



a) 110 kV Capacitor Bank Charge Voltage



b) Response to Reference Step
Fig. 5 80 kV (110 A) Output Waveforms

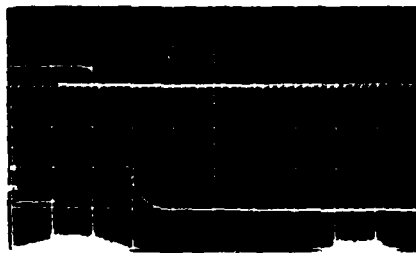
8 kV/div.
(baseline suppressed)



5 μ s/div.

a) Response to Reference Step (expanded sweep)

20 kV/div.



2 μ s/div.

b) Output Current Block

Fig. 6 Mod/Reg Output Response

References

1. Douglas B. Remsen, Jr., and Trevor H. Overett, "8 KVA Modulator Regulator For Neutral Beams", 1980 Fourteenth Pulse Power Modulator Symposium, June 3-5, 1980

A THYRATRON INVERTER CIRCUIT TO DRIVE A CAPACITIVE LOAD FOR THE PRODUCTION OF OZONE

H. Menown, B. P. Newton,
R. Sheldrake, R. L. Snelling
English Electric Valve Co., Ltd., U.K.

Ozone (O_3), a very powerful oxidising agent, is being used increasingly on an industrial scale for the purification of water and effluent. Since ozone is an unstable oxygen molecule and therefore difficult and expensive to transport, it is much more economic to manufacture on site as demand requires.

A highly efficient method for producing ozone has been developed whereby air is passed between electrodes on which a high voltage, high frequency square wave is impressed. The special inverter circuit used to drive the ozone generating cell is described, and the factors defining the choice of a suitable thyatron within the range of 30 kW to 1 MW are discussed.

Some types of load which are presented to inverter circuits are mainly capacitive and foremost among these are pulsed electrostatic precipitators and ozone generators.

The latter is particularly relevant and it may be worth while to discuss in brief the reason for its use.

Ozone is a very powerful oxidant and as such is used extensively in water and effluent purification plants. When made, ozone is so poisonous and so readily recombines with many substances that it is very difficult to transport. Thus it is usually made on site and used immediately. Ozone is the product of high voltage stress acting upon oxygen and as everyone who has dealt with high voltage equipment will know is not difficult to manufacture! In the water treatment plants it is usually made by passing air through co-axial pipes (capacitors) across which a voltage is impressed.

Low frequency A.C. voltages of say 12 kV rms and 50/60 Hz are used but these plants are so large and bulky that it has become necessary to condense their size and one way to achieve this has been to introduce high frequency systems (up to 3 kHz) which reduce the size of the equipments by between 10 and 20 times for the same output.

Thyristors can be employed but thyratrons possess a natural advantage in that they are

high voltage, high speed switches and, as such, can offer an extremely simple system without step up transformers.

Another advantage of thyratrons is their ability to readily operate at variable frequencies. For all other things being equal, the power output to the load is directly proportional to the frequency of operation.

As already stated, the load is of co-axial form with the flowing air stream forming the dielectric. Such a load is completely capacitive until ozone is formed. The only energy absorbed is by breakdown of the air. This may be represented as a perfect capacitor with a resistor in series.

Consider what happens when a perfect capacitor is charged from a no loss inverter circuit such as is shown in Fig. 1.

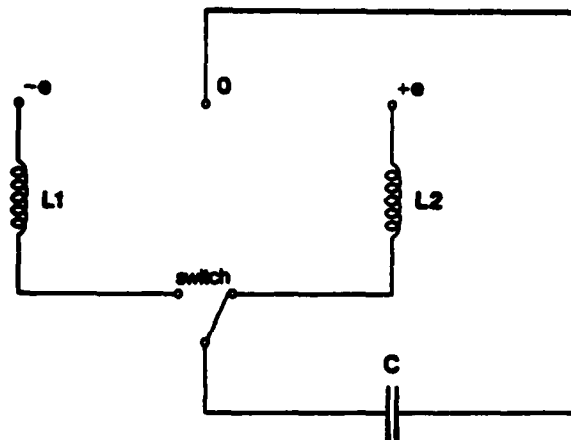


Figure. 1.

The first operation of the switch causes an inductive swing of $2e$ to be impressed on a capacitor. The next operation is impressed upon a capacitor which is already charged, therefore, $4e$ appears across it, then, successively, $6e$, $8e$ and so on. (Fig. 2).

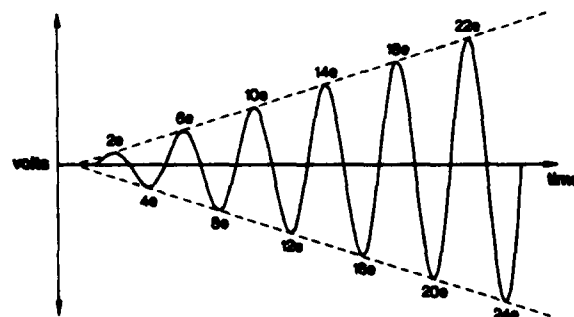


Figure. 2.

This behaviour is modified by the inclusion of a resistor in series with the capacitor. Fig. 3.

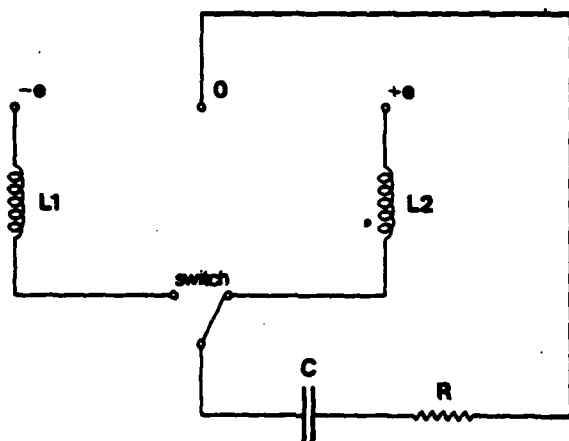


Figure. 3.

with $R = 0$ the voltage swings are as in Fig. 2 and, for a value of $R = 2\sqrt{\frac{L}{C}}$ which critically damps the circuit, the voltage across the circuit remains at $2e$. For other values between 0 and $R = 2\sqrt{\frac{L}{C}}$ the voltage across the capacitor increases but more slowly than in Fig. 2. Thus with values of R less than critical the circuit is unstable.

With a load such as an ozonizer we are fortunate that the process is self compensating; for, as the voltage rises the energy dissipation increases so does the series R , and as the voltage falls, so do the losses and the series R .

It can thus be seen that for this type of load, a very simple and efficient circuit can be made with a minimum of components. It is completely stable without feedback loops or other introduced controls.

Practical Circuit

Apart from the feed, trigger and safety circuits the only components used are the thyratrons and inductors, and with respect to these latter it is important to remember that losses in the circuit have the same effect as a series R , and, in the practical case the inductors $L1$ and $L2$ are air cored.

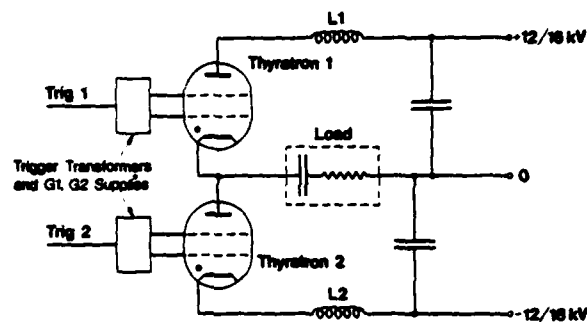
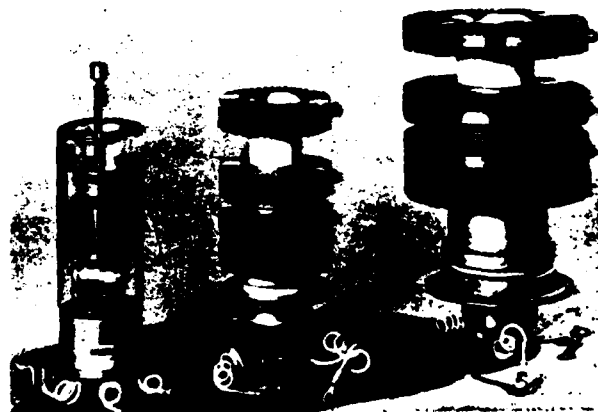


Fig. 4. Practical Circuit
Tube Life

In an industrial environment such as the one described, tube reliability and life are of paramount importance, and at the lower levels of power operation, running costs are also extremely important. Therefore, at the 30 kW level a long life glass tube based on the CX1159 has been produced. The aim is to provide at least one year continuous operation at full power and, although it is too early to be able to quote statistics, results look promising. In the case of 300 kW and 1 MW levels, two tubes already exist which have been specifically designed for continuous, industrial duty. These are the CX1526 and CX1527 respectively.



CX1552 CX1526 CX1527

Figure. 6.

Acknowledgements

The authors wish to thank the Directors of the English Electric Valve Co. Ltd. for permission to publish this paper.

Continuous Power Level	Supply Voltage	Pk Current Per Tube	Pulse Width	Average Current	Max. Frequency	Inductor Value	Tube Type
30 kW	12 kV	50 A	25 μ s	2.5 A	3 kHz	5 mH	CX1552
300 kW	15 kV	150 A	50 μ s	20 A	2.5 kHz	3.5 mH	CX1526
1 MW	16.5 kV	500 A	100 μ s	60 A	2 kHz	2.5 mH	CX1527

Fig. 5.

VACUUM ARC SWITCHED INVERTER OPERATION AT 10 KHZ*

A. S. Gilmour, Jr. and R. F. Hope III
State University of New York at Buffalo
4232 Ridge Lea Road
Amherst, NY 14226

R. N. Miller
University of Central Florida
7300 Lake Ellenor Drive
Orlando, FL 32809

Summary

This paper describes recent major advances in the operation of a vacuum arc switched inverter. Two alternately ignited vacuum arc switches have been used in a series-capacitor inverter circuit operating at frequencies up to 10 kHz for periods up to 0.2 second. The operating period has been limited by the power source, and not by the switches or the inverter circuit. Unloaded circuit operation will be described for ac current levels up to 1000A. Loss measurements at 10 kHz on all circuit elements, including the vacuum arc switches and the inverter transformer with its integral bridge rectifiers** will be reported. Finally, operation of the inverter under load will be described.

Introduction

A program of research and development on vacuum arc switched inverters is being carried out at the State University of New York at Buffalo (SUNYAB). Figure 1 shows the circuit diagram of the inverter, which is referred to as a half-bridge series-capacitor inverter. (1)

The circuit operates by alternately triggering VAS 1 (vacuum arc switch⁽²⁾ #1) and VAS 2. As each switch conducts a half-sinusoidal current waveform (with amplitude and period controlled primarily by the inductance and capacitance) is generated. Thus, the current waveform in the primary winding of the transformer is nearly sinusoidal. The bridge rectifier and filter capacitor convert the secondary transformer voltage to dc for application to the load.

Significant characteristics of the series capacitor inverter are:

- High efficiency
- Low weight and volume
- Relative insensitivity to load faults
- Ease of load regulation

Efficiencies of over 95 percent are expected to be achievable in very high-power versions of this circuit. These high efficiencies result from the sinusoidal nature of the operating waveforms and from the fact that switching occurs when the current in the circuit is zero. Of course, low-loss components and proper assembly techniques are also essential for high efficiency.

* Supported by the Air Force Aeropropulsion Laboratory through The Southeastern Center for Electrical Engineering Education, Contract F 33615-77-C-2059.

** Provided by Thermal Technology Laboratory, Inc.

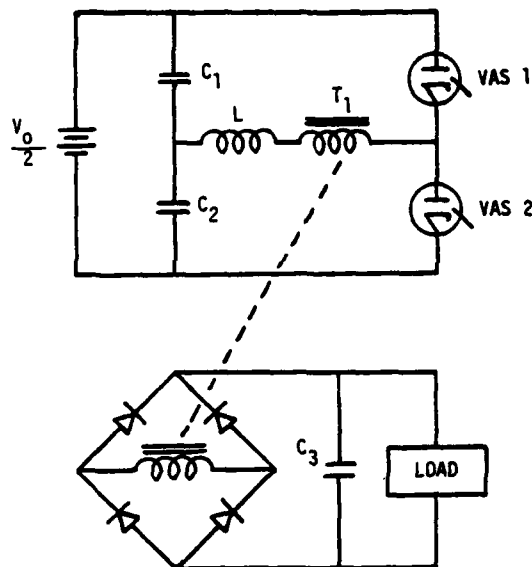


Figure 1. Circuit diagram for vacuum arc switched inverter.

Low weight and volume result from circuit operation at high frequencies. In the SUNYAB work, frequencies near 10 kHz are used. As a result, the series capacitors (C_1 and C_2 in Figure 1) have values of only 5 μF . An air core toroidal inductor (toroidal to minimize stray flux and associated losses) is used having an inductance of only 30 μH . The filter capacitor is about 0.1 μF when a 60:1 transformer and a 3 k Ω load are used.

The inverter is relatively insensitive to load faults because the current amplitude is controlled primarily by the inductance and capacitance.

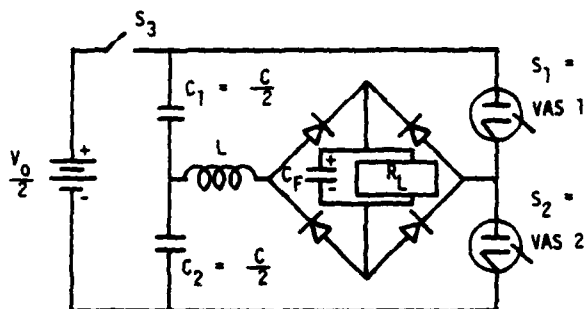
Load regulation is readily accomplished by controlling the triggering frequency of the switches. At low triggering frequencies the half-sinusoids of current are widely spaced and so the average current to the load is low. As triggering frequency is increased, current to the load is increased.

Single cycle and burst mode operation of the vacuum arc switched inverter have previously been described. (3) (4) (5) Recently, significant advancements in inverter operation have been achieved. The circuit has been operated at frequencies up to 10 kHz

for periods up to 0.2 sec. The operating period was limited by the power source, and not by the inverter. With the circuit unloaded (no transformer, rectifier or load attached to the circuit) operation at power levels in excess of one megawatt have been simulated. That is, the currents and voltages in the circuit were the same as they would be in a loaded circuit operating in excess of one megawatt. In addition, the circuit has been operated with the transformer, rectifier and load attached at power levels of a few tens of kilowatts. This paper describes the inverter circuit development and the results achieved.

Inverter Circuit Operation

The principles of operation of the inverter circuit are straightforward. To analyze the operation, assume first that the inverter transformer (T_1 in Fig. 1) is ideal. Then, the loaded bridge along with the filter capacitor may be transformed to the primary circuit as is shown in Fig. 2.



C_F = Transformed Filter Capacitance

R_L = Transformed Load Resistance

Figure 2. Inverter circuit after the transformation of the loaded bridge and filter capacitor to the primary circuit.

Next, assume:

- All circuit components are lossless.
- Switches S_1 and S_2 are ideal.
- The transformed capacitance, C_F , is much larger than C_1 and C_2 .

The initial operating conditions are that the voltages on capacitors C_1 and C_2 (V_{C_1} and V_{C_2}) are one half of the supply voltage, V_0 ; C_F is discharged; and switches S_1 and S_2 are open.

At time $t = 0$, if switch S_2 is closed, then the circuit in Fig. 2 becomes the equivalent circuit shown in Fig. 3. The waveforms for the current, I , for the voltage, V_C , across the series capacitor and for the

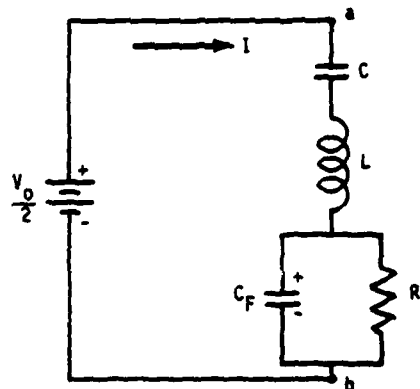


Figure 3. Equivalent circuit when S_2 is closed.

load voltage, V_L , are shown in Fig. 4. The current waveform is very nearly sinusoidal and the voltage waveforms are nearly cosinusoidal. The load voltage is much smaller than V_C because $C_F \gg C$. At the end of one half cycle, operation ceases because switch S_2 stops conducting.

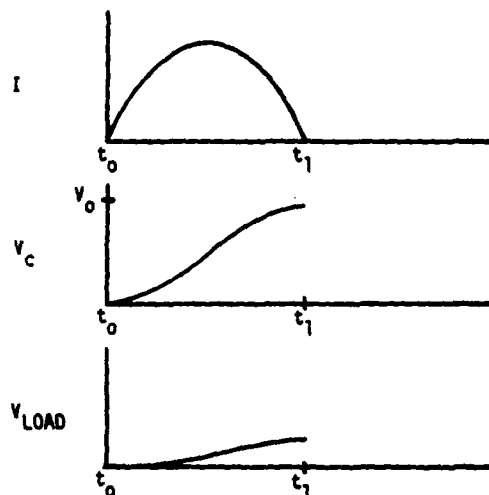


Figure 4. Waveforms for the current I , the series capacitor voltage V_C , and the load voltage, V_L , for the first half cycle of inverter operation.

The second half cycle of operation begins when switch S_1 closes. The equivalent circuit is shown in Fig. 5. Note that the operation of the switches (the bridge diodes as well as S_2 and S_1) has reversed points a and b relative to the source voltage but that the polarity of the load voltage relative to the source voltage is unchanged. Also, the initial voltage on C (which was the voltage on C at the end of the first half cycle of operation) is series aiding to the source voltage.

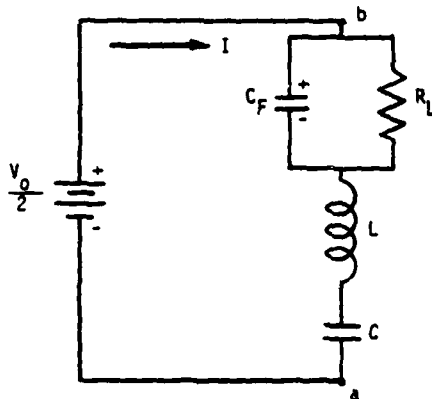


Figure 5. Equivalent circuit for the second half cycle of inverter operation.

The waveforms for the second half cycle (as well as the first) are shown in Fig. 6. Note that the maximum current is three times the value during the first half cycle. The series capacitor voltage, V_C , which reached a maximum value of V_o at $t = t_1$, reverses and goes to a maximum value of $2 V_o$ at the end of the second half cycle. The load voltage continues to increase during this half cycle because of the bridge rectifiers.

Figure 6 also shows the effect of R_L on the current I and the series capacitor voltage V_C . As can be seen (the dotted curves in the figure), when the load R_L has a value of 0, the magnitudes of the current I and the voltage, V_C , are at their greatest possible values. However, when the load $R_L \neq 0$, then I and V_C will have values less than the maximum values (as shown by the solid curves in the figure).

Except for the initial voltages on the series capacitor and the load, the analysis of the third and subsequent half cycles will be very similar to that of the first and second half cycles. As the inverter oscillates, the gradual increase of current and voltage will continue. The peak current value for the first half cycle was I_o ; for the second half cycle, it was near $3 I_o$. If the load resistance was 0, then the current would go to $5 I_o$, $7 I_o$, $9 I_o$, ..., increasing to infinity, as long as there is no loss in the circuit. If there is a load, then the current would build up to a steady state value.

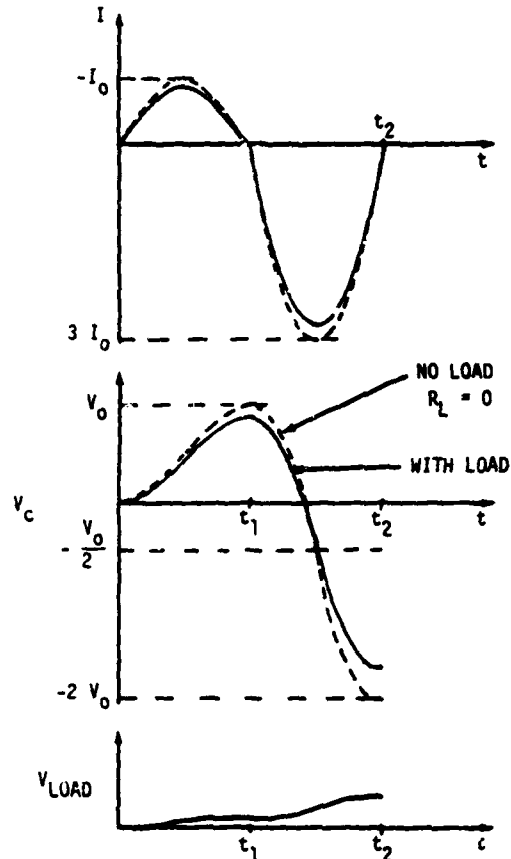


Figure 6. Waveforms for the current I , the series capacitor voltage V_C , and the load voltage, V_L , for the second half cycle of inverter operation.

The series capacitor voltage V_C also builds up as the circuit oscillates. If the load resistance is zero, then the voltage V_C would go as V_o , $2 V_o$, $3 V_o$, ..., to infinity. If there is a load, then the voltage V_C would build up to a steady state value.

The steady state condition occurs when the load voltage is very nearly equal to one half of the source voltage. The current and voltage waveforms from initial start up to steady state are shown in Figure 7.

At steady state, the average load current is

$$\begin{aligned} I_{L(\text{avg})} &= \frac{2}{\pi} I_{\text{peak}} \\ &= \frac{V_L}{R_L} \\ &= \frac{V_o}{2R_L} \end{aligned}$$

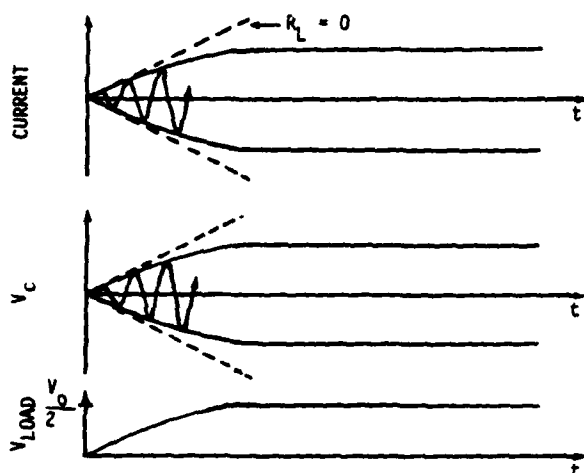


Figure 7. Current and voltage waveforms from initial start up to steady state.

and the capacitor voltage, V_C is

$$V_C = I_{\text{peak}} \sqrt{\frac{L}{C}}$$

where I_{peak} is the peak value of the ac current.

Use of Vacuum Arc Switches

The switching elements to be used in the inverter are required to have the following capabilities:

- Fast recovery time
- High voltage
- High current
- High frequency operation (10 kHz and over)

SCR's have conventionally been used as inverter switching elements. But at high power levels and high frequencies, SCR's must be substantially derated in current and voltage. As a result, series and parallel combinations of SCR's are required. The recovery time of an SCR is also a problem. At the very best, high power SCR's have a 7 μ s recovery time.

Since improved switching elements are needed for high power, high frequency applications, vacuum arc switches are being investigated for this application. In a vacuum arc switch, the constituent material of the negative electrode is vaporized and ionized by arc spots to provide the conducting medium.⁽²⁾ A vacuum arc discharge is an almost ideal medium for use in switching because it makes possible a high vacuum device having excellent insulation properties

when nonconducting and it becomes a plasma discharge device which, depending on the configuration of the electrodes, has a low voltage drop and high current capacity during conduction. Arc ignition in the SUNYAB vacuum arc switches is accomplished by applying a pulse of current sufficient to vaporize a portion of a thin metallic film on an insulator between the cathode and an igniter electrode.

The following capabilities have been demonstrated for vacuum arc switches:

- High voltage (10's of kilovolts)
- High current (kiloamperes to 10's of kiloamperes)
- Good recovery time ($\sim 2 \mu$ s demonstrated to date)

Thus, vacuum arc switches are superior to SCR's in all of these critical areas.

The primary deficiency in vacuum arc switches at this time is short life. For many applications, such as in certain multi-megawatt inverters for military use, the life demonstrated to date is adequate. In other cases, where long life is required, new concepts presently being considered at SUNYAB, must be developed.

Realities of Circuit Operation

The primary concern here is to assure that switch faults do not occur. The voltage source driving the inverter will be shorted if both switches (S_1 and S_2 in Fig. 2) conduct at the same time. A fault is most likely to occur during the recovery time at the end of the conduction period of a switch. If one of the switches has not fully recovered before the other is switched on, then there is high probability that both switches will conduct simultaneously. As a result, as is shown in Figure 8, there must be "off" periods between half cycles of operation. Clearly, the "off" period must be greater than the switch recovery time. For example, since vacuum arc switches have recovery times of $\sim 2 \mu$ s or less, the minimum "off" time must be no less than 2 μ s. For the high power SCR which was described in a previous section, the minimum delay time can be no less than 7 μ sec since the recovery times for those devices are 7 μ sec or greater. The duration of the "off" period not only depends on the type of switch used, but also on the frequency of operation and the power level of the circuit.

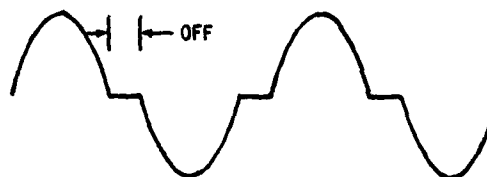


Figure 8. Current waveform with non conducting "off" period between half cycles of operation.

Next, the timing of switch conduction must be considered. The most important point here is to time the triggering of a switch on the basis of the end of the previous switch conduction period. The reason for doing this is shown in Figure 9. As can be seen, the time t_c at which conduction is initiated should be based on time t_b plus a predetermined delay, rather than on time t_a . Then the possibility of conduction overlap resulting from a triggering delay or an irregularity in conduction is avoided.

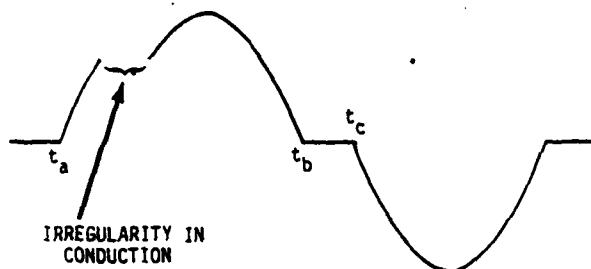


Figure 9. Switch triggering on basis of end of previous switch conduction period.

For high efficiency, of course, losses must be minimized. Some of the factors important in minimizing loss are:

- Litz wire should be used to reduce skin effect losses which occur at high frequencies.
- Torroidal inductors should be used since they generate very little stray magnetic flux.
- The capacitor dielectrics must have extremely low dissipation factors. Silicone oil and polypropylene are the best at present.
- V_o should be bypassed.
- Low loss bushings must be used throughout the circuit.

The accurate measurement of losses at high current levels and at resistance levels on the order of milliohms has previously been reported. (3) The technique is to use the ac elements of the circuit in series with a "perfect" switch and then to resonate the circuit. The resistive loss can be computed from the resulting exponential decay curve. The "perfect" switch consists of a pointed brass rod, a thin sheet of teflon (on the order of a few thousands of an inch thick) and a lead pad. The switch is activated by striking the brass rod with a hammer.

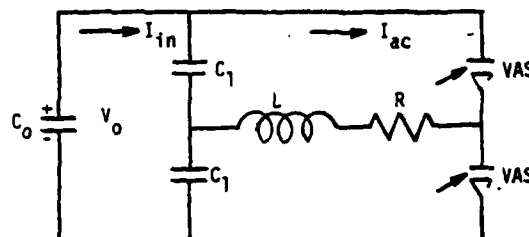
The major advantages of the resonance test method are:

- The technique is extremely simple and fast.
- Very accurate results are obtained.
- The test can be performed at full power.

- The test can be performed at the normal operating frequency.
- Non linearities can easily be detected from variations in the time constant.

Using this technique the overall circuit loss was reduced by a factor of 10 (from 0.1 Ω to 0.01 Ω).

Next, the losses of the circuit including the vacuum arc switches (VAS's) were determined. The circuit elements and quantities of significance are shown in Figure 10. To help in understanding the



C_o PROVIDES ENERGY SUPPLY (40,000 μF)

$C_1 = 5 \mu F$ SILICON OIL, POLYPROPYLENE

$L = 27 \mu H$ TORROIDAL INDUCTOR

$R =$ RESISTIVE LOSS OF CIRCUIT AND SWITCHES

Figure 10. Circuit elements and quantities of significance in analysis of inverter loss.

measurements that were made, a simple power flow analysis is required. With no load, under steady state operating conditions, the power supplied to the circuit, P_{in} , is equal to the power dissipated, P_{loss} . So,

$$P_{in} = P_{loss}$$

Assuming that all losses occur in R and as the result of the cathode-fall voltage, V_c , in each switch, then

$$\frac{2}{\pi} I_{in} V_o = \frac{1}{2} I_{ac}^2 R + \frac{2}{\pi} I_{ac} V_c$$

But,

$$I_{in} = \frac{1}{2} I_{ac}$$

so

$$\frac{1}{\pi} I_{ac} V_o = \frac{1}{2} I_{ac}^2 R + \frac{2}{\pi} I_{ac} V_c$$

$$\text{or } V_o = \frac{\pi}{2} I_{ac} R + 2 V_c$$

Thus, a plot of V_o vs I_{ac} should be a straight line with a slope of $\frac{\pi}{2} R$ and an intercept of $2 V_c$.

Steady state values of operating parameters of the circuit were determined by precharging one of the capacitors (C_1) to the voltage that it would have during steady state operation for a given input voltage, V_o .

The resulting data are shown in Figure 11, with a straight line drawn through the data points. Note that the intercept occurs at 40 volts, which indicates that the cathode fall voltage is 20 volts. From the slope of the line through the data points, R is determined to be .047 ohm. Now, since the resistance of the inductor and capacitor portions of the circuit were determined to be .011 ohm from the hammer switch tests, then the resistance of each vacuum arc switch must be .036 ohm. A portion of this resistance is in the switching plasma and the remainder in the cathode and anode feedthroughs and connections.

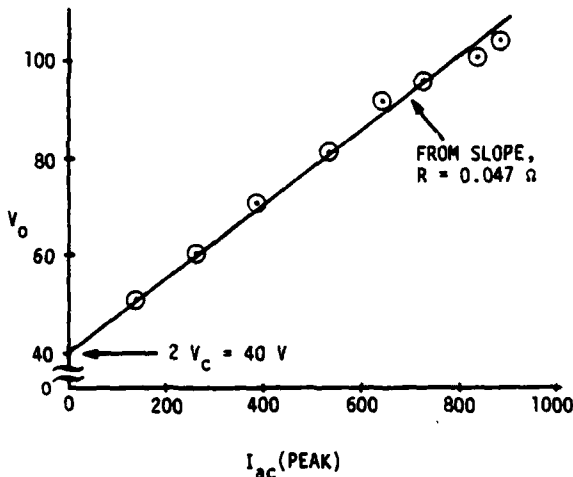


Figure 11. Plot of V_o vs I_{ac} is a straight line of slope $\frac{\pi}{2} R$ and intercept $2 V_c$.

Following the switch loss measurements, open and short circuit tests were performed, using the hammer switch technique, on the 200 kVA inverter transformer supplied by Thermal Technology Laboratory, Inc. This transformer is pie wound and contains 32 pie sections. The 32 individual primary windings are connected so that there are 16 pairs of windings all connected in parallel. The dc resistance of the resulting primary is calculated to be .0134 ohm. Each of the 32 secondary windings is connected to a full-wave bridge rectifier and the 32 bridge rectifiers are in series.

The total dc resistance of the secondary windings is calculated to be 33.4 ohms. The current-voltage characteristic for the diodes used in the bridge rectifiers is shown in Figure 12. The transformer turns ratio is 55.6:1.

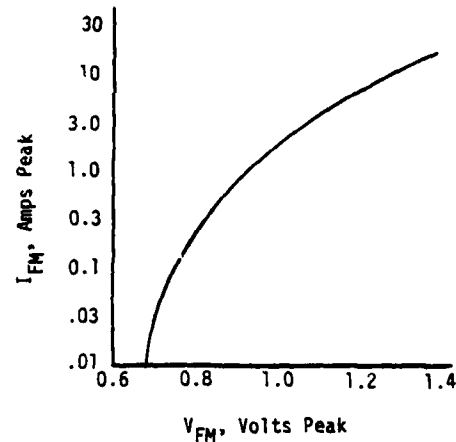
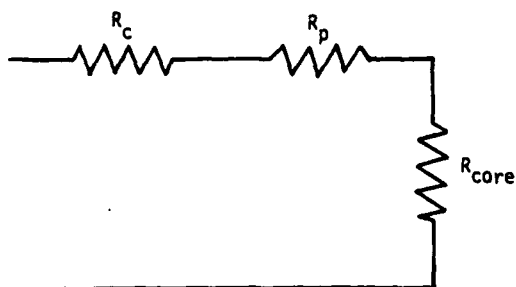


Figure 12. Typical instantaneous forward characteristics of General Instrument Corporation RGP 30 series rectifiers.

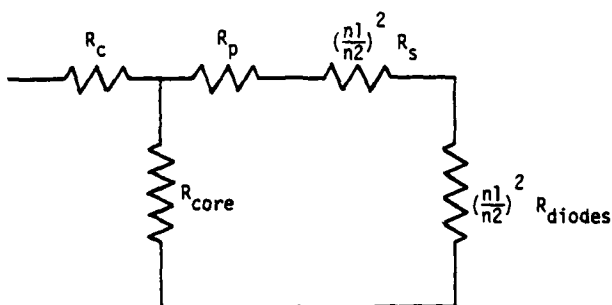
In the open circuit measurement the resistances involved, as is shown in Figure 13a, were the circuit resistance, R_c , which has been determined to be .0105 ohm; the primary resistance, R_p , and a resistance to represent the core loss, R_{core} . The resistance measured during the open circuit tests was .336 ohm so that the sum of R_p and R_{core} was .325 ohm. Thus, as would be expected, R_{core} was very large compared with the wire resistances.

Because R_{core} was large, the circuit for the short circuit tests can be represented as is shown in Figure 13b. The resistance measured during the short circuit tests was .108 ohm so that the transformer resistance was .097 ohm. Thus, the wire and diode resistance, reflected in the primary, was .138 ohm. Now, the complication in trying to compare the measured resistance with the calculated value is the nonlinear characteristics of the diodes. This was illustrated in Figure 12. A crude estimate of the expected resistance can be obtained by modeling the diodes as resistors. The short circuit tests were performed with a secondary current on the order of one ampere. At this current the diode voltage drop was about one volt so the resistance could be considered to be on the order of one ohm. The total number of diodes in series in the bridges during conduction was 64 so that the total diode resistance could be considered to be on the order of 64 ohms. This resistance was in series with the 33.4 ohm secondary winding. When transformed into the primary circuit, the equivalent secondary resistance was .632 ohm. This resistance added to the primary resistance of .013 ohm gives a calculated

resistance for the short circuit tests of .045 ohm, which is about one third of the measured value. The reasons for this discrepancy are not understood at present.



a) Open Circuit



b) Short Circuit

Figure 13. Resistive portions of transformer test circuits.

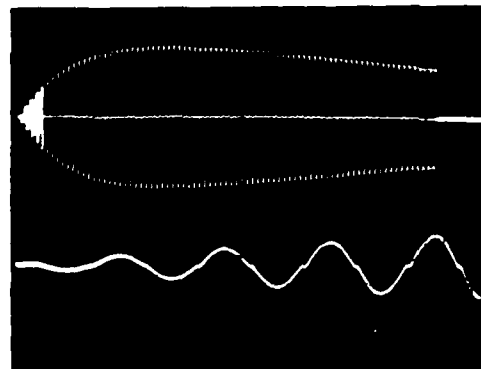
High Power Results

Unloaded and loaded high power tests have been carried out on the inverter. The results of these tests are as follows.

Unloaded Results

Unloaded testing was carried out with no load, filter capacitor, bridge rectifier or transformer in the circuit. Current and voltage amplitudes were limited only by circuit losses. Figure 14 shows an excellent example of the current waveform. The top trace shows the gradual buildup of current to its steady state value.* The bottom trace is a time expansion of the bright area of the top trace and this shows the initial buildup of current.

* It should be noted that the decreasing magnitude of the current waveform (after its greatest peak value) is due to an inadequate power supply. The current would not decrease if there was an adequate supply available.

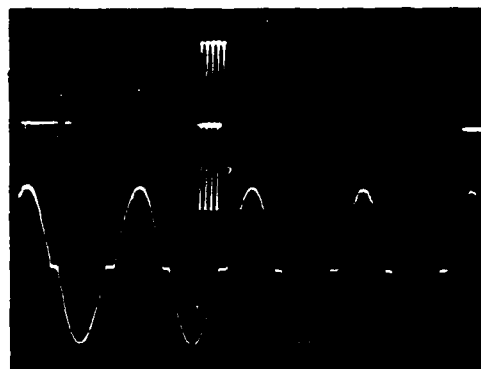


Upper waveform: 1 ms/div

Lower waveform: 50 μ s/div; 800 A/div

Figure 14. Current waveform shows gradual buildup to steady state.

The steady state condition of the current waveform is shown in the lower trace of Figure 15. Note that the "off" time between conduction cycles is clearly shown here.



Upper waveform: 1 ms/div

Lower waveform: 50 μ s/div; 800 A/div

Figure 15. Bottom trace shows steady state current waveform.

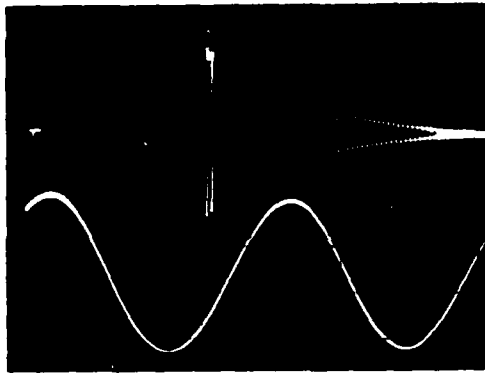
A switch fault is shown in Figure 16. Here it can be seen that the energy in the circuit oscillates at the resonant frequency of the circuit and decays exponentially.

To date, operating levels that have been achieved for unloaded inverter operation are:

Currents > 1 kA

Voltages > 1 kV

Effective power levels > 1 MW

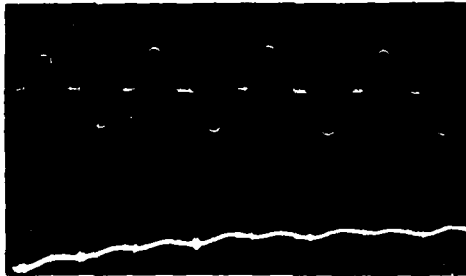


Upper waveform: 1 ms/div
Bottom waveform: 20 μ s/div; 400 A/div

Figure 16. Current waveform resulting from a switch fault.

Loaded Results

Next, loaded (200 kVA transformer, 3 k Ω load and 0.1 μ F filter capacitor) test results will be given. The top trace of Figure 17 shows the wave shape of the current in the primary winding of the transformer. Note that this waveform is the same as that for the unloaded case. The load voltage is shown in the bottom trace. Here it can be seen that the load voltage slowly builds up to its steady state value.



Upper waveform: 50 μ s/div; 400 A/div
Lower waveform: 50 μ s/div; 5 kV/div

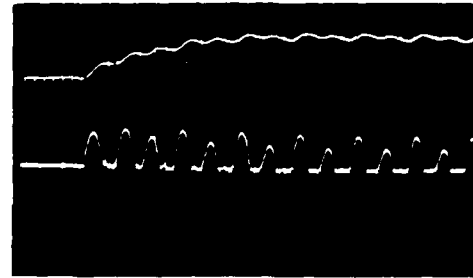
Figure 17. The primary current I (top trace) and load voltage V_L .

The load voltage and load current are shown in Figure 18. Notice that the load current stays fairly constant as the load voltage slowly builds up.

To date, power levels that have been achieved for loaded inverter operation are:

- Voltages \sim 10 kV
- Current \sim 3 A (avg.)
- Load power \sim 30 kilowatts

Loaded testing is continuing with the objective of achieving operation at the full 200 kVA rating of the transformer. New compact vacuum arc switches are being fabricated. These switches, which should be capable of operation to power levels in excess of one megawatt, are only 3 inches in diameter and 4 1/2 inches long.



Upper waveform: 0.1 ms/div; 5 kV/div
Lower waveform: 0.1 ms/div; 8 A/div

Figure 18. The load voltage V_L (top trace) and the primary current I.

Conclusions

To date, testing of the vacuum arc switched inverter has produced the following conclusions:

- Very good agreement is found between theoretical and experimental results.
- Inverter circuit operation at high power levels has demonstrated successful use of vacuum arc switches.
- The resonance loss measurement technique is simple, fast, reliable and accurate.
- Successful loaded test results show promise for the use of the vacuum arc switched inverter for future pulse power applications.

References

1. F. C. Schwarz, "Controllable, load insensitive power converters," U.S. Patent 3,663,940, May 1972.
2. A. S. Gilmour, Jr. and D. L. Lockwood, "Interruption of vacuum arcs at high dc voltages," IEEE Trans. Electron Devices, vol. ED-22, A4, 1975.
3. A. S. Gilmour, Jr. and D. C. Hopkins, "Recent results of vacuum-arc switched multimegawatt inverter tests," Proc. International Pulsed Power Conference, Texas Tech. University, Lubbock, Texas, Nov. 1974.
4. R. N. Miller, C. J. King, A. Pedano, R. Dollinger and A. S. Gilmour, Jr., "A multi-megawatt vacuum arc switched inverter for airborne applications," IEEE Conference Record of 1978 Thirteenth Pulse Power Modulator Symposium, Buffalo, N.Y., June, 1978.
5. R. N. Miller and A. S. Gilmour, Jr., "Vacuum arc switched inverter tests at 2.5 MVA," Proc. IEEE 2nd International Pulsed Power Conference, Texas Tech. University, Lubbock, Texas, June 1979.

COMMUTATION SWITCH VOLTAGE LIMITING BY CURRENT WAVEFORM CONTROL

A. S. Gilmour, Jr.
State University of New York at Buffalo
4232 Ridge Lea Rd.
Amherst, NY 14226

Summary

In some high power switching devices¹, the current waveform can be controlled by the device. As a result, it is possible in a commutation circuit to tailor the current waveform so that excessive voltage does not appear on the switching device during commutation. The ideal current waveform, when stray inductances are taken into consideration and a parallel capacitance is used, is cosinusoidal. Switching times, energies, and voltages will be discussed. In the case of the vacuum arc switch, the magnetic field waveform will be described along with the effects of deviations from the ideal waveform.

Introduction

When an opening switch is used for current commutation, large voltage transients may be produced that may cause damage to the switch and/or prevent the switch from opening properly. In an opening switch in which the current waveform can be controlled, these voltage transients can be controlled or even eliminated. As the following analysis shows, the ideal switch current waveform is cosinusoidal with a period equal to the period of the series resonant circuit consisting of stray inductances and a voltage limiting capacitor.

Analysis

The following is an analysis of the voltage appearing at the terminals of a commutation device, CD, during the commutation process. The circuit considered is shown in Figure 1. The capacitor, C, limits the rate of rise of voltage on CD and the resistor, R, may be used as a final energy dump. Inductors L_1 , L_2 & L_3 are stray inductances.

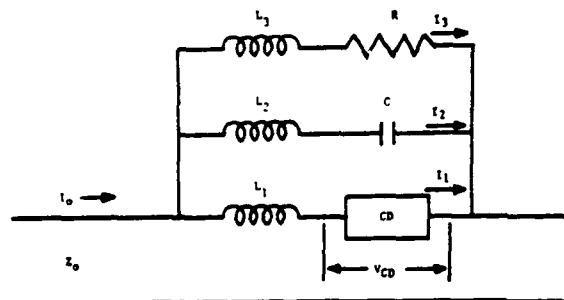


Figure 1. Circuit considered in commutation voltage analysis.

The commutation circuit is assumed to be in series with an inductive circuit carrying current I_0 . For the purposes of this analysis, it is assumed that the commutation process occurs in a few microseconds. During this period, the inductive circuit appears as a current source so that I_0 remains constant during the commutation process.

The variation of current I_1 as a function of time is assumed to be an independent variable that can be controlled in the design of the commutation device. For example, in the vacuum arc switch⁽¹⁾, the dependence of the current through the device on the applied magnetic field is

$$I = \frac{I_0}{1 + KB^2}$$

where I_0 is the current when the field B is zero.

The factor K in the above expression is a constant. The variation of current with time can be controlled by controlling the variation of magnetic field with time.

Because the commutation times to be considered are small and because the currents are large (kiloperes to tens of kiloperes), it is necessary to include in the analysis the effects of stray inductances. It is anticipated that the values of L_1 and L_2 , which would probably consist primarily of lead inductances, would be only a few microhenries. The value of L_3 would probably be an order of magnitude larger than L_1 and L_2 because it would consist primarily of the inductance of resistor R . Because of the necessity for this resistor to dissipate large pulses of energy it would necessarily have large dimensions and a relatively large inductance (compared with L_1 and L_2). During the commutation period, the voltage across the commutation device, V_{CD} is controlled primarily by the charging of capacitor C and by the inductive surges produced by L_1 and L_2 . The voltage across C is

$$V_C = \frac{1}{C} \int_0^t I_2 dt.$$

and the voltage across CD is

$$V_{CD} = \frac{1}{C} \int_0^t I_2 dt + L_2 \frac{dI_2}{dt} - L_1 \frac{dI_1}{dt}$$

but

$$I_2 = I_0 - I_1 - I_3$$

so

$$V_{CD} = \frac{I_0}{C} t - \frac{1}{C} \int_0^t I_1 dt - \frac{1}{C} \int_0^t I_3 dt - L_2 \frac{d}{dt} (I_1 + I_3) - L_1 \frac{dI_1}{dt}$$

Now, an acceptable solution to this equation can be obtained by first examining qualitatively what is happening during commutation. As CD opens, current is first transferred rapidly to C because L_1 and L_2 are small compared with L_3 . Then, current is gradually transferred to the L_3 -R circuit. These events are shown in Figure 2.

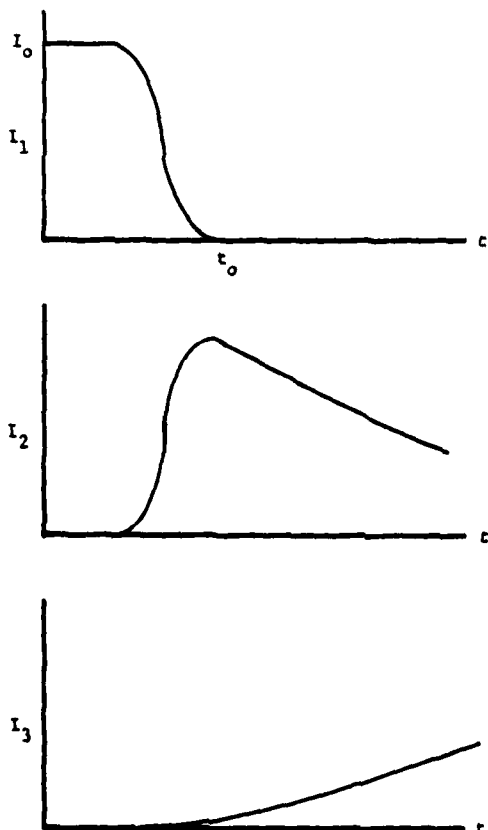


Figure 2. Current waveforms as a function of time during commutation.

Thus, it is seen that when t is small, I_3 is negligible. When t is large, I_1 and dI_1/dt are negligible. At all times, dI_3/dt is small. Thus, the equations for V_{CD} for small and large times are as follows:

for small t ,

$$V_{CD} \Big|_{t \text{ small}} = \frac{I_0}{C} t - \frac{1}{C} \int_0^t I_1 dt - (L_1 + L_2) \frac{dI_1}{dt}$$

and for large t ,

$$V_{CD} \Big|_{t \text{ large}} = \frac{I_0}{C} t - \frac{1}{C} \int_0^t I_1 dt - \frac{1}{C} \int_0^t I_3 dt$$

where, even though I_1 is small, the integrated effect of I_1 may be large. Once I_1 has been specified, V_{CD} can be readily determined for small times. For large times, it is possible to carry the analysis further because

$$V_{CD} \Big|_{t \text{ large}} = I_3 R$$

so, for large t

$$I_3 R = \frac{I_0}{C} t - \frac{Q_1}{C} - \frac{1}{C} \int_0^t I_3 dt$$

where

$$Q_1 = \int_0^{t_0} I_1 dt$$

so

$$I_3 = I_0 \left(1 - e^{-\frac{t}{RC}} \right) - \frac{Q_1}{RC} e^{-\frac{t}{RC}}$$

This means that for large times, the voltage across the commutation device is

$$V_{CD} \Big|_{t \text{ large}} = I_0 R \left(1 - e^{-\frac{t}{RC}} \right) - \frac{Q_1}{C} e^{-\frac{t}{RC}}$$

By choosing some representative values for parameters, it is possible to estimate the commutation voltage at the end of the commutation process. For example, if $I_0 = 10$ kA, $R = 10 \Omega$, $C = 1 \mu F$ and if it is assumed that the commutation process is completed in $3 \mu s$ with an average value of I_1 of 5 kA so that

$$\frac{Q_1}{C} = \frac{1}{C} \int_0^t I_1 dt = 15 \text{ kV},$$

then V_{CD} for times greater than $3 \mu s$ is as shown in Figure 3. Note that, for a commutation time of $5 \mu s$ or less, the voltage across the commutation device does not exceed 25 kV.

The next step in the analysis is to examine V_{CD} during commutation for various functional forms of I_1 . For a vacuum arc switch, a magnetic field that increases linearly with time until interruption occurs is frequently used. The variation of current with time is therefore

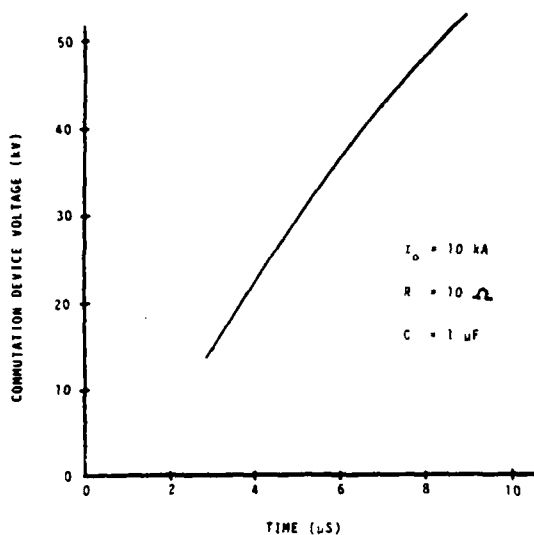


Figure 3. Commutation device voltage as a function of time for large times.

$$I_1(t) = \frac{I_0}{1 + \left(\frac{t}{\tau}\right)^2}$$

and is shown in Figure 4. To insure that $I_1(t)$ is at least in the range of instability (10 A) for an I_0 value of 10 kA, then t/τ should be on the order of 50. For commutation to occur with $t = 5 \mu s$, then $\tau = 10^{-7}$. Shown in Figure 5 is the resulting commutation device waveform for values of t from 0 to 4 μs for the following parameters:

$$\begin{aligned} I_0 &= 10 \text{ kA} & L_1 &= 1 \mu H \\ C &= 1 \mu F & L_2 &= 1 \mu H \\ \tau &= 1 \times 10^{-7} \end{aligned}$$

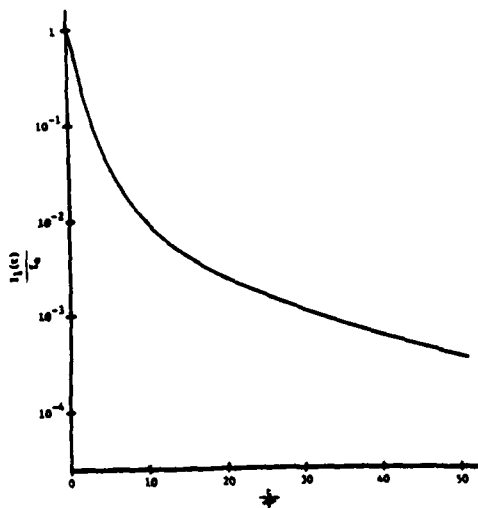


Figure 4. Vacuum arc switch current as a function of time when magnetic field increases linearly with time.

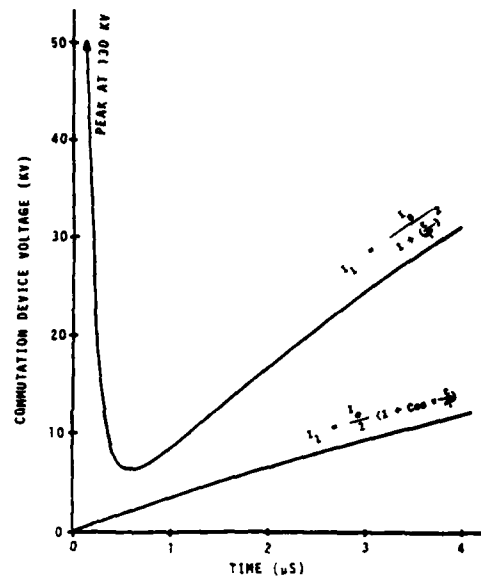


Figure 5. Commutation device voltage as a function of time for small times.

Notice that an extremely large voltage spike occurs for very small values of t . The peak value of this spike is 130 kV. Clearly, it is necessary to reduce the amplitude of this voltage spike to protect the commutation device and the other components of the commutation circuit. It is unlikely that the values of L_1 and L_2 can be substantially reduced, therefore current waveforms that change more slowly with time must be considered. If, for example, a cosinusoidal current waveform such as

$$I_1 = \frac{I_0}{2} (1 - \cos \pi \frac{t}{\tau})$$

is considered, then the commutation voltage becomes the lower curve shown in Figure 5. Notice that the voltage spike has been eliminated and that V_{CD} has been substantially reduced. The reason for this is, of course, that the choice of τ , C , L_1 and L_2 is such that a series resonance condition very nearly exists between C and L_1 and L_2 . It would appear in fact, that if the cosinusoidal current waveform could be produced, then the commutation process could be completed with voltages no larger than 15 kV being applied to the commutation device when

$$\begin{aligned} I_0 &= 10 \text{ kA} \\ R &= 10 \Omega \\ C &= 1 \times 10^{-6} \text{ F} \\ L_1 &= L_2 = 1 \times 10^{-6} \text{ H} \end{aligned}$$

The question remaining is that of the technique required to produce the cosinusoidal current waveform. Assuming that the following relation exists between current and magnetic flux density for the vacuum arc device

$$I_1(t) = \frac{I_0}{1 + K^2 \pi^2 \left(\frac{t}{\tau}\right)^2}$$

Then the flux density must vary as

$$\frac{1}{K} \left(\frac{2}{1 + \cos \pi \frac{t}{\tau}} - 1 \right)^{\frac{1}{2}}$$

There appears to be no reason why a flux density characteristic could not be generated in practice. Thus, it appears that the commutation voltage characteristic shown in Figure 5 for a cosinusoidal commutation current should be achievable.

¹ A. S. Gilmour, Jr. and D. L. Lockwood, "The Interruption of Vacuum Arcs at High DC Voltages," IEEE Transactions on Electron Devices, Vol. ED-11, No. 4, April 1975, pp. 173-180.

DRIVING PARALLEL FLASHLAMPS WITH A COMPENSATED PULSED ALTERNATOR*

B. M. Carder, B. T. Merritt, W. L. Gagnon
Lawrence Livermore Laboratory
P.O. Box 5508
Livermore, California 94550

W. L. Bird, W. F. Weldon, R. C. Zowarka
University of Texas
Center for Electromechanics
Austin, Texas 78712

Abstract

Test results are given for a prototype Compensated Pulsed Alternator that was operated up to its 5400 RPM design speed. The machine has delivered approximately 140 kilojoules of energy in a single 1.3 millisecond pulse into a load comprising sixteen parallel flashlamps. The energy delivered to the lamps follows a $W \propto (\text{RPM}/225)^4$ scaling law to about 4200 RPM. Beyond that speed, eddy current losses become significant with the present design. New codes are able to model the machine parameters, and the prototype is presently being rebuilt to reduce the high speed losses predicted by the codes and verified by experiment.

Summary

A prototype Compensated Pulsed Alternator, or "Compulsator" has been given its first proof of principle demonstration tests. It has been run to full speed -- 5400 RPM -- and it has been repeatedly discharged into a parallel flashlamp load, delivering up to 140 kilojoules of energy in a 1300 microsecond pulse. The purpose of the test was to measure the factors that determine the energy delivered by the Compulsator into a representative flashlamp load. The ultimate goal is to replace a capacitive energy store with a very large inertial energy store of the Compulsator type for new large lasers.

The test results indicate that the energy delivered to flashlamps follows a fourth-power scaling law with machine speed up to about 4250 RPM. At the optimum firing angle of about 45° before minimum inductance, the prototype delivered a net energy of $(\text{RPM}/225)^4$ joules to a 16-parallel lamp load, or 127 kJ at 4250 RPM.

At 4800 RPM, the energy delivered was 139 kJ, or only 67% of the fourth-power prediction. Computer circuit modeling indicated that this deficit is due to a probable eddy-current loss that becomes significant at the higher speeds.

New codes to model the Compulsator have now been developed that are being used to treat this problem quantitatively. A physical mockup of the machine windings has also been made, and tests are underway to

determine the optimum design for rewinding the prototype machine, including the use of eddy-current shields.

A new series of dynamic tests of the prototype Compulsator will be undertaken after the machine is reassembled. The results of this work will be used for the design of a large inertial-store pulse generator for application in very large future laser systems. It is anticipated that the next generation machine will deliver the order of 10 megajoules of energy to flashlamps in less than one millisecond.

Prototype Description

A picture of the prototype Compulsator is given in Fig. 1. It is surrounded by a steel torque frame and housed in a six-foot deep pit. It is driven by a timing belt and a 125 HP DC motor.

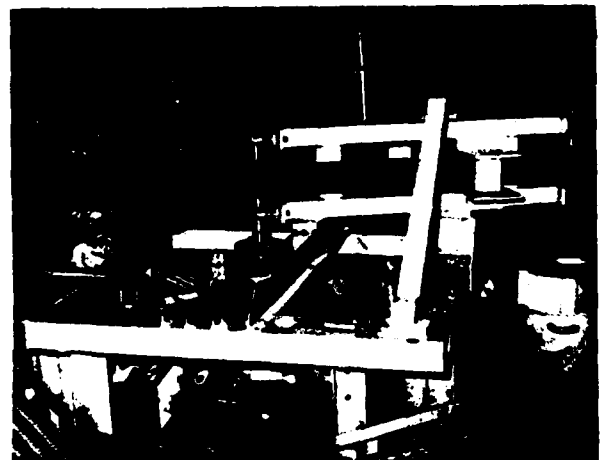


Figure 1. Prototype Compulsator Installation

An outline drawing of the machine is given in Fig. 2. It has a vertical shaft and a 15-inch diameter by four-foot long laminated steel rotor. The torque frame is about five feet square and six feet high

* Work performed by the Lawrence Livermore National Laboratory and the University of Texas at Austin under the auspices of the U.S. Department of Energy under Contract No. W-7405-Eng-48.

overall. The complete machine, including rotor, poles, backiron, bearings, and torque frame weighs 22,000 lb.

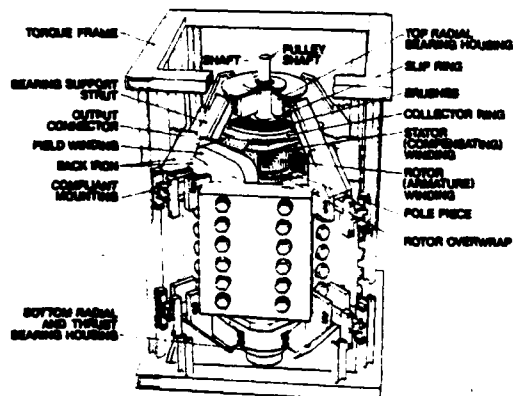


Figure 2. Components of the Prototype Compulsator

Electrical Test Circuit

The output of the prototype Compulsator was designed to drive sixteen parallel Shiva laser flashlamps. Each lamp is a 15-mm i.d. quartz tube, filled with 300 Torr xenon, and each lamp has a 44-inch arc length. The simplified test circuit that drives these lamps is given in Fig. 3.

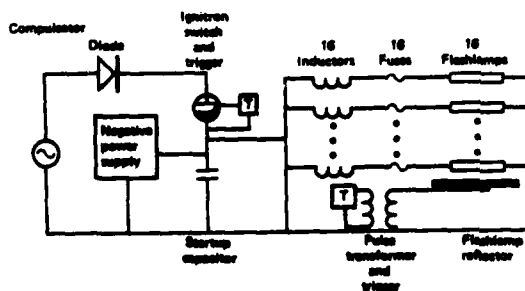


Figure 3. Simplified Test Circuit

Flashlamp balancing is achieved by use of the parallel inductors shown in each lamp circuit.¹ The fuses protect against faults in these circuits. The diodes in the Compulsator circuit are used to help the ignitron switch extinguish, preventing follow-on pulses. In addition, a vacuum relay that opens in about 11 milliseconds is located in the Compulsator circuit. This relay is timed to open soon after the first zero crossing of the output current pulse.

The startup capacitor serves the dual function of providing flashlamp trigger energy and initial current flow through the Compulsator. At the proper machine angle, the machine's computer sends a trigger pulse to a master timing unit. This unit then provides triggers to the vacuum relay and to the pulse transformer that bumps the flashlamp reflector, causing the lamps to

break down. The timing unit also fires the output ignitron switch.

The initial current in the flashlamps is in the negative direction, driven by the startup capacitor. Current also flows in the Compulsator circuit, and the voltage across the capacitor quickly reverses direction until it reaches the output voltage level of the machine. Current then flows in the positive direction through the flashlamps as energy is delivered by the Compulsator. The initial energy stored in the startup capacitor need only be 5% or 10% of the energy delivered by the machine. With a large Compulsator, this energy will probably be 2% or less.

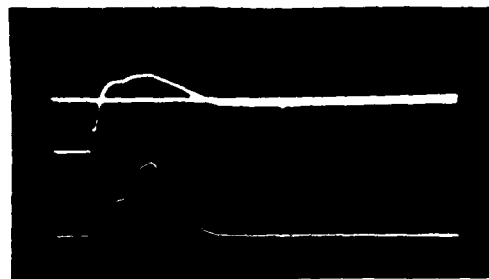
Electrical Monitors

The current in each flashlamp circuit was monitored with current transformers, or "bugs" designed for LLL. With these bugs, we determined that lamp balancing was achieved in all sixteen circuits to within a few percent. The current from four of the sixteen circuits was also monitored with a Pearson 50 kA current transformer. The voltage across the lamps was monitored with a differential pair of Tektronix high voltage probes. The calibrated accuracy of these monitors was measured to 2% or better. Tektronix storage scopes were used to record the data.

Measurements and Data Analyses

The flashlamp current was monitored on thirteen discharges of the prototype machine at nominal operational speeds from 2400 to 4800 RPM. A premature fault occurred inside the machine on a 5400 RPM shot that caused damage to the windings. As a result, this series of tests was terminated without obtaining the maximum speed, 5400 RPM data.

Flashlamp voltage was obtained on a few shots late in the series. Earlier measurements were invalid due to faulty calibration and noise in the voltage probes. The voltage and current traces from a 4800 RPM shot are presented in Fig. 4.



1 millisecond per division

Figure 4. Run number 121, 4840 RPM. Top Trace : Flashlamp Voltage, 5 kV/division Bottom Trace : Flashlamp Current, 16 kA/division

Because flashlamp current measurements were made on all shots that were set up to provide an electrical output, the data can be compared by use of the relationship,²

$$W_T = f k i_p^{3/2} \Delta t \quad (1)$$

This formula states that the total energy W_T delivered to the flashlamps is proportional to the peak current i_p to the three-halves power times the current pulse halfwidth Δt . Two constants of proportionality are used: k is the flashlamp constant and f is a waveshape form factor.^{1,2} In the present experiment, $k = 21.6$ for the sixteen parallel flashlamps.

The form factor f varied between 0.8 and about 1.0 on the series of shots. For simple triangular waveshapes, $f = 0.8$. With more complicated waveshapes, f was obtained by graphical integration via the formula.

$$f = (\int i^{3/2} dt) / i_p^{3/2} \Delta t \quad (2)$$

In reducing the data, the net energy W delivered to the flashlamps by the Compulsator was obtained by subtracting the energy stored in the startup capacitor from W_T , the total energy received by the lamps. This total energy, obtained by use of Equations (1) and (2), included the energy delivered to the lamps in the negative current pulse from the startup capacitor.

Test Results

Data from all of the runs that were set up to provide electrical pulses to the flashlamps are summarized in Table 1. In Fig. 5, the net energy delivered by the Compulsator to the lamps is plotted versus machine RPM. (Run number 120 is not included because of low field current on this shot.)

The curve $W = (RPM/225)^4$ is also plotted in Fig. 5. The delivered energy from the Compulsator appears to follow this fourth power curve rather closely. We therefore determined a figure of merit F from the formula,

$$F = W / (RPM/225)^4 \quad (3)$$

that quantizes the deviation from this fourth power relationship. This number is given in Table 1 for each run.

In order to assess the possible validity of a fourth power law, we plotted the figure of merit against the mechanical firing angle θ in Fig. 6. Here, θ is the mechanical position of the rotor when the switch triggers are fired. Zero degrees occurs at the position of minimum machine inductance. From the two sets of data, W versus RPM and F versus θ , we ascertain that the delivered energy is rather uniquely determined by the RPM of the machine and by the firing angle θ . This relationship holds up to 4255 RPM, provided the field is held constant. It can be summarized by the equation:

$$W = (m\theta + b) (RPM/225)^4 \quad (4)$$

Here, $m = -0.0160$ and $b = 0.286$ when the machine is fired after about minus 45° and $m = 0.0128$ and $b = 1.57$ if the machine fires earlier than this optimum 45° negative angle.

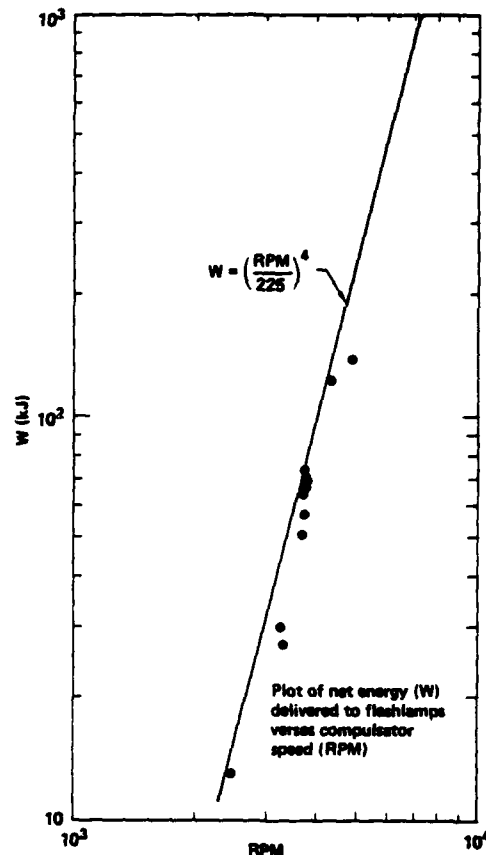


Figure 5

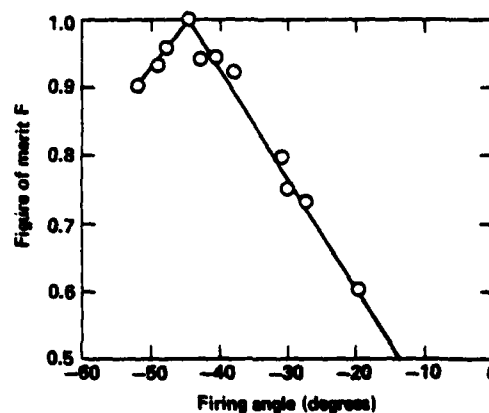


Figure of merit, F , versus firing angle for compulsator runs up to 4255 RPM

$$F = W / \left(\frac{RPM}{225} \right)^4$$

Figure 6

The percent deviation of the measured value of delivered energy versus the calculated value from Equation (4) is given in the last column of Table 1. Note that all measurements up through 4255 RPM fall within about 3% of the calculated value, or well within the errors introduced in data acquisition and reduction.

In two runs, numbers 84 and 85, the energy in the startup capacitor was increased significantly (to 31.5 kJ from 12.6 kJ). We had expected the net delivered output of the Compulsator to likewise increase. But this did not appear to happen, since the reduced data do not show any measurable difference in net energy. Because of this, it may be feasible to reduce the startup capacitor to well below the 12 kJ level without affecting the delivered output energy.

Three runs above 4255 RPM were made. Two were nominally 4800 RPM. The first of these, run number 120, was triggered when the field current was only 74.8% of full value. The second, run number 121, was a normal shot as far as we could determine. The delivered energy, however, only reached 67% of the value predicted by Equation (4) for the RPM and firing angle chosen. The last shot, run

number 122, was an attempt to determine the output energy at full rated machine speed. An internal fault caused damage to the machine windings, however, terminating this series of tests.

A computer model of the complete test circuit was made in order to describe the data of the 4840 RPM shot number 121. This model provides the best fit to the data when a resistive loss term is introduced that is a $(1-\cos\theta)$ function of the machine angle. From these results, it is apparent that eddy current losses become significant in this prototype machine at the higher speeds.

A new space harmonic model for the calculation of inductances and eddy currents in machines of this type has now been developed.³ Predictions with this model are presently being calibrated and verified by physical measurements, using a mock-up of the prototype Compulsator windings. The results of this work will be integrated into the rebuilding of the prototype machine. We expect thereby to extend the fourth-power scaling to higher speeds, and to deliver up to 200 kilojoules of energy into the flashlamps at the 5400 RPM design speed.

Table 1. Prototype Compulsator Electrical Test Summary

RUN NUMBER	RPM	FIRING ANGLE (DEGREES)	STARTUP CAPACITOR ENERGY (JOULES)	PEAK CURRENT i_p (AMPS)	CURRENT PULSE HALF-WIDTH Δt (μ sec)	NET ENERGY DELIVERED TO FLASH-LAMPS W (kJ)	FIGURE OF MERIT F	DEVIATION OF NET ENERGY FROM FOURTH POWER LAW (%)
69	2450	49	10976	8000	1420	13.1	0.935	-0.8
76	3280	20	10976	14300	1100	27.4	0.607	0.2
78	3200	28	10976	12900	1400	30.1	0.736	0.3
79	3640	30	10976	18500	1300	51.6	0.757	-1.1
80	3680	31	10976	18600	1520	57.2	0.798	2.1
81	3730	43	10976	18200	1820	71.0	0.943	-3.2
82	3640	41	12600	17400	1700	64.5	0.946	1.2
84	3700	38	31500	23800	1290	67.0	0.921	3.0
85	3700	45	31500	19200	1880	73.1	1.000	0.2
94	3750	52	12600	17500	154C	69.8	0.904	0.0
119	4255	48	12600	25300	1610	122.7	0.959	-0.4
120	4800	50	12600	20500	1290	69.6	0.336	-63.9
				LOW FIELD (74.8% OF NORMAL)				
121	4840	47	12600	30200	1300	139.3	0.589	-32.7
122	5360	-	12600	EARLY FAULT		-	-	-

References

1. B. M. Carder and B. T. Merritt, "Applying a Compensated Pulsed Alternator to a Flashlamp Load for Nova", UCRL-82473, prepared for 2nd IEEE International Pulsed Power Conference, Lubbock, Texas, June 12, 1979.
2. B. Carder and B. Merritt, "Compulsator Optimization" (Appendix 1), LLL Engineering Note EE78-192 (LEN 64), Nov. 29, 1978.
3. W. L. Bird and H. H. Woodson, "Detailed Design, Fabrication and Testing of an Engineering Prototype Compensated Pulsed Alternator", Final Report, UCRL-15213, March 1980.

NOTICE

This report was prepared as an account of work sponsored by the United States Government. Neither the United States nor the United States Department of Energy, nor any of their employees, nor any of their contractors, subcontractors, or their employees, makes any warranty, express or implied, or assumes any legal liability or responsibility for the accuracy, completeness or usefulness of any information, apparatus, product or process disclosed, or represents that its use would not infringe privately-owned rights.

Reference to a company or product name does not imply approval or recommendation of the product by the University of California or the U.S. Department of Energy to the exclusion of others that may be suitable.

HIGH POWER PULSE GENERATORS FOR FAST PULSED MAGNETS DEVELOPMENTS AND OPERATIONAL EXPERIENCE

H. Kuhn and G.H. Schröder
CERN, Geneva, Switzerland

SUMMARY

The paper describes in its first part the design of a prototype pulse generator for the new inflector of the CERN SPS. After a short explanation of the future SPS injection scheme, the electrical and mechanical design is treated in detail. The generator, equipped with 3 double ended ceramic thyristors, is designed for a short pulse rise time and low pulse to pulse jitter.

The paper presents furthermore the developments and the operational experience with 4 fast pulsed magnet systems, which contain 29 high voltage thyristors and 48 ignitrons and which are since 1976 in continuous operation in the SPS. The pulse modulators of these systems generate quasi rectangular pulses of up to 10 kA, 30 kV amplitudes and up to 25 μ s duration with a pulse repetition time of 1 to 10 s. The power switches are double ended ceramic thyristors, some of which are by-passed by 3 ignitrons in series.

1. Introduction

The European Organisation for Nuclear Research (CERN) operates since 1976 a Proton Synchrotron of a maximum energy of 400 GeV (SPS) located on the franco-swiss border near Geneva. The circular accelerator with a circumference of about 7 km is housed in a tunnel which is built in the stable rock down to 60 m underground. The accelerator is equipped with 4 different fast pulsed magnet systems for the deflection of the proton beam during one revolution of 23 μ s or part of it. They are used for :

- injection of the beam from a preaccelerator at an energy of 10 GeV
- fast extraction of the accelerated beam at energies between 200 and 400 GeV for beam transfer towards the experimental areas
- internal beam dumping onto an absorber block in case of equipment failure or operation faults
- the measurement of the betatron tunes of the machine.

A fast pulsed magnet system consists typically of :

- line type pulse generators supplying quasi rectangular current pulses of up to 10 kA amplitude and up to 25 μ s duration and located in a surface building
- coaxial transmission lines of up to 300 m length connecting the generator to the ferrite magnets located in the underground tunnel
- ferrite magnets, built as lumped parameter delay lines and working in ultra high vacuum
- termination resistors matched to the characteristic impedance of generator, transmission line and magnet and absorbing the pulse energy of up to 7.5 kJ energy supplied by the generator.

The systems used in the SPS have been presented at the 12th Modulator Symposium in 1976.¹

2. Prototype of a Line-type Pulse Generator for the new SPS Proton Inflector

2.1 Purpose

At present, the SPS accelerates about once every 10 s more than $2 \cdot 10^{13}$ protons which are shared between about 15 physics experiments. There is a need to increase this intensity and the SPS intensity improvement program established in 1977, foresees to bring the intensity to more than $3 \cdot 10^{13}$ protons per pulse, mainly by extending the rf system and modifying the injection scheme.² This requires, amongst other modifications, the construction of a faster and more powerful SPS inflector.

The presently used injection scheme is shown schematically in Fig. 1 :

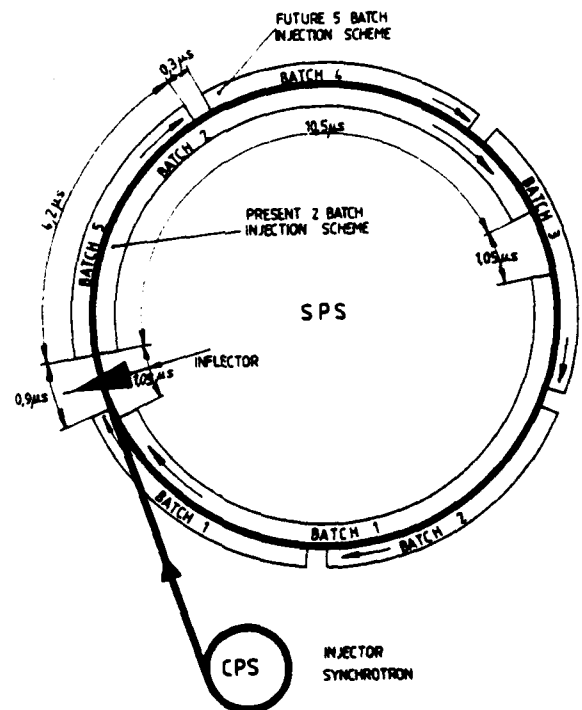


Fig. 1 - Present and future injection schemes of the SPS

The protons are injected with a momentum of 10 GeV/c from an injection synchrotron (CPS), the diameter of which is 11 times smaller than that of the SPS. The operation of the SPS started with extraction of the beam from the CPS during 10 CPS revolutions, filling in this way 10/11th of the SPS and leaving 1/11th (2.1 μ s) to allow the magnetic field in the inflector magnet to fall to zero before the circulating protons arrive again after their first revolution.

To increase the intensity of the SPS, the CPS can accelerate repeatedly protons which are extracted in batches of shorter duration and placed successively around the circumference of the SPS. They are held circulating at injection energy until the SPS ring is filled and their common acceleration can start. For the moment, two proton batches with a duration of 10.5 μ s

are injected. The presently installed inflector has a rise and fall time of the magnetic field of $0.75 \mu s$ which permits even 3-batch injection.

The SPS intensity improvement project foresees the injection of up to 5 proton batches and an accelerated intensity of at least $3 \cdot 10^{13}$ protons per pulse. In addition, the future part-time use of the SPS as a proton-antiproton collider at 270 GeV/c calls for the injection of up to 6 short proton bunches at 26 GeV/c.

The rise and fall times of the magnetic field of the presently installed inflector are too long to allow 5-batch injection and the deflection strength is insufficient for the injection of protons at 26 GeV/c. A new fast inflector is therefore under construction allowing the injection of 2 to 5 proton batches from the CPS.

The following chapters describe the design and the performances of a prototype system.

2.2 Design Principle

A fast pulsed magnet system must meet two requirements which are contradictory, i.e. a high deflection strength and a short rise time of the magnetic field. Both properties are, for a given operational voltage, proportional to the product of the electric current passing through the magnet and its length.

In order to meet the contradictory requirements, the length must be reduced by splitting the magnet system into several independently powered modules. The new inflector requires 12 magnet modules which are connected in pairs to 6 pulse generators. A block diagram of one fast pulsed magnet circuit is shown in Fig. 2.

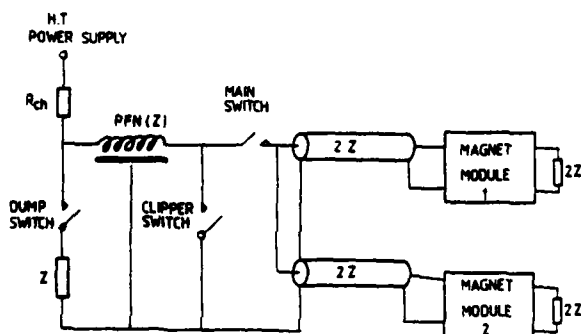


Fig. 2 - Bloc diagram of fast pulsed magnet circuit

A power supply charges the pulse forming network (pfn) to a maximum voltage of 60 kV. Then the pfn is discharged by fast electronic switches through matched transmission lines into the magnet modules which are terminated by matched resistors.

Three switches are necessary in order to get a fast rise and fall time and an adjustable pulse duration:³

- a main switch to initiate the discharge
- a clipper switch to shorten the fall time
- a dump switch to change the pulse length and to allow the absorption of the tail of the pulse in the dump resistor.

A transmission line of 180 m length connects the generators, housed in a building at surface level, to the magnets in the accelerator tunnel. Each line consists of several coaxial cables, type RG 220/U, with a characteristic impedance of 50 Ohm, connected in parallel.

Each fast pulsed magnet has an equivalent circuit in the form of a lumped parameter delay line with a characteristic impedance of twice that of the pfn. The pulse travels therefore through the magnet without major deformation and is absorbed in the terminating resistor.

To meet the requirements of the different injection schemes, the generator must have a pulse duration of up to $10.5 \mu s$ to allow 2-batch injection. For 5-batch injection a pulse duration of only $4.2 \mu s$ is required. For the purpose of testing the thyristors the prototype has been designed for a pulse duration of $24 \mu s$.

The kick rise time is determined by the distance between adjacent batches, whereas the kick fall time is given by the duration of the large gap between batch 5 and batch 1. Originally, the duration of the large gap was fixed to $1.5 \mu s$, leaving $0.15 \mu s$ as distance between adjacent batches. The kick rise time was therefore chosen to be $0.10 \mu s$. In the meantime, the large gap has been shortened and the distance between adjacent batches increased as shown in Fig. 1.

The main parameters of the prototype inflector are listed in Table 1:⁴

Table 1

Main System Parameters

Maximum generator voltage	60 kV
Characteristic impedance	8.33 Ohm
Current amplitude	3.6 kA
Pulse duration	0.5 μs to 24 μs
Generator rise time	40 ns
Generator fall time	380 ns
Magnet filling time	70 ns
Kick rise time (2 to 98%)	100 ns
Kick fall time (98 to 2%)	400 ns
Flat top ripple	< $\pm 1\%$
Pulse repetition time	5 pulses, 0.6 s apart within 12 s

2.3 Pulse Forming Network

2.3.1 Design Philosophy: Experience gained in recent years in the operation of high power pulse forming networks equipped with 3 independently triggered thyristor switches has shown that careful screening of the switches is necessary to avoid erratic firings of the 2nd and 3rd switch caused by electromagnetic pickup from the 1st switch.

Prototype test started in 1972 with all 3 switches housed in one common tank.⁵ Because of interference between the switches this design was abandoned in favour of a separate housing for the dump switch. Main and clipper switches, which have a common anode connection, remained however in the same tank. Both switch tanks were then connected via short cables to the pfn tank. This type of generator is operating in the SPS (Fig.3)¹

Nevertheless, special measures, described in chapter 3.2 had to be taken to avoid the clipper switch being triggered by the discharge of the main switch, especially for generators with a short rise time.



Fig. 3 - Pulse generators of the fast extraction system. The square tanks in the center house the pulse forming networks, the round tanks on the right hand side the main and the clipper switches and the round tank on the left hand side the dump switch

For the design of the new inflector whose rise time is particularly short, it appeared therefore imperative to house all three switches in separate tanks. To avoid stray inductances between the pfn and the switches, the latter are mounted directly on top of the pfn (Fig.4).

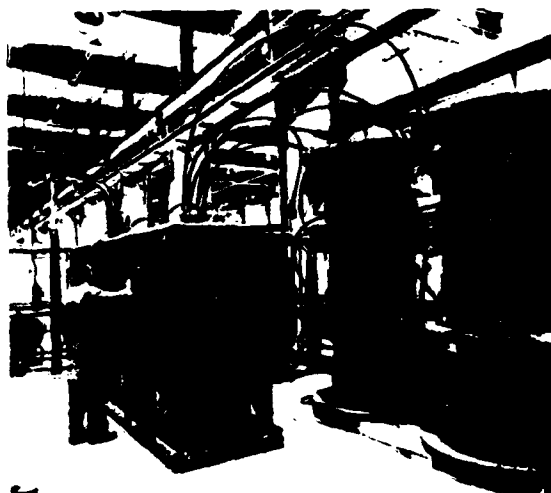


Fig. 4 - Prototype pulse generator of the new SPS inflector. The 3 switches are mounted in separate tanks on top of the pfn. The cylindrical housings of the capacitors are visible under the pfn tank. On the right the transmission line to the magnet, built up of 6 coaxial cables type RG 220/U connected in parallel.

The physical separation between the common anode connection of main and clipper switches introduces however a stray inductance which increases either the rise or the fall time of the pulse depending on the position of the front matching cell of the pfn. This stray inductance has been minimized by connecting a stripline

which is matched to the characteristic impedance of the pfn between the anodes of main and clipper switches. This stripline is housed in the pfn. At both ends of the stripline, front matching cells for rise time improvement are added.

The lowest ripple on the flat top of the current pulse is obtained when the cells of the pfn are aligned in one row. This arrangement is however inconvenient for the construction of the pfn tank. Experience with the existing pfn's has shown that a serpentine arrangement of the cells, which is more suitable for the tank construction has two major drawbacks:

- The ripple is relatively high because of a change in the mutual inductance between the cells at the position of the bends.
- The ripple changes when the pulse length is varied. This is due to electro-magnetic interference between two adjacent rows and is overcome by screening the coils.

In order to avoid these drawbacks the following layout has been chosen as illustrated in Fig. 5:

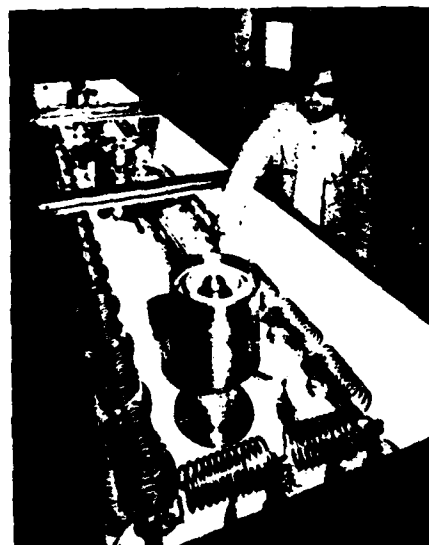


Fig. 5 - View into the tank of the pulse forming network. The LC-ladder network is mounted along the border of the tank. The coaxial connections to the 3 switches and the stripline are mounted along the central axis.

- The cells are aligned in only 2 1/2 rows as compared to 5 rows for the old inflector.
- The first 8 cells are arranged in a straight line in order not to perturb the beginning of the pulse which is particularly sensitive to mismatch.
- The 2 full rows are located near the tank borders in order to keep them separated.
- The coil diameter is rather small in order to confine better the strayfield.
- The connections to the 3 switches as well as the stripline are mounted along the central axis between the rows of cells.

- The 8 last cells on the axis are discharged at the end of the pulse and are therefore less sensitive to interference from the other rows.

The equivalent circuit of the pulse generator is given in Fig. 6.

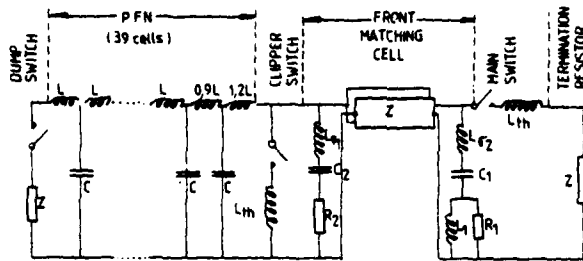


Fig. 6 - Equivalent circuit of the pulse generator

2.3.2 Rise Time: The rise time of the current pulse is mainly determined by the characteristic impedance of the pulse generator, the unmatched stray inductance of the main thyatron and its plasma formation time.

The unmatched stray inductance L_{th} of the main thyatron is estimated to be about 140 nH, giving a rise time contribution of about 25 ns.

The plasma formation time of the thyatron becomes shorter for a higher gas pressure in the tube. High gas pressure increases however the likelihood of premature firings.

To obtain a reliable operation at high gas pressure, the generator is charged via a resonant charging power supply which supplies voltage to the thyatron only a few milliseconds before its turn on.⁶ Erratic firing is thus strongly reduced even at high gas pressure, because of the short time that the thyatron has to withstand high voltage.

The contribution of the stray inductance of the front matching cell to the pulse rise time is small, because the stripline as part of the front matching cell has a very small stray inductance. The parameters of the two front matching cells at both ends of the stripline have been adjusted empirically.

The rising edge of the pulse at a reservoir voltage of 6 V is shown in Fig. 7.

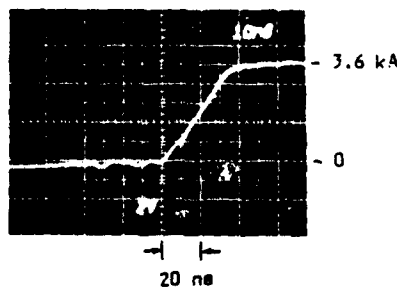


Fig. 7 - Pulse rise time and time jitter measured on one of the two termination resistors. For the jitter measurements, 2 x 5 pulses are superimposed within a time interval of 3 h.

2.3.3 Fall Time: The fall time of the current pulse is, in first instance, determined by the stray inductances in the branches of the clipper switch and the main switch and by the characteristic impedance of the pfn.

Due to the introduction of the matched stripline between main and clipper switches, the total stray inductance in the branch of the main switch could be kept small, resulting in a fall time of the current pulse of about 400 ns. Fig. 8 gives an oscillogram of the fall time.

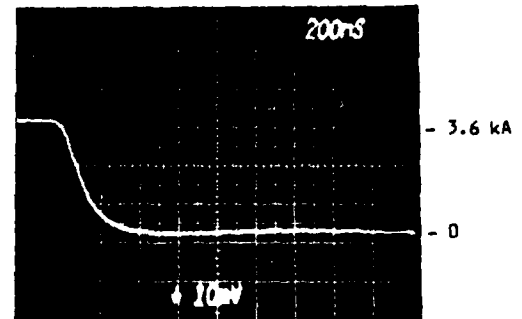


Fig. 8 - Pulse fall time

2.3.4 Flat Top Ripple: As a result of the comparably large number of 39 pfn cells and their arrangement in only 2 1/2 straight lines with few bends, a flat top ripple of less than $\pm 1\%$ is obtained as shown in Fig. 9. The pulsed magnet field of about 12 μ s duration as required for 2-batch injection is given in Fig. 10.

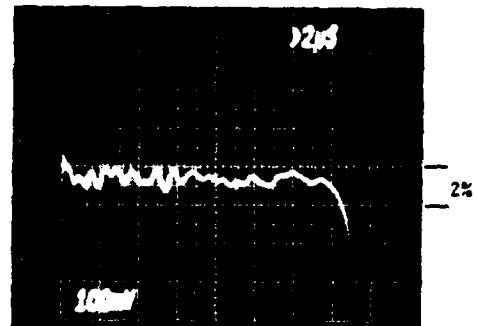


Fig. 9 - Flat top ripple

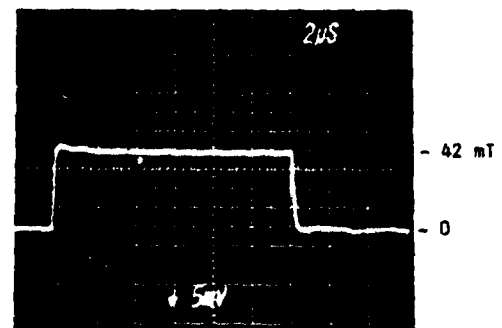


Fig. 10 - Pulse of the magnetic field in the kicker magnet, corresponding to a charging voltage of 60 kV.

2.3.5 Construction: The 39 regular cells of the pfn are composed of capacitors of 40 nF and solenoids of 2.78 μ H. The capacitors, made by LCC (France) have an insulating outer case of cylindrical shape with a length of 520 mm and a diameter of 170 mm.

The dielectric is a paper mylar mixture impregnated in mineral oil and designed for an operation voltage of 65 kV.

The capacitors are mounted in cylindrical stainless steel pots of 475 mm length and 180 mm diameter, which are fixed vertically into the base plate of the pfn tank. This type of construction provides a low inductance coaxial return path and minimises the quantity of silicon fluid required for insulation. The use of mineral oil is excluded because of fire hazards.

The inductor solenoids are copper spirals of 60 mm diameter and an adjustable length of about 200 mm. They are mounted horizontally between the h.t. electrodes of the capacitors as shown in Fig. 5.

2.4 Switches

2.4.1 Choice of Switch Type: CERN has excellent operational experience with the deuterium filled, three gap, double ended thyatron with a ceramic envelope, type CX11718, manufactured by English Electric Valve Company (EEV), for the switching of current pulses of up to 10 kA and a duration of up to 25 μ s. The tube is electrically symmetrical, with identical cathode and grid assemblies at both ends. The choice of this thyatron as switch for the new SPS inflector was therefore rather obvious.

The parallel connection of ignitrons, as in previous switches¹ was however avoided since this would have complicated considerably the switch construction. To obtain a fast rising pulse, the ignitron anode should be connected directly to the pfn and hence be at the bottom of the switch whereas the cathode should be near the top. This position is however not possible because of the liquid mercury cathode of the ignitrons.

Nevertheless, the switch has been tested with a pulse duration of 25 μ s in order to repeat in more detail earlier test on the switching behaviour of the thyatrons for pulses of long duration.

2.4.2 Electrical Design: The electrical circuit of the thyatron is shown in Fig. 11.

The voltage divider which provides the potentials for the gradient grids is mounted around the thyatron. Each of the three resistors of 10 MegOhm is made up of 36 agglomerated carbon resistors in series and compensated by ceramic capacitors of 500 pF and 30 kV.

It was found experimentally at English Electric Valve Co and at CERN that the voltage holding and hence the lifetime of the thyatron may be substantially improved, if the value of the two resistors which connect the gradient grids to the potential divider is increased from 47 Ohm to 470 Ohm.

2.4.3 Jitter: A large effort has been made to decrease the variation of the pulse to pulse anode delay (jitter). Measurements have been executed on a heated thyatron by observing the moment of breakdown of the trigger pulse on the control grid 2. This corresponds almost to the anode jitter and avoids to apply high voltage to the thyatron which facilitates experimentation.

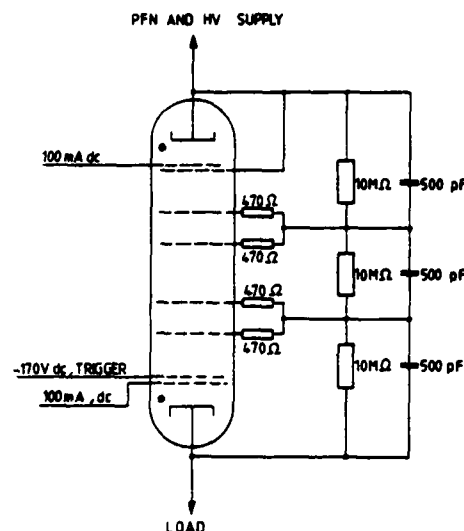


Fig. 11 - Electrical circuit of the double cathode thyatron CX 11718

It was found, that the jitter is independent of the voltage and the rise time of the trigger pulse, provided that the former is above 500 V, and the latter shorter than the anode delay time. The jitter became almost zero when the trigger pulse was synchronised with the mains, an indication that mains ripple is at the origin of the jitter.

Improved filtering of the dc supply to control grid 1 and stabilisation of the grid 1 current by means of constant current diodes brought a substantial improvement. Adding furthermore a filter capacitor to control grid 2 and splitting the trigger pulse via an R-C network between the control grids 1 and 2, resulted in a jitter of less than 2 ns. The improved cathode supply circuit is shown in Fig. 12. Jitter measurements at an anode voltage of 60 kV confirmed the results as given in Fig. 7.

2.5 Operational Results

The pulse generator has been operated at a charging voltage of 60 kV corresponding to a current of 3.6 kA and a peak power of 108 MW. The pulse length was adjusted to 25 μ s. The power supply was pulsed with a train of 5 pulses at 0.5 s interval followed by a rest period of 2.5 s. The reservoir voltage was initially set to 5.6 V and after 10^5 pulses increased to 6.0 V.

The main thyatron, which was still equipped with decoupling resistors in the gradient grid circuits of 47 Ohm, started to show signs of deterioration after $8 \cdot 10^5$ pulses. The rate of erratic firing became about 1 in 100 pulses. These results confirmed earlier tests carried out in 1973.⁵

A new thyatron was then installed and the pulse duration reduced to 17 μ s. It performed perfect at reservoir voltages of up to 6.1 V. The lifetest was stopped after 10^7 pulses at 60 kV. The rate of erratic firings was less than 1 in 10^5 pulses, which is our limit of detection. At the end of this test the jitter was still less than 2 ns. This second thyatron was equipped with decoupling resistors on the gradient grids of 470 Ohm, which may be, besides the reduction in pulse duration, a reason of its better performance.

The life expectancy for ignitrons is of the same order of magnitude as for thyratrons. Apart from the capacitor faults described above, at some rare occasions ignitrons failed to fire because the ohmic resistance between ignitor and cathode had strongly decreased.

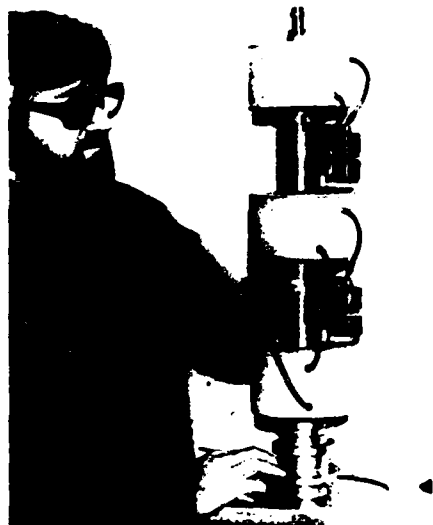


Fig. 14 - Ignitron chain assembled.
The resistors inside the voltage divider pots heat the anodes of the ignitrons, providing a temperature difference between anodes and cathodes which assures a very reliable operation.

3.3 The Screened Grid Thyatron

The pulse generators presently in operation at the SPS have a common tank for the main and the clipper switches in order to keep the inductance between both switches low. As already mentioned in chapter 2.3.1, the clipper switch has the tendency to turn-on prematurely with the discharges of the main switch so that the current pulse is shortcircuited.

One of the causes for the malfunctioning is the capacitance between the anode and the control grid 2 of the clipper switch which transmits the negative jump of the clipper anode at the trigger instant of the main switch to the clipper control grid. This causes oscillations of the clipper control grid, which can turn-on the switch.

To cure this effect, a capacitor of 500 pF in series with a resistor of 50 Ohm has been branched between control grid 2 and cathode of the clipper thyatron. This decreases the amplitude of the oscillations without too much attenuating of the trigger pulse. It does however not completely cure the problem. As the grid oscillation on the clipper depends strongly on the rate of rise of the current in the main switch, the reservoir voltage of the latter has also to be decreased in order to diminish the rate of rise of the pulse. In some cases, the reservoir voltage of the clipper has to be lowered in addition. These measures tend however to reduce the lifetime of the thyatron and can not be considered as a long term solution.

In order to solve the problem, EEV developed a thyatron with an additional screening grid on the anode side of control grid 2. The grid is connected to cathode potential and shortcircuits the capacitive cur-

rents coming from the anode before they can reach the control grids. This thyatron has the type designation CX 1171 C. It has the same outer dimensions as the type CX 1171 B and can therefore directly replace the latter.

A prototype has recently been tested in the fast extraction system of the SPS. It was installed in a main-clipper tank without the aforementioned blocking circuit between grid 2 and cathode.

Pulsing the generator with a charging voltage of 60 kV, the reservoir voltage of the main switch had to be raised from the original 4.8 V to 5.8 V before the effect reappeared. At a reservoir voltage of 5.6 V the new type of thyatron performed perfectly. The anode delay time is slightly larger compared to a thyatron of type CX 1171 B which is however of no importance in this application. The new thyatron CX 1171 C has a superior performance from the point of view of pulse voltage hold-off in the clipper position and will be used for all clipper thyratrons in the fast pulse generators of the SPS.

3.4 Limitations of Thyratrons to Switch Pulses of Long Duration

When in 1973 the "Thyragnitron" was chosen as main switch for the SPS kicker magnets, it could not be excluded completely that, for systems with comparably low pulse currents, the switch would also work reliably without bypassing ignitrons. For lack of time and in order to play it safe, ignitrons were installed in all systems working at a charging voltage of 60 kV. In the meantime, tests without ignitrons have however been pursued. First tests were made in one of the pulse generators of the fast extraction system, which operates at a charging voltage of 60 kV with a current amplitude of 3 kA. The maximum pulse power is 90 MW for 25 μ s. After several months of operation, corresponding to about 10^6 pulses, the thyratrons, not backed up by ignitrons, started to fail.

A second test was made, involuntarily, in the beam dumping system which works at a current amplitude of 10 kA and a pulse duration of 25 μ s, corresponding to a pulse power of almost 300 MW. Due to simultaneous faults of the ignitron trigger and the corresponding interlocks, the thyratrons had to conduct the total current. They were damaged already after about 1 000 pulses. A few pulses of 25 μ s duration in this power range may already destroy the thyatron whereas, if it is backed up by ignitrons, the average lifetime of the thyratrons in the beam dumping system is about 8 000 hours.

A third test is already described in chapter 2.5. A thyatron type CX 1171 B failed in switching current pulses of 3.6 kA with a duration of 25 μ s after about 10^6 pulses. When the pulse duration was reduced to 17 μ s another tube switched more than 10^7 pulses.

Furthermore, at the moment 7 thyratrons are under test which switch pulses with a current amplitude of 4.8 kA and a duration of 12 μ s. They work satisfactory.

The two last tests described are carried out with decoupling resistors of 470 Ohm between the voltage divider and the grids (see chapter 2.5), whereas all other tests described were made with resistors of 47 Ohm. Since the exact reasons for the influence of these resistors on the switching behaviour at higher ratings of current and pulse duration is not known, it is intended to continue these tests for higher ratings with the resistors of 470 Ohm.

The limitations of these thyratrons to switch pulses of long duration can not be determined in an exact way, because the field of applications is vast and the number of thyratrons tested is too small to make statistically relevant statements. Nevertheless, the results presented may help system designers to see the possibilities and the limits of these devices.

Conclusion

Double ended ceramic thyratrons bypassed by the series connection of 3 ignitrons have proven in recent years to be reliably operating switches for currents of at least 10 kA and pulse durations of at least 25 μ s, blocking voltages of at least 60 kV and repetition rates of at least 1 pps.

Their operational lifetime spans from about 8 000 h for current amplitudes of 10 kA to more than 15 000 h for pulses of 3 kA.

Thyratrons not being bypassed by ignitrons have switched pulses of 3.6 kA/17 μ s and 4.8 kA/12 μ s more than 10 million times. Current rise times to 3.6 kA within 40 ns and a pulse to pulse jitter as low as 2 ns over 3 h have been obtained.

In conclusion, these fast power switches offer a reliable and in nearly all aspects satisfactory behaviour in the day to day operation of fast kicker magnets installed in a large accelerator complex.

Acknowledgements

The work reported has benefitted from the constant support of W.C. Middelkoop and B. de Raad.

We would like to thank E. Frick for the mechanical design of the pulse generator and J.P. Zanesco, J. Bonthond and H. Verhegen for the construction of the command and interlock electronics.

R. Chappuis carried out the adjustment of the pfn and R. Tröhler participated in the life tests.

Last but not least it is our pleasure to thank H. Menown and R. Snelling of English Electric Valve Co for their close cooperation, especially in the development of the "screen grid" thyatron CX 1171 C.

References

1. P.E. Faugeras, E. Frick, C.G. Harrison, H. Kuhn, V. Rödel, G.H. Schröder, J.P. Zanesco
The SPS Fast Pulsed Magnet Systems
12th Modulator Symposium, New York, 1976
2. M.C. Crowley Milling, B. de Raad
Proposal to increase the Intensity of the SPS
CERN-SPS/AC/77-12
3. P.E. Faugeras
Calculations on the SPS Inflector Magnet
and its Pulse Generator
CERN LAB II/BI/72-1
4. H. Kuhn, G.H. Schröder, J.C. Soulié
SPS Inflector for Multibatch Injection,
CERN/SPS/ABT/nt/77-1
5. P.E. Faugeras, H. Kuhn, J.P. Zanesco
Generation of High Current, Long Duration
Rectangular Pulses
11th Modulator Symposium, New York, 1973
6. G.H. Schröder
Design and Tests of a 5 kJ, 60 kV Resonant Charging
Power Supply for the ISR Beam Dumping System

GENERATION OF CURRENT PULSES OF QUASI TRIANGULAR SHAPE WITH FAST POWER THYRISTORS

V. Rödel, G.H. Schröder, E.B. Vossenberg
CERN, Geneva, Switzerland

Summary

Fast resonant extraction of part of the circulating beam from the CERN 400 GeV Proton Synchrotron (SPS) is initiated by a quadrupole magnet with a linearly rising current. Efficient interruption of the extraction requires a change of current from the positive rate of rise to a negative one in a time interval which is short compared with the shortest uninterrupted spill of about 1 ms.

This paper describes the pulse generator which operates at a voltage of 3 kV and which is capable of changing the current in the inductive load within a time interval of less than 200 μ s from a positive rate of rise of 60 A/ms to a negative one of equal value.

The most critical components of the generator are three groups of three fast turn-off power thyristors in series, which provide the forced commutation of the current in the generator. The computer-aided design of the commutation circuit is presented as well as the selection criteria and the electrical layout of the thyristor chains. Measured pulse shapes and the operational results are discussed.

1. Introduction

The 400 GeV Proton Synchrotron (SPS) operated near Geneva by the European Organization for Nuclear Research (CERN) accelerates about once every 10 seconds more than 2×10^{13} protons to an energy of up to 400 GeV. After acceleration the protons are extracted from the synchrotron and sent to the experimental areas, where they are used for experiments in elementary particle physics. The following extraction schemes are used:

- Fast extraction:** Kicker magnets are used to extract protons over one revolution of the beam of 23 μ s¹. Shorter spill times can be obtained by shortening the pulses of the fast kicker magnets.
- Slow extraction:** The accelerator is tuned close to a resonance which increases the oscillations of the protons around their central orbit in a controlled way. The beam can then be spilt out continuously for more than two seconds.
- Fast resonant extraction:** This is used for spill times in the millisecond range². Also in this scheme the accelerator is brought close to a resonance. Then a capacitor bank is discharged through a quadrupole magnet which tunes the accelerator even closer to the resonance. The oscillations of the protons around their central orbit grow rapidly and the whole beam is extracted within a few milliseconds.

Once these various extraction schemes performed successfully, the need arose to extract a proton burst of a duration of about 1 to 2 ms at an intermediate energy (for example 350 GeV), and then to accelerate the remaining part of the beam to the highest energy. Initially the interrupted fast resonant extraction used two quadrupole magnets in suitable positions in the main ring. One of them was supplied with a linearly rising

current for exciting the resonance and initiating the extraction of the beam. When the desired spill-out was obtained, the second quadrupole magnet was excited with a current of the same waveform, but of opposite polarity. This tunes the accelerator away from the resonance and stops the spill-out of the protons. Also this scheme worked satisfactorily².

To simplify the operation and to save space in the main ring, a pulse generator was developed which can upon an external trigger signal reverse the slope of the current in a quadrupole magnet from a positive to a negative one. This made it possible to operate the required extraction mode with only one generator connected to one quadrupole magnet.

Efficient interruption of the extraction requires a polarity change fast with respect to the shortest spill time which is about 1 ms. By using power thyristors of the shortest available turn-off time, the reversal of the current slope could be achieved within 200 μ s for a current slope of 60 A/ms and a maximum current of 250 A.

2. Design principles

The extraction quadrupole can be considered as an inductance L . A linearly rising current is flowing through the inductance when a constant voltage is applied to its terminals. In order to reverse the current slope the voltage on the terminals must be reversed. The method used to reverse this voltage is shown in the basic equivalent circuit of Fig. 1.

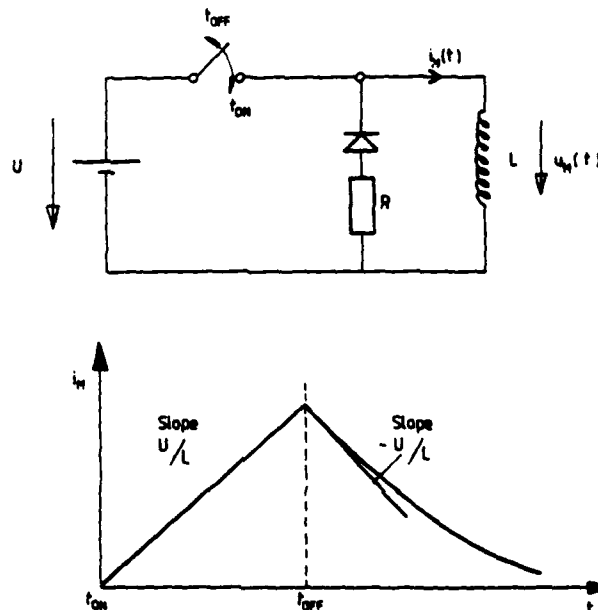


Fig. 1 Basic equivalent circuit and shape of current pulse

273

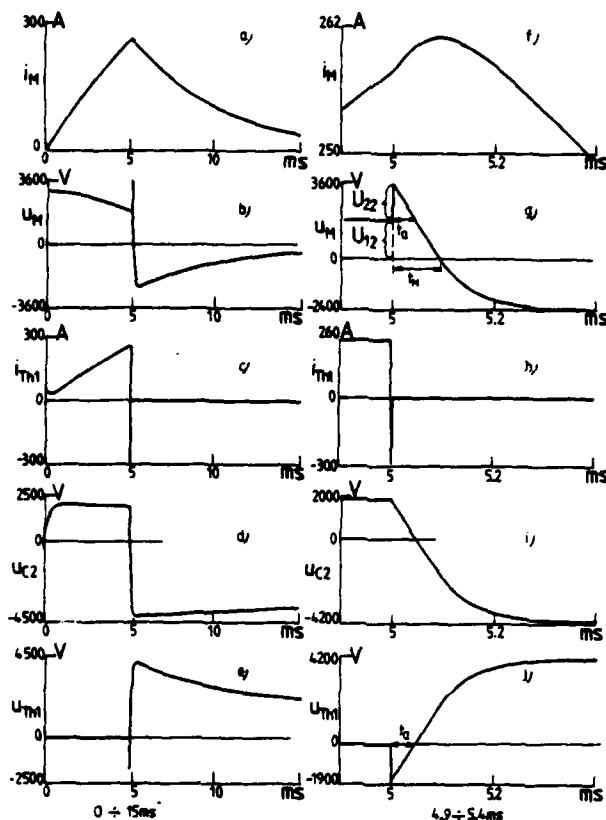


Fig. 4 Computed current and voltage waveforms

3.2 Interval 1 (current rise, $t_0 < t < t_1$)

The equivalent circuit for this interval is given in Fig. 5. The parallel branch C_2, C_3, R_3, R_5, R_6 charges the commutation capacitor C_2 approximately to the voltage:

$$U_2 = U_1 \frac{R_5}{R_3 + R_5 + R_6} \quad (2)$$

As $C_2, C_3 \ll C_1$ and $R_3, R_6 \gg \sqrt{L/C_1}$, this branch can be neglected here for the calculation of the current rise.

The current rises according to the following equation:

$$i_M(t) = \frac{U_1}{\omega L} e^{-\delta t} \sin \omega t \quad (3)$$

with

$$\omega^2 = \omega_0^2 - \delta^2 \quad (4)$$

$$\omega_0^2 = \frac{1}{LC_1} \quad (5)$$

and

$$\delta = \frac{R_6}{2L} \quad (6)$$

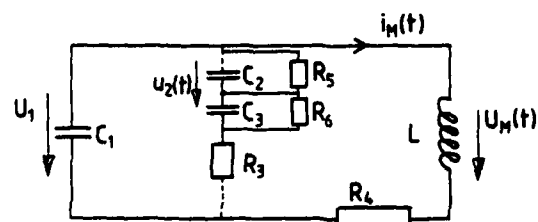


Fig. 5 Equivalent circuit for interval 1 (current rise)

If the commutation thyristor were not triggered the current would rise to:

$$I_M = \frac{U_1}{\omega L} e^{-\delta(\pi/\omega)} \quad (7)$$

The voltage falls according to:

$$u_1(t) = U_1 e^{-\delta t} \left[\cos \omega t + \frac{\delta}{\omega} \sin \omega t \right] \quad (8)$$

3.3 Interval 2 (main thyristor Th_1 turn-off, $t_1 < t < t_2$)

This interval starts with the triggering of the commutation thyristor Th_2 and it ends when the reverse main current in Th_1 has fallen below a threshold defined in Fig. 6. The equivalent circuit is given in Fig. 7.

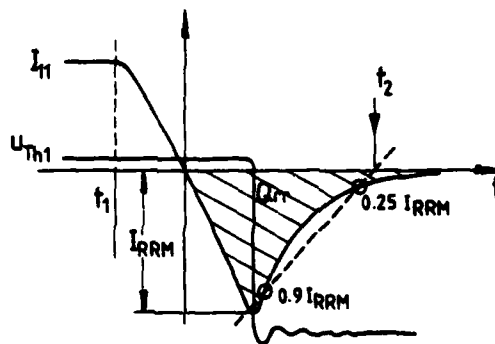


Fig. 6 Voltage and current of the main thyristor Th_1 during turn-off

When thyristor Th_2 is triggered, current flowing from the commutation capacitor C_2 decreases rapidly the current in the main thyristor Th_1 . The rate of decrease is determined by the inductance L_S in the loop consisting of Th_1 and Th_2 , and the voltage of the commutation capacitor C_2 :

$$\frac{-di_1}{dt} = \frac{U_{21}}{L_S} \quad (9)$$

where U_{21} is the voltage of C_2 at $t = t_1$.

As the rate of decrease of the current in thyristor Th_1 is faster than the recombination of the charge carriers, the thyristor remains conducting when the current reaches zero. The current rises therefore with the same di/dt in reverse direction to the peak reverse recovery current:

$$I_{RRM} = \sqrt{\left| -\frac{di}{dt} \right| 2Q_S} \quad (10)$$

The voltage of the commutation capacitor C_2 decreases during this interval by the amount:

$$\Delta U_2 = \frac{1}{C_2} \left[I_{11}(t_2 - t_1) - \frac{I_{11}^2 L_S}{2U_{21}} + Q_{rr} \right] \quad (11)$$

Q_S and Q_{rr} denote the lag charge and the reverse recovery charge of the main thyristor Th_1 , respectively. They depend both on amplitude and rate of fall of the forward current. They are given in the data sheets of the manufacturer. I_{11} is the current in thyristor Th_1 at $t = t_1$.

It should be noted that time interval 2 is much shorter than the other intervals considered.

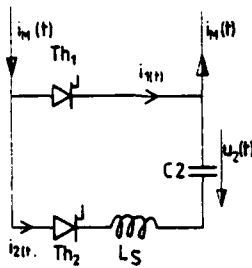


Fig. 7 Equivalent circuit for interval 2 (turn-off of the main thyristor Th_1)

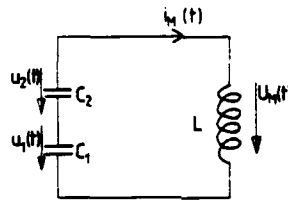


Fig. 8 Equivalent circuit for interval 3 (voltage reversal of the commutation capacitor C_2)

3.4 Interval 3 (voltage reversal on the commutation capacitor C_2 , $t_2 < t < t_3$)

This interval starts with the turn-off of main thyristor Th_1 and stops when the magnet current has reached its maximum value. Since the main thyristor is now in off-state the equivalent circuit of Fig. 8 is valid. Because of the high characteristic impedance of the circuit, the resistance R_a can be neglected. The commutation thyristor Th_2 has now completely taken over the load current. It is supplied from the capacitor bank C_1 and is reversing the voltage of the relatively small commutation capacitor C_2 (Fig. 4d). The circuit behaviour is described by the following equations:

$$u_M(t) = -I_{M_2} \sqrt{\frac{L}{C_S}} \sin \omega t + (U_{12} + U_{22}) \cos \omega t \quad (12)$$

$$i_M(t) = \frac{U_{12} + U_{22}}{\sqrt{L/C_S}} \sin \omega t + I_{M_2} \cos \omega t \quad (13)$$

$$u_2(t) = -I_{M_2} \frac{1}{\omega C_2} \sin \omega t + U_{22} \cos \omega t \quad (14)$$

with

$$\omega^2 = \frac{1}{LC_S} \quad (15)$$

and

$$C_S = \frac{C_1 C_2}{C_1 + C_2} \approx C_2, \text{ since } C_2 \ll C_1. \quad (16)$$

The initial conditions for this interval are

$$u_1(t_2) = U_{12} \quad (17)$$

$$u_2(t_2) = U_{22} \quad (18)$$

and

$$i_M(t_2) = I_{M_2} \quad (19)$$

At $t = t_2$, the main thyristor Th_1 turns off and branches the series connection of C_1 and C_2 to the magnet. The voltage of the magnet jumps then by the amount U_{22} . The magnet voltage is now given by Eq. (12). It decreases approximately linearly at a rate of I_{M_2}/C_2 . It crosses zero at $t = t_3$, which defines the beginning of the time interval 4. Due to the voltage spike on the magnet, the slope of the magnet current increases for a short moment as can be seen in Fig. 4f.

For the correct turn-off of the main thyristor Th_1 the circuit must provide a negative voltage to Th_1 long enough for its recovery. This time is called the circuit turn-off time t_Q and it must be longer than the turn-off time of the thyristor t_q specified by the manufacturer (Fig. 4g).

The circuit turn-off time t_Q is closely related to the duration of the interval $t_M = t_3 - t_2$ (see Fig. 4g and section 4). It is determined from Eq. (12) by setting $u_M(t) = 0$:

$$t_M = \frac{U_{12} + U_{22}}{I_{M_2}} C_S \approx \frac{U_{12} + U_{22}}{I_{M_2}} C_2. \quad (20)$$

Similarly, the circuit turn-off time is

$$t_Q \approx \frac{U_{22}}{I_{M_2}} C_2. \quad (21)$$

With the parameters of Section 3.1, $t_Q = 47 \mu s$.

During this time interval the magnet current continues to rise. This current increase is determined with Eq. (13) using Eq. (20). Remembering that I_{M_2} is the magnet current at the beginning of interval 3, the current rises during interval 3 by the relative amount

$$\frac{\Delta I_{M_2}}{I_{M_2}} = \frac{1}{2} \left[\frac{(U_{12} + U_{22})/I_{M_2}}{\sqrt{L/C_2}} \right]^2. \quad (22)$$

For the example considered in Section 3.1, $\Delta I_{M_2}/I_{M_2} = 1.3\%$.

3.5 Interval 4 (crowbar branch starts conducting, capacitors are still connected, $t_3 < t < t_4$)

The equivalent circuit is given in Fig. 9. It is characterized by the simultaneous conduction of the crowbar circuit and the branch of the commutation thyristor Th_2 . The circuit is now strongly damped owing to R_2 . The resistance R_a can be neglected, since $R_a \ll R_2$. The equations for voltage and currents are:

$$u_M(t) = -I_{M_2} \frac{1}{\omega C_S} e^{-\delta t} \sinh \alpha t \quad (23)$$

$$i_M(t) = I_{M_1} e^{-\delta t} \left[\frac{\delta}{\alpha} \sinh \alpha t + \cosh \alpha t \right] \quad (24)$$

$$i_1(t) = I_{M_1} e^{-\delta t} \left[-\frac{\delta}{\alpha} \sinh \alpha t + \cosh \alpha t \right] \quad (25)$$

with

$$\alpha^2 = \delta^2 - \omega_0^2 \quad (26)$$

$$\omega_0^2 = \frac{1}{LC_S} \quad (27)$$

and

$$\delta = \frac{1}{2R_2C_S} \quad (28)$$

The initial conditions are

$$u_M(t_3) = 0 \quad (29)$$

$$i_M(t_3) = I_{M_1} \quad (30)$$

When the current through the capacitors C_1 and C_2 falls below the holding current of the thyristor Th_2 the latter goes into open-state at the time t_4 .

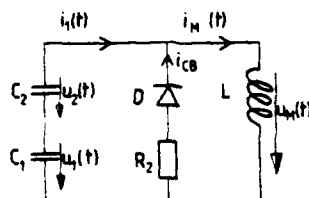


Fig. 9 Equivalent circuit for interval 4 (crowbar starts conducting)

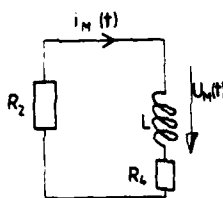


Fig. 10 Equivalent circuit for interval 5 (current fall)

3.6 Interval 5 (magnet current fall, $t > t_4$)

The equivalent circuit of Fig. 10 is now valid. All thyristors are in open-state and the capacitor bank C_1 is disconnected from the magnet. The magnet voltage and current are given by:

$$u_M(t) = -I_{M_0} (R_2 + R_4) e^{-t(R_2+R_4)/L} \quad (31)$$

$$i_M(t) = I_{M_0} e^{-t(R_2+R_4)/L}, \quad (32)$$

i.e., the current falls exponentially to zero with the time constant $L/(R_2+R_4)$.

The initial conditions are:

$$u_M(t_4) = -I_{M_0} (R_2 + R_4) \quad (33)$$

$$i_M(t_4) = I_{M_0} \quad (34)$$

4. Optimization of the commutation circuit

The aim of the optimization is to reverse the current slope as fast as possible. As discussed in Section 3.4, the magnet current continues to rise after the triggering of the commutation thyristor Th_2 . This is illustrated in the magnified view of the magnet current during commutation (Fig. 4f). The current reaches a maximum value after the time $t_M = t_1 - t_2$, which must be as short as possible.

According to Fig. 4g, the time t_M is approximately related to the circuit turn-off t_Q time by

$$t_M = t_Q \left(1 + \frac{U_{12}}{U_{22}} \right), \quad (35)$$

where U_{12} denotes the voltage on the capacitor bank C_1 , and U_{22} the voltage on the commutation capacitor C_2 at the time when the main thyristor Th_1 turns off (t_2). Thus, the ratio t_M/t_Q is only a function of the ratio U_{12}/U_{22} . The latter must be as small as possible.

The voltage ratio U_{12}/U_{22} is given by the voltage divider R_3 , R_5 , and R_6 . U_{12} is determined by the desired linearity of the magnet current as a function of time and U_{22} must be as high as possible. The maximum value of U_{22} is limited by the voltage rating of the magnet. If for the circuit parameters of Section 3.1, commutation is initiated after 5 ms, the voltage on the capacitor bank is $U_{12} = 1.8$ kV when thyristor Th_1 has turned off. The maximum rated voltage of the magnet being 3.6 kV, the optimum voltage of the commutation capacitor C_2 is then $U_{22} = 1.8$ kV and for the time t_M follows $t_M = 2 t_Q = 94 \mu s$.

The circuit turn-off time t_Q must be longer than the turn-off time of the thyristor t_Q . Normally the latter has a considerable spread among thyristors of the same type. Its value depends strongly on the junction temperature, the slope of the commutating current, and the reverse blocking voltage. It is therefore necessary to select thyristors with the shortest turn-off time t_Q and to choose a circuit turn-off time t_Q which is sufficiently long (see Section 5.3).

5. Construction

5.1 General layout

The CERN Super Proton Synchrotron (SPS) is located in a circular tunnel of about 7 km circumference, built in the stable rock down to 60 m underground. The pulse generator is housed in an auxiliary building on the surface and connected to the quadrupole magnet in the accelerator tunnel via a transmission line with a length of 1180 m. The generator is remotely controlled from the main control room, located at about 2 km from the auxiliary building.

5.2 Capacitor bank

The energy storage capacitor bank consists of 29 capacitors of 0.6 mF each. They are rated for 1500 V and a peak discharge current of 2000 A. The series inductance of each capacitor is less than 600 nH and the loss factor is less than 80×10^{-4} at 50 Hz. The dielectric consists of 4 layers of paper with a thickness of 10 μm . The dielectric stress at nominal voltage is 37.5 V/ μm . The capacitor is filled with castor oil.

The individual capacitors can be interconnected to different capacitance values at two different voltage levels: from 0.6 to 17.4 mF at 1.5 kV and from 0.3 to 4.2 mF at 3 kV. This allows operation of the generator with different current waveforms.

The capacitor bank is charged by a regulated power supply with a maximum output of 3 kV/3.3 A. The power supply regulates during the charging time the rate of voltage rise on the capacitor bank. Once the preset voltage is reached it stops charging and regulates the voltage to within $\pm 0.1\%$ of the preset value.

5.3 Thyristors

5.3.1 Ratings: The turn-off time of thyristors increases with their voltage ratings⁵. Therefore the choice of the thyristor configuration must be a compromise between the requirements of a short turn-off time and a high voltage capability.

The BBC thyristor type CSF 549-16 iwl has been chosen. It offers a relatively high voltage rating of 1.6 kV and a turn-off time of 30 μ s, the shortest available for this voltage rating. Three of these thyristors are connected in series. The main parameters are:

$$U_{DRM} = U_{RRM} = 1.6 \text{ kV}$$

$$\int i^2 dt = 320\,000 \text{ A}^2 \text{ s}$$

$$(di/dt)_{\max} = 400 \text{ A}/\mu\text{s}$$

$$t_q = 30 \mu\text{s}.$$

The required value for $\int i^2 dt$ of the thyristor is determined by the following. If the commutation fails, for example due to a missing trigger to the commutation thyristor, the main thyristor takes the complete half sine-wave of the current with an $\int i^2 dt$ considerably higher than for normal operation.

Each thyristor has connected in parallel a 30 k Ω resistor and a series connection of a capacitor of 0.1 μ F and a resistor of 10 Ω .

5.3.2 Voltage sharing: The voltage sharing of the three thyristors during the circuit turn-off time t_0 is influenced by the differences in the reverse recovery charge Q_{rr} of the thyristors. The higher the latter, the later the thyristor takes over forward voltage. Therefore the thyristors have been selected for approximately the same turn-off characteristics. Measurements confirm a satisfactory voltage sharing. Figure 11 shows the three traces of the voltages across the individual thyristors of the stack Th_1 during recovery. The spread in the circuit turn-off time t_0 is about 10%. This spread has to be considered for dimensioning the commutation capacitor C_2 as described by Eq. (21) of Section 3.4. The shortest circuit turn-off time t_0 in Fig. 11 is 44 μ s. This provides a sufficient safety margin compared with the thyristor turn-off time of 30 μ s.

The highest voltage to be blocked in the present design is 4.2 kV whereas the rated forward blocking voltage is 4.8 kV. This gives a safety factor of 1.14.

5.4 Crowbar circuit

The crowbar circuit consists of a series connection of a resistor and a diode. The maximum value of the resistance is critical, since it determines the maximum negative voltage on the magnet. To protect the quadrupole magnet against overvoltages due to component failures in the crowbar circuit, a spark gap has been installed in parallel to the quadrupole magnet.

5.5 Transmission line

The 1180 m long transmission cable between the pulse generator and the magnet has 4 aluminium conductors each with a cross-section of 95 mm². These conductors are diagonally connected in parallel to minimize the cable inductance.

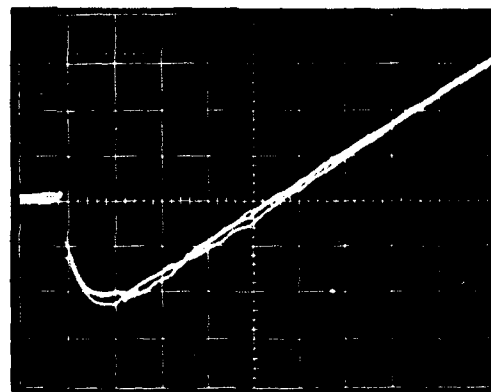


Fig. 11 Voltage sharing of the 3 thyristors of Th_1 . Vertical scale: 200 V/div., horizontal scale: 10 μ s/div.

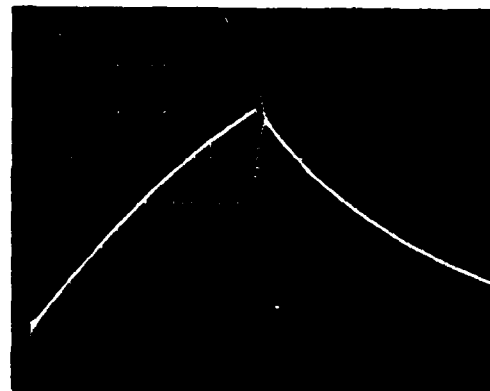


Fig. 12 Magnet current. Vertical scale: 50 A/div., horizontal scale: 1 ms/div.

5.6 Measured voltage and current waveforms, duration of slope reversal

Typical waveforms of the magnet current and the voltages on the magnet and the commutation capacitor C_2 are shown in Figs. 12 to 15. They correspond to the parameters given in Section 3.1 which proved to be optimal for the tuning of the extraction process. A comparison of the oscillograms with the computer plots shows a good agreement between calculations and measurements. In particular, it can be seen that the current rises with an initial rate of 60 A/ms, and that after a duration of about 200 μ s the slope is reversed to -60 A/ms (Fig. 16). Figure 17 shows a typical signal of the extracted beam. It has been taken from a beam current monitor in the extraction channel.

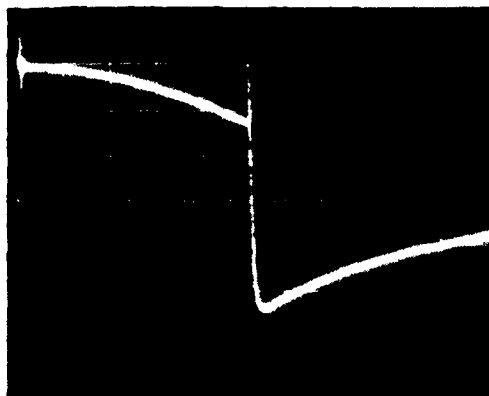


Fig. 13 Magnet voltage. Vertical scale: 1000 V/div., horizontal scale: 1 ms/div.

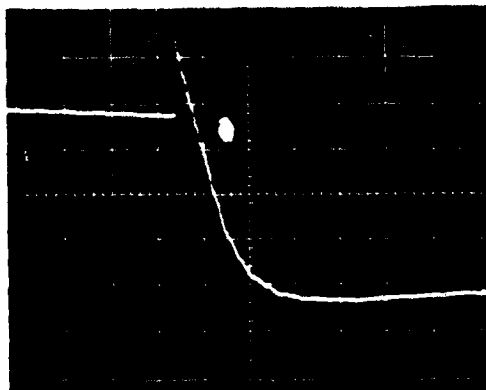


Fig. 14 Magnet voltage. Vertical scale: 1000 V/div., horizontal scale: 0.1 ms/div.

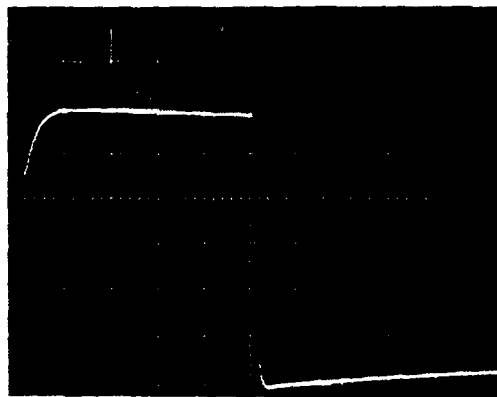


Fig. 15 Voltage of the commutation capacitor C_2 . Vertical scale: 1000 V/div., horizontal scale: 1 ms/div.

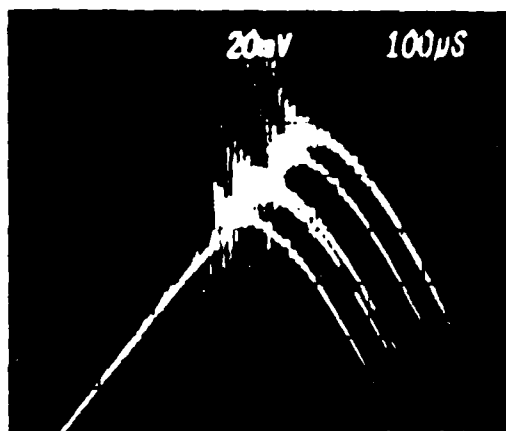


Fig. 16 Magnet current. The picture shows the top of the triangular waveform. Vertical scale: 2 A/div., horizontal scale: 0.1 ms/div.

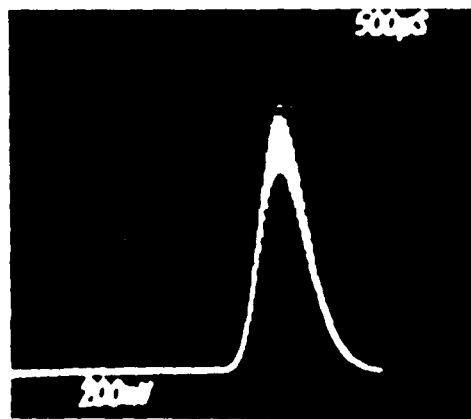


Fig. 17 Typical signal of extracted proton beam. Horizontal scale: 0.5 ms/div.

6. Operational experience

6.1 Commutation initiated by a signal from the beam

Instead of a fixed trigger delay between the initial trigger and the commutation trigger, the reversal of the current slope can also be initiated when a fixed amount of protons has been extracted. This is done with a signal derived from a beam current monitor in the extraction channel. When the number of protons has reached a preset value the commutation is initiated. In this way a constant intensity of protons is extracted from the SPS, independently of the intensity variations of the accelerated beam from one machine cycle to another. Figure 16 illustrates this mode of operation. It shows the upper part of the magnet current waveform for 5 consecutive pulses. Each current pulse is commutated at a different time corresponding to the intensity variations of the beam from one machine cycle to another.

6.2 Remote control

The generator is controlled from the main control room of the SPS, about 2 km away, via the SPS computer control system. This allows the remote turning on and off of the generator, the setting of a voltage on the capacitor bank, the setting of a fixed delay of the commutation trigger, or the setting of a threshold for the extracted current which triggers commutation. It is also possible to acquire the signal from the beam current monitor in the extraction channel, and to survey about 20 status signals which give information about the correct functioning of the generator.

7. Conclusion

The pulse generator has been working without any problems since its installation in September 1978. Up to now it has pulsed about 1.5 million times. The possibility to adjust the current slope and the pulse length proved to be very useful for optimizing the extraction process and for satisfying the changing demands of proton spill times.

References

1. P.E. Faugeras, C.G. Harrison, H. Kuhn, V. Rödel, G.H. Schröder and J.P. Zanasco, The SPS fast pulsed Magnet Systems, IEEE Conf. Record 12th Modulator Symposium, New York, 1976 (IEEE, NY, 1976), p. 147.
2. K.H. Kissler, J. Riche, W. Scandale and G.H. Schröder, Fast Resonant Extraction from the CERN SPS, Partic! Accelerator Conference, San Francisco, 1979, IEEE Trans. Nucl. Sci. NS-26, 3228 (1979).
3. R.W. Jensen and M.D. Lieberman, IBM Electronic Circuit Analysis Program (Prentice-Hall, Englewood Cliffs, New Jersey, 1968).
4. Thyristor Handbuch (Siemens, Berlin and München, 1976).
5. AEG-Telefunken, Leistungshalbleiter, Thyristoren, Erläuterungen (AEG-Telefunken, Belecke, 1975).

Acknowledgements

We are grateful to B. de Raad and W.C. Middelkoop for many discussions and their constant support. The fast resonant extraction mode was implemented in the SPS by K.H. Kissler. R. Chappuis and R. Tröhler have participated in the design and assembly of the generator, the design of the electronic circuits was made by J. Bonthond and J.L. Bretin. J. Riche and H. Verhagen implemented the computer control.

A TWO-STEP HIGH VOLTAGE PULSE GENERATOR

D.C. Fiander, D. Grier, K.D. Metzmacher, P. Pearce
CERN, Geneva, Switzerland.

Summary

A new extraction system for the transfer of protons between synchrotrons at CERN has necessitated the building of special high voltage pulse generators delivering two-step pulses. The maximum pulse power of each step is 100 MW in 15 ohm and is independently variable. The pulse length of each step, also independently variable, is 1.6 ± 0.5 μ s. Pulse rise and fall times are about 30 ns.

Introduction

A new type of high voltage, two-step pulse generator using multi-stage thyatron switches and SF₆ pressurised coaxial cable Pulse Forming Networks (PFN's) has been built at CERN. Two of these pulse generators excite fast pulse magnets in one of the proton synchrotrons; a simplified schematic of the pulse generator/magnet arrangement is shown in Fig. 1.

The output pulse of the generator may be either an ascending or descending two-step staircase or, theoretically, even a long rectangular pulse combining both steps at the same level. However, as will be seen later, certain limitations are met when small interstep voltages are demanded. The pulse width of each step is independently variable, with a maximum of 2.1 μ s for a single step and 4.2 μ s for the total pulse width. Resonant charging power supplies charge the two PFN's to a maximum of 80 kV in a few ms.

Previously designed multi-step pulse generators have suffered from the disadvantage that the step length of descending steps could not be controlled because of the impossibility of triggering the series switches when under reverse voltage¹. The generator now reported overcomes this difficulty by using a bi-directional double cathode thyatron as the series switch. This permits controlled switching independent of the switch polarity; hence ascending and descending pulses of precise duration can be produced.

Description of Pulse Generator

Design and Construction

The simplified schematic (Fig. 1) shows the principal elements of the pulse generator. The PFN's, resonant power supplies and thyatron switches T1 and T3 are identical to those used in previously designed CERN pulse generator systems and have already been described in some detail in an earlier Symposium²; they will be dealt with only briefly in this paper.

Each PFN is a low attenuation ionisation free cable which has tubular inner and outer conductors, the dielectric being multi-layer polythene tapes with SF₆ pressurisation to 9 bars. No semi-conductors are needed at the dielectric/conductor interfaces. Each resonant power supply is based on a high ratio 50 Hz step-up transformer which when pulsed from a large primary electrolytic capacitor permits charge transfer to the PFN. Pre-bias of the transformer core is used and system flexibility is improved by the inclusion of a high voltage diode between power supply and PFN. Switches T1 and T3 both use the CX 1171A single cathode thyatron, operating in a close fitting coaxial housing; insulation to ground is by solid/oil dielectrics, the oil being circulated for cooling purposes. The T1 cathode is pulsed to at least half the PFN1 voltage in operation

and the T1 supplies are insulated accordingly. The T3 cathode is at earth potential and the T3 supplies are therefore conventional. Power supply PS1 charges PFN1 directly and PFN2 is charged by power supply PS2 via the terminating resistor R3.

The series switch T2 uses a double cathode bi-directional version of the CX 1171A thyatron, known as the CX 1171B. The electrical schematic and mechanical layout of T2, both simplified for clarity, are shown in Figs. 2a and 3 respectively. Both extremities of T2 can be charged to 80 kV and its supplies therefore have to be suitably insulated from ground; this not only applies to the heater and reservoir supplies but also the biasing and triggering associated with each cathode. In addition to supporting relatively slow charging voltages the T2 supplies must also withstand high fast pulse voltages of either polarity when the generator is triggered. The provision of reliable insulation of the T2 supplies, whilst retaining the ability to trigger either control grid rapidly and precisely, is perhaps the biggest technological difficulty in the generator design; the solutions adopted are therefore described in some detail.

T2 is installed in a coaxial housing in similar manner and with the same dielectrics as T1 and T3. The symmetry of T2 requires that identical techniques be used for the insulation of the supplies associated with its two cathodes. The solution adopted is to supply each heater directly from the secondary of an oil-immersed, screened isolating transformer, insulated to withstand full charging and pulse voltages. Fed in parallel with the heater is a Faraday cage, located outside the main oil filled switch housing but within an earthed cylindrical cover pressurised to 0.2 bar SF₆ (Fig. 2b). This cage contains the supplies for the reservoir heater, the "keep alive" grid G1, the trigger grid G2 bias and the trigger pulse source. The trigger box on the outside of the cylindrical cover is linked to the Faraday cage by a quartz light pipe which transmits the G2 trigger pulse from an I-R emitter diode. The light pipe can also be rotated and so serves as an insulated adjusting rod for the Faraday cage-mounted potentiometer controlling the reservoir heater voltage. A second I-R emitter diode link from the Faraday cage back to the trigger box prevents charging of the PFN's if a fault occurs in the tube supplies.

The reliability of the T2 switch auxiliary supplies thus largely revolves around the adequacy of design of one 50 Hz high voltage isolating transformer per cathode, which for the voltages involved presents no significant difficulty. The more delicate trigger pulse isolation is easily provided by the quartz rod and Faraday cage in an SF₆ environment.

Principle of Operation

The lattice time diagram for representative switching instants t_1 , t_2 and t_3 of thyatrons T1, T2 and T3 respectively is shown in Fig. 4. For a charging voltage of PFN1 of $2V_1$, the first step amplitude is V_1 , and its length is

$$P_1 = (t_2 - t_1) + \tau_1 \quad (1)$$

where τ_1 is the propagation delay of PFN1 and provided $\tau_1 > (t_2 - t_1) > -\tau_1$

AD-A119 663

PALISADES INST FOR RESEARCH SERVICES INC NEW YORK
IEEE CONFERENCE RECORD OF 1980 FOURTEENTH PULSE POWER MODULATOR--ETC(U)
1980
80-CH-1573-5-ED

F/G 9/5

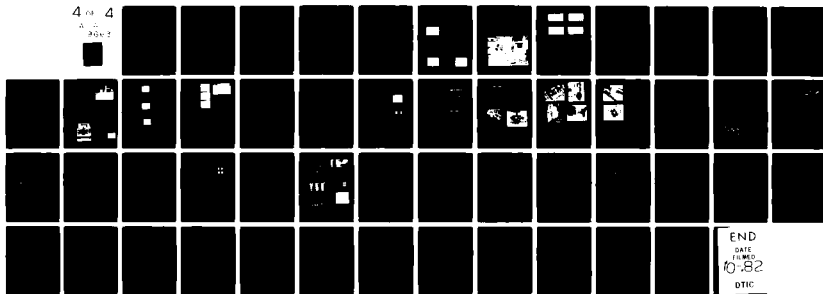
UNCLASSIFIED

NL

4 of 4

4 of 4

30x3



END
DATE
FILMED
10-82
DTIC

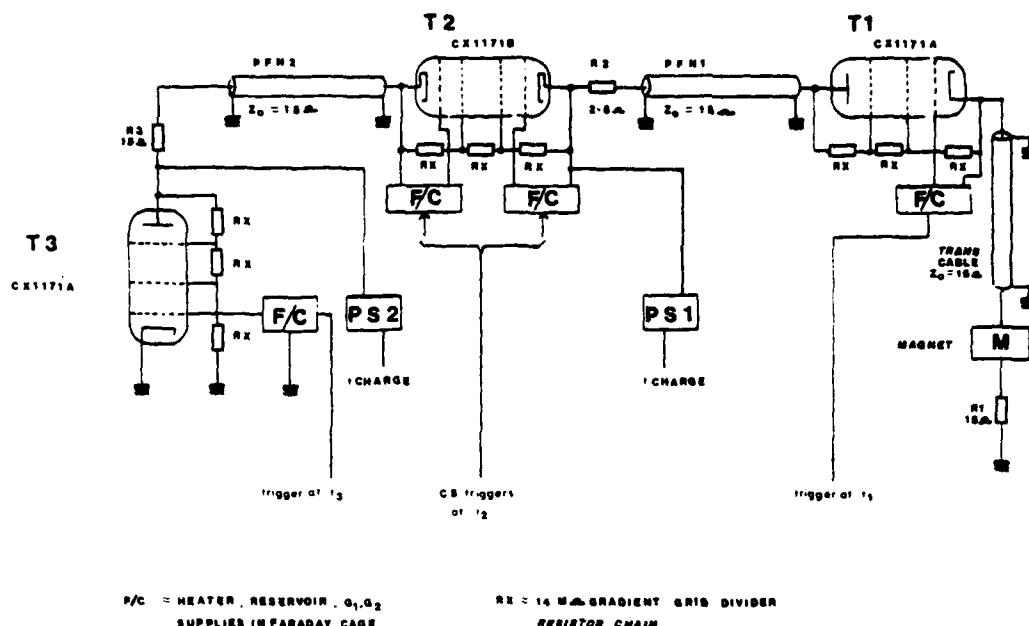


Fig. 1. Simplified schematic of the pulse generator

Likewise for a charging voltage of PFN2 of $2V_2$ the second step amplitude is V_2 and its length is

$$P_2 = (t_3 - t_2) + T_2 \quad (2)$$

where T_2 is the propagation delay of PFN2 and provided $T_2 > (t_3 - t_2) > -T_2$

In theory the output pulse length of each step may be made infinitely small. In practice, and bearing in mind the required generator service, the triggering delays have a range which restricts the minimum step length to about 1.1 μ s.

Thyratron T1 determines the first step rise, T2 determines the interstep rise or fall and T3 determines the second step fall. For positive PFN charging voltages and minimum step 1 length of 1.1 μ s the current in T1 is always positive. That in T2 is either positive or negative depending on the relative charging levels of PFN's 1 and 2. The current in T3 must be also always positive, a condition which is satisfied irrespective of the PFN1/PFN2 charging levels. Care must be taken not to exceed the maximum permissible step 1 length if a hole is to be avoided between step 1 and step 2. Likewise correct switching of T3 requires that the step 2 length is not excessive. Typical theoretical ascending and descending waveforms are shown in Fig. 5.

Particularities of Series Switch T2

Triggering

In unidirectional switching applications of the double cathode thyatron the trigger grid (G2) at the "virtual anode" is connected directly to the local cathode and, in fact, carries a large part of the switched current. For bi-directional switching applications, such as T2, this G2 has to be connected to its cathode via a trigger pulse transformer and filter, both of which have non-negligible impedance. Voltage

transients with an amplitude of 40% of the tube operating voltage and width of the order of 100 ns then can occur between this G2 and its cathode. This transient energy, if not by-passed, is dissipated in the trigger pulse supply circuits, and apart from distorting the rising edge of the switched current, can cause thyatron and trigger circuit damage.

It is found that this grid transient voltage can be suppressed partially by triggering both ends of the thyatron simultaneously to provide a region of pre-ionised gas in the G2 cathode space (Fig. 6). More effective suppression, however, is obtained by bridging G2 to cathode with a non-linear resistor (VDR) of the zinc oxide type. These have a fast response and a plateau voltage of about 2 kV at 2 kA. G2 to cathode waveforms showing voltage transients with and without VDR are shown in Fig. 7.

The self capacitance of the VDR degrades the incoming grid trigger pulse rise, and thus the size and hence maximum energy dissipation of the VDR is limited. In order to increase the operating lifetime of the VDR and to limit spike amplitude in the event of VDR failure the simultaneous pulsing of both trigger grids is maintained for all operating modes of T2. An additional margin of safety could be achieved by further development of the G2 trigger pulse source to allow use of a larger VDR, or by the application of VDR's of a type having higher energy dissipation capability and lower intrinsic capacity.

The G2 trigger pulse circuit is isolated from ground by a 10 mm diameter 200 mm long quartz rod with optically polished ends for minimum light loss. The infra-red trigger light pulse in this rod is detected by a photo transistor which triggers a fast SCR circuit into a 10:1 step-up pulse transformer with a 700 V peak output pulse. The circuit is simple and reliable and gives good switch output pulse jitter and drift performance. However the photo-transistor response is slow

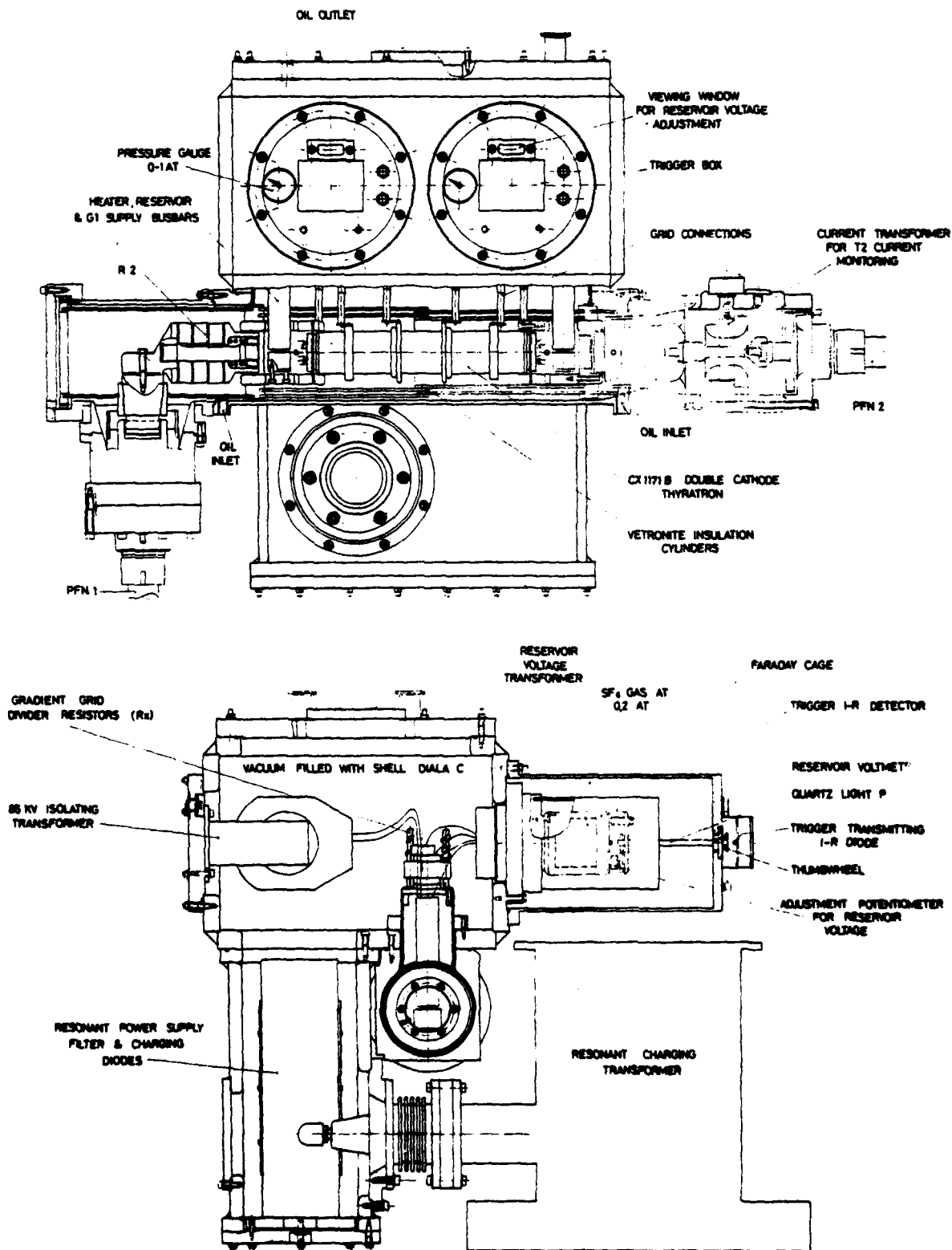


Fig. 3. Mechanical assembly of T2.

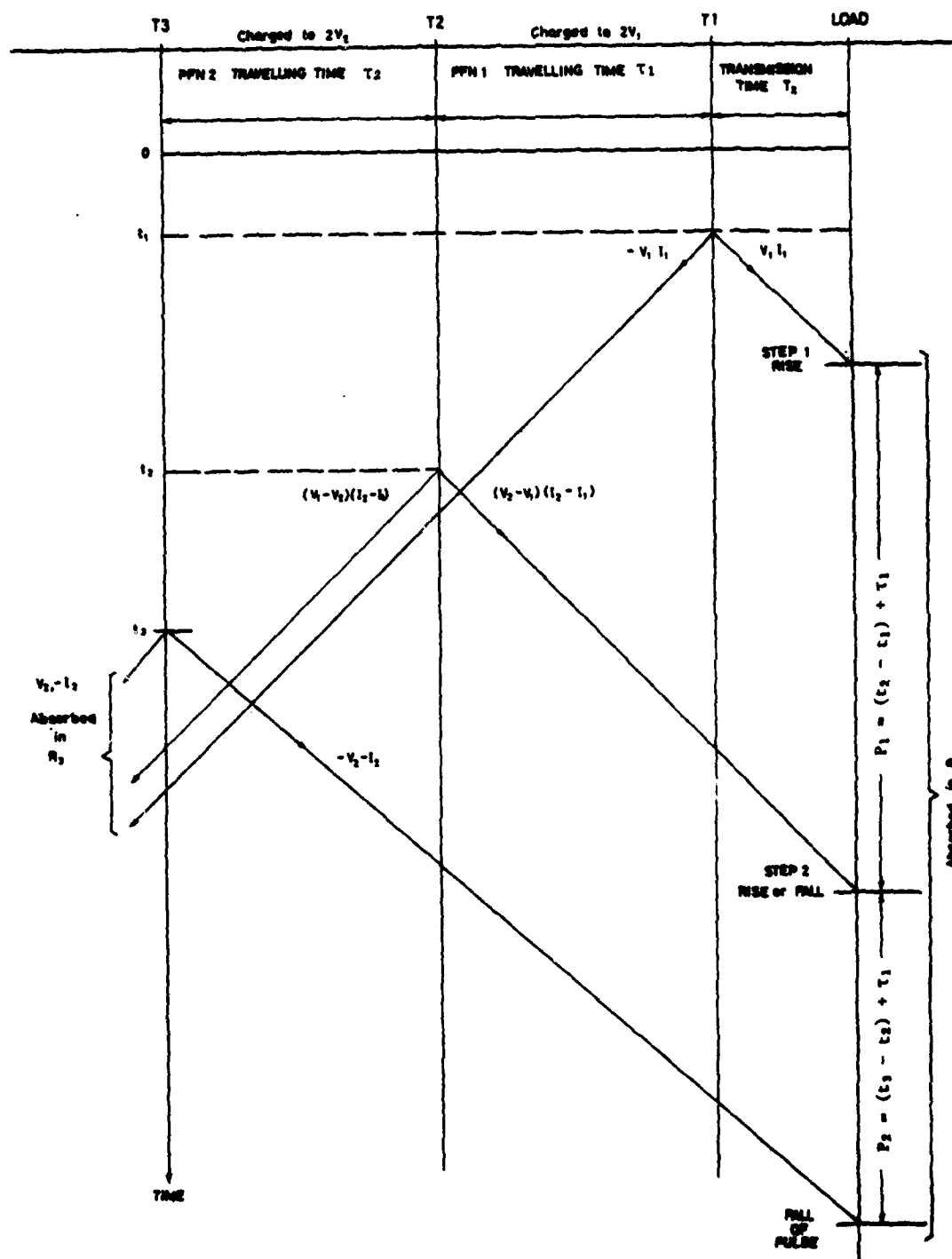


Fig. 4. Lattice time diagram.

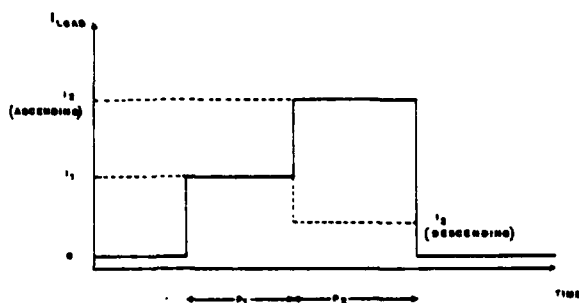


Fig. 5. Theoretical output pulse

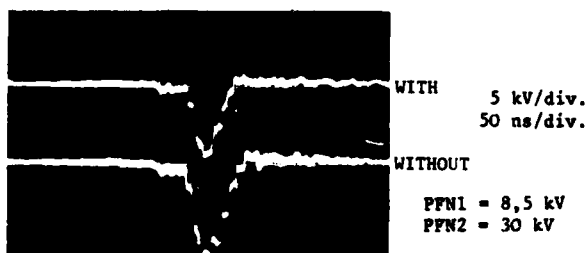


Fig. 6. Effect of simultaneous triggering

$$I = 2 \frac{(V_2 - V_1)}{2Z_0 + R_2} \quad (3)$$

The current from the switching of T1, having traversed PFN1, is partially reflected at R2. This reflected current is:

$$I_y = \frac{-V_1 R_2}{Z_0 (2Z_0 + R_2)} \quad (4)$$

Addition of I_x and I_y to the already established step 1 current, $\frac{V_1}{Z_0}$, gives the amplitude of the step 2 current, $\frac{2V_2}{Z_0}$

which can be shown to be

$$I_2 = \frac{2V_2}{2Z_0 + R_2} \quad (5)$$

From this expression it can be seen that the effective PFN2 voltage for creating the step 2 amplitude has been reduced by the factor $1 + \frac{R_2}{2Z_0}$.

Thus for $R_2 = 2.5 \Omega$, $Z_0 = 15 \Omega$ a flat-top 4.2 μs pulse without switching defects can be produced provided the PFN1 voltage exceeds 60 kV. An undesirable side effect of the addition of R2 is that a small intermediate step is introduced between steps 1 and 2 (Fig. 8). The intermediate step current is higher than the step 2 current by the value of expression (4). The length of the intermediate step is given by;

$$t_i = t_1 - (t_2 - t_1) \quad (6)$$

from which it may be deduced that the length of the intermediate step tends to zero as the length of step 1 approaches the two way travelling time of PFN1. Considerations of correct switching and required step length variation put a practical limit of about 100 ns on the minimum length of this step. Such a short distortion is considered acceptable because of the integrating characteristic of the magnet load. It will be appreciated that the deadband in the operating range of the pulse generator has not been eliminated, but merely shifted. Reduction of the absolute deadband could be envisaged by reducing the minimum operating voltage of the thyatron; improvements in this direction may be possible by the addition of C/R networks across the tube gradient grids, or by simultaneous triggering of gradient grids and control grid.

Operating Experience

A prototype two-step pulse generator was built in 1978 and operated for about 4000 hours, during which time small but nevertheless important improvements were introduced. A total of 15 million output pulses of varied waveform was produced. There were no thyatron failures nor was there any degradation in their performance during this prolonged test.

Encouraged by this result, three generators for the excitation of fast beam transfer magnets were manufactured during 1979 and have recently been installed and commissioned (Fig. 9). The characteristics of these generators are summarised in Table 1, where the performance data relates to the generators pulsing into 15 Ω closely coupled matched resistive loads.

The following comments can be made concerning thyatron performance. The rise of step 1, due to T1, can be as little as 26 ns (10 - 90%) but is generally slowed down to 30 ns by reduction of thyatron gas pressure to minimise any tendency to spontaneous breakdown. The step 1 to step 2 rise or fall, due to T2, measured in the resistive load is about 40 ns; this is larger than the same rise or fall measured directly at T2, about 35 ns, because of PFN 1 attenuation and mismatch in T1. The adjustment of the two reservoir voltages of T2 is critical if good risetime is to be obtained. Severe imbalance of the two reservoirs leads to gas pumping from one end of the tube to the other, with resulting significant polarity dependence of the

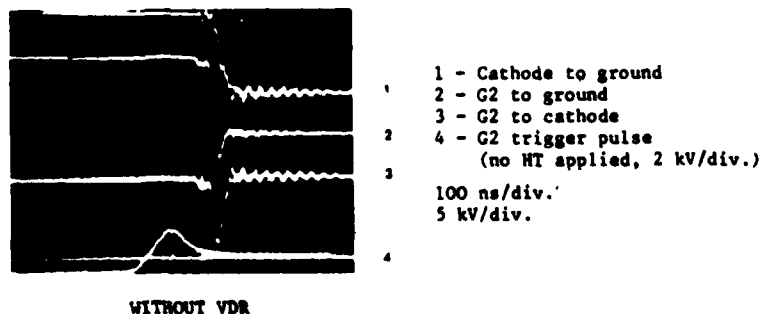


Fig. 7. The effect of VDR's and simultaneous triggering.

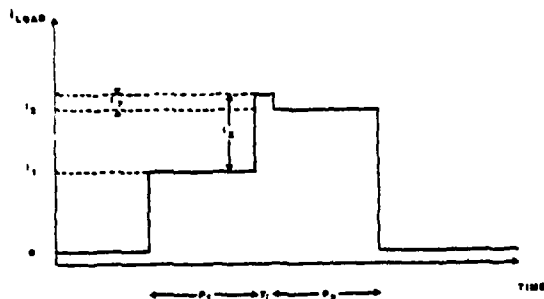


Fig. 8. Theoretical output pulse with R2. risetime and reduction of voltage hold-off for both polarities. In general, the double cathode thyatron seems to de-condition more easily than the single cathode version and needs to be run-in more carefully. It also has a greater tendency to spark discharge. The final step 2 fall, due to T3, measured in the resistive load is about 40 ns; the T3 rise of about 28 ns is considerably degraded by the attenuation of PFN's 1 and 2 and by the mis-matches of T1 and T2. An appreciable "cable tail" follows the main pulse.

Figs. 10 and 11 show waveforms of the output pulse in a matched resistive load for a generator with dead-band shifting resistor R2 of 1,7 ohms. The ascending pulse (Fig. 10a) results from PFN1 and 2 charging voltages of 40 and 50 kV respectively; the corresponding figures for the descending pulse (Fig. 10b) are 80 and 30 kV. The short (200 ns) intermediate level due to R2

Table 1. Generator Characteristics

Impedance Z_0	15 ohms
Number of steps	2
Max. voltage	85 kV either PFN
Min. voltage	5 kV
PFN charging time	4 ns
Output pulse length	$1,6 \pm 0,5 \mu s$ per step
Voltage deadband	$\pm 5 kV$
Absolute jitter	5 ns
Short term drift	< 5 ns/day
Long term drift	± 30 ns/month
Max. pulse rate	1 pulse/0,6s continuous
Pulse risetime (min.)	30 ns 1st step rise
10 - 90% into resistive load	40 ns 2nd step rise/fall
	40 ns fall of 2nd step
Spontaneous breakdown rate	< 1 pulse in 10^5

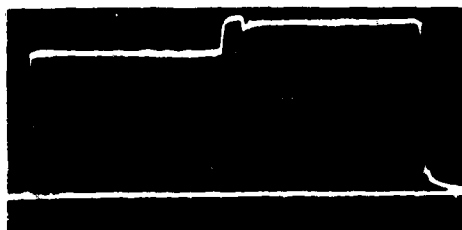
is clearly visible in both photos. The slight hole appearing at the start of the step 2 level occurs because of inductive mis-match in T2 which partially reflects the backward travelling wavefront generated by the initial switching of T1.

Conclusion

A flexible and reliable high voltage two-step pulse generator can be built from two series-connected PFN's. The choice of a bi-directional thyatron as the switch



Fig. 9. General view of switch installation.

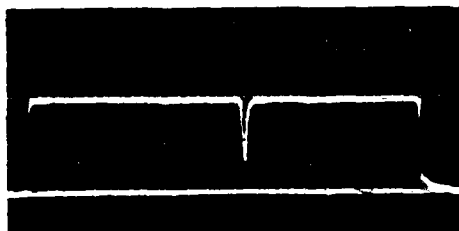


a) Ascending staircase pulse
PFN1 = 40 kV, PFN2 = 50 kV 500 ns/div.

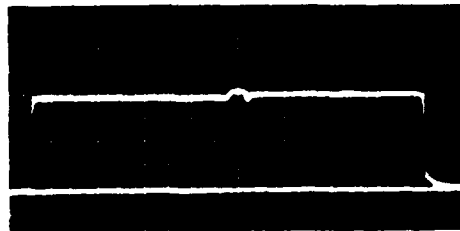


b) Descending staircase pulse
PFN1 = 80 kV, PFN2 = 30 kV 500 ns/div.

Fig. 10. Typical staircase output pulses.



a) Flat-top pulse with hole
PFN1 = 65 kV, PFN2 = 67 kV, 500 ns/div.



b) Flat-top pulse
PFN1 = 65 kV, PFN2 = 70 kV 500 ns/div.

Fig. 11. Flat-top pulse with and without hole.

between the PFN's permits the production of precise ascending and descending staircase pulses over a very wide voltage range and with accurate control of pulse length. The technological problem of insulating and triggering this series switch are resolved by standard engineering techniques.

Acknowledgements

The authors wish to thank the Directors General of CERN and the Division Leader of its PS Division for permission to publish this paper. They also wish to acknowledge helpful discussions with the English Electric Valve Co. Limited, particularly for the development of the bi-directional thyatron switch.

References

1. "A Modulated Fast Ramp for the CPS Continuous Transfer", D.C. Flander et al, Proceedings of 1977 Accelerator Conference, Chicago.
2. "High Voltage Pulse Generators for Kicker Magnet Excitation", D.C. Flander et al, 11th IEEE-ACED Modulator Symposium Proceedings, P. 129, New York 1973.

RAPID CYCLING SYNCHROTRON (RCS) SINGLE STAGE KICKER MAGNET*

Dale E. Suddeth and Gerald J. Volk
Argonne National Laboratory
Argonne, Illinois 60439

Abstract

A new single stage kicker magnet system is designed and is being fabricated for the RCS accelerator of the Intense Pulsed Neutron Source (IPNS-I) at the Argonne National Laboratory. This system will replace the two stage kicker in present use.

The magnet aperture is 10 cm wide by 5 cm high and the magnetic length is 0.89 m. The magnetic field intensity is 0.1021 T for a 25 milliradian kick to the 500 MeV proton beam. A field rise time (10 to 90%) of 80 ns and a flat top of 100 ns is needed. The magnetic field fall time is not critical so a lumped parameter magnet with a 7.2 ohm load will be used. The electric current required through the single turn magnet is 4863 A. A new energy storage and switching system is designed and is being fabricated for energizing the magnets.

The techniques and hardware used will be described along with some of the experience gained in the use of the two stage system which will help to improve the new design.

Introduction

Single stage as it is used in this paper means that the kicker magnet is in a single straight section of the accelerator as opposed to the magnets being placed in two different straight sections.

The previous design expectations were such that the kicks of the two separate magnets would add directly to give a 25 milliradian kick.¹ Actual RCS operation demonstrated that the betatron phase shift between the two magnets was not correct for "in phase" effect. This left the kicked orbit displaced from the extraction septum far enough to prevent efficient extraction.

Magnet Specifications

The magnet requirements are more constrained than in the two stage system in that the magnetic length is now 0.89 m where before there were two lengths of 0.56 m each. The total 1.12 m length should, however, be corrected to an equivalent 0.84 m since one magnet was energized to one half the field of the second magnet. Figure 1 shows a cross section of the magnet.

$$\text{Magnetizing current } I = \frac{Bh_g}{\mu_0} = \frac{0.1021 \times 0.057}{4\pi \times 10^{-7}} = 4631 \text{ A} \quad (1)$$

where

h_g = gap height in m.

*Work supported by the U.S. Department of Energy.

The calculated current value assumes zero ferrite reluctance and the current is 4863 A with a 5% allowance for ferrite reluctance.

As in the previous system, each leg of the magnet will be driven separately from opposite corners for minimum magnet voltage. A result of this type of excitation is that there is no "steady state" electric field affecting beam deflection. A special Belden type YR 10914, 14 ohm coaxial cable will be used for the pulse forming network (PFN) and transmission line. Two of these, each with a 14 ohm load, are connected in parallel. This fixes the magnet and load voltage at 4863 A x 7 ohms = 34 kV.

$$\begin{aligned} \text{Inductance per unit length} &= \frac{\mu_0 W_g}{h_g} \\ &= 2.51 \times 10^{-6} \text{ H/m} \quad (2) \end{aligned}$$

where

W_g = gap width (same units as h_g).

The value for each leg of the magnet = 1.25×10^{-6} H/m. The inductance of a 0.89 m long magnet leg = 1.1×10^{-6} H. The magnetic field fill time for the magnet is approximately $L/R = 159$ ns. This is about a factor of two too long so the magnet will have to be divided into at least two modules. Figure 2 shows a view of the magnet system.

To form a transmission line magnet by adding capacitance to match such a low impedance load is impractical particularly where the length is constrained and the basic magnet impedance is 113 ohms. The required capacitance per unit length would be $1.25 \times 10^{-6} \times 7^2 = 0.0255 \mu\text{F/m}$. It is difficult to obtain such capacitance and keep stray inductance to a small fraction of the magnet inductance.

With a lumped inductance magnet and 7 ohm transmission line, the pulse voltage jumps up nearly to the PFN voltage at the magnet input which helps to make the field rise time nearly equal to the L/R time. Of course, one must be careful to account for this mismatched condition in its effect on the rest of the system. Some help in reducing rise time, although minor, can be expected in matching the magnet to the load with capacitance; 0.011 μF per leg per module is needed. Series parallel combinations of low cost, high voltage, door knob type, ceramic capacitors have been successfully used for this application. An additional effect of the capacitors is in the field flat top characteristics.

A model of one module of the magnet was fabricated for low level tests. Figure 3 shows the B field photograph using a mercury relay as the switch and 50 ohm lines in parallel as the PFN and transmission lines. This, of course, is an optimistic case since

the high voltage, high current interconnections will add some stray inductance.

One might expect that the use of three modules each with filling time of 53 ns would be a further improvement. One must weigh the expected fill time reduction against the added PFN and switch cost and complexity and additional stray inductance for the interfaces. The economies of scale may actually be less for a three module magnet.

Since the RCS is of the first harmonic operation and therefore extracts only one bunch per pulse, the magnetic field fall time is of minor consideration since it affects only load dissipation. The magnet will be enclosed with an aluminum case which will act as a Faraday shield and also serve as a low impedance interface with the coaxial cable shields.

Switch Considerations

Figure 4 is a block diagram of the system components. Four English Electric Valve (EEV), CX-1192 deuterium thyratrons will be used as switches. ($V_{\text{maximum}} = 120 \text{ kV}$, $I_{\text{maximum}} = 6000 \text{ A}$).

It is physically impossible to match the thyratron and its housing to 7 ohms because high voltage considerations limit the spacing between the housing and the thyratron plasma. An improvement in the bandwidth is expected over nonmatching even with a 14 ohm assembly.

One of the major operating cost considerations for the RCS is the thyratron replacement costs. Lifetime data is thus of prime importance. No standard data is available, as far as we know, and it is difficult to compile since parameters such as dI/dt , I_{maximum} ,

I_{average} , V_{maximum} , V_{reverse} , allowable time jitter and repetition rate all affect lifetime. After some frighteningly short lifetimes of approximately 1 million pulses during shakedown testing and initial operation of the RCS, we now have two thyratrons in service that have seen over 200 million pulses. These operate at $dI/dt = 3.5 \times 10^{10} \text{ A/s}$, $I_{\text{maximum}} = 3500 \text{ A}$, $I_{\text{average}} = 0.011 \text{ A}$, $V_{\text{maximum}} = 74 \text{ kV}$, $V_{\text{reverse}} = 7 \text{ kV}$ for 50 ns and time jitter < 10 ns. These lifetimes are certainly more encouraging than what we had expected.

We are remaining optimistic for the new system although we recognize that the higher $dI/dt = 4.9 \times 10^{10} \text{ A/s}$, $I_{\text{maximum}} = 4863 \text{ A}$, $I_{\text{average}} = 0.044 \text{ A}$ will have a bearing on the lifetime. The new system is designed to run up to 45 Hz versus 30 Hz for the previous system.

The solid state thyratron trigger circuit has been improved to provide a 3.5 A, 1 μs wide pulse to the thyratron grid. Solid state transient suppressors have been added at strategic points where failures had occurred

from thyratron voltage kickbacks. The 47 V avalanche transistor voltage was increased to 62 V. The avalanche transistor 2N3262 was replaced with a 2N3229. Six of these transistors, each with its own primary winding, drive the pulse transformer.

PFN and Charge Circuits

Belden type YR-10914, 14 ohm coaxial cable will be used instead of RG 220-U for the PFN for reasons of simplicity and hopefully reliability. The special 14 ohm cable is supposed to be capable of 100 kV pulsed operation. Both ends of the PFN cable will terminate in oil as also the input end of the transmission line to the magnet. This arrangement should reduce the cable breakdown problems which we had with previous cable which was potted with silicone rubber. We plan to lay the 75 feet of PFN cables in an insulated tray so as to minimize physical stress and to reduce noise from cable to ground corona discharge. No connector is used with the 14 ohm cable but rather inner and outer braids are clamped with as short a separation length as possible at their terminations.

We have had good reliability with the hard tube, series regulator charging circuits and we will use this method replacing the 4PR250C with the Eimac 8960. The 4800 W capability of four tubes in series will provide adequate dissipation for charging four, 14 ohm, 75 foot cables to 80 kV at 45 Hz.

An oil to water heat exchanger will be used to remove the heat from the tanks in order to maintain temperature to less than 35°C.

Load Description

We had excellent results terminating the 50 ohm coaxial cable with a Carborundum coaxial power resistor connected so as to resemble a lossy transmission line. This load, however, has insufficient dissipation for the revised system. We are trying to extend the technique by using Carborundum type AS, washer style, high power, ceramic resistors with the 14 ohm cable. Each of the eight loads must be capable of 1600 W dissipation.

Summary

Although this project is not pushing the state-of-the-art for thyratrons, the application engineering is challenging since it is pushing the limits for some of the components. It will be rewarding to see that the goals are attained.

References

1. D. E. Suddeth and G. J. Volk, "Intense Pulsed Neutron Source (IPNS-I) Accelerator 500 MeV Fast Kickers," IEEE Transactions on Nuclear Science, Vol. NS-26, No. 3, pp. 3024-3025 (June 1979).

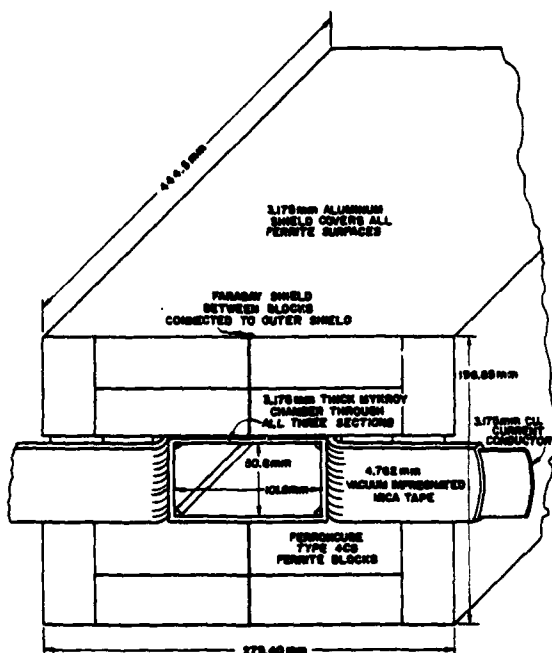


Fig. 1. RCS Kicker Cross Section

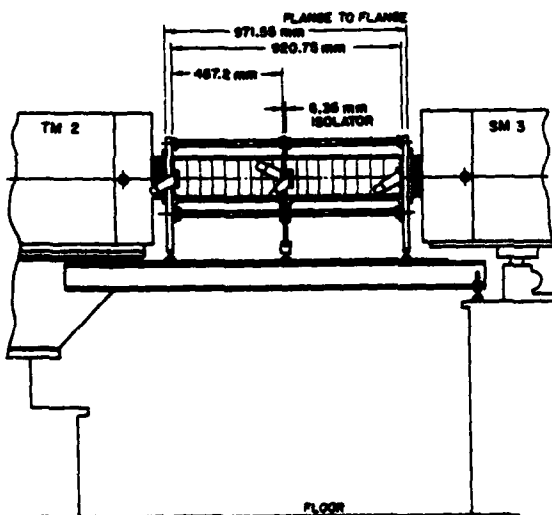


Fig. 2. RCS Kicker Elevation

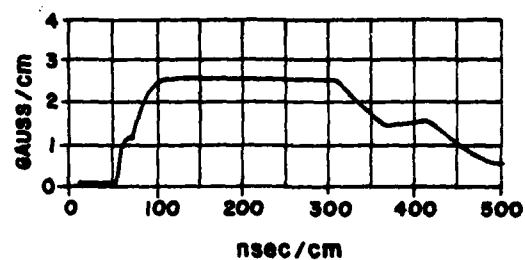


Fig. 3. Field versus Time of RCS Kicker Magnet Model

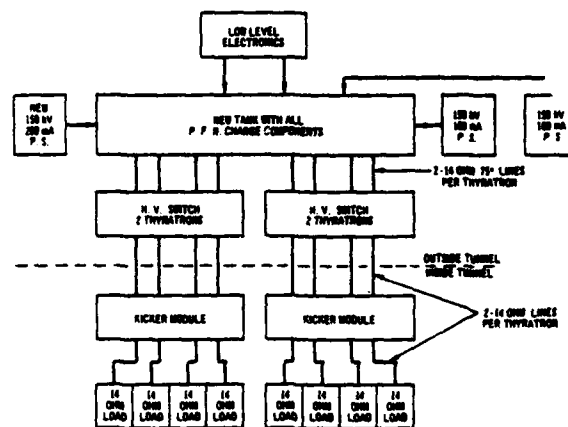


Fig. 4. Kicker System Layout

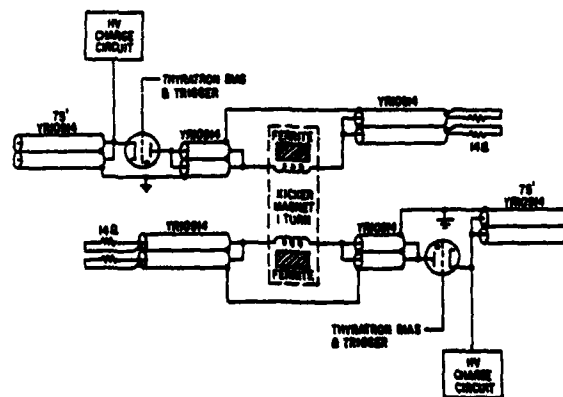


Fig. 5. Kicker Schematic Diagram

FAST-EXTRACTION MODULATORS FOR LOS ALAMOS SCIENTIFIC LABORATORY PROTON STORAGE RING

W. C. Nunnally, D. W. Hudgings, and W. J. Sarjeant
Los Alamos Scientific Laboratory
P. O. Box 1663
Los Alamos, NM 87545

Introduction

The Proton Storage Ring (PSR) now being designed at the Los Alamos Scientific Laboratory (LASL) will accumulate 800 MeV of protons from the Los Alamos Meson Physics Facility linear accelerator and deliver them in intense bursts to neutron production targets at the Weapons Neutron Research Facility. Two modes of operation are planned. In the short-bunch mode, the protons are accumulated for 110 μ s into six circulating bunches, each of nanosecond width every 8.3 ms, and are extracted at a rate of 720 bunches/s. In the long-bunch mode, a single 270-ns bunch is accumulated in 750 μ s every 67 ms. Each bunch is extracted within a few microseconds after accumulation is completed. The circulation period of protons in the PSR is 360 ns.

Design and Reliability Considerations

A bunch trajectory deflection of 6 mrad is required for extraction from the PSR. This requires a magnetic field path of 300 G-m (Gauss-meter). Because of the requirement for fast risetime and good pulse fidelity, the "magnet" is a parallel-plate transmission line 4 m long, schematically illustrated in Fig. 1. The force on a proton moving between the plates is $|F| = q|\mathcal{E} + \mathbf{v} \times \mathbf{B}| = q\mathcal{E}(1 \pm \beta)$, where $\beta = v/c = 0.84$ is the proton velocity expressed as a fraction of the velocity of light, and $|\mathcal{E}| = |\mathbf{E}|$ for TEM wave propagation in vacuum. The deflection pulse is propagated in the direction opposite that of the protons to get additive effects of electric and magnetic forces.

The two sides of the transmission lines are driven with pulses of opposite polarity, resulting in a virtual ground at the midplane. The impedance seen by the pulse generator is 50 Ω for each plate relative to ground. For a 10 cm aperture (separation between stripline elements), a voltage of ± 50 kV is required. The pulse parameters for the short- and long-bunch-mode modulators are listed in Table I.

A number of design requirements follow from the application of the modulators in a working accelerator

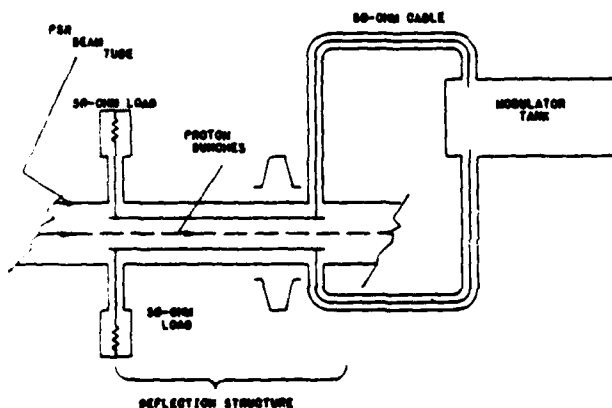


Fig. 1. PSR extraction modulator schematic.

TABLE I
PSR FAST EXTRACTION MODULATOR
PULSE PARAMETERS

PARAMETER	SHORT BUNCH MODE	LONG BUNCH MODE
PURPOSE	Remove Single Two Proton Bunches	Remove Single 270 ns Proton Bunch
PULSE VOLTAGE (+ & -) 80kV	(+ & -) 80kV	(+ & -) 80kV
PULSE CURRENT (+ & -) 1kA	(+ & -) 1kA	(+ & -) 1kA
PULSE RISETIME	< 30ns	< 30ns
PULSE FALLTIME	< 30ns	Not critical
PULSE BASE WIDTH	< 80ns	> 300ns
PERCENT AFTER PULSE RINGOUT	< 2%	Not critical
PULSE REPETITION RATE	720 Hz	12 - 120 Hz
PEAK POWER	100kW	100kW
AVERAGE POWER	4.3kW	0.43 - 4.3kW

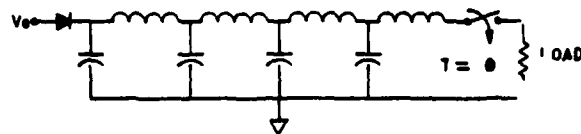
facility. Because of the limited downtime acceptable to the user and the limited operating budgets, all of the modulator components must have a long lifetime. High reliability is essential since the consequence of improper deflection is beam spillage, which makes the PSR radioactive. Thus the failure rate in the long-bunch mode should not exceed 10^{-4} .

Pulse-Generator Systems

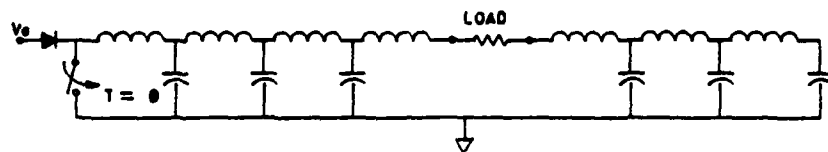
The development of the short-bunch mode, fast-extraction modulator prototype is detailed in this report. Similar systems will be used for the long-bunch mode, fast-extraction modulator. The short-bunch-mode modulator presents the largest technological challenge; the long-bunch modulator problems are similar but less demanding.

A symmetrical generator system is desired to reduce the deflection voltage levels required with respect to ground. In addition, it is desirable to use some type of voltage multiplication system to reduce the required switch operating voltage and thus increase reliability. Several pulse-forming network (PFN) type pulse-generator systems were evaluated because of the square pulse shape desired. The requirement for minimum prepulse favors a switched PFN that prevents charging transients in the load as shown in Fig. 2a. However, the switch of Fig. 2a must operate at twice the desired output voltage, and some form of voltage inversion (transformer) or double, oppositely charged, system must be used to obtain the required push-pull output. The basic Blumlein system of Fig. 2b can be used to reduce the switch operating voltage to that of the desired output-pulse voltage, but the line charging current must flow through the load, causing a prepulse. A dual, oppositely charged, Blumlein-line scheme can be configured to provide push-pull outputs as shown in Fig. 2c, but again the switch must operate at twice the single output voltage and must be dc isolated with respect to ground for the charging potentials.

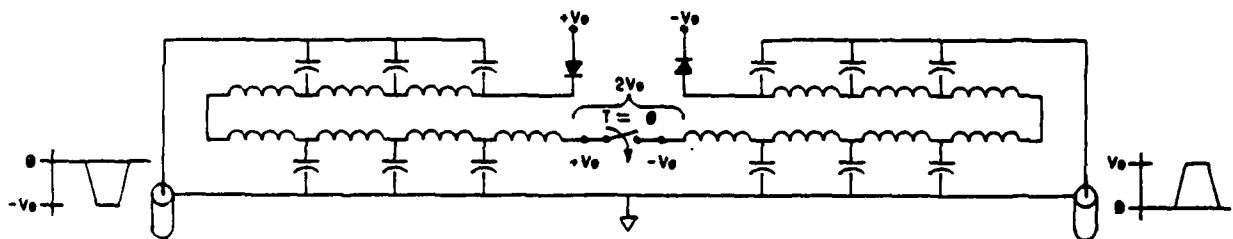
A new Ferrite-Isolated Blumlein-(FIB) line circuit was developed at LASL to alleviate the above problems and is shown in Fig. 3. This circuit uses one element to switch two Blumlein lines in parallel (instead of in series as in Fig. 2c) and ferrite inductive isolation to provide bipolar output pulses. Computer network analysis indicates that the sum of the output pulses is <0.01% of the absolute value of each. The FIB line circuit can also reduce the charging currents that flow



(A) SWITCHED PFN CIRCUITS



(B) BASIC BLUMLEIN LINE CIRCUIT



(C) PLUS-MINUS DUAL BLUMLEIN LINE CIRCUIT

Fig. 2. Pulse generator circuits.
(A) Switched PFN circuit.
(B) Basic Blumlein-line circuit.
(C) Plus-minus charged dual Blumlein-line circuit.

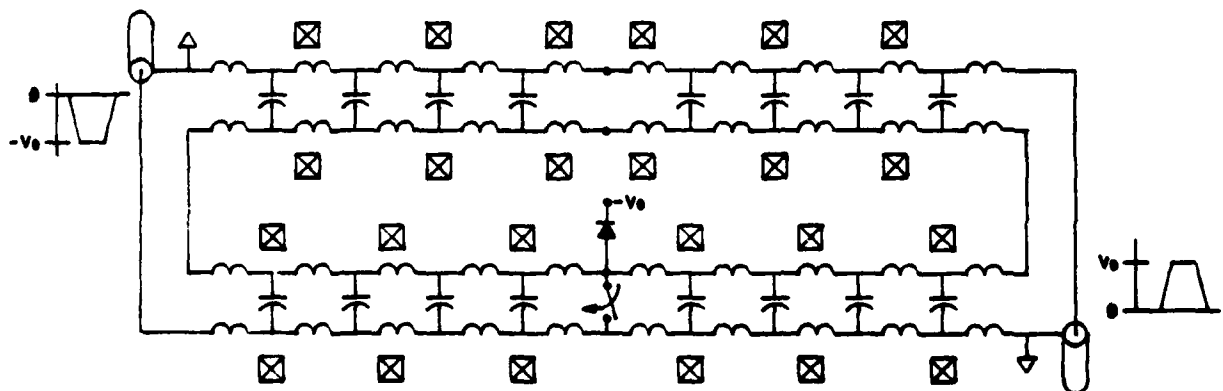


Fig. 3. Ferrite-Isolated Blumlein (FIB) circuit.

through the loads. If the circuit is charged at two points from the same source, the prepulses can be reduced to $<1\%$ of the output voltage.

The pulse-generator system of Fig. 3 was fabricated using 45 ns (15 ft), 23- Ω coaxial cable (17/14) lines and 50- Ω output cables. Sixty Ferrocube Type C38, 2-in. o.d. ferrite toroids per line provide sufficient inductive isolation for the short-bunch mode when the cable is threaded through them, as shown in Fig. 4. The assembly is switched with an EG&G HY-3024 gradient-grid thyatron for increased voltage hold-off reliability. The tube is mounted, as shown in Fig. 5, in a low-inductance shroud on an EG&G TM-42HV isolation system. The switch tube rises to one-half the output voltage during the pulse. Initially, the tube was triggered with a 2.5-kV positive pulse (unloaded) from an SCR-switched PFN added to the negative bias at grid G2 and a positive bias on G1, as shown in Fig. 6a. The resulting pulse shape, shown in Fig. 6b, indicates an unacceptably long turn-on time for the tube. Several other trigger configurations were investigated and are shown with their resultant output pulses in Figs. 7 and 8. The jitter for the trigger arrangements of Figs. 6-8 was excessive, ranging from ± 10 to ± 200 ns. A trigger booster consisting of an 8.5- Ω , 1- μ s PFN switched by an EG&G HY-6 thyatron in the cathode follower circuit of Fig. 9a was inserted between the original trigger unit and the HY-3024. Three overlays of the resulting output pulse shape are shown in Fig. 9b, indicating low total system jitter (1-2 ns) and very good circuit-limited pulse shape. The voltage on the trigger booster was reduced from 4 kV to 1 kV with little deterioration in pulse rise- and falltime ($<10\%$ increase). The delay time from booster anode voltage fall to HY-3024 anode fall is about 55 ns. The trigger booster pulse length was reduced from 1 μ s to 250 ns without any observable change in delay, jitter, or output pulse shape. Note that the after-pulse ringout is greater than that desired, but can be reduced by matching the pulse generator to the load more closely.

Charging System

The charging system is required to charge the Blumlein lines (~ 5 nF) to 50 kV. The desire for high reliability is manifest in the choice of a charging system that uses a combination of resonant and transformer pulse charging. The charging circuit is shown

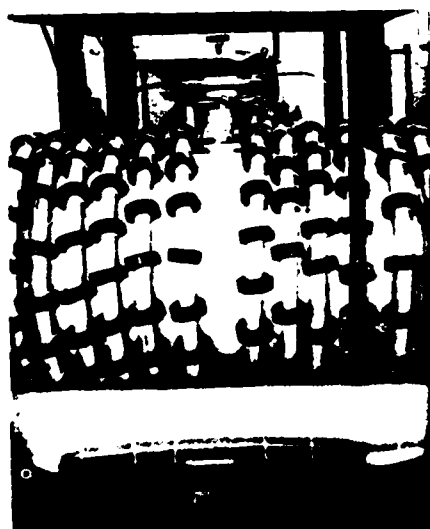


Fig. 4. FIB line.

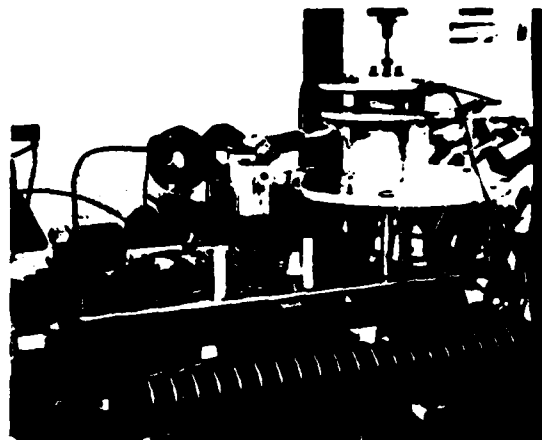


Fig. 5. Thyatron shroud and deck.

in Fig. 10. Ideally, a 10:1 voltage step-up transformer would be used to charge the Blumlein lines to 50 kV from an intermediate capacitor resonantly charged to 5 kV. However, the stray capacitances are a sizable fraction of the FIB line. Thus the intermediate energy storage capacitor must be resonantly charged to 6.2 kV in order to charge the FIB line to 50 kV. The intermediate energy storage capacitor is resonantly charged in 250 μ s. Then the transformer system charges the Blumlein lines to 50 kV in ~ 4 μ s. The main Blumlein-line switch is triggered within 100 μ s after charging so that the high-voltage system is energized for only a short time, reducing prefire probability. The transformer backswing also assists in turning off the charge thyatron (initially an EG&G HY-3002) so that both switches are not closed simultaneously to reduce fault problems. The charge thyatron is a 25-kV unit, but it is operated at only 6.2 kV to reduce prefires and increase reliability. The voltage on the intermediate energy storage capacitor is regulated with a reactive de"Q" circuit, also illustrated in Fig. 10. The voltage on the intermediate capacitor is monitored during the charging cycle and the de"Q" switch is closed when the voltage reaches the desired value. Closing the switch returns any residual energy stored in the charging choke to the low-impedance power-supply filter capacitor and thus prevents the intermediate energy storage capacitor from charging further. The charge thyatron and blocking diodes require the largest average and rms currents. The switch-tube and diode requirements are listed in Table II. The charge thyatron will probably have to be a 5-in. EG&G tube (123 A rms) to provide reliable long-life operation at the 43 A rms current required. A complete computer

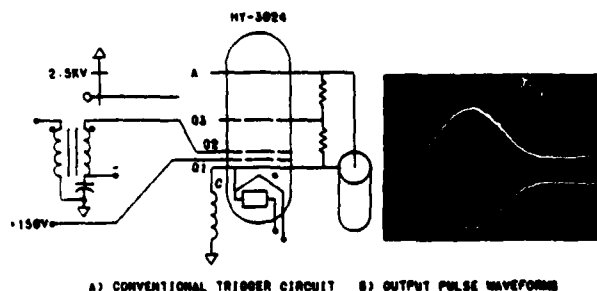


Fig. 6. Initial trigger circuit and pulse output.

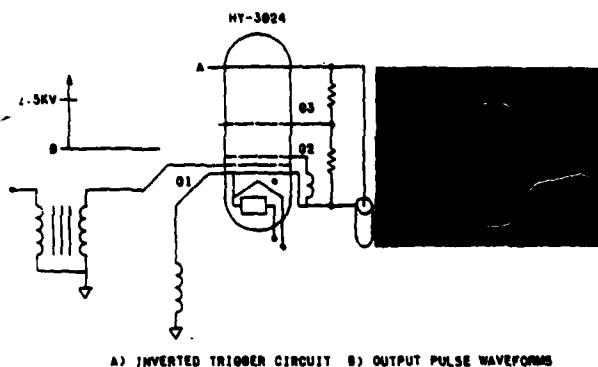


Fig. 7. Inverted trigger circuit and pulse output.

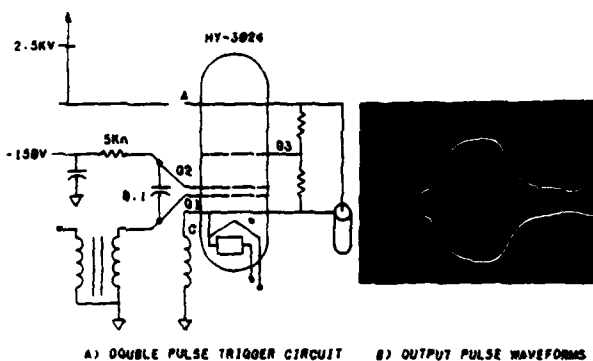


Fig. 8. Double pulse trigger circuit and pulse output.

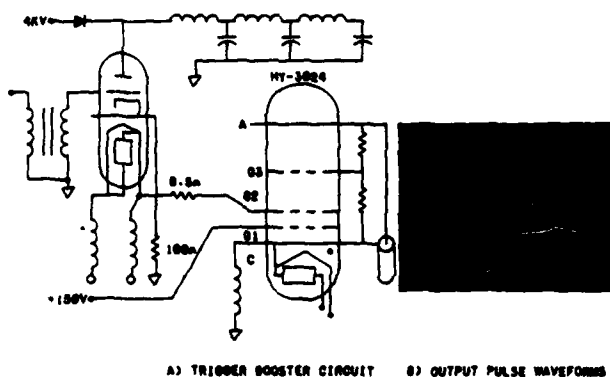


Fig. 9. Trigger booster circuit and pulse output.

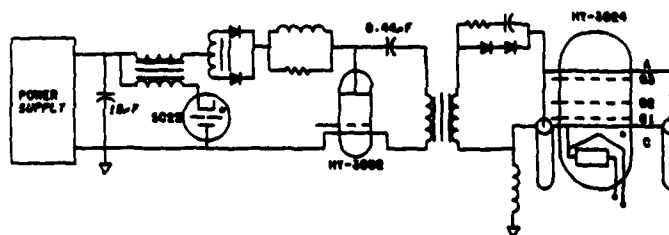


Fig. 10. Two-stage resonant and transformer charge circuit.

TABLE II
SHORT-BUNCH MODE
EXTRACTION MODULATOR SWITCH AND DIODE PARAMETERS

Parameters	Charging Switch	Output Switch	Charging Diode
Operating voltage	6.2 kV	50 kV	50 kV
Peak current	1.3 kA	4.3 kA	120 A
Repetition rate	720 Hz	720 Hz	720 Hz
Pulse width	3.5 μs	50 ns	250 μs
Average current	2.0 A	1.5 A	2.0 A
RMS current	43 A	18 A	6.0 A
Lifetime	>10 ⁴ H	>10 ⁴ H	>10 ⁴ H

model of the charge system was used to check the thyatron performance and the charging efficiency of the transformer circuit. The system charging, excluding the power supply, is about 80% efficient for this particular circuit; most of the energy is lost to the transformer stray capacitance, which is close to 10% of the Blumlein-line capacitance. The remainder is lost in the charge thyatron, the diode snubber, the diode forward resistance, and the transformer magnetizing reactance.

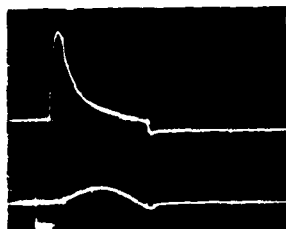
Charging Diode Tests

The charging diodes for the fast (4 μs) transformer charge system present several unusual requirements. First, the rms and average currents are large, as listed in Table II. Second, the charging diodes must turn on in less than one-tenth of the current pulse to prevent large anode dissipation, and must recover in less than one-tenth of the current pulse time to prevent energy from returning to the transformer primary energy store. Several manufacturers' diodes were tested for I-V turn-on characteristics, and also life tested singly at the current levels and repetition rates present in the actual circuit. The voltage and current waveforms for several diodes from different manufacturers are shown in Fig. 11.

System Considerations

The entire modulator system is mounted on a hydraulic scissor lift table inside a tank of transformer oil, as shown in Fig. 12. The output cables are routed to the deflection structure within the proton storage ring and then on to 50-Ω loads for dissipation. The lift table permits easy access to the components for modification and maintenance. Two separate kicker systems (short-bunch and long-bunch modes) will be used separately with the same deflection structure. The modulator system will be equipped with computer-programmable time-delay units and power supplies to permit

TOP: VOLTAGE 50V/DIV
 BOTTOM: CURRENT 50A/DIV
 1 μ s/DIV



a) DIODE A

TOP: VOLTAGE 50V/DIV
 BOTTOM: CURRENT 50A/DIV
 1 μ s/DIV



b) DIODE B

TOP: VOLTAGE 20V/DIV
 BOTTOM: CURRENT 50A/DIV
 1 μ s/DIV



c) DIODE C

Fig. 11. Diode voltage and current waveforms.

computer control. The time-delay units will be interfaced to the modulator system by LASL fiber optic trigger links.

Life test of the prototype system and components at the desired operating conditions will provide reliability data for the final modulator systems.



Fig. 12. Picture of short-bunch-mode modulator prototype.

Conclusions

The development of a short-bunch mode fast-extraction modulator for the LASL proton storage ring has made necessary the design and development of a resonant transformer charging circuit and the design of a new FIB line circuit to provide bipolar pulse outputs with low prepulse, postpulse, and an optimum high-voltage switch environments. The systems are now being developed to operate reliably at the high-average powers required. The short-bunch mode fast-extraction modulator prototype is presently operating. The initial construction of the long-bunch mode fast-extraction modulator prototype is under way, with results expected within the year.

References

1. G. T. Coate, L. R. Swain, Jr., *High-Power Semiconductor-Magnetic Pulse Generators*, MIT Press, Cambridge, Massachusetts, 1966, pp. 57-67.

OVERVIEW OF THE ETA/ATA PULSE POWER*

L. L. Reginato & R. E. Hester

University of California
Lawrence Livermore National Laboratory
Livermore, California

Introduction

A pulsed electron accelerator has been constructed and is now in operation at the Lawrence Livermore Laboratory¹. This Experimental Test Accelerator (ETA) a 5 MeV, 10 kA, 50 ns FWHM, five pulse burst at 1 kHz, was designed to be the front end or injector for the Advanced Test Accelerator (ATA). The ATA is presently under construction and will have the following parameters: beam energy - 50 MeV, beam current - 10 kA, pulse length - 70 ns, repetition rate in a ten pulse burst - 1 kHz.

The parameters which make the pulse power components unique for these machines are the high repetition rate in a burst and a high degree of regulation in the system to insure pulse to pulse repeatability. Because of the larger number of components required for the ATA, a much higher degree of reliability will be required. Improvements and modifications continue to be made on the ETA which is serving as a base of development for all ATA pulse power components. Furthermore, all ATA pulse power components will be tested at length in a test stand before beginning mass production to insure proper design to meet voltage, current, rep-rate and life requirements.

Overall System

A block diagram of the overall system is shown in Figure 1. Although many of the major components for the ATA are similar or identical to the ETA's, there are several changes in overall design that are being made and several proposed ones for improved performance.

Charging System

The ETA adapted the existing modulators in a constant current charging mode as the primary regulated power source while the ATA will utilize a much simpler and less expensive capacitor-limited voltage doubler system. The high degree of regulation required for pulse to pulse repeatability will be achieved by one of two ways, depending on the switch chassis system adopted. If the ETA technique of sequential firing of parallel chassis is adopted to achieve high repetition rates, then a crowbar will be used to accurately stop charging when the proper voltage is reached and simultaneously the primary AC power switch is opened. A serial rep-rateable system is also under consideration. If adopted, the regulation will be

obtained by the de-queing of a command resonance charging system. In either case the capacitor limited doubler will yield a leading power factor which is beneficial in partially canceling some of the magnet system lagging power factor.

Switch Chassis and Resonant Transformer

The load to the charging system is the 12 Blumlein capacitance, about 14 nF. A resonant transformer is still the logical choice for charging the water Blumlein. The ETA utilizes a coupling coefficient of 0.525 thus avoiding a bidirectional switch². All existing systems were capable of handling the extra power required by the less efficient coupling. In the case of the ATA, however, because of the much larger energy involved, it became imperative, that we adopt the more efficient coupling coefficient of $K = 0.6$ for the resonant transformer. This type of transformer is extensively used for charging capacitive loads and yields optimum conditions for energy transfer from the primary capacitance to the secondary. At the peak of the secondary or Blumlein voltage, the primary voltage and current and secondary current are all zero resulting in almost all the energy being transferred to the Blumlein and then out to the load by the spark gap. In order to carry the reverse current through the switch a thyatron in the reverse direction has been added. This type of a switch will be adopted with either the parallel delivery system or the series rep-rate system. Figure 2 is the schematic for the pulse power conditioning system.

A quick look at SCR technology showed that many advancements have been made in di/dt , but a considerable development program would be necessary before a direct replacement for the thyatron could be made. Schedule, rep-rate and life considerations did not allow us to pursue the usage of a low voltage spark gap as a primary switch.

In comparing the parallel delivery system with the series rep-rate one, there is little doubt that the series one offers less interaction between components, is easier to maintain, and is more flexible. It carries with it a new set of problems such as regulation, frequency response and a large energy storage bank. The parallel one, however, offers the capability of higher repetition rate during a burst since the switch has to handle only one pulse in a burst and recover before the next one fires. This is at the cost of more components.

*Lawrence Livermore National Laboratory is operated by the University of California for the Department of Energy under Contract No. W-7405-Eng-48.

*ATA Project Work is performed by LLNL for the Department of Defense under DARPA (DOD) ARPA Order 3718, Amendment #14, monitored by NSMC under Contract No. N60921-80-PO-W0003

Spark Gap and Blumlein

The Blumlein for the ATA accelerator has been increased in diameter from 15" to 18". This should yield fewer breakdowns at the 250 kV levels. This design is expected to hold voltage in the full ringing mode at 280 kV without breakdown. Figure 3 shows a typical ringing test at full rep-rate. We are also attempting to equalize the length of the inner and outer lines, but difficulty in air bubble removal from the water dielectric may make this design impractical. We have further deviated from the ETA design in that we have traded some impedance for length to obtain a 70 ns FWHM. The Blumlein impedance is now 12 Ω and the overall result is an increase in the total energy stored.

The spark gap³ has undergone considerable redesign in order to adapt to the new larger diameter Blumlein. The new design reduces the inductance from the Blumlein to the spark gap electrodes. The electrodes and the spacing remain essentially unchanged. ETA has shown that the coaxial cylindrical geometry allows the trigger electrode to wear uniformly in the axial direction with no change in electrical characteristics resulting in long life. The coaxial geometry further assures high gas velocities to achieve the one kHz burst mode repetition rate.

Accelerator Cell and Transmission Lines

The accelerator consists of a 2.5 MeV electron gun and 190 accelerator induction units. Each accelerator unit generates 250 kV. The energy at each gap is achieved the same way as in the ETA;⁴ the induction electric field is generated by a changing magnetic flux in the ferrite materials. The ATA cavities have been tested and have shown that they can support the 70 ns FWHM required. The ferrite cores were carefully selected so that they would automatically be reset to reverse saturation by the Blumlein charging current. One major

difference between the ETA and ATA accelerator cell is the added ferrite pieces on the feed points and back plane of the cell to suppress the beam breakup mode frequencies.⁵ (Figure 4) This has eliminated the need for pulsed magnetic fields to insure beam stability. The magnet power supplies require a stability of 0.02% to insure a stable beam.

Trigger System

Even with the voltage limitations imposed by the cables, the jitter on the ETA was quite acceptable. On the ATA, however, we will use higher voltage cables which will allow us to increase the trigger voltage level by 50% and easily insure the low jitter. A similar fan-out system as the ETA will be used until sufficient outputs are available to trigger the whole accelerator (Figure 5). The timing of the accelerator gap voltages relative to each other is adjusted by cable lengths. The same switch-chassis, resonant transformer and spark gap as the rest of the system will be used except for the Blumlein which will store less energy.

- ¹The Experimental Test Accelerator (ETA), by R.E. Hester, et al, IEEE Transactions on Nuclear Science, Volume NS26, No. 3, June 1979
- ²Off-Resonance Transformer Charging For 250 kV Water Blumlein by E. Cook, L. Reginato, Thirteenth Pulse Power Symposium, Buffalo, New York 1978
- ³High Repetition Rate Burst-Mode Spark Gap, by A. Faltens et al Thirteenth Pulse Power Symposium, Buffalo, New York 1978
- ⁴Pulsed Ferrite Core Tests For 50 ns Linear Induction Accelerator, by L. Reginato, E. Cook, W. Dexter, J. Schmidt at The International Magnetics Conference, Florence, Italy May 9-12, 1978
- ⁵Reduction of The Beam Breakup Mode Q Values In The ETA/ATA Accelerating Cell by Daniel Bix, UCID #18630.

NOTICE

This report was prepared by the UCLLL as an account of work sponsored jointly by the U.S. Department of Energy and the Defense Advanced Research Projects Agency. Neither the U.S. Government, nor any of its employees, nor any of its contractors, subcontractors, or their employees, makes any warranty, express or implied, or assumes any legal liability or responsibility for the accuracy, completeness or usefulness of any information, apparatus, product or process disclosed, or represents that its use would not infringe privately owned rights.

NOTICE

Reference to a company or product name does not imply approval or recommendation of the product by the University of California, the U.S. Department of Energy, or the Defense Advanced Research Projects Agency.



Summary

Sandia National Laboratories is completing the construction phase of the Particle Beam Fusion Accelerator-I (PBFA-I). Testing of the 36 module, 30 TW, 1 MJ output accelerator is in the initial stages. The 4 MJ, PBFA Marx generator has provided 3.6 MA into water-copper sulfate load resistors with a spread from first to last Marx firing between 15 to 25 ns and an output power of 5.7 TW. This accelerator is a modular, lower voltage, pulsed power device that is capable of scaling to power levels exceeding 100 TW. Research on the upgrade of PBFA-I to PBFA-II is already underway.¹ PBFA-II will be a 100 TW, 3.5 MJ output accelerator which will provide a testbed for breakeven target experiments.

This type of accelerator's high efficiency and low cost make it an attractive candidate for a fusion energy reactor system. Present accelerator efficiencies range between 30 to 40 percent from the Marx generator to the electron or ion beam diode and construction costs are less than ten dollars per joule. The elements of the PBFA technology and their integration into an accelerator system for particle beam fusion will be discussed.

Overall Program Update

During the last 12 months, the Electron Beam Fusion Accelerator² (EBFA) has been modified to accelerate either electrons or ions and renamed the Particle Beam Fusion Accelerator (PBFA). This modification was accomplished with a slight cost increase and with no change in delivery time and represents an example of the flexibility of this approach to fusion. Figure 1 shows ion beam focussing progress which initiated the change. Recently, the focussed ion power density was increased by a factor of ten. Simultaneously, target design improvements (shown as circles labelled SL and LLL) resulted in a several fold reduction in the required beam intensity for breakeven. These two factors indicate that scientific feasibility demonstration of ICF can be accomplished on PBFA-II, our next accelerator upgrade.³ Present ion current densities approaching 1 MA/cm² and present ion output energies over 150 kJ have been achieved in separate experiments.³ Reasons for choosing ions over electrons are shown in Figure 2.

The changes involved between PBFA-I and PBFA-II are shown in Figure 3. The present .8 TW modules will be upgraded within the same volume and the accelerating voltage will be increased from 2 to 4 MV for better coupling to the targets and more flexible magnetically-insulated outputs. The present 36 modules will be increased to 72 and the upgrade will be preassembled and then placed into the present tankage. The installation of the upgrade will require one year. PBFA-II will be described in more detail at this conference by D. L. Johnson.¹

PBFA-I Accelerator Description

As seen in Figure 4, the electromagnetic power is obtained by operating 36 modules in parallel. Each module has a sequence of energy stores which are

*This work was supported by the U. S. Department of Energy under Contract DE-AC04-76-DP00789.

Light Ion Beam ICF

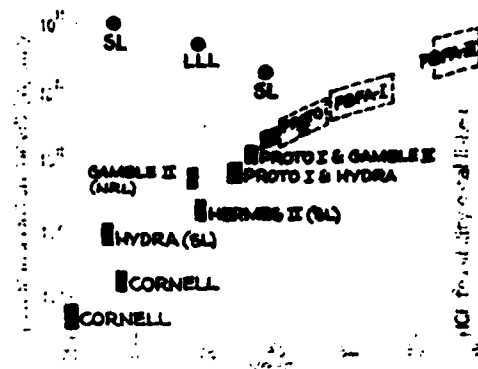


Fig. 1. Light Ion Beam ICF.

Light Ion Features

- preheat minimized \Rightarrow improved pellet performance
- ~100 % energy absorption
- ~80 % transfer of electric power to ions
- economical pulse power systems for ions or electrons
- rep rate possible
- increase effective power by bunching
- less channel energy for beam transport

EBFA \rightarrow PBFA

Fig. 2. Light Ion Features.

separated by synchronized switches. The primary energy store is a 112 kJ Marx generator composed of capacitors charged to ± 100 kV. The Marx switching is accomplished with triggered gas switches. The Marx energy is transferred to a water intermediate storage capacitor in 800 nanoseconds while achieving a peak power of 7 TW with the 4 MJ transfer. The water capacitors then transfer the energy to the pulse forming line in 200 nanoseconds through 36 triggered gas switches. This triggered switch provides the timing synchronization for all modules and has a rms uncertainty of 1.6 ns. The modules each have two parallel pulse forming lines which are switched into a wave mixer using self-breakdown, multichannel, water-dielectric switches.

PSFAI → PSFAK

particle type	e	→	i
power/module	.8TW	→	1.3TW
pulse length	40ns	→	40ns
voltage	2MV	→	4MV
number of modules	36	→	72
	(module operational)		(module under development)

- upgrade will take 1 year - mid '83-'84
- same tank, controls, etc.

Fig. 3. PSFA-II Changes.

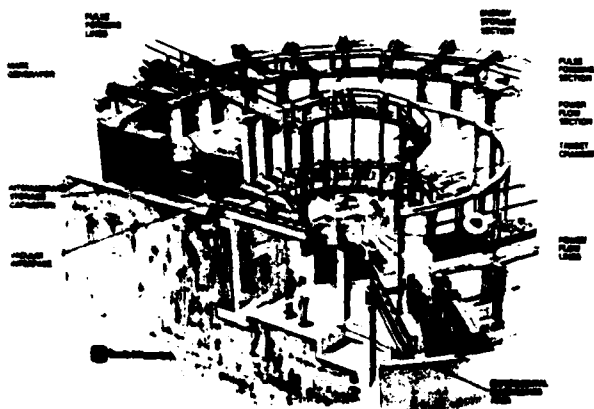


Fig. 4. PSFA-I Artist's Conception.

The output pulse (40 ns) then flows through a line transformer to the vacuum insulator. The resulting 2 MV pulse is placed on the magnetically-insulated transmission lines⁴ and transported at stresses of 2 MV/cm to the target chamber. Diodes then convert the electromagnetic energy to particle beam energy between 20 cm and 90 cm away from the target. The ions are then focussed or transported in plasma channels to the target.

Present Construction Status

The accelerator building has been completed and the accelerator is nearing completion. The first accelerator output is expected by July 1980. A photograph of the tank is shown as Figure 5. The Marxes are fully modularized and can be replaced simply by removing one unit with the crane and inserting the next unit. The Marxes are positioned by I-beam supports as shown in Figure 6. The Marx Pulser Unit (MPU), which triggers four Marx generators, is shown on the tank floor. It is located behind the main Marx as shown in Figure 7. These MPU's are developed by Maxwell Laboratories for Sandia.

A safety switch which can direct a trigger pulse either to ground or the main Marx is included and will be discussed later. The Marx generator output is switched mechanically between the water/oil feedthrough insulator and a water resistor load as shown in Figure 8. These components are in the oil-insulated section.

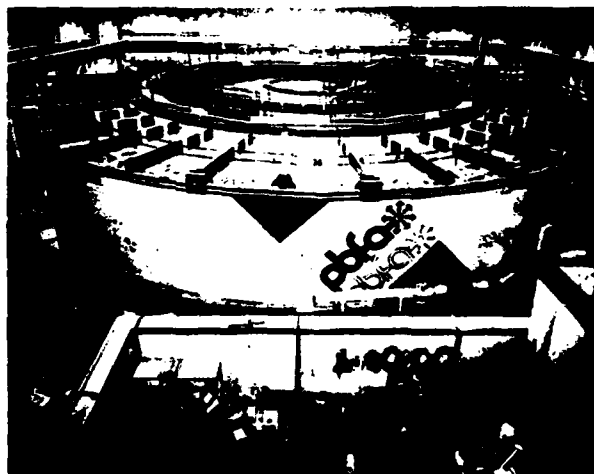


Fig. 5. PSFA-I Tankage.



Fig. 6. PBFA-I Marx Generator.

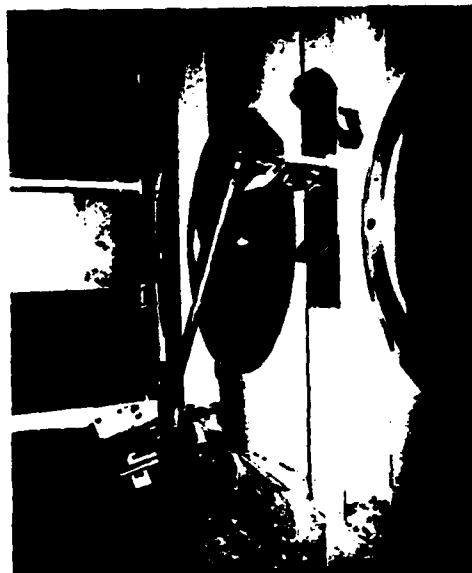


Fig. 8. Marx Safety Switch.

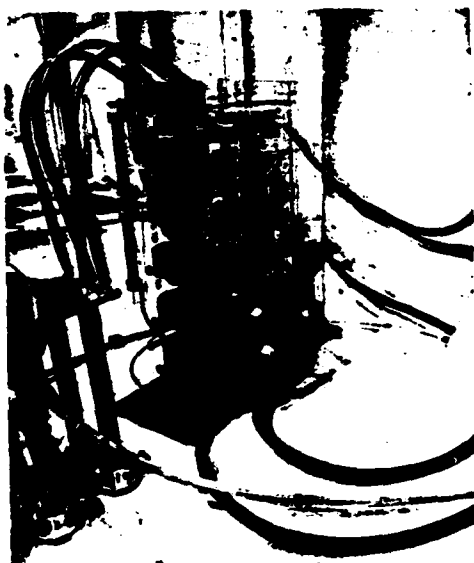


Fig. 7. PBFA-I MPU.



Fig. 9. PBFA-I Water Switch.

The 21 nfd water-insulated energy storage capacitors are shown in Figure 9 along with a 3 MV-triggered switch. These components are all in the water section.

The front of the pulse forming lines connect through a water-insulated line transformer to the vacuum interface. The front of the vacuum interfaces and the magnetically insulated lines are shown as Figure 10. Thirty-six of these lines then converge on the pellet chamber as shown in Figure 11. Note the four technicians to provide relative scale.

Module Protective and Testing Devices

A common failure mode for modular pulse power accelerators is a prefire. This occurs when the Marx generators are being charged or are waiting for the trigger pulse. When a prefire occurs and no protective devices are available, two consequences can occur. First, the experiment, which usually takes many manhours to install, is destroyed. Second, the 3 MV gas trigger system may not fire and the water capacitors will arc

over and destroy themselves. To prevent these problems, three energy diverter switches were installed as shown in Figure 12. The first switch, between the trigger Marx and the main Marx, will divert any prefiring timing circuit or trigger pulse generating circuits up to a few seconds before accelerator operation. In addition, this system will be exercised from the control room to show correct operation of the triggering system prior to the experiment. The second switch, which connects the Marx generator with the intermediate store, is normally connected to a dump resistor. In case of a main Marx prefire, the energy is routed into these dump resistors. Again those resistors are used to test the timing and firing of the entire accelerator to this point just prior to a chamber experiment. The previously described switches are remotely operated. The third switch must be manually set and connects the SP_6 triggered switch to a dump resistor. The resistor connection is made to check the main gas switch trigger, trigger systems, and switch functions. By using these built-in test points and exercising the



Fig. 10. Magnetically-Insulated Transmission Lines.

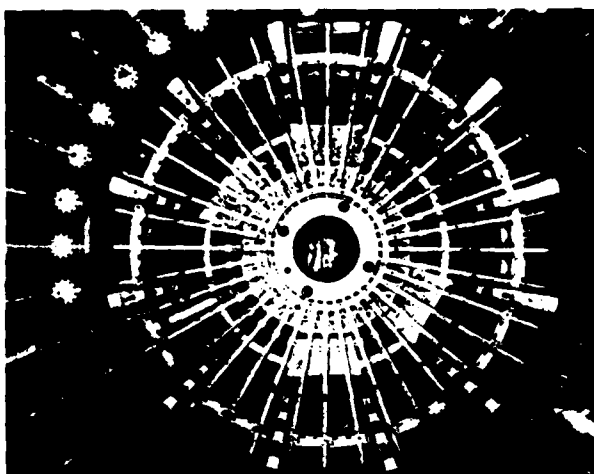


Fig. 11. PBFA-I Central Section.

accelerator frequently, the accelerator should provide reliable pulses for experimenters and yet allow relatively standard, lower reliability components to be utilized in the accelerator.

Marx Generator Experimental Results

The thirty-six Marx generators have been charged to ± 100 kV which places approximately 4 MJ total energy in the banks. The Marx was then discharged into its resistive loads and the voltage and currents were measured.

The voltage monitors generally have more electrical noise than the lower impedance, better shielded current monitors. Subsequently, all timing data was obtained from the current monitors. The current monitor outputs were recorded using a fast time sweep to provide more accurate data. A composite trace showing six Marx generator currents into their 14 ohm loads is shown in Figure 13. The Marx generator erection transient and discharge currents are similar in both time and amplitude. A total current of 2.6 MA at a power of 2.6 TW for 70 kV Marx charge is shown.

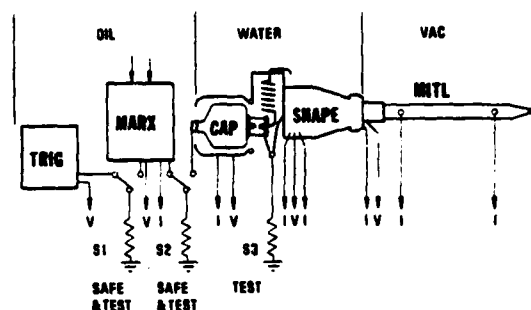


Fig. 12. PBFA-I Diverter Test.

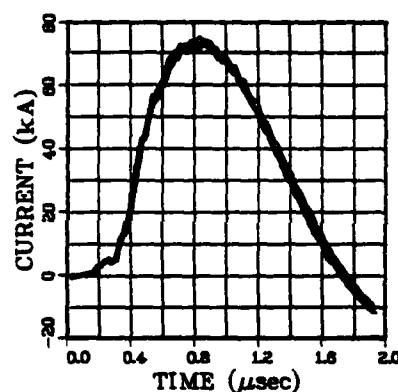


Fig. 13. Marx Generator Output Data.

The generator timing spreads were measured by using Tektronix 7912 digital recorders and data processing equipment. The time between first and last Marx current traces were measured and the total spread was obtained. See Figure 14. Spreads between 15 and 25 nsec were typical. This spread indicates a one-sigma jitter between 4 and 6 nanoseconds for these generators. Most of the testing was performed at a 70 kV Marx charge (approximately 2 MJ) then several proof shots were performed at a 100 kV charge and 4 MJ stored. The spread measured contains all jitter due to trigger generators, trigger Marx generators and the main Marx generator.

This series of tests showed the Marx generators, charging systems, and triggering systems to be operating well with lower jitter than expected. Installation of the water section components is almost completed and the power flow lines are installed. Initial operation of the accelerator is expected this month.

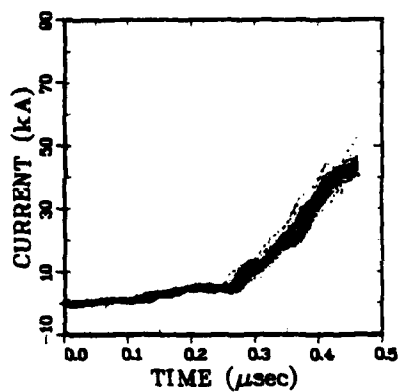


Fig. 14. Marx Generator Timing Data.

References

1. D. L. Johnson, J. P. VanDevender, and T. H. Martin, Preliminary PBFA-II Design, to be presented at the 1980 Fourteenth Pulse Power Modulator Symposium, Orlando, FL, June 3-5, 1980.
2. T. H. Martin, J. P. VanDevender, G. W. Barr, and D. L. Johnson, EBFA—Pulsed Power for Fusion, presented at the Third International Topical Conference on High Power Electron and Ion Beams, Novosibirsk, USSR, July 3-6, 1979.
3. G. W. Kuswa, Progress Toward Fusion with Light Ions, to be presented at the Eighth International Conference on Plasma Physics and Controlled Nuclear Fusion Research, Brussels, Belgium, July 1-10, 1980.
4. J. P. VanDevender, J. Appl. Phys. 50, 3928 (1979).

Abstract

The upgrade of Sandia National Laboratories particle beam fusion accelerator, PBFA I, to PBFA II presents several interesting and challenging pulsed power design problems. PBFA II requires increasing the PBFA I output parameters from 2 MV, 30 TW, 1 MJ to 4 MV, 100 TW, 3.5 MJ with the constraint of using much of the same PBFA I hardware. The increased PBFA II output will be obtained by doubling the number of modules (from 36 to 72), increasing the primary energy storage (from 4 MJ to 15 MJ), lowering the pulse forming line (PFL) output impedance, and adding a voltage doubling network.

A prototype accelerator, called Supermite, is being fabricated for use in the development and testing of PBFA II components. Supermite tankage will accommodate four PBFA II modules. However, only one is initially used for research and development. In Supermite, a 208 kJ Marx generator charges a water insulated transfer capacitor which in turn charges four water insulated pulse forming lines through a triggered gas switch. The self closing PFL output switches feed the 1.25 MV power pulse into a pulse conditioner which increases the voltage to 4 MV at 400 kA.

Details and data from the module development program and an analysis of the effects of component and module jitters on PBFA II output parameters will be presented.

Introduction

Sandia National Laboratories particle beam fusion accelerator, PBFA I, shown in Fig. 1 will be operational in July 1980. The 2 MV, 30 TW, 1 MJ accelerator consists of 36 modules housed in a 100 foot diameter tank. The 16 foot wide outer section is oil insulated and contains the Marx generators. The 14 foot wide water insulated section contains the intermediate storage capacitor, SF_6 trigatron switch, pulse forming network, and vacuum interface. The final inner section of the machine contains the magnetically insulated vacuum transmission lines and the diodes.

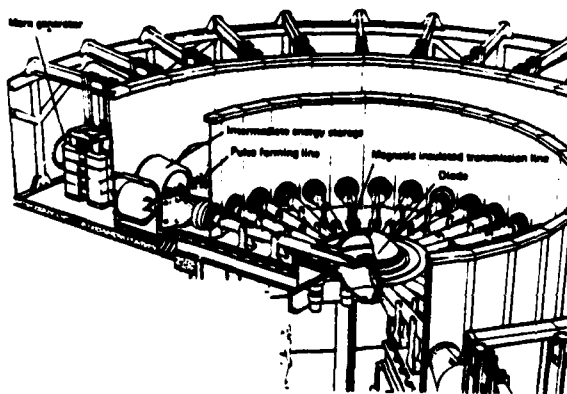


Fig. 1. PBFA I accelerator.

*This work was supported by the U.S. Dept. of Energy, under Contract DC-AC04-76-DPO0789.

Originally the upgrade of PBFA I to PBFA II was to have been the simple addition of 36 more PBFA I modules to the accelerator. These were to be included as a second layer of modules, above the existing modules. The output parameters would just be twice those of PBFA I or 2 MV, 60 TW, 2 MJ.

The rapid progress that has been made in exploring the ion option¹ for PBFA has shifted the emphasis from having an electron output to an ion output. The decision to make PBFA II a light ion accelerator allows a more powerful accelerator to be produced. Target and ion focusing requirements make increasing the output voltage from 2 MV to 4 MV advantageous. This increased voltage allows the accelerator output to be increased from 60 TW to 100 TW with the same reliability from the pulsed power and power flow technologies that we have in PBFA I.

In addition to doubling the number of modules, the upgrade to 4 MV, 100 TW will require increased energy storage in the Marx generators, twice the number of pulse forming lines per module, and the development of a voltage multiplying transition between the output switch and the vacuum insulator. Constraints imposed by size and space limitations and in self breakdown water switching prevent the formation of the 4 MV pulse at earlier stages in the machine. The upgrade must be accomplished within the PBFA I tankage and, to reduce cost, as much as possible of the PBFA I hardware should be utilized. Low system jitter with high reliability must also be maintained.

To facilitate the necessary research, development, and testing for PBFA II, a machine called Supermite, shown in Fig. 2, has been constructed. The Supermite tankage is a 20° sector of the PBFA tank which can house up to four accelerator modules. Development and testing of PBFA II designs and components will be performed on one or more of the Supermite modules. The full four module capability will later be used as a demonstration of the engineering design of the PBFA II system.

Marx Generators

The present Marx generators used on PBFA I store insufficient energy for the PBFA II upgrade. Capacitors with energy greater than the presently used 0.7 μF , 100 kV, 3.5 kJ units are required. Commercial suppliers are able to produce capacitors with an increased energy, 6.5 kJ, and similar voltage in the same size can as the PBFA I capacitors. Use of these capacitors increases the Marx generator energy by 86 percent from 112 kJ to 208 kJ or 15 MJ total for the 72 PBFA II Marxes.

Tests of two Marx generators, using the 6.5 kJ capacitors have begun on the Mite² and Supermite facilities. While lifetime and reliability data have not been obtained, the Marx generators have passed full power and voltage tests. Figure 3 gives the equivalent circuit obtained during the Marx generator tests.

Figure 4 shows a cross sectional view of the PBFA tank with two levels of Marx generators installed. The inductances of the high voltage connections from the Marx generators to the oil/water interfaces are different for the two positions. This will cause different charging times of the two intermediate storage capacitors. A compensating inductor must be

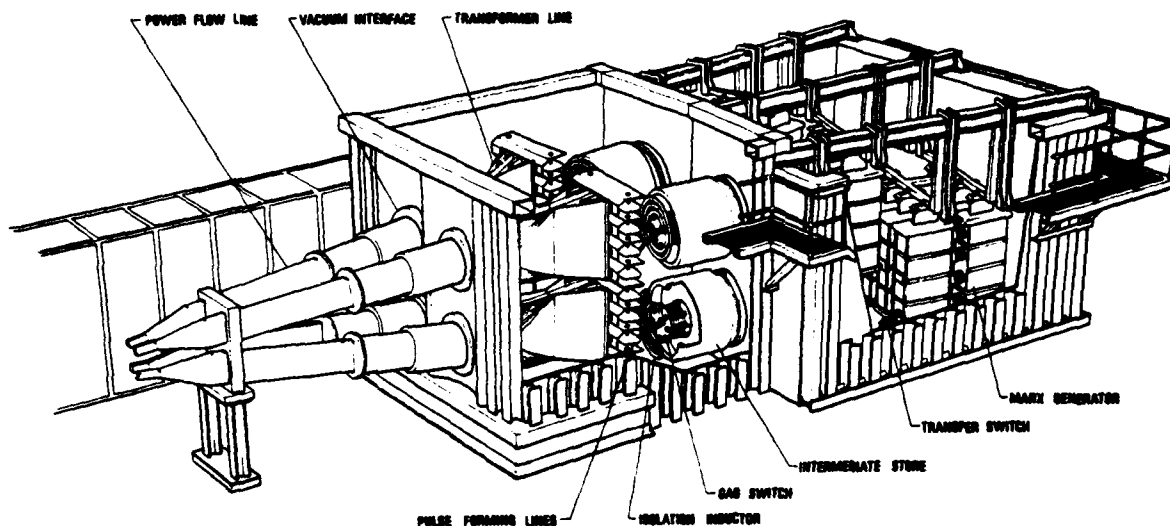


Fig. 2. Supermite, PBFA II research and demonstration module.

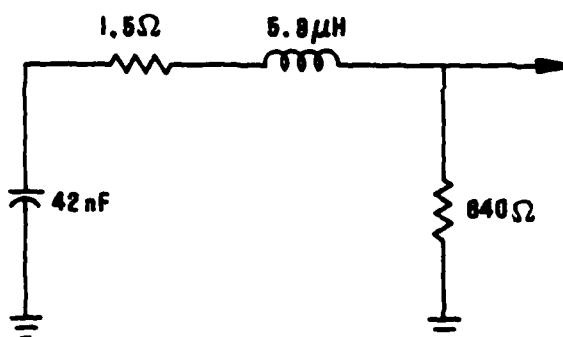


Fig. 3. PBFA II Marx generator equivalent circuit.

inserted in the upper charge feed to equalize the charging times. This overall increased charge time due to the added inductance and increased Marx generator capacitance is expected to reduce the hold off strength of the interface and water capacitor to 93 percent of the PBFA I value.

Circuit Calculations

Circuit calculations of the Marx to intermediate store to pulse forming lines charging circuit were made using the SCEPTRE³ circuit analysis program. The circuit used is shown in Fig. 5. A 1.5 μH inductance was used for the Marx generator high voltage feed and a 0.6 μH inductor represented the inductance of the gas trigatron and feed to the pulse forming lines. The shunt resistances across the water capacitor and pulse forming line capacities are consistent with 2 MΩ-cm water.

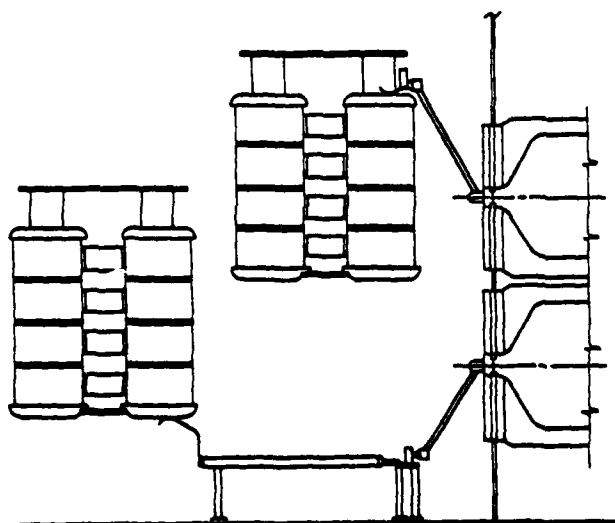


Fig. 4. Cross section of PBFA II Marx tank.

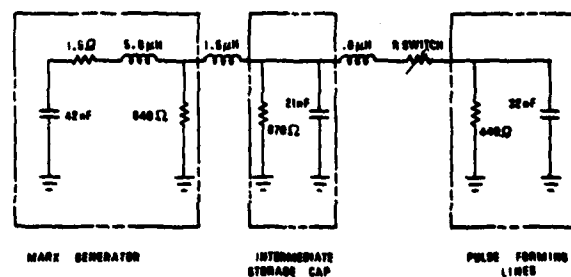


Fig. 5. Circuit used in SCEPTRE simulation.

Table I shows the results of the circuit calculations for various switching times of the trigatron switch. The peak voltages and energies on the pulse forming lines are relatively insensitive to switching times from 0.7 to 1.0 μs. Early switching times would be advantageous to reduce the time the voltage is across the intermediate storage capacitor.

TABLE I

Results of SCEPTRE Circuit Calculations

Switching Time (μ s)	Voltage on Intermediate Store (MV)	Voltage on Pulse Forming Lines (MV)	Charging Time of Pulse Forming Lines (ns)	Current thru Gas Switch (kA)
0.6	2.39	2.68	300	452
0.7	3.13	2.93	291	510
0.8	3.55	3.06	285	549
0.9	3.8	2.96	258	555
1.0	3.89	2.93	264	552

4 MV Pulse Forming Network

To provide as much room as possible in the 14 foot long water section to achieve the required 4 MV, a modification to the PBFA I intermediate storage capacitor was designed and fabricated. Figure 6a shows the original (PBFA I) capacitor/trigatron/inductor geometry and Fig. 6b shows the new geometry. The inductor which provides the trigger pulse to the trigatron switch was changed from a helical coil to a flat spiral. Equipotential field plots from the Jason⁴ computer code show only slight differences in the voltage grading across the trigatron switch for the two geometries. An additional 2 feet of length was gained by this modification.

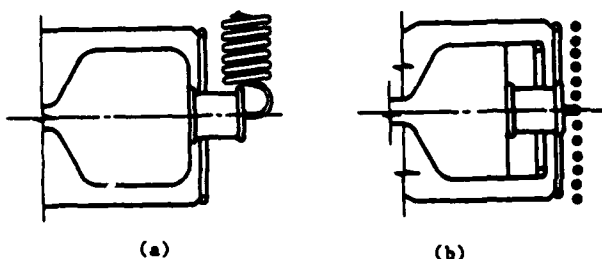


Fig. 6. Water capacitor and gas switch.

- a. PBFA I
b. PBFA II

Convolute, water dielectric transmission lines have reduced prepulses, provided pulse-forming-line stacking in parallel, and reversed the output polarity in high current accelerators.⁵ A new convolute design stacks lines in series to provide the accelerator voltage gain required for PBFA II. Experiments on a scale model have demonstrated the feasibility of the concept.

Flat plate pulse forming lines provide equal and oppositely directed fields when switched into two back-to-back transmission lines. If one side of the line has a polarity reversal convolute, as shown in Fig. 7, the electric fields of the two waves (top and bottom) will be in the same direction and a traveling voltage wave of twice the amplitude and impedance will be transmitted from the convolute.

An experiment was designed for Mite to check the efficiency of wave additions with triplate, water-dielectric lines. The initial pulse forming lines provide a two sided, 1.5 MV, 0.8 TW, 40 ns output into the transmission lines. One side of this output was inverted and both sides were transformed to higher voltage and impedance and then added. The convolute, Fig. 7, was one meter long. Resistive loads were connected directly across the high voltage terminals

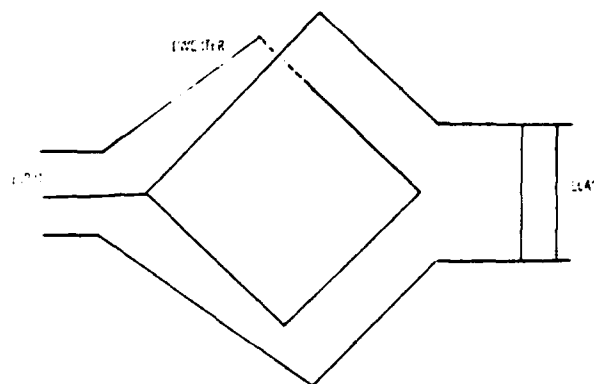


Fig. 7. Convolute for reversing polarity and stacking transmission lines.

and the accelerator load line, shown in Fig. 8, was determined. The output impedance of the pulse forming network was 18 Ω .

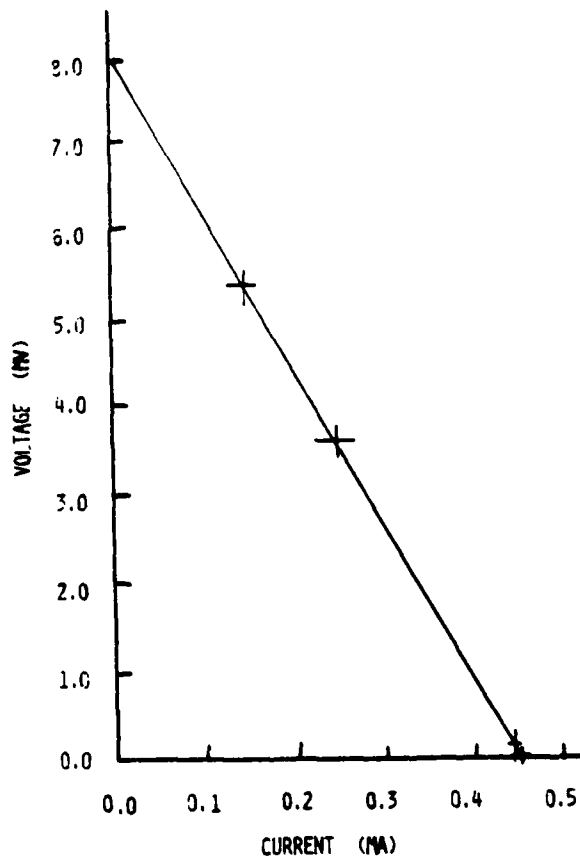


Fig. 8. Load line from convolute.

The voltage multiplication from 1.5 MV to 4 MV was accomplished with nearly a 100 percent peak power efficiency. This concept of inverting and stacking and introducing impedance mismatches has been incorporated into an experimental pulse conditioner. Low voltage, model tests of a similar pulse conditioning network for application to PBFA II have been completed. Figure 9 shows the geometry of the network. The transmission lines are vertical flat parallel plates driven by horizontal triplate pulse forming lines at the input end with the output ends connected in series. The output voltage is thus the sum of the voltage in each of the transmission lines. The series lines were terminated in a 2:1 impedance mismatch to achieve an additional voltage gain. Test results have shown an energy transfer efficiency of 61 percent, which is 86 percent of the efficiency calculated from a simple transmission line model that ignores parasitic, back impedance effects. The impedance mismatches in a PBFA II design are less than those in the low voltage test; so that energy efficiency is expected to be 71 percent in the PBFA II design.

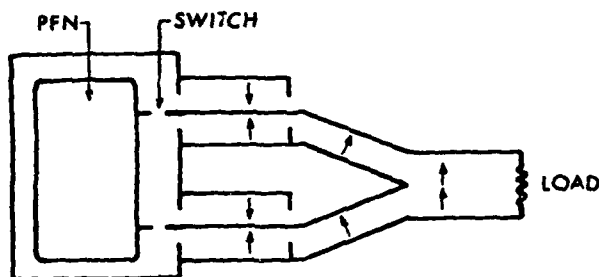


Fig. 9. Model of PBFA II pulse conditioning network.

Gas Switch Program

PBFA II places greater demands on gas switch performance than does PBFA I. Increased current and charge transfer capabilities with low jitter and greater reliability are required. While the present trigatron switch performance is adequate for initial PBFA I tests, this switch is not satisfactory for long term PBFA I or for PBFA II use. Proto I switching data show that after 30 to 100 shots, PBFA I type trigatrons degrade to unacceptable simultaneity. A gas switch research program has been initiated to develop a reliable, low jitter, long lifetime switch for the PBFA accelerators. The program includes material studies, investigations of breakdown processes in SF_6 , small and full scale testing of improved trigatron switches and alternatives to trigatron switches. Two alternative switches are being investigated at Sandia. They are a laser triggered switch and an x-ray triggered switch. In addition, switches under development by industry are being considered as alternatives to the trigatron.

The trigatron experiments are directed towards improving the reliability and lifetime of the trigatrons and, hence improving the performance of Proto II and PBFA I. Towards this goal, experiments on Hydrumite, Supermite, and Proto II are planned. Erosion of electrodes and degradation of switch jitter will be measured using several different electrode materials. The trigatron geometry (e.g., hole and trigger pin sizes and shapes) will be varied in an attempt to reduce the increase in switch jitter caused by electrode erosion.

A 1 MV, transformer driven test stand will provide voltage to study the breakdown physics in SF_6 insulated trigatrons. A basic understanding of the breakdown processes should lead to improved trigatron design.

Successful experiments⁷ by LLL on laser triggered switching of a SF_6 insulated gap using a few mJ KrF laser has prompted an investigation by Sandia into laser triggered switching for the PBFA Program. Studies of U.V. absorption, laser induced excitation, ionization, and their effects on the dielectric properties of pure SF_6 , commercial grade SF_6 , and SF_6 with selected trace additives are underway. In addition large scale testing on Supermite of a KrF triggered switch is also scheduled.

Vacuum Insulator and Power Flow Lines

The 4 MV, 10 Ω power pulse requires a new vacuum insulator section and modified power flow lines. A conceptual design for the vacuum insulator is complete and detailed field plots for determining the final design are underway. Magnetic insulation at the higher voltage should be more efficient than it was at 2 MV because the vacuum gap between the electron flow and the positive conductor in a self-magnetically insulated transmission line increases with increasing voltage.

Jitter Effect on Output Power

A statistical analysis of PBFA module simultaneity was performed and measured values of gas and water switch jitter were used to predict the output power from a 72 module system. Data from Mite¹⁰ showed that the rms standard deviation in breakdown time of a single water dielectric switch was 6 ns. Each PBFA II module will have 16 of these water switches in parallel. The mean time to closure of the 16 switches was selected as the random variable to be used as the water switch closure time. The rationale for this selection was that significant power would not begin to flow from that module until half of the switches had closed. Each of the 16 switches were assumed to be independent and normally distributed. This assumption, while not entirely correct, is probably acceptable since the switches are transient time isolated from one another. The standard deviation of the mean time is then

$$\sigma_{\text{mean}} = \frac{\sigma_{\text{one switch}}}{\sqrt{16}}$$

The module output time is equal to the sum of the times to closure of the gas and water switches plus a fixed delay.

$$T_{\text{out}} = t_{\text{gas switch}} + t_{\text{water switch}} + t_{\text{delay}}$$

Measurements of the trigatron switch timing on Hydrumite yielded ≈ 2 ns standard deviation for the gas switch time. The standard deviation of T_{out} is then

$$\sigma_{\text{out}} = \sqrt{\sigma_{\text{gas}}^2 + \frac{\sigma_{\text{water}}^2}{16}} = 2.5 \text{ ns}$$

The expected value of the range of firing time ($R = T_{\text{last}} - T_{\text{first}}$) for all 72 PBFA II modules is

$$E[R] = 4.78 \sigma_{\text{out}} = 12 \text{ ns}$$

The effect of the module jitter was estimated using order statistics for 72 normally distributed random variables. A $\sin^2 \theta$ pulse with 40 ns FWHM was assumed for the output pulse from each module. Figure 10 shows the normalized output pulse. The amplitude was reduced by 1 percent and the pulse width increased by less than 1 ns.

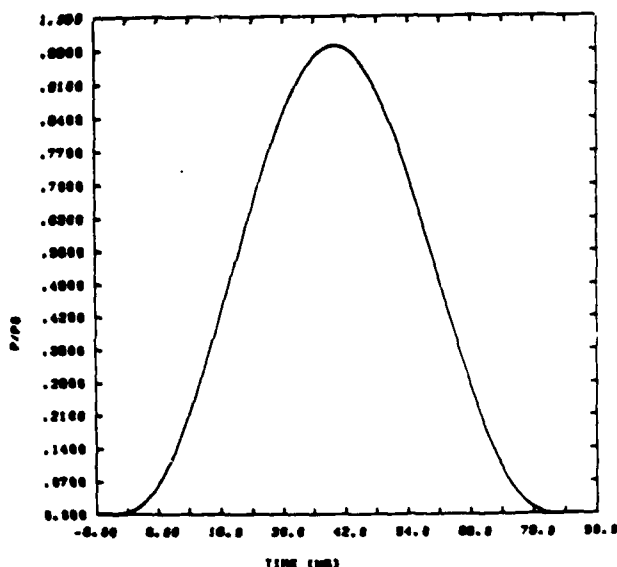


Fig. 10. Output of PBFA II with module jitter.

Summary

The conceptual design for the 4 MV, 100 TW PBFA II accelerator has been completed. The critical issues in the design have been identified and research programs are underway to address these issues. The results of these programs indicate that the conceptual design is a sound one and the project is currently on schedule.

References

1. D. J. Johnson, et al., Phys. Rev. Lett., Vol. 42, No. 9, p. 610 (1979).
2. T. H. Martin, D. L. Johnson and D. H. McDaniel, Proc. of the 2nd Int'l. Topical Conf. on High Power Electron and Ion Beam Res. and Tech., Ithaca, NY, p. 807 (1977).
3. J. C. Bowers and S. R. Edore, SCRIPTER: A Computer Program for Circuit Analysis (Prentice Hall, Englewood Cliffs, NJ, 1971).
4. S. J. Sackett, Jason--A Code for Solving General Electrostatics Problems, Lawrence Livermore Laboratory Report UCID-17814 (June 1978).
5. T. H. Martin, et al., Proc. of the 3rd Int'l. Topical Conf. on High Power Electron and Ion Beams, Novosibirsk, USSR (to be published).
6. E. L. Neau, X-Ray Triggered Switching in SF₆ Insulated Gaps, 14th Pulse Power Modulator Symposium, Orlando, FL, June 3-5, 1980.
7. W. R. Rapoport, J. Goldhar, J. R. Murry, "KrF Laser-Triggered SF₆ Spark Gaps for Low Jitter Timing", to be published in IEEE Transactions on Plasma Science on the subject of Plasma Switches and Switch Plasmas, a special issue.
8. E. L. Neau, Sandia National Laboratories, private communication.
9. J. P. VanDevender, Proc. of the Nat'l. Electronics Conf., Vol. 23, Chicago, IL, p. 258 (1979).
10. D. L. Johnson, J. P. VanDevender and T. H. Martin, High Power Density Water Dielectric Switching to be published in a special issue of IEEE Transactions on Plasma Science on the subject of Plasma Switches and Switch Plasmas.

COMPUTER MODELS IN THE DESIGN OF FXR*
G. E. Vogtlin & R. W. Kuenning
Lawrence Livermore National Laboratory
Livermore, California 94550

Summary

Lawrence Livermore National Laboratory is developing the FXR (Flash X-Ray Facility) 15-20 MEV electron accelerator with a beam current goal of 4 kA. This accelerator will be used for flash radiography and has a requirement of high reliability. Components being developed include spark gaps, Marx generators, water Blumleins and oil insulation systems.

A SCEPTRE model was developed that takes into consideration the non-linearity of the ferrite and the time dependency of the emission from a field emitter cathode. This model was used to predict an optimum charge time to obtain maximum magnetic flux change from the ferrite. This model and its application will be discussed.

JASON was used extensively to determine optimum locations and shapes of supports and insulators. It was also used to determine stresses within bubbles adjacent to walls in oil. Computer results will be shown and bubble breakdown will be related to bubble size.

* * *

The FXR linear induction accelerator is being designed and constructed at Lawrence Livermore National Laboratory. This accelerator has a goal of 500 R at one meter and will be used for flash radiography. Each acceleration stage will increase the electron beam energy by 400 kV. Effectively, the beam is accelerated by a transformer, the primary being fed by a Blumlein pulse generator and the secondary being the beam itself. The transformer core is ferrite with volt-seconds being limited by the B-H curve of the core material. A section of the accelerating cavity is shown in Figure 1.

High voltage breakdown is of concern due to the high electrical stresses and the possibility of trapped bubbles in the liquid dielectric throughout the high voltage system. The oil and water systems are degassed and filtered.

Large bubbles in the oil and water system will slowly be absorbed. A concern in the design of FXR is that a small bubble might ionize and grow until it causes a breakdown. FXR is to be fired once every three seconds. Bubbles in the water system will exit through circulation passages at the top of all cavities. The accelerator cavity oil system (Figure 1) could not be designed to totally eliminate trapped bubbles.

Oil that has been degassed can absorb bubbles. The absorption rate is a function of oil circulation, gas saturation and time. The rate of bubble absorption is proportional to the surface area. If other variables are constant, then the decrease in diameter versus time should be constant. Measurements with degassed mineral oil have shown absorption rates of from 2 to 6 microns per minute.

Bubbles can break down and increase their dimensions by cracking the surrounding oil. Figure 2 is a plot of Paschen breakdown distance versus voltage stress at atmospheric pressure. The implication of this curve is the smaller the bubble the greater the voltage stress before breakdown.

The breakdown phenomenon has been modeled with JASON in Figures 3 through 8. Figure 3 shows a

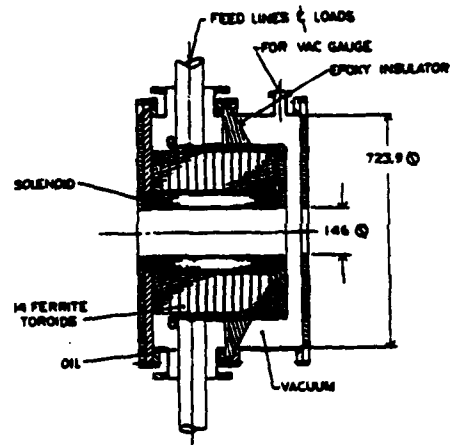


FIGURE 1 - Accelerator Cavity

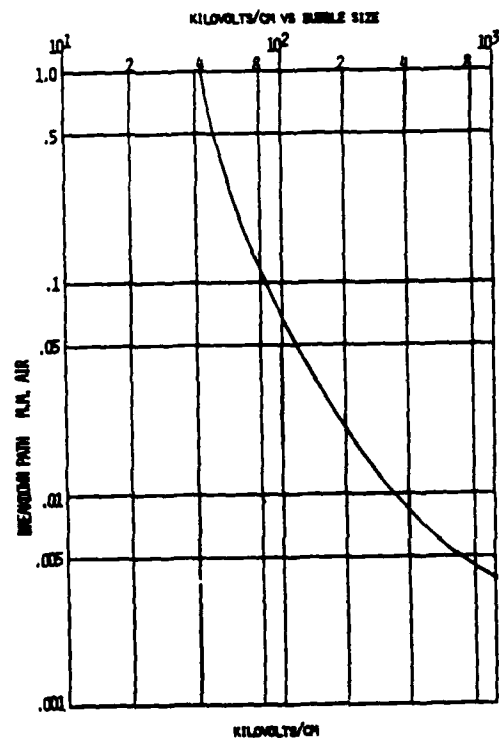


FIGURE 2 - Paschen's Curve

spherical bubble with a dielectric constant of 1 in oil of dielectric constant = 2.2. The right side of the figure is charged to 100, with the left a conductor at zero potential. The stress enhancement in the bubble is about 1.2 times the oil

*Work performed under the auspices of the U.S. Department of Energy by the Lawrence Livermore National Laboratory under contract No. W-7405-Eng-48.

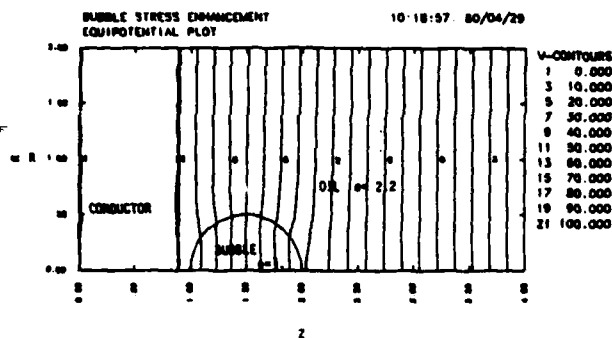


FIGURE 3 - Air Bubble in Oil

stress. Figure 4 is identical to Figure 3 except a dielectric constant of 200 is chosen for the bubble. This is equivalent to treating it as a floating conductor, or as if the air had ionized. The stress in the oil is increased to a factor of 3:1. Figure 5 assumes the ionized bubble is connected to the wall. The enhancement appears to be approximately 4:1.

Another possible situation in FXR is bubble growth in oil between a conducting wall and ferrite. Figures 6 through 8 includes ferrite in the model. This would only be the case when the bubble had grown to be the dimensions of the oil space. The stress in the bubble is 1.12 times the oil stress with ferrite occupying the space from 1.00 to 3.00 along the Z axis in Figure 6. Figure 7 is the case where the bubble becomes a conductor, or becomes ionized. The oil stress enhancement is close to a factor of 4:1. Figure 8 is the case where the bubble is electrically connected to the wall and ionized. The stress enhancement in the oil in this case is 6.5.

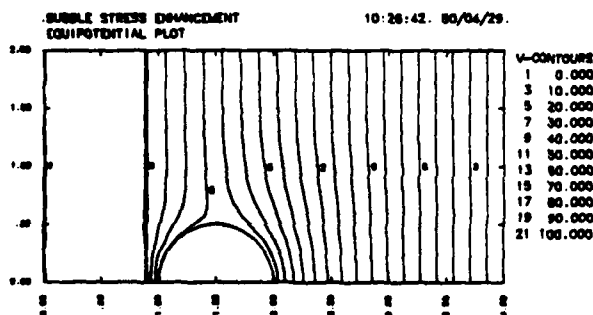


FIGURE 4 - Ionized Air Bubble in Oil

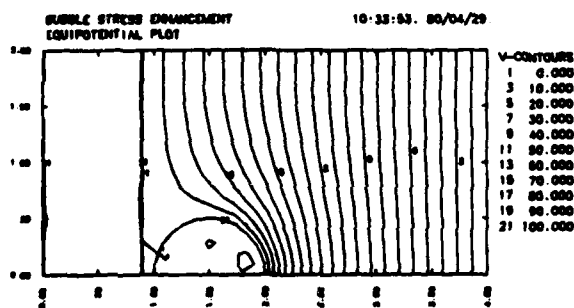


FIGURE 5 - Ionized Bubble Connected to Wall

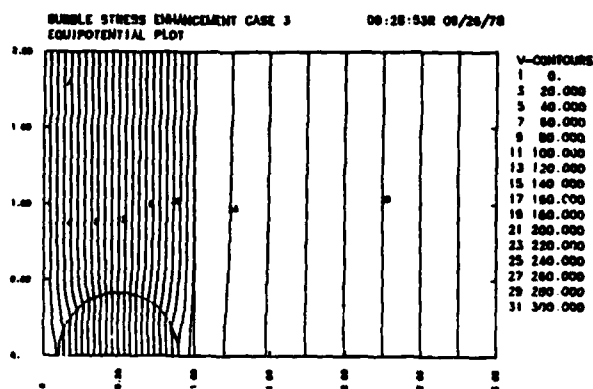


FIGURE 6 - Air Bubble Between Wall & Ferrite

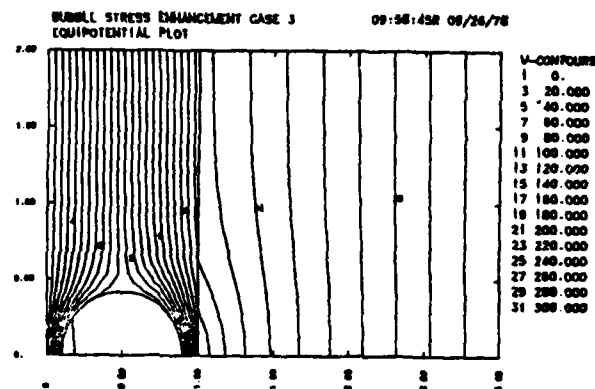


FIGURE 7 - Ionized Bubble Between Wall & Ferrite

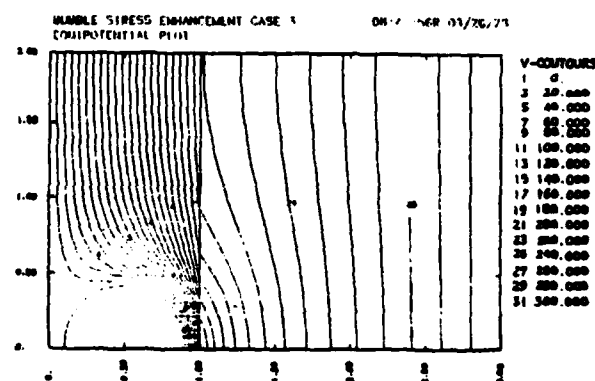


FIGURE 8 - Ionized Bubble Connected to Wall

Linear induction accelerators constructed at Lawrence Livermore National Laboratory have used magnetic materials as transformer cores in accelerating electron beams. These cores are excited by a pulse generator and act as a 1:1 turns ratio transformer to the beam. The pulse is generated in the FXR machine by the discharge of a spark gap fired water Blumlein. An illustration is shown in Figure 9. The water Blumlein is charged from a Marx generator.

This system has been modeled using the Sceptre Circuit Analysis Code. This circuit is shown in Figures 10 & 11. The ferrite is represented by a



The top section of the page contains a perspective view of a mechanical assembly, likely a pump or motor, showing its internal components and external housing. Below this, there are two large rectangular areas, each containing a top-down view of a circular component, possibly a valve or a piston. To the right of these are two smaller rectangular areas, each containing a side view of a cylindrical component. The bottom section of the page contains two large rectangular areas, each containing a cross-sectional view of a mechanical assembly, showing the internal components and their arrangement.

FIGURE 11 - Feedline & Cavity Model

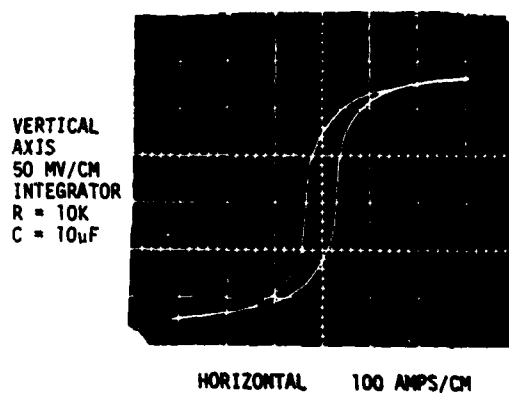


FIGURE 12 - B-H Curve of Ferrite

312

Figure 13 is an example of the ferrite saturation from the Sceptre model with a 1.2 microseconds charge time. At 1.2 microseconds, the available flux change is reduced about 35%.

Figure 14 is the Blumlein charge voltage. The Blumlein reaches full charge at 1200 nanoseconds while the ferrite goes out of saturation at 850 nanoseconds.

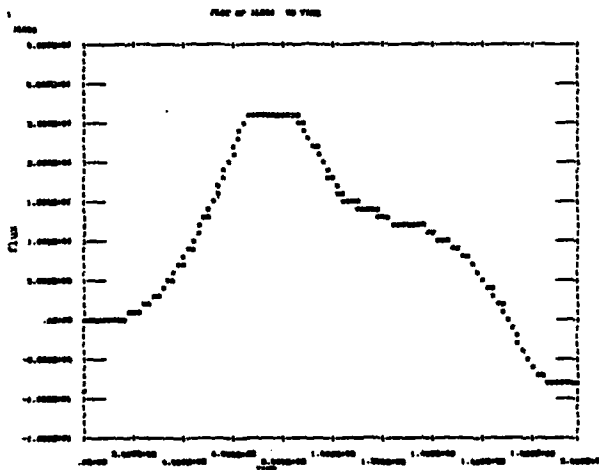


FIGURE 13 - Ferrite Saturation Curve (1.2 μ s)

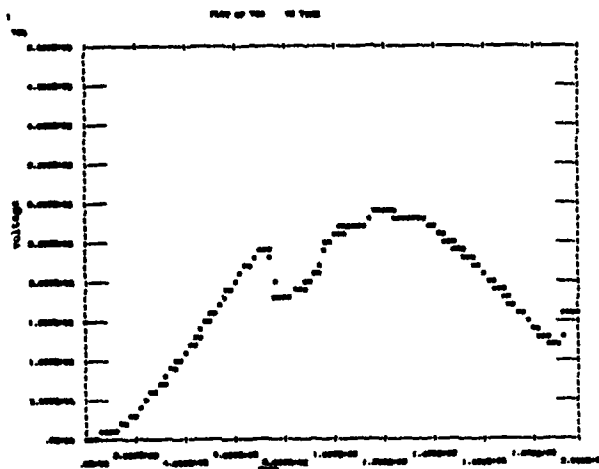


FIGURE 14 - Blumlein Charge Curve (1.2 μ s)

Figure 15 shows a longer charge time with a second saturation peak that coincides with the Blumlein charge shown in Figure 16. The location of the notch in the charge waveform gives an indication of the state of the ferrite. All testing to date has shown a consistent state for a given voltage level and charge time.

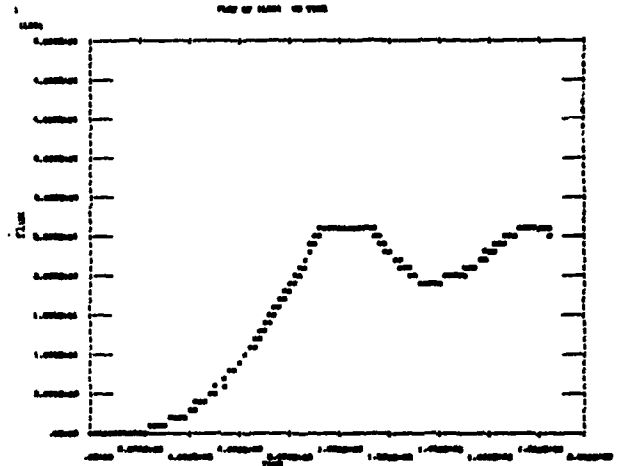


FIGURE 15 - Ferrite Saturation Curve (1.8 μ s)

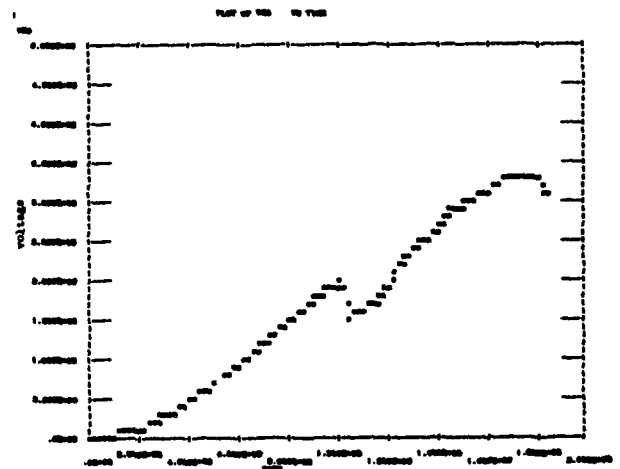


FIGURE 16 - Blumlein Charge Curve (1.8 μ s)

The result of the modeling has increased the available volt-seconds of ferrite by at least 30%. This technique is dependent on the charge current level, the amount of ferrite and the charge time.

NOTICE

"This report was prepared as an account of work sponsored by the United States Government. Neither the United States nor the United States Department of Energy, nor any of their employees, nor any of their contractors, subcontractors, or their employees, makes any warranty, express or implied, or assumes any legal liability or responsibility for the accuracy, completeness or usefulness of any information, apparatus, product or process disclosed, or represents that its use would not infringe privately-owned rights."

Reference to a company or product name does not imply approval or recommendation of the product by the University of California or the U.S. Department of Energy to the exclusion of others that may be suitable.

A VERSATILE 0.5 TW ELECTRON BEAM FACILITY FOR POWER CONDITIONING STUDIES OF LARGE RARE-GAS/HALIDE LASERS*

J. J. Ramirez

Sandia National Laboratories, Albuquerque, New Mexico 87185

Abstract

Rare-gas/halide lasers which are being developed for Inertial Confinement Fusion will require large area, low impedance electron beam drivers. A wide range of electron beam parameters are being considered for future systems in an effort to optimize the overall system design. A number of power conditioning issues must be investigated in order to obtain a better understanding of the various trade-offs involved in making such optimizations. The RAYITO electron beam accelerator is being designed and built at Sandia National Laboratories and will be used for such investigations. It will be capable of operating in either a 2 or 4 ohm configuration at 1 MV, 50 ns or 0.8 MV, 200 ns. Design details for RAYITO are presented in this paper. Experiments planned for this facility are also discussed.

Introduction

Investigations of electron beam generation and control using low impedance, large area diodes are of critical importance to the advanced laser program for inertial confinement fusion. Diodes which operate above the critical current for pinching require the use of an externally applied guide magnetic field. The magnitude of the magnetic field which is required is uncertain but could be several times the beam self-magnetic field, thus the energy required for the magnetic field coils could be much greater than the energy in the electron beam itself. It is also difficult to calculate the effect of the applied magnetic field on the efficiency, uniformity and profile of the electron beam energy deposition in the gas. RAYITO will provide a testbed to investigate various aspects of power conditioning including the trade-offs which result from various operating conditions. Since a wide range of electron beam parameters are still being considered for these high energy lasers, the RAYITO design incorporates substantial flexibility in the output beam parameters.

System Overview

RAYITO is to be a single sided diode, 0.8-1.0 MV, 50 and 200 ns, 2 and 4 ohm electron beam accelerator capable of generating a 0.3 m x 1.0 m beam. A block diagram of the facility is shown in Fig. 1. A Marx generator, intermediate energy store and triggered gas switch are contained within a 3.6 m x 2.4 m x 2.7 m oil tank. The pulse forming and transmission line assembly is placed inside of a 6.1 m x 1.5 m x 1.2 m water tank. The two tanks are connected by a short coaxial section with an oil/water insulating diaphragm. An artist's concept is shown in Fig. 2.

The 3.2 MV, 32 nF Marx generator is identical to those used in PBFA modules.¹ It pulse charges a 15 nF intermediate energy store, which consists of two Proto II water capacitors,² in ~800 ns. These capacitors are discharged by a triggered gas switch into the 150 ns water line. The water pulse forming and transmission lines are of the triplate geometry used in Proto II,³ Mita,⁴ and PBFA¹ and are equipped with self-breaking water switches. For this geometry the impedance of the lines is given by

$$Z_L = 1/2 \left(\frac{377}{\sqrt{\epsilon_r}} \frac{d}{W} \right) \quad (1)$$

where ϵ_r is the relative dielectric constant of water, W is the width of the lines and d is the spacing between the high voltage and ground electrodes. In our design $W = 1.07$ m so that $d = 0.1$ m and 0.2 m for the 2 and 4 ohm configurations respectively. The lines are held together by nylon support rods which makes it easy to change the line impedance. The convolute to the diode requires two sets of ground electrodes for the two impedance configurations.

The low inductance diode was designed with the capability of generating a 0.3 m x 1.0 m electron beam. Calculations show that the diode insulator will hold off 1.3 MV and 1.0 MV for the 50 ns and 200 ns output pulse widths respectively. No significant voltage overshoot will be seen in the 200 ns mode and a maximum of 12 percent will be experienced in the 50 ns, 2 ohm mode. The design provides an 18-20 percent safety factor in the insulator breakdown strength at the 1.0 MV, 50 ns and 0.8 MV, 200 ns output levels desired.

The 50 ns Configuration

In this mode the 150 ns line (Line 1) is charged by the water capacitors via a triggered gas switch in 350 ns. It then acts as a second intermediate energy store for fast charging of the 50 ns pulse forming line (PFL). Line 1 will be configured with the 0.2 m spacing in order to obtain a better capacitive match with the water capacitors. It is equipped with one, two or three self breaking water switches set to close at ~85 percent of the peak voltage. The number of switches employed will be chosen to obtain a charge time of ~150 ns on the PFL.

The 50 ns PFL is equipped with seven self breaking water switches set to close at ~85 percent of the peak voltage. The behavior of high power, water dielectric switching has been described by Johnson, et al.⁵ The 10 to 90 percent risetime of the output pulse for an exponentially rising waveform is given by $2.2 \tau_e$ where τ_e is the e-folding risetime of the switch. This consists of an inductive and a resistive term which are added in quadrature, thus

$$\tau_e^2 = \tau_L^2 + \tau_R^2 \quad (2)$$

In multichannel switching of a PFL, τ_e is given, in MKS units, by

$$\tau_e^2 = (L/NZ)^2 + (232/(NZ\epsilon)^{1/3})^2 \quad (3)$$

where L is the inductance per switch channel, Z is the sum of the PFL and load impedance, ϵ is the mean electric field in the switch and N is the number of channels. The inductance is given by

$$L = 1.4 \times 10^{-6} X \quad (4)$$

where X is the length of the channel in meters. For an effective charge time t (the time when the voltage is greater than 63 percent of the breakdown value) X is given by

$$X = 4 \times 10^{-4} v^{1.1} t^{0.67} \quad (5)$$

*This work supported by the U.S. Dept. of Energy, under Contract DE-AC04-76-DP00789.

where V is the breakdown voltage. The above equations can be used to calculate the output pulse risetime of the 50 ns PFL. Given the fast charging time, it can be expected that all seven switch points will close (see Ref. 4). Table I gives a summary of these calculations.

TABLE I

Calculated Output Risetimes
for a 1 MV, 50 ns Output Pulse

	2 ohms	4 ohms
X(m)	0.042	0.042
L(nH)	58.0	58.0
T _L (ns)	2.1	1.1
T _R (ns)	4.4	3.5
T _g (ns)	4.9	3.7
T(10/90)(ns)	10.8	8.2

The output of the PFL is fed to the diode via a transmission line/convolute assembly. A third set of water switches is used to reduce the amplitude of the prepulse voltage applied to the diode. The jitter of the system is determined by the combined jitter of the gas switch and water switches. It has been found experimentally that the jitter of the water switches increases linearly with X and the charge time of the line.⁴ Thus

$$\sigma = 3.3 \times 10^{-4} \sqrt{1.1} \tau_{1.67} \quad (6)$$

This expression yields a σ of 6.8 ns and 1.6 ns for the switches of Line 1 and the PFL respectively. Assuming a σ of 3 ns for the triggered gas switch, the overall rms system jitter is estimated at ~8 ns.

The 200 ns Configuration

In order to obtain a 200 ns output, the two water capacitors are removed from the system, the 150 and 50 ns lines are tied together and are charged directly by the Marx generator in ~1 μ s. At these long charge times, multichannel water switching becomes very difficult because the jitter of the self closing switches approaches 30 ns. The switch performance which might be obtained with the 200 ns, 4 ohm line can be calculated using the above formulas and is shown in Table II. The last column in this table is an approximate value of the energy dissipated in the switch.

TABLE II

Calculated Output Risetimes for a
200 ns, 4 ohm Line Charged to 1.6 MV

N	T _L (ns)	T _R (ns)	T _g (ns)	T(10/90) (ns)	T _R V ² /4Z (kJ)
1	20.5	35.4	40.8	90	2.8
2	10.3	28.1	30.0	66	2.3
3	6.8	24.5	25.5	56	2.0
4	5.1	22.3	22.9	50	1.8
5	4.1	20.7	21.1	46	1.7

It is calculated that only one channel will close using the criteria given in Ref. 4. The number of channels might be increased by slitting the ground electrodes in order to further isolate the switch points from each other; however it can be seen from Table II that even with four channels the expected

output risetime is marginal. This table also shows that the resistive term dominates for 2 or more channels and that slow improvement in the risetime is made after N = 3. One possibility for ameliorating this problem is the use of a peaking capacitor (the water capacitors) to charge the line faster. Another possibility, one which has a greater impact on the long term goals of the advanced laser program, is to develop multichannel gas switches for the strip transmission lines. Our first step in this direction is the development of a gas switch with an inductance of 100 nH. In as much as the resistive phase of a gas switch is minimal, the output risetime is entirely dominated by the switch inductance. The e-folding risetime of a 100 nH inductance switch would be 25 ns and 12.5 ns for the 2 ohm and 4 ohm configuration respectively. The first experiments on RAYITO will be directed at the development of this switch.

The Diode

The diode has a calculated inductance of ~14 nH. It is made of thin walled stainless steel to allow for the penetration of an externally applied magnetic field. The design allows for cathodes up to 0.3 m x 1.0 m. Under matched conditions at 1 MV this area yields current densities of 167 A/cm² and 83 A/cm² for the 2 ohm and 4 ohm configurations which correspond to anode-cathode spacings of 3.74 cm and 5.31 cm respectively. The critical current for pinching of a uniform rectangular beam of length L and width W (with L >> W) is approximately given by

$$I_c = \frac{8500 \beta \gamma L/s}{1 + \ln \left(\frac{2L}{W} \right)} \quad (7)$$

where s is the anode-cathode spacing and $\beta \gamma$ is the usual relativistic factor.⁵ At 500 kA the diode will be operating at 2.3 times the calculated critical current. It will thus be possible to study various methods for controlling the beam self-pinch; e.g., using externally applied magnetic fields or magnetically isolated segmented cathodes.

The Magnetic Field Coils

The externally applied magnetic field is supplied by two rectangular coils arranged in a Helmholtz pair configuration. The coils are 0.8 m x 1.5 m and are separated by 0.43 m. Each coil will be made of 50 turns of 0.4 cm diameter copper wire wound around a fiber-glass frame. When driven by a 155 kJ capacitor bank, these coils will produce a "free-space" field of 0.47 Tesla at the edge of the cathode. Although it is difficult to calculate the exact diffusion of the magnetic field through the complex metal structure of the diode, it is estimated that the B-field will be reduced to about 0.3 Tesla after penetrating the metal structure when the capacitor bank is crowbarred at peak current. This value is slightly higher than the 0.25 Tesla self-field produced by the 500 kA electron beam at the same point on the cathode.

Summary

A versatile 0.5 terawatt electron beam accelerator (RAYITO) is being constructed at Sandia National Laboratories. The design utilizes Sandia's modular pulse power concepts developed for the Particle Beam Fusion program. The accelerator can be configured for either a 2 ohm or 4 ohm output impedance at 1 MV, 50 ns or 0.8 MV, 200 ns. The experimental program planned for this facility is aimed at power conditioning studies for large rare-gas/halide lasers. Various schemes for controlling the beam self-pinch in the

diode and the gas region will be investigated. Special attention will be given to reducing the magnitude of the applied magnetic field while maintaining system efficiency and uniformity of the beam energy deposition profiles.

The assembly of RAYITO is presently underway. The completion of this process and the beginning of pulse power tests are scheduled for August of this year.

References

1. T. H. Martin, J. P. VanDevender, G. W. Barr and D. L. Johnson, Proc. of the 3rd Int'l. Topical Conf. on High Power Electron and Ion Beams, Novosibirsk, USSR, July 3-6, 1979.
2. T. H. Martin, J. P. VanDevender, D. L. Johnson, D. H. McDaniel and M. Aker, Proc. of the Int'l. Topical Conf. on Electron Beam Research and Technology, Vol. 1, p. 450, Albuquerque, NM, November 3-5, 1975.
3. J. P. VanDevender, J. Appl. Phys. 50, 3928, (1979).
4. D. L. Johnson, J. P. VanDevender and T. H. Martin, IEEE Trans. on Plasma Science (to be published).
5. L. G. Schlitt and L. P. Bradley, Proc. of the Int'l. Topical Conf. on Electron Beam Research and Technology, Vol. 2, p. 230, Albuquerque, NM, November 3-5, 1975.

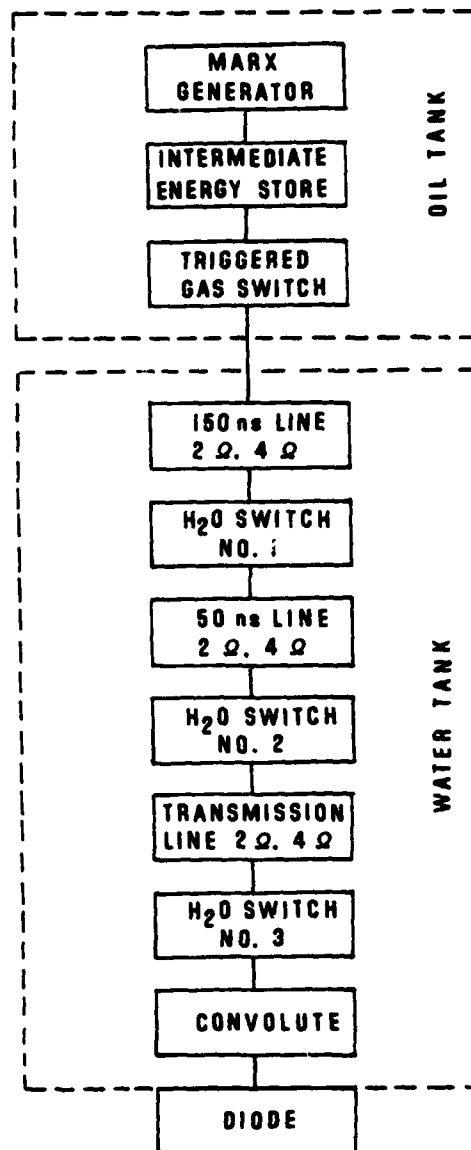


Fig. 1. Block diagram of RAYITO accelerator.

ANALYSIS OF PERFORMANCE OF RAILGUN ACCELERATORS POWERED BY DISTRIBUTED ENERGY STORES

Richard A. Marshall and William F. Weldon

Center for Electromechanics
Taylor Hall 167
The University of Texas at Austin
Austin, Texas 78712

Summary

It has been established that centimeter sized projectiles weighing several grams can be accelerated by electrical forces to velocities in excess of five kilometers per second in a classical railgun. The technologies required to do this are adequately understood, at least in the case where a single energy store is connected to the breech end of the gun.

There are two disadvantages to using a single energy store. It is generally desirable to keep gun current as nearly constant as possible and this is difficult to achieve with a single store without making the store excessively large. Rail resistance also becomes a dominating factor as higher velocities are reached because higher velocities require greater gun lengths and correspondingly larger gun resistances.

One way to by-pass these limitations is to distribute energy stores along the length of the gun. Not only does this reduce the average rail resistance by reducing the length of rail that carries current at anytime, but it permits inductive energy to be usefully transferred down the gun rather than allowing it to dissipate resistively in the rails.

This paper shows how the performance of such a gun may be simulated, by computing the instantaneous rate of change of current in each energy store and by using these values to obtain projectile acceleration. Two specific rail gun systems are examined, the first being a "scientific railgun" designed to propel a three gram projectile to a speed of 20 kilometers per second, and the second being a "space-launch railgun" to accelerate one metric ton to 7.5 kilometers per second.

Introduction

The basic concept of the parallel-rail railgun accelerator has been known for a long time. The accelerating force is obtained by the interaction of the current in the driven armature with the magnetic field produced by the current in the rails, the armature and rails being connected in series. The recent work done in Canberra has shown that an electric arc can successfully be used as a railgun armature.¹ The other important contribution made was the realization that current control was essential to success, and that the use of an inductor was one way to achieve such control.² Projectiles with a mass of three grams were accelerated to velocities of up to 5.9 km/s in the Canberra railgun.

There are other ways of achieving current control in railguns. A program at present being conducted by a LLL-LASL group involves the use of explosive flux compression generators.³ This very flexible generation scheme makes it possible to generate currents which vary in time in a wide variety of ways.

The use of a single current generator connected to the breech of a railgun has two disadvantages. As gun rails become longer to obtain higher performance, then a larger proportion of the input energy is lost resistively in the rails.⁴ The other is that the inductive energy remaining in the gun at projectile exit represents a considerable inefficiency. A way of circumventing both of these problems is to distribute energy stores along the length of the gun.^{5,6,7,8} It should be noted that the use of many power supplies along an accelerator is not new. It is commonly employed in atomic particle accelerators, and has been proposed for use in travelling magnetic wave macroparticle accelerators.⁹ It has also been used in the MIT Massdriver.¹⁰ The aim in all these cases is to deliver energy to a projectile in small increments many times.

In this paper we present a method by which the distributed inductive energy store railgun can be analysed, and apply this analysis to two railgun systems.

Analysis

The schematic representation of a railgun with inductive energy stores distributed along its length is shown in Fig. 1. Stores have inductance L and resistance R and are spaced at intervals 2 along the rails. Each is delivering current I_n into the railgun at a voltage of E_n . The projectile has moved a distance x into gun section number 1 . It has a mass of m and a velocity of x . The railgun has an inductance and resistance of L' and R' per unit length.

The current flowing in each gun section is the sum of the currents being delivered by each energy store up to and including the one in that gun section. Current is prevented from flowing backwards in the inductors. The arc armature driving the projectile is assumed to have a volt drop MV (so called because this is the voltage that is measured from rail to rail at the gun's muzzle.)

In order to compute the performance of the rail gun, it is first necessary to find the rates of change of the inductor currents, I_n . The first step in doing this is to write the equations for the power supply circuits (LH side below Fig. 1) and for the railgun sections (RH side below Fig. 1). These are then solved for I_n which are obtained from the matrix equation (1).¹¹

The simulation is now performed in the following manner. At any instant, x and \dot{x} are known as are all I_n . When an appropriate value for MV is chosen then all the terms in [A] and [C] are known. Thus [B] is found, enabling new values of current to be calculated for the next step of the simulation. New values of \dot{x} and x are also found from the calculated value of \dot{x} .

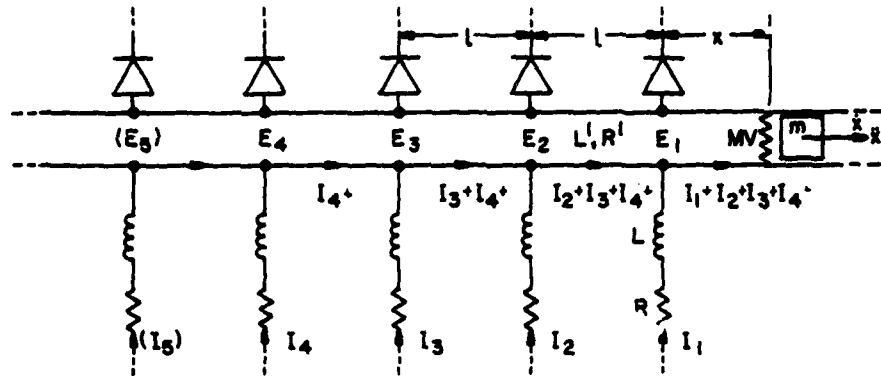


Fig. 1. Circuit diagram showing parameters and variables used in the analysis.

$$\begin{aligned}
 -E &= L\dot{I}_1 + RI_1 & E_1 &= L'x(I_1+I_2+I_3+I_4) + (L'x + R'x)(I_1+I_2+I_3+I_4) + MV \\
 -E_2 &= L\dot{I}_2 + RI_2 & E_2-E_1 &= L'\ell(I_2+I_3+I_4) + R'\ell(I_2+I_3+I_4) \\
 -E_3 &= L\dot{I}_3 + RI_3 & E_3-E_2 &= L'\ell(I_3+I_4) + R'\ell(I_3+I_4) \\
 -E_4 &= L\dot{I}_4 + RI_4 & E_4-E_3 &= L'\ell(I_4) + R'\ell(I_4) \\
 & & & \dots
 \end{aligned}$$

Eliminating the voltages E_n gives

$$\begin{aligned}
 L(\dot{I}_1) + L'x(\dot{I}_1+\dot{I}_2+\dot{I}_3+\dot{I}_4) &= R(-I_1) - (L'x + R'x)(I_1+I_2+I_3+I_4) - MV \\
 L(-\dot{I}_1+\dot{I}_2) + L'\ell(\dot{I}_2+\dot{I}_3+\dot{I}_4) &= R(I_1-I_2) - R'\ell(I_2+I_3+I_4) \\
 L(-\dot{I}_2+\dot{I}_3) + L'\ell(\dot{I}_3+\dot{I}_4) &= R(I_2-I_3) - R'\ell(I_3+I_4) \\
 L(-\dot{I}_3+\dot{I}_4) + L'\ell(\dot{I}_4) &= R(I_3-I_4) - R'\ell(I_4) \\
 & \dots
 \end{aligned}$$

giving

$$\begin{bmatrix} (L+L'x) & L'x & L'x & L'x & \dots \\ -L & (L+L'\ell) & L'\ell & L'\ell & \dots \\ 0 & -L & (L+L'\ell) & L'\ell & \dots \\ 0 & 0 & -L & (L+L'\ell) & \dots \\ \dots & \dots & \dots & \dots & \dots \end{bmatrix} \begin{bmatrix} \dot{I}_1 \\ \dot{I}_2 \\ \dot{I}_3 \\ \dot{I}_4 \\ \dots \end{bmatrix} = \begin{bmatrix} R(-I_1) - (L'x + R'x)(I_1+I_2+I_3+I_4) - MV \\ R(I_1-I_2) - R'\ell(I_2+I_3+I_4) \\ R(I_2-I_3) - R'\ell(I_3+I_4) \\ R(I_3-I_4) - R'\ell(I_4) \\ \dots \end{bmatrix}$$

Defining the matrix equation as

$$[A][B] = [C]$$

then values of the rates of change of the currents, \dot{I}_n , are obtained from the equation $[B] = [A^{-1}][C]$.

(1)

which is given by $\dot{x} = L'(I_1)^2/(2m)$.

At each step the value of x is tested and when it gets greater than L , it is replaced by $(x-L)$ and at the same time all the currents are shifted one gun stage, i.e., I_2 is replaced by I_1 , I_3 by I_2 , I_4 by I_3 , etc. and I_1 is set equal to the assumed initial value of current from the next energy store. The appropriate dimensions of the matrices are also in-

creased by one because there is now one more power circuit in use.

At each step also, the magnitude of the current in the rearmost energy store is checked and when it goes negative, that store is "removed" by reducing the dimensions of the matrices by one.

The "Scientific Railgun"

As an example of the method, a simulation has been made of a railgun for accelerating a three gram projectile to 20 km/s. The first point to note about the design of the system is that constant average acceleration of the projectile is both desirable and possible. Since energy equals force times distance, this means that the energy stores should be uniformly distributed. Aiming at an average current of around 375 kA (I) and assuming a gun inductance (L') of 0.6 $\mu\text{H/m}$ give a force on the projectile of 42 kN ($=0.5 L'I^2$), giving an acceleration to the projectile of 14 m/s^2 . Thus, the length of gun required to reach 20 km/s is 14 m.

The kinetic energy of the projectile at exit is 600 kJ. If the gun were to be 100% efficient, and each store held 10 kJ of energy, then these would have to be spaced 0.23 meters apart. For the simula-

tion spacing of 5 stores per meter was assumed.

The arc armature volt drop (MV) is assumed to be 160 V, the value that was observed in the Canberra railgun. The rail resistance (R') is taken as 0.002 Ω/m , being the resistance of copper rails 1.5 mm thick by 13 mm high. The inductor resistance is taken as 0.001 Ω .

The inductor current, when fully charged, has been taken as 125 kA and with the 10 kJ inductor energy gives a calculated inductance of 1.28 μH .

The resulting simulation is shown in Fig. 2. It has been assumed that the projectile is injected into the gun breech with a velocity of 1,000 m/s. The overall efficiency indicated is 70%, 598 kJ kinetic energy being obtained for the expenditure of 850 kJ (10 kJ from each of 85 energy stores). The stage efficiencies rise down the gun, starting from around 20% in the first few stages and rising to 84% in the last stage.

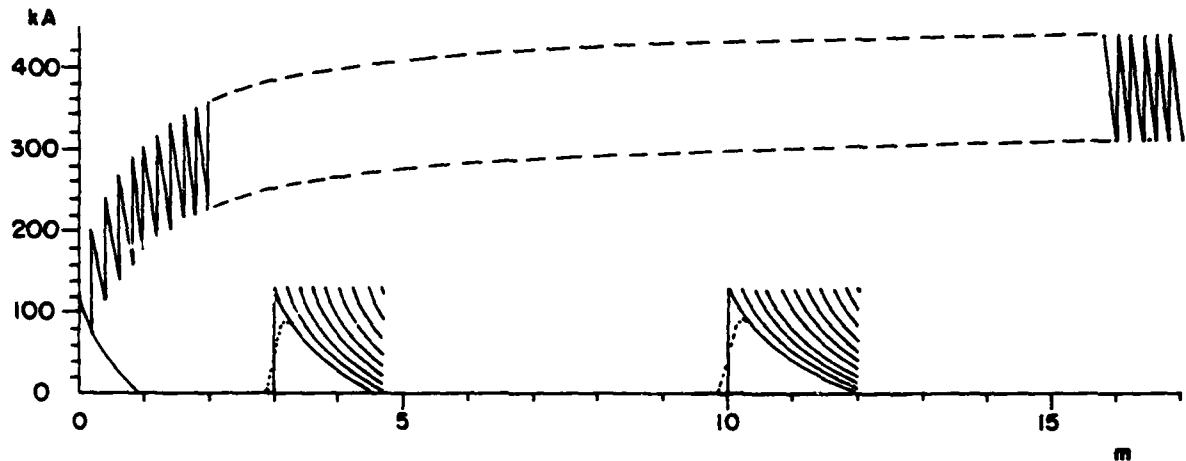


Fig. 2. Simulation of the "scientific railgun" showing current (kA) as a function of projectile travel (m) down the gun. The upper curve shows the total current. The lower curves (only partially drawn) show the currents in individual energy stores. The three gram projectile reaches a velocity of 20 km/s in the 17 m of gun length.

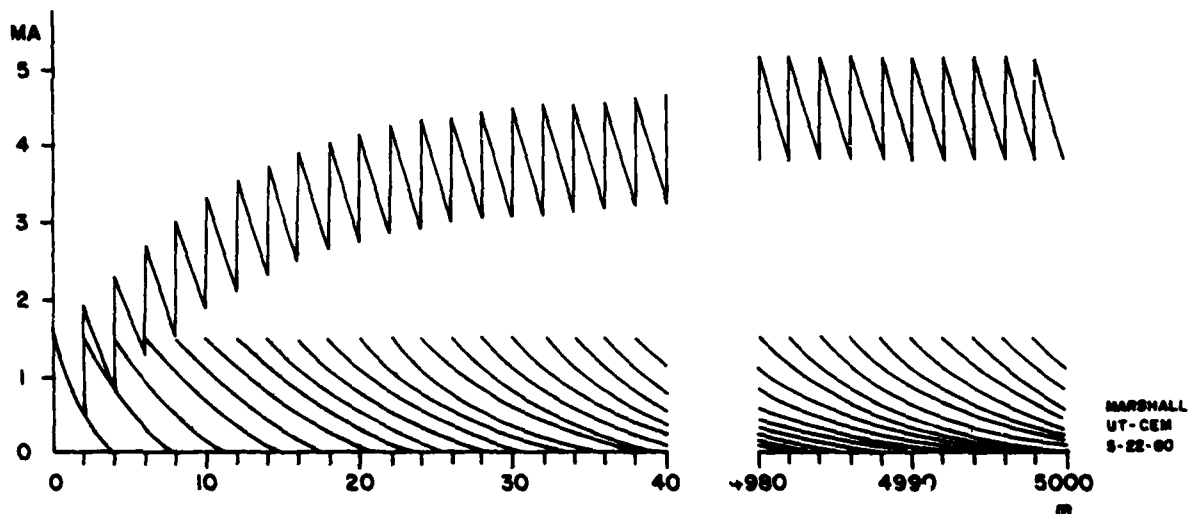


Fig. 3. Simulation of the "space-launch railgun" showing current (MA) as a function of projectile travel (m) down the gun. The curves are discontinuous, the length from 40 m to 4,980 m being omitted. The upper curve is the total current; the lower curves show the currents in individual energy stores. The one tonne projectile reaches a velocity of 7,500 m/s in the 5,000 m gun length.

The "Space-Launch Railgun"

A simulation has also been made of the acceleration of a relatively large mass, 1000 kg, to earth orbit velocity of 7,500 m/s. An acceleration of 500 gravities is assumed which gives a required gun length of 5,700 m. The kinetic energy of the projectile at gun exit is 28.1 GJ which means that about 5 MJ of energy must be delivered to the projectile each meter of travel down the gun barrel. It is assumed that 12 MJ inductors are distributed along the gun at a spacing of 2 m. The total average current required to give the assumed acceleration is 4 MA.

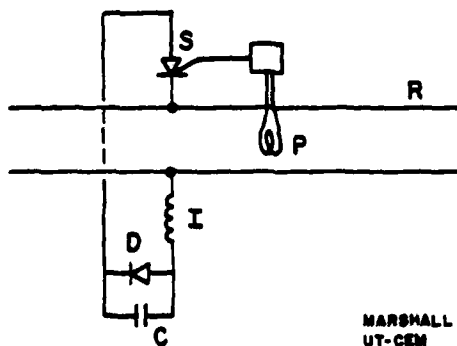
The peak inductor currents are taken as 1.5 MA, requiring an inductance of 10.7 μ H.

In the absence of any better information, the arc armature volt drop is again taken as 160 V. Rails of one meter high by three centimeters thick are assumed giving a gun resistance of 2 $\mu\Omega$ /m. The coil inductance has the same value as about 20 m of gun, the resistance of which is 40 $\mu\Omega$. Thus, a reasonable value to take for inductor resistance is 20 $\mu\Omega$.

The results of the simulation are shown in Fig. 3. The projectile reaches its desired velocity in a gun length of 5000 m, i.e., with the expenditure of 30 GJ, being 2500 energy stores of 12 GJ each. Thus, the overall efficiency is 93.8%. Again, the stage efficiency starts low (~20%) but rises rapidly as speed increases to reach a value of 98% at the exit end of the gun.

Switching

Accelerators of the type described above can only be made to work if the current from each energy store is switched into the gun at exactly the right moment. Synchronism with projectile position is crucial. There are many ways that the arrival of the projectile at any point along the gun can be detected. One obvious way is to interrupt a light beam. There are two other ways in which projectile passage can be used to provide very strong signals. The first is to use the arrival of the high pressure plasma of the armature. A small part of this could be allowed to pass through a vent from the gun base to trigger a switch. Radiation from the arc might be used for the same purpose. The second possibility is to use the magnetic field produced by the driving current to do the triggering. This field rises very fast as the armature passes, and can be used to give a strong, noise immune, signal accurately synchronized with the armature position.⁵ This signal could be used directly to activate a switch as indicated in Fig. 4.



MARSHALL
UT-CGM
6-20-80

Fig. 4. Schematic of an energy store circuit, showing railgun R, inductor I, capacitor C, diode D, switch S, and pick-up loop P.

When the switch (it can be an SCR) is activated, the energy in the capacitor transfers quickly to the inductor. When the transfer is completed, the diode then effectively removes the capacitor from the circuit. The switch S must also behave like a diode to prevent current from flowing in reverse through the inductor after the latter is discharged.

In the case of the space-launch railgun, the currents are sufficiently high that the use of solid state switches may be expensive. A possible low cost solution may be to have the gun's driving field do the switching directly as shown in Fig. 5.

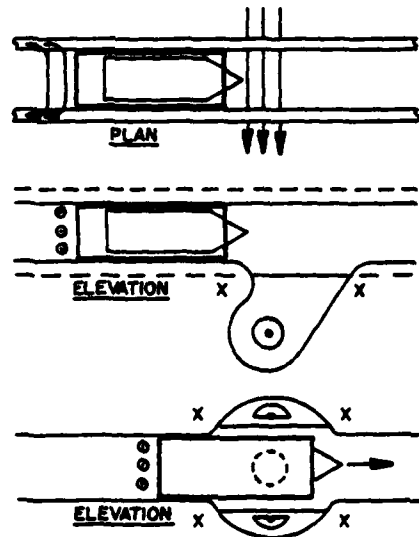


Fig. 5. Direct switching of current into a rail gun using the gun's driving field.

It may be possible to establish an arc, carrying the current from the energy store, between the rails (or electrodes embedded therein) in front of the moving projectile, the arc being stabilized by suitable placement of the current supply leads, xx. As the projectile passes, the arc responds to the driving field and moves in behind the projectile to form part of the armature current. It may be possible to trap the arc as shown in the lower elevation. The projectile would then divide the arc, to have it join the armature behind the projectile after it has passed.¹²

Discussion

The simulations assume that the energy stores consist of precharged inductors which are switched in instantaneously. The method can be expanded to include such effects as the current rise in the inductor which will be roughly as shown by dotted lines in Fig. 2. Note that a parameter not used is the capacitor voltage. In a real system choice of this would be made to provide appropriate rates of rise of inductor currents. Increasing capacitor voltage will probably be desirable with distance down the gun.

Decreasing skin depth in the rails down the gun has not been included, and the assumption of 160 V for the arc drop in the space-launch railgun may not be correct.

No attempt has been made to optimize the two systems studied. If desired, the efficiency of the scientific railgun will improve by using smaller energy stores closer together. The indicated efficiency of the space-launch railgun is surprisingly good. However, the overall efficiency in a real system will be reduced somewhat because the efficiency

of transfer of energy from homopolar generators (which will be required as primary stores) to inductors is lower than the transfer from electrostatic capacitors to inductors. The railgun space-launcher would seem to be a good candidate for firing H. Koim's telegraph-pole atmosphere penetrators. 13

Conclusion

The outlines presented of the two inductively driven railgun systems shown how the simple parallel-rail railgun macroparticle accelerator may be used to impart high velocities to "micro-macro" particles (gram-sized) and to "macro-macro" particles (tonne-sized) with good efficiency.

Acknowledgments

This work was conducted with the support of the Texas Atomic Energy Research Foundation.

References

1. Rashleigh, S.C. & Marshall, R.A., "Electromagnetic acceleration of macroparticles to high velocities," J. Appl. Phys. 49(4) April 1978.
2. Barber, J.P., "The acceleration of Macroparticles and a Hypervelocity Macroparticle Accelerator," Ph.D. Thesis, Australian National University, Canberra 1972.
3. Hawke, R.S., Scudder, J.K. of LLL, and Fowler, C.M., Peterson, D.R. of LASL, The LLL-LASL flux compressor railgun program.
4. Hawke, R.S., Scudder, J.K., "Magnetic Propulsion Railguns: their Design and Capabilities," presented at the Second International Conference on Megagauss Magnetic Field Generation and Related Topics, Washington, D.C. (1979).
5. Marshall, R.A., "Railgun Overview," presented at the DOE Impact Fusion Workshop held at LASL, July 1979.
6. Muller, R.A., et al., "Impact Fusion with a Segmented Rail Gun," *ibid.*
7. Hawke, R.S., "Railgun Accelerators for Launching 0.1-g Payloads at Velocities Greater than 150 km/s," *ibid.*
8. Tidmen, Derek A. and Goldstein, Shyke A., "Mass Accelerator for Producing Hypervelocity Projectiles using a Series of Imploding Annular Discharges," *ibid.*
9. Winterberg, F., Plasma Physics 8, 541 (1966).
10. Koim, H.H., "Basic Coaxial Mass Driver Reference Design," Proc. Princeton Conference on Space Manufacturing, May 1977.
11. Marshall, R.A., "A Method of Numerically Simulating the Performance of Railguns Powered by Distributed Energy Stores," presented at the DARPA/ARRADCOM Review, Washington, D.C., 9 April 1980.
12. Weldon, W.F. & Marshall, R.A., "Work in Progress at U.T., C.E.M." presented at the DARPA/ARRADCOM Review, Washington, D.C., 19 Sept. 1979.
13. Koim, H. et al., "Electromagnetic Propulsion Alternatives," presented at the Princeton Symposium on Space Manufacturing, 1979.

LIST OF ATTENDEES

1980 FOURTEENTH PULSE POWER MODULATOR SYMPOSIUM

Steven T. Adams	Norden Systems, Inc.
Harry R. Allen	Los Alamos Scientific Laboratory
E. Altshul	Aydin Energy Division
Hermann M. Amaya	Sperry Microwave Electronics
Phillip A. Arnold	University of South Carolina
Don G. Ball	Lawrence Livermore Laboratory
Edwin D. Ball	Naval Surface Weapons Center
William R. Barkley	EIMAC Division of Varian
David M. Barrett	Physics International Company
Jon E. Barth	Barth Electronics, Inc.
William C. Beggs	
Thomas L. Berger	Naval Surface Weapons Center
Bernie Bernstein	Physics International Company
Jerry Ray Bettis	U. S. Air Force
K. James Bickford	Los Alamos Scientific Laboratory
Stanley R. Bishop	
John G. Blackburn	Pan American World Airways
John Bohan	Aydin Energy Division
Laird Bradley	Lawrence Livermore Laboratory
Leonard Braverman	GTE Sylvania
David F. Brower	
Jacques Buchet	Commissariat a l'Energie Atomique
Tom R. Burkes	Texas Tech University
Robert R. Butcher	Los Alamos Scientific Laboratory
J. Clark Butterworth	
Malcolm T. Buttram	Sandia National Laboratories
William Caldwell	Lawrence Livermore Laboratory
J. E. Calpin	Westinghouse
Nguyen-N-Can	Thomson-CSF
Bruce Carder	Lawrence Livermore Laboratory
Port Caristi	EG & G, Inc.

LIST OF ATTENDEES

Robert Casolare	
John E. Celto	Naval Ocean Systems Center
Matija Cenanovic	Ontario Hydro Research Division
Phil Champney	Physics International Company
William O. Chapin	Lawrence Livermore Laboratory
Y. G. Chen	Physics International Company
A. Chesnel	Thomson-CSF
Al Chesterman	Lawrence Livermore Laboratory
S. Richard Childerhose	Veradyne Corporation
Raymond S. Clark	Sandia National Laboratories
Dominick Conte	R & D Associates
Edward Cook	Lawrence Livermore Laboratory
Robert A. Cooper	Maxwell Laboratories, Inc.
Carl R. Crager	Litton Industries
John E. Creedon	U. S. Army ERADCOM
J. Terry Crow	Sandia National Laboratories
Dave Cummings	Physics International Company
Jack L. Cutting	Lawrence Livermore Laboratory
Joseph H. Dableh	Ontario Hydro Research Division
C. L. Dailey	TRW
Harvey W. Dain	Hughes Aircraft Company
Terence E. DeHart	Math Sciences N. W.
Robert DeWitt	Naval Surface Weapons Center
Marco S. Di Capua	Physics International Company
John A. Dinkel	Fermilab
Rudy Ecken	
Carl J. Eichenauer	General Electric Company
Jack N. Elkins	United Technologies Research Center
Larry Epifanio	Sperry Microwave Elect.
George F. Erickson	Los Alamos Scientific Laboratory
David B. Fenneman	Naval Surface Weapons Center
Pete Fenoglio	General Electric Company
Karl Ferdi	MIT-Plasma Fusion Center

LIST OF ATTENDEES

Maurice Fialkoff	Garrett-Airesearch
Ward A. Fitch	Precipco, Inc.
William A. Fitzsimmons	National Research Group, Inc.
Richard Ford	Naval Research Laboratory
William L. Fox	Maxwell Laboratories, Inc.
George Frazier	Physics International Company
Herbert Friedman	Avco Research Laboratories
Steven Friedman	EG & G, Inc.
John D. Galbraith	Los Alamos Scientific Laboratory
Robert A. Gardenghi	Westinghouse Electric Corporation
Thomas B. Geary	Westinghouse
Woo F. Gee	Lawrence Livermore Laboratory
Victor H. Gehman, Jr.	Naval Surface Weapons Center
Leonard Genova	Standard Linear Accelerator Center
A. S. Gilmour, Jr.	SUNY at Buffalo
Harry Goldie	Westinghouse Defense Center
Ferry A. Goldlust	Dielectric Sciences
Albert A. Goodman	Lawrence Livermore Laboratory
A. E. Gordon	ITT Corporation
Bob Gray	Rome Air Development Center
Michael Greenspan	McDonnell Douglas Corporation
Ronald Gripshover	Naval Surface Weapons Center
Glen Grotz	GSB Electronics
Arthur H. Guenther	Air Force Weapons Laboratory
Marion Hagler	Texas Tech University
J. R. Hall	Rocketdyne Division of Rockwell
Ward Halverson	Spire Corporation
Ken Hanks	Los Alamos Technical Associates
Jack N. Hardwick	Los Alamos Scientific Laboratory
N. W. Harris	Ion Physics Company
John L. Harrison	Maxwell Laboratories, Inc.
R. E. Hartline	Systems Science & Software
Wm Harvey	Hughes Research Laboratories

LIST OF ATTENDEES

Alain Handuocour.....	Commissariat a l'Energie Atomique
R. S. Hawke.....	Lawrence Livermore Laboratory
Monson H. Hayes, Jr.	Maxwell Laboratories, Inc.
Philip C. Herren, Jr.....	AF Wright Aeronautical Laboratory
Stuart Hesselton.....	EEV, Inc.
Ross E. Hester.....	Lawrence Livermore Laboratory
Steve Hibbs.....	Lawrence Livermore Laboratory
Ronald W. Holloway.....	Lawrence Livermore Laboratory
Edward H. Hooper.....	Westinghouse Electric Corporation
Robert F. Hope, III.....	SUNYAB
Jim Ivers.....	Cornell University
David L. Johnson.....	Sandia National Laboratories
Richard T. Jones.....	Naval Surface Weapons Center
J. Kawecki.....	Raytheon Company
Ronald Kihara.....	Lawrence Livermore Laboratory
Dean O. Kippenhan.....	Lawrence Livermore Laboratory
Hugh C. Kirbie.....	Texas Tech University
Stanley L. Kokoszka.....	Raytheon Company
Alan Kolb.....	Maxwell Laboratories, Inc.
Marc Kolpin.....	Physics International Company
George Krauss.....	Los Alamos Scientific Laboratory
Peter Krickhahn.....	Maxwell Laboratories, Inc.
M. Kristiansen.....	Texas Tech University
Robert W. Kuenning.....	Lawrence Livermore Laboratory
Matt Kuhn.....	Bell Northern Research
E. Kunhardt.....	Texas Tech University
David S. Ladd.....	
Ron F. Lankshear.....	New England Nuclear Corporation
Charles Larson.....	Lawrence Livermore Laboratory
Eugene J. Lauer.....	Lawrence Livermore Laboratory
Benjamin Leon.....	Westinghouse Electric Corporation
Jeff Levatter.....	DECC
Samuel Levinson.....	Norden Systems, Inc.

LIST OF ATTENDEES

Roger G. Little	Spire Corporation
Weth G. Longenecker	Westinghouse-SCD
Lawrence H. Luesen	Naval Surface Weapons Center
James S. Lunsford	Los Alamos Scientific Laboratory
Richard A. Marshall	University of Texas at Austin
Thomas H. Martin	Sandia National Laboratories
M. L. Matnick	Axel Electronics, Inc.
Ralph E. McCotter	Lawrence Livermore Laboratory
Dillon H. McDaniel	Sandia National Laboratories
G. Glen McDuff	Los Alamos Scientific Laboratory
H. Bruce McFarlane	Lawrence Livermore Laboratory
Sterling G. McNeas	EIMAC Division of Varian
Hugh Menown	English Electric Valve Co., Ltd.
Bernard T. Merritt	Lawrence Livermore Laboratory
Spencer Merz	EG & G, Inc.
R. Mgrdechian	Axel Electronics, Inc.
Kenneth Mikkelson	Lawrence Livermore Laboratory
Wise A. Miles	Naval Surface Weapons Center
A. R. Miller	Maxwell Laboratories, Inc.
Richard N. Miller	University of Central Florida
Richard D. Milton	Army Missile Command
Al Mims	SPACE Microwave Laboratory, Inc.
John J. Moriarty	Raytheon Company
George Mullany	Mathematical Sciences N. W.
John J. Mulrey	EG & G, Inc.
R. J. Nawrocky	Brookhaven National Laboratory
Chris Neale	English Electric Valve Co., Ltd.
Eugene L. Neau	Sandia National Laboratories
L. K. Neher	Los Alamos Scientific Laboratory
William H. Nevins	The Machlett Laboratories, Inc.
Mark Newton	Lawrence Livermore Laboratory
Nigel S. Nicholls	Royal Signal & Radar Establishment
Wiam North	GTE Sylvania

LIST OF ATTENDEES

William C. Nunnally.....	Los Alamos Scientific Laboratory
R. F. Nylander	Exxon Nuclear Company
Minoru Obara.....	Keio University
Joseph C. O'Connell.....	U. S. Army ERADCOM
Henry B. Odom, III	Naval Surface Weapons Center
Joseph P. O'Donnell.....	Axel Electronics, Inc.
Peter Oettinger.....	Thermo Electron Corporation
Jeffrey A. Oicles.....	Lawrence Livermore Laboratory
Dennis J. Okula	Varian Associates
John E. Olbrych	Avco Everett Research Laboratory
Carl W. Olson.....	Stanford Linear Accelerator Center
Edward L. Orham.....	Lawrence Livermore Laboratory
Donald Osias	Physics International Company
John L. Pack	Westinghouse R & D Center
Robert D. Parker	Hughes Aircraft Company
Peter Pearce.....	C. E. R. N.
Todd A. Pelley	Lawrence Livermore Laboratory
Thomas M. Petach.....	Lawrence Livermore Laboratory
Edward M. Piechowiak	Westinghouse Electric Corporation
Wayne Pollard	Lawrence Livermore Laboratory
Kenneth R. Prestwich.....	Sandia National Laboratories
D. L. Pruitt.....	RCA Corporation
Juan J. Ramirez	Sandia National Laboratories
Al Ramrus	Maxwell Laboratories, Inc.
W. Ross Rapoport	Lawrence Livermore Laboratory
Louis Reginato.....	Lawrence Livermore Laboratory
Aaron Reich	Soreq Nuclear Research Center
Douglas B. Remsen, Jr.	General Atomic Company
Barry Resler	Universal Voltronics Corporation
Ben G. Rice.....	ITT Corporation
Volker Rödel.....	C. E. R. N.
Doyle Rogers, Jr.	Lawrence Livermore Laboratory
Gerald J. Rohwein	Sandia National Laboratories

LIST OF ATTENDEES

Gary Rondeau.....	Cornell University
Frank Rose.....	Naval Surface Weapons Center
Randall I. Ross.....	
Robert Rowe.....	Stanford Linear Accelerator Center
Rodney R. Rubert.....	Lawrence Livermore Laboratory
Kenneth R. Rust.....	Los Alamos Scientific Laboratory
W. J. Sarjeant.....	Los Alamos Scientific Laboratory
John A. Sathowski.....	Office of Naval Research
Raymond D. Scarpetti.....	Lawrence Livermore Laboratory
Leland Schlitt.....	Lawrence Livermore Laboratory
Sol Schneider.....	Consultant
David B. Seidel.....	Sandia National Laboratories
John Shannon.....	Maxwell Laboratories, Inc.
Ronald R. Shenhan.....	Lawrence Livermore Laboratory
Roger Shower.....	Hi Voltage Components, Inc.
Merrald B. Shrader.....	Elmac Division of Varian
David Shurtz.....	NV & EOL
Richard K. Simcox.....	Raytheon Company
Kenneth M. Smalley.....	Raytheon Company
Carl H. Smith.....	Allied Chemical
Ian D. Smith.....	Ian Smith, Inc.
Roger Soelling.....	English Electric Valve Co., Ltd.
Richard J. Sojka.....	GTEsylvania
Thomas E. Springer.....	Los Alamos Scientific Laboratory
Jerre D. Stabley.....	RCA Corporation
Brian Steer.....	Varian Canada, Inc.
Jeremy M. Stein.....	EG & G/WASC, Inc.
Howard Stern.....	Aydin Energy Division
Alex G. Stewart.....	Harry Diamond Laboratories
Joe V. Storer.....	Hughes Aircraft Company
Dale E. Suddeth.....	Argonne National Laboratories
Jan Sundström.....	L. M. Ericsson
Swan.....	E. M. I. Varian, Ltd.

LIST OF ATTENDEES

Rod S. Taylor	N. R. C. of Canada
Jim Thompson	University of South Carolina
Keith Tolk	Sandia National Laboratories
William T. Tomlin	Stanford Linear Accelerator Center
Alvin W. Trivelpiece	Science Applications, Inc.
Donald R. Trout	RCA Corporation
Peter J. Turchi	R & D Associates
David Turnquist	EG & G, Inc.
Vance I. Valencia	Exxon Nuclear Company
Fred Van Haaften	Los Alamos Scientific Laboratory
'S' James Veraldi	Veradyne Corporation
Ihor Vitkovitsky	Naval Research Laboratory
George E. Vogtlin	Lawrence Livermore Laboratory
George Wakalopoulos	Hughes Aircraft Company
Curt D. Walker	Boeing Aerospace Co., Inc.
Fenneth D. Ware	Los Alamos Scientific Laboratory
F. Thomas Warren, Jr.	University of South Carolina
Roger Warren	Los Alamos Scientific Laboratory
Richard J. Wasneski	Naval Air Systems Command
Maurice Weiner	U. S. Army ERADCOM
William Weiss	Lawrence Livermore Laboratory
S. E. Wheatley	Rocketdyne Division of Rockwell
John White	Lawrence Livermore Laboratory
Kenneth Whitham	Lawrence Livermore Laboratory
Paul Wildt	University of Texas at Austin
Roy R. Williams	Sandia National Laboratories
Andy R. Wilson	Los Alamos Scientific Laboratory
Joseph R. Woodworth	Sandia National Laboratories
Boris Yen	Physics International Company
Charles T. Zavalas	Cober Electronics, Inc.
Robert Zeret	Reynolds Industry, Inc.
ey Zwalg	Axel Electronics, Inc.

AUTHOR INDEX

NAME—SESSION NO.—PAPER	PAGE	NAME—SESSION NO.—PAPER	PAGE
Adams, S.T.—VI-3	169	Krausse, G.J.—VI-1	161
Ahn, B.H.—IV-4, V-6	104, 144	Kruger, B.—IV-6	115
Alcock, A.J.—I-9	32	Kuenning, R.W.—XI-4	310
Aslin, H.—IX-3	241	Kuhn, H.—X-1	264
Barr, G.W.—XI-2	300	Ladd, D.S.—VI-2	164
Barrett, D.A.—I-7	25	Lauer, E.J.—I-2	5
Beattie, W.—VI-4	179	Leopold, K.E.—I-9	32
Berger, T.L.—III-2	73	Levinson, S.—IV-5	110
Bettis, J.R.—I-8	28	Lindberg, D.D.—I-5	17
Bird, W.L.—IX-7	259	Little, R.G.—V-4	134
Bradley, L.P.—I-10	38	Lynch, T.—II-1	46
Braucht, J.R.—I-10	38	Mace, P.N.—V-1	122
Burkes, T.R.—I-7, V-2	25, 125	Marshall, R.A.—XI-6	318
Burton, J.K.—I-8	28	Martin, T.H.—XI-2, XI-3	300, 305
Butterworth, J.C.—VI-2	164	McDaniel, D.H.—VIII-4	227
Buttram, M.T.—VII-2	195	McDuff, G.—V-1	122
Carder, B.M.—IX-7	259	McFarlane, H.B.—I-3	9
Conte, D.—III-1	68	McNees, S.G.—II-3, II-4	56, 65
Cook, E.G.—I-2	5	Menown, H.—II-2, IX-3	54, 245
Crow, J.T.—VIII-2	219	Merritt, B.T.—IX-6	259
Cummings, D.B.—VI-6	187	Merz, S.S.—II-1	46
Dalton, C.G.—VI-1	161	Metzmacher, K.D.—X-3	280
Donaldson, T.P.—II-2	54	Mgrdechian, R.—VI-3	169
Ewanizky, T.F.—VII-1	191	Miles, L.A.—III-1	68
Ewell, G.W.—VI-2	164	Miller, J.E.—IV-4, V-6	104, 144
Felber, F.S.—VIII-1	214	Miller, R.N.—III-4, IX-4	80, 247
Fellers, R.G.—III-5	85	Moriarty, J.J.—VI-5	183
Fenneman, D.B.—V-7, V-8	150, 154	Naff, J.T.—I-6	21
Fiander, D.C.—X-3	280	Neale, C.V.—II-2	54
Fitzsimmons, N.A.—V-3	130	Neau, E.L.—I-11	42
Fujioka, T.—VII-3	201	Newton, B.P.—II-2, IX-3	54, 245
Gagnon, W.L.—IX-6	259	Nicholls, N.S.—IV-2, IX-1	97, 230
Gehman, V.H.—V-8	154	Nolting, E.E.—III-1	68
Gilmour, A.S., Jr.—III-4, IX-5, IX-6	80, 247, 255	North, W.—IV-6	115
Goplen, B.C.—VIII-3	222	Nunnally, W.C.—X-5	292
Gray, B.R.—II-3	56	Obara, M.—VII-3	201
Grier, D.—X-3	280	Olson, T.—VII-4	209
Gripshover, R.J.—I-5, V-7	17, 150	Orhain, E.L.—I-10	38
Guenther, A.H.—I-8	28	Overett, T.H.—IX-2	237
Halverson, W.—V-4	134	Parker, R.D.—V-5	137
Hanna, G.—IV-6	115	Parker, R.K.—I-8	28
Harrison, J.—VII-4	209	Parkison, C.D.—I-4	12
Hartline, R.—IX-3	241	Pearce, P.—X-3	280
Harvey, R.J.—III-3	77	Peterson, G.D.—VIII-2	219
Herndon, M.—I-8	28	Petr, R.A.—I-7	25
Hester, R.E.—XI-1	297	Piechowiak, E.M.—IV-1	92
Hooper, E.H.—IV-3	98	Ramirez, J.J.—XI-5	314
Hope, R.F., III—III-4, IX-4	80, 247	Reginato, L.L.—I-2, XI-1	5, 297
Horowitz, D.J.—IV-4	104	Reinhardt, N.—II-1	46
Hudgings, D.W.—X-5	292	Remsen, D.B., Jr.—IX-2	237
Ishibashi, Y.—VII-3	201	Rice, J.W.—I-5	17
Johnson, D.L.—XI-2, XI-3	300, 305	Rödel, V.—X-2	272
Kang M.—V-3	130	Rodgers, D.—I-2	5
Kent, H.—VII-4	209	Rodgers, J.	115
Kettle, L.J.—II-2	54	Rohwein, G.J.—I-1	1
Kihara, R.—I-3	9	Rust, K.—V-1	122
Kinkad, A.K.—I-8	28	Santamaria, G.—VII-4	209
Kobiela, E.J.—I-8	28	Sarjeant, W.J.—V-1, V-2, VI-1, X-5	122, 125, 161, 292
		Scarpetti, R.D.—I-4	12
		Schmidt, J.A.—I-2	5
		Schroder, G.H.—X-1, X-2	264, 272

AUTHOR INDEX

NAME—SESSION NO.—PAPER	PAGE	NAME—SESSION NO.—PAPER	PAGE
Seidel, D.B.—VIII-3	222	VanDevender, J.P.—VIII-1, XI-2, XI-3	222, 300, 305
Shannon, J.P.—VIII-1	214	Vitkovitsky, I.M.—III-1	68
Sheldrake, R.—II-2, IX-3	54, 245	Vogtlin, G.—XI-4	310
Shurtz, R.R.—IV-4, V-6	104, 144	Volk, G.J.—X-4	289
Simcox, G.K.—VI-5	183	Vossenber, E.B.—X-2	272
Snelling, R.L.—IX-3	245		
Sojka, R.J.—I-6	21	Warren, F.T., Jr.—III-5	85
Stinnett, R.W.—VIII-4	227	Weiner, M.—VI-4	179
Stowers, I.F.—I-10	38	Weldon, W.F.—IX-7, XI-6	259, 318
Sudarshan, T.S.—III-5	85	White, R.—VII-4	209
Suddeth, D.E.—X-4	289	White, R.A.—XI-2	300
Sunderland, R.—IX-1	230	Williams, R.R.—VIII-4	227
Suzuki, S.—VII-3	201		
		Yen, B.—VI-6	187
Taylor, R.S.—I-9	32		
Thompson, J.E.—III-5	85	Zeehandelaar, E.P.—I-6	21
Trussell, C.W.—IV-4, V-6	104, 144	Zowarka, R.C.—IX-6	259
Turnquist, D.—II-1	46		

FILME
0-8